From the Department of Pediatric Oncology, Hematology and Clinical Immunology,
Medical Faculty, Heinrich Heine University Düsseldorf

(Director: Univ.-Prof. Dr. med. Arndt Borkhardt)

New Therapeutic Approaches to Address Drug Resistance in Pediatric Acute Leukemia

Habilitation thesis

for the conferral of the Venia legendi for the subject of Molecular Medicine of the Faculty of Medicine of the Heinrich-Heine-University Dusseldorf

presented by

Dr. rer. nat. Sanil Bhatia

Düsseldorf

2025

1. Abbreviations

ABL1	ABL proto-oncogene 1
ALL	Acute lymphoblastic leukemia
ALDH4A1	Aldehyde dehydrogenase 4 family member A1
AML	Acute myeloid leukemia
AX	Aminoxyrone
BCL-2	B-cell lymphoma 2
BCR	Breakpoint cluster region
BCP-ALL	B-cell precursor acute lymphoblastic leukemia
CA1	Coumermycin A1
CDK	Cyclin-dependent kinase
CLL	Chronic lymphocytic leukemia
CML	Chronic myeloid leukemia
dDSS	Differential drug sensitivity score
FDA	Food and drug administration
FLT3::ITD	FMS-like tyrosine kinase 3 :: internal tandem duplication
HDAC	Histone deacteylase
HSF-1	Heat shock factor-1
HSP	Heat shock protein
HSP90i	HSP90 inhibitor
HSR	Heat shock response
HTDS	High throughput drug screening
JAK	Janus kinase

KD	Knockdown
KMT2A	Histone-lysine N-methyltransferase 2A
KO	Knockout
LSCs	Leukemia stem cells
Mcl-1	Myeloid cell leukemia-1
MD	Middle domain
MS	Mass spectrometry
NF-κB	Nuclear factor kappa-light-chain-enhancer of activated B cells
NSG	NOD scid gamma
NTD	N-terminal domain
PBMC	Peripheral blood mononuclear cell
PDX	Patient-derived xenograft
Ph+	Philadelphia chrmosome positive
PROTACs	Proteolysis targeting chimeras
PTPRC	Protein tyrosine phosphatase, receptor type, C
PUHr	PU-H71 resistant
RNAPII	RNA-Polymerase II
SCID	Severe combined immune deficiency
STAT	Signal transducer and activator of transcription
TKI	Tyrosine kinase inhibitor
TM	Tanespimycin
PI3K	Phosphoinositide 3-kinases
UPR	Unfolded protein response

2. Introduction

Pediatric acute leukemia is a rapidly progressing blood cancer that originates in the bone marrow, where immature blood cells, known as blasts, multiply uncontrollably. It is the most common cancer in children, with acute lymphoblastic leukemia (ALL) being the most frequent subtype, followed by acute myeloid leukemia (AML). Despite significant advances in treatment, pediatric acute leukemia remains one of the leading cause of cancer-related mortality in children.[2-4] Furthermore, the toxicity and quality of life burden following polychemotherapy protocols are significant, even for pediatric leukemia patients classified as "low risk." The treatment-related mortality for first-line therapy ranges from 1-10%, depending on the patient's age and risk group. Additionally, approximately 20% of patients experience serious adverse events that substantially influence their quality of life and place a considerable burden of care on their families.[5-7] Therefore, it is still crucial to find new therapeutic approaches for patients, especially displaying high-risk features, where typically harsher treatments are required.[8] Consequently, the goal of future therapies should be to achieve a sustained molecular response, de-escalation of chemotherapy backbone and reducing the need for hematopoietic stem cell transplant.

Despite advancements in treatment, the occurrence of relapse continues to pose a significant challenge to achieving curative outcomes for pediatric leukemia patients, as existing therapeutic modalities prove insufficient in effectively preventing or overcoming resistance.[3,4] Drug resistance refers to the reduced effectiveness of therapeutic agents over time, leading to diminished treatment outcomes. This phenomenon poses a formidable obstacle to the success of anticancer therapies, as malignant cells acquire mechanisms to evade the cytotoxic effects of drugs. Mechanisms of drug resistance involve genetic alterations, epigenetic plasticity, altered drug metabolism, enhanced DNA repair mechanisms and the presence of cancer stem cells, among others (**Figure 1)**.[1] The acquisition of drug resistance in acute leukemia underscores the dynamic and adaptive nature of cancer cells, necessitating continuous research efforts to elucidate the intricate molecular mechanisms underlying this phenomenon. Therefore, understanding the molecular

basis of drug resistance is crucial for developing new therapeutic strategies to overcome these obstacles and improve outcomes for acute leukemia patients. Potential interventions may include developing novel anti-cancer drugs and identifying effective combination therapies to address multiple resistance mechanisms.

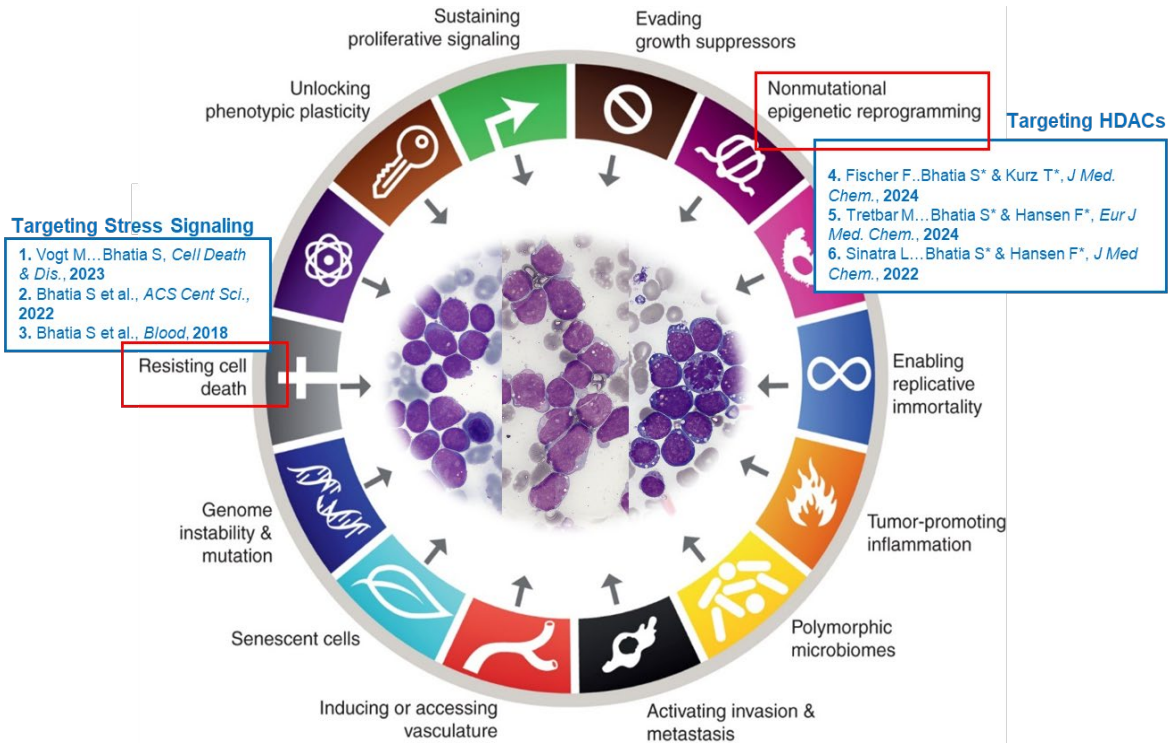

***Figure 1**: Schematic overview of the overarching topics addressed in this habilitation thesis, focusing on (i) stress signaling pathways involved in resisting cell death, and (ii) targeting nonmutational epigenetic reprogramming by inhibiting histone deacetylases (HDACs). Publications are numbered 1-6, illustrating specific contributions within these domains. The schematic is adapted from Douglas Hanahan's review, Hallmarks of Cancer: New Dimensions,[1] capturing critical pathways and therapeutic interventions. The adaptation was created by S. Bhatia.*

The overarching topics of this thesis, illustrated in **Figure 1**, focus on (i) targeting stress-signaling related molecular chaperones, especially heat shock proteins (HSPs) involved in resisting cell death (summarized in **Publication 1 - 3**) and (ii) targeting epigenetic modifiers, specifically histone deacetylase (HDAC) enzymes and finding their combinatorial partners (summarized in **Publication 4 - 6**) for synergistic targeting of therapy-resistant leukemia cells. Furthermore, the drug repurposing approach was applied on the initial or relapse pediatric leukemia samples using ex vivo high throughput drug screening (HTDS) platform to find new therapeutic vulnerabilities. The drug repurposing approach is not part of the six publications comprising the cumulative thesis.

I. Targeting stress signaling related molecular chaperones

Cells encounter diverse external stressors and stimuli, including radiation, heat, hypoxia, and infections.[9,10] In such circumstances, it is crucial for cellular processes to remain functional. Under these circumstances, heat shock proteins (HSPs) carry out this role, which act as molecular chaperones and assist in protein refolding and stability. These chaperone proteins help malignant cells cope with cellular stress, prevent apoptosis, and maintain the stability of oncoproteins crucial for cancer cell survival.[11] Tumor cells, due to their constant need to reprogram metabolic pathways, exhibit characteristics of highly stressed cells and thus depend on elevated HSP expression for survival. This heightened reliance on HSPs contributes to their increased resistance to cell death mechanisms, whether of natural origin or induced by therapeutic interventions.

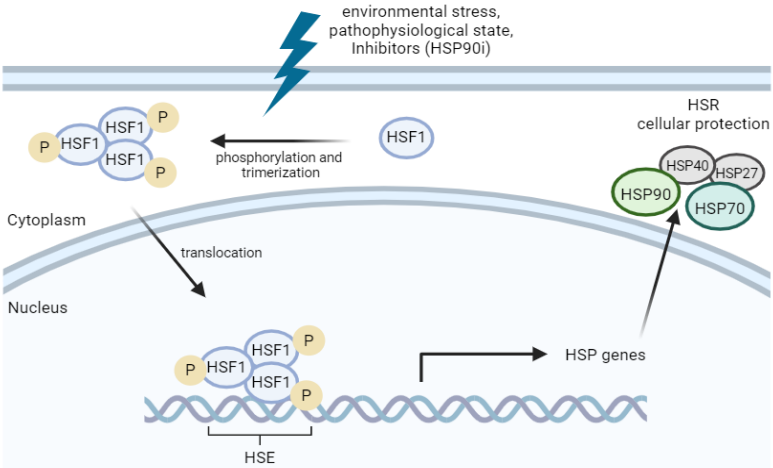

Figure 2: *Schematic representation of the initiation of the heat shock response including activation of heat shock proteins (HSP90, HSP70, HSP40, and HSP27) due to cellular stressors. The illustration is created using Biorender by S.Bhatia.*

HSPs play a significant role in cancer progression, including in leukemia.[12] By protecting cancer cells from various stressors, including those induced by therapeutic interventions, HSPs contribute to the development of drug resistance in leukemia. This makes HSPs potential targets for novel therapeutic approaches in leukemia treatment, with ongoing research exploring ways to inhibit or modulate HSP function to enhance the efficacy of existing therapies and overcome treatment resistance. In leukemia, HSPs are often overexpressed and contribute to the survival and proliferation of malignant cells.[11,12] HSPs are differentiated according to their molecular weight, such as HSP90, HSP70, HSP40 or HSP27 (**Figure 2**).

Among these, HSP90 stands out as a ubiquitous molecular chaperone pivotal for protein stabilization and folding.[13] Although HSP90 plays a crucial role in maintaining normal cellular function, excessive expression of this protein has been associated with a range of diseases, including cancer. In cancer cells, HSP90 is frequently overexpressed and protects mutated and overexpressed oncogenes from degradation.[14] Such HSP90 client proteins, including kinases or transcription factors or other mutated oncogenes and translocated proteins (such as BCR::ABL1 kinase, mutant-TP53, STAT3 and c-MYC), are often responsible for proliferation, survival and resistance to apoptosis. Cancer cells are more dependent on HSP90 chaperone activity than normal cells.[12,16,17] Besides, elevated HSP90 expression is reported in solid tumors and several resistant leukemia subtypes such as Philedelphia chromosome-positive (Ph+) CML/BCP-ALL, FLT3::ITD-driven acute myeloid leukemia (AML) and Ph-like BCP-ALL (**Figure 3**).[18-21] Therefore, the significant engagement of HSP90 in multiple oncogenic pathways and its heightened expression in leukemia subgroups with poor prognoses underscores its importance as a therapeutic target.[16]

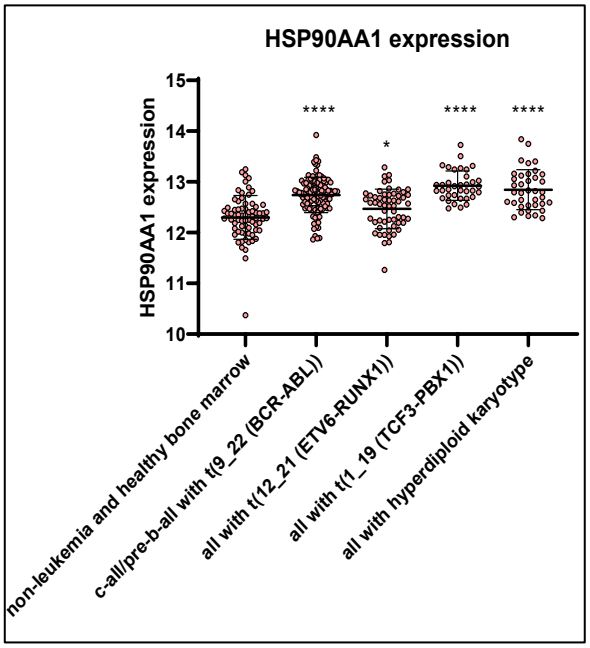

Figure 3: *HSP90AA1 (HSP90α) expression in different leukemia subtypes showing significant increased expression levels compared to non-leukemia and healthy bone marrow. Data were taken from R2 genomics analysis and visualization platform (Data set: Mixed Leukemia - MILE - 2004 - MAS5.0 - u133p2; http://r2.amc.nl/). The illustration is created by S.Bhatia.*

An appealing approach involves destabilizing the BCR::ABL1 protein (both p210 and p190) and its associated downstream pathways by targeting HSP90.[22,23] HSP90i have demonstrated effectiveness against leukemia stem cells (LSCs) resistant to tyrosine kinase inhibitors (TKIs) and leukemia cells carrying the gatekeeper BCR::ABL1^{T315I} mutation (**Figure 4**). Consistently, a recent report demonstrated that

inhibiting HSP90 slows down the progression of *BCR::ABL1*⁺ BCP-ALL when combined with TKI (Imatinib).[24]

HSP90 is a flexible homodimer, and each monomer consists of three major functional domains: N-terminal domain (NTD), middle domain (MD), and C-terminal domain (CTD). In mammalian cells, there are two dominant cytosolic isoforms of HSP90, HSP90α, the stress-inducible isoform (*HSP90AA1* gene; located at 14q32–33) and HSP90β, the constitutively expressed isoform (*HSP90AB1* gene; located at 6p21).[25] These isoforms share a high degree (86%) of amino acid sequence identity. Although HSP90α and HSP90β isoforms exhibit comparable affinities for their client proteins and can often compensate for each other effectively [26], exceptions have been reported that indicate distinctive binding tendencies [27-29]. This is emphasized by their different roles in development and cell survival [30]. For instance, HSP90α-KO mice develop normally or occasionally with few congenital disabilities [31], while the knockout of HSP90β causes embryonic lethality in mice, which cannot be compensated by HSP90α [32]. In previous *ex vivo* studies, cultured HSP90α-KO cells exhibited normal cell morphology and growth rates, while the generation of HSP90β-KO cells was not achieved [26].

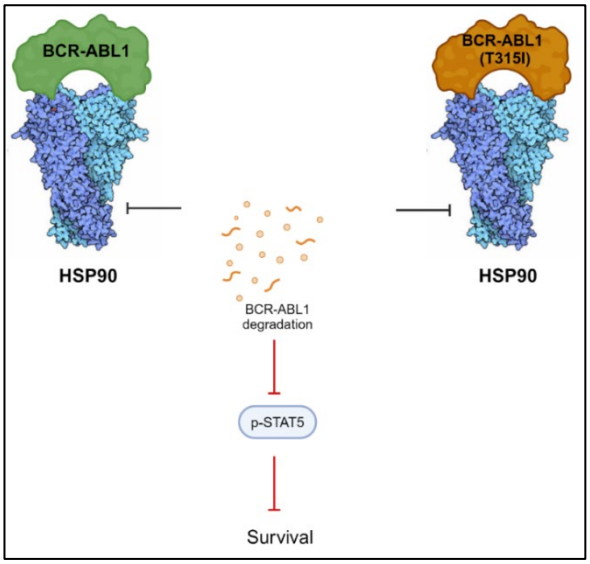

Figure 4: *Destabilisation of wt-BCR::ABL1 and mutated BCR::ABL1^{T315I} upon targeting of HSP90. Figure: Created with BioRender.com. The illustration is created using Biorender by S.Bhatia.*

In the past, several HSP90 inhibitors (HSP90i) have been evaluated in over 60 clinical trials, however associated resistance with their use have thus far precluded clinical approval.[33] This is mainly due to the induction of the pro-survival resistance mechanism, the heat shock response (HSR) and dose-limiting toxicity, such as hepatotoxicity and retinal dysfunction.[34] While the activation of a pro-survival HSR is now recognized as a most prominent contributor to acquired resistance against HSP90i,[35] the precise mechanism driving HSR induction remains poorly elucidated. Although named for its association with heat, HSR is not solely responsive to changes

in temperature but serves as a conserved cellular defense mechanism maintaining proteostasis.[36] HSR can be induced by stressors like glucose depletion, oxidative stress, misfolded protein accumulation and HSP90 inhibition (**Figure 2**).[36] HSP90's activity depends on the binding and hydrolysis of ATP at the NTD and on its dimerization via the CTD. Several HSP90i target the ATP binding site in the NTD of HSP90, causing the release of a transcription factor called heat shock factor-1 (HSF-1).[16] Upon release, HSF-1 is phosphorylated, trimerized and translocated to the nucleus. Activated HSF-1 binds to heat shock responsive DNA elements (HSEs) within the nucleus, thereby inducing the transcription of other heat shock proteins (HSPs), including HSP90α, HSP70, HSP40, and HSP27 (**Figure 2**).[11,37] These HSPs serve as anti-apoptotic chaperones, protecting oncogenic proteins from degradation, thus diminishing the cytotoxic effects of HSP90i.[38] Therefore, despite showing early clinical promise, the widespread utilization of HSP90i in the clinic has been limited. Conversely, modulators that target the CTD of HSP90 have shown not to induce the HSR, making them a promising strategy for selective HSP90 inhibition.[35]

Earlier results have shown that the HSP90 C-terminal dimer opens and closes with fast kinetics.[39] Based on computational predictions and subsequent experimental validation, Ile688 (i), Tyr689 (i + 1), Ile692 (i + 4), and Leu696 (i + 8) were identified (by our collaborator, Prof. Holger Gohlke) as critical hot spot amino acid residues in the C-terminal dimerization interface of HSP90.[40] Starting from the hot spot amino acid residues and the

Publication 1

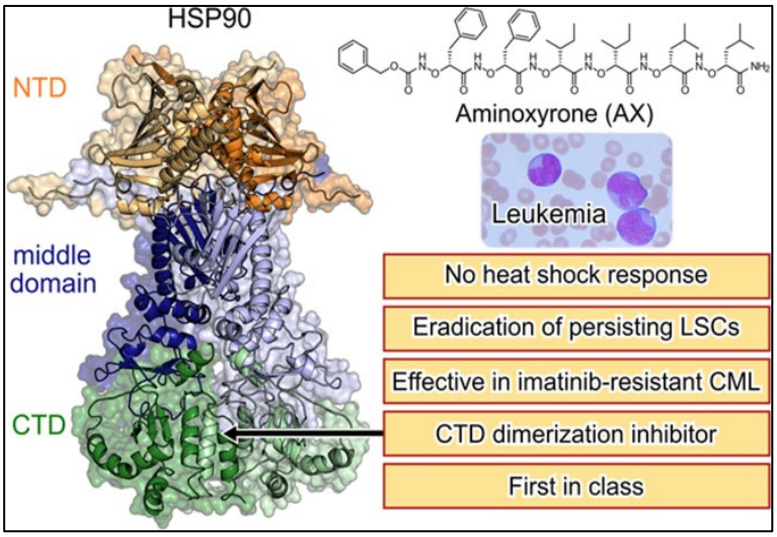

Figure 5: *Graphical abstract showing the development of first-in-class peptidomimetic inhibitor (aminoxyrone or AX) targeting HSP90 C-terminal dimerization that is effective against TKI-resistant CML and leukemic stem cells without inducing heat shock resistance as a resistance mechanism. Use of Illustration is permitted under standard copyright under 'Blood' journal in accordance with 18 USC section 1734.*

peptidic dimerization inhibitors,[41] the aminooxypeptide aminoxyrone (AX) was developed (**Publication 1**).[22] AX is the first-in-class peptidomimetic C-terminal HSP90 dimerization inhibitor (**Figure 5**). Subsequent functional studies have revealed that AX is a promising candidate for inducing apoptosis in both the leukemic stem cell fraction ($CD34^{+}CD38^{-}$) and the leukemic bulk ($CD34^{+}CD38^{+}$) of primary chronic myeloid leukemia (CML) as well as in TKI-resistant *BCR::ABL1*$^{+}$ BCP-ALL cells. AX downregulates the expression of BCR::ABL1 oncoprotein and associated pro-oncogenic cellular responses. Notably, targeting the HSP90 C-terminus with AX does not induce the heat shock response (HSR) as a resistance mechanism in vitro or in vivo. AX may offer a novel therapeutic option for patients with therapy refractory *BCR::ABL1*$^{+}$ leukemia due to its low toxicity profile and lack of HSR induction. However, drawbacks are the complex structure and the difficult chemical synthesis. In addition, the peptidomimetic structure of AX leads to poor aqueous solubility, which is commonly associated with low oral bioavailability.[42]

Structural simplification and optimization of AX towards the first generation small-molecule C-terminal HSP90 inhibitors provided the optimized hit 5b (or LSK82), which was the most active inhibitor within the first series of seven tripyrimidonamides (**Publication 2**).[43] 5b, targets the HSP90 C-terminal domain (CTD) dimerization interface. This inhibitor is based on a tripyrimidonamide scaffold, designed through structure-based molecular

Publication 2

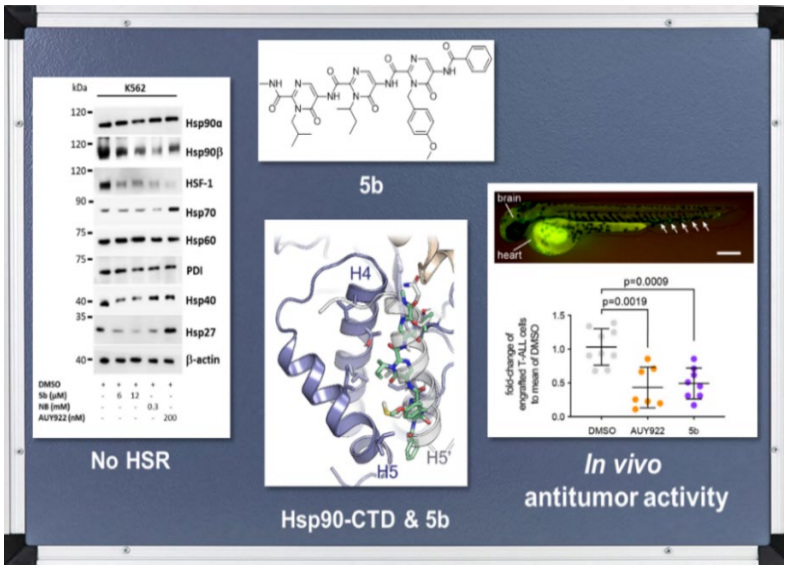

Figure 6: *Graphical abstract showing the development of first-in-class small molecule inhibitor tareting C-terminal dimerization of HSP90 inhibitor (5b or LSK82) that has in vivo anti-leukemic activity in zebrafish model without inducing heat shock response as a resistance mechanism. Use of illustration is permitted by 'ACS Central Science' journal with open access under a CC BY license.*

design, followed by chemical synthesis, binding mode model prediction, and assessment of biochemical affinity (**Figure 6**). Compound 5b (or LSK82) significantly reduced leukemia burden in the zebrafish xenotransplantation model and triggered apoptosis in TKI-resistant BCR::ABL1^{T315I}, BCR::ABL1^{E255K}, and BCR::ABL1^{M351T} mutant cells. This effect was achieved by targeting BCR::ABL1 kinase, thereby disrupting associated downstream signaling pathways, without inducing a heat shock response (HSR) as a resistance mechanism. However, the clinical application of compound 5b (or LSK82) is limited by challenges related to its solubility and complex molecular structure. In particular, the compound's poor thermodynamic aqueous solubility has hindered its further preclinical evaluation in murine models. Currently, efforts are being undertaken by our collaborators to optimize the pharmacokinetic and pharmacodynamic profiles of newly developed analogs of 5b. These efforts aim to enhance solubility and bioavailability, thereby facilitating more robust preclinical assessments and advancing the therapeutic potential of these compounds. Additionally, we have recently developed a HSP90 inhibitor (Geldanamycin) based proteolysis targeting chimera (PROTAC) or degrader targeting HSP90.[44] Our leading degrader, 3a, effectively reduced HSP90α and HSP90β levels in cells by utilizing the ubiquitin-proteasome pathway.

Despite the innovative design of HSP90 CTD targeting HSP90i or HSP90-PROTACs, their poor pharmacological properties limit their further development for clinical use. Consequently, our focus was shifted towards enhancing the efficacy of currently available HSP90 (NTD-targeting) inhibitors, which have advanced to clinical trials.[45,46] However, to fully exploit the potential of HSP90i for clinical application, it is crucial to achieve a comprehensive understanding of: (i) the distinct roles of cytosolic HSP90 isoforms (HSP90α and HSP90β) in sustaining malignant cell growth, and (ii) the mechanisms underlying the acquisition of resistance to HSP90i.

Loss of HSP90β leads to the upregulation of the stress-inducible isoform HSP90α: First, we aimed to improve the understanding of the impact of the two cytosolic HSP90 isoforms (HSP90α and HSP90β) and their involvement in the development of acquired resistance to HSP90i (**Publication 3**).[47] To this end, we generated CRISPR/CAS9 mediated knockout (KO) and siRNA mediated knockdown

(KD) models of HSP90 isoforms (α and β) in *BCR::ABL1*$^{+}$ leukemia cell line K562, established from CML. This cell line displays high levels and strong dependency of HSP90 inhibition.[48] Furthermore, an additional KO model was established using other the *BCR::ABL1*$^{+}$ (CML) KCL-22 cell line to corroborate the findings. The loss of HSP90β in the K562 and KCL-22 cell lines resulted in an upregulation of HSP90α at the mRNA and protein level investigated *via* western blot (WB) analysis. Further investigation of HSR-related proteins also showed upregulation of HSF1, HSP70 and HSP40. The same effect (upregulation of HSP90α and HSP70) was observed in the HSP90β-KD cell lines investigated *via* automated western blot.[47] In contrast, the loss of HSP90α had no effect on the HSP90β level and HSR-related proteins (HSF1, HSP70, HSP40, and HSP27). Likewise, the expression of clients such as AHA1, CDC37 and SURVIVIN was not affected. Moreover, examination of alterations in other non-cytosolic HSP90 paralogues, such as HSP75/TRAP1 (localized in mitochondria), GRP94 (located in the endoplasmic reticulum), and co-chaperones of HSP90 (AHA1 and CDC37), showed no significant changes in their expression following the loss of HSP90α/β. Taken together, targeting HSP90β elicits resistance via inducing the expression of pro-survival HSR-related proteins, including HSP90α and HSP70.

Depletion of HSP90α isolform results in downregulation of PTPRC (or CD45) expression and suppresses the in vivo engraftment of *BCR::ABL1*+ leukemia cells: HSP90 is critically involved in the folding and subcellular localization of the BCR::ABL1 protein and consistent with findings from a prior study,[49] we also noted that HSP90β interacts with and stabilizes BCR::ABL1 protein with greater efficacy than HSP90α.[47] In our HSP90α-KO cells, where only the HSP90β isoform was expressed, this led to heightened kinase activity of BCR::ABL1 and its associated downstream pro-survival signaling pathways. Next, we employed multi-omics methodologies, incorporating transcriptomics and proteomics analyses, to investigate the potential effects on specific signaling pathways following the depletion of HSP90α/β isoforms. Multi-omics analysis, coupled with rescue experiments, consistently revealed a significant downregulation of PTPRC (CD45) expression following the depletion of the HSP90α isoform. This downregulation had a notable impact on downstream p-LCKY505 and LCK expression.[47] Additionally, we investigated the transplantation efficiency of HSP90α/β-KO K562 cells in an immunodeficient NSG mouse model.

Of note, HSP90α-KO cells exhibited a significantly reduced engraftment capacity compared to HSP90β-KO or the control group (Fig. 2A). This finding was supported by a notable increase in overall survival of 19 days among the animals with HSP90α-KO leukemia cells when compared to HSP90α-KO or respective controls (**Figure 7**).[47]

Results from Publication 3

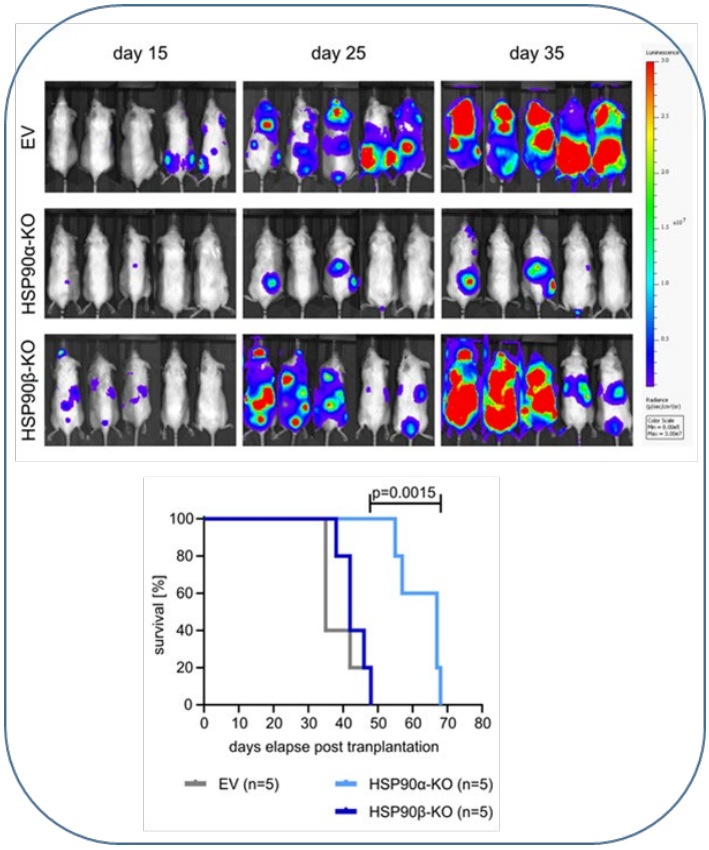

Figure 7: *Images of NSG mice (n=5 mice/group) transplanted with luciferase-GFP+ HSP90α/β-KO or control K562 cells on the days depicted outside image panel. Below, kaplan-Meier survival curves showing significantly prolonged overall survival of NSG mice transplanted with HSP90α-KO compared to HSP90β-KO or EV (K562) control cells (n=5 mice/group, p = 0.0015, Log-rank Mantel-Cox test). Use of illustration is permitted by 'Cell Death Diesease' journal with open access under a CC BY license.*

HSP90α is secreted extracellularly (eHSP90α) and plays a critical role in promoting tumor cell invasion and metastasis.[50-54] To explore the effects of HSP90α/β isoform depletion on the secreted protein profile, we conducted MS-based secretome analysis. This revealed significant alterations in protein expression following the loss of either HSP90α or HSP90β. Notably, eHSP90α secretion was markedly reduced in HSP90α-KO cells, while its expression significantly increased in HSP90β-KO cells. This may likely suppress the *in vivo* migration and invasion capability of HSP90α-KO cells in NSG mouse model.

Prolonged exposure to the HSP90i PU-H71 results in genetic alterations of the *HSP90AA1* gene and promotes HSP90α overexpression: Recently, the HSP90i PU-H71 (Zelavespib) has received orphan drug designation from the FDA for the

treatment of myelofibrosis and was administered for compassionate use for treating AML.[45] To investigate the mechanisms underlying resistance to pharmacological inhibition of HSP90, we generated HSP90i-resistant cell lines targeting either the NTD of HSP90 with PU-H71 and 17-AAG (Tanespimycin) or the CTD with Coumermycin A1 (CA1). Clonal selection was achieved through repeated cycles of treatment with progressively increasing inhibitor concentrations. Notably, PU-H71-resistant (PUHr) cells exhibited cross-resistance to Tanespimycin, another HSP90-NTD-targeting inhibitor. PUHr cells also showed significant upregulation of HSP90α relative to their

Results from Publication 3

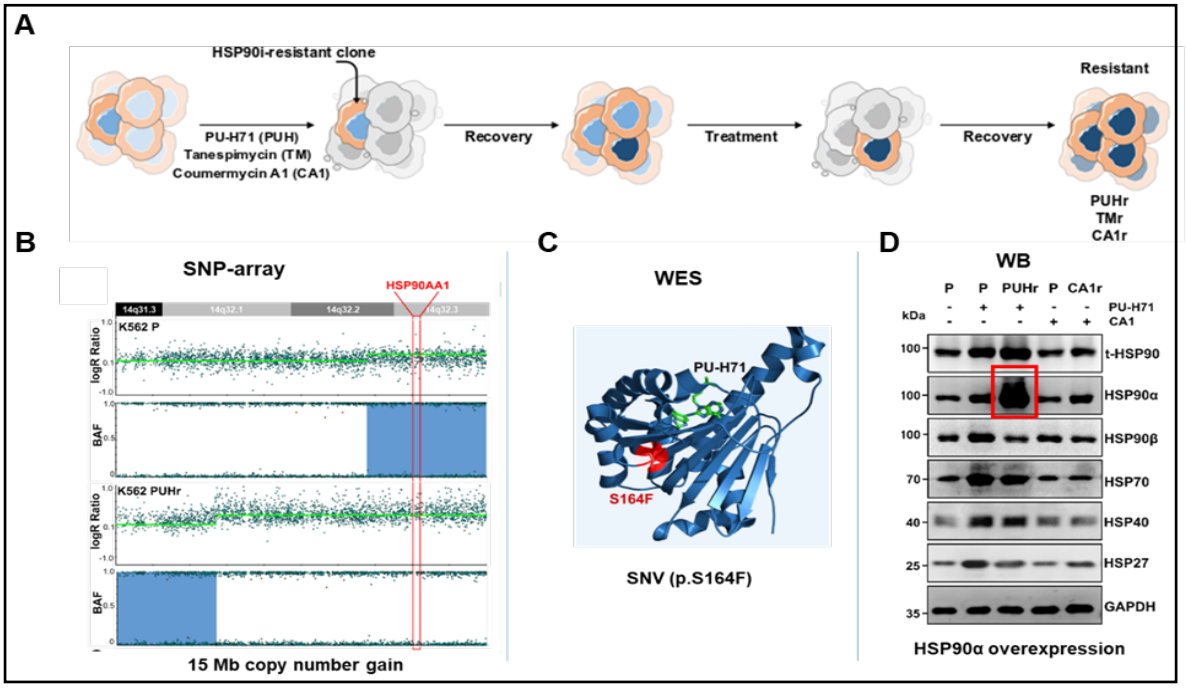

Figure 8: *(A) Schematic depiction of the workflow of generating HSP90 inhibitor resistant cells, through chronic exposure of HSP90-N-terminal domain- (PU-H71 and Tanespimycin or TM) or HSP90-C-terminal domain-targeting (Coumermycin A1 or CA1) inhibitors in K562 cells. (B) SNP array results of PUHr cells in comparison to the parental (P) counterpart revealed an acquired 15 Mb copy number gain in 14q32.1q32.3 encompassing the HSP90AA1 gene locus (C) Structural model of the N-terminal domain of HSP90α bound to PU-H71 (based on PDB ID 2fwz). The substitution site S164F is highlighted in red. (D) WB analysis of PUHr, CA1r and control parental (P) cells after re-treatment with CA1 (2 µM), PU-H71 (500 nM) or vehicle (-) for 24 h. GAPDH served as a loading control. Use of illustration is permitted by 'Cell Death Diesease' journal with open access under a CC BY license.*

parental lines, accompanied by an increase in total HSP90, AKT, and SRC protein levels.. Consistent with the elevated HSP90α levels, SNP array analysis revealed a 15 Mb copy number gain on chromosome 14q32.12q32.3 in PUHr cells, encompassing

the *HSP90AA1* gene locus. Whole-exome sequencing further identified two single-nucleotide variants (SNVs) within *HSP90AA1*, including a missense variant, p.(S164F) (chr14:102085796G>A). These data indicate that upregulation and genetic alteration of the HSP90α isoform contribute significantly to resistance against the clinically relevant HSP90 inhibitor PU-H71 (**Figure 8**). In contrast to resistance acquired against Tanespimycin and Coumermycin A1 was primarily mediated through amplification of the ABCB1 locus and MDR1 efflux pump overexpression.[47]

Combined CDK7 and HSP90 inhibition exhibit synergistic effects against TKI-resistant *BCR::ABL1*⁺ CML and BCP-ALL cells: We next performed ex vivo high throughput drug screening (HTDS) to identify novel therapeutic vulnerabilities upon ablation of HSP90α/β isoforms. HSP90α-KO cells showed increased sensitivity toward the CDK7 inhibitor (THZ1) and standard chemotherapeutics. In line, a pronounced increase in CDK7 expression in HSP90α-KO K562, KCL22, and SUPB15 cells was observed.[47] Therefore, we proceeded to conduct combinatorial drug screenings utilizing HSP90i PU-H71 together with the CDK7 inhibitor THZ1. The screenings were performed using *BCR::ABL1*⁺ CML cell lines and their TKI-resistant counterparts. Additionally, we included TKI-resistant *BCR::ABL1*⁺ BCP-ALL cell lines (SUPB15),[22] three relapsed *BCR::ABL1*⁺ BCP-ALL patient samples. We also employed a murine BA/F3 cell line model expressing TKI-resistant BCR::ABL1(T315I) mutant cells resistant to the third-generation TKI Ponatinib.[22] Notably, a significant synergistic interaction was observed in all tested cells. Subsequently, we evaluated the effects of combining PUH71 and THZ1 on peripheral blood-derived mononuclear cells (PBMCs) collected from three healthy individuals. Remarkably, healthy PBMCs exhibited significantly lower sensitivity to the PUH71 + THZ1 combination compared to leukemia cells (**Publication 3**).[47] Further mechanistic studies revealed suppression of HSR-related proteins including HSP90α upon combinational treatment of HSP90i with CDK7i (Fig. 2C/D). CDK7 (TFIIH subunit of RNA polymerase II) can activate RNA polymerase II (RNAPII) *via* phosphorylation of the CTD (pS5), and inhibiting CDK7 can therefore trigger a cascade of abnormalities in the initiation, proximal pausing, and elongation phases of RNAPII.[55] Consistently, decreased RNAPII (pS5) levels were

detected in cells treated with either CDK7i alone or in combination with HSP90i. As a result, we observed a potent synergistic effect between inhibitors targeting HSP90 and CDK7, which acted by hindering the transcription of pro-survival HSR-related genes mediated by RNAPII (**Figure 9**).[47]

Results from Publication 3

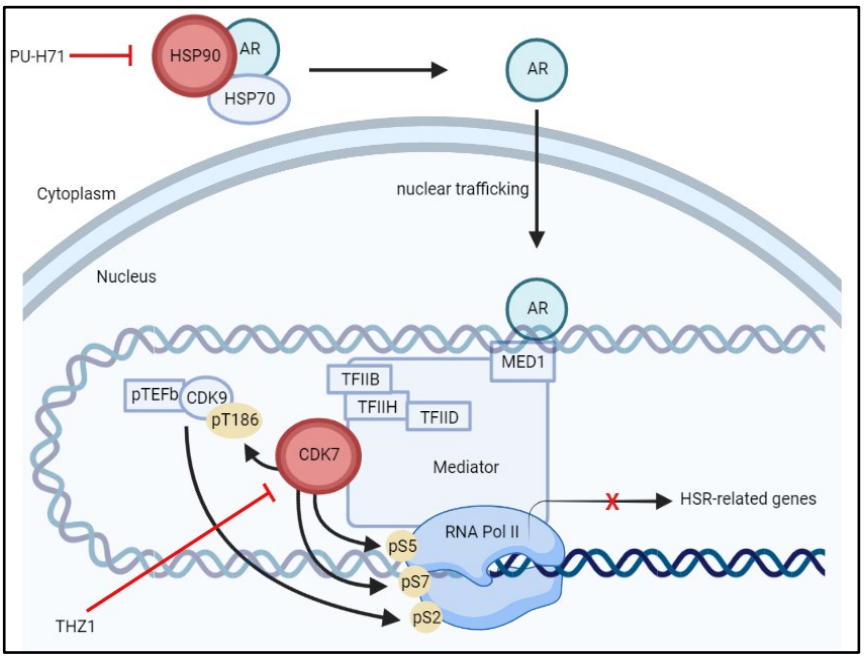

Figure 9: *Schematic depiction of CDK7 inhibition via THZ1 on the expression of heat shock response-related genes. Use of illustration is permitted by 'Cell Death Diesease' journal with open access under a CC BY license.*

Our recent unpublished studies have demonstrated that commonly used chemotherapeutics and targeted therapies can also activate the expression of stress signaling-related molecular chaperones. Thus, it may be beneficial to combine modulators that inhibit the expression of these stress-related molecular chaperones with these standard therapies. Additionally, we plan to identify and characterize new modulators capable of overcoming drug resistance beyond CDK7 inhibition. In an alternative approach to target HSP90, we will continue to develop novel HSP90 CTD targeting inhibitors with our collaboration partners at the Institute of Pharmaceutical and Medicinal Chemistry, HHU Düsseldorf.

II. Targeting epigenetic modifiers: histone deacetylases (HDACs)

Non-genetic modifications encompass a diverse range of cellular and molecular processes that intricately modulate the responsiveness of cancer cells to therapeutic agents, all without involving changes in the DNA sequence. The challenges posed by

these mechanisms are significant in the clinical context, given that existing approaches predominantly centered on identifying gene mutations to predict treatment outcomes.[56] In fact, epigenetic dysregulation, considered a commonality in human cancers, is proposed as a causative mechanism driving various hallmarks of cancer, including proliferation, evasion of growth suppressors, and resistance to apoptosis.[57,58] Therefore, the intricate landscape of epigenetic dysregulation in cancer cells, including hematological malignancies, presents a promising target for innovative therapies. Epigenetic modifications are crucial in regulating the expression of hematopoietic lineage-specific genes.[59]

Histones, essential elements of chromatin structure, are subject to acetylation and deacetylation processes that regulate gene expression. Two opposing classes of enzymes, histone deacetylases (HDACs) and histone acetyltransferases (HATs), play a central role in this process. HATs promote gene transcription by acetylating lysine residues on histone tails, resulting in chromatin relaxation and increased accessibility for transcriptional machinery.[60] Conversely, epigenetic modifications play a crucial role in the development, progression, and treatment of leukemia. Among these modifications, histone deacetylases (HDACs) have emerged as key players in leukemogenesis and potential therapeutic targets. Studies have shown that HDACs are frequently overexpressed in various types cancers,[61] including leukemia.[62] This overexpression is associated with poor prognosis and increased resistance to conventional therapies. HDACs exert a repressive effect on gene expression by removing acetyl groups from histones, leading to chromatin condensation and transcriptional silencing. Mammalian HDACs are composed of 18 highly conserved genes, categorized based on phylogenetic analysis and sequence homology to yeast factors. These enzymes are classified into five groups: Class I (HDAC1, 2, 3 and 8), Class IIa (HDAC4, 5, 7 and 9), Class IIb (HDAC6 and 10), Class III (SIRT1-7), and Class IV (HDAC11).

Role of HDACs in normal and aberrant hematopoiesis: HDACs play a significant role in the development of multiple hematopoietic lineages, including the hematopoietic stem cell (HSC)-progenitor lineage, granulocyte-monocyte lineage, erythropoietic lineage, and lymphoid lineage.[59] Throughout the process of

hematopoiesis, HDACs are integral to the assembly of various transcriptional complexes. The interaction between HDACs and transcription factors (TFs) or other cofactors are crucial for modulating histone acetylation levels, influencing TF activity, and regulating the function of transcriptional complexes.[59] These processes collectively affect the expression of numerous genes associated with hematopoiesis. For instance, class I HDAC1 and HDAC2 are critical regulators of hematopoietic stem cell (HSC) formation and homeostasis. The simultaneous deletion of these two enzymes leads to the loss of HSCs and, subsequently, early hematopoietic progenitors.[63] Furthermore, class I HDAC3 has been show to regulate the development of HSCs by interaction the TFs, such as Ncor2 and GATA2.[64,65] HDAC8, another member of Class I HDACs, is highly expressed in long-term hematopoietic stem cells (LT-HSCs), multipotent progenitors (MPPs), and lymphoid-primed multipotent progenitors (LMPPs). HDAC8 is crucial for maintaining the functional integrity of LT-HSCs through the deacetylation of p53.

HDAC inhibitors and acute myeloid leukemia (AML): AML is a heterogeneous disease, albeit its incidence is more common in adults, AML accounts for around 20% of childhood leukemias. While polychemotherapy regimens have increased the overall survival of childhood ALL to around 90%, still the 5-year survival rates of children with AML is comparatively lower (65 - 70%). Furthermore, in case of relapse (seen in 30-40% patients), prognosis is generally worse.[4,66] The therapy regimen of AML also known as “7+3” consists of 7 days of treatment with cytarabine, and 3 days with an anthracycline has been used for more than four decades. However, it is poorly tolerated. In cases where the patients are not suitable for this intensive therapy, combinations with different drugs (e.g. BCL-2 inhibitors and IDH1 and 2 inhibitors) and/or lower dosages of the cytarabine and anthracycline must be employed. A great part of recurring mutations in AML involves the epigenetic machinery, which form a strong argument for the use of epigenetic therapies. As a consequence, numerous epigenetic drugs are currently under investigation in clinical studies for treating AML.[67,68]

Single-agent therapies against AML have shown limited efficacy, so the most promising results with epigenetic drugs are achieved through combination therapies.

These include combinations of epigenetic drugs with other epigenetic agents (e.g., azacitidine plus an HDAC inhibitor), immunotherapies (e.g., checkpoint inhibitors), and targeted therapies (e.g., NEDD8 inhibitors, FLT3 inhibitors), which are actively being evaluated in clinical trials.[67,69,70] At present, HDAC inhibitor (HDACi)-based combinations are the focus of six active or recruiting clinical trials (ClinicalTrials.gov). In three of these trials, vorinostat is combined either with azacitidine alone (NCT03843528, NCT00392353) or with azacitidine, fludarabine, and cytarabine (NCT03263936). The combination of azacitidine with chidamide is also under study (NCT03031262). Another promising regimen involves the NEDD8 inhibitor pevonedistat with the HDAC inhibitor belinostat (NCT03772925), while a phase III trial is evaluating the role of panobinostat in maintenance therapy following stem cell transplantation (NCT04326764).

Development of HDAC class specific inhibitors and PROTACs: The currently approved HDAC inhibitors (HDACis) are pan-HDACis, meaning they non-selectively target multiple HDAC isoforms, which are involved in normal cellular functions. This lack of specificity contributes to a broad range of side effects, some of which can be severe or life threatening, including myelosuppression, cardiac toxicity, and gastrointestinal disturbances.[71-73] These adverse effects often necessitate discontinuation of HDACi-based therapies to prevent serious complications. Targeting specific isoforms could limit the inhibition to select cellular functions, potentially reducing the occurrence and severity of side effects, thereby improving tolerability. HDAC6, in particular, is an attractive target due to its involvement in key cellular processes relevant to cancer.[74] HDAC6 is a distinct member of the family of HDAC class IIb, primarily localized in the cytoplasm, where it regulates a variety of cellular functions. It deacetylates a range of substrates, including α-tubulin, cortactin, and heat shock protein HSP90α, thereby influencing numerous cellular processes.[75] Recent studies have shown that inhibiting HDAC6 reduces the expansion of leukemia stem cells, potentially by modulating the Hedgehog signaling pathway.[76] Besides, HDAC6 is overexpressed and plays a significant role in the progression of various cancers, including several subtypes of leukemia such as chronic lymphocytic leukemia (CLL), acute myeloid leukemia (AML), and ALL.[77] Furthermore, analysis of the TARGET AML dataset indicates that high levels of HDAC6 are associated with poor survival in AML

patients. Therefore, targeting HDAC6 specifically holds considerable potential for clinical application in the treatment of in hematological malignancies.[78]

In collaborative research attempts with Prof. Thomas Kurz from the University of Düsseldorf and Prof. Finn K. Hansen from the University of Bonn, we have developed a spectrum of HDAC inhibitors, spanning from specific, preferential, to pan-HDAC inhibitory profiles.[79-85] For combination therapy, the most thoroughly studied synergy involving HDAC inhibitors (HDACi) is with proteasome inhibitors (PIs).[86] In our previous work, this combination achieves dual inhibition of proteasome and aggresome pathways, leading to the accumulation of misfolded proteins and triggering apoptosis.[79] In recent years, multitarget drugs have emerged as a promising alternative to combination chemotherapy. Although several multitarget drugs based on HDAC inhibitors (HDACi) have been developed, no dual HDAC-proteasome inhibitor had been reported until now. In this study, we designed and synthesized RTS-V5 as the first dual inhibitor targeting both HDAC and proteasome activity (**Figure 10**). Our findings demonstrate that RTS-V5 effectively inhibits HDAC6 and chymotrypsin-like proteasome activity at submicromolar concentrations. In the KMT2A-rearranged BCP-ALL SEM cell line, RTS-V5 induces apoptosis, activates the heat shock response

Publication 4

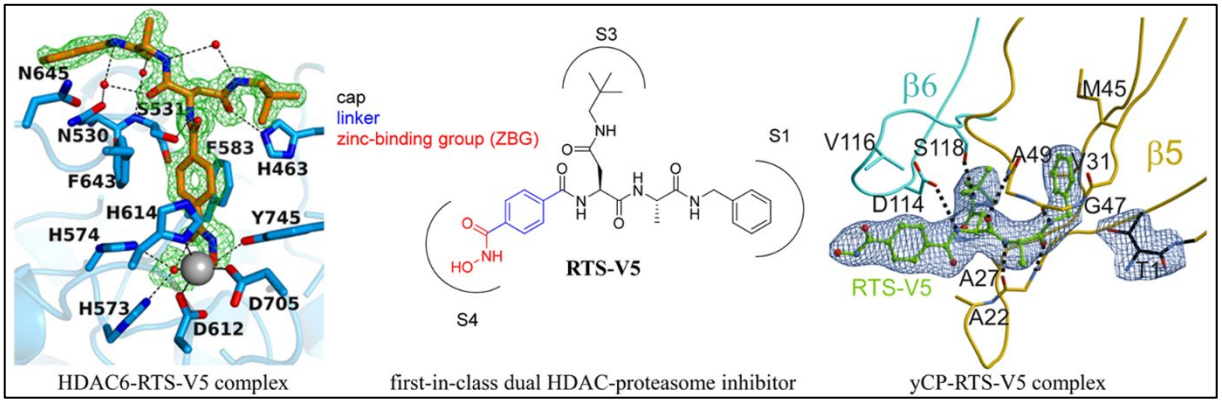

Figure 10: *Visual abstract showing the development of a first-in-class dual inhibitor, RTS-V5, which targets both HDAC and proteasome pathways. RTS-V5's engagement with these targets was confirmed through biochemical assays, cellular studies, and X-ray crystal structures of the 20S proteasome and HDAC6. Use of illustration is permitted by 'Journal of Medicinal Chemistry' journal with open access under a CC BY license.*

(HSR), initiates the unfolded protein response (UPR), and promotes autophagy. Additionally, RTS-V5 inhibits cell cycle progression, colony formation, and aggresome

accumulation. Significantly, RTS-V5 displayed potent anticancer activity across a range of chemosensitive and chemoresistant leukemic and multiple myeloma cell lines, as well as in therapy-refractory primary leukemia cells derived from patients, all without showing toxicity toward peripheral blood mononuclear cells (PBMCs) from healthy donors. This promising efficacy profile suggests RTS-V5 as a valuable candidate for further development in cancer therapy (**Publication 4**).[87] Over the years, we have developed highly selective HDAC6 inhibitors and demonstrated their synergistic interaction with DNA methyltransferase inhibitors, such as decitabine, with differential activity against AML cells.[80,81,88]

In a distinctive approach to target HDAC6, we generated proteolysis targeting chimeras (PROTACs) or degraders which selectively target HDAC6 without affecting other HDAC isoforms (**Publication 5**),[89] such as HDAC1 (class I) and HDAC4 (class IIa). Quantitative analysis via automated capillary Western blotting confirmed high degradation efficiency for the leading HDAC6 degraders, with DC_{50} values in the low nanomolar range and Dmax values exceeding 80% (**Figure 11**). Pretreatment with an HDAC inhibitor, a CRBN ligand, or the proteasome inhibitor MG132 prevented HDAC6 degradation, suggesting that degradation occurs through a ternary complex formation and the ubiquitin-proteasome pathway. To assess degradation kinetics, HDAC6 in K562 cells was CRISPR-tagged and monitored over 24 hours using HiBiT+LgBiT complementation technology, which allowed real-time tracking of HDAC6 level reduction. Furthermore, quantitative mass spectrometry (MS) data showed no significant changes in the overall cellular proteome profile after treating K562 cells with 1 µM of PROTACs (A6 or B4). Subsequently, HDAC6 degradation and the intracellular localization of a fluorescein-labeled PROTAC (A7) were examined using fluorescence microscopy. This analysis revealed that PROTAC (A7) predominantly localized within the cytoplasm and at the nuclear-cytoplasmic interface. PROTAC (A6) demonstrated promising anti-proliferative activity in three AML cell lines and induced apoptosis in MOLM13 cells through Caspase 3/7 activation by arresting cells in the sub-G1 phase. Overall, given their potent ability to degrade HDAC6, these PROTACs represent valuable tools for studying HDAC6 biology.

Publication 5

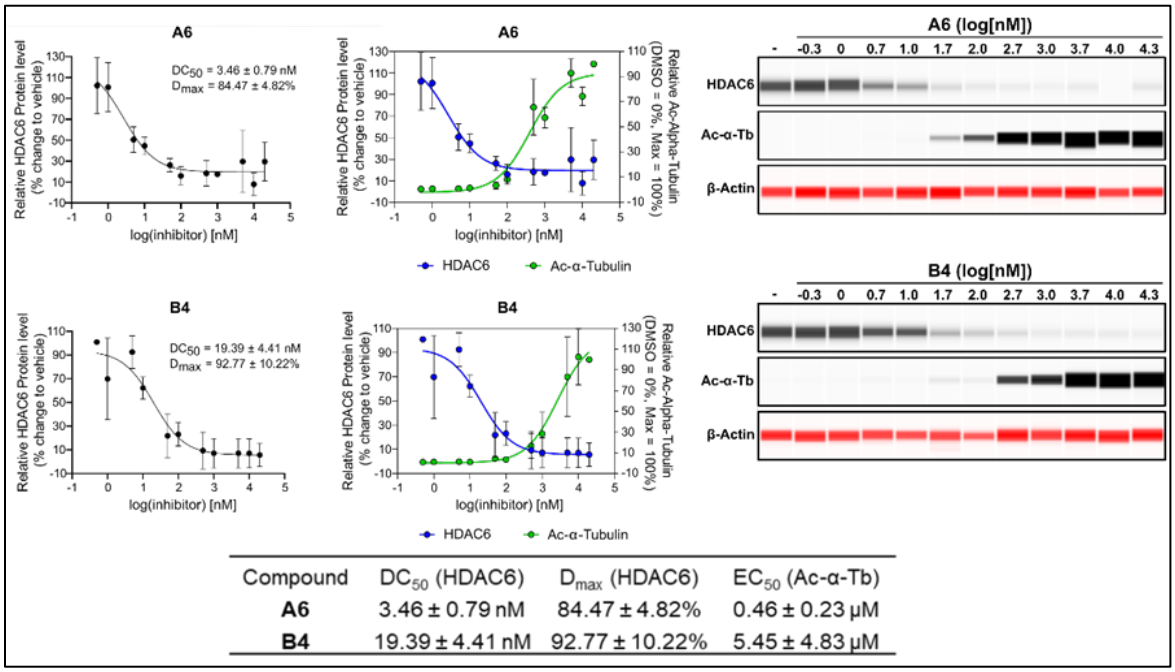

Compound	DC_{50} (HDAC6)	D_{max} (HDAC6)	EC_{50} (Ac-α-Tb)
A6	3.46 ± 0.79 nM	84.47 ± 4.82%	0.46 ± 0.23 µM
B4	19.39 ± 4.41 nM	92.77 ± 10.22%	5.45 ± 4.83 µM

Figure 21: *Quantitative simple western immunoassay shows dose-dependent degradation of HDAC6 with subsequent increased levels of acetyl-α-tubulin. HL-60 cells were treated with the indicated concentrations of PROTACs (A6 and B4) and the resulting lysates were analysed utilizing simple western immunoassay technology (BioTechne). DC50 and Dmax were calculated using nonlinear regression (log(inhibitor) vs response (three hree independent simple western immunoassay runs on the treated samples from two independent biological replicates. Use of illustration is permitted by 'Journal of Medicinal Chemistry' journal with open access under a CC BY license.*

In our recently published study, we aimed to design and synthesize HDAC inhibitors with a specific focus on their efficacy against therapy-resistant leukemia cells, while minimizing toxicity (**Publication 6**).[90] Through structural optimization, we developed HDACi compounds with nanomolar inhibitory activity against class I and IIb HDAC enzymes. The novel HDAC inhibitors (4d and 4m) demonstrated significantly enhanced anti-leukemic efficacy compared to several clinically approved HDAC inhibitors across (n = 35) leukemia cell lines and patient-derived leukemia samples originated from different subgroups including from the myeloid and lymphoid lineage. Notably, both HDAC inhibitors exhibited selective activity against leukemia cells, with minimal impact on healthy human cells, providing a safety advantage over commonly used HDAC inhibitors like vorinostat, romidepsin and ricolinostat (**Figure 12**).

Results from Publication 6

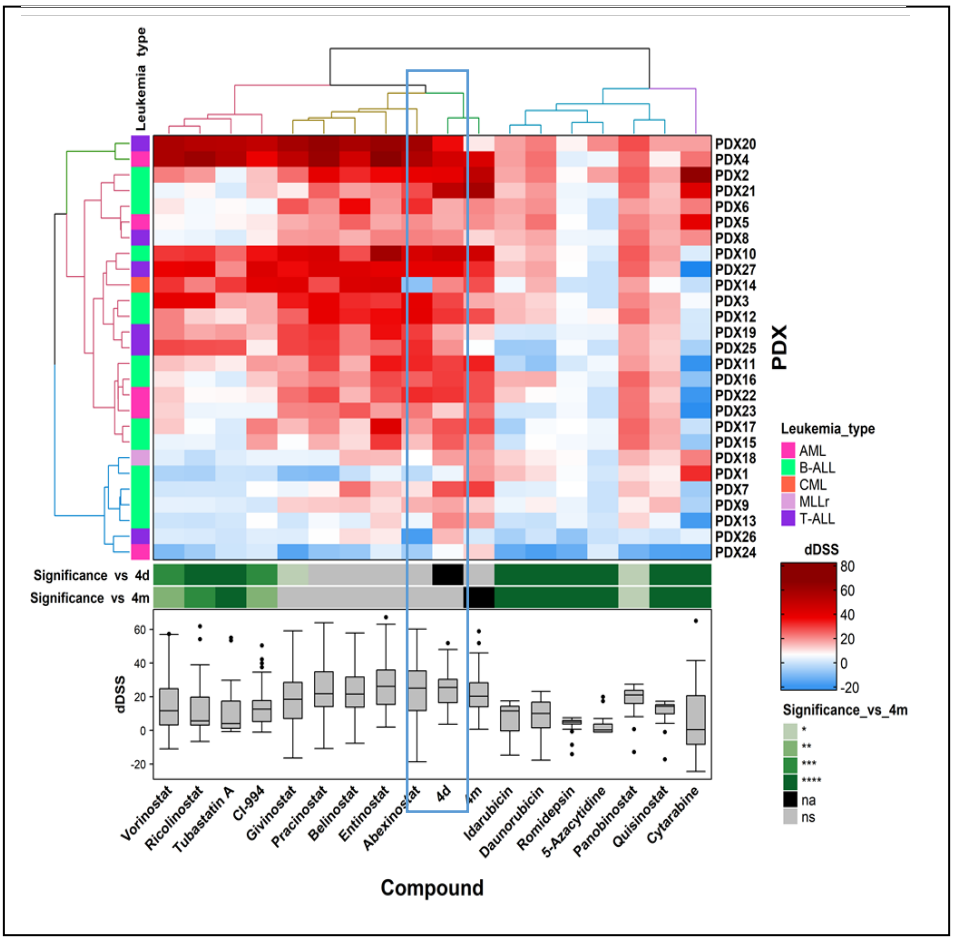

Figure 32: *Unsupervised clustered heatmap displaying differential drug sensitivity score (dDSS) of A) leukemia cell lines and B) patient derived xenografts (PDX) grown leukemia cells. The statistical analysis was conducted using one way ANOVA, n=1. ALL = acute lymphoblastic leukemia, AML = acute myeloid leukemia, B-ALL = B-cell acute lymphoblastic leukemia, CML = chronic myeloid leukemia, MLLr = MLL rearranged leukemia, T-ALL = T-cell acute lymphoblastic leukemia, na = not applicable, ns= not significant, * = p(adj) > 0.05, **= p(adj) > 0.01, ***= p(adj) > 0.001, ****= p(adj) > 0.0001. Use of illustration is permitted by 'Journal of Medicinal Chemistry' journal with open access under a CC BY license.*

Additionally, 4d and 4m showed strong synergistic effects when combined with standard chemotherapeutics, including decitabine and clofarabine, indicating their potential for use in combination therapy to overcome resistance and improve treatment outcomes. In vitro pharmacokinetic analyses revealed that 4d had the most favorable profile, with intermediate microsomal stability, excellent plasma stability and concentration-independent plasma protein binding. Following our in vitro pharmacokinetic findings, an in vivo pharmacokinetic study of 4d was conducted in

three C57BL/6 mice. Notably, the dose-adjusted overall exposure of 4d was higher in mice than that of vorinostat, measuring (47 vs. 12 h*kg*ng/ml/mg). Similar to vorinostat (t½ = 0.75 hours), 4d demonstrated a short elimination half-life of 0.35 hours, suggesting substantial metabolism and elimination of 4d in mice. The strong cytotoxic effect of 4d on leukemia cells, along with its promising pharmacokinetic profile in both

Results from Publication 6

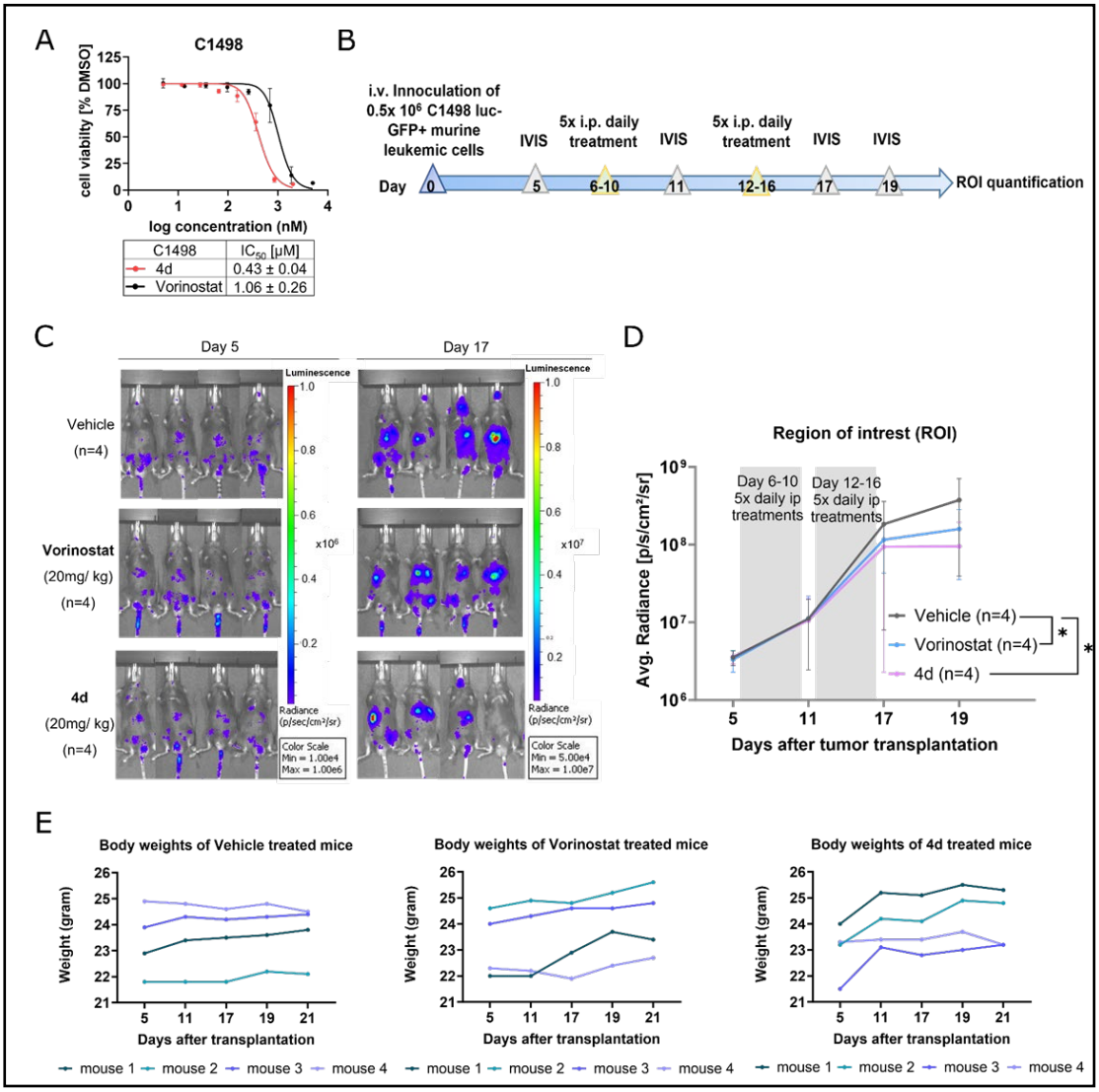

Figure 43: *(A) Dose-response curve with IC50 value showing the inhibitory effect of vorinostat and compound 4d on the proliferation of C1498 cell line. B) Schematic timeline of the experimental design. Each mouse received 0.5 × 10^6 C1498 luc-GFP+ murine leukemic cells. C) IVIS images of treated mice were taken on day 5 and 17. (D) ROI values at various time points, representing the measurement of leukemia cell growth. Statistical analysis was performed using a Two-way mixed ANOVA with Greenhouse-Geisser correction. E) Changes in body weight of each mouse from the three treatment groups before and after the treatment course. Use of illustration is permitted by 'Journal of Medicinal Chemistry' journal with open access under a CC BY license.*

in vitro and in vivo settings, motivated us to assess its efficacy in a preclinical leukemic xenograft model using human AML cells (MV4-11) in NSG mice. In this model, 4d significantly inhibited the proliferation of MV4-11 leukemia cells in vivo without inducing toxicity. Given the emerging immunomodulatory effects of HDAC inhibitors in cancer therapy,[91] we further evaluated 4d in an allograft leukemia model. In this model, leukemia was established by intravenous injection of murine AML (C1498) cells (derived from C57BL/6 mice) into immunocompetent wild-type C57BL/6 mice (**Figure 13**). Compared to the vehicle control group, both the vorinostat-treated ($p = 0.0249$) and 4d-treated ($p = 0.0326$) groups showed a significantly reduced leukemia burden after the second treatment cycle, with the difference becoming even more pronounced by day 19. These findings support 4d as novel lead candidate for further preclinical development (**Figure 14**). Compound 4d not only exhibit a favorable therapeutic window but also show promising anti-leukemic effects, particularly in combination with established anti-leukemic agents.[90]

Summary of Publication 6

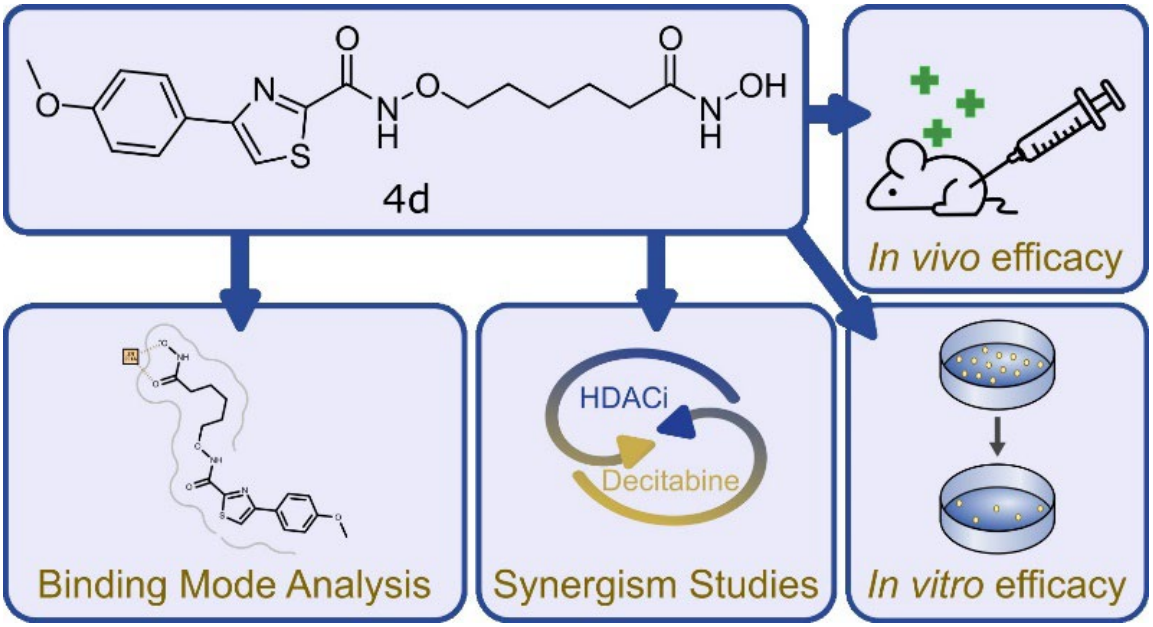

Figure 54: *Illustration of the lead compound 4d, highlighting it's in vitro antileukemic effects and synergistic potential with the hypomethylating agent Decitabine. The visual abstract also depicts the in vivo anti-leukemic activity of 4d, alongside its binding mode with the target. Use of illustration is permitted by 'Journal of Medicinal Chemistry' journal with open access under a CC BY license.*

III. Drug repurposing via high throughput drug screening platform

Targeted therapy has revolutionized the standard care of some leukemia subtypes. However, the clinical response to the targeted anticancer agents is rather heterogeneous. Predicting more accurately the drug responses before the treatment will not only improve the response rates but would also reduce redundant medication, lower side effects related to organ toxicity and also would be more economical for the patients. In our previous efforts, we mapped the dependencies on various signaling pathways using our ex vivo high throughput drug screening (HTDS) platform (**Figure 15**). The compound library includes FDA or EMA approved chemotherapeutics and kinase inhibitors, routinely used for the treatment of leukemia, inhibitors in early to late clinical phase and new promising compounds waiting to enter clinical trials (e.g. PI3K/AKT-, HDAC-, NF-κB-, JAK/STAT-, Aurora kinase-, Raf-MEK-ERK-, BCL-2-, MYC-, β-catenin etc. targeting inhibitors). The drugs and the cells are dispensed in a semi-automated fashion, allowing us to work with fewer cell numbers, which is very useful when analyzing primary patient samples and decreasing the possibility of human errors. Utilizing an industry standard (miniaturized) 384/1536-well plate format approach, essential due to the inherent scarcity of primary patient samples. Our efforts have encompassed the screening of over 150 diagnostic, relapsed leukemia or lymphoma or in vivo xenograft amplified patient samples.[92-96]

For instance, in a recent investigation, we utilized drug screening platform to pinpoint potentially efficacious hits for pediatric BCP-ALL patients exhibiting unfavorable prognosis, notably those with Dwn Syndrome or harboring rearrangements in the PAX5 or KMT2A/MLL genes.[97] Furthermore, we have recently identified that trametinib (MEKi) or venetoclax (BCL2i) synergize effectively with the HDACi inhibitor givinostat (ITF2357) in CRLF2-rearranged pediatric BCP-ALL.[96] This high-risk subtype, often found in children with Down Syndrome, is associated with poor outcomes and increased susceptibility to treatment-related toxicity.

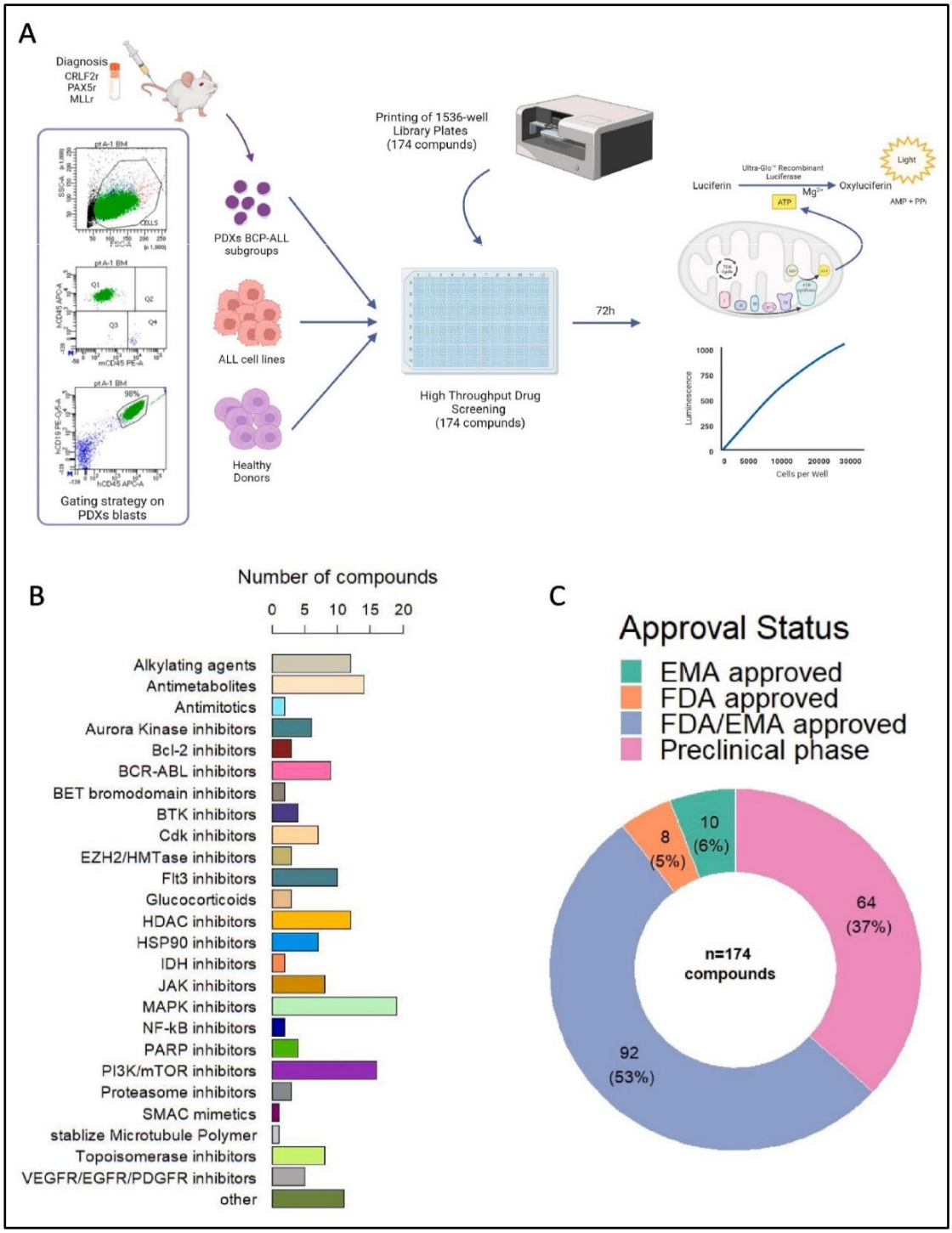

Figure 65: *Schematic representation of a high-throughput drug screening (HTDS) platform. (A) Overview of the experimental workflow, showing the stages of drug screening from initial assay setup to data analysis. (B) Categorization of drugs within the screening library, with classification by therapeutic area or target specificity. (C) Approval status breakdown of the custom drug library, highlighting the proportion of FDA/EMA-approved, investigational, and experimental compounds. Use of illustration is permitted by 'Biochemical Pharmacology' journal with open access under a CC BY license.*

3. Discussion

The cumulative work presented in this habilitation thesis explores the development of novel therapeutic strategies for pediatric acute leukemia. Firstly, a key focus of the research was the targeting of molecular chaperone proteins, specifically heat shock protein 90 (HSP90), which activate in response to stress signaling. The client proteins of HSP90 fulfill essential roles in cellular processes, such as signal transduction, cell cycle progression and transcriptional regulation. Among HSP90 clients are transcription factors, various kinases, steroid receptors, and several cell cycle regulators.[98-100] Notably, several of these HSP90 clients are associated with the six hallmarks of cancer: self-sufficiency in growth signaling, insensitivity to antigrowth signals, evasion of apoptosis, sustained angiogenesis, limitless replicative potential, tissue invasion and metastasis.[14] Hence, inhibiting the activity of HSP90 is a promising strategy for the development of novel anti-cancer drugs. Furthermore, overexpression of HSP90 is associated with poor prognosis in multiple cancers, including hematological malignancies, positioning it as a promising therapeutic target.[18-21] Most HSP90 inhibitors that have advanced to clinical trials target N-terminal domain (NTD) of HSP90,[33,35,101] however the clinical application of these inhibitors is primarily limited due to the induction of pro-survival HSR mechanism and the associated toxicity.[16,33,34] In contrast, modulators targeting the C-terminal domain (CTD) of HSP90 do not elicit HSR, making them a promising alternative for HSP90 inhibition.[35] Previous findings have shown that the C-terminal dimer of HSP90 undergoes rapid conformational changes.[39] Based on computational predictions and subsequent experimental validation, key amino acid residues at the C-terminal dimerization interface of HSP90 were identified, leading to the development of aminoxyrone (AX), a first-in-class protein-protein interaction peptidomimetic inhibitor (**Publication 1**).[22] Functional studies demonstrated that AX can effectively target multi-tyrosine kinase inhibitor-resistant leukemia cells, including the leukemia stem cell fraction. Additionally, in vivo experiments showed that AX inhibits leukemia cell engraftment without inducing a pro-survival heat shock response as a resistance mechanism, offering a potential therapeutic option for patients with TKI-resistant leukemia. However, AX's complex structure poses challenges for chemical synthesis, and its peptidomimetic nature results in poor aqueous solubility, limiting oral bioavailability.

Subsequently, we initiated an optimization process for AX to develop a first-generation small-molecule inhibitor targeting HSP90 C-terminal dimerization. This effort yielded an optimized candidate, designated as compound 5b or LSK82 (**Publication 2**).[43] Compound 5b significantly reduced leukemia burden in a zebrafish xenotransplantation model and induced apoptosis in TKI-resistant BCR::ABL1 mutants, specifically BCR::ABL1^{T315I}, BCR::ABL1^{E255K} and BCR::ABL1^{M351T}. This anti-leukemic effect was achieved through destabilization of the BCR::ABL1 protein, which in turn disrupted its downstream signaling pathways, notably without activating the heat shock response (HSR). However, clinical application of compound 5b was also hindered by poor thermodynamic aqueous solubility and structural complexity, which posed challenges for preclinical studies, particularly in mouse models. Collaborative efforts are currently underway to improve the pharmacokinetic (PK) and pharmacodynamic (PD) profiles of these novel class of inhibitors targeting HSP90 C-terminal dimerization. Specifically, these modifications aim to enhance solubility and bioavailability, thereby supporting more comprehensive preclinical evaluations and increasing the therapeutic potential of these compounds. In parallel, we have recently developed a HSP90 inhibitor (Geldanamycin) based proteolysis targeting chimeras (PROTACs), which are designed to degrade HSP90. Our lead PROTAC candidate, 3a, effectively reduces cellular levels of HSP90α and HSP90β through the ubiquitin-proteasome pathway, offering a novel approach to HSP90-targeted therapy.[44]

Despite the innovative design of HSP90 C-terminal domain-targeting inhibitors and HSP90-PROTACs, poor pharmacological properties hinder their clinical development. Therefore, we shifted our focused on enhancing the efficacy of existing HSP90 inhibitors that have advanced to clinical trials. For instance, the HSP90i PU-H71 (Zelavespib) has been granted orphan drug status by the US Food and Drug Association (FDA) to treat myelofibrosis and was administered for compassionate use to treat AML.[45] Nevertheless, the induction of HSR is acknowledged as one of the most prominent causes of acquired resistance toward using N-terminal targeting HSP90i, such as PU-H71.[22,35] Therefore, understanding the specific roles (cytosolic) HSP90 isoforms (HSP90α and HSP90β) in supporting malignant cell growth and the mechanisms driving resistance to HSP90 inhibitors (HSP90i) is essential to harness full clinical potential of HSP90 inhibitors. Through multi-omics analyses, we identified

that loss of (consitituvely expressing isoform) HSP90β induces compensatory overexpression of (stress induced isoform) HSP90α and extracellular HSP90α (eHSP90α). However Notably, depletion of HSP90α led to downregulation of CD45 (PTPRC) expression, restricting the in vivo growth of *BCR::ABL1*$^{+}$ leukemia cells. Additionally, chronic exposure to the advanced HSP90i PU-H71 (Zelavespib) resulted in copy number gain and mutation (p.S164F) in the HSP90AA1 gene, along with elevated HSP90α levels. In contrast, resistance to other HSP90i, such as Tanespimycin and Coumermycin A1, was associated with overexpression of the MDR1 efflux pump. Notably, combined inhibition of CDK7 and HSP90 demonstrated synergistic effects against therapy-resistant *BCR::ABL1*$^{+}$ leukemia cells from patients. This combination mitigates the stress signaling linked to HSR by inhibiting RNA polymerase II, thereby enhancing the efficacy of HSP90-targeted therapies (**Publication 3**).[47] Our recent (unpublished) data have demonstrated that commonly used chemotherapeutics and targeted therapies can also activate the expression of stress signaling-related molecular chaperones like HSP90 N-terminal targeting inhibitors. Thus, it may be beneficial to combine modulators (such as CDK7 inhibitors) that inhibit the transcription of these stress-related molecular chaperones (involved in drug resistance) with the standard therapies. Additionally, we plan to identify and characterize new modulators capable beyond CDK7 inhibition.

Another critical research area included in this thesis involves targeting epigenetic modifications, particularly histone deacetylases (HDACs). In leukemia, aberrant HDAC activity contributes to the dysregulation of genes involved in cell proliferation, differentiation, and apoptosis.[102,103] The established clinical success of HDACi in the treatment of hematological malignancies instigated their investigation against different types of leukemia, including acute myeloid leukemia (AML).[104] Currently approved HDAC inhibitors (HDACis) are non-selective, or pan-HDACis, targeting multiple HDAC isoforms that play essential roles in normal cellular functions. Although HDAC inhibitors demonstrate promising therapeutic efficacy, their lack of specificity is linked to a wide range of side effects, which can range from gastrointestinal disturbances to severe, potentially life-threatening toxicities such as cardiac complications and myelosuppression.[71-73] These adverse effects frequently require the discontinuation of HDACi-based therapies to mitigate the risk of serious

complications. Additionally, HDACis are rarely used as monotherapy and are typically administered in combination with other drugs,[69,70] further complicating treatment. Given the severity of the side effects associated with pan-HDACis, the development of isoform-specific HDAC inhibitors would represent a significant therapeutic advancement.

Therefore, we have focused on targeting isoform-specific HDAC inhibitors. Of the different HDACs, class IIb related HDAC6 is an attractive molecular target as it is widely expressed across leukemia cells.[74,77] HDAC6 is primarily localized in the cytoplasm of the cells, making it more accessible for inhibitors, whereas most of the other HDAC isoforms are localized in nucleus. HDAC6 has two catalytic domains (CD1 and CD2), and confirmed substrates of CD2 include α-tubulin, cortactin, tau, and the chaperone protein HSP90. Furthermore, HDAC6 is unique by possessing an ubiquitin-binding domain that is involved in the regulation of the aggresome-autophagy pathway, an important protein degradation mechanism next to the 26S proteasome.[105] Thus, the dual inhibition of the proteasome and aggresome pathways through combinations of HDAC6 and proteasome inhibitors leads to the accumulation of misfolded proteins, thereby promoting apoptosis, which is an effective mechanism against cancer cells that are resistant to conventional treatments. However, despite these advances, the limitations of combination therapy, such as potential drug-drug interactions and increased toxicity, have fueled the development of multi-target drugs that consolidate multiple inhibitory functions into a single molecule. We developed RTS-V5 as a pioneering dual HDAC-proteasome inhibitor, effectively combining HDACi activity with proteasome inhibition (**Publication 4**).[87] RTS-V5 was found to simultaneously inhibit HDAC6 and chymotrypsin-like proteasome activity at submicromolar concentrations, thus inducing apoptosis, unfolded protein response (UPR) and autophagy in leukemia cells, particularly in the KMT2A-rearranged BCP-ALL SEM cell line. Importantly, RTS-V5 demonstrated significant efficacy across chemosensitive and chemoresistant leukemia and multiple myeloma cell lines, while maintaining selectivity against healthy peripheral blood mononuclear cells (PBMCs). These results underscore RTS-V5's potential as a therapeutic candidate for resistant hematological cancers.

Expanding on this approach, PROTACs (proteolysis-targeting chimeras) were developed to target HDAC6 selectively, without impacting other HDAC isoforms (**Publication 5**).[89] In this study, PROTACs (A6 and B4) effectively degraded HDAC6 with minimal effects on the cellular proteome, showing selective intracellular localization. PROTAC A6, in particular, displayed potent anti-proliferative effects in multiple AML cell lines and induced apoptosis in MOLM13 cells via caspase 3/7 activation. Given the specificity of these HDAC6-targeting PROTACs, they present valuable tools for studying HDAC6's unique roles in cancer biology and offer a selective strategy for targeting HDAC6 in cancer therapy.

In parallel, in our recent study novel HDAC inhibitors (4d and 4m) were synthesized with a focus on targeting therapy-resistant leukemia cells while minimizing toxicity (**Publication 6**).[90] These inhibitors exhibited nanomolar inhibitory activity against class I and IIb HDAC enzymes and surpassed clinically approved HDAC inhibitors such as vorinostat, romidepsin, and ricolinostat in anti-leukemic activity. Notably, 4d and 4m maintained selectivity for leukemia cells, sparing healthy cells, which highlights their therapeutic potential for reducing off-target effects. When combined with standard chemotherapeutics, 4d and 4m showed strong synergy, particularly with decitabine and clofarabine, supporting their application in combination therapies for enhanced efficacy against resistant leukemia. In vitro pharmacokinetic analyses further substantiated the potential of 4d, revealing favorable plasma stability and concentration-independent plasma protein binding. In vivo studies in C57BL/6 mice confirmed rapid absorption, with a t_max of 0.25 hours and a high dose-adjusted exposure compared to vorinostat. Although 4d exhibited a short half-life, it effectively reduced leukemia proliferation in a preclinical NSG mouse model with MV4-11 AML cells, without inducing toxicity. Considering the immunomodulatory effects of HDAC inhibitors, additional investigations in an immunocompetent allograft leukemia model demonstrated that both 4d and vorinostat significantly reduced leukemia burden by the second treatment cycle, further validating the anti-leukemic potential of 4d. These findings position 4d as a promising lead structure for clinical development. Moving forward, optimizing the in vivo pharmacokinetics of 4d through a lead optimization program will be essential to maximize their therapeutic potential and to address current

limitations, ultimately advancing them as viable candidates for therapy-resistant AML treatment.

Additionally, using CRISPR/Cas9-edited HDAC6-knockout models, we have identified an immunomodulatory role for HDAC6 (manuscript in preparation). Considering the critical role of immunotherapy in oncology, we plan to investigate the effects of combining HDAC inhibitors with immunotherapy in the future. With strong collaboration partners in HHU Düsseldorf, we will continue to develop novel selective HDAC inhibitors, with the aim to mitigate the side effects and resistance associated with the currently available HDAC inhibitors.

A key challenge in pediatric cancer treatment is minimizing harmful side effects, addressing difficult-to-treat subtypes, and overcoming drug resistance. In the ever-evolving landscape of cancer treatment, the intersection of high-throughput drug sensitivity and resistance profiles with holistic genetic, transcriptomic, and epigenetic data offers a refined stratification for uncovering under-recognized biomarkers and novel therapeutic targets. In our drug repurposing approach, we explored the interdependencies of signaling pathways by correlating drug sensitivity and resistance patterns with a curated drug library, ranging from FDA-approved cancer treatments (such as chemotherapeutics and targeted inhibitors) to emerging compounds currently in clinical trials. Utilizing an industry standard essential due to the inherent scarcity of primary patient samples; our efforts have encompassed the screening of over 150 diagnostic, relapsed leukemia or lymphoma or in vivo xenograft amplified patient samples.[92-94,96,97] For instance, in pediatric BCP-ALL patients with high-risk profiles, such as those with CRLF2/PAX5/KMT2A rearrangements, we identified promising compounds that selectively targeted leukemic cells with minimal toxicity to healthy cells.[97] This approach highlights potential therapeutic candidates and underscores the utility of tailored drug screening for personalized leukemia treatment.

4. Summary – English

Pediatric acute leukemia continues to present significant challenges despite therapeutic advancements, with polychemotherapy and immunotherapy regimens contributing to considerable toxicity and impairing the quality of life for patients. Relapse rates remain around 15-20%, which complicates outcomes, particularly for high-risk cases. Future strategies should focus on achieving sustained molecular responses, reducing chemotherapy intensity, and minimizing the reliance on hematopoietic stem cell transplantation.

I. HSP90 as a Therapeutic Target in Leukemia: HSP90, a molecular chaperone, is often overexpressed in leukemia, stabilizing mutated or overexpressed oncogenes by preventing their degradation. Critical HSP90 client proteins in leukemia include mutant-BCR::ABL1, TP53, FLT3::ITD and MYC. While HSP90 inhibition has therapeutic potential, conventional HSP90 inhibitors often activate a pro-survival heat shock response (HSR) as a resistance mechanism, limiting their clinical efficacy. To circumvent this, we developed two novel HSP90 inhibitors targeting the C-terminal dimerization: Aminoxyrone (AX) and 5b. These inhibitors target *BCR::ABL1*$^{+}$ leukemia cells of myeloid or lymphoid origin that exhibit resistance to multiple tyrosine kinase inhibitors, including BCR::ABL1(T315I)-driven disease. They achieve this by disrupting BCR::ABL1 kinase-associated signaling pathways and can also induce apoptosis in leukemia stem cell fraction, importantly, without inducing a HSR. Though limitations in pharmacokinetics currently restrict their clinical applicability. As an alternative approach, our recent findings emphasize the pivotal role of the stress-inducible HSP90α isoform in driving resistance to HSP90 inhibitors. We have developed a novel combination strategy with CDK7 inhibitors, which suppresses the transcription of HSR-related genes, thus enhancing the efficacy of HSP90-targeted therapies.

II. Targeting epigenetic modifiers: Another research focus examines epigenetic modifiers, particularly histone deacetylase (HDAC) enzymes. Due to the severity of side effects associated with pan-HDAC inhibitors, developing isoform-specific HDAC inhibitors would be a substantial therapeutic advancement. HDAC6 inhibitors exhibit synergy with proteasome inhibitors, which led us (i) to the development of novel dual HDAC6-proteasome inhibitor (RTS-V5), with a potent anti-leukemia activity, especially

against KMT2A-r BCP-ALL cells. (ii) In a different approach, highly selective PROTACs (A6 and B4) that degrade HDAC6 were developed, providing an alternative strategy for precise HDAC6 targeting. (iii) Recently, we introduced novel isoform specific HDAC inhibitors (4d and 4m), especially designed to address therapy resistance in leukemia cells with reduced off-target toxicity. Notably, these inhibitors exhibited superior anti-leukemic efficacy compared to clinically approved pan-HDAC inhibitors. Inhibitor 4d displayed a strong synergy with standard chemotherapeutics, showed favorable pharmacokinetic properties and notable leukemia suppression in preclinical models.

III. High throughput drug screening: Through tailored drug repurposing screens, we identified hits that selectively targeting high-risk pediatric BCP-ALL cells, particularly with PAX5/KMT2A/CRLF2 rearrangements, underscoring the potential of personalized drug screening to reveal novel therapeutic options.

Together, these strategies offer new avenues for enhancing pediatric leukemia treatment.

5. Summary – Deutsch

Akute Leukämien im Kindesalter stellen trotz therapeutischer Fortschritte weiterhin eine erhebliche Herausforderung dar, da Polychemotherapie- und Immuntherapie-Regime erhebliche Toxizitäten verursachen und die Lebensqualität der Patienten beeinträchtigen. Die Rezidivrate liegt bei etwa 15–20 %, was die Prognose insbesondere bei Hochrisikopatienten erschwert. Zukünftige Strategien sollten darauf abzielen, nachhaltige molekulare Remissionen zu erreichen, die Chemotherapie-Intensität zu reduzieren und die Abhängigkeit von hämatopoetischen Stammzelltransplantationen zu minimieren.

I. HSP90 als therapeutisches Ziel bei Leukämie: HSP90, ein molekulares Chaperon, ist bei Leukämie häufig überexprimiert und stabilisiert mutierte oder überexprimierte Onkogene, indem es deren Abbau verhindert. Zu den entscheidenden HSP90-Klientenproteinen in der Leukämie gehören mutiertes BCR::ABL1, TP53, FLT3::ITD und MYC. Während die Hemmung von HSP90 ein therapeutisches Potenzial hat, aktivieren herkömmliche HSP90-Inhibitoren oft eine pro-survival

Hitzeschockreaktion (HSR) als Resistenzmechanismus, was ihre klinische Wirksamkeit einschränkt. Um dies zu umgehen, entwickelten wir zwei neuartige HSP90-Inhibitoren, die die C-terminale Dimerisierung anvisieren: Aminoxyrone (AX) und 5b. Diese Inhibitoren zielen auf *BCR::ABL1*$^{+}$ Leukämiezellen myeloischer oder lymphatischer Herkunft ab, die eine Resistenz gegenüber mehreren Tyrosinkinase-Inhibitoren aufweisen, einschließlich der BCR::ABL1(T315I)-getriebenen Krankheit. Sie erreichen dies durch die Störung der mit der BCR::ABL1-Kinase assoziierten Signalwege und können zudem Apoptose in der leukämischen Stammzellfraktion induzieren – ohne jedoch eine HSR auszulösen. Einschränkungen in der Pharmakokinetik begrenzen jedoch derzeit ihre klinische Anwendbarkeit. Alternativ dazu zeigen unsere neuesten Ergebnisse, dass die stressinduzierbare HSP90α-Isoform eine entscheidende Rolle bei der Resistenz gegenüber HSP90-Inhibitoren spielt. Wir haben eine neuartige Kombination mit CDK7-Inhibitoren entwickelt, die die Transkription von HSR-bezogenen Genen unterdrückt und die Wirksamkeit der auf HSP90 abzielenden Therapien verbessert.

II. Zielgerichtete epigenetische Modifikatoren: Ein weiterer Forschungsschwerpunkt untersucht epigenetische Modifikatoren, insbesondere Histondeacetylase (HDAC)-Enzyme. Angesichts der schweren Nebenwirkungen, die mit pan-HDAC-Inhibitoren verbunden sind, würde die Entwicklung von isoformspezifischen HDAC-Inhibitoren einen erheblichen therapeutischen Fortschritt darstellen. HDAC6-Inhibitoren zeigen Synergien mit Proteasominhibitoren, was uns dazu veranlasste, (i) den dualen HDAC6-Proteasominhibitor RTS-V5 zu entwickeln, der eine starke Anti-Leukämie-Aktivität insbesondere gegen KMT2A-r BCP-ALL-Zellen aufweist. (ii) In einem anderen Ansatz wurden hochselektive PROTACs (A6 und B4) entwickelt, die HDAC6 abbauen und eine präzise Ansteuerung von HDAC6 ermöglichen. (iii) Kürzlich führten wir neuartige isoformspezifische HDAC-Inhibitoren (4d und 4m) ein, die speziell entwickelt wurden, um Therapieresistenz in Leukämiezellen mit reduzierter Off-Target-Toxizität zu adressieren. Bemerkenswerterweise zeigten diese Inhibitoren eine überlegene anti-leukämische Wirksamkeit im Vergleich zu klinisch zugelassenen pan-HDAC-Inhibitoren. Inhibitor 4d zeigte eine starke Synergie mit Standard-Chemotherapeutika und günstige

pharmakokinetische Eigenschaften sowie eine signifikante Leukämieunterdrückung in präklinischen Modellen.

III. Hochdurchsatz-Drogenscreening: Durch Drug-Repurposing-Screenings identifizierten wir Wirkstoffe, die gezielt hochriskante pädiatrische BCP-ALL-Zellen mit PAX5-, KMT2A- oder CRLF2-Rearrangements angreifen. Dies unterstreicht das Potenzial personalisierter Medikamentenscreenings zur Entdeckung neuer Therapieoptionen.

Zusammen bieten diese Strategien vielversprechende Ansätze zur Verbesserung der Behandlung akuter Leukämien im Kindesalter.

6. References

1. Hanahan, D. Hallmarks of Cancer: New Dimensions. *Cancer Discov* **12**, 31-46 (2022).
2. Hunger, S.P. & Mullighan, C.G. Acute Lymphoblastic Leukemia in Children. *N Engl J Med* **373**, 1541-1552 (2015).
3. Pagliaro, L.*, et al.* Acute lymphoblastic leukaemia. *Nat Rev Dis Primers* **10**, 41 (2024).
4. Egan, G. & Tasian, S.K. Relapsed pediatric acute myeloid leukaemia: state-of-the-art in 2023. *Haematologica* **108**, 2275-2288 (2023).
5. Eiser, C.*, et al.* Prospective evaluation of quality of life in children treated in UKALL 2003 for acute lymphoblastic leukaemia: A cohort study. *Pediatr Blood Cancer* **64**(2017).
6. Vora, A.*, et al.* Treatment reduction for children and young adults with low-risk acute lymphoblastic leukaemia defined by minimal residual disease (UKALL 2003): a randomised controlled trial. *Lancet Oncol* **14**, 199-209 (2013).
7. Schmiegelow, K.*, et al.* Consensus definitions of 14 severe acute toxic effects for childhood lymphoblastic leukaemia treatment: a Delphi consensus. *Lancet Oncol* **17**, e231-e239 (2016).
8. He, J.*, et al.* Biological Markers of High-Risk Childhood Acute Lymphoblastic Leukemia. *Cancers (Basel)* **16**(2024).
9. Matz, J.M., Blake, M.J., Tatelman, H.M., Lavoi, K.P. & Holbrook, N.J. Characterization and regulation of cold-induced heat shock protein expression in mouse brown adipose tissue. *American Journal of Physiology-Regulatory, Integrative and Comparative Physiology* **269**, R38-R47 (1995).
10. Cao, Y.*, et al.* TGF-β1 mediates 70-kDa heat shock protein induction due to ultraviolet irradiation in human skin fibroblasts. *Pflügers Archiv* **438**, 239-244 (1999).
11. Zuo, W.F.*, et al.* Heat shock proteins as hallmarks of cancer: insights from molecular mechanisms to therapeutic strategies. *J Hematol Oncol* **17**, 81 (2024).
12. Cabaud-Gibouin, V.*, et al.* Heat-Shock Proteins in Leukemia and Lymphoma: Multitargets for Innovative Therapeutic Approaches. *Cancers (Basel)* **15**(2023).
13. Calderwood, S.K. & Gong, J. Heat Shock Proteins Promote Cancer: It's a Protection Racket. *Trends in Biochemical Sciences* **41**, 311-323 (2016).

14. Whitesell, L. & Lindquist, S.L. HSP90 and the chaperoning of cancer. *Nature Reviews Cancer* **5**, 761-772 (2005).
15. Pick, E.*, et al.* High HSP90 Expression Is Associated with Decreased Survival in Breast Cancer. *Cancer Research* **67**, 2932-2937 (2007).
16. Butler, L.M., Ferraldeschi, R., Armstrong, H.K., Centenera, M.M. & Workman, P. Maximizing the therapeutic potential of HSP90 inhibitors. *Molecular cancer research : MCR* **13**, 1445-1451 (2015).
17. Wang, Y., Koay, Y.C. & McAlpine, S.R. How Selective are Hsp90 Inhibitors for Cancer Cells over Normal Cells? *ChemMedChem* **12**, 353-357 (2017).
18. Mahalingam, D.*, et al.* Targeting HSP90 for cancer therapy. *British journal of cancer* **100**, 1523-1529 (2009).
19. Khajapeer, K.V. & Baskaran, R. Hsp90 Inhibitors for the Treatment of Chronic Myeloid Leukemia. *Leukemia research and treatment* **2015**, 757694 (2015).
20. Lazenby, M., Hills, R., Burnett, A.K. & Zabkiewicz, J. The HSP90 inhibitor ganetespib: A potential effective agent for Acute Myeloid Leukemia in combination with cytarabine. *Leukemia research* **39**, 617-624 (2015).
21. Miyata, Y., Nakamoto, H. & Neckers, L. The therapeutic target Hsp90 and cancer hallmarks. *Current pharmaceutical design* **19**, 347-365 (2013).
22. Bhatia, S.*, et al.* Targeting HSP90 dimerization via the C terminus is effective in imatinib-resistant CML and lacks the heat shock response. *Blood* **132**, 307-320 (2018).
23. Peng, C.*, et al.* Inhibition of heat shock protein 90 prolongs survival of mice with BCR-ABL-T315I-induced leukemia and suppresses leukemic stem cells. *Blood* **110**, 678-685 (2007).
24. Zhang, P.*, et al.* Inflammation accelerates BCR-ABL1+ B-ALL development through upregulation of AID. *Blood Adv* **6**, 4060-4072 (2022).
25. Subbarao Sreedhar, A., Kalmár, É., Csermely, P. & Shen, Y.-F. Hsp90 isoforms: functions, expression and clinical importance. *FEBS Letters* **562**, 11-15 (2004).
26. Tang, X.*, et al.* Heterogeneous Responses and Isoform Compensation the Dim Therapeutic Window of Hsp90 ATP-Binding Inhibitors in Cancer. *Mol Cell Biol* **42**, e0045921 (2022).
27. Taherian, A., Krone, P.H. & Ovsenek, N. A comparison of Hsp90alpha and Hsp90beta interactions with cochaperones and substrates. *Biochem Cell Biol* **86**, 37-45 (2008).
28. Sanchez, E.R. Chaperoning steroidal physiology: lessons from mouse genetic models of Hsp90 and its cochaperones. *Biochim Biophys Acta* **1823**, 722-729 (2012).
29. Hoter, A., El-Sabban, M.E. & Naim, H.Y. The HSP90 Family: Structure, Regulation, Function, and Implications in Health and Disease. *Int J Mol Sci* **19**(2018).
30. Sreedhar, A.S., Kalmar, E., Csermely, P. & Shen, Y.F. Hsp90 isoforms: functions, expression and clinical importance. *FEBS Lett* **562**, 11-15 (2004).
31. Tang, X.*, et al.* Heat shock protein-90alpha (Hsp90alpha) stabilizes hypoxia-inducible factor-1alpha (HIF-1alpha) in support of spermatogenesis and tumorigenesis. *Cancer Gene Ther* **28**, 1058-1070 (2021).
32. Voss, A.K., Thomas, T. & Gruss, P. Mice lacking HSP90beta fail to develop a placental labyrinth. *Development* **127**, 1-11 (2000).
33. Koren, J., 3rd & Blagg, B.S.J. The Right Tool for the Job: An Overview of Hsp90 Inhibitors. *Adv Exp Med Biol* **1243**, 135-146 (2020).
34. Rajan, A.*, et al.* A Phase I Study of PF-04929113 (SNX-5422), an Orally Bioavailable Heat Shock Protein 90 Inhibitor, in Patients with Refractory Solid Tumor Malignancies and Lymphomas. *Clinical Cancer Research* **17**, 6831-6839 (2011).
35. Wang, Y. & McAlpine, S.R. N-terminal and C-terminal modulation of Hsp90 produce dissimilar phenotypes. *Chemical communications* **51**, 1410-1413 (2015).

36. Mendillo, M.L., Pincus, D. & Scherz-Shouval, R. *HSF1 and Molecular Chaperones in Biology and Cancer*, (Springer International Publishing, 2020).
37. Dayalan Naidu, S. & Dinkova-Kostova, A.T. Regulation of the mammalian heat shock factor 1. *The FEBS Journal* **284**, 1606-1627 (2017).
38. Wang, Y. & McAlpine, S.R. Heat-shock protein 90 inhibitors: will they ever succeed as chemotherapeutics? *Future Med Chem* **7**, 87-90 (2015).
39. Ratzke, C., Mickler, M., Hellenkamp, B., Buchner, J. & Hugel, T. Dynamics of heat shock protein 90 C-terminal dimerization is an important part of its conformational cycle. *Proceedings of the National Academy of Sciences of the United States of America* **107**, 16101-16106 (2010).
40. Ciglia, E.*, et al.* Resolving hot spots in the C-terminal dimerization domain that determine the stability of the molecular chaperone Hsp90. *PLoS One* **9**, e96031 (2014).
41. Bopp, B.*, et al.* Design and biological testing of peptidic dimerization inhibitors of human Hsp90 that target the C-terminal domain. *Biochim Biophys Acta* **1860**, 1043-1055 (2016).
42. Byrd, J.C. HSP90 inhibition without heat shock response. *Blood* **132**, 241-242 (2018).
43. Bhatia, S.*, et al.* Development of a First-in-Class Small-Molecule Inhibitor of the C-Terminal Hsp90 Dimerization. *ACS Central Science* **8**, 636-655 (2022).
44. Wurnig, S.*, et al.* Development of the first geldanamycin-based HSP90 degraders. *Frontiers in Chemistry* **11**(2023).
45. Pillarsetty, N.*, et al.* Paradigms for Precision Medicine in Epichaperome Cancer Therapy. *Cancer Cell* **36**, 559-573 e557 (2019).
46. Hoy, S.M. Pimitespib: First Approval. *Drugs* **82**, 1413-1418 (2022).
47. Vogt, M.*, et al.* Co-targeting HSP90 alpha and CDK7 overcomes resistance against HSP90 inhibitors in BCR-ABL1+ leukemia cells. *Cell Death & Disease* **14**, 799 (2023).
48. DepMap, Broad (2019): DepMap 19Q4 Public. figshare. Dataset doi:10.6084/m9.figshare.11384241.v2
49. Peng, Y.*, et al.* Effect of HSP90AB1 and CC domain interaction on Bcr-Abl protein cytoplasm localization and function in chronic myeloid leukemia cells. *Cell Commun Signal* **19**, 71 (2021).
50. Eustace, B.K.*, et al.* Functional proteomic screens reveal an essential extracellular role for hsp90α in cancer cell invasiveness. *Nature Cell Biology* **6**, 507-514 (2004).
51. Stellas, D., El Hamidieh, A. & Patsavoudi, E. Monoclonal antibody 4C5 prevents activation of MMP2 and MMP9 by disrupting their interaction with extracellular HSP90 and inhibits formation of metastatic breast cancer cell deposits. *BMC Cell Biology* **11**, 51 (2010).
52. Tsutsumi, S.*, et al.* A small molecule cell-impermeant Hsp90 antagonist inhibits tumor cell motility and invasion. *Oncogene* **27**, 2478-2487 (2008).
53. Zou, M.*, et al.* Evolutionarily conserved dual lysine motif determines the non-chaperone function of secreted Hsp90alpha in tumour progression. *Oncogene* **36**, 2160-2171 (2017).
54. Wang, X.*, et al.* The regulatory mechanism of Hsp90alpha secretion and its function in tumor malignancy. *Proc Natl Acad Sci U S A* **106**, 21288-21293 (2009).
55. Fisher, R.P. Cdk7: a kinase at the core of transcription and in the crosshairs of cancer drug discovery. *Transcription* **10**, 47-56 (2019).
56. Cheng, Y.*, et al.* Targeting epigenetic regulators for cancer therapy: mechanisms and advances in clinical trials. *Signal Transduct Target Ther* **4**, 62 (2019).
57. Timp, W. & Feinberg, A.P. Cancer as a dysregulated epigenome allowing cellular growth advantage at the expense of the host. *Nat Rev Cancer* **13**, 497-510 (2013).
58. Bates, S.E. Epigenetic Therapies for Cancer. *N Engl J Med* **383**, 650-663 (2020).
59. Wang, P., Wang, Z. & Liu, J. Role of HDACs in normal and malignant hematopoiesis. *Mol Cancer* **19**, 5 (2020).

60. Yang, X.J. & Seto, E. HATs and HDACs: from structure, function and regulation to novel strategies for therapy and prevention. *Oncogene* **26**, 5310-5318 (2007).
61. Barneda-Zahonero, B. & Parra, M. Histone deacetylases and cancer. *Mol Oncol* **6**, 579-589 (2012).
62. Liu, X.L.*, et al.* Role of epigenetic in leukemia: From mechanism to therapy. *Chem Biol Interact* **317**, 108963 (2020).
63. Heideman, M.R.*, et al.* Sin3a-associated Hdac1 and Hdac2 are essential for hematopoietic stem cell homeostasis and contribute differentially to hematopoiesis. *Haematologica* **99**, 1292-1303 (2014).
64. Wei, Y.*, et al.* Ncor2 is required for hematopoietic stem cell emergence by inhibiting Fos signaling in zebrafish. *Blood* **124**, 1578-1585 (2014).
65. Ozawa, Y.*, et al.* Histone deacetylase 3 associates with and represses the transcription factor GATA-2. *Blood* **98**, 2116-2123 (2001).
66. Conneely, S.E. & Stevens, A.M. Acute Myeloid Leukemia in Children: Emerging Paradigms in Genetics and New Approaches to Therapy. *Curr Oncol Rep* **23**, 16 (2021).
67. Fennell, K.A., Bell, C.C. & Dawson, M.A. Epigenetic therapies in acute myeloid leukemia: where to from here? *Blood* **134**, 1891-1901 (2019).
68. Nair, R., Salinas-Illarena, A. & Baldauf, H.M. New strategies to treat AML: novel insights into AML survival pathways and combination therapies. *Leukemia* **35**, 299-311 (2021).
69. Suraweera, A., O'Byrne, K.J. & Richard, D.J. Combination Therapy With Histone Deacetylase Inhibitors (HDACi) for the Treatment of Cancer: Achieving the Full Therapeutic Potential of HDACi. *Front Oncol* **8**, 92 (2018).
70. Zhou, M.*, et al.* Combining histone deacetylase inhibitors (HDACis) with other therapies for cancer therapy. *Eur J Med Chem* **226**, 113825 (2021).
71. Shah, R.R. Safety and Tolerability of Histone Deacetylase (HDAC) Inhibitors in Oncology. *Drug Saf* **42**, 235-245 (2019).
72. Chen, J., Ren, J.J., Cai, J. & Wang, X. Efficacy and safety of HDACIs in the treatment of metastatic or unresectable renal cell carcinoma with a clear cell phenotype: A systematic review and meta-analysis. *Medicine (Baltimore)* **100**, e26788 (2021).
73. Gryder, B.E., Sodji, Q.H. & Oyelere, A.K. Targeted cancer therapy: giving histone deacetylase inhibitors all they need to succeed. *Future Med Chem* **4**, 505-524 (2012).
74. Li, T.*, et al.* Histone deacetylase 6 in cancer. *J Hematol Oncol* **11**, 111 (2018).
75. Li, Y., Shin, D. & Kwon, S.H. Histone deacetylase 6 plays a role as a distinct regulator of diverse cellular processes. *FEBS J* **280**, 775-793 (2013).
76. Pezzotta, A.*, et al.* HDAC6 inhibition decreases leukemic stem cell expansion driven by Hedgehog hyperactivation by restoring primary ciliogenesis. *Pharmacol Res* **183**, 106378 (2022).
77. Losson, H., Schnekenburger, M., Dicato, M. & Diederich, M. HDAC6-an Emerging Target Against Chronic Myeloid Leukemia? *Cancers (Basel)* **12**(2020).
78. Hackanson, B.*, et al.* HDAC6 as a target for antileukemic drugs in acute myeloid leukemia. *Leukemia research* **36**, 1055-1062 (2012).
79. Alves Avelar, L.A.*, et al.* Synergistic induction of apoptosis in resistant head and neck carcinoma and leukemia by alkoxyamide-based histone deacetylase inhibitors. *Eur J Med Chem* **211**, 113095 (2021).
80. Pflieger, M.*, et al.* Oxa Analogues of Nexturastat A Demonstrate Improved HDAC6 Selectivity and Superior Antileukaemia Activity. *ChemMedChem* **16**, 1798-1803 (2021).
81. Ressing, N.*, et al.* Multicomponent Synthesis, Binding Mode, and Structure-Activity Relationship of Selective Histone Deacetylase 6 (HDAC6) Inhibitors with Bifurcated Capping Groups. *J Med Chem* **63**, 10339-10351 (2020).

82. Schaker-Hubner, L.*, et al.* 4-Acyl Pyrrole Capped HDAC Inhibitors: A New Scaffold for Hybrid Inhibitors of BET Proteins and Histone Deacetylases as Antileukemia Drug Leads. *J Med Chem* **64**, 14620-14646 (2021).
83. Selg, C.*, et al.* Borinostats: solid-phase synthesis of carborane-capped histone deacetylase inhibitors with a tailor-made selectivity profile. *Chem Sci* **12**, 11873-11881 (2021).
84. Sinatra, L.*, et al.* Hydroxamic Acids Immobilized on Resins (HAIRs): Synthesis of Dual-Targeting HDAC Inhibitors and HDAC Degraders (PROTACs). *Angew Chem Int Ed Engl* **59**, 22494-22499 (2020).
85. von Bredow, L.*, et al.* Synthesis, Antiplasmodial, and Antileukemia Activity of Dihydroartemisinin-HDAC Inhibitor Hybrids as Multitarget Drugs. *Pharmaceuticals (Basel)* **15**(2022).
86. Hideshima, T., Richardson, P.G. & Anderson, K.C. Mechanism of action of proteasome inhibitors and deacetylase inhibitors and the biological basis of synergy in multiple myeloma. *Mol Cancer Ther* **10**, 2034-2042 (2011).
87. Bhatia, S.*, et al.* Discovery of the First-in-Class Dual Histone Deacetylase-Proteasome Inhibitor. *J Med Chem* **61**, 10299-10309 (2018).
88. Tretbar, M.*, et al.* Preferential HDAC6 inhibitors derived from HPOB exhibit synergistic antileukemia activity in combination with decitabine. *Eur J Med Chem* **272**, 116447 (2024).
89. Sinatra, L.*, et al.* Solid-Phase Synthesis of Cereblon-Recruiting Selective Histone Deacetylase 6 Degraders (HDAC6 PROTACs) with Antileukemic Activity. *J Med Chem* **65**, 16860-16878 (2022).
90. Fischer, F.*, et al.* Deciphering the Therapeutic Potential of Novel Pentyloxyamide-Based Class I, IIb HDAC Inhibitors against Therapy-Resistant Leukemia. *J Med Chem* (2024).
91. Hull, E.E., Montgomery, M.R. & Leyva, K.J. HDAC Inhibitors as Epigenetic Regulators of the Immune System: Impacts on Cancer Therapy and Inflammatory Diseases. *Biomed Res Int* **2016**, 8797206 (2016).
92. Flumann, R.*, et al.* An Autochthonous Mouse Model of Myd88- and BCL2-Driven Diffuse Large B-cell Lymphoma Reveals Actionable Molecular Vulnerabilities. *Blood Cancer Discov* **2**, 70-91 (2021).
93. Palmi, C.*, et al.* Definition and Prognostic Value of Ph-like and IKZF1plus Status in Children With Down Syndrome and B-cell Precursor Acute Lymphoblastic Leukemia. *Hemasphere* **7**, e892 (2023).
94. Fazio, G.*, et al.* PAX5 fusion genes are frequent in poor risk childhood acute lymphoblastic leukaemia and can be targeted with BIBF1120. *EBioMedicine* **83**, 104224 (2022).
95. Stachura, P.*, et al.* Unleashing T cell anti-tumor immunity: new potential for 5-Nonloxytryptamine as an agent mediating MHC-I upregulation in tumors. *Mol Cancer* **22**, 136 (2023).
96. Oikonomou, A.*, et al.* Synergistic drug interactions of the histone deacetylase inhibitor givinostat (ITF2357) in CRLF2-rearranged pediatric B-cell precursor acute lymphoblastic leukemia identified by high-throughput drug screening. *Heliyon* **10**, e34033 (2024).
97. Oikonomou, A.*, et al.* High-throughput screening as a drug repurposing strategy for poor outcome subgroups of pediatric B-cell precursor Acute Lymphoblastic Leukemia. *Biochem Pharmacol* **217**, 115809 (2023).
98. Schopf, F.H., Biebl, M.M. & Buchner, J. The HSP90 chaperone machinery. *Nature reviews. Molecular cell biology* **18**, 345-360 (2017).
99. Sanchez, J., Carter, T.R., Cohen, M.S. & Blagg, B.S. Old and New Approaches to Target the Hsp90 Chaperone. *Current cancer drug targets* (2019).
100. Geller, R., Taguwa, S. & Frydman, J. Broad action of Hsp90 as a host chaperone required for viral replication. *Biochim Biophys Acta* **1823**, 698-706 (2012).

101. Sanchez, J., Carter, T.R., Cohen, M.S. & Blagg, B.S.J. Old and New Approaches to Target the Hsp90 Chaperone. *Current cancer drug targets* **20**, 253-270 (2020).
102. Hosseini, M.S., Sanaat, Z., Akbarzadeh, M.A., Vaez-Gharamaleki, Y. & Akbarzadeh, M. Histone deacetylase inhibitors for leukemia treatment: current status and future directions. *Eur J Med Res* **29**, 514 (2024).
103. Goldman, S.L.*, et al.* Epigenetic Modifications in Acute Myeloid Leukemia: Prognosis, Treatment, and Heterogeneity. *Front Genet* **10**, 133 (2019).
104. San Jose-Eneriz, E., Gimenez-Camino, N., Agirre, X. & Prosper, F. HDAC Inhibitors in Acute Myeloid Leukemia. *Cancers (Basel)* **11**(2019).
105. Kawaguchi, Y.*, et al.* The deacetylase HDAC6 regulates aggresome formation and cell viability in response to misfolded protein stress. *Cell* **115**, 727-738 (2003).

7. Acknowledgements

I am deeply thankful to Prof. Dr. Arndt Borkhardt for his encouragement and support. From my very first days in his department, I have thrived in an intellectually stimulating environment, and I feel incredibly privileged to work under his guidance. His mentorship has been invaluable to my growth as a scientist.

I would also like to express my gratitude to my other mentors, Prof. Julia Hauer, Prof. Aleksandra Pandyra, Prof. Holger Gohlke and Dr. Ute Fischer. Each of you has imparted skills and wisdom that have shaped me, ranging from scientific rigor to teaching, presenting research and remaining calm when faced with challenges. Aleks, in particular, has consistently encouraged me to complete my habilitation and has been a supportive guide, not only as a colleague but also as a friend. I am also grateful to collaborators such as Prof. Finn K. Hansen and Prof. Thomas Kurz; working with both of you has been a pleasure.

My deepest thanks go to my team, “Team Target”—Melina Vogt, Julian Schliehe-Diecks, Jia-Wey Tu, Titus Watrin, Marie Kemkes, Katerina Scharov, Philip Gebing, Niklas Dienstbier, Astrid Götz, Melf Sönnichsen, Julian Hogenkamp and Silke Furlan. Your hard work and dedication have been essential to this work. I am grateful for your commitment and trust throughout our journey together.

To my colleagues and friends in the lab, Daniel Scholtyssik, Dr. Rabea Wagener and Daniel Picard, thank you for your company and support.

Lastly, I would like to extend a special thanks to my wife, Supriya, for her unwavering encouragement (nagging) and support, and to my family for their love and support.

8. Thesis Publications

In this habilitation thesis the following original works are summarized:

IF is from 2023, (Shared last author)*

1. **Bhatia S**, Diedrich D, Frieg B, Ahlert H, Stein S, Bopp B, Lang F, Zang T, Kröger T, Ernst T, Kögler G, Krieg A, Lüdeke S, Kunkel H, Rodrigues Moita AJ, Kassack MU, Marquardt V, Opitz FV, Oldenburg M, Remke M, Babor F, Grez M, Hochhaus A, Borkhardt A, Groth G, Nagel-Steger L, Jose J, Kurz T, Gohlke H, Hansen FK, Hauer J. Targeting HSP90 dimerization via the C terminus is effective in imatinib-resistant CML and lacks the heat shock response. Blood. 2018 Jul 19;132(3):307-320. doi: 10.1182/blood-2017-10-810986. PubMed PMID: 29724897. IF: 21

2. **Bhatia S**, Spanier L, Bickel D, Dienstbier N, Woloschin V, Vogt M, Pols H, Lungerich B, Reiners J, Aghaallaei N, Diedrich D, Frieg B, Schliehe-Diecks J, Bopp B, Lang F, Gopalswamy M, Loschwitz J, Bajohgli B, Skokowa J, Borkhardt A, Hauer J, Hansen FK, Smits SHJ, Jose J, Gohlke H, Kurz T. Development of a First-in-Class Small-Molecule Inhibitor of the C-Terminal Hsp90 Dimerization. **ACS Cent Sci. 2022** May 25;8(5):636-655. doi: 10.1021/acscentsci.2c00013. Epub 2022 Apr 27. PubMed PMID: 35647282. IF: 12.7

3. Vogt, M.; Dienstbier, N.; Schliehe-Diecks, J.; Scharov, K.; Tu, J.-W.; Gebing, P.; Hogenkamp, J.; Bilen, B.-S.; Furlan, S.; Picard, D.; Remke, M.; Yasin, L.; Bickel, D.; Kalia, M.; Iacoangeli, A.; Lenz, T.; Stühler, K.; Pandyra, A. A.; Hauer, J.; Fischer, U.; Wagener, R.; Borkhardt, A.; **Bhatia, S**. Co-targeting HSP90 alpha and CDK7 overcomes resistance against HSP90 inhibitors in BCR-ABL1+ leukemia cells. **Cell Death & Disease 2023**, 14 (12), 799. PubMed PMID: 38057328. IF: 8.1

4. **Bhatia S**, Krieger V, Groll M, Osko JD, Reßing N, Ahlert H, Borkhardt A, Kurz T, Christianson DW, Hauer J, Hansen FK. Discovery of the First-in-Class Dual Histone Deacetylase-Proteasome Inhibitor. **J Med Chem. 2018** Nov 8. doi: 10.1021/acs.jmedchem.8b01487. PubMed PMID: 30365892. IF: 6.9

5. Sinatra L, Yang J, Schliehe-Diecks J, Dienstbier N, Vogt M, Gebing P, Bachmann LM, Sönnichsen M, Lenz T, Stühler K, Schöler A, Borkhardt A, **Bhatia S***, Hansen FK*. Solid-Phase Synthesis of Cereblon-Recruiting Selective Histone Deacetylase 6 Degraders (HDAC6 PROTACs) with Antileukemic Activity. **J Med Chem. 2022** Dec 22;65(24):16860-16878. doi: 10.1021/acs.jmedchem.2c01659. Epub 2022 Dec 6. PubMed PMID: 36473103. IF: 6.9

6. Fischer F, Schliehe-Diecks J, Tu JW, Gangnus T, Ho YL, Hebeis M, Alves Avelar LA, Scharov K, Watrin T, Kemkes M, Stachura P, Daugs K, Biermann L, Kremeyer J, Horstick N, Span I, Pandyra AA, Borkhardt A, Gohlke H, Kassack MU, Burckhardt BB, **Bhatia S***, Kurz T*. Deciphering the Therapeutic Potential of Novel Pentyloxyamide-Based Class I, IIb HDAC Inhibitors against Therapy-Resistant Leukemia. J Med Chem. 2024 Nov 27;. doi: 10.1021/acs.jmedchem.4c02024. PubMed PMID: 39602240.IF: 6.9

9. Declarations

I hereby declare that with regards to the work presented in my habilitation thesis, ethical principles to ensure good scientific practice were adhered to by me.

Düsseldorf, 02.12.2024 Dr. rer. nat. Sanil Bhatia

I hereby declare that no other habilitation procedures have been initiated or and that there have been no other unsuccessful habilitation attempts.

Düsseldorf, 02.12.2024 Dr. rer. nat. Sanil Bhatia

I hereby declare in lieu of an oath that I have independently made that the contributions to the publications on which on which my habilitation thesis is based have been made independently.

Düsseldorf, 02.12.2024 Dr. rer. nat. Sanil Bhatia

10. Appended Publications

The publications included in this habilitation thesis are presented with the kind permission of the respective publishers or under their free copyright agreements, where applicable.

Die in dieser Habilitationsschrift enthaltenen Publikationen werden mit der freundlichen Genehmigung der jeweiligen Verlage oder im Rahmen ihrer freien Copyright-Vereinbarungen, soweit zutreffend, eingebunden.

blood®

Regular Article

MYELOID NEOPLASIA

Targeting HSP90 dimerization via the C terminus is effective in imatinib-resistant CML and lacks the heat shock response

Sanil Bhatia,[1] Daniela Diedrich,[2] Benedikt Frieg,[2,3] Heinz Ahlert,[1] Stefan Stein,[4] Bertan Bopp,[5] Franziska Lang,[1] Tao Zang,[6,7] Tobias Kröger,[2] Thomas Ernst,[8] Gesine Kögler,[9] Andreas Krieg,[10] Steffen Lüdeke,[11] Hana Kunkel,[4] Ana J. Rodrigues Moita,[2] Matthias U. Kassack,[2] Viktoria Marquardt,[1,2,12,13] Friederike V. Opitz,[1] Marina Oldenburg,[1] Marc Remke,[1,12,13] Florian Babor,[1] Manuel Grez,[4] Andreas Hochhaus,[8] Arndt Borkhardt,[1] Georg Groth,[14] Luitgard Nagel-Steger,[6,7] Joachim Jose,[5] Thomas Kurz,[2] Holger Gohlke,[2,3] Finn K. Hansen,[2,15,*] and Julia Hauer[1,*]

[1]Department of Pediatric Oncology, Hematology and Clinical Immunology, Medical Faculty, and [2]Institute for Pharmaceutical and Medicinal Chemistry, Heinrich Heine University Düsseldorf, Düsseldorf, Germany; [3]John von Neumann Institute for Computing, Jülich Supercomputing Centre, Institute for Complex Systems–Structural Biochemistry (ICS-6), Forschungszentrum Jülich GmbH, Jülich, Germany; [4]Institute for Tumor Biology and Experimental Therapy, Georg-Speyer-Haus, Frankfurt, Germany; [5]Institute for Pharmaceutical and Medicinal Chemistry, PharmaCampus, Westphalian Wilhelms University, Münster, Germany; [6]Institute for Physical Biology, Heinrich Heine University Düsseldorf, Düsseldorf, Germany; [7]Institute of Complex Systems, Structural Biochemistry (ICS-6), Forschungszentrum Jülich GmbH, Jülich, Germany; [8]Hematology/Oncology, Internal Medicine II, Jena University Hospital, Jena, Germany; [9]Institute for Transplantation Diagnostics and Cell Therapeutics and [10]Department of Surgery (A), Heinrich Heine University Düsseldorf, Düsseldorf, Germany; [11]Institute of Pharmaceutical Sciences, University of Freiburg, Freiburg, Germany; [12]Institute of Neuropathology, Medical Faculty, Heinrich Heine University Düsseldorf, Düsseldorf, Germany; [13]Division of Pediatric Neuro-Oncogenomics, German Cancer Consortium, partner site University Hospital Düsseldorf, Düsseldorf, Germany; [14]Institute for Biochemical Plant Physiology, Heinrich Heine University Düsseldorf, Düsseldorf, Germany; and [15]Pharmaceutical/Medicinal Chemistry, Institute of Pharmacy, Leipzig University, Leipzig, Germany

KEY POINTS

- **We have developed a first-in-class C-terminal HSP90 inhibitor (AX) that is effective against TKI-resistant CML and leukemic stem cells.**
- **Unlike the majority of HSP90 inhibitors, AX does not induce the HSR as a resistance mechanism.**

Heat shock protein 90 (HSP90) stabilizes many client proteins, including the BCR-ABL1 oncoprotein. BCR-ABL1 is the hallmark of chronic myeloid leukemia (CML) in which treatment-free remission (TFR) is limited, with clinical and economic consequences. Thus, there is an urgent need for novel therapeutics that synergize with current treatment approaches. Several inhibitors targeting the N-terminal domain of HSP90 are under investigation, but side effects such as induction of the heat shock response (HSR) and toxicity have so far precluded their US Food and Drug Administration approval. We have developed a novel inhibitor (aminoxyrone [AX]) of HSP90 function by targeting HSP90 dimerization via the C-terminal domain. This was achieved by structure-based molecular design, chemical synthesis, and functional preclinical in vitro and in vivo validation using CML cell lines and patient-derived CML cells. AX is a promising potential candidate that induces apoptosis in the leukemic stem cell fraction ($CD34^+CD38^-$) as well as the leukemic bulk ($CD34^+CD38^+$) of primary CML and in tyrosine kinase inhibitor (TKI)–resistant cells. Furthermore, BCR-ABL1 oncoprotein and related pro-oncogenic cellular responses are downregulated, and targeting the HSP90 C terminus by AX does not induce the HSR in vitro and in vivo. We also probed the potential of AX in other therapy-refractory leukemias. Therefore, AX is the first peptidomimetic C-terminal HSP90 inhibitor with the potential to increase TFR in TKI-sensitive and refractory CML patients and also offers a novel therapeutic option for patients with other types of therapy-refractory leukemia because of its low toxicity profile and lack of HSR. (*Blood*. 2018;132(3):307-320)

Introduction

Heat shock protein 90 (HSP90) acts as a molecular chaperone, thereby ensuring correct protein folding of several oncogenic proteins involved in leukemia such as BCR-ABL1 and its downstream signaling partners.[1-5] HSP90 expression is also enriched in several leukemia subtypes, making HSP90 a promising therapeutic approach in the treatment of therapy-refractory leukemia, such as BCR-ABL1+ leukemia,[1,6-8] FLT3-ITD+ acute myeloid leukemia (AML)[9-11] and Philadelphia chromosome (Ph)-like B-cell precursor acute lymphoblastic leukemia (BCP-ALL).[12,13] Several HSP90 inhibitors have been developed, but none have been clinically approved by the US Food and Drug Association (supplemental Table 1, available on the *Blood* Web site).[8,14] The majority of the HSP90 inhibitors target the adenosine triphosphate binding pocket

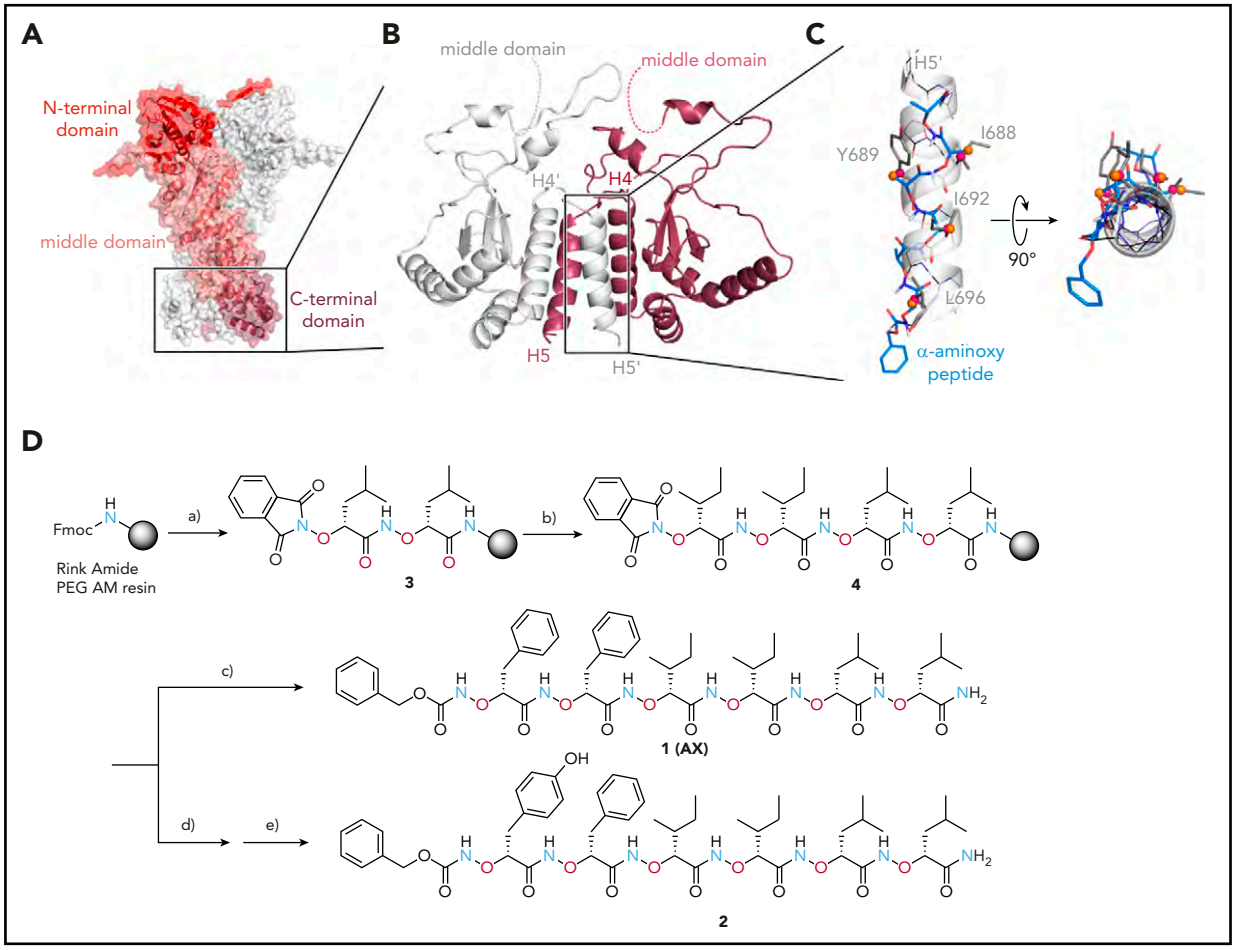

Figure 1. Design and synthesis of HSP90 CTD dimerization inhibitors. (A) Crystal structure of the HSP90 dimer from *Saccharomyces cerevisiae* (Protein Data Bank [PDB] accession number 2CG9[56]), shown as a transparent surface with cartoon representation. One monomer is colored in white and one in red, with 3 domains (N terminal, middle, and C terminal) colored in different shades of red. (B) Dimeric CTD from human HSP90 (PDB accession number 3Q6M[57]). Both subunits are colored differently. Helices H4, H4′, and H5, H5′ form the CTD dimerization interface. Dashed lines show where the middle domains would be located. (C) Overlay of a hexameric α-aminoxy peptide with all-methyl side chains (blue sticks) onto C_β atoms of hot spot amino acids I688, Y689, I692, and L696[34] (gray sticks) on helix H5′ (sequence P681 to D699) shown in transparent cartoon representation, with backbone atoms shown as black lines. The right panel shows the structures rotated by 90° such that the helix C terminus is oriented toward the viewer. C_β reference atoms of hot spot amino acids are depicted as magenta spheres and C_β atoms of the α-aminoxy peptide as orange spheres. (D) Solid-phase synthesis of α-aminoxy hexapeptides 1 (AX) and 2. Reagents and conditions: a), (i) 20% piperidine in *N,N*-dimethylformamide (DMF), room temperature, 2 × 15 min; (ii) Phth-^{NO}Leu-^{NO}Leu-OH, BOP, HOBt, *N*-ethylmorpholine (NEM) in DMF, room temperature, 24 hours; b) 5% hydrazine hydrate in MeOH, 2 × 15 min; (ii) Phth-^{NO}Ile-^{NO}Ile-OH, BOP, HOBt, NEM in DMF, room temperature, 24 hours; c) (i) 5% hydrazine hydrate in MeOH, 2 × 15 min; (ii) Cbz-^{NO}Phe-^{NO}Phe-OH, BOP, HOBt, NEM in DMF, room temperature, 24 hours; (iii) trifluoroacetic acid/triethylsilane (98:2, v:v), room temperature, 1.5 hours; d) (i) 5% hydrazine hydrate in MeOH, 2 × 15 min; (ii) Phth-^{NO}Phe-OH, BOP, HOBt, NEM in DMF, room temperature, 24 hours; e) 5% hydrazine hydrate in MeOH, 2 × 15 min; (ii) Cbz-^{NO}Tyr (*t*-Bu)-OH, BOP, HOBt, NEM in DMF, room temperature, 24 hours; (iii) trifluoroacetic acid/triethylsilane (98:2, v:v), room temperature, 1.5 hours. PEG AM resin, polyethylene glycol aminomethyl-polystyrene resin.

in the HSP90 N terminus,[14,15] leading to dissociation of heat shock factor-1 (HSF-1), which gets subsequently phosphorylated, trimerized, and translocated to the nucleus.[16] Here, HSF-1 induces the transcription of other HSPs, such as HSP70, HSP40, or HSP27, that act as antiapoptotic chaperones and protect proteins from degradation, thereby inducing a resistance mechanism called the heat shock response (HSR),[17] which potentially weakens the cytotoxic effect of HSP90 inhibitors.[14,15,18-22] C-terminal inhibitors of HSP90, such as novobiocin and its analogs, do not trigger an HSR.[23,24] The reason for the induction of the HSR by classical HSP90 inhibitors is not well understood. It has been hypothesized that inhibition of HSP90 might trigger cellular effects through mechanisms that involve targets other than HSP90 (off-target effects).[23,25] The off-target effects hypothesis is further supported by the significant difference (100-fold) between the efficiency of N-terminal inhibitors in killing cancer cells and their binding affinity to HSP90 in biochemical assays.[23] For instance, the well-known N-terminal HSP90 inhibitor AUY922 induces cell death at low nanomolar concentrations but binds to HSP90 with micromolar affinity.[23] In contrast, C-terminal HSP90 inhibitors are likely selective for HSP90 given that their cytotoxicity against cancer cells correlates with their binding affinity for HSP90.[23,24] Thus, targeting the HSP90 C-terminal domain may ultimately be the most promising route to discover safe and efficacious HSP90 inhibitors.

In the present study, we evaluated a novel HSP90 inhibitor aminoxyrone (AX) in chronic myeloid leukemia (CML), a stem cell disease that can in most cases be controlled by tyrosine kinase inhibitor (TKI) treatment, but treatment-free remission (TFR) is still not satisfactory. Approximately 40% to 60% of patients who discontinue TKI treatment develop molecular relapse and need to restart them.[26] TKIs target proliferating leukemic clones but are unable to eradicate persisting leukemia stem cells (LSCs).[27,28] This implicates long-term dependence on them with consequences for patients' quality-of-life

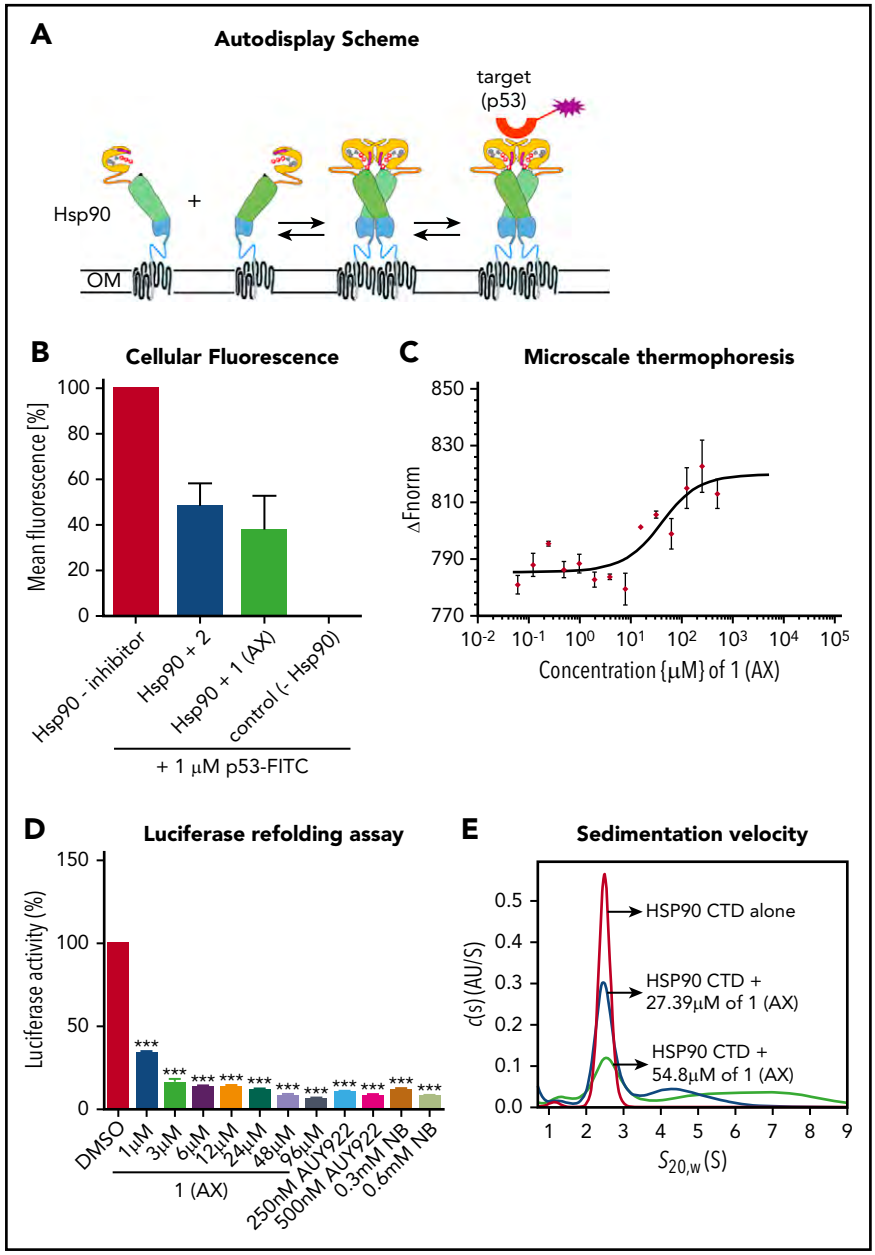

Figure 2. Selective binding of compound 1 (AX) and 2 to the HSP90 C terminus. (A) Scheme of the HSP90 dimerization assay using Autodisplay. HSP90 is displayed on the surface of *E coli* cells via the Autodisplay technique. The motility of the anchoring domain within the outer membrane of *E coli* facilitates the dimerization of Hsp90. Dimerized HSP90 on the surface of *E coli* is capable of binding to fluorescein isothiocyanate (FITC)–labeled p53. This leads to an increase of cellular fluorescence, which can then be detected via flow cytometry. Blocking the dimerization of surface displayed Hsp90 inhibits the binding of FITC-labeled p53 to HSP90 and thus leads to a decrease of cellular fluorescence.[33] (B) Inhibition of dimerization of on *E coli* cells displayed HSP90 measured via flow cytometry. Experiments were performed 3 times independently (n = 3), and error bars denote the standard deviation. Incubation of *E coli* BL21 (DE3) cells displaying HSP90 with 1 µM FITC-labeled p53 leads to a high cellular fluorescence, indicating dimerization of HSP90, whereas no cellular fluorescence was detectable in *E coli* cells without displaying HSP90 (control cells). Preincubation of cells with surface displayed HSP90 with 50 µM of 1 (AX) and 2, respectively, leads to a loss in cellular fluorescence, indicating a lowered binding affinity of FITC-labeled p53 to surface-displayed HSP90. (C) Determination of the apparent K_d value of the NT-647–labeled C-terminal domain of HSP90 and 1 (AX) via MST. A constant amount of the 50 nM–labeled C-terminal domain of HSP90 was used (n = 3). The resulting mean values were determined and used in the K_d fit formula. This yielded an apparent K_d of 27.39 µM for 1 (AX). (D) A cell-based HSP90-dependent luciferase assay was performed on stably expressing K562-luciferase cells. The extent of thermally denatured luciferase refolding (3 minutes at 50°C) in the presence of 1 (AX), NB, and AUY922 was monitored after 180 minutes. (E) Influence of 1 (AX) on the size distribution of HSP90 CTD revealed by sedimentation velocity analysis. 20 µM HSP90 CTD alone (purple), 20 µM HSP90 CTD plus 27.4 µM 1 (AX) (blue), and 20 µM HSP90 CTD plus 54.8 µM 1 (AX) (cyan) were analyzed at 50 000 rpm at 20°C, and the continuous c(s) model was applied to evaluate the data. The *s*-values were standardized to $s_{20,w}$-values. Columns depict the mean of 3 independent experiments (n = 3). Significance analyses of normally distributed data with variance similar between groups used paired, 2-tailed Student *t* test. *$P < .05$, **$P < .005$, ***$P < .001$.

and economic resources. Patients feel chronically ill, which is not related to their CML but due to the moderate to severe TKI side effects, which ~30% of patients experience.[29] For instance, acute side effects of imatinib (IM) are impaired physical and mental health status in patients <60 years of age,[30] whereas dasatinib can cause pleural effusion and arterial hypertension,[31] and nilotinib causes vascular events.[32] The use of TKIs is especially controversially discussed in young adults and children, because none of the TKIs are recommended during pregnancy and/or lactation, and their effects on fertility and skeletal growth have not been systematically analyzed. Hence, the development and characterization of novel therapeutic agents that specifically target CML LSCs and are capable of inducing sustained TFR are of enormous clinical and economic value.

We show that AX targets LSCs in CML patients and is effective in TKI-resistant CML subtypes and therefore promising in adding value to sustained TFR. In addition, inhibition of the HSP90 C terminus is effective in high-risk BCR-ABL1+ BCP-ALL, FLT3-ITD+ AML, and Ph-like BCP-ALL, comprising a relevant proportion of therapy-resistant leukemia in adults and children.

Methods

Chemical synthesis and 2-dimensional nuclear magnetic resonance spectroscopy

See supplemental Note 1 for general methods, synthetic protocols, compound characterization, and spectral data.

Circular dichroism (CD) spectroscopy

CD spectra in trifluoroethanol (50 µM, 1 mm path length) and sodium phosphate buffer (10 µM, 5 mm path length) were recorded on a J-810 Spectropolarimeter (Jasco) at 20°C and background corrected by solvent subtraction.

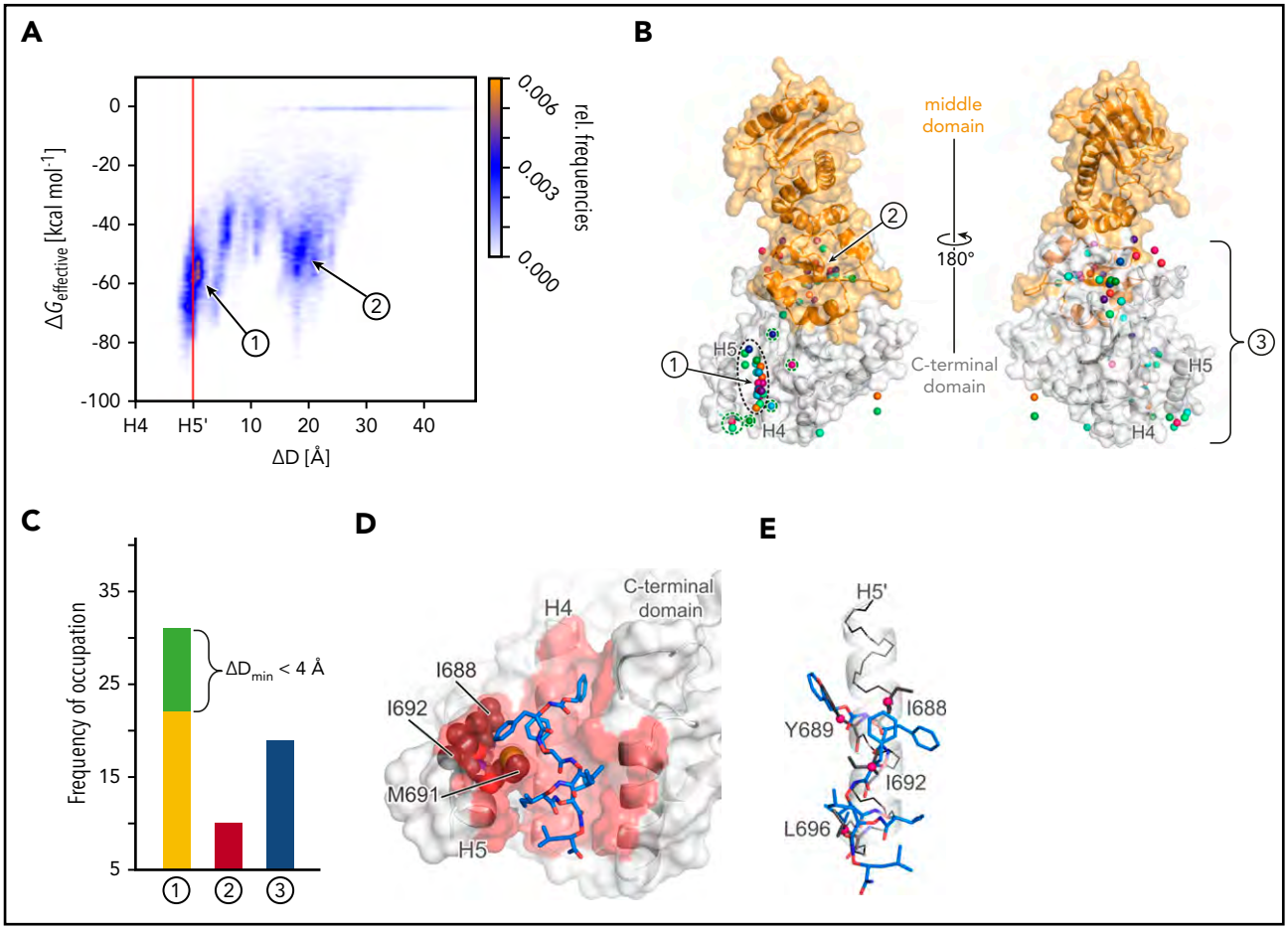

Figure 3. Results of MD simulations of free diffusion of AX. (A) Relative frequencies of ligand pose (see color scale) as a function of the relative distance between the center of mass of AX and helix H4 (ΔD) and computed effective energies of binding ($\Delta G_{effective}$). (B) Locations of the center of mass of AX (spheres) after 60 MD simulations of 400 nanosecond length each, with each simulation result colored differently. The black dashed line highlights all conformations that are bound to dimerization interface 1 with $\Delta D_{min} \leq 0$ Å, and the green dashed line highlights those with $\Delta D_{min} < 4$ Å. The protein structure is shown as surface representation with the middle domain (not present during MD simulations) in orange and the CTD in white. In the panel, the structure is rotated by 180° around the y-axis. (C) Frequency of occupation of binding sites 1 (yellow), close to 1 (green; see definition in the main text), 2 (red), or 3 (blue) by AX across 60 MD simulations. (D) Binding mode model of AX. A representative conformation of AX bound to the CTD, extracted from the MD trajectory. Residues I688, I692, and M691 (gray spheres) bind to the side chain that distinguishes AX from 2. (E) An overlay of AX onto helix H5′ (Figure 1B-C) extracted from the crystal structure (PDB accession number 3Q6M[57]). In panels D and E, AX is depicted as blue sticks; hot spot amino acids I688, Y689, I692, and L696[34] as gray sticks with C_β atoms as magenta spheres; helix H5′ as a white cartoon with black backbone atoms; and the CTD in the left panel as surface representation, with all residues within 3 Å of AX colored in red. In panels A-C, 1, 2, and 3 denote the binding sites of AX, where 3 represents all binding sites besides 1 and 2.

Autodisplay dimerization assay

Surface display of HSP90 on *Escherichia coli* BL21 (DE3) cells was performed as described before.[33] See supplemental Note 2 for further details.

Microscale thermophoresis (MST)

The HSP90 CTD was purified as described before[34] and labeled with the Monolith NT Protein Labeling Kit RED-NHS (Amine-reactive; NanoTemper Technologies GmbH, Munich, Germany) according to the manufacturer's protocol. See supplemental note 2 for further details.

Analytical ultracentrifugation

Sedimentation velocity experiments were carried out using a Beckman Proteome Laboratory XL-A ultracentrifuge (Beckman Coulter, Indianapolis, IN) equipped with an absorbance detection system and an 8-hole rotor. See supplemental Note 2 for further details.

Luciferase refolding assay

The luciferase assay was performed with K562 cells stably expressing luciferase transgene, as described previously,[24] with some modifications. See supplemental Note 2 for further details.

Drug-affinity responsive target stability (DARTS)

The DARTS assay was carried to evaluate the protease protection of AX from thermolysin, as described previously.[24] See supplemental Note 2 for further details.

Western blot (WB) and Blue-native gel

Cell lysates were generated after 48-hour treatment of leukemic cells with AX, IM, novobiocin (NB), or AUY922. Blue-native gels were performed following the manufacturer's instructions (Invitrogen) and as described previously.[24] See supplemental Note 2 for further details.

Table 1. IC_{50} values after treament with AX

Cell line	Origin	Growth inhibition (IC_{50}), μM
K562 and K562 IMr	CML (BCR-ABL1+)	5.72 ± 0.31 and 6.24 ± 0.52
KCL22 and KCL22 IMr	CML (BCR-ABL1+)	2.74 ± 0.52 and 2.86 ± 0.63
BA/F3	Murine pro B cell line	3.12 ± 0.09
BA/F3 (T315I)	Murine pro–B-cell line (BCR-ABL1+)	3.02 ± 0.22
BA/F3 (T315I) PNr	Murine pro–B-cell line (BCR-ABL1+)	4.02 ± 0.22
BA/F3 (M351T)	Murine pro–B-cell line (BCR-ABL1+)	3.11 ± 0.12
BA/F3 (E255K)	Murine pro–B-cell line (BCR-ABL1+)	3.02 ± 0.41
SUP-B15 and SUP-B15 IMr	BCP-ALL (BCR-ABL1+)	2.9 ± 0.67 and 3.97 ± 0.47
HL60	AML	7.17 ± 1.7
Mutz-2	AML	10.10 ± 0.46
Kasumi	AML	6.0 ± 0.03
SEM	BCP-ALL	5.9 ± 0.07
697	BCP-ALL	3.9 ± 0.10

IM-sensitive/resistant human- and murine-derived pro–B-cell lines expressing clinically relevant BCR-ABL1 mutant isoforms (T315I, T315I (PNr), M351T, and E255K) were treated with AX at different concentrations for 72 hours, and the average IC_{50} was then determined by CellTiter-Glo assay (n = 3).

IMr, IM resistant; PNr, ponatinib resistant.

Molecular dynamics (MD) simulations and computation of effective binding energies

To provide a structural model of the binding mode of AX at the HSP90 CTD, we performed 60 MD simulations of at least 400 nanosecond length of free diffusion[35] of AX in the presence of the CTD. During the MD simulations, AX was not biased by any guiding force. Resulting MD trajectories were analyzed with respect to potential binding sites of AX and its binding mode. Furthermore, effective binding energy calculations of AX binding to the CTD were performed.[36] See supplemental Note 3 for further details.

Cell culture

K562, KCL22, HL60, Kasumi, 697, SEM, and Mutz-2 leukemic cell lines were cultured in RPMI 1640 supplemented with 10% fetal calf serum (FCS) and maintained at 37°C with 5% CO_2, except for the Mutz-2[37] and SUP-B15 (BCR-ABL1) BCP-ALL cell lines, which were cultured in McCoy 5A supplemented with 20% FCS (DSMZ, Braunschweig, Germany). Normal Ba/F3 (murine pro-B cell line) or expressing BCR-ABL1$^{T315I,\ M351T,\ and\ E255K}$ mutants[38] were cultured in RPMI 1640 (10% FCS) supplemented with or without interleukin-3 (IL-3) (10 ng/mL), respectively. The BA/F3^{T315I} ponatinib-resistant cell line was generated as described previously[39] and is referred to as BA/F3$^{T315I\ (PNr)}$. In addition, the IM-resistant K562 (1 μM), KCL22 (2.5 μM), and SUP-B15 (2 μM) lines were generated as described previously[40] and are referred to as K562 IMr, KCL22 IMr, and SUP-B15 IMr, respectively. In IM-resistant cell line models, ABL1 kinase domain was sequenced for BCR-ABL1 point mutation using Sanger sequencing, including K562 and K562 IMr, KCL22 (T315I, F317L) and KCL22 IMr (T315I and F317L), SUP-B15 (T315I) and SUP-B15 IMr (T315I), BA/F3^{T315I} (T315I and Y272H), and BA/F3$^{T315I\ (PNr)}$ (T315I and Y272H).

Primary cell culture

Fresh cord blood (CB) samples were obtained from the Institute for Transplantation Diagnostics and Cell Therapeutics (Heinrich Heine University, Duesseldorf) after informed consent approval of the local ethical committee. Mononuclear cells (MNCs) were isolated by Ficoll density gradient centrifugation using standard procedures and later cultured in Mononuclear Cell Medium (PromoCell, Heidelberg, Germany). $CD34^+$ cells were later sorted from these MNCs using magnetic-activated cell sorting (MACS; Miltenyi Biotec, Bergisch Gladbach, Germany).[37] Primary T ($CD3^+$), natural killer (NK) ($CD56^+$), and B ($CD19^+$) cells were isolated from PB MNCs from healthy individuals after using MACS (Miltenyi Biotec). Cytokine profiling was performed on supernatant recovered from primary T, NK, and B cells after 48-hour treatment with respective compounds using Cytokine 25-Plex Human ProcartaPlex Panel 1B (Thermo Fisher Scientific) following the supplier's guidelines.

Primary patient samples were obtained from newly diagnosed or relapsed patients (supplemental Table 2) after informed consent approval of the local ethics committee and were cultured either in Stemline II Hematopoietic Stem Cell Expansion Medium (Sigma-Aldrich) or in Mononuclear Cell Medium (PromoCell). CML and BCR-ABL1+ BCP-ALL samples were sorted for $CD34^+CD38^{+/-}$ using the $CD34^+CD38^-$ Cell Isolation Kit, human (Miltenyi Biotec).

Viability assay

Inhibitors were printed on white 96-well or 384-well plates (Thermo Fisher Scientific) with their increasing concentration (50 nM to 25 μM) along with respective controls by using a digital dispenser (D300e; Tecan, Männedorf, Switzerland). Cell viability

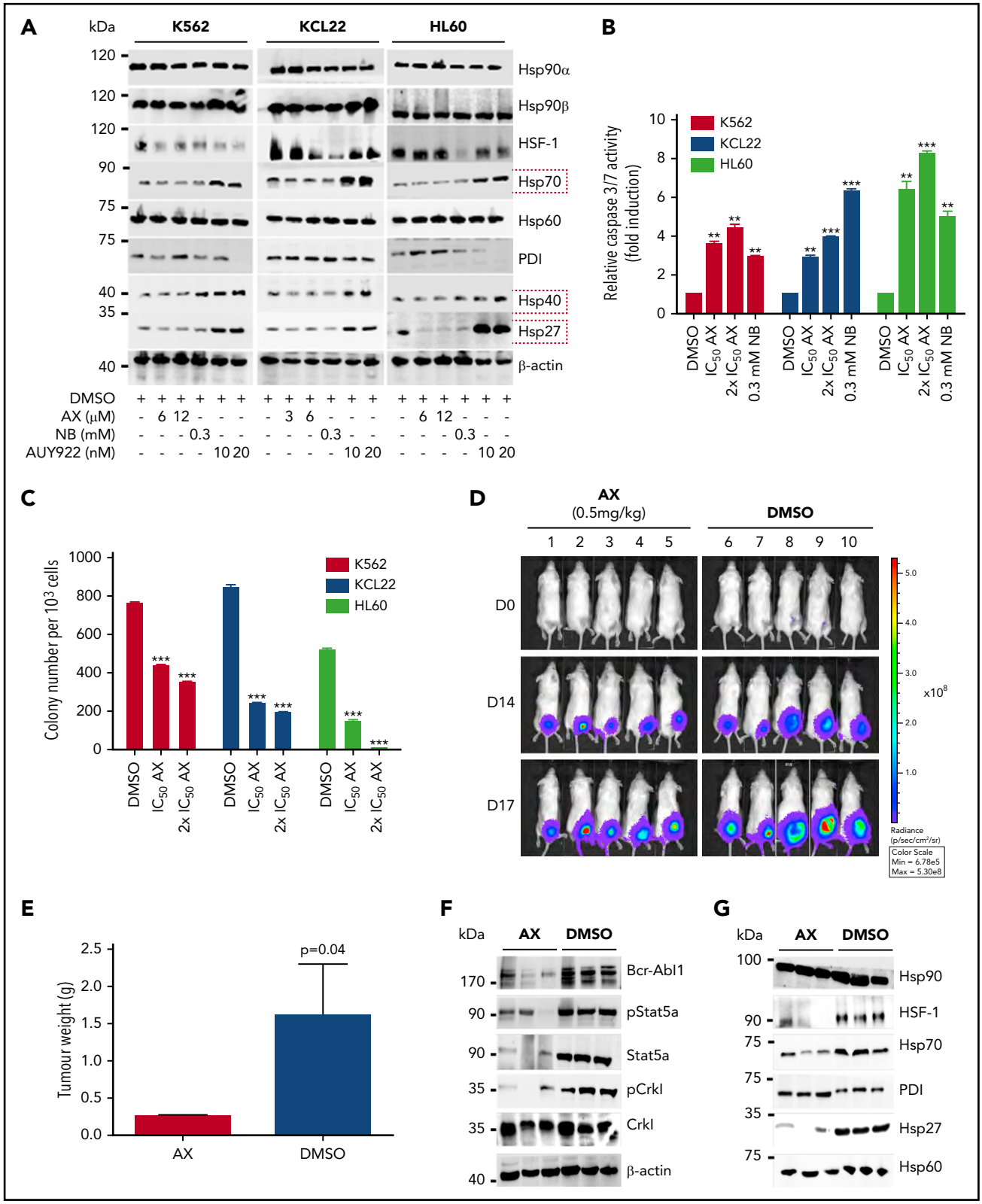

Figure 4. AX is a potent inhibitor in leukemic cell lines without inducing any HSR. (A) K562, KCL22, and HL60 were treated with the indicated (cytotoxic) concentration of AX, NB and AUY922 for 48 hours, and protein lysates were later subjected to immunoblot analysis. AX and NB (C-terminal HSP90 inhibitors) do not induce expression of HSP70, HSP40, and HSP27, whereas AUY922 (an N-terminal HSP90 inhibitor) demonstrates HSR induction by triggering their expression. HSP60 (primarily present in mitochondria) and PDI (primarily present in endoplasmic reticulum) served as controls for the HSR in the cytoplasm, in response to inhibition of HSP90 dimerization via the CTD. (B) K562, KCL22, and HL60 (Mutz-2; data not shown) were treated with AX for 48 hours, and enzymatic activity of caspase-3/7 was later examined by caspase-3/7–dependent Glo assay (absorbance at 405 nm). (C) K562, HL60, KCL22 cells were seeded in methylcellulose medium containing respective compounds at indicated concentration after treatment in liquid medium for 24 hours. Colonies were counted after 14 days. (D) 5 × 10^5 luciferase-expressing K562 cells were subcutaneously transplanted into NSG mice. Starting the day after

was monitored after 72 hours using CellTitre-Glo luminescent assay (Promega, Madison, WI) using a microplate reader (Spark, Tecan). The 50% inhibitory concentration (IC_{50}) for compounds (all inhibitors were bought from MedChemExpress) were determined by plotting raw data (normalized to controls) using sigmoid dose curve and nonlinear regression (GraphPad Prism, San Diego, CA).

Proliferation assay

Cell proliferation was examined after treatment with respective compounds using an automated cell counter, which uses trypan exclusion method (Vi-CELL XR, Beckman Coulter). Proliferation was measured after every 24-hour interval.

Cell cycle assay

AX- or NB-treated cells (48 hours) were fixed with chilled (70%) ethanol for 24 hours to allow the access of propidium iodide (PI) to the DNA. Fixed cells were treated with ribonuclease to digest RNA and later incubated with 200 μL PI (50 μg/mL stock) for 10 minutes at 37°C and immediately subjected to fluorescence-activated cell sorter (FACS) analysis.

Annexin V staining

To evaluate apoptosis, cells treated with respective compounds or control for 48 hours were stained with Annexin V and PI and later subjected to FACS following the supplier's guidelines (Invitrogen, Carlsbad, CA).

Caspase-3/7-Glo assay

Cells were treated with respective compounds or control in white 96-well or 384-well plates. Enzymatic activity of caspase-3/7 was then examined by caspase-3/7–dependent Glo assay (absorbance at 405 nm) following the manufacturer's instructions (Promega) using a microplate reader (Spark, Tecan).

FACS

FACS was performed on FACSCalibur (Becton Dickinson, Heidelberg, Germany) using fluorochrome-coupled monoclonal antibodies along with the following matched isotype controls: anti-CD34 (8G12; BD Biosciences), anti-CD11b (Bear1), anti-CD14 (RMO52), anti-CD13 (Beckman Coulter), and anti-CD33 (Miltenyi Biotec)

Colony-forming unit assay

Colony-forming unit assays were performed initially by treating cells in the liquid medium for 24 hour. Later, treated cells were seeded in a semisolid methylcellulose-based medium containing respective compounds or control.[37] Colonies were counted after 14 days.

In vivo xenograft tumor model

A total of 5×10^5 K-562-luciferase–expressing (stably transduced) cells mixed with Matrigel matrix (Corning) were injected subcutaneously in the dorsal flank of NSG (B6 NOD.Cg-Prkdc^{scid} Il2rg^{tm1Wjl}/SzJ) mice (005557; The Jackson Laboratory, Bar Harbor, ME). Engraftment was monitored by measuring luminescence 3 or 4 days after intraperitoneal injection of 150 μg/100 μL D-Luciferin Firefly sodium salt monohydrate (Biosynth, Staad, Switzerland) using the Caliper IVIS Lumina II Multispectral Imaging System (Perkin Elmer, Rodgau, Germany) and Living Image Software. AX (0.5 mg/kg dose) or vehicle (dimethyl sulfoxide [DMSO]) was administered starting from the day after the transplantation by peritumoral injection for 17 days (n = 5 per group). Mice were sacrificed on day 17, and excised tumors were weighed and subjected to WB analysis. No blinding experiment was performed. Animal husbandry and experiments were conducted in accordance with the German Animal Welfare Act at the Institute for Tumor Biology and Experimental Therapy, Georg-Speyer-Haus, Frankfurt, Germany.

Results

Design and synthesis of HSP90 CTD dimerization inhibitors

HSP90 is a homodimer, with each monomer consisting of three major functional domains, of which the C-terminal domain (CTD) mediates HSP90 dimerization (Figure 1A). The CTD dimerization interface is formed by a characteristic 4-helix bundle (Figure 1B).[41] We recently resolved hot spots in the HSP90 CTD dimerization interface (I688, Y689, I692, and L696; Figure 1C) and identified the first peptidic inhibitors shown to bind to the CTD.[33,34] Subsequently, we demonstrated that α-aminoxy peptides, a novel class of peptidomimetic foldamers, can fold into a unique 2_8-helical conformation.[42] Molecular modeling studies revealed that this 2_8-helix can mimic the spatial arrangement of peptide side chains in α-helices.[42] Herein, we found that side chains of an α-aminoxy hexapeptide can accurately mimic the HSP90 dimerization hot spots (Figure 1C). Based on this knowledge, we designed 2 tailor-made potential HSP90 CTD dimerization inhibitors (α-aminoxy hexapeptides 1 (later referred to as AX) and 2, Figure 1D). A combination of solution- and solid-phase supported methods was used to synthesize 1 (AX) and 2 (Figure 1D; supplemental Note 1). Our investigation of the conformational properties by 2-dimensional nuclear magnetic resonance spectroscopy (supplemental Figures 1 and 2) and CD spectroscopy (supplemental Figure 3) confirmed that 1 (AX) and 2 are able to fold into the desired 2_8-helical conformation indicating that they can adopt the required secondary structure to mimic the HSP90 CTD dimerization hot spots.

AX inhibits HSP90 dimer formation and specifically binds to the CTD of HSP90

To elucidate the biological properties of 1 (AX) and 2, we first showed by means of a dimerization assay based on the autodisplay technology[33] that 1 (AX) and 2 inhibit HSP90 dimer formation (Figure 2A-B). Furthermore, binding of 1 (AX) and 2 to the CTD of HSP90 was revealed by MST measurements with the

Figure 4 (continued) transplantation, animals were treated by peritumoral injection (15 μg) of compound AX (0.5 mg/kg dose) or solvent only (DMSO). One control DMSO-treated mouse was sacrificed earlier (on day 16) because of large tumor size. Luminescence was monitored every 3 or 4 days after intraperitoneal injection of 100 μL luciferin, and the final analysis was performed on day 17 (n = 5 mice per group). (E) AX reduced tumor burden with respect to tumor weight 0.24 ± 0.01 g vs vehicle 1.6 ± 0.6 g ($P = .04$; 1-tailed *t* test). (F) Immunoblot analysis of tumor samples derived from mice treated with AX revealed downregulation of BCR-ABL1 kinase activity and its associated downstream signaling pathways involving Stat5a and Crkl. (G) Immunoblot analysis of tumor samples derived from mice after treatment with AX. Samples displayed no HSR, as evaluated by expression of HSF-1, HSP70, and HSP27; PDI and HSP60 were used as controls. Columns depict the mean of 3 independent experiments (n = 3). Significance analyses of normally distributed data with variance similar between groups used paired, 2-tailed Student *t* test. $^*P < .05$, $^{**}P < .005$, $^{***}P < .001$.

purified, recombinant, NT-647 labeled CTD of HSP90 (1 (AX): K_d = 27.4 μM; 2: K_d = 44.2 μM; Figure 2C; supplemental Figure 4A).

A cell-based luciferase refolding assay[24] using K562 cells revealed a dose-dependent reduction in the luciferase activity after application of 1 (AX) or 2 comparable to NB (CTD HSP90 inhibitor) and AUY922 (NTD HSP90 inhibitor) (Figure 2D; supplemental Figure 4B). Hence, 1 (AX) (IC_{50}: 5.72 ± 0.31 μM [K562]; 7.1 ± 1.7 μM [HL60]) was selected for further experiments due to the higher efficacy in autodisplay, MST, the luciferase refolding assay, and the viability assay compared with 2 (IC_{50}: 16.8 ± 0.11 μM [K562]; 17.4 ± 0.4 μM [HL60]) (supplemental Figure 4C). We proved specific binding of AX to HSP90 complexes by native gel analysis, resulting in a more potent disruption of HSP90α and HSP90β (also HSP40 and HSP27) complexes (including their monomers/dimers) at cytotoxic concentrations (supplemental Figure 5A) than NB and AUY922. In contrast, treatment with AUY922 resulted in an elevated expression of HSR-associated protein complexes (including their monomers/dimers) of HSP40 and HSP27 (supplemental Figure 5A). AX protected recombinant HSP90α protein from degradation against thermolysin digestion, an assay commonly used to quantify DARTS[24] (supplemental Figure 5B). Immunoblotting was performed under reducing (+dithiothreitol) and nonreducing (−dithiothreitol) conditions, which revealed that AX acts on HSP90 oligomers, in contrast to NB but in concordance with AUY922 (supplemental Figure 5C). Sedimentation velocity analysis revealed that AX influences the size distribution of HSP90 CTD, in that AX is able to either dissociate oligomeric species of or suppress HSP90 CTD oligomerization (Figure 2E; supplemental Note 2).

In summary, these results reveal that AX specifically binds to the CTD of HSP90 and inhibits its dimerization.

AX is predicted to bind to the HSP90 CTD dimerization interface and mimic hot spot residues on helix H5′

To provide a binding mode model of AX at the HSP90 CTD, we performed 60 MD simulations of at least 400 nanosecond length of free diffusion of AX in the presence of the CTD (supplemental Figure 7 and supplemental Note 3). In 22 simulations, AX binds between helices H4 and H5 in the dimerization interface (site 1 in Figure 3A; supplemental Figure 7). In the remaining cases, AX either binds to a hydrophobic site occupied by the middle domain in full-length HSP90 (site 2 in Figure 3A-B; supplemental Figures 7 and 8) or gets trapped in locations scattered across the CTD (site 3 in Figure 3B-C; supplemental Figures 7 and 9). Effective binding energy calculations corroborate these results in that the most favorable energies are found for AX at site 1 (Figure 3A; supplemental Figures 10 and 11). The conformations of AX at site 1 revealed side chains partially aligned with side chains of hot spot residues of helix H5′ (Figure 3D-E). The side chain that distinguishes AX from 2 (Figure 1D) binds to a hydrophobic groove formed by I688, I692, and M691 (Figure 3D), where the additional polar hydroxyl group in 2 would be disfavorable, which may explain the lower apparent K_d of 2. Taken together, the computational results suggest that AX binds to the HSP90 CTD dimerization interface and mimics hot spot residues on helix H5′.[34]

AX destabilizes BCR-ABL1 without inducing HSR in vitro and in vivo

HSP90 expression is high in BCR-ABL1$^{+/-}$ leukemia cell lines such as HL60, K562, and Mutz-2 (supplemental Figure 12A). Later, we determined the average IC_{50} for AX in selected leukemic cell lines (Table 1). Upon 48-hour exposure to AX, K562 and KCL22 cells downregulated BCR-ABL1 levels as well as downstream signaling pathways such as STAT5a and CRKL, as evaluated by WB analysis (supplemental Figure 12B). AX additionally reduced pAKT-S473, pS6 expression, and expression of client proteins associated with HSP90 chaperone activity, involving *t*-AKT, *t*-STAT5a, *t*-CRKL, cMYC, and BCL2 (supplemental Figure 12B).

Furthermore, AX triggered the degradation of HSP90 client proteins without elevating the expression of HSPs (HSP70, HSP40, and HSP27) involved in the HSR, in contrast to AUY922 (Figure 4A; supplemental Figure 5A). We observed inhibition of cell proliferation (supplemental Figure 12C) and induction of both late apoptotic (Annexin$^+$PI$^+$) and necrotic (Annexin$^-$PI$^+$) cells after the exposure to AX at its IC_{50} concentration (Table 1) in K562, HL60, and KCL22 cell lines (supplemental Figure 12D). Caspase-3/7 enzyme–dependent apoptosis assays with an induction of approximately three- to fivefold of apoptotic cells in K562, HL60, Mutz-2 (data not shown), and KCL22 corroborated the observations from cell proliferation studies, similarly to exposure with NB (Figure 4B). K562 cells were dose-dependently arrested in G1 phase, and we observed a reduction in G2/M phase after exposure to AX (supplemental Figure 12E). Furthermore, AX facilitated early differentiation in a liquid medium, as measured by expression of myelomonocytic antigens markers involving CD13 and CD38 in K562 cells and CD11b in HL60 cells (supplemental Figure 12F). Moreover, 48-hour exposure of AX to K562, HL60, Mutz-2 (data not shown), and KCL22 significantly reduced their colony-forming capacity (Figure 4C) in accordance to NB, whereas AX was effective at micromolar concentrations ~100-fold below those of NB in the millimolar range. We additionally transplanted K562-Luc (stably expressing the luciferase reporter gene) in an in vivo xenograft model and treated the tumor locally with AX (0.5 mg/kg dose) for 17 days. We obtained a significant reduction in tumor weight (Figure 4D-E), indicating that AX has an antioncogenic potential in vivo. BCR-ABL1 protein and its downstream signaling pathways (STAT5a and CRKL) (Figure 4F) were downregulated, and HSR was not initiated in the excised tumors (Figure 4G).

In summary, these data confirm a potent anti–BCR-ABL1 effect of AX in the absence of HSR induction and at low cytotoxic concentrations in vitro and in vivo.

AX is effective in TKI-resistant leukemic cell line models

BCR-ABL1$^{T315I,\ E255K,\ \text{and}\ M351T}$ are the clinically relevant mutations leading to constitutive ABL1 kinase activity and a severe TKI-resistance profile. The effect of AX is superior to that of IM and other second- and third-generation TKIs (including PN) in murine BA/F3 cell line models encompassing BCR-ABL1$^{T315I,\ T315I\ (PNr),\ E255K,\ \text{and}\ M351T}$ mutants (supplemental Figure 13A; Figure 5A). In these cell line models, AX reduced cell viability (IC_{50} ~3-4 μM) (Table 1) and proliferation (supplemental Figure 13B) and induced apoptosis (Figure 5B) in a manner similar to NB (0.3 mM). Additionally, after

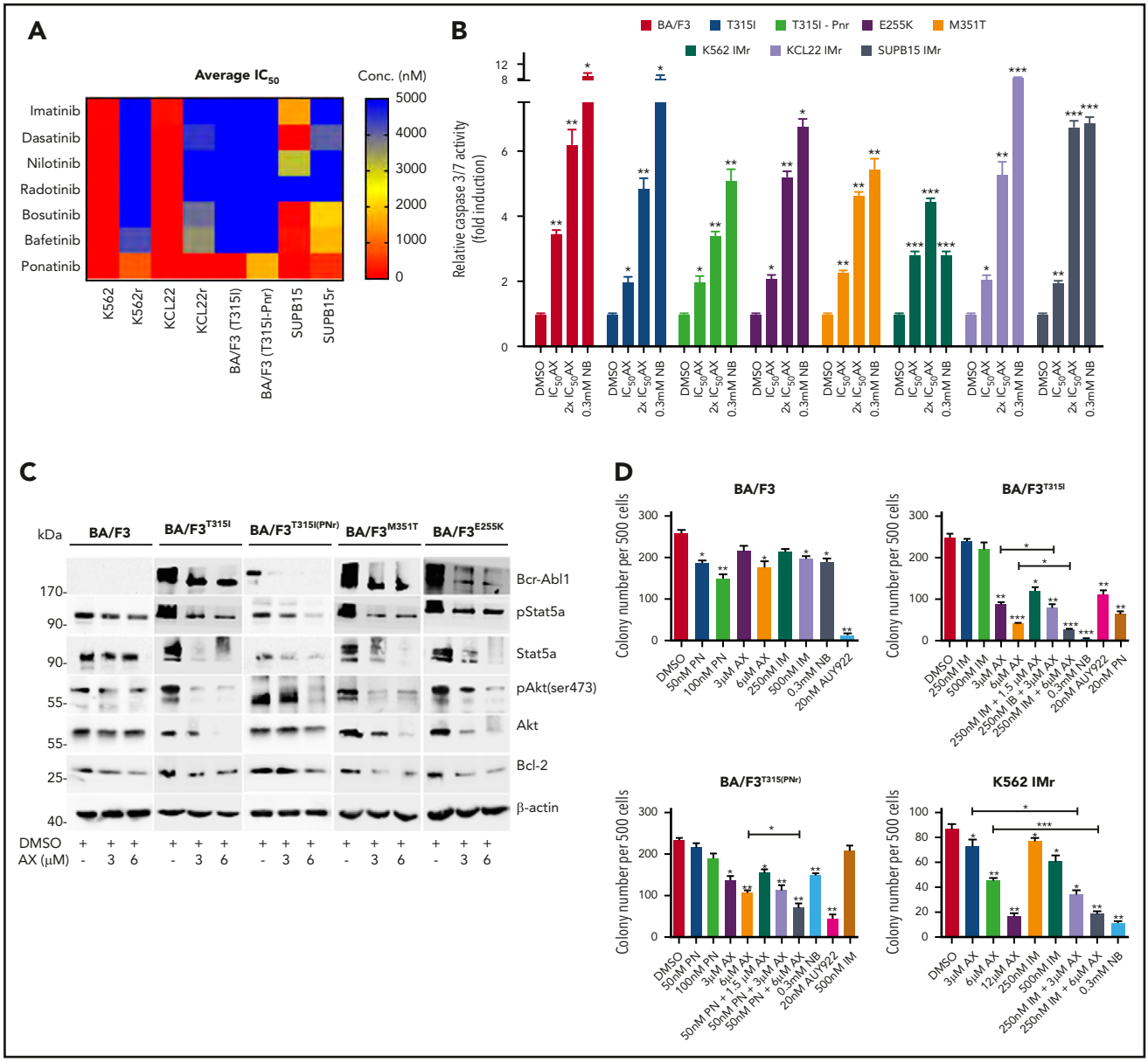

Figure 5. Efficacy of AX in TKI-resistant leukemic cell line models. (A) IM-resistant K562, KCL22, SUP-B15, and BA/F3-expressing BCR-ABL1$^{T315I,\ T315I\ (PNr)}$ along with their respective normal cell lines were treated with second- and third-generation TKIs (dasatinib, nilotinib, radotinib, bosutinib, befetinib, and ponatinib) at 7 different concentrations (ranging from 50 nM to 25 μM) for 72 hours. Later, the average IC_{50} was determined and plotted on a heat map. (B) BA/F3 cells expressing BCR-ABL1$^{T315I,\ T315I\ (PNr),\ M351T,\ and\ E255K}$ mutants, K562 IMr, KCL22 IMr, and SUP-B15 IMr cells were treated with the indicated concentration of AX (48 hours) and later enzymatic activity of caspase-3/7 were examined by caspase-3/7 dependent-Glo assay (absorbance at 405 nm). (C) Likewise, in human leukemia cell lines, AX causes downregulation of BCR-ABL1 and subsequently its associated downstream signaling pathways, including Stat5a, Akt, and Bcl-2 in BA/F3 cells expressing BCR-ABL1$^{T315I,\ T315I\ (PNr),\ M351T,\ and\ E255K}$ mutants. (D) Normal BA/F3 cells, BA/F3-expressing BCR-ABL1$^{T315I\ and\ T3151\ (PNr)}$ mutants, and K562 IMr cells were seeded in methylcellulose medium containing respective compounds at indicated concentration after treatment in liquid medium for 24 hours. Colonies were counted after 14 days. Significance analysis of normally distributed data with variance similar between groups used paired, 2-tailed Student *t* test. $^{*}P < .05$, $^{**}P < .005$, $^{***}P < .001$.

application of AX, BCR-ABL1 oncoprotein was destabilized, and downstream signaling pathways (AKT, STAT5a, and BCL-2) were blocked with increasing concentrations of AX, which is comparable to the results from TKI-sensitive leukemic cell lines and in vivo xenograft model (Figure 5C). To evaluate the effect of AX in combination with IM, colony-forming assays were performed in which AX was administered alone or coadministered (at lower doses) with IM. Coadministration of AX with IM further reduced the colony-forming capacity of BCR-ABL1$^{T315I\ and\ T315I\ (PNr)}$ cells when compared with treatment with AX alone, NB, AUY922, and PN, which were taken as controls (Figure 5D). Furthermore, we have generated human BCR-ABL1+ IM resistant cell lines, including K562 IMr, KCL22 IMr, and SUP-B15 IMr.[40] These cell lines were also found to be resistant to second- and third-generation TKIs when compared with their normal counterparts (Figure 5A). In analogy to murine BA/F3 cell line models and respective sensitive cell lines, AX reduced the viability of human IM-resistant cell lines at nearly similar IC_{50} concentrations (Table 1) and in addition inhibited proliferation, induced apoptosis, destabilized BCR-ABL1 oncoproteins,

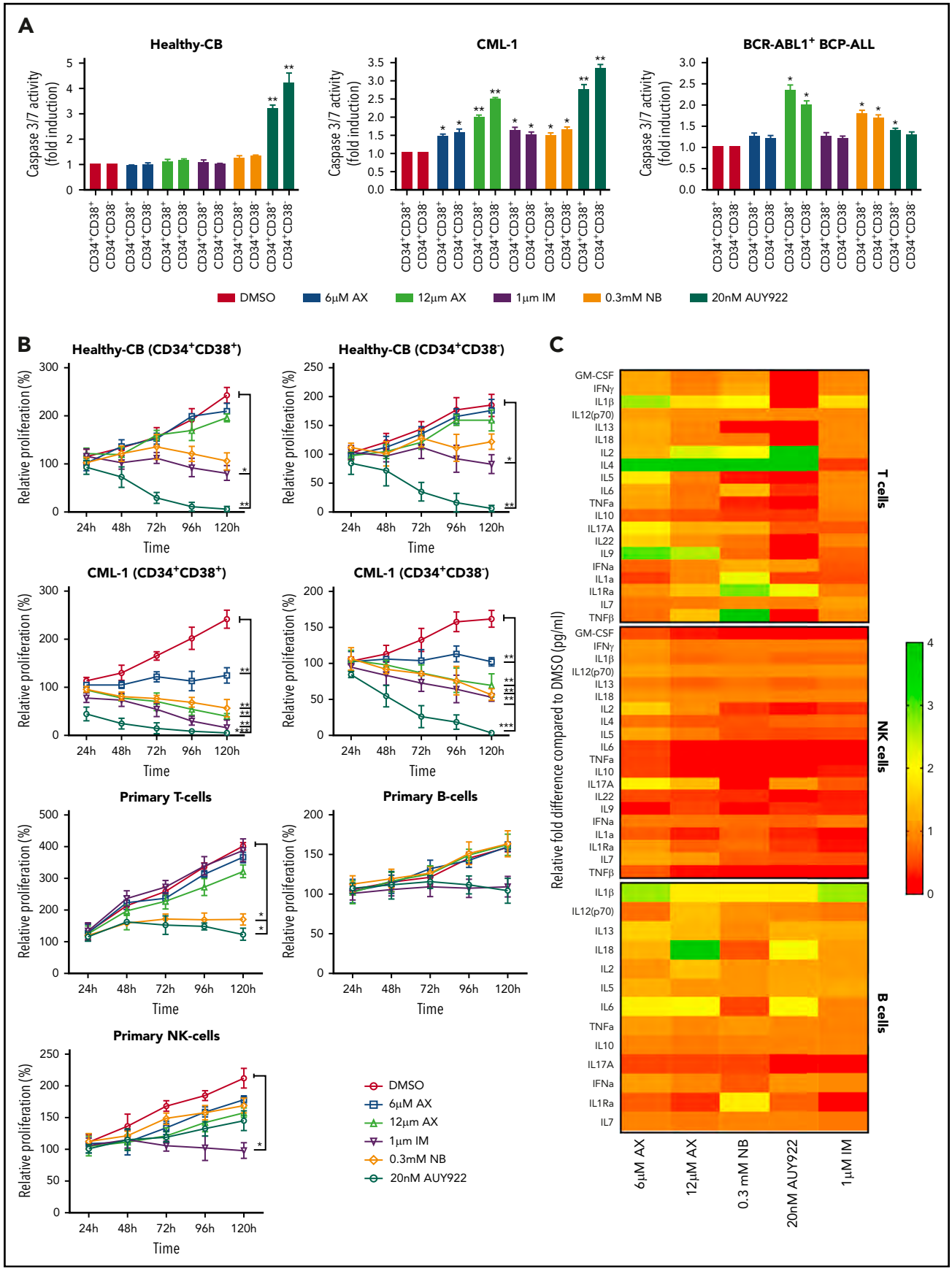

Figure 6.

Figure 6. (Continued).

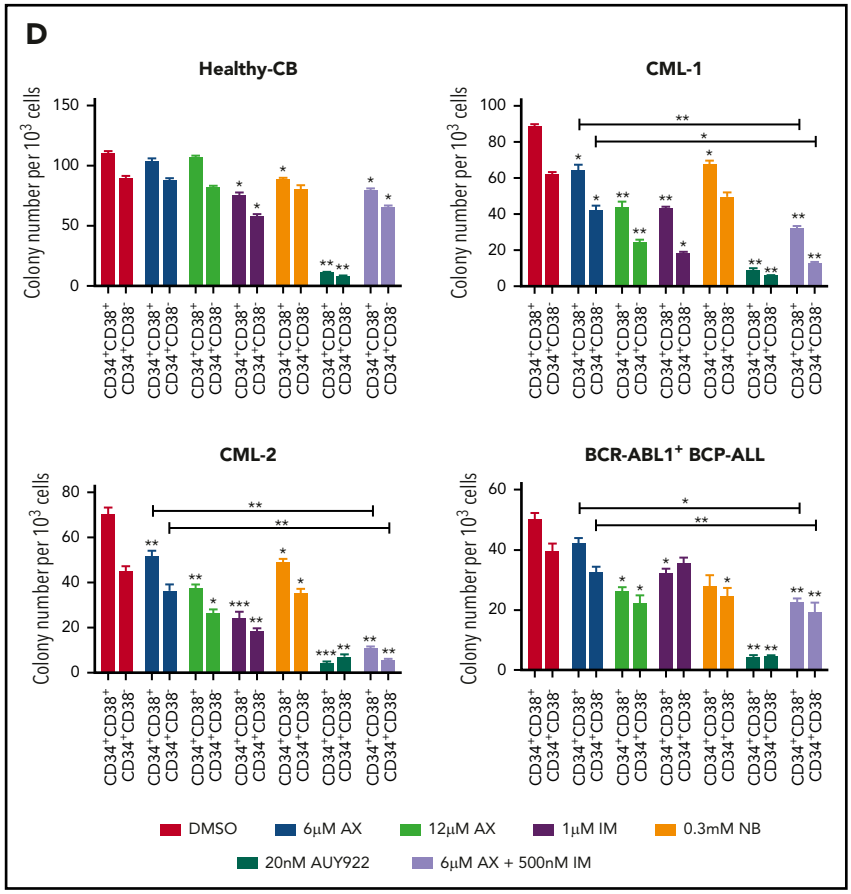

blocked downstream signaling, and further reduced colony-forming ability when used in combination with IM as compared with AX treatment alone (Figure 5D; supplemental Figures 14-16).

AX suppresses human LSCs and acts in a reasonable therapeutic window

The major challenge in treating CML and other stem cell diseases is the elimination of LSCs to establish sustained TFR.[43,44] We therefore have cell sorted 2 patient-derived CML samples taken from diagnosis without prior treatment (clinical data provided in supplemental Table 2) and 1 relapse BCR-ABL1+ BCP-ALL sample for $CD34^+CD38^-$ as markers for CML/BCP-ALL LSCs. AX did not differentiate between $CD34^+CD38^+$ and $CD34^+CD38^-$ subpopulations and significantly inhibited cell growth and induced apoptosis in these leukemic fractions as compared with healthy-CB-derived $CD34^+CD38^+$ or $CD34^+CD38^-$ counterparts, where IM, NB, and AUY922 were used as a control (Figure 6A-B; supplemental Figure 17A-B). The clinical value of AX depends on its therapeutic window. In this regard, we have evaluated the average IC_{50} (20.94 ± 3.07 μM) (supplemental Figure 18A) similar to leukemic cell lines and assessed the cell viability using trypan exclusion method in healthy-CB MNCs (supplemental Figure 18B) after exposure to AX. The cytotoxic effect of AX was significantly less pronounced on healthy fraction than on leukemia cell line models (Table 1). Unlike in leukemic cell lines, AX did not induce early differentiation of CB-$CD34^+$ cells in liquid medium (supplemental Figure 18C) and did not affect the cell proliferation of different healthy blood fractions, including, T, NK, and B cells (Figure 6b). Cytokine profiling (25 cytokines) was performed from the supernatants obtained from these healthy blood cell fractions after treatment with AX (Figure 6C; supplemental

Figure 6. AX suppresses human LSCs and acts in a reasonable therapeutic window. (A) One BCR-ABL1+ CML patient sample and a relapse BCP-ALL patient sample, along with a healthy human-CB-derived $CD34^+CD38^{+/-}$ (sorted by MACS) sample, were treated with increasing concentrations of AX or controls (NB, AUY922, or IM). Later, the enzymatic activity of caspase-3/7 was examined using a caspase-3/7–dependent Glo assay after 5 days of treatment. (B) Primary patient samples along with healthy control cells (including primary B, T, and NK cells) were treated with the indicated concentration of AX or controls (NB, AUY922, or IM), and viable cells were counted after every 24-hour interval for 5 days. AX specifically targets leukemic samples (both the leukemic bulk and leukemic stem cell fractions) contrary to healthy control cells. (C) Supernatants were collected from primary T, NK, and B cells after 48-hour treatment with respective compound and then evaluated for the detection of 25 different human cytokines. Heat maps depict the fold difference relative to the control (DMSO) in picograms per milliliter. Some cytokines were omitted from the analysis because their concentration was below the detection limit. (D) $CD34^+CD38^{+/-}$ cells from 2 BCR-ABL1+ CML (CML-1 and CML-2) patient samples and 1 TKI-resistant BCR-ABL1+ BCR-ALL patient sample, along with healthy CB controls, were seeded in methylcellulose medium containing respective compounds at the indicated concentration after treatment in liquid medium for 24 hours. Colonies were counted after 14 days (n = 5). Significance analysis of normally distributed data with variance similar between groups used a paired, 2-tailed Student *t* test. $^*P < .05$, $^{**}P < .005$, $^{***}P < .001$. IFNa, interferon α; GM-CSF, granulocyte-macrophage colony-stimulating factor; TNFa, tumor necrosis factor α.

Table 3). As compared with AUY922, there was a modest change in the cytokine profile with AX, especially in T cells, with the exception for IL-17a in NK cells and IL-6 in B cells (Figure 6C; supplemental Table 3). Moreover, AX specifically inhibited the colony-forming capacity of the CML (n = 3) and BCP-ALL (n = 1) patient-derived $CD34^+CD38^+$ and $CD34^+CD38^-$ fraction as compared with their healthy-CB-derived counterparts (Figure 6D; supplemental Figure 17C). The co-administration of AX along with IM further blocked the colony formation of both $CD34^+CD38^+$ and $CD34^+CD38^-$ leukemic fractions (Figure 6D). Like in leukemic cell lines, AX did not inflict any HSR (supplemental Figure 19A) and induced early differentiation in CML^{CD34+} in liquid medium (supplemental Figure 19B).

As HSP90 is involved in chaperoning several other oncoproteins besides BCR-ABL1,[4,45] which is involved in several other leukemia subtypes, we evaluated the effect of AX on BCR-ABL1− leukemia involving, FLT3 ITD+ AML (n = 2), Ph-like ALL (n = 1), and CLL (n = 1) clinical samples. Likewise, in BCR-ABL1+ CML samples, AX inhibited growth and induced apoptosis in FLT3-ITD+ AML and reduced colony formation in all 4 patient samples (Figure 6D; supplemental Figures 20 and 21).

Discussion

The involvement in a plethora of oncogenic pathways has positioned HSP90 as a prominent therapeutic target. Malignant cells are particularly sensitive to HSP90 inhibition.[14,46] Over the last decade, ~15 different inhibitors targeting the adenosine triphosphate binding pocket in HSP90's N terminus have been assessed in >40 different clinical trials; however, the entire class of these inhibitors instigates an HSR.[8,14,15,18-22,24,47-49] Ocular toxicity is a major concern with HSP90 inhibitors; for instance, in a phase 1 clinical trial, the maximum tolerated dose of AUY922 induced night blindness in 20% of patients, and ~7% of the patients developed grade ≥3 eye disorders (supplemental Table 1).[45,50] These reports suggest that the nonselectivity of N-terminal HSP90 inhibitors leads to toxicity and to induction of the HSR, which could be why N-terminal HSP90 inhibitors fail in advanced clinical trials.[8,14,45] Functional assays have shown that the silencing of HSF-1, HSP70, and HSP27 in addition to HSP90 considerably enhances the cytotoxic effect of HSP90 inhibitors against malignant cells.[18,20,21] Accordingly, some HSP90 C-terminal inhibitors have been developed that appear not to induce any HSR; however, they have not yet entered clinical trials.[15,23,24,51,52] None of these inhibitors have been reported to act as protein–protein interaction inhibitors that interfere with CTD dimerization.[23,51,53,54] Here, we developed the α-aminoxy hexapeptide AX, which blocks HSP90 function by specifically binding to the CTD of HSP90 and then either dissociating oligomeric species or suppressing HSP90 CTD oligomerization, which ultimately leads to inhibition of HSP90 dimer formation.

The CTD is essential for the dimerization of HSP90 and therefore crucial for HSP90 function.[41] Targeting protein–protein interactions is generally considered challenging due to the size, hydrophobicity, and lack of deep binding pockets at the protein–protein interfaces.[55] Based on our MD simulation, AX binds to the HSP90 CTD dimerization interface and mimics hot spot residues on helix H5′. Thus, the mode of action of AX differs from all other known HSP90 inhibitors, which makes AX the first-in-class HSP90 C-terminal dimerization inhibitor. The absence of HSR upon administration of AX is in agreement with previous reports that the modulation of HSP90 function via the C terminus does not trigger an HSR response.[15,23,24,51,52]

We evaluated AX in CML and showed that it targets BCR-ABL1–expressing precursor cells, which are dependent on BCR-ABL1 expression, and CML LSCs, which are independent of BCR-ABL1 expression and therefore not targetable by TKIs. We showed that this mechanism also applies to highly resistant BCP-ALL, including BCR-ABL1+ BCP-ALL, in which AX is equally effective. Especially in Ph-like BCP-ALL, inhibition of HSP90 by AX is of major importance because of its poor response to TKI treatment and its 3-times-higher frequency compared with BCR-ABL1+ BCP-ALL, especially in young adults. Thus, in the future, AX or its analogs might also be applied to other leukemia entities that still have an intolerably poor prognosis, such as BCR-ABL1+ BCP-ALL, Ph-like BCP-ALL, and FLT3-ITD+ AML. Moreover, AX constitutes a promising compound in many solid tumor entities, which are characterized by expression of HSP90 client proteins (eg, AKT, HER2, BRAF, and EGFR) with key functions in multiple myelomas and solid carcinomas (supplemental Table 4).

Acknowledgments

The authors thank all members of their groups for useful discussions and critical reading of the manuscript. Kathleen Mohs is acknowledged for her technical assistance during animal experiments.

J.H. is supported by the German Cancer Aid (Project 110997 and Translational Oncology Program 70112951), the German Jose Carreras Leukemia Foundation (DJCLS 02R/2016), the Kinderkrebsstiftung (2016/17), the Deutsches Konsortium für Translationale Krebsforschung (DKTK) Joint funding (Targeting MYC L*10), and the Elterninitiative Kinderkrebsklinik. F.K.H. acknowledges financial support from the Fonds der Chemischen Industrie and the Strategischer Forschungsfonds of Heinrich Heine University (HHU) (SFF - F 2012/79-17). T. Kurz, H.G., G.G., and M.U.K. are supported by funds from the Strategischer Forschungsfonds of HHU. Computational support and infrastructure were provided by the Centre for Information and Media Technology at HHU Düsseldorf (Germany). We are grateful to the John von Neumann Institute for Computing (NIC) and the Jülich Supercomputing Centre for computing time on the supercomputer JURECA (NIC project HKF 7 (H.G., B.F.). Financial support by Deutsche Forschungsgemeinschaft through funds to purchase the hybrid computer cluster used in this study (INST 208/704-1 FUGG) (H.G.) is gratefully acknowledged. The Deutsche Forschungsgemeinschaft is acknowledged for funds used to purchase the UHR-TOF maXis 4G, Bruker Daltonics, Bremen HRMS instrument used in this research. V.M. is supported by the Düsseldorf School of Oncology (funded by the Comprehensive Cancer Centre Düsseldorf/Deutsche Krebshilfe and the Medical Faculty of the Heinrich Heine University Düsseldorf). The Georg-Speyer-Haus is funded jointly by the German Federal Ministry of Health and the Ministry of Higher Education, Research and the Arts of the State of Hessen. A.B. is supported by the German Children's Cancer Foundation and the Federal Ministry of Education and Research (Bonn, Germany).

Authorship

Contribution: H.G., T. Kurz, F.K.H., and J.H. contributed to conception and design of the project and supervision of the study; D.D., B.B., S.B., H.A., B.F., T.Z., T. Kröger, S.L., A.J.R.M., H.K., S.S., F.V.O., M.O., F.L., and V.M. acquired data; S.B., T.E., G.K., A.K., D.D., B.F., A.B., A.H., F.B., M.G., G.G., M.R., M.U.K., T. Kurz, H.G., F.K.H., and J.H. developed methodology; S.B., D.D., B.F., B.B., S.L., A.J.R.M., M.U.K., S.S., A.B., A.H., G.G., L.N.-S., J.J., T. Kurz, H.G., F.K.H., and J.H. were responsible for analysis and interpretation of data; and S.B., D.D., B.F., S.L., M.U.K., G.G.,

L.N.-S., J.J., T. Kurz, H.G., F.K.H., and J.H. wrote, reviewed, and/or revised the manuscript.

Conflict-of-interest disclosure: The authors declare no competing financial interests.

ORCID profiles: S.B., 0000-0001-6494-7744; B.F., 0000-0002-7877-0262; T. Kurz, 0000-0002-9474-4224; H.G., 0000-0001-8613-1447; F.K.H., 0000-0001-9765-5975; J.H., 0000-0002-4058-3058.

Correspondence: Julia Hauer, Department of Pediatric Oncology, Hematology and Clinical Immunology, Medical Faculty, Heinrich Heine University Düsseldorf, Düsseldorf, Germany; e-mail: julia.hauer@med.uni-duesseldorf.de; and Finn K. Hansen, Pharmaceutical/Medicinal Chemistry, Institute of Pharmacy, Leipzig University, Leipzig, Germany; e-mail: finn.hansen@uni-leipzig.de.

Footnotes

Submitted 12 October 2017; accepted 19 April 2018. Prepublished online as *Blood* First Edition paper, 3 May 2018; DOI 10.1182/blood-2017-10-810986.

*F.K.H. and J.H. contributed equally to this study.

The online version of this article contains a data supplement.

There is a *Blood* Commentary on this article in this issue.

The publication costs of this article were defrayed in part by page charge payment. Therefore, and solely to indicate this fact, this article is hereby marked "advertisement" in accordance with 18 USC section 1734.

REFERENCES

1. Mahalingam D, Swords R, Carew JS, Nawrocki ST, Bhalla K, Giles FJ. Targeting HSP90 for cancer therapy. *Br J Cancer*. 2009;100(10):1523-1529.
2. Khajapeer KV, Baskaran R. Hsp90 inhibitors for the treatment of chronic myeloid leukemia. *Leuk Res Treatment*. 2015;2015:757694.
3. Lazenby M, Hills R, Burnett AK, Zabkiewicz J. The HSP90 inhibitor ganetespib: A potential effective agent for Acute Myeloid Leukemia in combination with cytarabine. *Leuk Res*. 2015;39(6):617-624.
4. Miyata Y, Nakamoto H, Neckers L. The therapeutic target Hsp90 and cancer hallmarks. *Curr Pharm Des*. 2013;19(3):347-365.
5. Yamaki H, Nakajima M, Shimotohno KW, Tanaka N. Molecular basis for the actions of Hsp90 inhibitors and cancer therapy. *J Antibiot (Tokyo)*. 2011;64(9):635-644.
6. Wu LX, Xu JH, Zhang KZ, et al. Disruption of the Bcr-Abl/Hsp90 protein complex: a possible mechanism to inhibit Bcr-Abl-positive human leukemic blasts by novobiocin. *Leukemia*. 2008;22(7):1402-1409.
7. Blagosklonny MV, Toretsky J, Neckers L. Geldanamycin selectively destabilizes and conformationally alters mutated p53. *Oncogene*. 1995;11(5):933-939.
8. Wang M, Shen A, Zhang C, et al. Development of heat shock protein (Hsp90) inhibitors to combat resistance to tyrosine kinase inhibitors through Hsp90-kinase Interactions. *J Med Chem*. 2016;59(12):5563-5586.
9. Reikvam H, Hatfield KJ, Ersvaer E, et al. Expression profile of heat shock proteins in acute myeloid leukaemia patients reveals a distinct signature strongly associated with FLT3 mutation status–consequences and potentials for pharmacological intervention. *Br J Haematol*. 2012;156(4):468-480.
10. Flandrin P, Guyotat D, Duval A, et al. Significance of heat-shock protein (HSP) 90 expression in acute myeloid leukemia cells. *Cell Stress Chaperones*. 2008;13(3):357-364.
11. Zong H, Gozman A, Caldas-Lopes E, et al. A hyperactive signalosome in acute myeloid leukemia drives addiction to a tumor-specific Hsp90 species. *Cell Reports*. 2015;13(10):2159-2173.
12. Kucine N, Marubayashi S, Bhagwat N, et al. Tumor-specific HSP90 inhibition as a therapeutic approach in JAK-mutant acute lymphoblastic leukemias. *Blood*. 2015;126(22):2479-2483.
13. Wells J, Jain N, Konopleva M. Philadelphia chromosome-like acute lymphoblastic leukemia: progress in a new cancer subtype. *Clin Adv Hematol Oncol*. 2017;15(7):554-561.
14. Butler LM, Ferraldeschi R, Armstrong HK, Centenera MM, Workman P. Maximizing the therapeutic potential of HSP90 inhibitors. *Mol Cancer Res*. 2015;13(11):1445-1451.
15. Wang Y, McAlpine SR. Heat-shock protein 90 inhibitors: will they ever succeed as chemotherapeutics? *Future Med Chem*. 2015;7(2):87-90.
16. Whitesell L, Santagata S, Lin NU. Inhibiting HSP90 to treat cancer: a strategy in evolution. *Curr Mol Med*. 2012;12(9):1108-1124.
17. Duerfeldt AS, Blagg BS. Hsp90 inhibition: elimination of shock and stress. *Bioorg Med Chem Lett*. 2010;20(17):4983-4987.
18. Maloney A, Clarke PA, Naaby-Hansen S, et al. Gene and protein expression profiling of human ovarian cancer cells treated with the heat shock protein 90 inhibitor 17-allylamino-17-demethoxygeldanamycin. *Cancer Res*. 2007;67(7):3239-3253.
19. Bagatell R, Paine-Murrieta GD, Taylor CW, et al. Induction of a heat shock factor 1-dependent stress response alters the cytotoxic activity of hsp90-binding agents. *Clin Cancer Res*. 2000;6(8):3312-3318.
20. McCollum AK, Teneyck CJ, Sauer BM, Toft DO, Erlichman C. Up-regulation of heat shock protein 27 induces resistance to 17-allylamino-demethoxygeldanamycin through a glutathione-mediated mechanism. *Cancer Res*. 2006;66(22):10967-10975.
21. Guo F, Rocha K, Bali P, et al. Abrogation of heat shock protein 70 induction as a strategy to increase antileukemia activity of heat shock protein 90 inhibitor 17-allylamino-demethoxy geldanamycin. *Cancer Res*. 2005;65(22):10536-10544.
22. Hall JA, Forsberg LK, Blagg BS. Alternative approaches to Hsp90 modulation for the treatment of cancer. *Future Med Chem*. 2014;6(14):1587-1605.
23. Wang Y, McAlpine SR. N-terminal and C-terminal modulation of Hsp90 produce dissimilar phenotypes. *Chem Commun (Camb)*. 2015;51(8):1410-1413.
24. Eskew JD, Sadikot T, Morales P, et al. Development and characterization of a novel C-terminal inhibitor of Hsp90 in androgen dependent and independent prostate cancer cells. *BMC Cancer*. 2011;11(1):468.
25. Wang Y, Koay YC, McAlpine SR. How selective are Hsp90 inhibitors for cancer cells over normal cells? *ChemMedChem*. 2017;12(5):353-357.
26. Hughes TP, Ross DM. Moving treatment-free remission into mainstream clinical practice in CML. *Blood*. 2016;128(1):17-23.
27. Wieczorek A, Uharek L. Management of chronic myeloid leukemia patients resistant to tyrosine kinase inhibitors treatment. *Biomark Insights*. 2016;10(Suppl 3):49-54.
28. Ursan ID, Jiang R, Pickard EM, Lee TA, Ng D, Pickard AS. Emergence of BCR-ABL kinase domain mutations associated with newly diagnosed chronic myeloid leukemia: a meta-analysis of clinical trials of tyrosine kinase inhibitors. *J Manag Care Spec Pharm*. 2015;21(2):114-122.
29. Williams LA, Garcia Gonzalez AG, Ault P, et al. Measuring the symptom burden associated with the treatment of chronic myeloid leukemia. *Blood*. 2013;122(5):641-647.
30. Efficace F, Baccarani M, Breccia M, et al; GIMEMA. Health-related quality of life in chronic myeloid leukemia patients receiving long-term therapy with imatinib compared with the general population. *Blood*. 2011;118(17):4554-4560.
31. Kantarjian HM, Shah NP, Cortes JE, et al. Dasatinib or imatinib in newly diagnosed chronic-phase chronic myeloid leukemia: 2-year follow-up from a randomized phase 3 trial (DASISION). *Blood*. 2012;119(5):1123-1129.
32. Chai-Adisaksopha C, Lam W, Hillis C. Major arterial events in patients with chronic myeloid leukemia treated with tyrosine kinase inhibitors: a meta-analysis. *Leuk Lymphoma*. 2016;57(6):1300-1310.
33. Bopp B, Ciglia E, Ouald-Chaib A, Groth G, Gohlke H, Jose J. Design and biological testing of peptidic dimerization inhibitors of human Hsp90 that target the C-terminal domain. *Biochim Biophys Acta*. 2016;1860(6):1043-1055.
34. Ciglia E, Vergin J, Reimann S, et al. Resolving hot spots in the C-terminal dimerization domain that determine the stability of the

molecular chaperone Hsp90. *PLoS One*. 2014;9(4):e96031.

35. Gohlke H, Hergert U, Meyer T, et al. Binding region of alanopine dehydrogenase predicted by unbiased molecular dynamics simulations of ligand diffusion. *J Chem Inf Model*. 2013; 53(10):2493-2498.

36. Miller BR III, McGee TD Jr, Swails JM, Homeyer N, Gohlke H, Roitberg AE. MMPBSA.py: an efficient program for end-state free energy calculations. *J Chem Theory Comput*. 2012;8(9):3314-3321.

37. Bhatia S, Reister S, Mahotka C, Meisel R, Borkhardt A, Grinstein E. Control of AC133/CD133 and impact on human hematopoietic progenitor cells through nucleolin. *Leukemia*. 2015;29(11):2208-2220.

38. Ernst T, Gruber FX, Pelz-Ackermann O, et al. A co-operative evaluation of different methods of detecting BCR-ABL kinase domain mutations in patients with chronic myeloid leukemia on second-line dasatinib or nilotinib therapy after failure of imatinib. *Haematologica*. 2009;94(9):1227-1235.

39. Okabe S, Tauchi T, Tanaka Y, Katagiri S, Kitahara T, Ohyashiki K. Activity of omacetaxine mepesuccinate against ponatinib-resistant BCR-ABL-positive cells. *Blood*. 2013;122(17): 3086-3088.

40. Mahon FX, Deininger MW, Schultheis B, et al. Selection and characterization of BCR-ABL positive cell lines with differential sensitivity to the tyrosine kinase inhibitor STI571: diverse mechanisms of resistance. *Blood*. 2000;96(3): 1070-1079.

41. Pearl LH, Prodromou C. Structure and mechanism of the Hsp90 molecular chaperone machinery. *Annu Rev Biochem*. 2006;75(1): 271-294.

42. Diedrich D, Moita AJ, Rüther A, et al. α-Aminoxy oligopeptides: synthesis, secondary structure, and cytotoxicity of a new class of anticancer foldamers. *Chem Eur J*. 2016; 22(49):17600-17611.

43. Shah NP, Nicoll JM, Nagar B, et al. Multiple BCR-ABL kinase domain mutations confer polyclonal resistance to the tyrosine kinase inhibitor imatinib (STI571) in chronic phase and blast crisis chronic myeloid leukemia. *Cancer Cell*. 2002;2(2):117-125.

44. Gorre ME, Mohammed M, Ellwood K, et al. Clinical resistance to STI-571 cancer therapy caused by BCR-ABL gene mutation or amplification. *Science*. 2001;293(5531):876-880.

45. Jhaveri K, Ochiana SO, Dunphy MP, et al. Heat shock protein 90 inhibitors in the treatment of cancer: current status and future directions. *Expert Opin Investig Drugs*. 2014; 23(5):611-628.

46. Trepel J, Mollapour M, Giaccone G, Neckers L. Targeting the dynamic HSP90 complex in cancer. *Nat Rev Cancer*. 2010;10(8):537-549.

47. Hsu HS, Lin JH, Huang WC, et al. Chemoresistance of lung cancer stemlike cells depends on activation of Hsp27. *Cancer*. 2011;117(7):1516-1528.

48. Gandhi N, Wild AT, Chettiar ST, et al. Novel Hsp90 inhibitor NVP-AUY922 radiosensitizes prostate cancer cells. *Cancer Biol Ther*. 2013;14(4):347-356.

49. Modi S, Saura C, Henderson C, et al. A multicenter trial evaluating retaspimycin HCL (IPI-504) plus trastuzumab in patients with advanced or metastatic HER2-positive breast cancer. *Breast Cancer Res Treat*. 2013;139(1): 107-113.

50. Zhou D, Liu Y, Ye J, et al. A rat retinal damage model predicts for potential clinical visual disturbances induced by Hsp90 inhibitors. *Toxicol Appl Pharmacol*. 2013;273(2): 401-409.

51. Koay YC, McConnell JR, Wang Y, et al. Chemically accessible hsp90 inhibitor that does not induce a heat shock response. *ACS Med Chem Lett*. 2014;5(7):771-776.

52. Sellers RP, Alexander LD, Johnson VA, et al. Design and synthesis of Hsp90 inhibitors: exploring the SAR of Sansalvamide A derivatives. *Bioorg Med Chem*. 2010;18(18): 6822-6856.

53. Marcu MG, Chadli A, Bouhouche I, Catelli M, Neckers LM. The heat shock protein 90 antagonist novobiocin interacts with a previously unrecognized ATP-binding domain in the carboxyl terminus of the chaperone. *J Biol Chem*. 2000;275(47):37181-37186.

54. Yun BG, Huang W, Leach N, Hartson SD, Matts RL. Novobiocin induces a distinct conformation of Hsp90 and alters Hsp90-cochaperone-client interactions. *Biochemistry*. 2004;43(25):8217-8229.

55. Metz A, Ciglia E, Gohlke H. Modulating protein-protein interactions: from structural determinants of binding to druggability prediction to application. *Curr Pharm Des*. 2012; 18(30):4630-4647.

56. Ali MMU, Roe SM, Vaughan CK, et al. Crystal structure of an Hsp90-nucleotide-p23/Sba1 closed chaperone complex. *Nature*. 2006; 440(7087):1013-1017.

57. Lee CC, Lin TW, Ko TP, Wang AH. The hexameric structures of human heat shock protein 90. *PLoS One*. 2011;6(5):e19961.

ACS central science

http://pubs.acs.org/journal/acscii

Research Article

Development of a First-in-Class Small-Molecule Inhibitor of the C-Terminal Hsp90 Dimerization

Sanil Bhatia,*,▲ Lukas Spanier,▲ David Bickel, Niklas Dienstbier, Vitalij Woloschin, Melina Vogt, Henrik Pols, Beate Lungerich, Jens Reiners, Narges Aghaallaei, Daniela Diedrich, Benedikt Frieg, Julian Schliehe-Diecks, Bertan Bopp, Franziska Lang, Mohanraj Gopalswamy, Jennifer Loschwitz, Baubak Bajohgli, Julia Skokowa, Arndt Borkhardt, Julia Hauer, Finn K. Hansen, Sander H. J. Smits, Joachim Jose, Holger Gohlke,*,▲ and Thomas Kurz*,▲

Cite This: https://doi.org/10.1021/acscentsci.2c00013

Read Online

ABSTRACT: Heat shock proteins 90 (Hsp90) are promising therapeutic targets due to their involvement in stabilizing several aberrantly expressed oncoproteins. In cancerous cells, Hsp90 expression is elevated, thereby exerting antiapoptotic effects, which is essential for the malignant transformation and tumor progression. Most of the Hsp90 inhibitors (Hsp90i) under investigation target the ATP binding site in the N-terminal domain of Hsp90. However, adverse effects, including induction of the prosurvival resistance mechanism (heat shock response or HSR) and associated dose-limiting toxicity, have so far precluded their clinical approval. In contrast, modulators that interfere with the C-terminal domain (CTD) of Hsp90 do not inflict HSR. Since the CTD dimerization of Hsp90 is essential for its chaperone activity, interfering with the dimerization process by small-molecule protein−protein interaction inhibitors is a promising strategy for anticancer drug research. We have developed a first-in-class small-molecule inhibitor (**5b**) targeting the Hsp90 CTD dimerization interface, based on a tripyrimidonamide scaffold through structure-based molecular design, chemical synthesis, binding mode model prediction, assessment of the biochemical affinity, and efficacy against therapy-resistant leukemia cells. **5b** reduces xenotransplantation of leukemia cells in zebrafish models and induces apoptosis in BCR-ABL1^{+} (T315I) tyrosine kinase inhibitor-resistant leukemia cells, without inducing HSR.

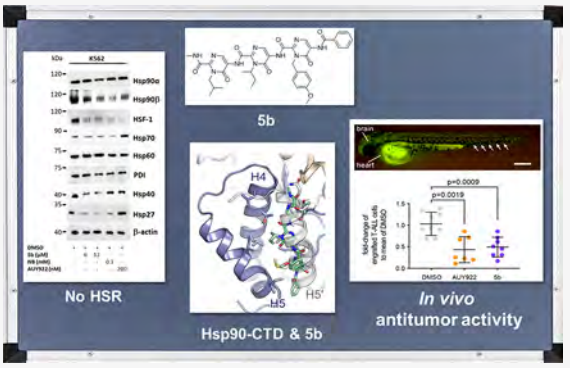

INTRODUCTION

The heat shock proteins of 90 kDa (Hsp90) are abundant, molecular chaperones that modulate the folding, stabilization, and maturation of over 400 client proteins in eukaryotes that are involved in essential processes such as signal transduction, cell cycle progression, and transcription regulation.[1] In cancer cells, Hsp90 is overexpressed and involved in uncontrolled proliferation and antiapoptotic effects and, in that way, is essential for the malignant transformation and progression of several cancer types, including in acute and chronic myeloid leukemia (AML and CML).[2−4] Thus, cancer cells are more dependent on Hsp90 activity than normal cells.[5,6] Multiple signal transduction-promoting oncoproteins are client proteins of Hsp90, including BCR-ABL1 fusion kinase, which is a molecular hallmark of CML.[7] Hence, inhibiting the activity of Hsp90 is a promising strategy for the development of anticancer therapy. Several Hsp90 inhibitors (Hsp90i) have been developed so far, for instance, targeting Hsp90 N- or C-terminal domain (NTD or CTD) or with isoform selectivity, whereas most of the inhibitors studied in clinical trials target the Hsp90 NTD ATP binding site and with a pan-inhibitory profile.[5,8−20] However, adverse events including dose-limiting ocular and cardiac toxicity and poor patient stratification have precluded their clinical approval.[5] Another clinical challenge with the use of Hsp90 NTD-targeting inhibitors is the induction of the prosurvival heat shock response (HSR).[5,8] The HSR is a stress response mechanism mediated by heat shock factor 1 (HSF-1), which leads to the expression of other heat shock proteins (HSPs) including Hsp27, Hsp40, and Hsp70, as a rescue mechanism upon Hsp90 inhibition that eventually weakens the cytotoxic effects of Hsp90i.[5,8,13−16] In addition, Hsp90 NTD-targeting inhibitors potentially inflict cytotoxicity through mechanisms that involve targets other than Hsp90 (off-target effects).[6,21] The off-target effect hypothesis is

Received: January 5, 2022

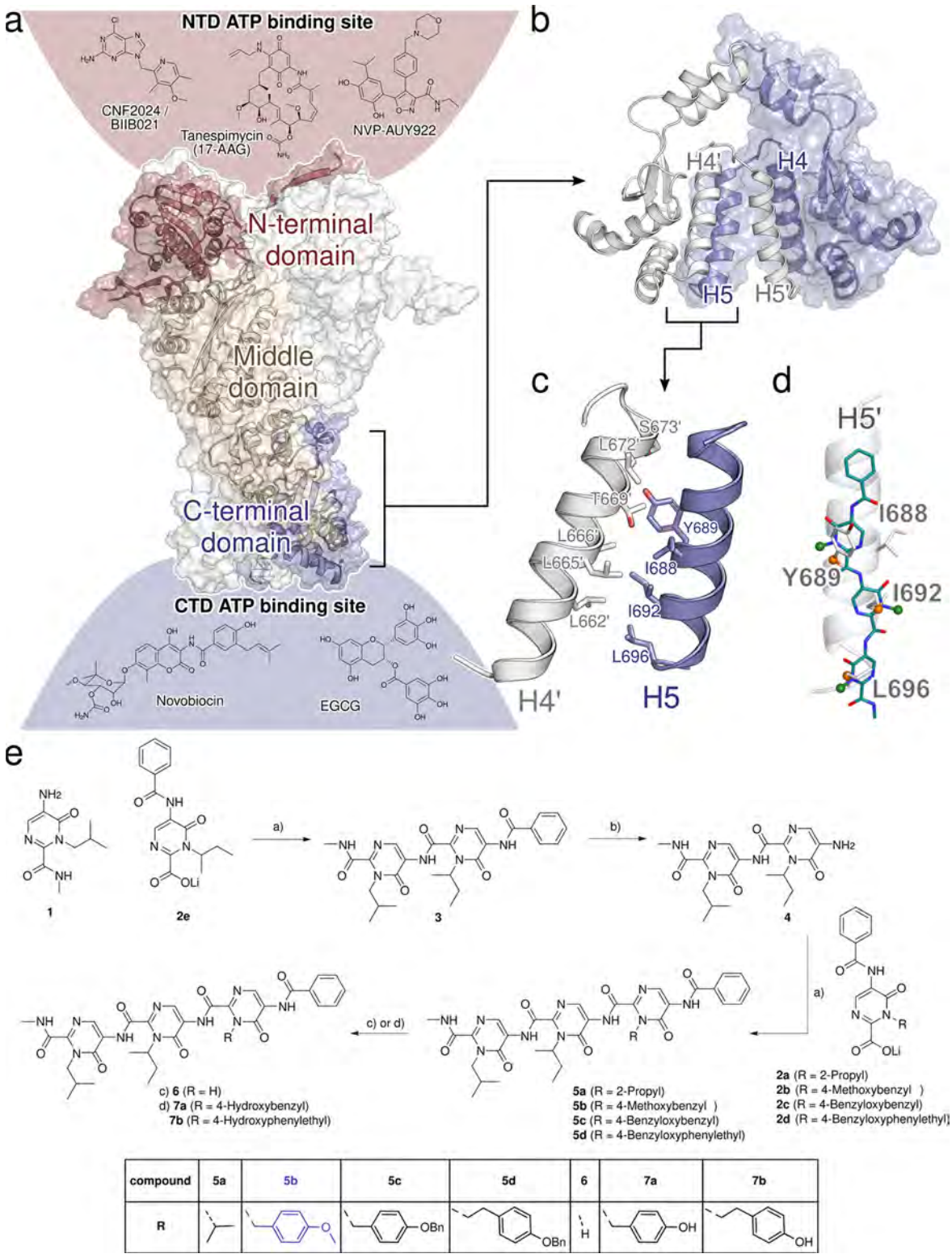

Figure 1. Rational design and synthesis of tripyrimidonamides. (a) Cryo-EM structure of the dimer of human Hsp90β (PDB ID 5FWK),[39] shown in surface and cartoon representations. For one of the Hsp90 monomers, the N-terminal domain (NTD) is colored in red, the middle domain in beige, and the C-terminal domain (CTD) in blue. Above and below the protein structure, the structures of Hsp90i and their potential binding sites (see refs 40−44, color-coded according to the domains) are shown. (b) Dimeric CTD of human Hsp90β with the two monomers in blue and white. Helices H4, H4′, H5, and H5′ of the CTDs form the dimerization interface. (c) Residues forming the CTD dimerization interface in human Hsp90α are primarily located on helices H4, H4′, H5, and H5′.[34] (d) Tripyrimidones can adopt conformations resembling the side chain orientation of an α-helix in i, $i + 4$, and $i + 7$ positions.[38] (e) Synthesis of tripyrimidonamides: (a) COMU, DMF, r.t., 18 h; (b) NaOH, MeOH, 80 °C, 6 h; (a) **2a−2d**, COMU, DMF, r.t., 18 h; (c) **6** via **5b**, BBr_3, DCM, −78 °C, 1 h, r.t., 1 h; (d) via **7a** via **5c** and **7b** via **5d**, H_2, Pd(C), MeOH, DCM, r.t., 1 h.

https://doi.org/10.1021/acscentsci.2c00013
ACS Cent. Sci. XXXX, XXX, XXX−XXX

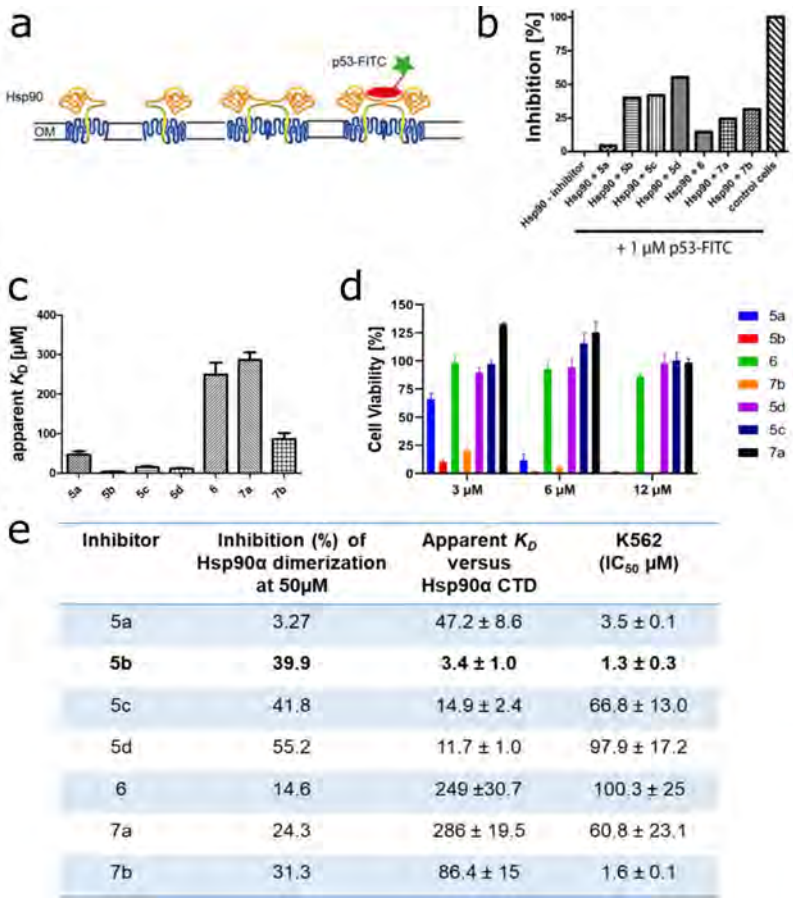

e

Inhibitor	Inhibition (%) of Hsp90α dimerization at 50µM	Apparent K_D versus Hsp90α CTD	K562 (IC_{50} µM)
5a	3.27	47.2 ± 8.6	3.5 ± 0.1
5b	**39.9**	**3.4 ± 1.0**	**1.3 ± 0.3**
5c	41.8	14.9 ± 2.4	66.8 ± 13.0
5d	55.2	11.7 ± 1.0	97.9 ± 17.2
6	14.6	249 ±30.7	100.3 ± 25
7a	24.3	286 ± 19.5	60.8 ± 23.1
7b	31.3	86.4 ± 15	1.6 ± 0.1

Figure 2. Selection of **5b** as a lead candidate. (a) Schematic view of the Hsp90 dimerization assay using Autodisplay. (b) Flow cytometry measurements of the inhibition of dimerized Hsp90α displayed on *E. coli* cells.[36] *E. coli* BL21 (DE3) cells displaying Hsp90α incubated with 1 μM FITC-labeled p53 lead to a high cellular fluorescence indicating dimerization of Hsp90α. The value obtained was set as 0% inhibition. In contrast, *E. coli* cells without displaying Hsp90α (control cells) show no cellular fluorescence. The value obtained here was set as 100% inhibition. Preincubation of *E. coli* cells with surface-displayed Hsp90α with 50 μM of the respective substance leads to a lowered cellular fluorescence intensity indicating a lowered binding affinity of FITC-labeled p53 to surface-displayed Hsp90α. These values were set in relation to obtain the relative inhibition of dimerization. (c) Apparent K_D values of the purified CTD of Hsp90α and the respective substance measured via the MST method. A constant amount of 50 nM labeled CTD of Hsp90 was used, and three independent measurements were performed. The resulting mean values were determined and used in the K_D fit formula. (d) Cellular viability assessment of a leukemic cell line (K562) measured by incubating with the indicated inhibitors for 72 h, followed by a viability measurement using an ATP-based Celltiter Glo assay. (e) Selection of **5b** as a lead candidate on the basis of high inhibition of Hsp90α dimerization, low apparent K_D, and low IC_{50} (μM) in a tested leukemic cell line.

also supported by the significant differences between cytotoxicity concentrations of Hsp90 NTD-targeting inhibitors vs their binding affinity to Hsp90.[21] Furthermore, there are two major cytosolic isoforms of Hsp90 (Hsp90α and Hsp90β) expressed in humans. Hsp90α is an inducible isoform, overexpressed in several cancer types, whereas the Hsp90β isoform is expressed constitutively. Thus, targeting Hsp90 with isoform-specific inhibitors can afford a therapeutic window.[20,22] However, the Hsp90α and Hsp90β isoforms share a high degree of similarity (Figure S21), making it challenging to develop isoform-selective inhibitors.[22]

Hsp90 is a flexible homodimer, and each monomer consists of three major functional domains: NTD, middle domain, and CTD. The activity of Hsp90s depends on the binding and hydrolysis of ATP at the NTD and on its dimerization via the CTD.[2] The middle domain (MD) that connects the NTD and the CTD mediates the binding of clients and cochaperones. The CTD is connected to the MEEVD motif, which interacts with the subset of tetratricopeptide repeat (TPR) domain-containing cochaperones.[2] To our knowledge, inhibiting Hsp90 dimer formation by targeting the CTD dimerization interface constitutes a so far unexplored mode of action (MOA) of small-molecule Hsp90i. In contrast to Hsp90i targeting the N-terminal ATP binding site, C-terminal inhibitors do not generally induce HSR.[8,21,23−25] The most important classes of C-terminal inhibitors are (1) inhibitors binding to the C-terminal nucleotide binding site (e.g., novobiocin and analogues), (2) modulators of the Hsp90-CDC37 interaction (e.g., celastrol, induces HSR[26]), (3) modulators of the Hsp90−p23 interaction (e.g., gedunin), (4) modulators of the Hsp90−HOP interaction (e.g., LB76), (5) modulators addressing an allosteric binding site between CTD and MD, and (6) aminoxyrone (AX), the first nonpeptidic inhibitor of the C-terminal dimerization of Hsp90.[21,27−31]

Following a strategy recently introduced by us to identify protein−protein interaction (PPI) inhibitors,[32,33] we initially identified hot spot residues in the CTD dimerization interface that accounted for most of the binding affinity[34] and identified the first peptidic inhibitors shown to bind to the CTD of Hsp90.[35] Furthermore, we developed AX, the first peptidomi-

https://doi.org/10.1021/acscentsci.2c00013
ACS Cent. Sci. XXXX, XXX, XXX−XXX

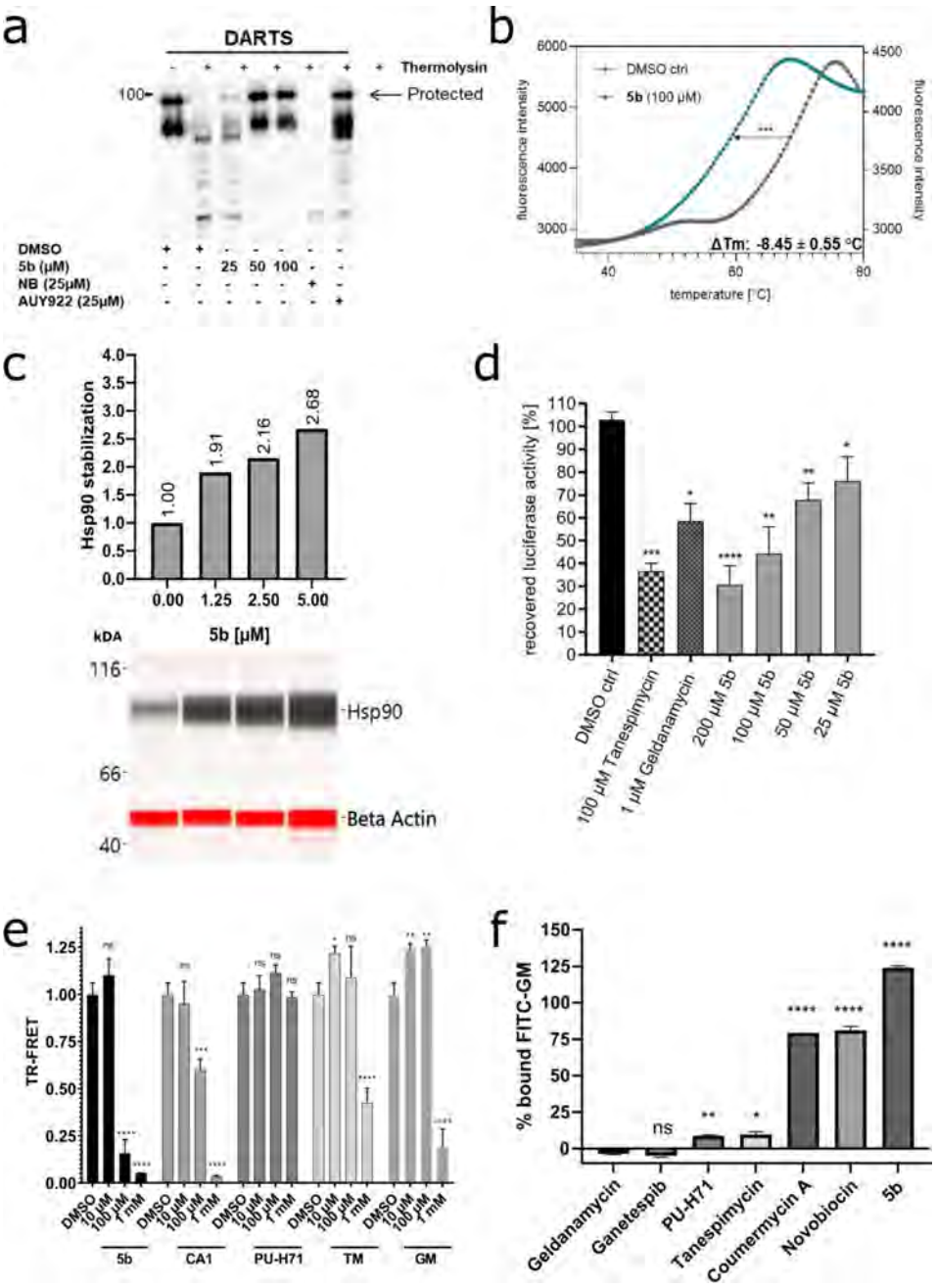

Figure 3. Specificity of **5b** against Hsp90 CTD and its cochaperone function. (a) Recombinant (full-length) Hsp90α (1 μg) was incubated with **5b** at indicated concentrations, followed by digestion with thermolysin. Treated protein samples were electrophoresed (SDS-PAGE) and immunoblotted with anti-Hsp90α for detecting the protection of Hsp90α protein by **5b** (the upper band is protected from proteolysis). (b) A cell-free thermal shift assay was performed by incubating recombinant Hsp90α CTD protein with **5b** at an increasing temperature (up to 95 °C). The melting temperature (T_m) without inhibitors (DMSO) was used as a control. (c) Dose-dependent intracellular (K562 cells) thermal stabilization ($CETSA_{ITDRF}$) of Hsp90 after **5b** incubation (24 h) at its increasing concentration (1.25−5 μM). (d) **5b** inhibits the Hsp90α chaperone function, comparable to TM and GM, in the cell-free luciferase refolding assay, where the incubation of the inhibitors prevented the rabbit reticulocyte lysate (a source of Hsp90)-assisted refolding of denatured luciferase. (e) Incubation of **5b** blocked the binding of Hsp90 CTD-interacting cochaperone (PPID) in TR-FRET measurements. (f) **5b** did not reduce the amount of Hsp90-bound FITC-labeled GM and, therefore, does not compete for the GM binding pocket of full-length Hsp90α. Unlabeled GM, GP, PUH71, and TM served as positive controls and NB and CA1 as negative controls.

metic Hsp90 CTD dimerization inhibitor,[36] which is a promising lead candidate effective against BCR-ABL1$^+$ TKI-resistant leukemic cells.[36] Based on these experiences, here, we report the rational design, chemical synthesis, binding mode model, biochemical affinity, and biological *in vitro* evaluation of a first-in-class small-molecule inhibitor (**5b**) of Hsp90 CTD dimerization based on a tripyrimidonamide scaffold.

■ RESULTS

Design of Tripyrimidonamides as CTD Hsp90 Inhibitors. Based on computational predictions and subsequent experimental validation, we identified the spatially clustered hot spot residues I688, Y689, I692, and L696 in the Hsp90 CTD interface, which are located on α-helix H5, form a functional epitope, and account for most of the protein dimerization

https://doi.org/10.1021/acscentsci.2c00013
ACS Cent. Sci. XXXX, XXX, XXX−XXX

energy.[34] Furthermore, conformational analysis by 2D NMR and MD simulations revealed for the recently introduced tripyrimidonamide scaffold that it can act as a potential α-helix mimetic, mimicking side chains at positions i, $i + 4$ (dimeric compound) or i, $i + 4$, $i + 8$ (trimeric compound).[37,38] This side chain pattern is concordant with the succession of the hot spot residues in the Hsp90 CTD interface.

Together, this provided the incentive for us to design and synthesize the tripyrimidonamide **5a**, which mimics the hot spots I688, I692, and L696. In compound **5a**, the side chain of V was used instead of I to avoid diastereomers. **6**, which lacks the isopropyl side chain, was also designed to probe the influence of the absence of the third side chain in a tripyrimidonamide. Next, we aimed to design compounds that can also form polar interactions, as these should confer specificity of binding.[34] In addition, the binding to a well-defined cleft or groove in a PPI region has been described to yield a particularly effective PPI inhibitor.[34] The Y689 side chain of **7a** should be accommodated in an indentation in the binding epitope of helix H4′ (Figure 1);[34] we also designed the homologue **7b** with a prolonged (4-hydroxy-phenyl)-ethyl side chain. Although both compounds mimic the three hot spots Y689, I692, and L696, with the longer side chain in **7b**, we intended to accommodate for the apparent mismatch between the preferred side chain orientations in tripyrimidonamides and the side chain pattern of the hot spots (i, $i + 3$, $i + 4$). The side chain patterns of **5b** and **7a** are almost identical to that of the α-aminoxy-peptide AX, which was shown to bind to the CTD.[36]

Further analysis of the physicochemical properties of the CTD dimerization interface revealed a particular hydrophobic patch there (Figure 1). Interestingly, the 4-methoxy-benzyl side chain of **5b** should act as a (weak) hydrogen bond acceptor for S673′ and T669′ on helix H4′ but, at the same time, decrease the side chain's hydrophilicity for a more favorable burial in the overall hydrophobic interface. To probe this with a larger substituent, we also designed the benzyloxy derivatives **5c** and **5d**, which are also precursors of **7a** and **7b**, respectively.

Synthesis of Tripyrimidonamides. The monomeric building blocks **1** and **2a−2e** were prepared according to our previously published protocol.[38] Subsequently, the designed tripyrimidonamides **5a−5d** were synthesized using a modular approach. Briefly, a COMU-mediated amide coupling of the lithium carboxylate **2e** with 5-aminopyrimidone **1** afforded the benzoyl-protected dimer **3** in 75% yield. Deprotection of the benzoyl-group by treatment of **3** with sodium hydroxide in methanol at 80 °C afforded the unprotected dimer **4** (77% yield). Additional coupling reactions of **4** with the respective lithium salts **2a−2d** in the presence of COMU furnished the tripyrimidonamides **5a−5d** in 39−76% yield. Compound **6** with an *N*-unsubstituted N-terminal pyrimidone ring was synthesized by treating the corresponding 4-methoxybenzyl-substituted derivative **5b** with BBr_3 in DCM (Scheme S1). Finally, the tripyrimidonamides **7a** and **7b** with free phenolic groups were prepared by catalytic hydrogenation of their respective *O*-benzyl-protected precursors **5c** and **5d** (40% and 87% yield).

Selection of 5b as a Lead Candidate. To evaluate the inhibition of Hsp90 dimerization, *Escherichia coli* BL21 (DE3) pETSH-3 cells were used to display Hsp90α on their surface (Figure 2a).[35] Passenger-driven dimer formation of Hsp90α is facilitated through the motility of the β-barrel domain within the outer membrane of *E. coli*, as reported for other proteins.[45] To demonstrate the functionality of dimerized Hsp90 on the surface of *E. coli*, the transcription factor p53, a natural client protein of Hsp90, was labeled with fluorescein isothiocyanate (FITC) and added to cells displaying Hsp90 on their surface. A subsequent flow cytometer analysis revealed a high green fluorescence for cells displaying Hsp90, indicating dimerized and functional Hsp90 (Figure 2b). Compounds **5a**, **6**, and **7a** showed only weak inhibition of 3.27%, 14.65%, and 24.35%, respectively. In contrast, **5b−5d** and **7b** showed moderate inhibition of 39.92%, 41.83%, 55.23%, and 31.33%, respectively (Figure 2b).

Later, the binding affinity of the compounds was determined with microscale thermophoresis (MST) measurements using the NT-647-labeled recombinant CTD of the Hsp90α protein.[36] A nonlinear regression curve was fitted with the KD formula, and as expected, substances showing weak inhibition have high dissociation constants (**6**, 249 μM; **7a**, 286 μM; Figure 2c,e). The lowest KD value was observed for **5b** (3.42 ± 1.0 μM) and the second lowest for **5d** (11.74 ± 1.0 μM) (Figure 2c,e). These findings are paralleled by the *in vitro* cytotoxicity assessment of compounds **5a−5d**, **6**, **7a**, and **7b**, which also revealed **5b** as the most promising candidate (with low IC_{50}: 1.3 ± 0.3 μM) in a BCR-ABL1$^+$ tested leukemia cell line K562 (Figure 2d,e).

Based on the inhibition of Hsp90α CTD dimerization, the low apparent K_D value for the Hsp90α CTD, and the potent antileukemic activity, **5b** was selected for further detailed affinity and efficacy assessments.

5b Binds Specifically to CTD of Hsp90α and Blocks Its Cochaperone Function. One of the major limitations of NTD-targeting inhibitors is their off-target activity.[6,21] Hence, it is important that the selected hit **5b** has a high degree of selectivity against its target, the CTD of Hsp90. To assess the selectivity of **5b**, biochemical cell-free and cellular assays were performed. First, we evaluated the affinity of **5b** against Hsp90 in a cell-free assay, where **5b** protected recombinant (full-length) Hsp90α protein in a dose-dependent fashion from degradation against thermolysin enzyme digestion, an assay commonly used to quantify drug affinity-responsive target stability (DARTS)[23,46] (Figure 3a). Next, we performed the cell-free thermal shift assay[47] to determine the potential binding affinity of **5b** to recombinant Hsp90α CTD and NTD protein. **5b** specifically destabilized the CTD of Hsp90α protein Hsp90 CTD (ΔT_m: −8.45 ± 0.55 °C), whereas reference CTD-targeting Hsp90i coumermycin A1 (CA1) stabilized Hsp90α CTD protein (Figure 3b, Figure S22 and Table S1). NTD-targeting Hsp90i tanespimycin (TM) and PUH-71 served as a positive (Hsp90α NTD) or negative (Hsp90α CTD) control in this assay. The thermostabilizing effect of **5b** to its target (total Hsp90) was also assessed in a cellular setup, termed the cellular thermal shift assay (CETSA),[47−49] a biophysical method based on the ligand-induced thermal stabilization of the protein to directly probe the target engagement in the living cells (Table S1 and Figure S23). The protein quantification for CETSA was performed using a digital Western blotter for a sensitive and quantitative evaluation of the ligand-protected intracellular Hsp90, whereas TM and PU-H71 served as controls. Next, the thermal stability of intracellular Hsp90 in an increasing concentration of **5b** (at a fixed temperature) was determined, a method termed isothermal dose−response fingerprint $ITDRF_{CETSA}$.[48] **5b** induced the thermal stability of Hsp90 in a dose-dependent fashion, confirming its intracellular and specific target engagement (Figure 3c, Table S1).

Next, to assess the ability of **5b** to inhibit the Hsp90 chaperone function, a cell-free luciferase-refolding assay[50−52] was performed using rabbit reticulocyte lysates as a source of

https://doi.org/10.1021/acscentsci.2c00013
ACS Cent. Sci. XXXX, XXX, XXX−XXX

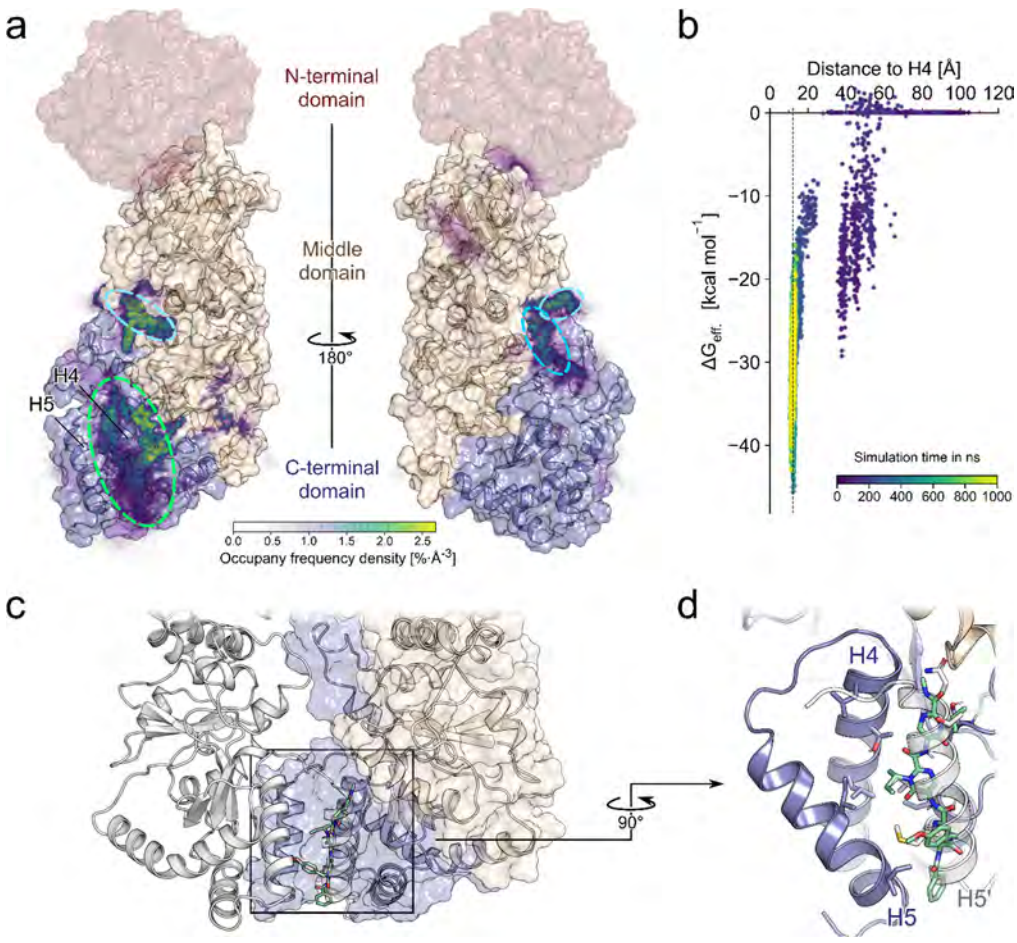

Figure 4. MD simulations of **5b** diffusion and effective binding energy calculations to predict the binding mode. (a) The relative densities of the bound poses of **5b** after 500 ns are mapped on the Hsp90α monomer fragment used in the simulations (PDB ID 3q6m). The missing NTD is shown in red, based on the Hsp90β structure (PDB ID 5fwk). Particularly high densities are observed in the region between H4 and H5 (green circle). A second, less preferred site is in the cleft between the CTD and middle domain (blue circles). (b) Effective binding energy calculations over a single trajectory that resulted in **5b** binding in the C-terminal helix interface as a function of the center-of-mass distance between **5b** and H4 and the simulation time (see the color scale). The dashed line at 12.1 Å corresponds to the H4−H5′ distance in the crystal structure of PDB ID 3q6m. (c) Possible binding mode of **5b** in the helix interface, where **5b** mimics H5′. (d) Blow-up of the possible binding mode of **5b** showing how its side chains mimic side chains of H5′.

Hsp90. Exposure of **5b** decreased the luciferase refolding capacity in a dose-dependent manner by blocking the chaperone function of Hsp90 (Figure 3d). The known Hsp90 NTD inhibitors geldanamycin (GM) and TM served as positive controls. In addition, to assess the specific effect of **5b** in obstructing Hsp90 CTD-interacting cochaperones, a time-resolved fluorescence resonance energy transfer (TR-FRET) assay was conducted.[53] **5b** blocked the binding of PPID (or cyclophilin D, an Hsp90 CTD-interacting chaperone) to recombinant Hsp90α or Hsp90β CTD protein comparable to the CA1 treatment, whereas PU-H71, TM, and GM served as negative controls (Figure 3e, Table S1). To rule out the possible interaction of **5b** with the NTD of Hsp90α, a fluorescence polarization (FP) competitive assay was carried out using FITC-labeled GM[50] (Figure 3f, Table S1). As expected, **5b** did not show any interaction with the NTD of Hsp90, whereas unlabeled Hsp90 NTD-targeting inhibitors GM, ganetespib (GP), TM, and PU-H71 served as positive controls.

Binding Mode Prediction of 5b at Hsp90α. To provide structural insights into how **5b** binds to the CTD of human Hsp90, we performed 40 independent molecular dynamics (MD) simulations of free diffusion of **5b** in the presence of truncated monomeric Hsp90α (aa 294−699) using the Amber 18 suite of molecular simulation programs[54] and the ff14SB[55] and a modified GAFF[38,56] force field for protein and ligand. Initially, we generated 40 individual starting configurations by randomly placing **5b** and the CTD structure, leaving at least 10 Å between atoms in **5b** and the CTD structure. After minimization, thermalization, and density adaptation, we performed MD simulations of 500 ns length, in which the **5b** molecule diffused freely. To counter the high flexibility of the C-terminal helix interface, we introduced positional restraints on the backbone atoms, adjusting the reference coordinates every 100 ns to allow for moderate protein movements.

From the trajectories, first, we extracted all frames where **5b** is bound to Hsp90 (no-fit RMSD of **5b** $\leq$1.5 Å to the previous frame after superimposing Hsp90). Mapping the probability density of occurrence of **5b** onto the surface of Hsp90 (Figure 4a) revealed two main binding regions: one in the C-terminal helix interface (Figure 4a, green), where binding occurred in 10 out of the 40 replicas, and another in a cleft between the CTD and middle domain (Figure 4a, blue), where binding occurred in 6 out of 40 replicas. In the latter case, an area of high density with the shape of **5b** is observed (Figure 4a, light blue), which resulted from a single trajectory. This indicates that the ligand was kinetically trapped in this one case, although the position is

https://doi.org/10.1021/acscentsci.2c00013
ACS Cent. Sci. XXXX, XXX, XXX−XXX

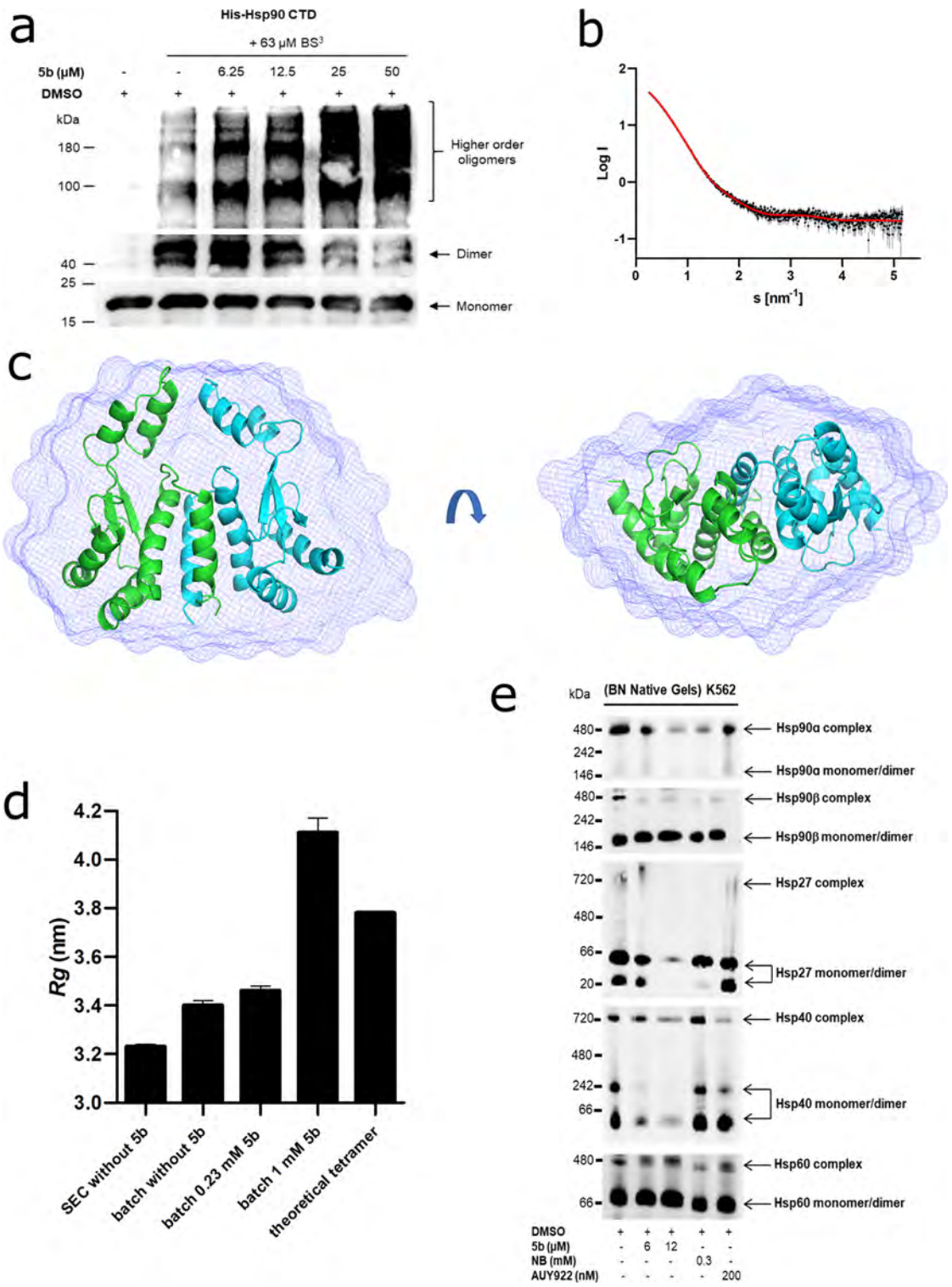

Figure 5. Effect of **5b** on Hsp90 oligomeric species and CTD-mediated dimerization. (a) Recombinant Hsp90α CTD was incubated with 63 μM BS^3 cross-linker with (at the indicated concentration) or without **5b**, followed by immunoblotting with the anti-Hsp90 (AC88) antibody. (b) The scattering data of Hsp90α CTD is shown in black dots, with gray error bars. The *ab initio* DAMMIF model fit is shown as a red line. The intensity is displayed as a function of momentum transfer *s*. (c) The volumetric envelope, calculated from the scattering data using DAMMIF,[65] is shown as a blue surface. The monomers of the predicted Hsp90 CTD dimer model are shown in green and cyan. Superimposing was performed using SUPCOMB.[65] (d) The radius of gyration (R_g) of the different Hsp90α CTD protein samples was calculated using the Guinier approximation.[66] The theoretical R_g of the tetramer was calculated using CRYSOL based on the structure PDB ID 3q6m.[67] (e) Native Hsp90 complexes in K-562 (24 h administration of **5b**) were identified by running blue native (BN) gels followed by immunoblotting analysis. The cytotoxic concentration of **5b** resulted in the potent disruption of Hsp90α, Hsp90β, Hsp40, and Hsp27 complexes and monomers/dimers. AUY922 exposure elevated the expression of HSR associated protein complexes and monomers/dimers (Hsp40 and Hsp27), whereas Hsp60 served as loading controls.

https://doi.org/10.1021/acscentsci.2c00013
ACS Cent. Sci. XXXX, XXX, XXX−XXX

thermodynamically not favorable. By contrast, the densities in the C-terminal interface are more ambiguously shaped, indicating that, while binding there is favorable, the ligand can still explore multiple binding modes, which are also seen to interchange.

To further study these binding modes, we clustered the bound frames of **5b** mapped on the protein surface with respect to their RMSD after superimposing Hsp90. Among the binding modes were several that form interactions to the C-terminal helix interface, with **5b** positioned such that it mimics interactions formed by H5′ in the dimer (Figure 4c,d). To corroborate that this binding mode is favorable, we computed the effective binding free energies by the MM-GB/SA approach for the trajectory that led to it. The first transient interactions with the protein already resulted in effective energies down to ∼−30 kcal mol^{-1}. The effective energies decreased further to ∼−45 kcal mol^{-1} once the ligand was bound in the C-terminal interface, thereby forming interactions with Hsp90 that remained stable even when the trajectory was extended to 1 μs, indicating that such poses are particularly favorable (Figure 4b). Regarding the magnitude of the effective energies, note that configurational entropy contributions were not considered, since estimating such contributions by a normal-mode analysis may introduce additional uncertainties.[57,58]

Overall, the probability density of bound **5b** poses, the proportion of replicas, and the results of the MM-GB/SA computations indicate that **5b** preferentially binds to the C-terminal helix interface, where it can adopt poses that mimic H5′.

Comparison to 5b Binding at Hsp90*β*. We then set out to study whether there is an isoform specificity for the binding of **5b** because the helical interface regions differ in three positions: *α*, S641; *β*, P633; *α*, S658; *β*, A650; *α*, A685; *β*, S677 (Figure S21). Using the same setup as before, we performed MD simulations of free ligand diffusion around Hsp90*β*. The probability density of bound **5b** again revealed that the C-terminal helix interface is the most preferred region, followed by the cleft between the CTD and middle domain (Figure S24). Notably, no high density in this cleft was then found, in contrast to Hsp90*α*, confirming that the observation there resulted from kinetic trapping. Hence, despite the few sequence variations in the C-terminal helix interface between Hsp90*α* and Hsp90*β*, the same preferred binding region of **5b** was found in both cases.

5b Interferes with Hsp90*α* CTD Dimers and Disrupts Intracellular Hsp90 Multiprotein Complexes. CTD dimerization of Hsp90 is necessary for its function.[59,60] To study the effect of **5b** exposure on the dissociation of Hsp90 dimers in a cell-free assay, we used Hsp90*α* CTD protein after incubation with amine-reactive cross-linker BS^3, as previously described.[50,53] A dose-dependent reduction of Hsp90*α* CTD dimers along with an increase in the high-order oligomeric species was noticed upon incubation with **5b** (Figure 5a). Next, we performed small-angle X-ray scattering (SAXS) with the Hsp90*α* CTD protein, which was coupled to a size exclusion chromatography column (SEC-SAXS) at the ESRF beamline BM29 in Grenoble.[61,62] In the absence of **5b**, a clear dimeric profile of the Hsp90*α* CTD protein was visible on the chromatogram, with an additionally minor tetrameric species (Figure S25). We used the program CHROMIXS[63] to merge the frames containing the dimer from this SEC-SAXS profile. Buffer frames were then subtracted using PRIMUS.[64] From the SAXS data, a radius of gyration (R_g) of 3.23 nm was calculated, which describes the average particle dimension in solution. The *ab initio* model fit from DAMMIF[65] shows a χ^2 of 1.127, indicating good agreement with the experimental data (Figure 5b and Table S2). The corresponding dimeric envelope is highlighted in Figure 5c, superimposed with the calculated dimeric model of Hsp90*α* CTD. Further, we tested the effect of **5b** on the Hsp90 CTD dimer using SAXS (Figure 5d). Due to the low solubility of **5b**, we needed to measure the sample as an ensemble of species in solution. First, we tested Hsp90*α* CTD without **5b** on Xeuss 2.0 with the Q-Xoom system and observed an increase of R_g to 3.40 nm. This increase is likely due to the small amount of tetramer in solution in the ensemble. Theoretically, the R_g of a tetrameric Hsp90*α* CTD species is 3.78 nm, using CRYSOL, indicating that, even in batch mode SAXS measurements, the Hsp90*α* CTD protein is predominantly in a dimeric state. We added **5b** with an equimolar concentration to Hsp90*α* CTD protein, and the R_g value slightly increased from 3.40 to 3.46 nm. However, with an increasing concentration of **5b** to 1 mM, the R_g value increased to 4.11 nm. Compared to the theoretical R_g value of 3.78 nm for the tetramer, we observed that **5b** induces oligomerization of Hsp90*α* CTD to species even larger than the tetrameric form (Figure 5e). It is unclear, however, if the oligomers are formed from Hsp90*α* CTD monomers or dimers, as the single species could not be resolved in the ensemble measurement.

In a cellular context, Hsp90 acts in multiprotein complexes.[23] Therefore, interfering with Hsp90 function may lead to the disruption of these complexes. In a cellular assay, Western blotting was performed under reducing (+dithiothreitol or +DTT) and nonreducing (−DTT) conditions after **5b** incubation of the K562 cells.[36] Similarly to AX,[36] **5b** inhibited the formation of Hsp90 higher-order multimeric species, in contrast to novobiocin (NB) but in concordance with AUY922 (Figure S26). Next, to study the effect of **5b** exposure on Hsp90 native multiprotein complexes, blue native (BN) PAGE analysis was carried out with K562 cell lysates after **5b** incubation.[23,36] At cytotoxic concentrations of **5b**, Hsp90*α* and Hsp90*β* multiprotein complexes were disrupted, including monomers/dimers of Hsp40 and Hsp27; Hsp60 (primarily in mitochondria) multiprotein complexes, serving as a loading control, were not affected (Figure 5e). The extent of Hsp90*α* or *β* complex/monomer/dimer disruption by **5b** was comparable to the controls (NB and AUY922). Moreover, the expression of detected Hsp90*α* monomeric/dimeric species was prominently lower than the Hsp90*β* monomeric/dimeric species in the blue native PAGE analysis, which makes it difficult to conclude whether **5b** had any intracellular isoform selectivity, especially in disrupting Hsp90 dimerization.

Taken together, these results confirm that **5b** interferes with the Hsp90*α* CTD dimerization, induces oligomerization, and disrupts intracellular Hsp90 multiprotein complexes.

Basic Physicochemical Properties and Microsomal Stability of 5b. Next, we assessed the aqueous solubility, chemical stability, and *in vitro* metabolic stability of **5b** (Supporting Information). The thermodynamic solubility of **5b** was determined in phosphate-buffered saline (PBS, 25 °C, pH 7.4) after 4 and 24 h of incubation. Ondansetron was used as a reference compound with a high solubility of 95 μM. The thermodynamic solubility of **5b** was low, ranging from 5 μM after 4 h to 8 μM after 24 h (n = 2). To study the chemical stability of **5b** at physiological pH, the compound was dissolved in a mixture of Tween20/ethanol/phosphate buffer pH 7.5 (7/3/90) and monitored over 24 h. After 24 h, almost no decomposition was detected (0.7% drug decomposition, n = 2).

https://doi.org/10.1021/acscentsci.2c00013
ACS Cent. Sci. XXXX, XXX, XXX−XXX

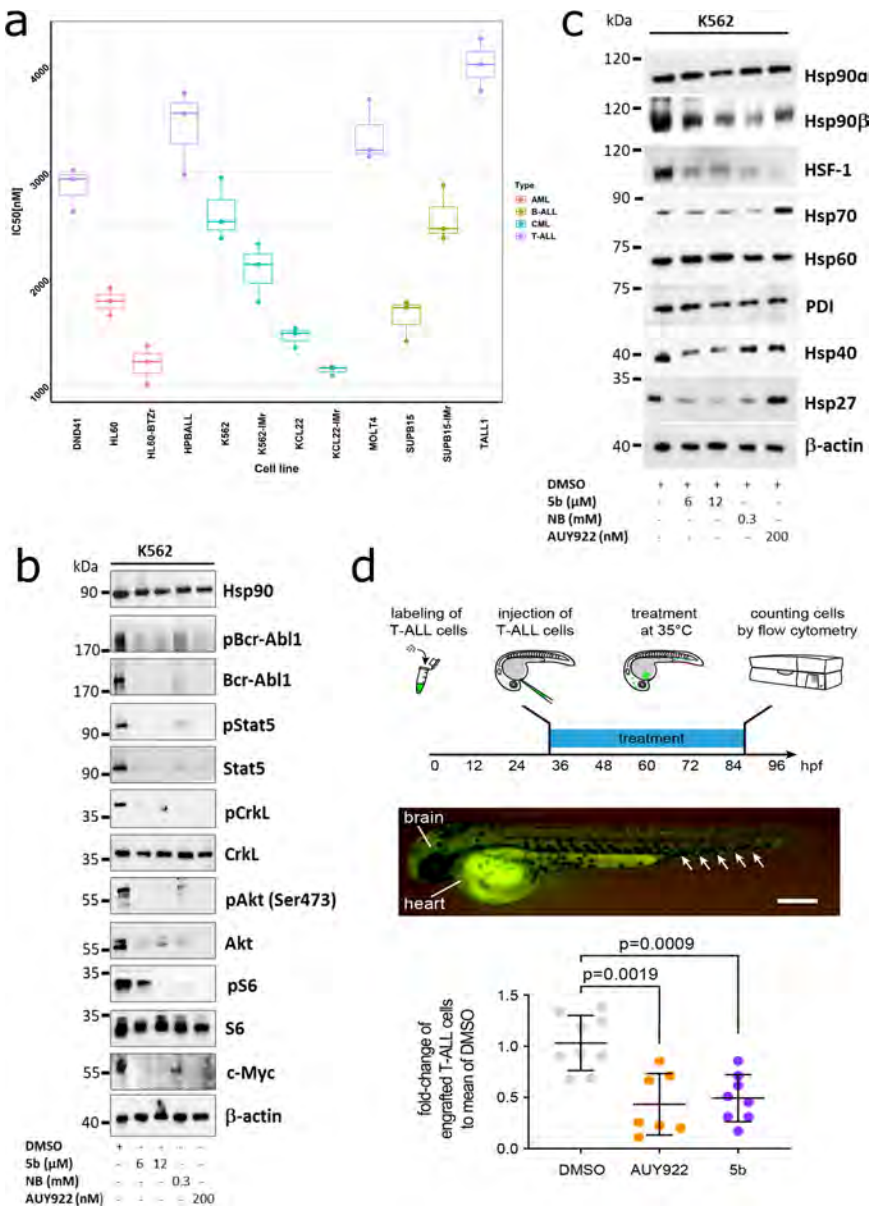

Figure 6. 5b is effective against human leukemic cell lines without inducing any HSR. (a) Comparative cytotoxicity assessment of different subgroups of leukemic cell lines (K562, KCL22, SUPB15, HL60, MOLT4, DND41, TALL1, and HPBALL), imatinib-resistant cell lines (K562-IMr, KCL22-IMr, SUPB15-IMr), and the bortezomib-resistant cell line (HL60-BTZr) after 72 h of exposure to **5b**. The IC_{50} data was plotted as a clustered heat map, followed by unsupervised hierarchical clustering. The vertical axis of the dendrogram exemplifies the dissimilarity between clusters, whereas the color of the individual cell is related to its position along a log IC_{50} (μM) gradient. (b) The treatment of K562 cells with **5b** and respective controls (AUY922 and NB) for 48 h resulted in the downregulation of BCR-ABL1$^+$ and subsequent downstream signaling pathways including phosphorylated and unphosphorylated Stat5a, Crkl, Akt, S6 (mTOR), and cMyc. (c) K562 cells were treated with the indicated (cytotoxic) concentration of **5b**, NB, and AUY922 for 48 h, and later, protein lysates were subjected to immunoblot analysis. As expected, **5b** and NB did not induce expression of Hsp70, Hsp40, and Hsp27, whereas AUY922 led to HSR induction. Hsp60 (primarily present in mitochondria) and PDI (endoplasmic reticulum) served as a control. (d) (upper) description of the experimental rationale; (middle) representative image of a xenotransplanted zebrafish embryo at 32 hpf [scale bar, 250 μm; note that human T-ALL cells (green) were distributed in the yolk, brain, and hematopoietic tissue (arrows)]; (lower) fold-change of labeled cells normalized to the average percentage of labeled cells in the DMSO-treated group. Each dot represents three embryos pooled as one biological sample. Data are mean $\pm$ standard deviation. The p-values were calculated with the Mann−Whitney test.

The chemical stability of **5b** at acidic pH was determined by dissolving **5b** in a mixture of Tween20/ethanol/phosphate buffer pH 2 (7/3/90) and monitoring over 24 h. After 24 h, only slight decomposition was detected (1.3% drug decomposition, $n = 2$).

A metabolic stability screening of **5b** in human liver microsomes revealed 91% stability after a 40 min incubation at 37 °C. Propanolol, a reference drug with medium to high metabolic stability, showed 74% of the parent compound remaining and therefore demonstrated slightly decreased stability compared with **5b**. Calculated results for the intrinsic clearance suggest that **5b** [6 μL/(min mg)] is a low-clearance compound with an estimated long half-life ($n = 2$).

5b Is Effective against Resistant Leukemia Cells and in the Zebrafish Xenotransplantation Model. Elevated Hsp90 expression is reported in several resistant leukemia

https://doi.org/10.1021/acscentsci.2c00013
ACS Cent. Sci. XXXX, XXX, XXX−XXX

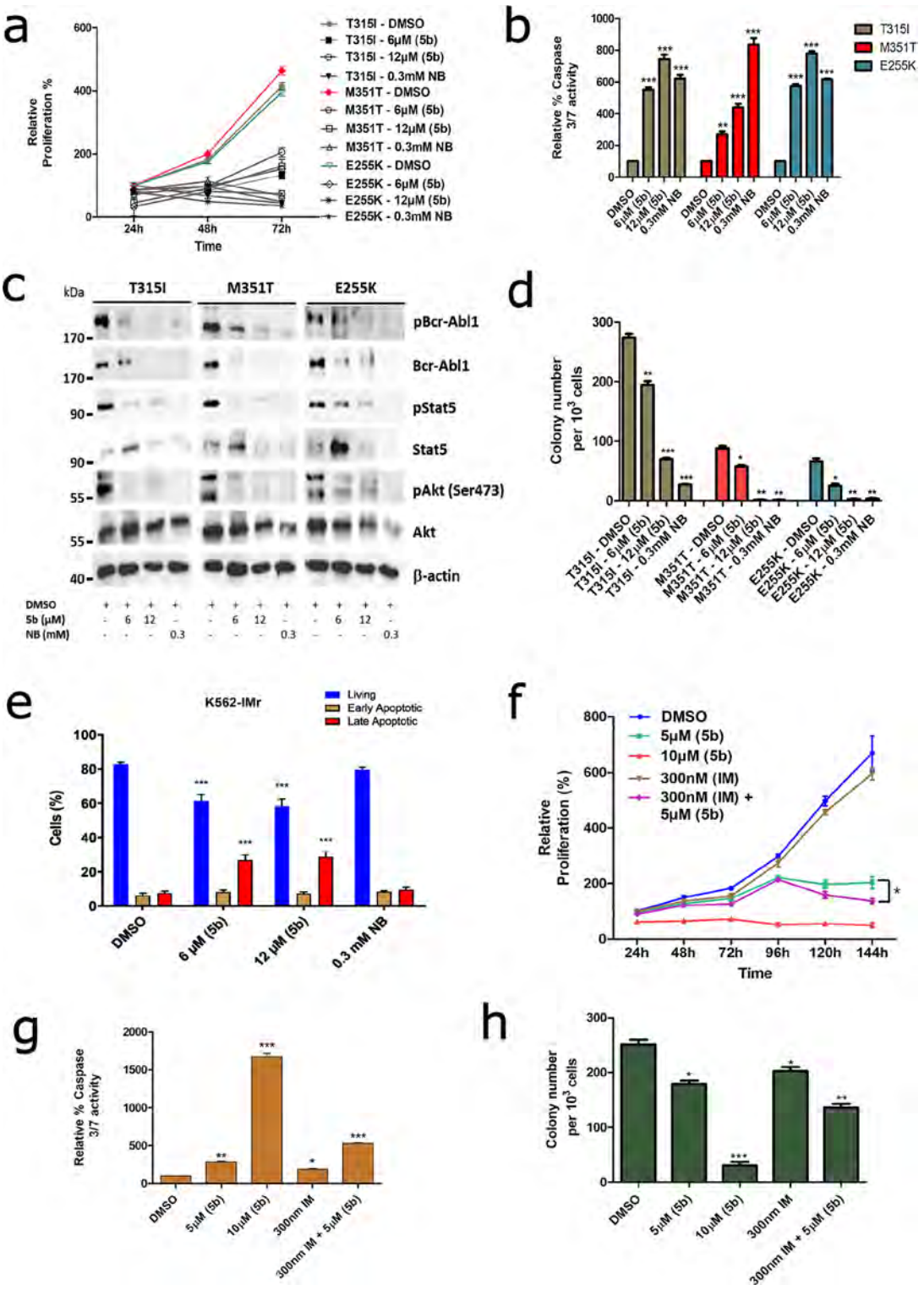

Figure 7. 5b as a potent inhibitor against the TKI-resistant BCR-ABL1 mutant and a primary patient sample. (a) BA/F3 cells expressing BCR-ABL1 mutants (T315I, M351T, and E255K) were treated with the indicated concentration of **5b**, and later, viable cells were counted after every 24 h interval for 3 days. (b) Apoptosis induction of the same cells after 48 h of incubation of the compounds at the indicated concentration, determined by a caspase 3/7 dependent Glo assay. (c) Exposure of **5b** to these cells destabilizes BCR-ABL1 and, subsequently, its associated downstream signaling pathways. (d) BA/F3 BCR-ABL1 mutant-expressing cells were seeded in methylcellulose-based semisolid medium after 24 h of treatment with **5b**. Colonies were counted after 14 days. (e) K562-IMr cells were treated with the indicated concentration of **5b** for 48 h, later dually stained with annexin V/PI, and subsequently measured by FACS. (f) Primary CML^{CD34+} patient cells were treated with the indicated concentration of **5b** or IM alone or in combination, and later, viable cells were counted after every 24 h interval for 6 days. (g) Apoptosis induction in primary CML^{CD34+} patient cells after exposure of **5b** or IB alone or in combination. (g) Primary CML^{CD34+} patient cells were seeded in methylcellulose medium after 24 h of treatment with **5b**, IM alone, or both in combination. Colonies were counted after 14 days. Columns depict the mean of three independent experiments ($n = 3$).

https://doi.org/10.1021/acscentsci.2c00013
ACS Cent. Sci. XXXX, XXX, XXX−XXX

subtypes such as BCR-ABL1$^+$ CML/BCP-ALL, FLT3-ITD-driven AML, and Ph-like BCP-ALL.[68−71] In addition, client proteins of Hsp90 include several kinases (e.g., AKT, BCR-ABL1, BRAF, EGFR2, HER2, and JAK1/2), growth and steroid receptors, and apoptotic factors (e.g., BCL-2 and mutant p53), which are often aberrantly regulated in several malignancies.[2,72] Therefore, we determined the efficacy of **5b** on therapy-resistant cell lines obtained from different leukemia subtypes (B-ALL, T-ALL, CML, and AML), including imatinib (IM) and multi-TKI-resistant and bortezomib (BTZ)-resistant leukemic cell lines.[36] Average IC_{50} values of **5b** in these cell lines were determined using an ATP-based viability assay and were plotted in a clustered heat map, indicating the superior efficacy against BCR-ABL1$^+$ and AML leukemic cell lines when compared to T-ALL cell lines (Figure 6a).

As previously performed with AX,[36] we next determined the destabilizing effect of **5b** on BCR-ABL1 expression and associated downstream signaling. In K562 cells, 48 h of exposure of **5b** downregulated the phospho-BCR-ABL1 and total-BCR-ABL1 levels as well as the related downstream signaling pathways, as evaluated by an immunoblot analysis (Figure 6b). **5b** additionally reduced the expression of client proteins associated with Hsp90 chaperone activity, involving Akt, Stat5, and c-Myc (Figure 6b). In contrast to AUY922, the exposure of **5b** on the K562 cells did not induce the expression of Hsp70, Hsp40, and Hsp27 involved in HSR (Figure 6c). Exposure of **5b** to the leukemic cell lines (K562, KCL22, and HL60) inhibited their proliferation (Figure S27) and induced apoptosis in a caspase 3/7 enzyme-dependent assay, with an induction of an approximately 2- to 8-fold increase of apoptotic cells, in accordance to the reference Hsp90 CTD-targeting inhibitor, novobiocin (NB) (Figure S28). In addition, **5b** facilitated early differentiation measured by the expression of differentiation markers involving CD14 vs CD11b in HL60 cells and CD133 vs CD11b in Mutz-2 cells (Figure S29). In this line, a 48 h exposure of **5b** to K562 cells significantly reduced the colony-forming capacity (Figure S30). To further evaluate the efficacy of **5b** on leukemic cells, we used the zebrafish xenotransplantation model[73] (Figure 6d). MOLT-4 cells were transplanted into zebrafish embryos at 32 h postfertilization (hpf). At this stage, the adaptive immune system is not yet developed; therefore, human cells can be tolerated by the host. The transparency of zebrafish embryos also enabled us to monitor the distribution of human cells, which were stained with a vital fluorescent dye. Xenotransplanted embryos were treated with AUY922 (500 nM) and **5b** (500 nM) for 48 h, whereas DMSO was used as a negative control. No toxicity of drugs at the given concentration was noticed on the development of xenotransplanted embryos. We then determined the number of MOLT4 cells in each treated group using flow cytometry. Compared to the DMSO-treated group, the number of transplanted cells was significantly reduced in AUY922- and **5b**-treated embryos.

To conclude, this data confirms the antileukemic effect of **5b** without inducing HSR.

5b Acts on TKI-Resistant BCR-ABL1$^+$ Leukemic Cells. The integration of specific tyrosine kinase inhibitors (TKI) such as imatinib (Gleevec) into polychemotherapy treatment protocols has significantly improved the response rate in BCR-ABL1$^+$ leukemia patients (initial remission went from 35% to 88%).[74] However, stable remission cannot be sustained in many cases as the leukemic cells pursue several escape mechanisms against TKI treatment; one of them is the occurrence of mutations in the ABL1 kinase domain. In particular, in the BCR-ABL1^{T315I} mutant, only ponatinib (TKI) is effective,[75] albeit with severe cardiovascular side effects.[76] As Hsp90 facilitates the correct folding of several oncogenic newly synthesized or denatured proteins, among them BCR-ABL1,[77−79] targeting Hsp90 with small-molecule inhibitors would destabilize BCR-ABL1 and can serve as a therapeutic target.[5,12] Therefore, we next tested the efficiency of **5b** in a murine BA/F3 cell line stably expressing clinically relevant mutants (BCR-ABL1^{T315I}, BCR-ABL1^{E255K}, and BCR-ABL1^{M351T}) with prominent TKI resistance profiles.[36] As expected, similar to K562 cells, exposure of **5b** significantly reduced proliferation (Figure 7a) and induced apoptosis (Figure 7b) at 6 and 12 μM, comparable to NB (at 0.3 mM) in BA/F3 cells expressing BCR-ABL1^{T315I}, BCR-ABL1^{E255K}, or BCR-ABL1^{M351T} mutants. Additionally, after the application of **5b**, BCR-ABL1 oncoprotein was destabilized, and downstream signaling pathways (Akt and Stat5) were blocked with increasing concentrations of **5b**, comparable to the human leukemic cell lines (Figure 7c). Furthermore, 24 h of exposure of **5b** on BCR-ABL1^{T315I}, BCR-ABL1^{E255K}, or BCR-ABL1^{M351T} mutant-expressing BA/F3 cells significantly inhibited the colony formation ability (Figure 7d). In addition, in our generated human BCR-ABL1$^+$ IM-resistant cell line models (K562-IMr and KCL22-IMr),[36] **5b** did not differentiate in inducing apoptosis between IM-resistant vs IM-sensitive clones, proposing a superior effect of **5b** in human IM-resistant BCR-ABL1-positive cells (Figure 7e and Figure S31). Encouraged by these results, we next tested **5b** on three primary CML^{CD34+} IM-resistant patient samples in the range of cytotoxic concentrations (5−10 μM) obtained from leukemic cell lines. Similar to BCR-ABL1$^+$ leukemic cell lines, the exposure of **5b** reduced the proliferation, induced apoptosis, and reduced the colony-forming ability of CML^{CD34+} IM-resistant patient cells and also revealed a potent combinatorial inhibitory effect when used in combination with IM (Figure 7f−h).

■ DISCUSSION

The CTD of Hsp90 contains several binding areas: the C-terminal ATP binding site, the MEEVD motif at the end of the CTD, the region at the border between the MD and the CTD (located ∼60 Å away from the NTD ATP binding site, which has been indicated to host a druggable allosteric binding site), and the primary dimerization interface of Hsp90.[28,80,81] The C-terminal nucleotide binding site is only available upon occupation of the N-terminal ATP binding pocket and binds purine and pyrimidine nucleotides, while the N-terminal ATP binding site (NTD) is more specific for adenine derivatives.[82] The MEEVD motif binds the TRP-domain of cochaperones such as Hop and immunophilins, which is formed by a four-helix bundle and is crucial for Hsp90 dimerization.[2] For the mitochondrial Hsp90 paralog TRAP1, small-molecule inhibitors were rationally found that target the allosteric site,[30] and found Hsp90 activators were indicated to also act via this site.[29] Protein−protein interactions in the interface of the four-helix bundle maintain the dimeric state of Hsp90.[59]

In this study, we present the development of a first-in-class small-molecule inhibitor of Hsp90, **5b**, which was rationally designed to target the C-terminal dimerization interface. Based on our prior hotspot prediction[34] and the prototype compound AX,[36] we successfully performed scaffold-hopping from the aminoxy peptide-backbone toward more druglike tripyrimidones. **5b** mimics α-helical side-chains that form hotspot residues located on H5 in the dimerization interface. A 3-fold difference in the K_D between **5b** and **5d** was reported, which is

https://doi.org/10.1021/acscentsci.2c00013
ACS Cent. Sci. XXXX, XXX, XXX−XXX

likely because of the larger 4-benzyloxyphenylethyl substituent compared to 4-methoxybenzyl (Figure 1e) that sterically interferes when binding to the H4/H5 interface. In contrast to the 4-methoxy-benzyl side chain of **5b**, the 4-benzyloxyphenylethyl substituent of **5d** cannot mimic the Y689′ hot spot, and the 4-methoxy-benzyl side chain of **5b** does mimic it and should also act as a (weak) hydrogen bond acceptor for S673′ and T669′. To independently predict the binding site and mode of **5b**, we performed extensive MD simulations, in which the inhibitor was allowed to diffuse freely around an MD-CTD construct of Hsp90α, similar to our analysis on AX binding[36] and related studies.[83−85] The results revealed the C-terminal dimerization interface as the most likely binding region of **5b**, which was confirmed by effective binding energy computations, corroborating the hypothesis underlying the design of **5b**. Following the high sequence-identity in the interface region, similar results were obtained for Hsp90β, suggesting that **5b** does not exhibit isoform specificity. Furthermore, in the TR-FRET assay by taking Hsp90α and β CTD recombinant proteins, **5b** did not display any Hsp90 isoform selectivity in blocking the binding of a CTD interacting chaperone (PPID).

Next, the selective binding of **5b** to Hsp90 was validated in a variety of biochemical and cellular assays, including DARTS, thermal, and isothermal shift assays, whereas intracellular Hsp90 engagement and disruption of Hsp90 multiprotein complexes were established via CETSA and $ITDRF_{CETSA}$ assays and immunoblotting under reducing conditions (±DTT) and nondenaturing (BN-PAGE) conditions. Moreover, a cross-linker and autodisplay dimerization assay, as well as SEC-SAXS measurements, repeatedly confirmed the destabilization of Hsp90α CTD dimers upon **5b** incubation, whereas no unspecific binding of **5b** was reported on the Hsp90α NTD protein in an FP-based competitive assay. However, during SAXS measurements, which were performed on an ensemble of species in solution, we were unable to determine whether **5b**-induced oligomers originated from Hsp90α CTD monomeric or dimeric species. In addition, **5b** blocks the chaperone function of Hsp90, as determined by the TR-FRET assay and in the cell-free luciferase refolding assay. Markedly, even though there are differences in the inhibitory concentrations against tested leukemia cells between **5b** (IC_{50} in a sub-micromolar range) and reference Hsp90 NTD control inhibitors (IC_{50} in sub-nanomolar range), a comparative selectivity profile (in cell-free or cell-based biochemical assays) toward Hsp90 was observed between **5b** and Hsp90 NTD reference inhibitors. This data indicates that the conventional Hsp90 NTD inhibitors induce cellular inhibitory effects through their off-target activity, in addition to targeting Hsp90.[6,21]

Moreover, **5b** exhibited potent *in vitro* anticancer activity against a broad spectrum of therapy-resistant leukemia cell lines (including TKI and proteasome inhibitor-resistant) and primary TKI-resistant (BCR-ABL1$^+$) leukemia patient cells. **5b** significantly reduced the leukemia burden in the zebrafish xenotransplantation model and induced apoptosis in TKI-resistant BCR-ABL1^{T315I}, BCR-ABL1^{E255K}, or BCR-ABL1^{M351T} mutant cells by destabilizing the BCR-ABL1 expression and, thereby, hampering related downstream signaling cascades without HSR induction. This data collectively established **5b** as a first-in-class small-molecule inhibitor that targets the C-terminal dimerization interface.

■ CONCLUSION

Through structure-based molecular design, chemical synthesis, a molecular simulations-based prediction of the binding mode, and an evaluation of biochemical affinity, we have developed the first low-molecular-weight compound interfering with the Hsp90 CTD dimerization. The C-terminal Hsp90 inhibitor **5b** contains a tripyrimidonamide scaffold and is active against therapy-resistant leukemia cells as well as in a zebrafish xenotransplantation model without exhibiting the prosurvival resistance mechanism HSR.

■ METHODS

Chemical Synthesis. See the Supporting Information for general methods, synthetic protocols, compound characterization, and spectral data (Figures S1−S20).

Expression and Purification of Recombinant Hsp90. Human Hsp90α CTD (563−732 amino acids) recombinant protein purification was performed as previously described.[34] Human Hsp90α NTD (amino acids 9−236; Addgene 22481) protein was expressed in *E. coli* BL21-DE3 cells.[86] BL21-DE3 expression strains were grown overnight and used to inoculate LB medium at 37 °C supplemented with 100 μg/mL ampicillin to an OD_{600} = 0.5−0.8, followed by overnight induction of protein expression with 0.5 mM isopropyl β-D-1-thiogalactopyranoside (IPTG) at 25 °C. After induction, cells were harvested by centrifugation at 5000*g* and lysed using B-PER bacterial protein extraction reagent (ThermoFisher Scientific, Wesel, Germany). GST-tagged Hsp90 CTD and NTD proteins were affinity purified using spin columns (ThermoFisher Scientific) and eluted using glutathione elution buffer. Protein aliquots were made and supplemented with 5% glycerol and stored at −80 °C.

Microscale Thermophoresis (MST). The labeling of the CTD of Hsp90 (Hsp90 CTD) has been described before.[34,36] For a determination of the apparent KD value of Hsp90 CTD and the respective inhibitor, 10 μL of 50 nM labeled Hsp90 CTD in PBS containing 0.5% BSA and 0.1% Tween-20 was mixed with 10 μL of the respective inhibitor in different concentrations ranging from 15 nM to 500 μM and incubated for 15 min at room temperature (RT) in the dark. Thermophoresis of each mixture was induced at 1475 ± 15 nm and measured using a Monolith NT.115 instrument (NanoTemper Technologies GmbH, München, Germany).[87] The measurement was repeated three times independently for each sample, and each measurement was performed at 25 °C for 25 s at 70% LED power and 40% infrared laser power. The resulting fluorescence values were plotted against the concentration of the titrant, and the apparent KD was calculated using the KD fit formula $Y = E + (A - E)/2 \times (T + x + \mathrm{KD} - \mathrm{sqrt}((T + x + \mathrm{KD})^2 - 4 \times T \times x))$ by GraphPad Prism software (GraphPad Software, Inc. La Jolla, CA). *T*, the concentration value for the labeled Hsp90 CTD, was set to 50 nM.

Autodisplay Dimerization Assay. *E. coli* strain BL21 (DE3) [B, F−, dcm, ompT, lon, hsdS (rB−mB−), gal, λ(DE3)] pETSH-3 Hsp90 encoding CtxB signal peptide, AIDA-I autotransporter, and Hsp90 was used for the surface display of Hsp90.[35,36] *E. coli* strain BL21 (DE3) [B, F−, dcm, ompT, lon, hsdS (rB−mB−), gal, λ(DE3)] pETSH-3 SDH08 encoding CtxB signal peptide, AIDA-I autotransporter, and sorbitol dehydrogenase was used as a control.[45] Recombinant bacteria were routinely grown at 37 °C in lysogeny broth (LB) containing carbenicillin (100 μg/mL). Cells were grown to

https://doi.org/10.1021/acscentsci.2c00013
ACS Cent. Sci. XXXX, XXX, XXX−XXX

the mid-log phase (OD_{600} = 0.5), and the protein expression was induced by adding 1 mM IPTG for 16 h at 30 °C. Cells were then washed three times and suspended in PBS to an OD_{600} = 0.35 in a final volume of 100 μL. Prior to p53-FITC incubation at a final concentration of 1 μM for 1 h at RT in the dark, cells were incubated for 15 min either with or without inhibitor. Subsequently, cells were washed three times with PBS containing 0.1% Tween-20 to avoid unspecific binding. The cellular fluorescence was measured with a FACS Aria III instrument (BD, Heidelberg, Germany) using 488 nm as the excitation wavelength and 530 nm for detection, and a mean fluorescence value of at least 50 000 events for each measurement was determined.

Drug Affinity Responsive Target Stability (DARTS). A DARTS assay was performed to assess protease protection of Hsp90 protein from thermolysin digestion after incubation of Hsp90i, as described previously.[23,36] Briefly, 1 μg of recombinant Hsp90α was incubated on ice for 15 min with 25, 50, and 100 μM **5b**, NB, AUY922, and DMSO. After incubation, the samples were treated with thermolysin (1:50 of protein) for 5 min. The reaction was halted by the addition of 50 mM EDTA and later examined by immunoblot analysis.

Luciferase Refolding Assay. A luciferase refolding assay was performed using recombinant firefly luciferase from *Photinus pyralis* (Sigma-Aldrich, St. Louis, MO; 10×10^{10} units/mg), which was diluted (1:100) in denaturation buffer (25 mM Tricine, pH 7.8, 8 mM $MgSO_4$, 0.1 mM EDTA, 1% Triton X-100, 10% glycerol, and 10 mg/mL BSA) at 38 °C for 8 min.[50−52,88] Rabbit reticulocyte lysate (Promega, Madison, WI) was diluted 1:1 by the addition of cold mix buffer (100 mM Tris, pH 7.7, 75 mM $Mg(OAc)_2$, 375 mM KCl, and 15 mM ATP), creatine phosphate (10 mM), and creatine phosphokinase (16 U/mL) and was preincubated at 30 °C with the respective inhibitors and controls for 1 h. Afterward, 1 μL of denatured luciferase or active luciferase (as a control) was added to 20 μL of a rabbit reticulocyte mixture. As a control, denatured or active luciferase was incubated without reticulocyte lysate in buffer containing 20 mM Tris, pH 7.5, 150 mM NaCl, 1% hemoglobin, and 4% BSA. At desired time points, 1.5 μL samples were removed and added to 40 μL of assay buffer (25 mM Tricine, pH 7.8, 8 mM $MgSO_4$, 0.1 mM EDTA, 33 μM DTT, 0.5 mM ATP, and 0.5 mM luciferin), and the luminescence was read using a Spark microplate reader (Tecan). Percent luciferase refolding was determined using luminescence of DMSO at 120 min as 100% and comparing all samples to this value.

Thermal Shift Assay. CTD or NTD of r-Hsp90α (5 μM) protein and inhibitors at the indicated concentrations were mixed together in the assay buffer (1× PBS, pH = 7.5) and were incubated for 2 h. Then, 6× SYPRO orange dye (Sigma-Aldrich) was added to the mixture (20 μL), which binds to the exposed hydrophobic residues of unfolded protein (during thermal exposure) thereby showing an increase in fluorescence.[47,89] 96-well polymerase chain reaction (PCR) plates and a PCR system (BioRad, CFX Connect real-time system) were used to heat the samples from room temperature to 95 °C in increments of 0.5 °C for 10 s, with the excitation wavelength at 470 nm and emission wavelength at 570 nm. For a determination of protein melting temperature values (T_m), the melting curve for each data set was analyzed by GraphPad Prism 8.0.2 and fitted with the sigmoidal Boltzmann fit. Melting temperatures without the inhibitors were used as a control.

An isothermal shift assay was performed following a procedure similar to that for the thermal shift assay. However, increasing indicated concentrations of the inhibitors (98 nM to 200 μM) were used and were incubated with either C-terminal or N-terminal Hsp90 (5 μM) in the assay buffer (1× PBS, pH = 7.5) for 2 h. The samples were heated to 46 °C after the addition of 6× SYPRO orange dye (Sigma-Aldrich). Percent unfolding was calculated by normalizing to 100% unfolding and comparing to the vehicle control (DMSO).

Cellular Thermal Shift Assay (CETSA). A CETSA assay was performed as described previously,[47−49] with minor modifications. K562 cells were incubated with the indicated inhibitors (or DMSO) for 24 h. Cells were harvested by centrifugation (400*g* for 5 min at RT) and washed three times with PBS. The pellets were dissolved in PBS and later equally divided into 200 μL PCR tubes. Solutions were heated at the indicated temperature gradient for 3 min (T-Gradient Cycler, Biometra). Aliquots were then snap-frozen in liquid nitrogen and thawed at 25 °C in a thermal cycler (GeneAMP PCR System2700, Applied Biosystems) three times, followed by centrifugation at 10 000*g* for 20 min at 4 °C. The supernatants were harvested, and protein levels were measured by a quantitative simple western immunoassay (JESS, BioTechne, Minneapolis, MN). Protein levels represented by the area under the curve of the electropherograms were normalized to the lowest temperature set as 0% degradation. ΔT_m values for compounds were determined by plotting normalized data using a sigmoid dose curve and nonlinear regression (GraphPad Prism 8.0.2).

Isothermal Dose-Dependent Fingerprint (ITDRF) CETSA. Based on the previously determined IC_{50} values, K562 cells were treated with the indicated dilution range of inhibitor for 24 h. Then, cells were harvested by centrifugation (400*g* for 5 min at RT) and washed three times with PBS. The pellets were dissolved in 200 μL of PBS and transferred into PCR tubes (Eppendorf). Results of prior CETSA runs were utilized to determine the optimal melting temperature of 54.1 °C for Hsp90. Samples were heated once at 54.1 °C for 3 min (T-Gradient Cycler, Biometra) and then snap-frozen in liquid nitrogen and thawed at 25 °C in a thermal cycler (GeneAMP PCR System2700, Applied Biosystems) three times, followed by centrifugation at 10 000*g* for 20 min at 4 °C. The supernatants were harvested, and protein levels were measured by a quantitative simple western immunoassay (JESS, BioTechne, Minneapolis MN). Protein levels are calculated by the area under the curve of the electropherograms.

Simple Western Immunoassay. Fluorescent (5×) master mix, DTT, and biotinylated ladder were prepared following the manufacturer's instructions (BioTechne). Lysates were diluted with 0.1× sample buffer and mixed 5:1 with fluorescent 5× master mix to obtain a target sample concentration of 0.40 μg/μL per well. Samples were then denatured for 5 min at 95 °C in a PCR cycler (GeneAMP PCR System2700, Applied Biosystems). The assay plate was loaded following the manufacturer's instructions and centrifuged for 5 min at 1000*g* at RT. The immunoassay was performed using a 12−230 kDaA separation module with 25 cartridges (SM-W004, BioTechne). Lysates were separated for 25 min at 375 V, blocked for 5 min with antibody diluent 2, and incubated for 30 min with primary antibody and for 30 min with secondary antibody, subsequently. Primary antibody multiplex mix consisted of 1:100 anti-Hsp90 (4877S, Cell Signaling Technology, Danvers, MA) and 1:50 anti-β-actin (MAB8929, R&D) diluted in antibody diluent 2. Signals were detected using a JESS antirabbit detection module

https://doi.org/10.1021/acscentsci.2c00013
ACS Cent. Sci. XXXX, XXX, XXX−XXX

(DM-001, BioTechne) multiplexed with an antimouse secondary NIR antibody (043-821, BioTechne).

Time-Resolved Fluorescence Resonance Energy Transfer (TR-FRET). An evaluation of the Hsp90 binding affinity to PPID (cyclophilin D) was performed using the Hsp90 CTD TR-FRET assay kit (50289, BPS Bioscience, San Diego, CA). Terbium (Tb)-labeled donor and dye-labeled acceptor were diluted 100-fold in (1×) Hsp90 assay buffer 2. A 10 μL portion of diluted Tb-labeled donor and 10 μL of diluted dye-labeled acceptor were mixed with 4 μL of inhibitor (at the indicated concentration), 10 μL of 3 ng/μL PPID-GST-tag (BPS Bioscience), and 6 μL of 2 ng/μL biotin-labeled CTD of Hsp90 (BPS Biosciences). For the positive control, the inhibitor was substituted for DMSO, and for the negative control, PPID-GST-tag was substituted for 1× Hsp90 assay buffer. Samples were incubated for 2 h at RT protected from light and measured with a microplate-reader (SPARK10M, Tecan). Fluorescence was measured using a time-resolved reading mode with two subsequent measurements: The first measurement was performed using a 340 nm/620 nm (excitation/emission) wavelength with a lag time of 60 μs and integration time of 500 μs. The second measurement was performed using a 340 nm/665 nm (excitation/emission) wavelength with a lag time of 60 μs and integration time of 500 μs. A data analysis was performed using the TR-FRET ratio (665 nm emission/620 nm emission). The TR-FRET ratios are normalized to % activity by setting the negative control as 0% activity and the positive control as 100% activity

$$[(\mathrm{FRET}_{\mathrm{sample}} - \mathrm{FRET}_{\mathrm{neg}})/(\mathrm{FRET}_{\mathrm{pos}} - \mathrm{FRET}_{\mathrm{neg}}) \times 100\%]$$

Fluorescence Polarization (FP) Measurements. An evaluation of the binding affinity of compounds toward the ATP pocket of Hsp90 NTD was determined by a competitive binding assay against FITC-labeled geldanamycin (GM) using the Hsp90 NTD assay kit (50293, BPS Bioscience).[50] The inhibitor sample wells were filled with 15 μL of 1× Hsp90 assay buffer, 5 μL of 40 mM DTT, 5 μL of 2 mg/mL BSA, 40 μL of H_2O, 5 μL of FITC-labeled GM (100 nM), and 10 μL of inhibitor (at the indicated concentration). The reaction was initiated by adding 20 μL of Hsp90 (17 ng/μL) and incubating at room temperature for 3 h with slow shaking. Background wells (master mix only), negative controls (FITC-labeled GM, buffer, and DMSO), and positive controls (FITC-labeled GM, buffer, DMSO, and Hsp90) were also included within the assay plate. Fluorescence was measured at a 470 nm excitation wavelength and 525 nm emission wavelength in a microtiter-plate reader (Infinite M1000pro by Tecan). Polarization was calculated using $(I_{\mathrm{II}} - G(I_{\perp})/(I_{\mathrm{II}} + G(I_{\perp})) \times 1000$ and a g-factor of 1.187. The percentage of Hsp90-bound FITC-labeled GM was calculated using

$$P_{\mathrm{norm}} = (P_{\mathrm{Inhibitor}} - P_{\mathrm{neg}})/(P_{\mathrm{pos}} - P_{\mathrm{neg}}) \times 100$$

Molecular Dynamics (MD) Simulations. The structures of Hsp90α and β (PDB IDs 3q6m and 5fwk, respectively) were prepared using Schrödinger Maestro.[90] For each of the isoforms, 40 individual MD simulations were performed. The initial random placement of **5b** and solvation in TIP3P water[91] was done using PACKMOL,[92] neutralizing the system by the addition of sodium ions. ff14SB was used as the force field for the protein and a modified GAFF version 1.5 for **5b**.[34,56] All simulations were carried out using the Amber18 software package.[54] To treat long-range electrostatics, the particle mesh Ewald method[93] was used with a cutoff of 9.0 Å for equilibration and 10.0 Å for production. The SHAKE algorithm[94] and hydrogen mass repartitioning[95] were used to allow for simulation steps of 2 fs in the equilibration and 4 fs in the production.

Initially, the systems were energy-minimized using the steepest descent (500 steps) and conjugate gradient (2000 steps) methods and placing positional restraints with a force constant of 5 kcal mol^{-1} Å^{-2} on all protein atoms; the restraints were reduced in a second energy minimization to a force constant of 1 kcal mol^{-1} Å^{-2} (for 2000 steps of steepest descent followed by 8000 steps of conjugate gradient) and removed in a third one (for 1000 steps of steepest descent followed by 4000 steps of conjugate gradient). Placing positional restraints with a force constant of 1 kcal mol^{-1} Å^{-2} on the backbone atoms, first, the system was heated to 100 K in 50 ps of NVT MD and further heated to 300 K in 5 ps of NPT MD. A further 65 ps of NPT MD was performed for density equilibration, still applying the backbone restraints. Afterward, over the course of a further 300 ps of NPT MD, the backbone restraints were gradually reduced to a force constant of 0.2 kcal mol^{-1} Å^{-2}.

After the thermalization, 500 ns of NPT MD simulation was carried out with positional restraints with a force constant of 0.1 kcal mol^{-1} Å^{-2} on the backbone atoms. The Langevin thermostat with a collision frequency of 1 ps^{-1} and the Monte Carlo barostat with a pressure relaxation time of 1 ps were used. The reference coordinates for these restraints were readjusted every 100 ns to allow for moderate protein flexibility. For Hsp90α, these simulations were later extended to 1 μs. The trajectories were postprocessed and analyzed with CPPTRAJ,[96] and results were visualized with PyMol.[86]

MM-GB/SA Computations. Effective binding energies were computed over one MD trajectory that resulted in binding of **5b** in the CTD dimerization interface and led to a binding mode in which **5b** mimics H5′. In the computations, the single trajectory approach was used, where complex, protein, and ligand configurations were extracted from the complex trajectory.[97] After removing water molecules and counterions, gas-phase energies (van der Waals and electrostatic contributions) were evaluated on every frame sampled at an interval of 200 ps using MMPBSA.py;[98] the polar contribution to the solvation free energy was calculated using the "OBC II" generalized Born model,[99] together with mbondi2 radii and a dielectric constant of 1 for the solute and 80 for the solvent. The ionic strength was set to 150 mM of a 1:1 salt. The nonpolar contribution to the solvation free energy was calculated as a function of the solvent-accessible surface area using 0.0050 kcal mol^{-1} Å^{-2} as the surface tension. No absolute binding free energies can be derived from this approach since configurational entropy contributions are not considered here to reduce the uncertainty in the computations.[57,58] However, the sum of gas-phase energies and solvation free energies, the effective energy, is suitable to estimate relative differences in binding free energies for differential binding poses.[36]

WB and Blue Native Gels. Cells were treated with the indicated concentration of the compound or vehicle (DMSO) for 48 h. An immunoblot analysis was performed by following a standard protocol using antibodies: anti-Hsp90 (4877), anti-Hsp70 (4872), anti-Hsp40 (4871), anti-Hsp27 (2402), anti-HSF-1 (4356), anti-Hsp60 (12165), anti-PDI (2446), anti-Hsp90α (8165), anti-Hsp90β (5087), anti-c-Abl (2862), antiphospho-c-Abl (2865), anti-Stat5 (9363), antiphospho-Stat5 (9351), anti-CrkL (3182), antiphospho-Crkl (3181),

https://doi.org/10.1021/acscentsci.2c00013
ACS Cent. Sci. XXXX, XXX, XXX−XXX

anti-Akt (2920), antiphospho-Akt (4060), anti-S6 ribosomal protein (2217), antiphospho-S6 ribosomal protein (4858), and anti-c-Myc (13987) from Cell Signaling Technology and anti-β-actin (Sigma-Aldrich). Blue native (BN) gels were performed following the manufacturer's instructions (Invitrogen) and as performed previously.[36] Briefly, lysates were generated from the K562 cell line after 48 h of treatment with inhibitors (at the indicated concentration) using a NativePAGE Sample Prep kit (Invitrogen) by 2−3 freezing−thawing cycles followed by centrifugation at 20 000*g* for 25−30 min at 4 °C.

Dimerization Assay. Hsp90 CTD dimerization was evaluated using an amine-reactive chemical cross-linker bis-(sulfosuccinimidyl) suberate (BS^3) (Pierce).[50,53] Hsp90α CTD protein (2 μM) was diluted in Na_2HPO_4 (25 mM; pH 7.4) and treated with different concentrations of the inhibitor to make a final volume of 25 μL. The reaction mixture was incubated at RT for 1 h. The amine-reactive cross-linker BS^3 was added to a final concentration of 63 μM, and the samples were incubated for 1 h at RT. Cross-linking was quenched by the addition of SDS sample buffer and subsequent heating for 5 min at 95 °C. Samples were run in 12% SDS-PAGE gels followed by Western blotting. Blots were probed with anti-Hsp90 (AC88, Abcam) antibody.

SEC-SAXS. We collected the SEC-SAXS data on beamline BM29 at the ESRF Grenoble.[61,62] The BM29 beamline was equipped with a PILATUS 2M detector (Dectris) at a fixed distance of 2.827 m. The measurement of Hsp90 CTD (18 mg/mL) was performed at 20 °C on a Superdex 200 increase 3.2/300 column (Buffer 50 mM TRIS pH 7.5, 100 mM NaCl) with a flow rate of 0.075 mL/min, collecting one frame every two seconds. The data was scaled to absolute intensity against water. Further, we collected SAXS data on our Xeuss 2.0 Q-Xoom system from Xenocs, equipped with a PILATUS 3 R 300 K detector (Dectris) and a GENIX 3D CU ultralow divergence X-ray beam delivery system. The chosen sample to detector distance for the experiment was 0.55 m, resulting in an achievable q-range of 0.10−6 nm^{-1}. All measurements were performed at 20 °C with protein concentrations of 9.7 and 10.8 mg/mL. Compound **5b** was added and incubated for 30 min at 20 °C. Samples were injected in the low-noise flow cell (Xenocs) via an autosampler. For each sample, 18 frames with an exposure time of 10 min were collected. Data were scaled to absolute intensity against water. All programs used for data processing were part of the ATSAS software package (version 3.0.3).[100] Primary data reduction was performed with the programs CHROMIXS and PRIMUS.[63,64] With the Guinier approximation,[66] we determine the forward scattering $I(0)$ and the radius of gyration (R_g). The program GNOM[101] was used to estimate the maximum particle dimension (D_{max}) with the pair-distribution function $p(r)$. Low-resolution *ab initio* models were calculated with DAMMIF.[65] A superimposition of the predicted model was done with the program SUPCOMB.[102]

Physicochemical Properties of 5b (See the Supporting Information for More Details). *Aqueous Solubility of **5b**.* The aqueous thermodynamic solubility of **5b** was determined in phosphate-buffered saline (PBS, pH 7.4) after 4 and 24 h of incubation time at 25 °C. Ondansetron was used as a reference compound with high solubility of 95 μM. The thermodynamic solubility of **5b** was ranging from 4 μM after 4 h to 8 μM after 24 h (n = 2). For detailed information, see Bienta, Enamie Biological Services study reports.

*Chemical Stability of **5b**.* Drug decomposition was determined by high-performance liquid chromatography (HPLC, Method 1): instrument, Knauer HPLC system in combination with a Knauer UV Detector Azura UVD 2.1L; column, KNAUER Eurospher II 100-5 C18, 150 × 4 mm; mobile phase 1, linear gradient (90−0%) of water with 0.1% trifluoroacetic acid; mobile phase 2, linear gradient (10−100%) of acetonitrile with 0.1% of trifluoroacetic acid; run time, 20 min, followed by an isocratic elution with 100% acetonitrile for 10 min; flow rate, 1 mL/min; detection, 254 nm.

5b was dissolved in a mixture of Tween20/ethanol/phosphate buffer pH 7.4 (7/3/90) and the stability monitored over a period of 24 h at 37 °C. After 24 h, almost no decomposition was detected (0.7% drug decomposition, n = 2).

The stability of **5b** at acidic pH was determined by dissolving **5b** in a mixture of Tween20/ethanol/phosphate buffer pH 2 (7/3/90), and the stability was monitored over a period of 24 h at 37 °C. After 24 h, only slight decomposition was detected (1.3% drug decomposition, n = 2).

*In Vitro Metabolic Stability of **5b** in Human Liver Microsomes.* The metabolic stability screening of **5b** in human liver microsomes revealed 91% stability after a 40 min incubation at 37 °C. Propanolol, a reference drug with medium to high metabolic stability showed 74% of the parent compound remaining and therefore demonstrated slightly decreased stability compared with **5b**. Calculated results for the intrinsic clearance suggest that **5b** (6 μL/(min mg)) is a low-clearance compound with an estimated long half-life (n = 2). For detailed information, see Bienta, Enamie Biological Services study reports.

Cell Culture. K562, KCL22, SUPB15 (BCR-ABL1$^+$ CML/BCP-ALL), Mutz-2 (50 ng/mL SCF), HL-60 (AML), DND41, HPBALL, TALL1, and MOLT4 (T-ALL) leukemic cell lines (DSMZ, Braunschweig, Germany) were cultured in RPMI1640 GlutaMAX (ThermoFisher Scinetific) supplemented with 10−20% FCS (Sigma-Aldrich, St. Louis, MO) and penicillin/streptomycin (Invitrogen, Carlsbad, CA) and maintained at 37 °C with 5% CO_2. Normal BA/F3 and BA/F3 cells expressing BCR-ABL1 mutants (T315I, M351T, and E255K) (murine pro B cell line) were cultured in RPMI1640 GlutaMAX (10% FCS) supplemented with or without IL-3 (10 ng/mL), respectively. BA/F3 cells expressing BCR-ABL1 mutants were resistant against imatinib (IM) until ∼10 μM.[36] IM-resistant BCR-ABL1$^+$ K562 (K562-IMr), KCL22 (KCL22-IMr), and SUPB15 (SUPB15-IMr) were generated by a gradual increase (1−2.5 μM) in the concentration of IM (Sigma-Aldrich, St. Louis, MO) over a period of 3 months.[36,103] Bortezomib (BTZ)-resistant clones (80 nM) of HL60 (HL60-BTZr) were established following a protocol similar to that described to pick IM resistant clones. Primary patient derived CML^{CD34+} blast cells were cultured in mononuclear cell medium (PromoCell, Heidelberg, Germany).

Hsp90 CTD/NTD-Targeting Reference Inhibitors. Coumermycin A1 (CA1) and novobiocin (NB) were purchased from Sigma-Aldrich, and Hsp90 NTD-targeting reference control inhibitors, geldanamycin (GM), tanespimycin (TM), and PUH-71, were purchased from Selleckchem.

Viability Assay. Cells were seeded in a white 96-well plate (Corning, NY) with an increasing concentration (50 nM to 25 μM) of inhibitors and respective controls for 48 h. Cell viability was monitored using a Celltiter Glo luminescent assay (based on the ATP quantification), following the manufacturer's guidelines (Promega).[36] IC_{50} values for compounds were determined by plotting raw data (normalized to controls) using a sigmoid dose curve and nonlinear regression (GraphPad Prism).

https://doi.org/10.1021/acscentsci.2c00013
ACS Cent. Sci. XXXX, XXX, XXX−XXX

Proliferation Assay. Cell proliferation was examined after treatment with the compounds at their indicated concentration with the trypan exclusion method using an automated cell counter (Vi-CELL XR-Beckman Coulter, Fullerton, CA) after every 24 h interval.

Annexin V Staining. For evaluating apoptosis, cells treated with inhibitor for 48 h were stained with annexin V and propidium iodide (PI), following the supplier's guidelines (Invitrogen, Carlsbad, CA), and later, the stained cells were subjected to FACS (Cytoflex, Beckman Coulter).

Caspase 3/7 Glo Assay. Cells were incubated with the respective inhibitors or control for 48 h, and later, the enzymatic activity of caspase 3/7 was examined (SPARK10M, Tecan) by using a caspase 3/7-dependent Glo assay (absorbance at 405 nm), following the manufacturer's instructions (Promega).[36]

Zebrafish. A Zebrafish wild-type TE strain was maintained according to standard protocols and handled in accordance with European Union animal protection directive 2010/63/EU and the local government (Tierschutzgesetz §11, Abs. 1, Nr. 1, husbandry permit 35/9185.46/Uni TÜ). All experiments described in this study were conducted on embryos younger than 5 days postfertilization (dpf), prior to the legal onset of animal life.

Xenotransplantation in Zebrafish Embryos. A xenotransplantation experiment was performed as described previously.[73] Briefly, MOLT-4 cells were labeled with a Vybrant CFDA SE cell tracer kit (Invitrogen) following the manufacturer's instructions and were then suspended in PBS at a density of 1×10^8 cells/mL. An approximately 1 nL portion of cell suspension (around 200 cells) was injected into the perivitelline space of embryos at 32 hpf. Injected embryos were first incubated at 28 °C for 1 h. Only embryos with good engraftment were selected for treatment with DMSO (control group), AUY922 (500 nM), or **5b** (500 nM) for 48 h at 35 °C. This temperature enables the maintenance of embryos with grafted cells without compromising zebrafish development. Drug-treated embryos were dissociated by passing through a 40 μm cell strainer (Greiner Bio-One) and then analyzed using a BD LSR II flow cytometer. The fold change of engrafted MOLT4 cells was calculated using the mean of DMSO-treated embryos. GraphPad Prism software (version 7) was used for graphing and statistical analysis.

Differentiation Assay. FACS measurements were performed after incubating the respective inhibitors at the indicated concentration for 48 h using fluorochrome-coupled monoclonal antibodies (mAbs) along with matched isotype controls: anti-CD11b (Bear1; Beckman Coulter), anti-CD14 (RMO52; Beckman Coulter), and anti-CD133 (AC133; MiltenyiBiotec, Gladbach, Germany).[46]

Colony Forming Unit (CFU) Assay. A CFU assay was performed by plating inhibitor treated cells (48 h) in methylcellulose medium (Methocult H4100, StemCell Technologies, Vancouver, BC, Canada) supplemented with 50 ng/mL SCF, 10 ng/mL IL-3, 10 ng/mL GM-CSF (Peprotech, Hamburg, Germany), and 3 U/mL erythropoietin (eBioscience, San Diego, CA).[46] Colonies were counted after 14 days ($n = 3$).

Significance analyses of normally distributed data with variances similar between groups used a paired, two-tailed Student's t test: *, $p < 0.05$; **, $p < 0.005$; and *** $p < 0.001$, unless stated otherwise.

■ ASSOCIATED CONTENT

Supporting Information

The Supporting Information is available free of charge at https://pubs.acs.org/doi/10.1021/acscentsci.2c00013.

Additional methods, data, and figures including chemical synthesis, general methods, compound characterization, spectral data, a determination of the aqueous solubility of **5b**, and an assessment of the metabolic stability of **5b** (PDF)

Transparent Peer Review report available (PDF)

■ AUTHOR INFORMATION

Corresponding Authors

Sanil Bhatia − *Department of Pediatric Oncology, Hematology and Clinical Immunology, Medical Faculty, Heinrich Heine University Düsseldorf, Düsseldorf 40225, Germany;* orcid.org/0000-0001-6494-7744; Phone: (+49) 211 81 04896; Email: sanil.bhatia@med.uni-duesseldorf.de

Holger Gohlke − *Institute for Pharmaceutical and Medicinal Chemistry, Heinrich Heine University Düsseldorf, Düsseldorf 40225, Germany; John von Neumann Institute for Computing (NIC), Jülich Supercomputing Centre (JSC), Institute of Biological Information Processing (IBI-7: Structural Biochemistry) & Institute of Bio- and Geosciences (IBG-4: Bioinformatics), Forschungszentrum Jülich GmbH, Jülich 52425, Germany*; Phone: (+49) 211 81 13662; Email: gohlke@uni-dueseldorf.de

Thomas Kurz − *Institute for Pharmaceutical and Medicinal Chemistry, Heinrich Heine University Düsseldorf, Düsseldorf 40225, Germany;* orcid.org/0000-0002-9474-4224; Phone: (+49) 211 81 14984; Email: thomas.kurz@uni-duesseldorf.de

Authors

Lukas Spanier − *Institute for Pharmaceutical and Medicinal Chemistry, Heinrich Heine University Düsseldorf, Düsseldorf 40225, Germany*

David Bickel − *Institute for Pharmaceutical and Medicinal Chemistry, Heinrich Heine University Düsseldorf, Düsseldorf 40225, Germany*

Niklas Dienstbier − *Department of Pediatric Oncology, Hematology and Clinical Immunology, Medical Faculty, Heinrich Heine University Düsseldorf, Düsseldorf 40225, Germany*

Vitalij Woloschin − *Institute for Pharmaceutical and Medicinal Chemistry, Heinrich Heine University Düsseldorf, Düsseldorf 40225, Germany*

Melina Vogt − *Department of Pediatric Oncology, Hematology and Clinical Immunology, Medical Faculty, Heinrich Heine University Düsseldorf, Düsseldorf 40225, Germany*

Henrik Pols − *Institute for Pharmaceutical and Medicinal Chemistry, Heinrich Heine University Düsseldorf, Düsseldorf 40225, Germany*

Beate Lungerich − *Institute for Pharmaceutical and Medicinal Chemistry, Heinrich Heine University Düsseldorf, Düsseldorf 40225, Germany*

Jens Reiners − *Center for Structural Studies, Heinrich Heine University Düsseldorf, Düsseldorf 40225, Germany*

Narges Aghaallaei − *Department of Hematology, Oncology, Clinical Immunology and Rheumatology, University Hospital Tübingen, Tübingen 72076, Germany*

Daniela Diedrich − *Institute for Pharmaceutical and Medicinal Chemistry, Heinrich Heine University Düsseldorf, Düsseldorf 40225, Germany*

Benedikt Frieg − *Institute for Pharmaceutical and Medicinal Chemistry, Heinrich Heine University Düsseldorf, Düsseldorf 40225, Germany; John von Neumann Institute for Computing (NIC), Jülich Supercomputing Centre (JSC), Institute of Biological Information Processing (IBI-7: Structural Biochemistry) & Institute of Bio- and Geosciences (IBG-4: Bioinformatics), Forschungszentrum Jülich GmbH, Jülich 52425, Germany*

Julian Schliehe-Diecks − *Department of Pediatric Oncology, Hematology and Clinical Immunology, Medical Faculty, Heinrich Heine University Düsseldorf, Düsseldorf 40225, Germany*

Bertan Bopp − *Institute for Pharmaceutical and Medicinal Chemistry, PharmaCampus, Westphalian Wilhelms University, Münster 48149, Germany*

Franziska Lang − *Department of Pediatric Oncology, Hematology and Clinical Immunology, Medical Faculty, Heinrich Heine University Düsseldorf, Düsseldorf 40225, Germany*

Mohanraj Gopalswamy − *Institute for Pharmaceutical and Medicinal Chemistry, Heinrich Heine University Düsseldorf, Düsseldorf 40225, Germany*

Jennifer Loschwitz − *Institute for Pharmaceutical and Medicinal Chemistry, Heinrich Heine University Düsseldorf, Düsseldorf 40225, Germany*

Baubak Bajohgli − *Department of Hematology, Oncology, Clinical Immunology and Rheumatology, University Hospital Tübingen, Tübingen 72076, Germany;* orcid.org/0000-0002-7368-7523

Julia Skokowa − *Department of Hematology, Oncology, Clinical Immunology and Rheumatology, University Hospital Tübingen, Tübingen 72076, Germany*

Arndt Borkhardt − *Department of Pediatric Oncology, Hematology and Clinical Immunology, Medical Faculty, Heinrich Heine University Düsseldorf, Düsseldorf 40225, Germany*

Julia Hauer − *Department of Pediatrics, Pediatric Hematology and Oncology, University Hospital Carl Gustav Carus, Dresden 01307, Germany; Partner Site Dresden, National Center for Tumor Diseases (NCT), Dresden 01307, Germany*

Finn K. Hansen − *Pharmaceutical and Cell Biological Chemistry, Pharmaceutical Institute University of Bonn, Bonn 53121, Germany;* orcid.org/0000-0001-9765-5975

Sander H. J. Smits − *Center for Structural Studies and Institute of Biochemistry, Heinrich Heine University Düsseldorf, Düsseldorf 40225, Germany*

Joachim Jose − *Institute for Pharmaceutical and Medicinal Chemistry, PharmaCampus, Westphalian Wilhelms University, Münster 48149, Germany;* orcid.org/0000-0002-0666-2676

Complete contact information is available at: https://pubs.acs.org/10.1021/acscentsci.2c00013

Author Contributions

▲S.B. and L.S. contributed equally to this work. H.G. and T.K. share senior authorship. Conceptualization: H.G., T.K., S.B., and L.S. Development and application of methodology: D.B., N.D., M.V., B.F., H.P., B.L., V.W., F.L., M.G., J.L., B.B., D.D., N.A., Ba.B., J.S., J.S.-D., F.K.H., J.J., J.H., A.B., S.B., H.G., and T.K. Analysis of data: D.B., B.F., J.L., H.G., S.B., N.D., M.V., V.W., T.K., and L.S. S.S. and J.R. performed and analyzed the SAXS experiment. Manuscript writing: S.B., H.G., T.K., D.B., and V.W. The study was supervised by H.G., T.K., and S.B.

Notes

The authors declare no competing financial interest.

■ ACKNOWLEDGMENTS

This study was funded in part by the Deutsche Forschungsgemeinschaft (DFG, German Research Foundation), 270650915 (Research Training Group GRK 2158: TP4a to H.G., TP4b to S.S., TP2c to T.K., and TP 2d to S.B.). S.B., H.G., and T.K. are supported by Forschungskommission and DSO-Netzwerkverbundes, HHU Düsseldorf. S.B. additionally acknowledges the financial support by KinderKrebsForschung e.V. J.H. and A.B. were supported by the TransOnc priority program of the German Cancer Aid within grant 70112951 (ENABLE). J.H. was supported by ERC Stg 85222 "PreventALL" and ERA PerMED 2018 "GEPARD". T.K. and H.G. were supported by funds from the Strategischer Forschungsfonds of HHU. The Center for Structural studies is funded by the DFG (Grant 417919780 and INST 208/761-1 FUGG to S.S.). We are grateful for computational support by the "Zentrum für Informations und Medientechnologie" at the Heinrich-Heine-Universität Düsseldorf and the computing time provided by the John von Neumann Institute for Computing (NIC) to H.G. on the supercomputer JUWELS at Jülich Supercomputing Centre (JSC) (user IDs: HKF7, VSK33). A.B. acknowledges the financial support of Katharina-Hardt Foundation and Löwenstern e.V. for providing a Simple Western Instrument (JESS). We thank Anton Popov for the great support at BM29 as well as the whole ESRF Outstation Grenoble Team.

■ ABBREVIATIONS

TLC, thin-layer chromatography; MOA, mode of action; MD, molecular dynamics; MM-GB/SA, molecular mechanics generalized Born surface area; NTD, N-terminal domain; MD, middle domain; CTD, C-terminal domain; PPIs, protein−protein interactions; HSR, heat shock response

■ REFERENCES

(1) Sanchez, J.; Carter, T. R.; Cohen, M. S.; Blagg, B. S. Old and New Approaches to Target the Hsp90 Chaperone. *Current cancer drug targets* **2020**, *20*, 253.

(2) Schopf, F. H.; Biebl, M. M.; Buchner, J. The HSP90 chaperone machinery. *Nature reviews. Molecular cell biology* **2017**, *18* (6), 345−360.

(3) Flandrin, P.; Guyotat, D.; Duval, A.; Cornillon, J.; Tavernier, E.; Nadal, N.; Campos, L. Significance of heat-shock protein (HSP) 90 expression in acute myeloid leukemia cells. *Cell Stress Chaperones* **2008**, *13* (3), 357−64.

(4) Wang, M.; Shen, A.; Zhang, C.; Song, Z.; Ai, J.; Liu, H.; Sun, L.; Ding, J.; Geng, M.; Zhang, A. Development of Heat Shock Protein (Hsp90) Inhibitors To Combat Resistance to Tyrosine Kinase Inhibitors through Hsp90-Kinase Interactions. *Journal of medicinal chemistry* **2016**, *59* (12), 5563−86.

(5) Butler, L. M.; Ferraldeschi, R.; Armstrong, H. K.; Centenera, M. M.; Workman, P. Maximizing the therapeutic potential of HSP90 inhibitors. *Molecular cancer research: MCR* **2015**, *13* (11), 1445−51.

(6) Wang, Y.; Koay, Y. C.; McAlpine, S. R. How Selective are Hsp90 Inhibitors for Cancer Cells over Normal Cells? *ChemMedChem.* **2017**, *12* (5), 353−357.

(7) Wu, J.; Liu, T.; Rios, Z.; Mei, Q.; Lin, X.; Cao, S. Heat Shock Proteins and Cancer. *Trends Pharmacol. Sci.* **2017**, *38* (3), 226−256.

(8) Wang, Y.; McAlpine, S. R. Heat-shock protein 90 inhibitors: will they ever succeed as chemotherapeutics? *Future Med. Chem.* **2015**, *7* (2), 87−90.
(9) Hsu, H. S.; Lin, J. H.; Huang, W. C.; Hsu, T. W.; Su, K.; Chiou, S. H.; Tsai, Y. T.; Hung, S. C. Chemoresistance of lung cancer stemlike cells depends on activation of Hsp27. *Cancer* **2011**, *117* (7), 1516−28.
(10) Gandhi, N.; Wild, A. T.; Chettiar, S. T.; Aziz, K.; Kato, Y.; Gajula, R. P.; Williams, R. D.; Cades, J. A.; Annadanam, A.; Song, D.; et al. Novel Hsp90 inhibitor NVP-AUY922 radiosensitizes prostate cancer cells. *Cancer biology & therapy* **2013**, *14* (4), 347−56.
(11) Modi, S.; Saura, C.; Henderson, C.; Lin, N. U.; Mahtani, R.; Goddard, J.; Rodenas, E.; Hudis, C.; O'Shaughnessy, J.; Baselga, J. A multicenter trial evaluating retaspimycin HCL (IPI-504) plus trastuzumab in patients with advanced or metastatic HER2-positive breast cancer. *Breast cancer research and treatment* **2013**, *139* (1), 107−13.
(12) Wang, M.; Shen, A.; Zhang, C.; Song, Z.; Ai, J.; Liu, H.; Sun, L.; Ding, J.; Geng, M.; Zhang, A. Development of Heat Shock Protein (Hsp90) Inhibitors To Combat Resistance to Tyrosine Kinase Inhibitors through Hsp90-Kinase Interactions. *J. Med. Chem.* **2016**, *59*, 5563.
(13) Bagatell, R.; Paine-Murrieta, G. D.; Taylor, C. W.; Pulcini, E. J.; Akinaga, S.; Benjamin, I. J.; Whitesell, L. Induction of a heat shock factor 1-dependent stress response alters the cytotoxic activity of hsp90-binding agents. *Clin. Cancer Res.* **2000**, *6* (8), 3312−3318.
(14) McCollum, A. K.; Teneyck, C. J.; Sauer, B. M.; Toft, D. O.; Erlichman, C. Up-regulation of heat shock protein 27 induces resistance to 17-allylamino-demethoxygeldanamycin through a glutathione-mediated mechanism. *Cancer research* **2006**, *66* (22), 10967−75.
(15) Guo, F.; Rocha, K.; Bali, P.; Pranpat, M.; Fiskus, W.; Boyapalle, S.; Kumaraswamy, S.; Balasis, M.; Greedy, B.; Armitage, E. S.; et al. Abrogation of heat shock protein 70 induction as a strategy to increase antileukemia activity of heat shock protein 90 inhibitor 17-allylamino-demethoxy geldanamycin. *Cancer research* **2005**, *65* (22), 10536−44.
(16) Maloney, A.; Clarke, P. A.; Naaby-Hansen, S.; Stein, R.; Koopman, J. O.; Akpan, A.; Yang, A.; Zvelebil, M.; Cramer, R.; Stimson, L.; et al. Gene and protein expression profiling of human ovarian cancer cells treated with the heat shock protein 90 inhibitor 17-allylamino-17-demethoxygeldanamycin. *Cancer research* **2007**, *67* (7), 3239−53.
(17) Hall, J. A.; Forsberg, L. K.; Blagg, B. S. Alternative approaches to Hsp90 modulation for the treatment of cancer. *Future Med. Chem.* **2014**, *6* (14), 1587−605.
(18) Banerjee, M.; Hatial, I.; Keegan, B. M.; Blagg, B. S. J. Assay design and development strategies for finding Hsp90 inhibitors and their role in human diseases. *Pharmacol Ther* **2021**, *221*, 107747.
(19) Koren, J., 3rd.; Blagg, B. S. J. The Right Tool for the Job: An Overview of Hsp90 Inhibitors. *Adv. Exp. Med. Biol.* **2020**, *1243*, 135−146.
(20) Li, L.; Wang, L.; You, Q. D.; Xu, X. L. Heat Shock Protein 90 Inhibitors: An Update on Achievements, Challenges, and Future Directions. *Journal of medicinal chemistry* **2020**, *63* (5), 1798−1822.
(21) Wang, Y.; McAlpine, S. R. N-terminal and C-terminal modulation of Hsp90 produce dissimilar phenotypes. *Chem. Commun.* **2015**, *51* (8), 1410−3.
(22) Khandelwal, A.; Kent, C. N.; Balch, M.; Peng, S.; Mishra, S. J.; Deng, J.; Day, V. W.; Liu, W.; Subramanian, C.; Cohen, M.; et al. Structure-guided design of an Hsp90beta N-terminal isoform-selective inhibitor. *Nat. Commun.* **2018**, *9* (1), 425.
(23) Eskew, J. D.; Sadikot, T.; Morales, P.; Duren, A.; Dunwiddie, I.; Swink, M.; Zhang, X.; Hembruff, S.; Donnelly, A.; Rajewski, R. A.; et al. Development and characterization of a novel C-terminal inhibitor of Hsp90 in androgen dependent and independent prostate cancer cells. *BMC Cancer* **2011**, *11*, 468.
(24) Koay, Y. C.; McConnell, J. R.; Wang, Y.; Kim, S. J.; Buckton, L. K.; Mansour, F.; McAlpine, S. R. Chemically accessible hsp90 inhibitor that does not induce a heat shock response. *ACS medicinal chemistry letters* **2014**, *5* (7), 771−6.
(25) Sellers, R. P.; Alexander, L. D.; Johnson, V. A.; Lin, C. C.; Savage, J.; Corral, R.; Moss, J.; Slugocki, T. S.; Singh, E. K.; Davis, M. R.; et al. Design and synthesis of Hsp90 inhibitors: exploring the SAR of Sansalvamide A derivatives. *Bioorganic & medicinal chemistry* **2010**, *18* (18), 6822−56.
(26) Westerheide, S. D.; Bosman, J. D.; Mbadugha, B. N.; Kawahara, T. L.; Matsumoto, G.; Kim, S.; Gu, W.; Devlin, J. P.; Silverman, R. B.; Morimoto, R. I. Celastrols as inducers of the heat shock response and cytoprotection. *J. Biol. Chem.* **2004**, *279* (53), 56053−60.
(27) Strocchia, M.; Terracciano, S.; Chini, M. G.; Vassallo, A.; Vaccaro, M. C.; Dal Piaz, F.; Leone, A.; Riccio, R.; Bruno, I.; Bifulco, G. Targeting the Hsp90 C-terminal domain by the chemically accessible dihydropyrimidinone scaffold. *Chem. Commun.* **2015**, *51* (18), 3850−3.
(28) Bickel, D.; Gohlke, H. C-terminal modulators of heat shock protein of 90 kDa (HSP90): State of development and modes of action. *Bioorganic & medicinal chemistry* **2019**, *27* (21), 115080.
(29) Sattin, S.; Tao, J.; Vettoretti, G.; Moroni, E.; Pennati, M.; Lopergolo, A.; Morelli, L.; Bugatti, A.; Zuehlke, A.; Moses, M.; et al. Activation of Hsp90 Enzymatic Activity and Conformational Dynamics through Rationally Designed Allosteric Ligands. *Chemistry* **2015**, *21* (39), 13598−608.
(30) Sanchez-Martin, C.; Moroni, E.; Ferraro, M.; Laquatra, C.; Cannino, G.; Masgras, I.; Negro, A.; Quadrelli, P.; Rasola, A.; Colombo, G. Rational Design of Allosteric and Selective Inhibitors of the Molecular Chaperone TRAP1. *Cell Rep* **2020**, *31* (3), 107531.
(31) Mak, O. W.; Sharma, N.; Reynisson, J.; Leung, I. K. H. Discovery of novel Hsp90 C-terminal domain inhibitors that disrupt co-chaperone binding. *Bioorg. Med. Chem. Lett.* **2021**, *38*, 127857.
(32) Metz, A.; Pfleger, C.; Kopitz, H.; Pfeiffer-Marek, S.; Baringhaus, K. H.; Gohlke, H. Hot spots and transient pockets: predicting the determinants of small-molecule binding to a protein-protein interface. *J. Chem. Inf Model* **2012**, *52* (1), 120−33.
(33) Metz, A.; Schanda, J.; Grez, M.; Wichmann, C.; Gohlke, H. From determinants of RUNX1/ETO tetramerization to small-molecule protein-protein interaction inhibitors targeting acute myeloid leukemia. *J. Chem. Inf Model* **2013**, *53* (9), 2197−202.
(34) Ciglia, E.; Vergin, J.; Reimann, S.; Smits, S. H.; Schmitt, L.; Groth, G.; Gohlke, H. Resolving hot spots in the C-terminal dimerization domain that determine the stability of the molecular chaperone Hsp90. *PloS one* **2014**, *9* (4), No. e96031.
(35) Bopp, B.; Ciglia, E.; Ouald-Chaib, A.; Groth, G.; Gohlke, H.; Jose, J. Design and biological testing of peptidic dimerization inhibitors of human Hsp90 that target the C-terminal domain. *Biochimica et biophysica acta* **2016**, *1860* (6), 1043−55.
(36) Bhatia, S.; Diedrich, D.; Frieg, B.; Ahlert, H.; Stein, S.; Bopp, B.; Lang, F.; Zang, T.; Kroger, T.; Ernst, T.; et al. Targeting HSP90 dimerization via the C terminus is effective in imatinib-resistant CML and lacks the heat shock response. *Blood* **2018**, *132* (3), 307−320.
(37) Krieger, V.; Ciglia, E.; Thoma, R.; Vasylyeva, V.; Frieg, B.; de Sousa Amadeu, N.; Kurz, T.; Janiak, C.; Gohlke, H.; Hansen, F. K. alpha-Aminoxy Peptoids: A Unique Peptoid Backbone with a Preference for cis-Amide Bonds. *Chemistry* **2017**, *23* (15), 3699−3707.
(38) Spanier, L.; Ciglia, E.; Hansen, F. K.; Kuna, K.; Frank, W.; Gohlke, H.; Kurz, T. Design, synthesis, and conformational analysis of trispyrimidonamides as alpha-helix mimetics. *Journal of organic chemistry* **2014**, *79* (4), 1582−93.
(39) Verba, K. A.; Wang, R. Y.; Arakawa, A.; Liu, Y.; Shirouzu, M.; Yokoyama, S.; Agard, D. A. Atomic structure of Hsp90-Cdc37-Cdk4 reveals that Hsp90 traps and stabilizes an unfolded kinase. *Science* **2016**, *352* (6293), 1542−7.
(40) Marcu, M. G.; Chadli, A.; Bouhouche, I.; Catelli, M.; Neckers, L. M. The heat shock protein 90 antagonist novobiocin interacts with a previously unrecognized ATP-binding domain in the carboxyl terminus of the chaperone. *J. Biol. Chem.* **2000**, *275* (47), 37181−37186.
(41) Eccles, S. A.; Massey, A.; Raynaud, F. I.; Sharp, S. Y.; Box, G.; Valenti, M.; Patterson, L.; Brandon, A. D.; Gowan, S.; Boxall, F.; et al. NVP-AUY922: A novel heat shock protein 90 inhibitor active against xenograft tumor growth, angiogenesis, and metastasis. *Cancer research* **2008**, *68* (8), 2850−2860.

https://doi.org/10.1021/acscentsci.2c00013
ACS Cent. Sci. XXXX, XXX, XXX−XXX

(42) Yin, Z. Y.; Henry, E. C.; Gasiewicz, T. A. (−)-Epigallocatechin-3-gallate Is a Novel Hsp90 Inhibitor. *Biochemistry-Us* **2009**, *48* (2), 336−345.
(43) Lundgren, K.; Zhang, H.; Brekken, J.; Huser, N.; Powell, R. E.; Timple, N.; Busch, D. J.; Neely, L.; Sensintaffar, J. L.; Yang, Y. C.; et al. BIIB021, an orally available, fully synthetic small-molecule inhibitor of the heat shock protein Hsp90. *Mol. Cancer Ther* **2009**, *8* (4), 921−9.
(44) Pacey, S.; Gore, M.; Chao, D.; Banerji, U.; Larkin, J.; Sarker, S.; Owen, K.; Asad, Y.; Raynaud, F.; Walton, M.; et al. A Phase II trial of 17-allylamino, 17-demethoxygeldanamycin (17-AAG, tanespimycin) in patients with metastatic melanoma. *Invest New Drugs* **2012**, *30* (1), 341−9.
(45) Jose, J.; von Schwichow, S. Autodisplay of active sorbitol dehydrogenase (SDH) yields a whole cell biocatalyst for the synthesis of rare sugars. *Chembiochem* **2004**, *5* (4), 491−9.
(46) Bhatia, S.; Reister, S.; Mahotka, C.; Meisel, R.; Borkhardt, A.; Grinstein, E. Control of AC133/CD133 and impact on human hematopoietic progenitor cells through nucleolin. *Leukemia* **2015**, *29* (11), 2208−20.
(47) Wang, L.; Jiang, J.; Zhang, L.; Zhang, Q.; Zhou, J.; Li, L.; Xu, X.; You, Q. Discovery and Optimization of Small Molecules Targeting the Protein-Protein Interaction of Heat Shock Protein 90 (Hsp90) and Cell Division Cycle 37 as Orally Active Inhibitors for the Treatment of Colorectal Cancer. *Journal of medicinal chemistry* **2020**, *63* (3), 1281−1297.
(48) Liang, C.; Hao, H.; Wu, X.; Li, Z.; Zhu, J.; Lu, C.; Shen, Y. Design and synthesis of N-(5-chloro-2,4-dihydroxybenzoyl)-(R)-1,2,3,4-tetrahydroisoquinoline-3-carboxamid es as novel Hsp90 inhibitors. *European journal of medicinal chemistry* **2016**, *121*, 272−282.
(49) Jafari, R.; Almqvist, H.; Axelsson, H.; Ignatushchenko, M.; Lundback, T.; Nordlund, P.; Martinez Molina, D. The cellular thermal shift assay for evaluating drug target interactions in cells. *Nat. Protoc* **2014**, *9* (9), 2100−2122.
(50) Goode, K. M.; Petrov, D. P.; Vickman, R. E.; Crist, S. A.; Pascuzzi, P. E.; Ratliff, T. L.; Davisson, V. J.; Hazbun, T. R. Targeting the Hsp90 C-terminal domain to induce allosteric inhibition and selective client downregulation. *Biochimica et biophysica acta. General subjects* **2017**, *1861* (8), 1992−2006.
(51) McConnell, J. R.; Alexander, L. A.; McAlpine, S. R. A heat shock protein 90 inhibitor that modulates the immunophilins and regulates hormone receptors without inducing the heat shock response. *Bioorg. Med. Chem. Lett.* **2014**, *24* (2), 661−6.
(52) Galam, L.; Hadden, M. K.; Ma, Z.; Ye, Q. Z.; Yun, B. G.; Blagg, B. S.; Matts, R. L. High-throughput assay for the identification of Hsp90 inhibitors based on Hsp90-dependent refolding of firefly luciferase. *Bioorganic & medicinal chemistry* **2007**, *15* (5), 1939−46.
(53) Allan, R. K.; Mok, D.; Ward, B. K.; Ratajczak, T. Modulation of chaperone function and cochaperone interaction by novobiocin in the C-terminal domain of Hsp90: evidence that coumarin antibiotics disrupt Hsp90 dimerization. *J. Biol. Chem.* **2006**, *281* (11), 7161−71.
(54) Case, D. A.; Ben-Shalom, I. Y.; Brozell, S. R.; Cerutti, D. S.; Cheatham, T. E., III; Cruzeiro, V. W. D.; Darden, T. A.; Duke, R. E.; Ghoreishi, D.; Gilson, M. K.; et al. *AMBER 2018*; University of California: San Francisco, 2018.
(55) Maier, J. A.; Martinez, C.; Kasavajhala, K.; Wickstrom, L.; Hauser, K. E.; Simmerling, C. ff14SB: Improving the accuracy of protein side chain and backbone parameters from ff99SB. *J. Chem. Theory Comput.* **2015**, *11* (8), 3696−3713.
(56) Wang, J.; Wolf, R. M.; Caldwell, J. W.; Kollman, P. A.; Case, D. A. Development and testing of a general amber force field. *J. Comput. Chem.* **2004**, *25* (9), 1157−74.
(57) Sun, H. Y.; Duan, L. L.; Chen, F.; Liu, H.; Wang, Z.; Pan, P. C.; Zhu, F.; Zhang, J. Z. H.; Hou, T. J. Assessing the performance of MM/PBSA and MM/GBSA methods. 7. Entropy effects on the performance of end-point binding free energy calculation approaches. *Phys. Chem. Chem. Phys.* **2018**, *20* (21), 14450−14460.
(58) Gohlke, H.; Case, D. A. Converging free energy estimates: MM-PB(GB)SA studies on the protein-protein complex Ras-Raf. *J. Comput. Chem.* **2004**, *25* (2), 238−250.
(59) Pearl, L. H.; Prodromou, C. Structure and mechanism of the Hsp90 molecular chaperone machinery. *Annual review of biochemistry* **2006**, *75*, 271−94.
(60) Wayne, N.; Bolon, D. N. Dimerization of Hsp90 is required for in vivo function. Design and analysis of monomers and dimers. *J. Biol. Chem.* **2007**, *282* (48), 35386−95.
(61) Pernot, P.; Theveneau, P.; Giraud, T.; Fernandes, R. N.; Nurizzo, D.; Spruce, D.; Surr, J.; McSweeney, S.; Round, A.; Felisaz, F.; et al. New beamline dedicated to solution scattering from biological macromolecules at the ESRF. *Journal of Physics: Conference Series* **2010**, *247* (1), 012009.
(62) Pernot, P.; Round, A.; Barrett, R.; De Maria Antolinos, A.; Gobbo, A.; Gordon, E.; Huet, J.; Kieffer, J.; Lentini, M.; Mattenet, M.; et al. Upgraded ESRF BM29 beamline for SAXS on macromolecules in solution. *J. Synchrotron Radiat* **2013**, *20* (4), 660−4.
(63) Panjkovich, A.; Svergun, D. I. CHROMIXS: automatic and interactive analysis of chromatography-coupled small angle X-ray scattering data. *Bioinformatics* **2018**, *34*, 1944.
(64) Konarev, P. V.; Volkov, V. V.; Sokolova, A. V.; Koch, M. H. J.; Svergun, D. I. PRIMUS: a Windows PC-based system for small-angle scattering data analysis. *J. Appl. Crystallogr.* **2003**, *36*, 1277−1282.
(65) Franke, D.; Svergun, D. I. DAMMIF, a program for rapid ab-initio shape determination in small-angle scattering. *J. Appl. Crystallogr.* **2009**, *42*, 342−346.
(66) Guinier, A. Diffraction of x-rays of very small angles-application to the study of ultramicroscopic phenomenon. *Annales de Physique* **1939**, *11*, 161−237.
(67) Svergun, D.; Barberato, C.; Koch, M. H. J. CRYSOL - A program to evaluate x-ray solution scattering of biological macromolecules from atomic coordinates. *J. Appl. Crystallogr.* **1995**, *28*, 768−773.
(68) Mahalingam, D.; Swords, R.; Carew, J. S.; Nawrocki, S. T.; Bhalla, K.; Giles, F. J. Targeting HSP90 for cancer therapy. *British journal of cancer* **2009**, *100* (10), 1523−9.
(69) Khajapeer, K. V.; Baskaran, R. Hsp90 Inhibitors for the Treatment of Chronic Myeloid Leukemia. *Leukemia research and treatment* **2015**, *2015*, 757694.
(70) Lazenby, M.; Hills, R.; Burnett, A. K.; Zabkiewicz, J. The HSP90 inhibitor ganetespib: A potential effective agent for Acute Myeloid Leukemia in combination with cytarabine. *Leukemia research* **2015**, *39* (6), 617−24.
(71) Miyata, Y.; Nakamoto, H.; Neckers, L. The therapeutic target Hsp90 and cancer hallmarks. *Current pharmaceutical design* **2013**, *19* (3), 347−65.
(72) Lu, X.; Xiao, L.; Wang, L.; Ruden, D. M. Hsp90 inhibitors and drug resistance in cancer: the potential benefits of combination therapies of Hsp90 inhibitors and other anti-cancer drugs. *Biochemical pharmacology* **2012**, *83* (8), 995−1004.
(73) Morishima, T.; Krahl, A. C.; Nasri, M.; Xu, Y.; Aghaallaei, N.; Findik, B.; Klimiankou, M.; Ritter, M.; Hartmann, M. D.; Gloeckner, C. J.; et al. LMO2 activation by deacetylation is indispensable for hematopoiesis and T-ALL leukemogenesis. *Blood* **2019**, *134* (14), 1159−1175.
(74) Schultz, K. R.; Bowman, W. P.; Aledo, A.; Slayton, W. B.; Sather, H.; Devidas, M.; Wang, C.; Davies, S. M.; Gaynon, P. S.; Trigg, M.; et al. Improved early event-free survival with imatinib in Philadelphia chromosome-positive acute lymphoblastic leukemia: a children's oncology group study. *Journal of clinical oncology: official journal of the American Society of Clinical Oncology* **2009**, *27* (31), 5175−81.
(75) Gibbons, D. L.; Pricl, S.; Posocco, P.; Laurini, E.; Fermeglia, M.; Sun, H.; Talpaz, M.; Donato, N.; Quintas-Cardama, A. Molecular dynamics reveal BCR-ABL1 polymutants as a unique mechanism of resistance to PAN-BCR-ABL1 kinase inhibitor therapy. *Proc. Natl. Acad. Sci. U.S.A.* **2014**, *111* (9), 3550−5.
(76) Ariad suspends ponatinib sales. *Cancer discovery* **2014**, *4* (1), 6−7..
(77) Blagosklonny, M. V.; Toretsky, J.; Neckers, L. Geldanamycin selectively destabilizes and conformationally alters mutated p53. *Oncogene* **1995**, *11* (5), 933−939.

https://doi.org/10.1021/acscentsci.2c00013
ACS Cent. Sci. XXXX, XXX, XXX−XXX

(78) Chavany, C.; Mimnaugh, E.; Miller, P.; Bitton, R.; Nguyen, P.; Trepel, J.; Whitesell, L.; Schnur, R.; Moyer, J.; Neckers, L. p185erbB2 binds to GRP94 in vivo. Dissociation of the p185erbB2/GRP94 heterocomplex by benzoquinone ansamycins precedes depletion of p185erbB2. *J. Biol. Chem.* **1996**, *271* (9), 4974−7.

(79) Stepanova, L.; Leng, X.; Parker, S. B.; Harper, J. W. Mammalian p50Cdc37 is a protein kinase-targeting subunit of Hsp90 that binds and stabilizes Cdk4. *Genes & development* **1996**, *10* (12), 1491−502.

(80) D'Annessa, I.; Raniolo, S.; Limongelli, V.; Di Marino, D.; Colombo, G. Ligand Binding, Unbinding, and Allosteric Effects: Deciphering Small-Molecule Modulation of HSP90. *J. Chem. Theory Comput* **2019**, *15* (11), 6368−6381.

(81) Sanchez-Martin, C.; Serapian, S. A.; Colombo, G.; Rasola, A. Dynamically Shaping Chaperones. Allosteric Modulators of HSP90 Family as Regulatory Tools of Cell Metabolism in Neoplastic Progression. *Front Oncol* **2020**, *10*, 1177.

(82) Soti, C.; Racz, A.; Csermely, P. A Nucleotide-dependent molecular switch controls ATP binding at the C-terminal domain of Hsp90. N-terminal nucleotide binding unmasks a C-terminal binding pocket. *J. Biol. Chem.* **2002**, *277* (9), 7066−75.

(83) Frieg, B.; Gremer, L.; Heise, H.; Willbold, D.; Gohlke, H. Binding modes of thioflavin T and Congo red to the fibril structure of amyloid-beta(1−42). *Chem. Commun.* **2020**, *56* (55), 7589−7592.

(84) Milic, D.; Dick, M.; Mulnaes, D.; Pfleger, C.; Kinnen, A.; Gohlke, H.; Groth, G. Recognition motif and mechanism of ripening inhibitory peptides in plant hormone receptor ETR1. *Sci. Rep* **2018**, *8* (1), 3890.

(85) Gohlke, H.; Hergert, U.; Meyer, T.; Mulnaes, D.; Grieshaber, M. K.; Smits, S. H.; Schmitt, L. Binding region of alanopine dehydrogenase predicted by unbiased molecular dynamics simulations of ligand diffusion. *J. Chem. Inf Model* **2013**, *53* (10), 2493−8.

(86) Fontana, J.; Fulton, D.; Chen, Y.; Fairchild, T. A.; McCabe, T. J.; Fujita, N.; Tsuruo, T.; Sessa, W. C. Domain mapping studies reveal that the M domain of hsp90 serves as a molecular scaffold to regulate Akt-dependent phosphorylation of endothelial nitric oxide synthase and NO release. *Circ. Res.* **2002**, *90* (8), 866−73.

(87) Seidel, S. A.; Dijkman, P. M.; Lea, W. A.; van den Bogaart, G.; Jerabek-Willemsen, M.; Lazic, A.; Joseph, J. S.; Srinivasan, P.; Baaske, P.; Simeonov, A.; et al. Microscale thermophoresis quantifies biomolecular interactions under previously challenging conditions. *Methods* **2013**, *59* (3), 301−15.

(88) Thulasiraman, V.; Matts, R. L. Luciferase renaturation assays of chaperones and chaperone antagonists. *Methods Mol. Biol.* **1998**, *102*, 129−41.

(89) Lo, M. C.; Aulabaugh, A.; Jin, G.; Cowling, R.; Bard, J.; Malamas, M.; Ellestad, G. Evaluation of fluorescence-based thermal shift assays for hit identification in drug discovery. *Anal. Biochem.* **2004**, *332* (1), 153−9.

(90) *Schrödinger Release 2018-1: Maestro*; Schrödinger, LLC: New York, NY, 2018.

(91) Jorgensen, W. L.; Chandrasekhar, J.; Madura, J. D.; Impey, R. W.; Klein, M. L. Comparison of Simple Potential Functions for Simulating Liquid Water. *J. Chem. Phys.* **1983**, *79* (2), 926−935.

(92) Martinez, L.; Andrade, R.; Birgin, E. G.; Martinez, J. M. PACKMOL: A Package for Building Initial Configurations for Molecular Dynamics Simulations. *J. Comput. Chem.* **2009**, *30* (13), 2157−2164.

(93) Darden, T.; York, D.; Pedersen, L. Particle Mesh Ewald - an N.Log(N) Method for Ewald Sums in Large Systems. *J. Chem. Phys.* **1993**, *98* (12), 10089−10092.

(94) Ryckaert, J. P.; Ciccotti, G.; Berendsen, H. J. C. Numerical-Integration of Cartesian Equations of Motion of a System with Constraints - Molecular-Dynamics of N-Alkanes. *J. Comput. Phys.* **1977**, *23* (3), 327−341.

(95) Hopkins, C. W.; Le Grand, S.; Walker, R. C.; Roitberg, A. E. Long-Time-Step Molecular Dynamics through Hydrogen Mass Repartitioning. *J. Chem. Theory Comput* **2015**, *11* (4), 1864−74.

(96) Roe, D. R.; Cheatham, T. E. PTRAJ and CPPTRAJ: Software for processing and analysis of molecular dynamics trajectory data. *J. Chem. Theory Comput.* **2013**, *9* (7), 3084.

(97) Homeyer, N.; Gohlke, H. Free Energy Calculations by the Molecular Mechanics Poisson-Boltzmann Surface Area Method. *Mol. Inform* **2012**, *31* (2), 114−22.

(98) Miller, B. R., 3rd; McGee, T. D., Jr.; Swails, J. M.; Homeyer, N.; Gohlke, H.; Roitberg, A. E. MMPBSA.py: An Efficient Program for End-State Free Energy Calculations. *J. Chem. Theory Comput* **2012**, *8* (9), 3314−21.

(99) Onufriev, A.; Bashford, D.; Case, D. A. Exploring protein native states and large-scale conformational changes with a modified generalized born model. *Proteins* **2004**, *55* (2), 383−94.

(100) Manalastas-Cantos, K.; Konarev, P. V.; Hajizadeh, N. R.; Kikhney, A. G.; Petoukhov, M. V.; Molodenskiy, D. S.; Panjkovich, A.; Mertens, H. D. T.; Gruzinov, A.; Borges, C. ATSAS 3.0: expanded functionality and new tools for small-angle scattering data analysis. *J. Appl. Crystallogr.* **2021**, *54* (1), 343.

(101) Svergun, D. I. Determination of the Regularization Parameter in Indirect-Transform Methods Using Perceptual Criteria. *J. Appl. Crystallogr.* **1992**, *25*, 495−503.

(102) Kozin, M. B.; Svergun, D. I. Automated matching of high- and low-resolution structural models. *J. Appl. Crystallogr.* **2001**, *34*, 33−41.

(103) Mahon, F. X.; Deininger, M. W.; Schultheis, B.; Chabrol, J.; Reiffers, J.; Goldman, J. M.; Melo, J. V. Selection and characterization of BCR-ABL positive cell lines with differential sensitivity to the tyrosine kinase inhibitor STI571: diverse mechanisms of resistance. *Blood* **2000**, *96* (3), 1070−1079.

https://doi.org/10.1021/acscentsci.2c00013
ACS Cent. Sci. XXXX, XXX, XXX−XXX

CDDpress

www.nature.com/cddis

ARTICLE OPEN

Co-targeting HSP90 alpha and CDK7 overcomes resistance against HSP90 inhibitors in BCR-ABL1+ leukemia cells

Melina Vogt[1,13], Niklas Dienstbier[1,13], Julian Schliehe-Diecks[1], Katerina Scharov[1], Jia-Wey Tu[1], Philip Gebing[1], Julian Hogenkamp[1], Berna-Selin Bilen[1], Silke Furlan[1], Daniel Picard[1,2], Marc Remke[1,2], Layal Yasin[1], David Bickel[3,4], Munishikha Kalia[5,6], Alfredo Iacoangeli[5,6,7], Thomas Lenz[8], Kai Stühler[9], Aleksandra A. Pandyra[1,10,11], Julia Hauer[12], Ute Fischer[1,2], Rabea Wagener[1,2], Arndt Borkhardt[1,2] and Sanil Bhatia[1,2]✉

HSP90 has emerged as an appealing anti-cancer target. However, HSP90 inhibitors (HSP90i) are characterized by limited clinical utility, primarily due to the resistance acquisition via heat shock response (HSR) induction. Understanding the roles of abundantly expressed cytosolic HSP90 isoforms (α and β) in sustaining malignant cells' growth and the mechanisms of resistance to HSP90i is crucial for exploiting their clinical potential. Utilizing multi-omics approaches, we identified that ablation of the HSP90β isoform induces the overexpression of HSP90α and extracellular-secreted HSP90α (eHSP90α). Notably, we found that the absence of HSP90α causes downregulation of PTPRC (or CD45) expression and restricts in vivo growth of BCR-ABL1+ leukemia cells. Subsequently, chronic long-term exposure to the clinically advanced HSP90i PU-H71 (Zelavespib) led to copy number gain and mutation (p.S164F) of the *HSP90AA1* gene, and HSP90α overexpression. In contrast, acquired resistance toward other tested HSP90i (Tanespimycin and Coumermycin A1) was attained by MDR1 efflux pump overexpression. Remarkably, combined CDK7 and HSP90 inhibition display synergistic activity against therapy-resistant BCR-ABL1+ patient leukemia cells via blocking pro-survival HSR and HSP90α overexpression, providing a novel strategy to avoid the emergence of resistance against treatment with HSP90i alone.

Cell Death and Disease (2023)14:799; https://doi.org/10.1038/s41419-023-06337-3

INTRODUCTION

Cancer cells are widely known to hijack normal cytoprotective processes mediated by chaperone proteins to promote their survival and growth [1]. Among the chaperone proteins, HSP90 has been extensively studied due to their critical ATP-dependent chaperone activity, required by various oncoproteins implicated in malignant transformation [2, 3]. HSP90 facilitates the correct folding of newly synthesized and denatured oncoproteins, such as BCR-ABL1 [4, 5]. Consistently, in a recent report, inhibition of HSP90 delays the progression of BCR-ABL1+ leukemia in combination with tyrosine kinase inhibitor (TKI) [6]. Of note, HSP90i are effective against TKI-resistant BCR-ABL1+ leukemia stem cells and BCR-ABL1^{T315I} mutant cells [4, 7–9]. Furthermore, HSP90 expression is found enriched in other therapy refractory leukemia subtypes, including acute or chronic myeloid leukemia (AML or CML) [10–13] and BCR-ABL1-like BCP-ALL [14, 15]. The critical involvement of HSP90 in numerous oncogenic pathways and its overexpression in poor prognostic leukemia subgroups positioned it as an important therapeutic target [2]. Numerous pan-HSP90i or isoform-specific HSP90i have been developed over the past few years, exhibiting different binding modes [16, 17]. However, despite the early clinical promise, adverse events, including resistance-acquisition and dose-limiting toxicity in patients, have mostly barred widespread use of HSP90i in the clinic [2]. Recently, the HSP90i PU-H71 (Zelavespib) has been granted orphan drug status by the US Food and Drug Association (FDA) to treat myelofibrosis and was administered for compassionate use to treat AML [18]. Nevertheless, the induction of HSR is acknowledged as one of the most prominent causes of acquired resistance toward using HSP90i [4, 19].

In mammalian cells, there are two cytosolic isoforms of HSP90, i.e., a stress-inducible HSP90α isoform (encoded by the *HSP90AA1* gene located on chromosome 14q32–33) and a constitutively expressed HSP90β isoform (*HSP90AB1* gene; located on

[1]Department of Pediatric Oncology, Hematology and Clinical Immunology, Medical Faculty, Heinrich Heine University Düsseldorf, Düsseldorf, Germany. [2]German Cancer Consortium (DKTK), partner site Essen/Düsseldorf, Düsseldorf, Germany. [3]Interuniversity Institute of Bioinformatics in Brussels, ULB-VUB, Brussels, Belgium. [4]Structural Biology Brussels, Vrije Universiteit Brussel, Brussels, Belgium. [5]Department of Biostatistics and Health Informatics, King's College London, London, UK. [6]Department of Basic and Clinical Neuroscience, King's College London, Maurice Wohl Clinical Neuroscience Institute, London, UK. [7]National Institute for Health Research Biomedical Research Centre and Dementia Unit at South London and Maudsley NHS Foundation Trust and King's College London, London, UK. [8]Molecular Proteomics Laboratory, Biological Medical Research Center, Heinrich-Heine-University Düsseldorf, Düsseldorf, Germany. [9]Institute for Molecular Medicine, Proteome Research, University Hospital and Medical Faculty, Heinrich-Heine-University Düsseldorf, Düsseldorf, Germany. [10]Institute of Clinical Chemistry and Clinical Pharmacology, University Hospital Bonn, Bonn, Germany. [11]German Center for Infection Research (DZIF), Partner Site Bonn-Cologne, Bonn, Germany. [12]Department of Pediatrics and Children's Cancer Research Center, Children's Hospital Munich Schwabing, Technical University of Munich, School of Medicine, Munich, Germany. [13]These authors contributed equally: Melina Vogt, Niklas Dienstbier.
✉email: sanil.bhatia@med.uni-duesseldorf.de

Edited by Professor Marc Diederich

Received: 6 June 2023 Revised: 22 November 2023 Accepted: 23 November 2023
Published online: 06 December 2023

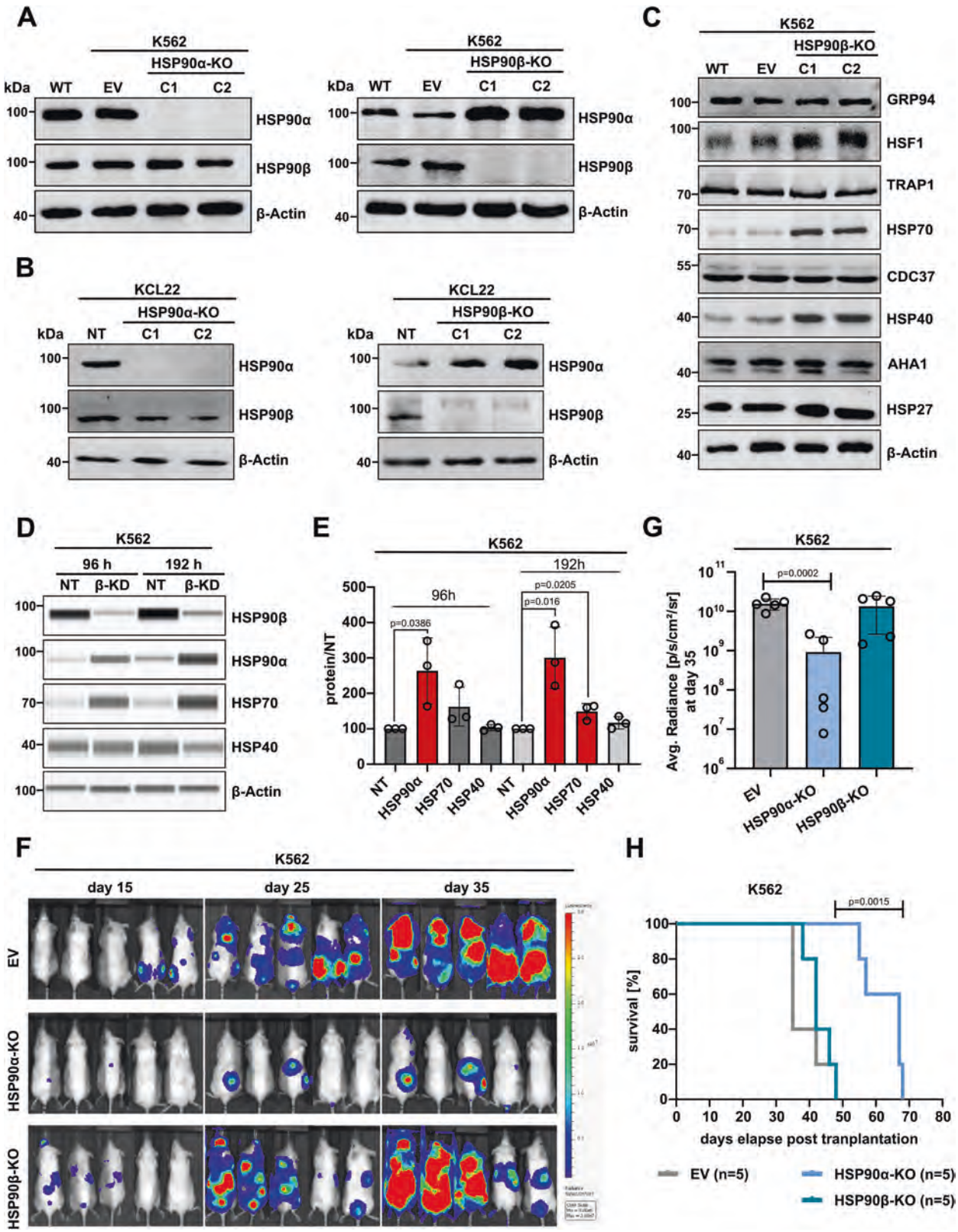

chromosome 6p21) [20]. These isoforms share a high degree (86%) of amino acid sequence identity. Although HSP90α and HSP90β isoforms exhibit comparable affinities for their client proteins and can often compensate for each other effectively [21], exceptions have been reported that indicate distinctive binding tendencies [22–24]. This is emphasized by their different roles in development and cell survival [20]. For instance, HSP90α-KO mice develop normally or occasionally with few congenital disabilities [25], while the knockout of HSP90β causes embryonic lethality in mice, which cannot be compensated by HSP90α [26]. In previous

Fig. 1 HSP90β ablation causes HSP90α and HSP70 upregulation, whereas HSP90α loss suppresses in vivo growth of BCR-ABL1+ leukemia cells and prolongs survival. Western Blot (WB) analysis of the stable CRISPR-Cas9 mediated knockout (KO) of HSP90α and HSP90β isoforms in K562 (**A**) and in KCL22 (**B**) cells. Clone (C), empty vector (EV), wild type (WT) and non-targeting (NT) control. Beta-actin (β-actin) served as a loading control. Representative immunoblots are shown from three independent repeats. **C** Expression of other non-cytosolic HSP90 paralogues (GRP94 and TRAP1), HSR-related proteins (HSP70, HSP40 and HSP27) and HSP90 co-chaperones (AHA1 and CDC37) in HSP90β-KO K562 cells. β-actin served as a loading control. **D** Expression of HSP70, HSP40 and HSP90α upon siRNA mediated HSP90β knockdown (KD) in K562 cells, analyzed by automated WB (JESS). β-actin served as a loading control. **E** Bars show average protein quantification measurements of HSP90α, HSP70 and HSP40 levels in HSP90β-KD cells compared to NT control cells. Error bars = SD of three independent replicates; *p*-values were calculated by unpaired two-tailed student's t-test. **F** Images of NSG mice ($n = 5$ mice/group) transplanted with luciferase-GFP + HSP90α/β-KO or EV K562 cells on the days depicted outside image panel. **G** Graph show mean ± SD ($n = 5$ mice/group) of the bioluminescence measurements of region of interest (radiance; p/s/cm2/sr) at day 35. Significant reduction in the transplantation of HSP90α-KO as compared to EV control K562 cells, determined by unpaired two-tailed student's t-test, $p = 0.0002$. **H** Kaplan–Meier survival curves showing significantly prolonged overall survival of NSG mice transplanted with HSP90α-KO compared to HSP90β-KO or EV (K562) control cells ($n = 5$ mice/group, $p = 0.0015$, Log-rank Mantel-Cox test).

ex vivo studies, cultured HSP90α-KO cells exhibited normal cell morphology and growth rates, while the generation of HSP90β-KO cells was not achieved [21].

In this study, we employed genetic KO and knockdown (KD) models of HSP90 isoforms (α and β) for extensive multi-omics-based in vitro and in vivo characterization and identified HSP90α as the primary driver of malignancy of the two isoforms in BCR-ABL1+ leukemia cells. Moreover, acquired resistance toward distinct HSP90i (exhibiting different binding modes) was studied in BCR-ABL1+ leukemia cells, highlighting the involvement of heightened HSP90α or MDR1 levels in mitigating the efficacy of HSP90 inhibition. Importantly, combinatorial ex vivo drug sensitivity screenings identified CDK7 inhibitors (CDK7i) as drugs synergizing with HSP90α inhibition. Thus our findings can augment HSP90i-based therapy and indicate a new therapeutic vulnerability, especially in cases of BCR-ABL1+ leukemia with reduced treatment response.

RESULTS

HSP90β loss induces overexpression of the stress-inducible HSP90α isoform in BCR-ABL1+ cell lines (K562 and KCL22)

To understand the precise role of HSP90 cytosolic isoforms (α and β), we generated CRISPR-Cas9 mediated knockout (KO), si- or inducible shRNA mediated knockdown (KD) models. Strikingly, the loss of HSP90β isoform in BCR-ABL1+ leukemia cell lines (K562 and KCL22) resulted in the upregulation of the HSP90α isoform both at protein and mRNA levels (Fig. 1A, B, Supplemental Fig. 1A–D). We next asked whether the observed high HSP90α expression upon loss of the HSP90β isoform was caused by genetic alterations of the *HSP90AA1* gene, as a long-term compensatory adaption carried out by HSP90β-KO cells. For that we performed SNP array analysis on the HSP90β-KO (K562) cells; however, no alterations were observed in the *HSP90AA1* locus (Supplemental Fig. 1E). Of note, HSP90α-KO did not induce the expression of HSR-related proteins (e.g., HSP70, HSP40, or HSP40), while HSP90β-KO resulted in the upregulation HSP70 and HSP40 (Fig. 1C, Supplemental Fig. 1F). Furthermore, analyzing changes in other non-cytosolic HSP90 paralogues, such as HSP75/TRAP1 (mitochondria), GRP94 (endoplasmic reticulum) and co-chaperones of HSP90 (AHA1 and CDC37) revealed no significant changes in their expression upon HSP90α/β loss (Fig. 1C, Supplemental Fig. 1F).

To corroborate the observed HSP90α overexpression in HSP90β-KO cells and to eliminate any potential off-target effects attributed to CRISPR-mediated targeting, we proceeded to employ a siRNA-mediated knockdown (KD) strategy using K562 cells. We observed that even a short-term KD of HSP90β, lasting either 96 or 192 h, induces a significant ($p < 0.05$) increase in HSP90α expression (Fig. 1D, E). However, a significant ($p < 0.05$) elevation in HSP70 expression following HSP90β-KD was only evident at a later time point (192 h). Conversely, HSP90β-KD did not affect the expression of HSP40 as seen in case of HSP90β-KO (Fig. 1D, E). In alternative models utilizing doxycycline-inducible shRNA to induce HSP90β-KD in K562 cells, we again validated increase in the HSP90α and HSP70 mRNA transcripts upon targeting of the HSP90β isoform (Supplemental Fig. 1G, H).

Following previous reports [22, 27–30], the binding preferences of specific client proteins (CDK4, CDK6, and SURVIVIN) toward distinct HSP90α/β isoforms were next analyzed. However, no changes were observed in the expression of these client proteins upon ablation of HSP90α/β isoforms (Supplemental Fig. 1I, J). On the other hand, the levels of other HSP90 client proteins, such as pan-AKT and FKBP5 [31, 32], were found enriched in both HSP90α- and HSP90β-KO cells (Supplemental Fig. 1I–K). Our subsequent focus was directed towards exploring the influence on the BCR-ABL1 oncoprotein following the depletion of HSP90α/β isoforms, considering the involvement of HSP90 in ensuring the accurate folding and subcellular positioning of the BCR-ABL1 protein [4, 5]. Relatively higher BCR-ABL1 activity (p-BCR-ABL^{Y412}) along with heightened downstream pro-survival signaling (p-STAT5a^{Y694} and p-CRKL^{Y207}) were noticed in HSP90α-KO cells compared to respective controls (Supplemental Fig. 1K, L). Moreover, immunofluorescence imaging of the HSP90α- and HSP90β-KO cells identified a comparatively higher abundance of BCR-ABL1-foci (in the cytoplasmic/nucleocytoplasmic region) in HSP90α-KO cells compared to HSP90β-KO and control cells (Supplemental Fig. 1M). These results are in agreement with a previous study [5], where HSP90β was shown to interact and stabilize BCR-ABL1 kinase with comparatively better potency than HSP90α. As in the case of our HSP90α-KO model, the exclusive expression of the HSP90β isoform resulted in the hyperactivation of BCR-ABL1 and the subsequent activation of downstream pro-survival signaling pathways.

Taken together, the loss of HSP90β isoform in BCR-ABL1 + CML cell lines (K562 and KCL22) leads to an increase in the HSP90α isoform, while loss of HSP90α doesn't induce changes in HSP90β levels.

Loss of HSP90α represses in vivo growth of BCR-ABL1 + (K562) leukemia cells

To test possible functional implications on the BCR-ABL1+ leukemia cells' growth upon loss of either HSP90α/β, we next performed in vitro and in vivo functional assays. CDK4 and CDK6 are well-recognized clients of HSP90β [27] and play a crucial role in cell cycle progression. In line with unchanged CDK4/6 expression (Supplemental Fig. 1I, J), no changes in the cell cycle progression was determined upon HSP90α/β-KO K562 cells (Supplemental Fig. 1N). Next, we performed colony forming unit (CFU) assays in the semi-solid medium (Supplemental Fig. 1O, P). HSP90β-KO (K562 and KCL22) cells formed fewer ($p < 0.05$) and morphologically smaller colonies in comparison to control and HSP90α-KO cells. In comparison, the colonies of HSP90α-KO (K562 and KCL22) cells had a dispersed and atypical phenotype, with

slightly higher (not significant) total colony numbers than the respective control cells. Further, the in vivo transplantation efficiency of HSP90α/β-KO (K562) cells in an immunodeficient NSG mouse model was examined. Interestingly, the engraftment capacity of HSP90α-KO cells was significantly ($p = 0.0002$) reduced in comparison to HSP90β-KO or the control group, which was corroborated by the significant ($p = 0.0015$) increase in the overall survival (19 days) of the animals (Fig. 1F–H). The differences between in vitro CFU assay and in vivo growth of HSP90α-KO cells likely appeared due to the absence of eHSP90α upon HSP90α-KO, which is known for promoting invasiveness and metastasis of the malignant cells [33–37], a function not relevant for ex vivo growth.

HSP90α loss causes downregulation of PTPRC (or CD45) expression in BCR-ABL1 + (K562 and KCL22) cells

We next utilized multi-omics approaches (including Transcriptomics, Proteomics and Secretomics) to evaluate the potential implications on the distinctive signaling pathways upon loss of HSP90α/β isoforms in K562 cells. Firstly, differential RNA expression analysis using RNA-sequencing (RNA-seq) was performed, which revealed 2095 genes (1090 up- and 1005 down-regulated) with consistent and significant (FDR < 0.05; log2(FC) < −1 or log2(FC) > 1) altered expression in HSP90α-KO cells in comparison to control cells (Fig. 2A, Supplemental Fig. 2A). In contrast, 903 genes (368 up- and 535 down-regulated) were altered in HSP90β-KO cells in comparison to control cells (Supplemental Fig. 2A, B). Fast gene set enrichment analysis (fGSEA) and clusterProfiler revealed significant enrichment in gene sets associated with the leukemic stem cell downregulation, MAPK/ERK signaling and immune cell development and activation in HSP90α-KO cells (Supplemental Fig. 2C, D). Strikingly, enrichment of a gene signature related to visual loss was found enriched in HSP90β-KO cells (Fig. 2B), which can be seen in line with ocular toxicity, a common side effect reported during clinical use of HSP90i [2, 38, 39].

Next, differential protein expression analysis using quantitative mass spectrometry (MS) based proteomic data revealed 375 proteins (180 up- and 195 down-regulated) with consistent and significant (p-value < 0.05; log2(FC) < −1 or log2(FC) > 1) altered expression in HSP90α-KO cells (Fig. 2C, Supplemental Fig. 2E), whereas 213 proteins (103 up- and 110 down-regulated) were found in HSP90β-KO cells in comparison to control (Supplemental Fig. 2E, F). Aligned with the previous WB results (Fig. 1C), higher levels of HSP90AA1 (HSP90α) and HSPA1A (HSP70) were identified in the MS data of HSP90β-KO cells (Supplemental Fig. 2F). fGSEA from the MS data identified enrichment in the gene sets involved in the cell cycle, chromosomal and cytoskeleton organization in HSP90α-KO cells (Supplemental Fig. 2G). Notably, both fGSEA and clusterProfiler identified significant downregulation in the oxidative phosphorylation-, cellular respiration- and energy metabolism-related gene signature in the HSP90α-KO cells (Fig. 2D, Supplemental Fig. 2G). The importance of HSP90 in coordinating and supporting a multitude of metabolic pathways necessary for energy generation and efficient cellular respiration has been shown in a previous study [40]. In contrast, there was no enrichment in the gene sets identified (in any of the biological processes) in HSP90β-KO cells compared to control. We then compared the overlap of genes between HSP90α- and HSP90β-KO cells on the mRNA and protein level and found 210 genes (100 up- and 110 down-regulated) shared between HSP90α- and HSP90β-KO cells (Supplemental Fig. 2H). Subsequently, we examined the overlap of some top differentially up- or down-regulated genes from RNA-seq and MS data in the KO cells (Fig. 2E, F).

HSP90α is secreted extracellularly (eHSP90α), which acts as mediator of tumor cell invasion and metastasis [33–36]. Therefore, we next performed MS-based secretome analysis to evaluate changes in the secreted protein profile in the extracellular space upon loss of HSP90α/β isoform. To identify and quantify the peptides/proteins, the human sequence database from Uni-ProtKB was used, and a total of 2051 protein groups were identified in the K562 cells (FDR = 0.01). Differential protein expression analysis revealed 149 proteins (87 up- and 62 down-regulated) with altered expression in the HSP90α-KO cells compared to the control cells (Fig. 3A). In contrast, 124 proteins (57 up- and 49 down-regulated) were found to be altered in the HSP90β-KO cells in comparison to the control cells (Supplemental Fig. 3A). As expected, secretion of HSP90α was found most significantly downregulated in HSP90α-KO cells, while eHSP90α expression went significantly up in HSP90β-KO cells (Fig. 3B).

Further, we validated some of the top hits shared in the proteogenomic characterization, such as TOP2A, LCP2 (SLP76) and PTPRC (CD45). A consistent upregulation of LCP2 and TOP2A upon HSP90α loss was validated in BCR-ABL1 + CML cell lines (K562 and KLC22) and in BCR-ABL1 + BCP-ALL cell line (SUP-B15) (Supplemental Fig. 3B). Next, as a functional validation step based on high TOP2A levels detected (at proteome and secretome levels) upon HSP90α loss, pharmacological drug screenings were performed by combining TOP2A and HSP90 inhibitors [41, 42]. Indeed, the combination of PU-H71 (HSP90i) along with Mitoxantrone (TOP2i) displayed a significant (ZIP Synergy score ≥ 20) synergistic interaction against two BCR-ABL1 + BCP-ALL (relapsed) patient derived xenograft (PDX) cells and BCR-ABL1 + CML leukemia cell lines (K562 and KCL22) (Fig. 3C, Supplemental Fig. 3C). Notably, in all multi-omics approaches we detected a consistent downregulation of PTPRC (or CD45) expression and secretion upon HSP90α loss. These results were corroborated in HSP90-KO K562 or KCL22 models (Fig. 3D–F). In addition, we evaluated the expression of downstream signaling partners of CD45, specifically LCK and LYN. Notably, there were no discernible changes in LYN and p-LYN^{Y507} expression, whereas the expression of LCK and p-LCK^{Y505} (phosphorylation site known to negatively influence LCK catalytic activity) [43], exhibited an increase following HSP90α-KO. However, no statistical difference in the p-LCK^{Y505}/LCK ratio was determined (Supplemental Fig. 3D), suggesting that the elevation in p-LCK^{Y505} expression is due to an overall increase in the LCK expression upon HSP90α-KO. We next performed recovery experiments, where transient re-expression of HSP90α in the HSP90α-KO cells restored CD45 expression (Fig. 3G and Supplemental Fig. 3E).

Enhanced CD45 expression is associated with the increased risk of relapse in B- or T-ALL [44], and the dependency of CD45 expression on HSP90α could serve as a predictive biomarker for evaluating the effectiveness of HSP90α inhibition [45].

Chronic exposure to HSP90 inhibitor PU-H71 promotes HSP90α overexpression in K562 cells

To better understand resistance mechanisms evoked during pharmacological inhibition of HSP90, we generated HSP90i resistant (K562) cells against the HSP90-N-terminal domain (NTD) targeting inhibitor (PU-H71 and 17-AAG or Tanespimycin) or against HSP90-C-terminal domain (CTD) targeting inhibitor (Coumermycin A1 or CA1). Briefly, the clonal selection was carried out by repetitive treatment cycles using increasing inhibitor concentrations (Fig. 4A). Dose–response curves of PU-H71 resistant (PUHr), Tanespimycin (TM) resistant (TMr) and CA1 resistant (CA1r) clones displayed significant shifts in IC_{50} (4.5, 17.6, and 4.4 fold, respectively) as compared to the parental cells (Fig. 4B, Supplemental Fig. 4A). PUHr, TMr, or CA1r cells also displayed cross-resistance toward other HSP90i with different modes of action (Fig. 4C, Supplemental Fig. 4B). Of note, upon re-treatment with the respective inhibitors, only PUHr cells displayed a strong upregulation of HSP90α in comparison to the parental counterpart (Fig. 4D, Supplemental Fig. 4C). Consequently, the total-HSP90 levels were also found higher in PUHr cells, whereas no changes in the HSR induction was noticed in the PUHr cells

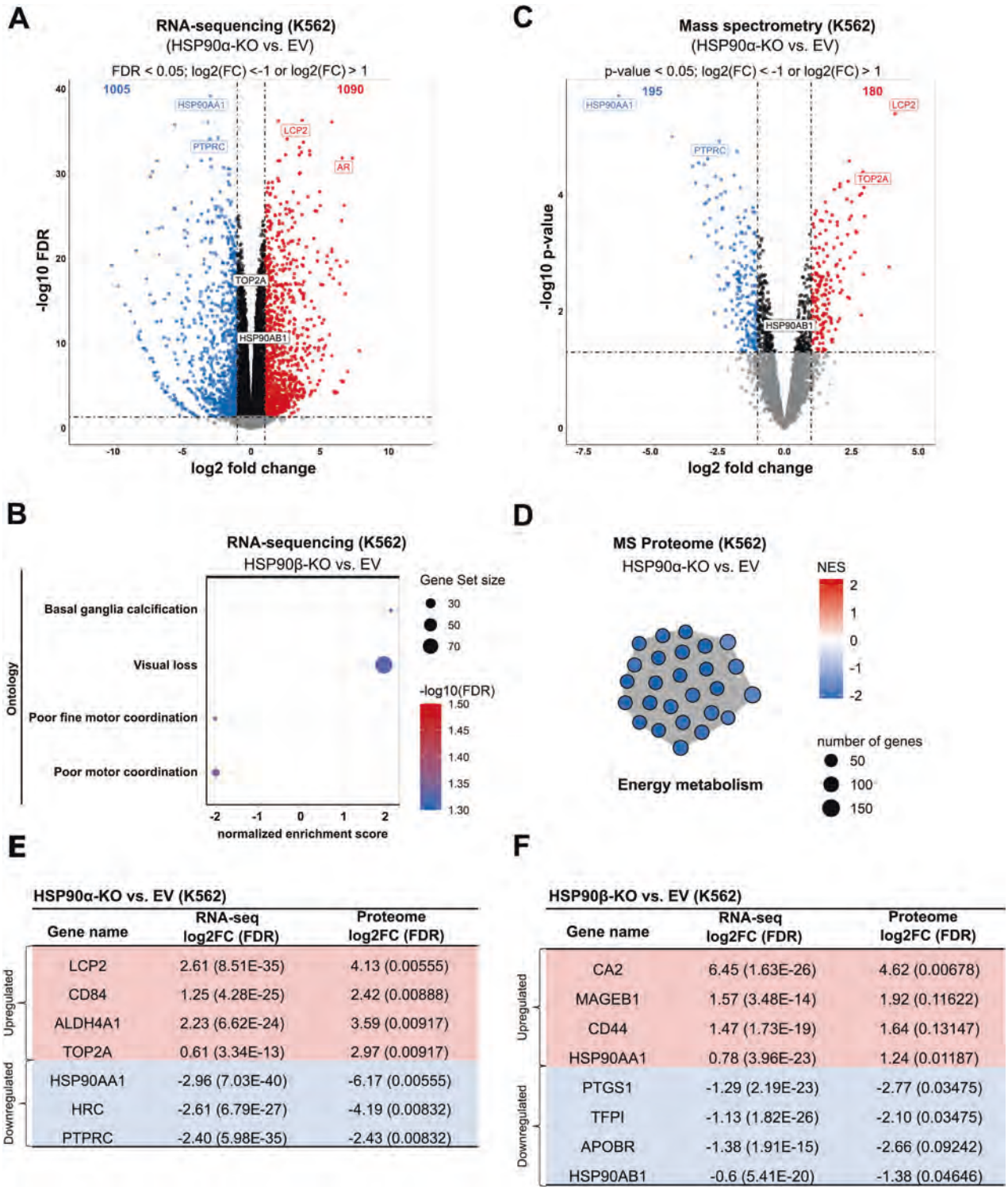

HSP90α-KO vs. EV (K562)

	Gene name	RNA-seq log2FC (FDR)	Proteome log2FC (FDR)
Upregulated	LCP2	2.61 (8.51E-35)	4.13 (0.00555)
	CD84	1.25 (4.28E-25)	2.42 (0.00888)
	ALDH4A1	2.23 (6.62E-24)	3.59 (0.00917)
	TOP2A	0.61 (3.34E-13)	2.97 (0.00917)
Downregulated	HSP90AA1	-2.96 (7.03E-40)	-6.17 (0.00555)
	HRC	-2.61 (6.79E-27)	-4.19 (0.00832)
	PTPRC	-2.40 (5.98E-35)	-2.43 (0.00832)

HSP90β-KO vs. EV (K562)

	Gene name	RNA-seq log2FC (FDR)	Proteome log2FC (FDR)
Upregulated	CA2	6.45 (1.63E-26)	4.62 (0.00678)
	MAGEB1	1.57 (3.48E-14)	1.92 (0.11622)
	CD44	1.47 (1.73E-19)	1.64 (0.13147)
	HSP90AA1	0.78 (3.96E-23)	1.24 (0.01187)
Downregulated	PTGS1	-1.29 (2.19E-23)	-2.77 (0.03475)
	TFPI	-1.13 (1.82E-26)	-2.10 (0.03475)
	APOBR	-1.38 (1.91E-15)	-2.66 (0.09242)
	HSP90AB1	-0.6 (5.41E-20)	-1.38 (0.04646)

Fig. 2 Transcriptomic (RNA-sequencing) and quantitative mass spectrometry (MS)-based proteomic analysis of HSP90α/β-KO cells. **A** Volcano plot showing significantly (FDR <0.05; log2(FC) < −1 or log2(FC) > 1, calculated using edgeR (F-Test & Benjamini-Hochberg correction) up- or down-regulated genes from RNA-sequencing data (obtained from three independent replicates) of HSP90α-KO compared to empty vector (EV) control K562 cells. Black dots represent genes that are not significantly regulated, while gray dots represent significantly regulated genes, but below log2(FC) threshold. Blue and red dots represent significantly downregulated and upregulated genes, respectively. **B** fGSEA on the RNA-seq data of HSP90β-KO cells, displaying significantly (FDR = 0.05) regulated ontology gene set signatures in comparison to EV control. **C** Volcano plot obtained from five independent replicates of HSP90α-KO compared to EV control K562 cells showing up- or down-regulated proteins based on MS-based proteomics data applying *p*-value < 0.05 and log2(FC) < −1 or log2(FC) > 1 as the specificity cutoff criteria. **D** Gene clusters obtained using clusterProfiler on the MS data of HSP90α-KO cells revealed significant downregulation (FDR = 0.05) of energy metabolism signature. Normalized enrichment scores (NES). Tables showing consistently up- or down-regulated genes in HSP90α-KO (**E**) or in HSP90β-KO (**F**) K562 cells from the RNA-seq and MS-based proteomics analysis.

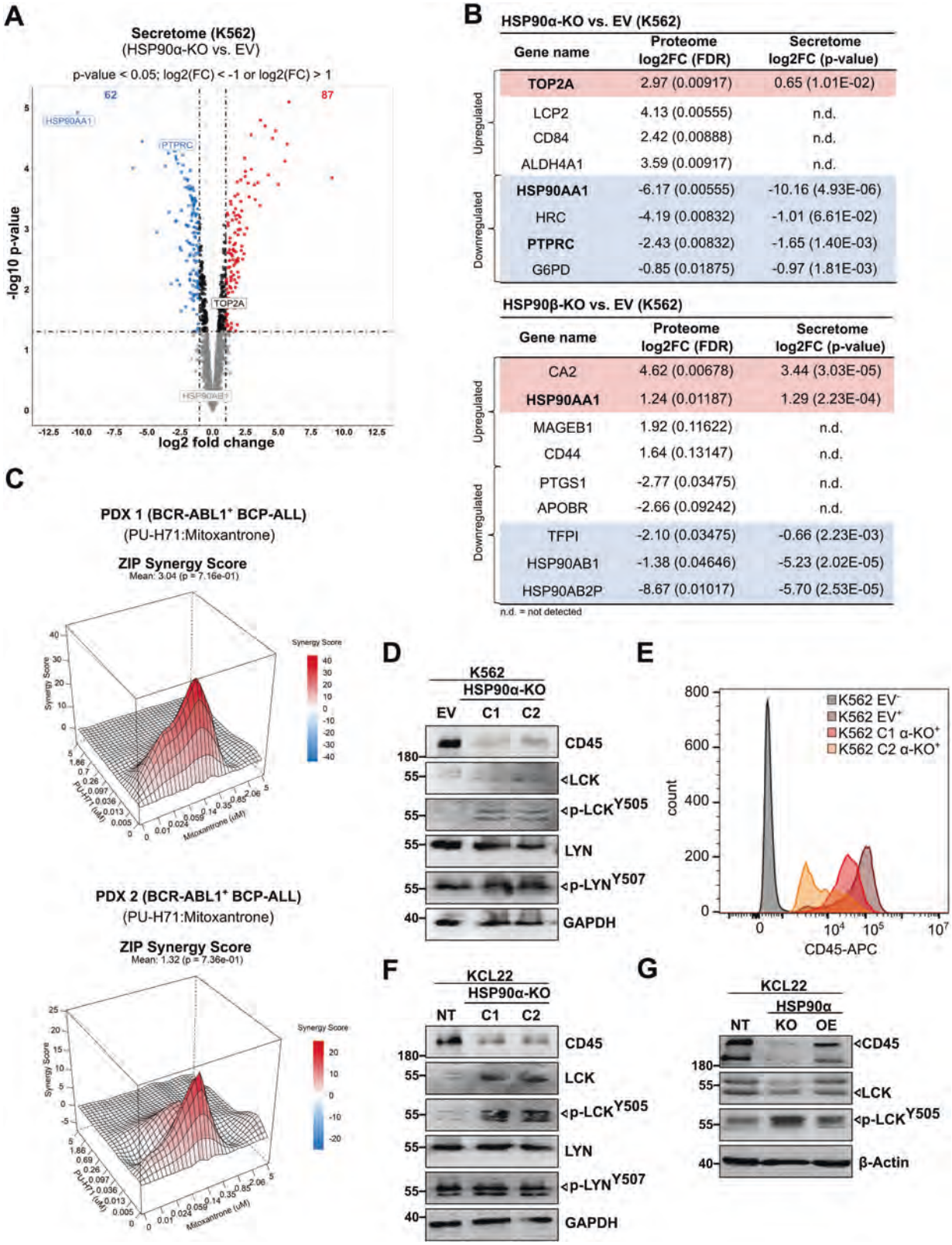

compared to respective parental cells. The resistance escape mechanisms against HSP90i are additionally facilitated through the activation of numerous kinases [46]. HSP90 inhibition can lead to the destabilization of the SRC-AKT-ERK kinase axis [47, 48]. In agreement, we also observed upregulation in the total-AKT or -SRC levels, implying an overall stabilization of these proteins by high HSP90α levels (Supplemental Fig. 4D). The elevated total-AKT levels later protected mTOR signaling from PU-H71 re-treatment, confirmed by recovery of the hallmark phosphorylation at the T389 site of the p70S6 kinase (p70S6K), maintaining the

Fig. 3 Quantitative MS-based secretome analysis validated PTPRC (CD45) as differentially regulated hit in HSP90α-knockout cells. **A** Volcano plot obtained from five independent replicates of HSP90α-KO compared to EV control K562 cells showing up- or down-regulated proteins based on MS-based secretomics data applying *p*-value < 0.05 and log2(FC) < −1 or log2(FC) > 1 as the specificity cutoff criteria. The third replicate of the EV control in the secretome data was omitted from the statistical analysis due to its significant deviation from the other four replicates. **B** Table showing consistently up- or down-regulated proteins from the MS-based proteomic and secretomic analysis in HSP90α-KO cells (upper panel) and HSP90β-KO K562 cells (lower panel). **C** Synergy maps of PU-H71 and Mitoxantrone combination matrix for two BCR-ABL1 + BCP-ALL patient derived xenograft (PDX) cells, using zero interaction potency (ZIP) method [79]. Visualization was done using SynergyFinder package. WB analysis of CD45 (intracellular domain) and respective inactivating phosphorylation levels of downstream effectors (p-LCK^{Y505} and p-LYN^{Y507}) in HSP90α-KO K562 (**D**) and KCL22 (**E**) cells. Glyceraldehyde 3-phosphate dehydrogenase (GAPDH) served as a loading control. **F** Fluorescence antibody staining (using FACS) validated downregulation of PTPRC (CD45) on the surface of K562 HSP90α-KO cells. **G** Rescue experiment was performed, in which HSP90α-KO KCL22 cells were transiently transfected with HSP90α-overexpression (OE) construct to re-express the HSP90α isoform.

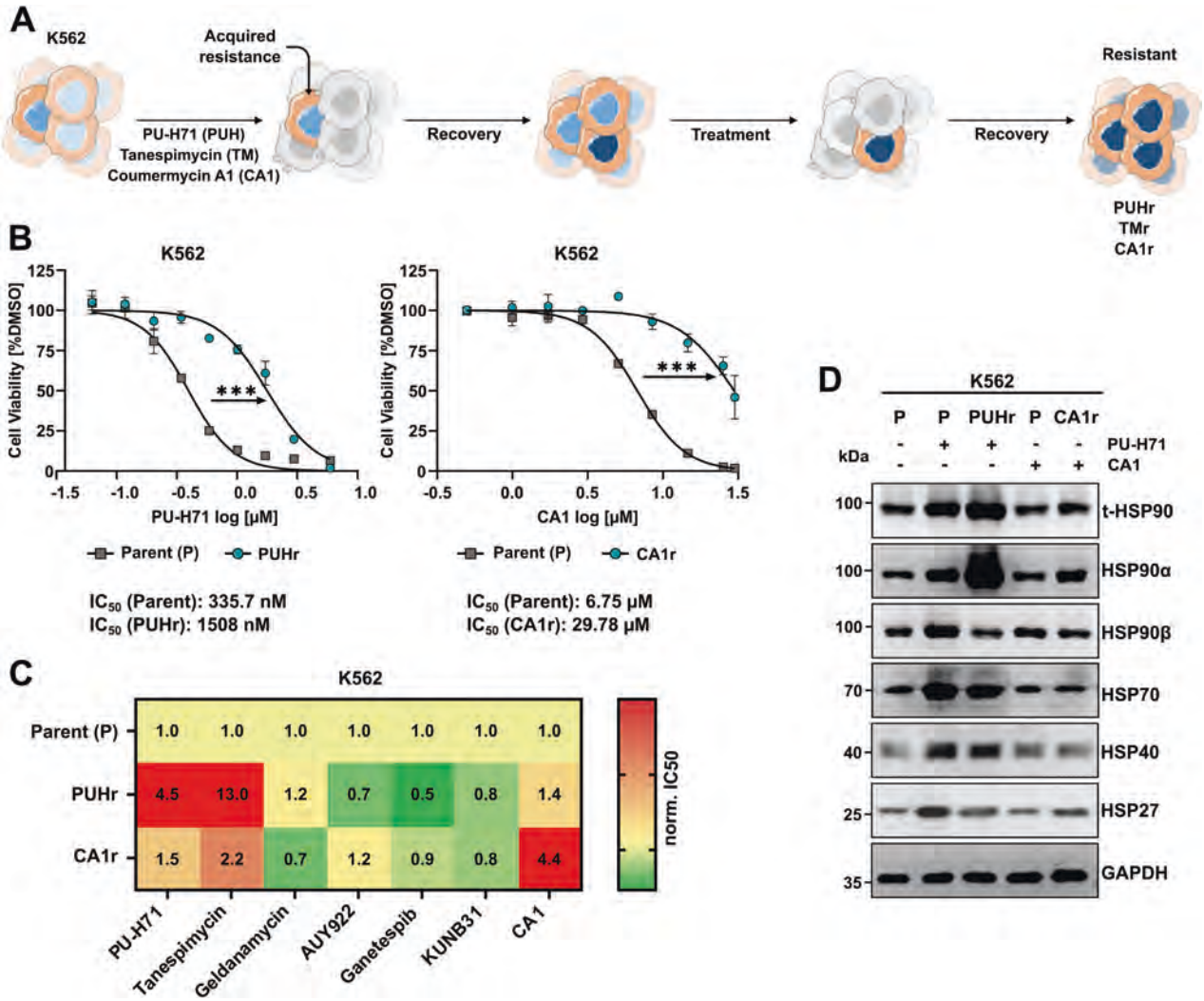

Fig. 4 Resistance against HSP90i PU-H71 is attained by HSP90α overexpression. **A** Schematic depiction of the workflow of generating HSP90 inhibitor (HSP90i) resistant cells, through chronic exposure of HSP90-N-terminal domain- (PU-H71 and Tanespimycin or TM) or HSP90-C-terminal domain-targeting (Coumermycin A1 or CA1) inhibitors in K562 cells. **B** Dose–response curves from three independent experiments showing significant (***$p \leq 0.001$, unpaired two-tailed student's t-test) increase in IC_{50} values for PU-H71-resistant (PUHr) and CA1-resistant (CA1r) cells in comparison to their parental (P) counterparts. **C** Cross-resistance of PUHr and CA1r cells to other HSP90i with similar or different modes of action (MoA). The numbers in the heat map indicate the normalized fold-change of the IC_{50} values of the resistant cell lines to the parental counterpart. The red color depicts an increase in IC_{50} value whereas green indicates a decrease in IC_{50} value in comparison to the parental control. **D** WB analysis of PUHr, CA1r and control parental (P) cells after re-treatment with CA1 (2 μM), PU-H71 (500 nM) or vehicle (-) for 24 h. GAPDH served as a loading control.

phosphorylation of ribosomal protein S6 (RPS6) at position S235/236 (Supplemental Fig. 4D). However, the reported dependency on the p90 RSK and ERK signaling cascade to confer resistance against the HSP90-NTD targeting inhibitor was not verified in our PUHr cells [46]. In contrast, CA1r cells exhibited a notable increase in the phosphorylation of RPS6 at the S240/244 site upon CA1 re-treatment (Supplemental Fig. 4D).

In general, these findings indicate that leukemia cells resistant to HSP90i employ specific adaptations to develop resistance against NTD- or CTD-targeting HSP90i (Supplemental Fig. 4E).

Prolonged treatment with PUH71 causes genetic alterations in the *HSP90AA1* (HSP90α) gene in K562 cells

To identify whether these changes mentioned above were solely short-term adaptive changes or if there was any underlying genetic cause, we subjected PUHr and CA1r cells to SNP array analysis (Fig. 5A, B). In accordance with elevated HSP90α level, PUHr cells harbored a 15 Mb copy number gain on 14q32.12q32.3, in which the *HSP90AA1* gene is located (Fig. 5A). Moreover, to identify single nucleotide variations (SNVs) and insertion/deletions (indels) during resistance acquirement toward HSP90i (PU-H71 and CA1), whole exome sequencing (WES) of PUHr and CA1r cells was next performed. WES identified 100 and 59 acquired variants in PUHr and CA1r cells, respectively, of which 6 were shared between each. Strikingly, we identified two distinct SNVs in the *HSP90AA1* gene. PUHr cells acquired the missense variant p.(S164F) (chr14:102085796 G > A), whereas the CA1r cells harbored the p.(L29F) (chr14:102086292 C > A) (Supplemental Table 1). Interestingly, both resistant cell lines also acquired distinct variants in the *CLMN* gene, with PUHr harboring a p.(S217N) and CA1r a p.(E588Q) (ENST00000298912.9) missense variant (Supplemental Table 1). Moreover, in CA1r cells SNP array identified 1.9 Mb copy number gain on 7q21.12q21.13, in which the *ABCB1* gene (encoding MDR1) is located (Fig. 5B).

To understand how the S164F substitution affects PU-H71 binding and HSP90α in general, we next modeled the S164F variant in silico and compared it to the wildtype structure (Fig. 5C). The substitution site is located in a solvent-exposed loop which is ~0.9 nm away from the PU-H71 binding site. Thus, the substitution is unlikely to interfere with the binding of the inhibitor directly. However, S164 forms multiple hydrogen bonds including to Y142, such that the substitution may lead to conformational changes in the NTD. To explore this possibility, we performed unbiased molecular dynamics (MD) simulations (1 μs length each) of the wildtype and the S164F protein to which PU-H71 is bound. We observed no difference in the binding mode of PU-H71, i.e., the ligand remained stably bound in both simulations (Supplemental Fig. 5A). Moreover, we did not observe major conformational changes in the variant with respect to the crystal structure. In fact, the S164F variant remained more stable throughout the simulation than the wildtype structure (Fig. 5D). This is likely due to the phenylalanine sidechain forming a hydrophobic core, thereby stabilizing the adjacent loop. While these changes do not affect the stability of bound PU-H71, they supposedly interfere with the binding pathway by introducing additional conformational constraints.

To determine the changes at a transcriptomic level in PUHr cells compared to the parental cells, we next performed RNA-seq analysis. A significant increase in the ALDH1A at mRNA and at protein level was determined in the PUHr cells as compared to CA1r and TMr cells (Fig. 5E, F). Further, fGSEA revealed enrichment in the WNT signaling and growth factor response related gene signatures and downregulation of immune related signatures in the PUHr cells (Supplemental Fig. 5B). In contrast, consistent with earlier studies [49–52] and supported by our SNP array findings (in CA1r cells), both CA1r and TMr cells exhibited elevated MDR1 expression (Fig. 5F).

These findings demonstrate that the HSP90α isoform is a prominent cause of resistance against clinically advanced HSP90i PU-H71. Therefore targeting HSP90α and identifying therapeutic combinations can effectively avert the development of resistance to treatment with HSP90 inhibitors alone.

CDK7 and HSP90 inhibitors act synergistically against BCR-ABL1+ leukemia cells by reducing heat shock response induction and HSP90α overexpression

In order to elucidate the actionable therapeutic targets in BCR-ABL1+ leukemia, we next screened HSP90α/β-KO (K562) models on the ex vivo high throughput drug screening platform, consisting of conventional chemotherapeutics and targeted inhibitors (Supplemental Table 2). Of note, HSP90α-KO cells were found hypersensitive toward CDK7i (THZ-1) and standard chemotherapeutics (Cytarabine and Clofarabine) (Fig. 6A). In line, a high CDK7 expression was observed upon loss of HSP90α isoform (Supplemental Fig. 6A). Moreover, in agreement, HSP90β isoform specific inhibitor (KUNB31) [27] was found differentially potent against HSP90α-KO cells. Conversely, HSP90β-KO cells (expressing high levels of HSP90α) displayed hypersensitivity toward several HSP90i (PU-H71, AUY922, BIIB021, and Ganetespib) (Supplemental Fig. 6B). Based on these differential vulnerabilities noticed in HSP90α-KO cells, we next performed combinatorial drug screenings using clinically advanced HSP90i (PU-H71) along with a CDK7i (THZ1). These screenings were carried out utilizing BCR-ABL1 + CML leukemia cell lines (K562 and KCL22) and their TKI-resistant counterparts [4], referred to as K562r, KCL22r, respectively (Supplemental Fig. 6D, E). Furthermore, TKI-resistant BCR-ABL1 + BCP-ALL cells designated as SUPB15r and three (relapsed) PDX cells were included, along with a murine BA/F3 cell line model expressing TKI-resistant BCR-ABL1^{T315I} mutant cells (made resistant to third generation TKI Ponatinib or PN) [4], referred to as BA/F3 BCR-ABL1$^{T315I\text{-}PNr}$ cells (Fig. 6B, Supplemental Fig. 6F–H). Notably, in all cases, the combination of PU-H71 along with THZ1 exhibited significant (Synergy score ≥ 15) synergistic interaction. Next, we tested the combination of PUH71 and THZ1 on peripheral blood derived mononuclear cells (PBMCs) obtained from three healthy individuals. Strikingly, we found out that healthy PBMCs are significantly less sensitive to the PUH71 + THZ1 combination in comparison leukemia K562 cells (Supplemental Fig. 6I).

The inhibition of CDK7 (TFIIH subunit of RNA polymerase II or RNAPII) can initiate a series of defects in the initiation, proximal pausing and elongation of RNAPII [53]. Consequently, we noticed a strong synergistic interaction between HSP90- and CDK7-inhibitors, which acted via impeding RNAPII-mediated transcription of pro-survival heat shock response (HSR)-related genes (Fig. 6C–G and Supplemental Fig. 6J). Of note, combined inhibition of both HSP90 and CDK7 also led to the restoration of HSP90α levels to their basal state, in contrast to the use of HSP90i (PU-H71) alone, demonstrating a promising approach for augmenting HSP90i-based therapy in the future.

DISCUSSION

The clinical response in BCR-ABL1 + BCP-ALL is only short lived, with relapses being driven by mutations in the BCR-ABL1 kinase or activation of independent circuitries [54]. TKIs are unable to eradicate persisting leukemic stem cells and the frequent development of reduced sensitivity to TKIs is also prevalent, thereby amplifying the risk of relapse [55–57]. Novel treatment approaches are therefore needed with the potential to increase treatment-free remission. One attractive strategy is via destabilization of BCR-ABL1 kinase and its related downstream circuitries by targeting HSP90 [4, 7–9]. However, the adverse events such as acquired resistance (through HSR induction) and toxicity associated with the clinical use of HSP90i have thus far halted their widespread clinical approval [2, 16, 58]. To our knowledge, we have shown here for the first time that the loss of HSP90β isoform induces high expression and secretion of HSP90α isoform (eHSP90a) and pro-survival HSR related protein (HSP70), while the converse outcome was not observed upon loss of HSP90α. Interestingly, HSP90α/β-KO cells displayed no changes in the expression of previously reported HSP90-isoform specific client proteins [22, 27–30], which is however in line with a recent study [21], suggesting a compensatory behavior among these cytosolic isoforms. However, our multi-omics profiling of HSP90α- vs. HSP90β-KO cells revealed overall prominent differences in the regulated signaling pathways, likely due to the diverse adaptions

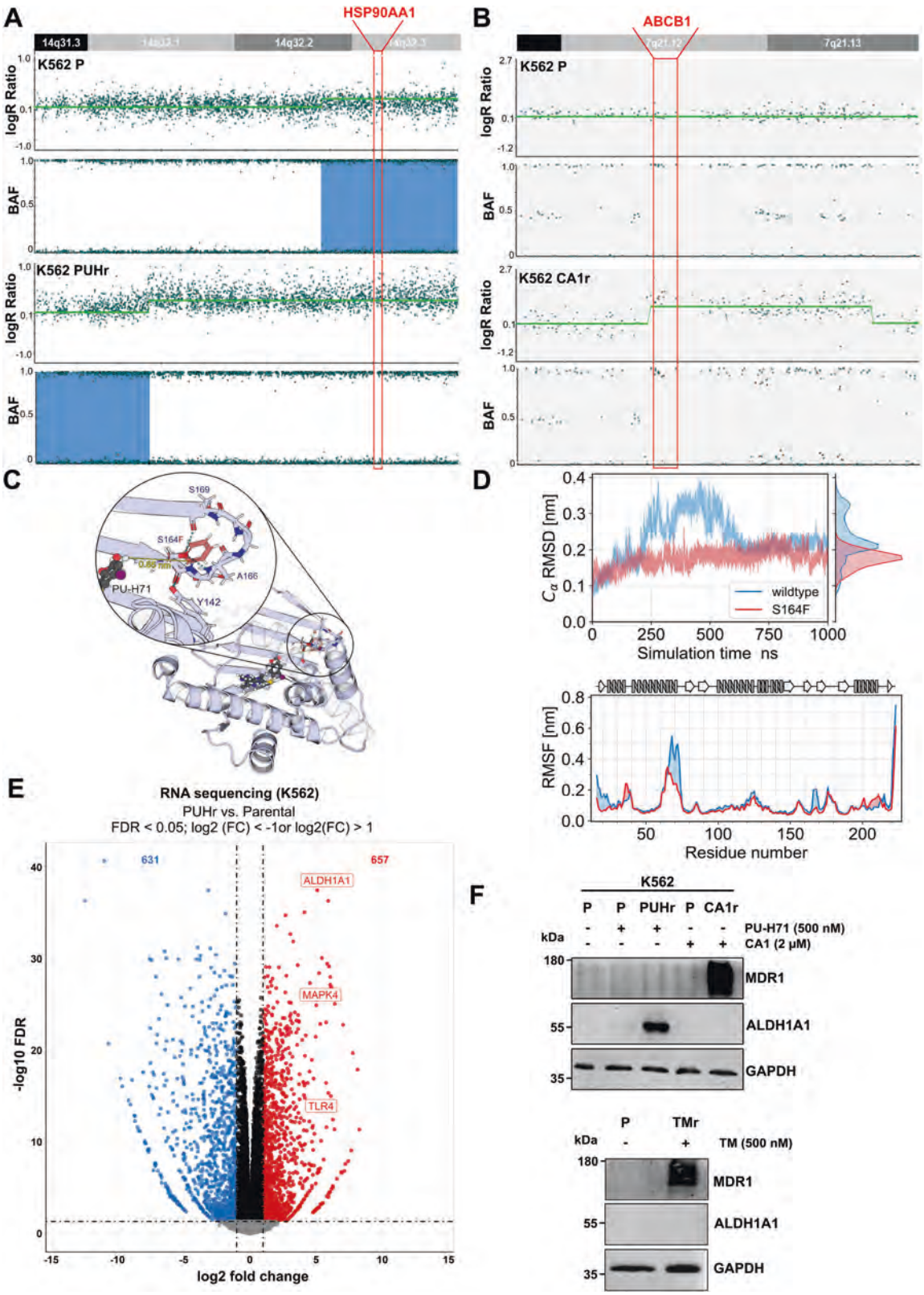

acquired by the cells to compensate for the loss [20, 24]. The tendency of HSP90α isoform to dimerize more frequently than HSP90β, which is required for the proper functioning of HSP90 [59], additionally outlines the differences observed in the regulated pathways. The HSP90β isoform is generally linked with long-term cellular adaptation and early embryonic development, whereas HSP90α is a fast-reactive and stress-inducible isoform [20]. In line, we observed fewer genes and respective pathways altered upon HSP90β-KO than HSP90α-KO [20, 24]. Our multi-omics analysis and rescue experiments consistently identified a

Fig. 5 PU-H71 resistant cells acquire copy number gain and mutation (S164F) in the *HSP90AA1* gene and overexpress ALDH1A1. A SNP array results of PUHr cells in comparison to the parental (P) counterpart revealed an acquired 15 Mb copy number gain in 14q32.1q32.3 encompassing the *HSP90AA1* gene locus (highlighted in red). The upper panel depicts the log2 ratio and the B-allele frequency (BAF) of the parental cells (K562 P), whereas the lower panel depicts the log2 ratio and the BAF of the resistant PUHr cells. **B** SNP array analysis of CA1r cells revealed an acquired copy number gain in 7q21.12q21.13 encompassing the *ABCB1* gene locus (highlighted in red), which is not present in the K562 parental (P) cells. **C** Structural model of the N-terminal domain of HSP90α bound to PU-H71 (based on PDB ID 2fwz). The substitution site S164F is highlighted in red. **D** Upper panel: Alpha carbon-root mean square deviation (C_α-RMSD) of wild type and variant (S164F) HSP90α over the course of the simulation. The wildtype HSP90α structure exhibits stronger conformational changes than the variant S164F, and these changes are reversible. Bottom panel: Alpha carbon-root-mean-square fluctuation (C_α-RMSF) of HSP90α identifies two major regions, which lead to the stronger fluctuations in RMSD observed in the wildtype HSP90α structure. One of these regions is directly adjacent to the mutation site S164F. Above the plot, a schematic representation of the secondary structure is given. **E** Volcano plot of the significantly (FDR<0.05; $-1 > \log2(FC) > 1$, calculated using edgeR (F-Test & Benjamini-Hochberg correction) up- or down-regulated genes in the mRNA expression profile (from RNA-sequencing data) of PUHr vs. parental K562 cells (from three independent replicates). **F** WB analysis of PUHr and CA1r cells (upper panel), Tanespimycin resistant (TMr) cells (lower panel) in comparison to control parental (or P) cells after re-treatment with respective inhibitors or vehicle (-) for 24 h. GAPDH served as a loading control.

strong downregulation of PTPRC (CD45) expression upon loss of HSP90α isoform, affecting downstream p-LCK^{Y505} and LCK expression [43, 48]. Interestingly, CD45 expression correlates positively with BCR-ABL1-induced malignant transformation and negatively with the efficacy of TKI treatment in individuals with CML [60]. In agreement, we noticed a reduction in the in vivo engraftment of BCR-ABL1+ leukemia cells upon HSP90α-KO. Elevated levels of HSP90 have been linked to a dismal prognosis in AML [12], whereas notably, heightened expression of HSP90α isoform is reported in acute leukemia cells and among untreated samples from leukemia patients [61–63]. Our secretome analysis revealed a significant decrease in eHSP90a expression in the HSP90α-KO cells, potentially leading to the suppression of in vivo migration and invasion capabilities of these leukemia cells [33–37].

As previously shown [51], we also observed that the resistance toward PU-H71 conferred cross-resistance only toward TM but not against other tested HSP90i. In our MD simulation analysis, the S164F substitution did not directly affect bound PU-H71; but changed the conformational dynamics of the HSP90-NTD, which may hinder the binding pathway. Interestingly, a missense variant at Y142, which is the hydrogen-bond interaction partner of S164, as well as a CN gain of *HSP90AA1* has been reported in PU-H71-resistant lung cancer cells [51]. Moreover, upregulation of ALDH1A1 was also detected in PUHr cells. Elevated ALDH1A1 levels are often associated with reduced responsiveness to therapy in other malignancies [64, 65]. In contrast, resistance acquired against HSP90i TM and CA1 is primarily mediated through amplification of the *ABCB1* locus and MDR1 efflux pump overexpression [49–52].

Heat shock causes an overall reduction of RNA polymerase II (RNAPII) occupancy across several genes, whereas its occupancy increases at specific pro-survival genes to minimize cellular stress during heat shock [66]. Of these pro-survival genes, HSP70 genes are actively transcribed utilizing a transcriptional mechanism called RNAPII promoter-proximal pausing [67]. In most cases, the exposure of pan- or HSP90-NTD targeting HSP90 inhibitors induces the expression of HSR related proteins (e.g., HSP70), which eventually weakens their cytotoxic effects [2, 4, 8, 16]. Employing high throughput and combinatorial drug screenings, we observed a strong synergism between HSP90 and CDK7 inhibitors, which acts via impeding RNAPII-assisted transcription [53] of pro-survival HSR-related genes and HSP90α. Interestingly, inhibitors of RNAPII has been shown to specifically target dormant leukemia cells [68]. What's more, we observed a robust synergistic effect between PU-H71 (HSP90 inhibitor) and Mitoxantrone (TOP2 inhibitor) (TOP2i), presumably also operated by inhibition of RNAPII-assisted transcription of pro-survival HSR-related genes and HSP90α by Mitoxantrone [69]. Altogether, combining HSP90 and CDK7 targeting inhibitors can serve as a promising therapeutic combination by mitigating HSP90i-related resistance against therapy refractory leukemia.

MATERIALS AND METHODS

Cell culture

BCR-ABL1+ chronic myeloid leukemia (CML) cell lines K562, KCL22 and B-cell precursor acute lymphoblastic leukemia (BCP-ALL) cell line SUPB15 (DSMZ, Braunschweig, Germany) were cultured in RPMI1640 GlutaMAX (Gibco, Thermo Fisher Scientific, Waltham, MA, USA) supplemented with 10–15% FCS and 1% penicillin/streptomycin (Sigma-Aldrich, St. Louis, MO, USA). A regular cell line authentication by short tandem repeat (STR) profiling and mycoplasma testing was performed.

si- or shRNA-mediated knockdown (KD) and CRISPR-Cas9 mediated knockout (KO) of HSP90α/β isoforms

siRNA pools (Accell SMARTPOOL) or tetracycline (Tet)-inducible microRNA-based lentiviral shRNA vectors (Horizon Discovery, Waterbeach, UK) were used for conditional knockdown of HSP90α/β isoforms. Guide RNAs (gRNAs) targeting *HSP90AA1* (HSP90α) or *HSP90AB1* (HSP90β) were either cloned into the lentiviral expression plasmid (in case of K562) or transfected using Alt-R CRISPR-Cas9 nuclease based system in case of KCL22 and SUP-B15 cells (IDT, Coralville, IA, USA). See supplemental methods for sequences and more details.

Immunofluorescence (IF) staining

IF stainings were performed as described earlier [70]. Briefly, the Lab-Tek II chamber slides (Thermo Fisher Scientific) were coated with a 50 µg/ml solution of Poly-D-Lysine or PDL (Thermo Fisher Scientific) and incubated for 24 h at 37 °C. For permeabilization, 0.1% Triton X-100 was used, followed by blocking with 10% goat serum (Sigma-Aldrich). Primary antibodies including, anti-BCR-ABL1 (#ab187831, 1:200, Abcam), anti-HSP70 (#4872, 1:200, Cell Signaling Technology Danvers, MA, USA) or anti-total HSP90 (#sc-69703, 1:100, Santa Cruz Biotechnology, Dallas, TX, USA) were used, followed by labeling with Alexa Flour 488 or 594 conjugated secondary antibody (Thermo Fisher Scientific). Antibody stained cells were embedded in ProLong Gold Antifade Mountant (Thermo Fisher Scientific) with DAPI (hydrochloride) (StemCell Technologies, Vancouver, Canada). Confocal laser scanning microscope (Fluoview3000, Olympus) with super apochromatic UPLSAPO 60X objective (Olympus) was used for imaging (at room temperature). FV31S-SW (Ver. 2.6.1.243) viewer software, along with the Omero image server were used to process and develop confocal images. Maximum intensity projections of data were generated directly within the Omero-figure plugin. Signal quantification was performed using Fiji software. The process involved loading images, splitting composite images into individual channels, and creating a Z-projection from all slices with maximum intensity. Subsequently, the images were converted to grayscale by changing the current look-up table (LUT) to grayscale. Square regions were then placed around the cells, and the mean gray values were measured. To ensure accuracy, background values were subtracted from all measurements.

Murine xenograft transplantation

Luciferase-GFP-positive control, HSP90α- or HSP90β-KO K562 (2.5×10^6 cells) cells were transplanted via intravenous (i.v.) tail injection in 8–12-week-old female *NOD.Cg-Prkdc^{scid} Il2rg^{tm1Wjl}/SzJ* (NSG) mice ($n = 5$ mice/group) (The Jackson Laboratory) [4]. Mice were be housed in sterile conditions using high-efficiency particulate arrestance filtered micro-isolators and fed with irradiated food and acidified water. The engraftment

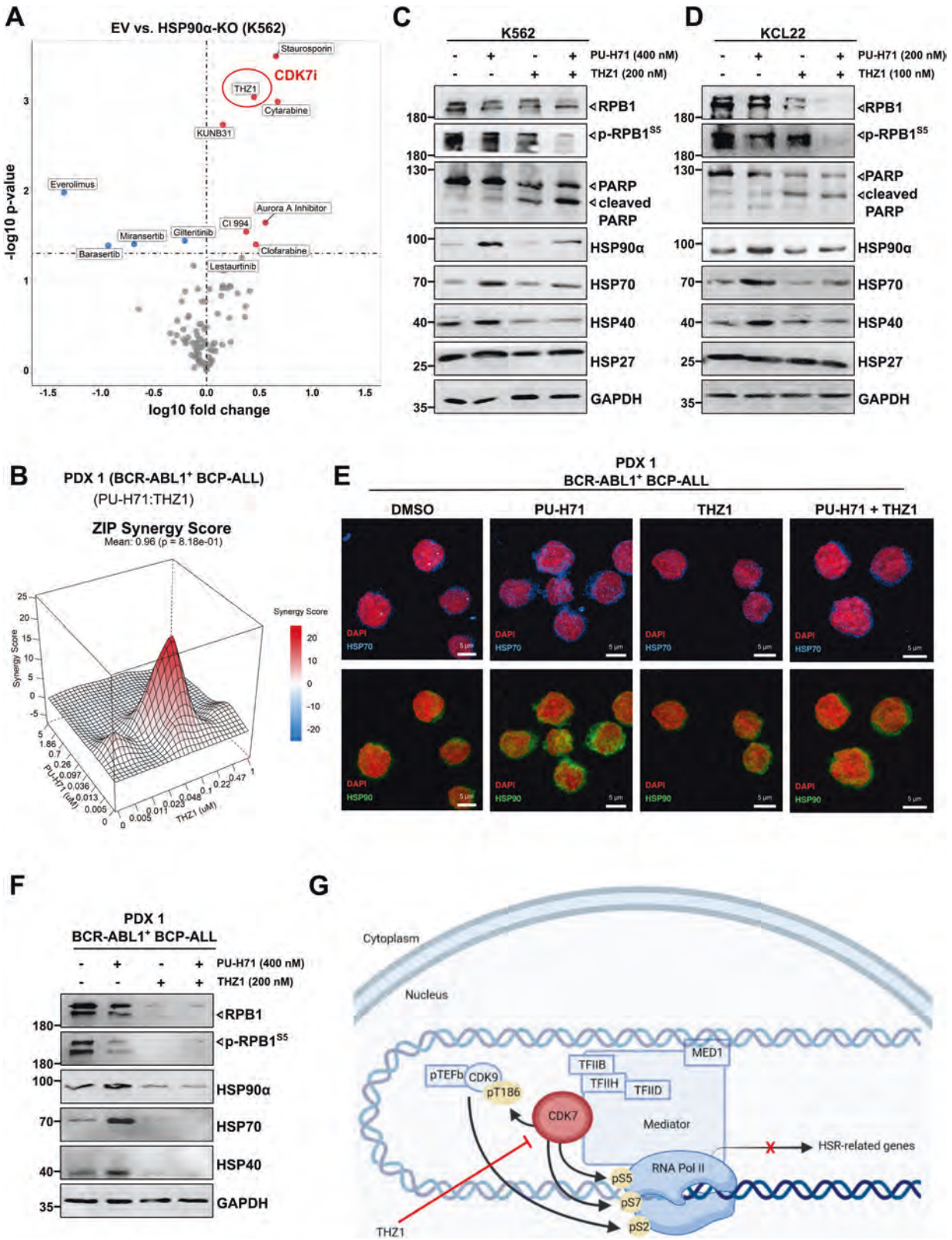

of the leukemia cells in the animals was monitored by measuring luminescence after i.p. injection of 150 µg per 100 µl D-Luciferin firefly sodium salt monohydrate (Biosynth, Staad, Switzerland), using the Caliper IVIS Lumina II Multispectral Imaging System and the Living Image Software (Perkin Elmer, Waltham, MA, USA). No blinding or randomization was performed.

In house BCR-ABL1 + BCP-ALL cells derived from the peripheral blood (PB) or bone marrow (BM) of three relapsed (TKI-resistant) patients after obtaining informed consent in accordance with the Declaration of Helsinki. The experiments were approved by the ethics committee of the medical faculty of the Heinrich Heine University (Study Nr.: 2019-566). Patient samples were transplanted intravenously in 8–12-week-old female NSG

Fig. 6 Combinatorial targeting of CDK7 and HSP90α acts synergistically against BCR-ABL1+ leukemia cells *via* blocking heat shock response induction. A Comparative cell viability was measured by luminescent-based ATP-Glo assay after screening HSP90α-KO K562 cells on an ex vivo high throughput drug screening platform, including 93 inhibitors. Average IC_{50} values from three independent replicates are depicted in the volcano plots compared to the empty vector (EV) control. Significance was calculated using unpaired t-test. **B** Synergy map of PU-H71 and THZ1 (CDK7i) combination matrix in a BCR-ABL1 + BCP-ALL PDX sample was generated using Zero Interaction Potency (ZIP) method. Visualization was performed using SynergyFinder package. The experiments were reproduced three times and representative synergy map is shown. WB analysis of K562 (**C**) and KCL22 (**D**) cells following (24 h) treatment with PU-H71, THZ1 alone, or in combination (at depicted concentrations). GAPDH served as a loading control. **E** Immunofluorescence imaging also confirmed a reduction in the HSP90 and HSP70 levels (in PDX1 cells) upon treatment with a combination of PU-H71 (200 nM) and THZ1 (100 nM), in contrast to the effects of PU-H71 (200 nM) treatment alone. **F** WB analysis of BCR-ABL1 + BCP-ALL PDX cells after treatment with PU-H71 and THZ1 alone or in combination (at depicted concentrations). GAPDH was used as a loading control. **G** Schematic depiction of CDK7 inhibition *via* THZ1 on the expression of HSR-related genes.

mice. The transplanted (≥90% human) leukemia cells obtained from BM and spleen of the mice were used to perform short-term ex vivo drug sensitivity assay. All animal experiments were conducted in accordance with the regulatory guidelines of the official committee at LANUV (Akt. 81-02.04.2017.A441), under the authorization of the animal research institute (ZETT) at the Heinrich Heine University Düsseldorf.

RNA-sequencing (RNA-seq)

RNA-seq was performed as described previously [71]. Briefly, RNA was isolated utilizing the Maxwell® RSC simplyRNA cells kit (Promega, Madison, WI, USA, #AS1390). Library preparation was carried out following supplier's guidelines, using the VAHTs Stranded mRNA-Seq Library Prep Kit (Illumina, San Diego, CA, USA). Total RNA (500 ng) was used for capturing of mRNA, fragmentation, cDNA synthesis, ligation of the adapters and library amplification. Purified libraries were normalized and sequenced on the NextSeq550 (Illumina) with 1 × 76 bp read setup. Followed by using bcl2fastq2 tool to convert the bcl files to fastq files.The raw sequencing data was uploaded to galaxy and an initial quality control was performed by FastQC and aggregated via MultiQC. After cutting the adapters with FASTQ Trimmer, the reads were aligned to the reference genome GRCh38 with RNA STAR. FastQC determined that at least 85% of all reads were uniquely mapped. In order to quantify the gene expression featureCounts was used, followed by edgeR to normalize the data to the sequencing depth. Differentially expressed genes were determined by an absolute log2 fold change of $>1/<-1$ and a FDR < 0.05. Differentially expressed genes with a low log2CPM (normalized log2CPM < −1) were treated preferentially.

Mass spectrometry (MS) based proteome and secretome analysis

Quantitative MS based proteome analysis was essentially performed as described previously [70]. For secretome analysis, K562 cells (EV, HSP90α-KO (C1), or HSP90β-KO (C1); five biological replicates) were washed three times with PBS and FCS-free medium. Later the cells were incubated for 24 h in FCS-free medium at a density of 1 million cells/mL. The conditioned medium was collected by centrifugation (5 min, 800 × *g*, 4 °C) and filtering through a 0.2 µm membrane (Acrodisc 32 mm Syringe Filter with 0.2 µm Supor Membrane; Pall, #4652). Aliquots were shock frozen in liquid nitrogen and stored at −80 °C. See supplemental methods for more details.

Gene set enrichment analysis (GSEA)

Volcano plots were generated with ggplot2. GSEA was performed with the fGSEA package and all nine major gene set collections of the molecular signature database. The gene ontology GSEA and the enrichment maps were generated by clusterProfiler.

Cell cycle

Nicoletti method (with Propidium Iodide staining) was used to measure the cell cycle of HSP90α/β-KO K562 cells. To this end, cells (500,000 cells/mL) were seeded onto a 6-well plate and treated with Vorinostat (3 µM) or DMSO. Cells were incubated for 48 h, counted and centrifuged. The pellet was resolved in Nicoletti buffer and cells were transferred to a 96-well plate, incubated for 15 min at room temperature and the DNA content was measure *via* flow cytometry.

Colony forming unit (CFU) assay

HSP90α/β-KO cells (K562 or KCL22) were seeded (50 cells/mL) in methylcellulose based medium (#H4100, STEMCELL Technologies). After 8 days, the colonies ($n = 5$) were counted and pictures were taken, as described previously [4].

Caspase 3/7 Glo assay

To measure the Caspase 3/7 activity, the luminescent Caspase-Glo® assay system (Promega, #G8090) was used. Peripheral blood derived mononuclear cells (PBMCs) (100.000 cells/mL) were seeded into a white 96-well plate and treated with PU-H71, THZ1 and with both inhibitors together with the indicated concentrations. Cells were incubated for 24 h and diluted with Caspase-Glo® 3/7 Reagent 1:1 (Caspase-Glo® 3/7 Substrate + Caspase-Glo® buffer was previously mixed according to manufacturer's instructions). The plate was incubated for 30 min at room temperature and luminescence was measured with the Tecan Spark.

Generation of HSP90 inhibitor-resistant cells

K562 cells were long-term treated with half of the IC_{50} concentration of PU-H71, Coumermycin A1 (CA1) and Tanespimycin (TM). The clonal evolution was reiterated with 10% increased inhibitor concentration over the course of 12–14 months (Fig. 4A). The individual resistant clones were picked using methylcellulose based medium (#H4100, STEMCELL Technologies). To account for the effect of long-term culture and solvent (DMSO) exposure, parental (P) clone was also treated with same concentration of DMSO and grown in parallel.

Single nucleotide polymorphism (SNP) array

Copy number analyses were performed using DNA from PUHr and CA1r cells using the CytoSNP-12 v2.1 array (Illumina) encompassing 299,140 SNP markers and were compared to the parental (P) K562 cells. Beeline 2.0.3.3 software was used to convert idat to gct files. Data were processed and analyzed using the BlueFuse Multi 4.5 software from Illumina. Partek Flow was used to identify chromosomal imbalances in resistant cells compared to parental cells. The human reference genome was GRCh38/hg38.

Whole exome sequencing (WES)

WES of PUHr and CA1r cells along with parental K562 cells was carried out as described before [72], with some modifications. Next-generation WES was performed using the Sure Select Human All Exon V7 kit (Agilent, Santa Clara, CA, USA). The library was paired-end sequenced on an Illumina NextSeq550 (2 × 150 bp) sequencer to yield an average on-target coverage of a minimum 100x. Sanger sequencing was performed to validate the herein-reported variants. See supplemental methods for more details.

Molecular dynamics (MD) simulation

The protein structure of human HSP90α bound to PU-H71 (2FWZ) was obtained from Protein Data Bank (PDB ID: 2fwz) [73, 74]. Missing atoms were added using the 'build' function in the PyMOL Molecular Graphics System (Version 2.1.0: Schrödinger, LLC) [75]. To generate the variant structure, the S164F substitution was introduced with the mutagenesis wizard in PyMOL, selecting the highest probability rotamer. See supplemental methods for more details.

Western blotting (WB)

Conventional WB and capillary based immunoassay (JESS, Bio-Techne, Minneaspolis, MN, USA) was performed as previously described [4, 70]. Refer supplemental methods for more details, including list of the

antibodies and their concentrations used in conventional WB or during JESS. See supplementary material for uncropped western blot images.

Ex vivo high throughput drug screening (HTDS)

A library containing 93 compounds was created for ex vivo HTDS of leukemic cell lines and patient samples [76]. DMSO dissolved compound library was purchased from Selleck Chemicals and MedChem Express. The compound selection involved the majority of FDA/EMA-approved routinely used chemotherapeutics and targeted drugs involved in the leukemia treatment protocols and inhibitors in the early to late clinical trial phase (see Supplemental Table S2 for the detailed list of drugs). Briefly, the DMSO dissolved compound library was dispensed with increasing concentrations of the inhibitors in 6 dilution steps (0.008–25 µM) on a white 384-well plate (Corning, New York, USA) using digital dispenser (D300e, Tecan, Maennedorf, Switzerland), ensuring precise and robotic compound application in randomized fashion. The cells (≥90% viability) were seeded on the thawed pre-dispensed inhibitor plates using an automated Multidrop Combi Reagent Dispenser (Thermo Fisher Scientific). Differential responses were monitored with ATP-dependent CellTiter-Glo Luminescent viability assay (Promega) after 72 h of inhibitor exposure using a microplate reader Spark 10 M (Tecan). Dose–response curves for the inhibitors were determined by plotting raw data (normalized to controls) with non-linear regression (log(inhibitor) vs. normalized response) variable slope function ($n = 3$ replicates). For combinatorial drug screening, respective inhibitors were printed on white 384-well plates with increasing concentrations in dose–response 8×8 matrices. The synergy score calculations were based on the ZIP reference model [77].

Replicates and statistical analysis

The experiments were reproduced a minimum of three times and representative data are shown. Error bar represent standard deviation (SD). Statistical analyses were conducted using Prism v8.0.2 (GraphPad Software, La Jolla, CA, USA) or using R. Statistical significance was considered for p values < 0.05 (*$p < 0.05$), < 0.01 (**$p < 0.01$), and <0.001 (***$p < 0.001$).

DATA AVAILABILITY

RNA-seq data have been deposited in the NCBI GEO database with the accession ID: GSE208005. The mass spectrometry based proteomics or secretomics raw and expression data have been deposited to the ProteomeXchange Consortium via the PRIDE [78] partner repository with the dataset identifier PXD041871. SNP array and WES data have been deposited in the EGA database with accession ID EGAS00001006385 and EGAS00001006381, respectively.

REFERENCES

1. Calderwood SK, Gong J. Heat shock proteins promote cancer: it's a protection racket. Trends Biochem Sci. 2016;41:311–23.
2. Butler LM, Ferraldeschi R, Armstrong HK, Centenera MM, Workman P. Maximizing the therapeutic potential of HSP90 inhibitors. Mol Cancer Res. 2015;13:1445–51.
3. Schopf FH, Biebl MM, Buchner J. The HSP90 chaperone machinery. Nat Rev Mol Cell Biol. 2017;18:345–60.
4. Bhatia S, Diedrich D, Frieg B, Ahlert H, Stein S, Bopp B, et al. Targeting HSP90 dimerization via the C terminus is effective in imatinib-resistant CML and lacks the heat shock response. Blood. 2018;132:307–20.
5. Peng Y, Huang Z, Zhou F, Wang T, Mou K, Feng W. Effect of HSP90AB1 and CC domain interaction on Bcr-Abl protein cytoplasm localization and function in chronic myeloid leukemia cells. Cell Commun Signal. 2021;19:71.
6. Zhang P, Qin M, Wang Y, Chen X, Miao Y, Yuan M, et al. Inflammation accelerates BCR-ABL1+ B-ALL development through upregulation of AID. Blood Adv. 2022;6:4060–72.
7. Peng C, Brain J, Hu Y, Goodrich A, Kong L, Grayzel D, et al. Inhibition of heat shock protein 90 prolongs survival of mice with BCR-ABL-T315I-induced leukemia and suppresses leukemic stem cells. Blood. 2007;110:678–85.
8. Bhatia S, Spanier L, Bickel D, Dienstbier N, Woloschin V, Vogt M, et al. Development of a first-in-class small-molecule inhibitor of the C-terminal Hsp90 dimerization. ACS Central Sci. 2022;8:636–55.
9. Zeng D, Gao M, Zheng R, Qin R, He W, Liu S, et al. The HSP90 inhibitor KW-2478 depletes the malignancy of BCR/ABL and overcomes the imatinib-resistance caused by BCR/ABL amplification. Exp Hematol Oncol. 2022;11:33.
10. Mahalingam D, Swords R, Carew JS, Nawrocki ST, Bhalla K, Giles FJ. Targeting HSP90 for cancer therapy. Br J Cancer. 2009;100:1523–9.
11. Reikvam H, Hatfield KJ, Ersvaer E, Hovland R, Skavland J, Gjertsen BT, et al. Expression profile of heat shock proteins in acute myeloid leukaemia patients reveals a distinct signature strongly associated with FLT3 mutation status-consequences and potentials for pharmacological intervention. Brit J Haematol. 2012;156:468–80.
12. Flandrin P, Guyotat D, Duval A, Cornillon J, Tavernier E, Nadal N, et al. Significance of heat-shock protein (HSP) 90 expression in acute myeloid leukemia cells. Cell Stress Chaperones. 2008;13:357–64.
13. Zong H, Gozman A, Caldas-Lopes E, Taldone T, Sturgill E, Brennan S, et al. A hyperactive signalosome in acute myeloid leukemia drives addiction to a tumor-specific Hsp90 species. Cell Rep. 2015;13:2159–73.
14. Kucine N, Marubayashi S, Bhagwat N, Papalexi E, Koppikar P, Sanchez Martin M, et al. Tumor-specific HSP90 inhibition as a therapeutic approach in JAK-mutant acute lymphoblastic leukemias. Blood. 2015;126:2479–83.
15. Wells J, Jain N, Konopleva M. Philadelphia chromosome-like acute lymphoblastic leukemia: progress in a new cancer subtype. Clin Adv Hematol Oncol. 2017;15:554–61.
16. Sanchez J, Carter TR, Cohen MS, Blagg BSJ. Old and new approaches to target the Hsp90 chaperone. Curr Cancer Drug Targets. 2020;20:253–70.
17. Koren J 3rd, Blagg BSJ. The right tool for the job: an overview of Hsp90 inhibitors. Adv Exp Med Biol. 2020;1243:135–46.
18. Pillarsetty N, Jhaveri K, Taldone T, Caldas-Lopes E, Punzalan B, Joshi S, et al. Paradigms for precision medicine in epichaperome cancer therapy. Cancer Cell. 2019;36:559–73.e7.
19. Wang Y, McAlpine SR. N-terminal and C-terminal modulation of Hsp90 produce dissimilar phenotypes. Chem Commun. 2015;51:1410–3.
20. Sreedhar AS, Kalmar E, Csermely P, Shen YF. Hsp90 isoforms: functions, expression and clinical importance. FEBS Lett. 2004;562:11–5.
21. Tang X, Chang C, Mosallaei D, Woodley DT, Schonthal AH, Chen M, et al. Heterogeneous responses and isoform compensation the dim therapeutic window of Hsp90 ATP-binding inhibitors in cancer. Mol Cell Biol. 2022;42:e0045921.
22. Taherian A, Krone PH, Ovsenek N. A comparison of Hsp90alpha and Hsp90beta interactions with cochaperones and substrates. Biochem Cell Biol. 2008;86:37–45.
23. Sanchez ER. Chaperoning steroidal physiology: lessons from mouse genetic models of Hsp90 and its cochaperones. Biochim Biophys Acta. 2012;1823:722–9.
24. Hoter A, El-Sabban ME, Naim HY. The HSP90 family: structure, regulation, function, and implications in health and disease. Int J Mol Sci. 2018;19:2560.
25. Tang X, Chang C, Hao M, Chen M, Woodley DT, Schonthal AH, et al. Heat shock protein-90alpha (Hsp90alpha) stabilizes hypoxia-inducible factor-1alpha (HIF-1alpha) in support of spermatogenesis and tumorigenesis. Cancer Gene Ther. 2021;28:1058–70.
26. Voss AK, Thomas T, Gruss P. Mice lacking HSP90beta fail to develop a placental labyrinth. Development. 2000;127:1–11.
27. Khandelwal A, Kent CN, Balch M, Peng S, Mishra SJ, Deng J, et al. Structure-guided design of an Hsp90beta N-terminal isoform-selective inhibitor. Nat Commun. 2018;9:425.
28. Mishra SJ, Khandelwal A, Banerjee M, Balch M, Peng S, Davis RE, et al. Selective inhibition of the Hsp90alpha isoform. Angew Chem Int Ed Engl. 2021;60:10547–51.
29. Didelot C, Lanneau D, Brunet M, Bouchot A, Cartier J, Jacquel A, et al. Interaction of heat-shock protein 90 beta isoform (HSP90 beta) with cellular inhibitor of apoptosis 1 (c-IAP1) is required for cell differentiation. Cell Death Differ. 2008;15:859–66.
30. Peterson LB, Eskew JD, Vielhauer GA, Blagg BS. The hERG channel is dependent upon the Hsp90alpha isoform for maturation and trafficking. Mol Pharm. 2012;9:1841–6.
31. Basso AD, Solit DB, Chiosis G, Giri B, Tsichlis P, Rosen N. Akt forms an intracellular complex with heat shock protein 90 (Hsp90) and Cdc37 and is destabilized by inhibitors of Hsp90 function. J Biol Chem. 2002;277:39858–66.
32. Li L, Lou Z, Wang L. The role of FKBP5 in cancer aetiology and chemoresistance. Br J Cancer. 2011;104:19–23.
33. Eustace BK, Sakurai T, Stewart JK, Yimlamai D, Unger C, Zehetmeier C, et al. Functional proteomic screens reveal an essential extracellular role for hsp90α in cancer cell invasiveness. Nat Cell Biol. 2004;6:507–14.
34. Stellas D, El Hamidieh A, Patsavoudi E. Monoclonal antibody 4C5 prevents activation of MMP2 and MMP9 by disrupting their interaction with extracellular HSP90 and inhibits formation of metastatic breast cancer cell deposits. BMC Cell Biol. 2010;11:51.
35. Tsutsumi S, Scroggins B, Koga F, Lee MJ, Trepel J, Felts S, et al. A small molecule cell-impermeant Hsp90 antagonist inhibits tumor cell motility and invasion. Oncogene. 2008;27:2478–87.
36. Zou M, Bhatia A, Dong H, Jayaprakash P, Guo J, Sahu D, et al. Evolutionarily conserved dual lysine motif determines the non-chaperone function of secreted Hsp90alpha in tumour progression. Oncogene. 2017;36:2160–71.

37. Wang X, Song X, Zhuo W, Fu Y, Shi H, Liang Y, et al. The regulatory mechanism of Hsp90alpha secretion and its function in tumor malignancy. Proc Natl Acad Sci USA. 2009;106:21288–93.
38. Jhaveri K, Ochiana SO, Dunphy MP, Gerecitano JF, Corben AD, Peter RI, et al. Heat shock protein 90 inhibitors in the treatment of cancer: current status and future directions. Expert Opin Investig Drugs. 2014;23:611–28.
39. Zhou D, Liu Y, Ye J, Ying W, Ogawa LS, Inoue T, et al. A rat retinal damage model predicts for potential clinical visual disturbances induced by Hsp90 inhibitors. Toxicol Appl Pharmacol. 2013;273:401–9.
40. Calvo-Vidal MN, Zamponi N, Krumsiek J, Stockslager MA, Revuelta MV, Phillip JM, et al. Oncogenic HSP90 facilitates metabolic alterations in aggressive B-cell lymphomas. Cancer Res. 2021;81:5202–16.
41. Barker CR, Hamlett J, Pennington SR, Burrows F, Lundgren K, Lough R, et al. The topoisomerase II-Hsp90 complex: a new chemotherapeutic target? Int J Cancer. 2006;118:2685–93.
42. Barker CR, McNamara AV, Rackstraw SA, Nelson DE, White MR, Watson AJ, et al. Inhibition of Hsp90 acts synergistically with topoisomerase II poisons to increase the apoptotic killing of cells due to an increase in topoisomerase II mediated DNA damage. Nucleic Acids Res. 2006;34:1148–57.
43. Saunders AE, Johnson P. Modulation of immune cell signalling by the leukocyte common tyrosine phosphatase, CD45. Cell Signal. 2010;22:339–48.
44. Cario G, Rhein P, Mitlohner R, Zimmermann M, Bandapalli OR, Romey R, et al. High CD45 surface expression determines relapse risk in children with precursor B-cell and T-cell acute lymphoblastic leukemia treated according to the ALL-BFM 2000 protocol. Haematologica. 2014;99:103–10.
45. Lin H, Kolosenko I, Bjorklund AC, Protsyuk D, Osterborg A, Grander D, et al. An activated JAK/STAT3 pathway and CD45 expression are associated with sensitivity to Hsp90 inhibitors in multiple myeloma. Exp Cell Res. 2013;319:600–11.
46. Chatterjee S, Burns TF. Targeting heat shock proteins in cancer: a promising therapeutic approach. Int J Mol Sci. 2017;18:1978.
47. Koga F, Xu W, Karpova TS, McNally JG, Baron R, Neckers L. Hsp90 inhibition transiently activates Src kinase and promotes Src-dependent Akt and Erk activation. Proc Natl Acad Sci USA. 2006;103:11318–22.
48. Mshaik R, Simonet J, Georgievski A, Jamal L, Bechoua S, Ballerini P, et al. HSP90 inhibitor NVP-BEP800 affects stability of SRC kinases and growth of T-cell and B-cell acute lymphoblastic leukemias. Blood Cancer J. 2021;11:61.
49. Agrawal M, Hanfstein B, Erben P, Wolf D, Ernst T, Fabarius A, et al. MDR1 expression predicts outcome of Ph+ chronic phase CML patients on second-line nilotinib therapy after imatinib failure. Leukemia. 2014;28:1478–85.
50. Triller N, Korosec P, Kern I, Kosnik M, Debeljak A. Multidrug resistance in small cell lung cancer: expression of P-glycoprotein, multidrug resistance protein 1 and lung resistance protein in chemo-naive patients and in relapsed disease. Lung Cancer. 2006;54:235–40.
51. Rouhi A, Miller C, Grasedieck S, Reinhart S, Stolze B, Dohner H, et al. Prospective identification of resistance mechanisms to HSP90 inhibition in KRAS mutant cancer cells. Oncotarget. 2017;8:7678–90.
52. Yin L, Yang Y, Zhu W, Xian Y, Han Z, Huang H, et al. Heat shock protein 90 triggers multi-drug resistance of ovarian cancer via AKT/GSK3beta/beta-catenin signaling. Front Oncol. 2021;11:620907.
53. Nilson KA, Guo J, Turek ME, Brogie JE, Delaney E, Luse DS, et al. THZ1 reveals roles for Cdk7 in co-transcriptional capping and pausing. Mol Cell. 2015;59:576–87.
54. Braun TP, Eide CA, Druker BJ. Response and resistance to BCR-ABL1-targeted therapies. Cancer cell. 2020;37:530–42.
55. Talpaz M, Shah NP, Kantarjian H, Donato N, Nicoll J, Paquette R, et al. Dasatinib in imatinib-resistant Philadelphia chromosome-positive leukemias. N Engl J Med. 2006;354:2531–41.
56. Gu Z, Churchman ML, Roberts KG, Moore I, Zhou X, Nakitandwe J, et al. PAX5-driven subtypes of B-progenitor acute lymphoblastic leukemia. Nat Genet. 2019;51:296–307.
57. Bhatia R. Targeting leukemia stem cell resistance in chronic myelogenous leukemia. Trans Am Clin Climatol Assoc. 2019;130:246–54.
58. Wang Y, McAlpine SR. Heat-shock protein 90 inhibitors: will they ever succeed as chemotherapeutics? Future Med Chem. 2015;7:87–90.
59. Prodromou C. Mechanisms of Hsp90 regulation. Biochem J. 2016;473:2439–52.
60. Drube J, Ernst T, Pfirrmann M, Albert BV, Drube S, Reich D, et al. PTPRG and PTPRC modulate nilotinib response in chronic myeloid leukemia cells. Oncotarget. 2018;9:9442–55.
61. Tian WL, He F, Fu X, Lin JT, Tang P, Huang YM, et al. High expression of heat shock protein 90 alpha and its significance in human acute leukemia cells. Gene. 2014;542:122–8.
62. Sedlackova L, Spacek M, Holler E, Imryskova Z, Hromadnikova I. Heat-shock protein expression in leukemia. Tumour Biol. 2011;32:33–44.
63. Yufu Y, Nishimura J, Nawata H. High constitutive expression of heat shock protein 90 alpha in human acute leukemia cells. Leuk Res. 1992;16:597–605.
64. Lei HM, Zhang KR, Wang CH, Wang Y, Zhuang GL, Lu LM, et al. Aldehyde dehydrogenase 1A1 confers erlotinib resistance via facilitating the reactive oxygen species-reactive carbonyl species metabolic pathway in lung adenocarcinomas. Theranostics. 2019;9:7122–39.
65. Uddin MH, Kim B, Cho U, Azmi AS, Song YS. Association of ALDH1A1-NEK-2 axis in cisplatin resistance in ovarian cancer cells. Heliyon. 2020;6:e05442.
66. Cardiello JF, Goodrich JA, Kugel JF. Heat shock causes a reversible increase in RNA polymerase II occupancy downstream of mRNA genes, consistent with a global loss in transcriptional termination. Mol Cell Biol. 2018;38:e00181–18.
67. Bunch H. RNA polymerase II pausing and transcriptional regulation of the HSP70 expression. Eur J Cell Biol. 2017;96:739–45.
68. Pallis M, Burrows F, Whittall A, Boddy N, Seedhouse C, Russell N. Efficacy of RNA polymerase II inhibitors in targeting dormant leukaemia cells. BMC Pharmacol Toxicol. 2013;14:32.
69. Chegini N, Safa AR, Tseng MT. Acute effects of mitoxantrone on the template activity of isolated nuclei from the T-47D human breast tumor cell line. Cancer Lett. 1984;21:329–36.
70. Sinatra L, Yang J, Schliehe-Diecks J, Dienstbier N, Vogt M, Gebing P, et al. Solid-phase synthesis of cereblon-recruiting selective histone deacetylase 6 degraders (HDAC6 PROTACs) with antileukemic activity. J Med Chem. 2022;65:16860–78.
71. Garcia-Ramirez I, Bhatia S, Rodriguez-Hernandez G, Gonzalez-Herrero I, Walter C, Gonzalez de Tena-Davila S, et al. Lmo2 expression defines tumor cell identity during T-cell leukemogenesis. EMBO J. 2018;37:e98783.
72. Gorre ME, Ellwood-Yen K, Chiosis G, Rosen N, Sawyers CL. BCR-ABL point mutants isolated from patients with imatinib mesylate-resistant chronic myeloid leukemia remain sensitive to inhibitors of the BCR-ABL chaperone heat shock protein 90. Blood. 2002;100:3041–4.
73. Immormino RM, Kang Y, Chiosis G, Gewirth DT. Structural and quantum chemical studies of 8-aryl-sulfanyl adenine class Hsp90 inhibitors. J Med Chem. 2006;49:4953–60.
74. Berman HM, Westbrook J, Feng Z, Gilliland G, Bhat TN, Weissig H, et al. The protein data bank. Nucleic Acids Res. 2000;28:235–42.
75. Janson G, Zhang C, Prado MG, Paiardini A. PyMod 2.0: improvements in protein sequence-structure analysis and homology modeling within PyMOL. Bioinformatics. 2017;33:444–6.
76. Flumann R, Rehkamper T, Nieper P, Pfeiffer P, Holzem A, Klein S, et al. An autochthonous mouse model of Myd88- and BCL2-driven diffuse large B-cell lymphoma reveals actionable molecular vulnerabilities. Blood Cancer Discov. 2021;2:70–91.
77. Ianevski A, He L, Aittokallio T, Tang J. SynergyFinder: a web application for analyzing drug combination dose-response matrix data. Bioinformatics. 2020;36:2645.
78. Perez-Riverol Y, Bai J, Bandla C, Garcia-Seisdedos D, Hewapathirana S, Kamatchinathan S, et al. The PRIDE database resources in 2022: a hub for mass spectrometry-based proteomics evidences. Nucleic Acids Res. 2022;50:D543–D52.
79. Ianevski A, He L, Aittokallio T, Tang J. SynergyFinder: a web application for analyzing drug combination dose-response matrix data. Bioinformatics. 2017;33:2413–5.

ACKNOWLEDGEMENTS

AB acknowledges the support from Katharina-Hardt Foundation, Christiane und Claudia Hempel-foundation and especially Löwenstern e.V. for funding the Simple Western system (JESS). JH is supported by ERC Stg 852222 "PreventALL". The computational resources and services used in this work were provided by the VSC (Flemish Supercomputer Center), funded by the Research Foundation - Flanders (FWO) and the Flemish Government. AI and MK are funded by Motor Neurone Disease Association and Spastic Paraplegia Foundation. We acknowledge the use of the research computing facility at King's College London, Rosalind (https://rosalind.kcl.ac.uk), which is delivered in partnership with the National Institute for Health Research (NIHR) Biomedical Research Centres at South London & Maudsley and Guy's & St. Thomas' NHS Foundation Trusts and part-funded by capital equipment grants from the Maudsley Charity (award 980) and Guy's and St Thomas' Charity (TR130505).

AUTHOR CONTRIBUTIONS

SB, ND, and MV performed study concept and design. MV, ND, JS-D, KS, JT, PG, RW, JHO, SF, DP, MR, LY, DB, MK, AI, TL, and KS performed development of methodology and investigation, analysis and interpretation of data. ND, MV, RW, TL, AP, JH, UF, AB, and SB performed writing, reviewing and editing of the paper. SB supervised the study. All authors discussed the results and commented on the manuscript.

FUNDING

SB acknowledges the financial support by Düsseldorf School of Oncology-Netzwerkverbundes (DSO) and Forschungskommission (2021-19) HHU Düsseldorf.

This study is funded in part by the Elterninitiative Kinderkrebsklinik e.V. and the Deutsche Forschungsgemeinschaft (DFG, German Research Foundation) – 270650915 (Research Training Group GRK2158, TP2d) and BH 162/4-1 (528968169) to SB. RW and SB additionally acknowledge the financial support from Gesellschaft für KinderKrebsForschung e.V. Open Access funding enabled and organized by Projekt DEAL.

COMPETING INTERESTS

The authors declare no competing interests.

ETHICS APPROVAL

All animal experiments were conducted in accordance with the regulatory guidelines of the official committee at LANUV (Akt. 81-02.04.2017.A441), under the authorization of the animal research institute (ZETT) at the Heinrich Heine University Düsseldorf. In house leukemia cells derived from the peripheral blood (PB) or bone marrow (BM) of three relapsed (TKI-resistant) patients after obtaining informed consent in accordance with the Declaration of Helsinki. The experiments were approved by the ethics committee of the medical faculty of the Heinrich Heine University (Study Nr.: 2019-566).

ADDITIONAL INFORMATION

Supplementary information The online version contains supplementary material available at https://doi.org/10.1038/s41419-023-06337-3.

Correspondence and requests for materials should be addressed to Sanil Bhatia.

Journal of Medicinal Chemistry

Article

Cite This: J. Med. Chem. XXXX, XXX, XXX−XXX

pubs.acs.org/jmc

Discovery of the First-in-Class Dual Histone Deacetylase−Proteasome Inhibitor

Sanil Bhatia,[†] Viktoria Krieger,[‡] Michael Groll,[§] Jeremy D. Osko,[∥] Nina Reßing,[⊥] Heinz Ahlert,[†] Arndt Borkhardt,[†] Thomas Kurz,[‡] David W. Christianson,[∥] Julia Hauer,[*,†] and Finn K. Hansen[*,⊥]

[†]Department of Pediatric Oncology, Hematology and Clinical Immunology, Medical Faculty, Heinrich Heine University Düsseldorf, Moorenstrasse 5, 40225 Düsseldorf, Germany

[‡]Institute for Pharmaceutical and Medicinal Chemistry, Heinrich Heine University Düsseldorf, Universitätsstrasse 1, 40225 Düsseldorf, Germany

[§]Center for Integrated Protein Science at the Department Chemie, Lehrstuhl für Biochemie, Technische Universität München, Lichtenbergstrasse 4, 85747 Garching, Germany

[∥]Roy and Diana Vagelos Laboratories, Department of Chemistry, University of Pennsylvania, 231 South 34th Street, Philadelphia, Pennsylvania 19104-6323, United States

[⊥]Pharmaceutical/Medicinal Chemistry, Institute of Pharmacy, Medical Faculty, Leipzig University, Brüderstraße 34, 04103 Leipzig, Germany

Supporting Information

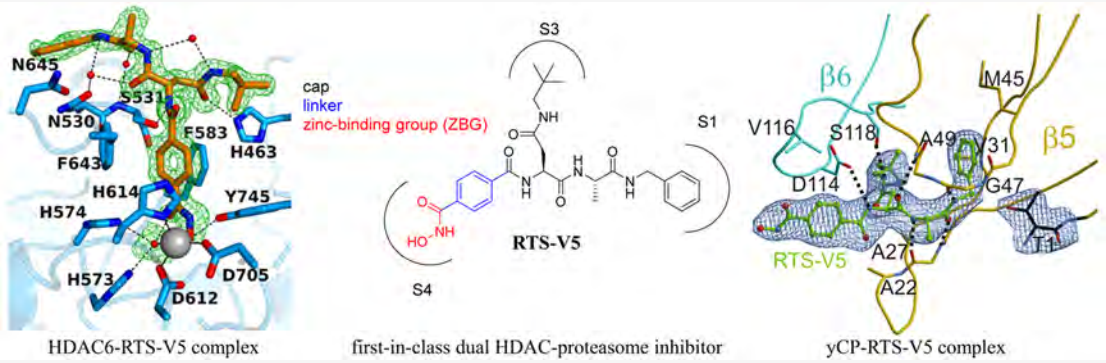

ABSTRACT: Dual- or multitarget drugs have emerged as a promising alternative to combination therapies. Proteasome inhibitors (PIs) possess synergistic activity with histone deacetylase (HDAC) inhibitors due to the simultaneous blockage of the ubiquitin degradation and aggresome pathways. Here, we present the design, synthesis, binding modes, and anticancer properties of RTS-V5 as the first-in-class dual HDAC-proteasome ligand. The inhibition of both targets was confirmed by biochemical and cellular assays as well as X-ray crystal structures of the 20S proteasome and HDAC6 complexed with RTS-V5. Cytotoxicity assays with leukemia and multiple myeloma cell lines as well as therapy refractory primary patient-derived leukemia cells demonstrated that RTS-V5 possesses potent and selective anticancer activity. Our results will thus guide the structure-based optimization of dual HDAC−proteasome inhibitors for the treatment of hematological malignancies.

■ INTRODUCTION

The approach "one drug multiple targets" or "multitarget drugs" is gaining major consideration in drug discovery and has been termed polypharmacology.[1] Despite the highly significant therapeutic relevance of combination therapies, potential advantages of a targeted therapy based on a single drug acting through two or more independent modes of action include (a) a more predictable pharmacokinetic profile, (b) increased patient compliance, and (c) the simultaneous presence of the molecule in tissues where the active principles are intended to work.[1]

Histone deacetylases (HDACs) are clinically validated cancer targets, and four inhibitors thereof (HDACi) have been approved by the FDA for cancer therapy.[2] HDACi are characterized by a cap−linker−zinc-binding group pharmacophore model (Figure 1).[3] Fortunately, the HDACi pharmacophore tolerates a variety of cap groups which allows scope for hybridization approaches.[4] Consequently, the incorporation of a second pharmacophore in the cap region has been used to engineer several HDACi-based multitarget drugs.[4] Notably, the dual kinase-HDAC inhibitors CUDC-101 and CUDC-907, the nitrogen mustard-HDACi hybrid tinostamustine, as well as the dual LSD1-HDAC inhibitor 4SC-202, are currently being

Received: September 24, 2018
Published: October 26, 2018

DOI: 10.1021/acs.jmedchem.8b01487
J. Med. Chem. XXXX, XXX, XXX−XXX

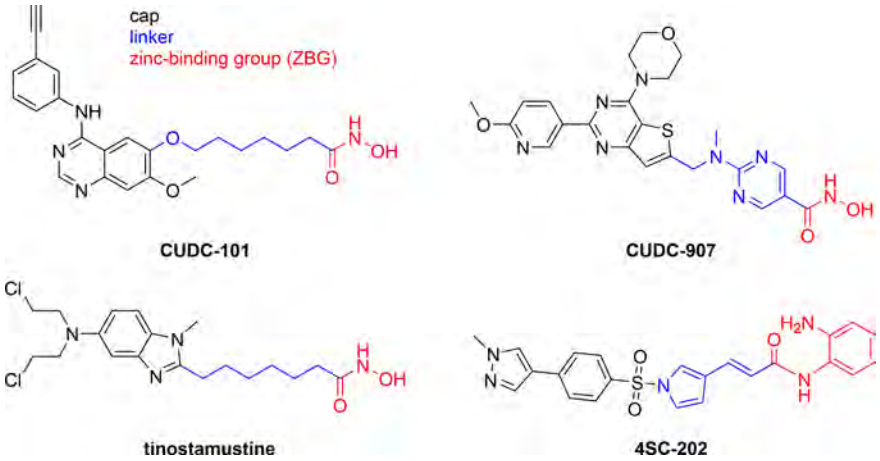

Figure 1. HDACi-based multitarget drugs in clinical trials.

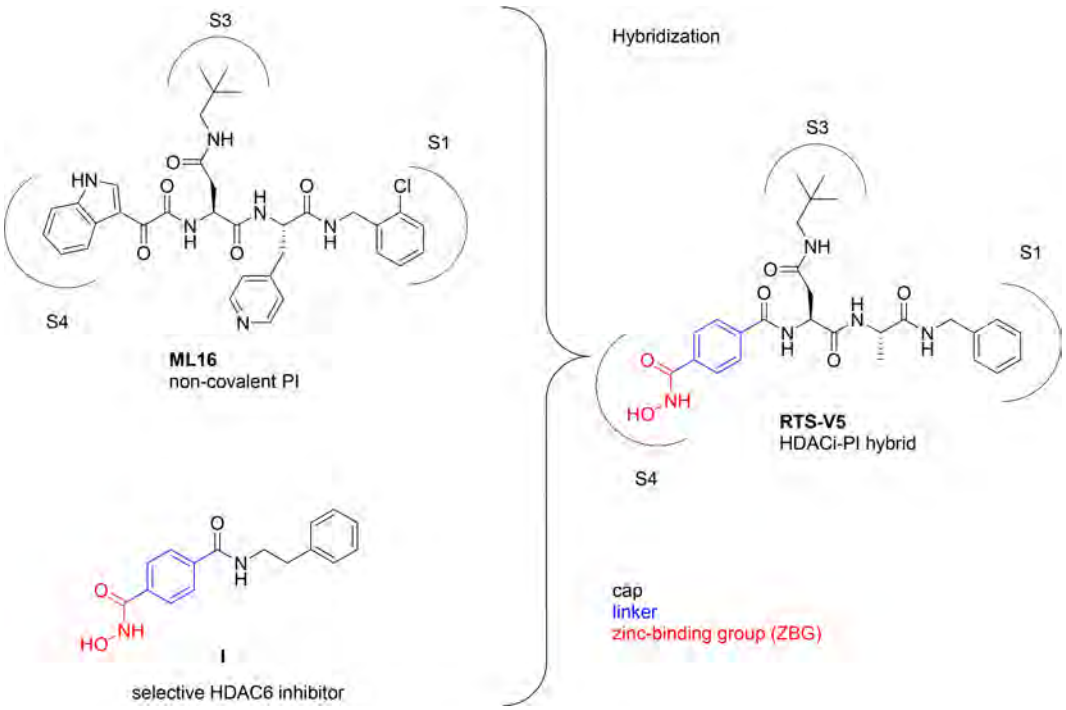

Figure 2. Design of RTS-V5 as the first-in-class dual HDAC-proteasome inhibitor.

investigated in clinical trials (Figure 1).[4,5] In regard to combination therapy, the best investigated synergism of HDACi has been identified with proteasome inhibitors (PIs), leading to dual proteasome and aggresome blockage and apoptosis induction due to the accumulation of misfolded proteins.[6] However, to the best of our knowledge, no dual HDAC-proteasome inhibitor has been reported so far.

Herein, we present the design, synthesis, biological evaluation, and binding modes of RTS-V5 as the first-in-class dual HDAC−proteasome inhibitor.

■ RESULTS

Design and Synthesis of RTS-V5. PIs can be divided into covalent and noncovalent binders.[7] We decided to focus on noncovalent scaffolds to suppress several drawbacks such as excessive reactivity, lack of specificity, and/or stability.[8] Moreover, highly reactive electrophilic warheads might cause chemical incompatibilities with the typical HDACi zinc-binding groups (ZBGs) such as hydroxamic acids, aminoanilides, or thioles. The first noncovalent PI was identified in the crystal structure of the yeast proteasome in complex with the natural product TMC-95A.[9] In the following years, binding modes of TMC-95A derivatives[10] as well as noncovalent linear peptide mimetics have been reported.[11] In particular, a promising PI turned out to be compound ML16 (Figure 2) obtained from an elaborate study published by Blackburn and colleagues.[11a] The high affinity of ML16 and several analogues is primarily achieved by a P3-neopentyl-Asn residue (Figure 2). The comparison of currently available crystal structures of the proteasome in complex with peptidic ligands[12] revealed that this bulky residue indeed represents a superb side chain to occupy the entire S3 specificity pocket of the chymotrypsin-like site of the 20S core particle. We, therefore, decided to use ML16 as a starting point for the design of dual HDAC−proteasome inhibitors. The S4 binding site does not resemble a pocket-like structure and a careful inspection of a series of X-

DOI: 10.1021/acs.jmedchem.8b01487
J. Med. Chem. XXXX, XXX, XXX−XXX

Scheme 1. Synthesis of RTS-V5[a]

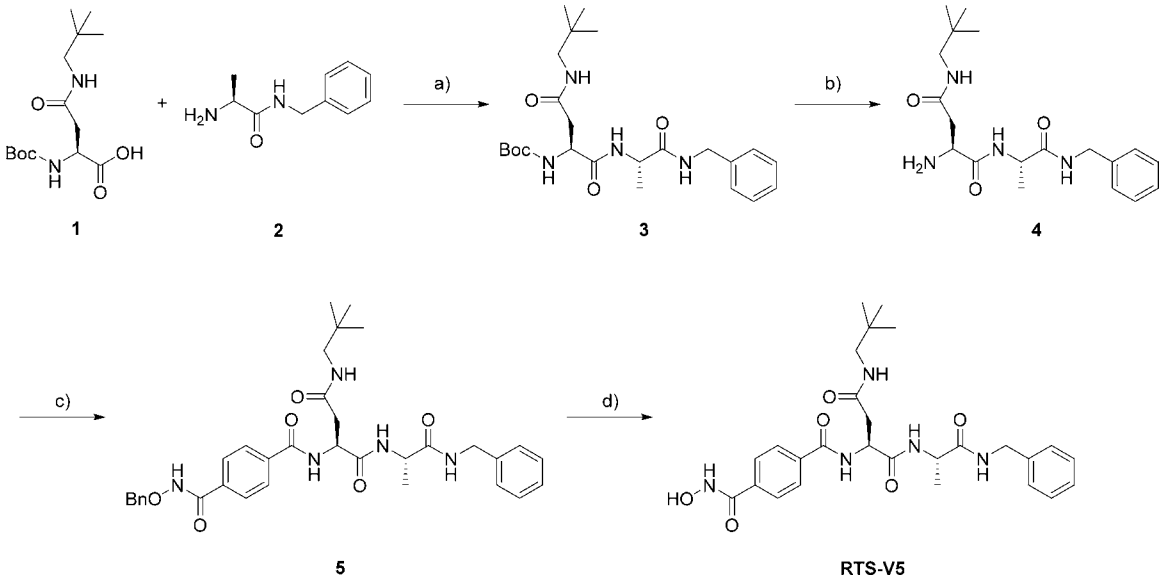

[a]Reagents and conditions: (a) HATU, DIPEA, DMF, rt, 16 h; (b) TFA, CH_2Cl_2, rt, 4 h; (c) 4-((benzyloxy)carbamoyl)benzoic acid, HATU, DIPEA, DMF, rt, 24 h; (d) Pd/C, H_2, rt, 4 h.

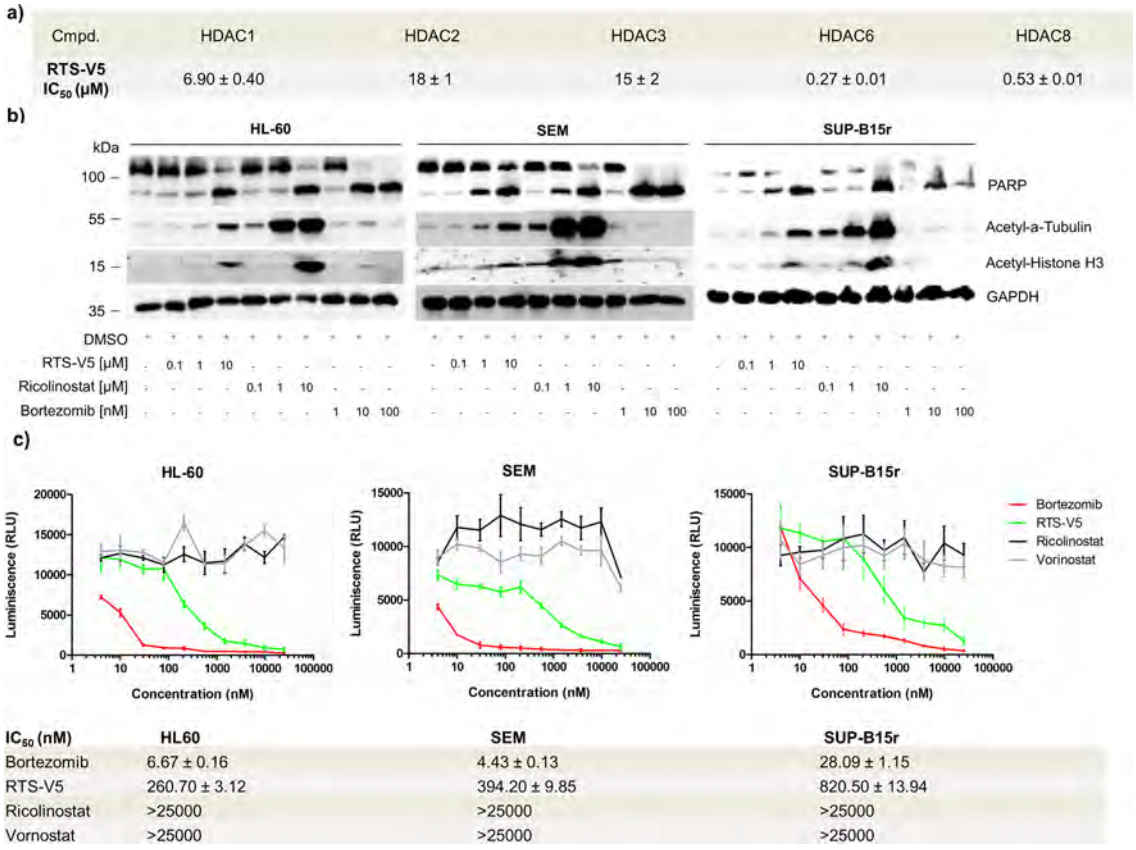

Figure 3. Functional specificity of RTS-V5 against HDAC6 and the proteasome. (A) Inhibitory activities of compounds RTS-V5 against HDAC isoforms 1, 2, 3, 6, and 8. (B) HL-60, SEM, and SUP-B15r cells were exposed to bortezomib, vorinostat, ricolinostat, and RTS-V5 at the indicated concentration for 24 h, after which lysates were immunoblotted with antiacetyl-α-tubulin, antiacetyl-histone H3, poly(ADP-ribose) polymerase (PARP), and antiglycerinaldehyd-3-phosphat-dehydrogenase (GAPDH) antibodies. (C) HL-60, SEM, and SUP-B15r cells were treated for 2 h with bortezomib, vorinostat, ricolinostat, and RTS-V5 at concentrations ranging from 4 nM to 25 μM. The proteasomal activity was measured after 2 h using the cell-based Proteasome-Glo chymotrypsin-like assay by taking Suc-LLVY-aminoluciferin (succinyl-leucine-leucine-valine-tyrosine-aminoluciferin) as a substrate. The compounds were printed on a 384-well plate using a randomization feature (n = 3).

DOI: 10.1021/acs.jmedchem.8b01487
J. Med. Chem. XXXX, XXX, XXX−XXX

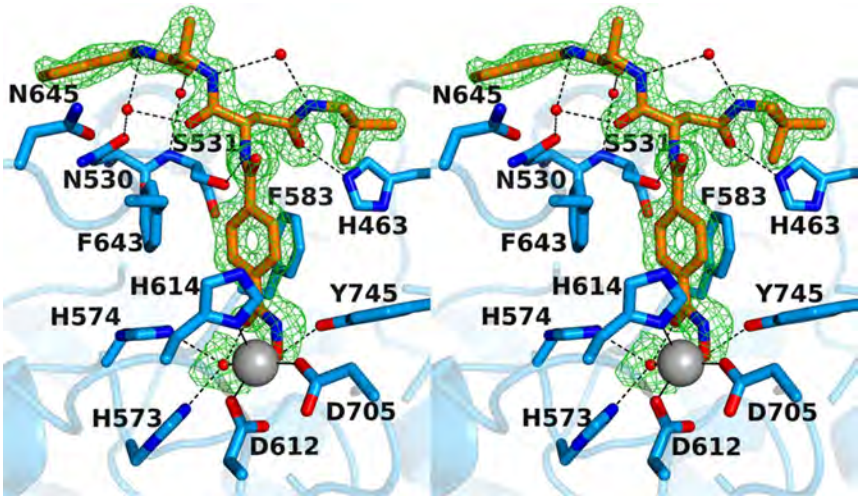

Figure 4. Stereoview of the Polder omit map of RTS-V5 bound to monomer A of HDAC6 (contoured at 3.0 σ) (PDB 6CW8). Atoms are color-coded as follows: C = orange (RTS-V5) or light blue (protein), N = blue, O = red, Zn^{2+} = gray sphere, and solvent = red spheres. Metal coordination and hydrogen bond interactions are indicated by solid and dashed black lines, respectively. The Zn^{2+} coordination geometry is pentacoordinate square pyramidal.

ray structures of ML16 and its analogues indicated that the P4 residue is solvent exposed.[7,11a] As a result, we aimed at the design of a HDAC−proteasome hybrid inhibitor by incorporating the HDACi part at the P4 position (Figure 2). The most obvious synergy between PIs and HDACi is derived from the inhibition of HDAC6.[6,13] Thus, we chose an *N*-hydroxybenzamide scaffold as HDACi part as this moiety provides HDAC6 selectivity.[14]

Compound **I** (Figure 2) is a representative example of a selective HDAC6 inhibitor based on an *N*-hydroxybenzamide group. Furthermore, the solvent-exposed 4-picolyl group in the P2 position was replaced by a methyl group in order to reduce the molecular weight of the hybrid compound. Our hybridization strategy thus yielded the prototype HDAC−proteasome hybrid inhibitor RTS-V5 (Figure 2).

RTS-V5 was synthesized as outlined in Scheme 1. The readily available building blocks **1** and **2** were combined by HATU-mediated coupling to generate dipeptide **3**. Next, the deprotection of **3**, followed by introduction of 4-((benzyloxy)-carbamoyl)benzoic acid via another amide coupling reaction, afforded the protected hydroxamic acid **5**. Finally, catalytic hydrogenolysis of **5** provided the target compound RTS-V5.

RTS-V5 Inhibits Histone Deacetylase and Proteasomal Activity. RTS-V5 was evaluated for its ability to inhibit both histone deacetylase and proteasomal activity. First, we tested the compound in a biochemical assay for activity against recombinant HDAC6. The screening demonstrated potent submicromolar activity with an IC_{50} value of 0.27 μM (Figure 3a). To assess the selectivity of RTS-V5 for HDAC6, it was further tested for activity against all class I isoforms (HDACs 1, 2, 3, and 8, Figure 3a). Our analysis revealed that RTS-V5 has low activity against HDACs 1, 2, and 3. However, HDAC8 was blocked at submicromolar concentrations as well (HDAC8 IC_{50}: 0.53 μM), which can be explained by the lowered rim of the catalytic channels of HDAC6 and HDAC8.[15]

In the following, we aimed to evaluate the inhibition of RTS-V5 against HDAC6 in a cellular environment. Therefore, we treated the acute myeloid leukemia (AML) cell line HL-60 as well as the B-cell precursor acute lymphoblastic leukemia (BCP-ALL) cell lines SEM and SUP-B15r (tyrosine kinase inhibitor (TKI) - resistant)[16] with RTS-V5, the preferential HDAC6 inhibitor ricolinostat, and the FDA-approved proteasome inhibitor bortezomib for 24 h. Next, the cell lysates were immunoblotted with antiacetyl-α-tubulin and acetyl-histone H3 antibodies (Figure 3b). Compared to bortezomib, the treatment with RTS-V5 enhanced the expression of acetyl-α tubulin and acetyl-histone H3 in accordance with ricolinostat. Furthermore, RTS-V5 upregulated the expression of cleaved PARP, a marker of apoptosis, corresponding to ricolinostat and bortezomib (Figure 3b). The inhibition of proteasome activity by RTS-V5 was evaluated using a cell-based chymotrypsin-like Glo assay (Promega) by taking bortezomib as a positive control and ricolinostat (HDAC6i) or vorinostat (pan-HDACi) as a negative marker (Figure 3c). In all selected leukemic cell lines (HL-60, SEM, and SUP-B15r), RTS-V5 blocked the chymotrypsin-like proteasome activity while vorinostat and ricolinostat were unable to inhibit the protease. Furthermore, it was shown that RTS-V5 acts specifically on the chymotrypsin-like activity, i.e., RTS-V5 was unable to inhibit the trypsin- and caspase-like proteasome activities (Figure S1a, S1b, Supporting Information). Thus, these results demonstrate that RTS-V5 is the first-in-class dual HDAC−proteasome inhibitor.

Cocrystal Structures of RTS-V5 in Complex with HDAC6 and the 20S Proteasome. Encouraged by the functional specificity of RTS-V5 against HDAC6 and the proteasome, we set out to elucidate its binding modes in the vastly differing targets. First, the crystal structure of catalytic domain 2 (CD2) of *Danio rerio* (zebrafish) HDAC6 complexed with RTS-V5 was determined at 1.90 Å resolution (R_{free} = 0.190, PDB 6CW8, Table S1, Supporting Information). The crystal structures of zebrafish and human CD2 enzymes are essentially identical,[17a] so zebrafish HDAC6 CD2 (henceforth simply "HDAC6") serves as a more readily studied surrogate of the human enzyme. The crystal structure of the enzyme−inhibitor complex depicts no major conformational changes between the inhibitor-bound and unliganded states of the enzyme, and the root-mean-square (rms) deviation is 0.14 Å for 287 Cα atoms (unliganded HDAC6, PDB 5EEM). Notably, there are two independent and essentially identical

DOI: 10.1021/acs.jmedchem.8b01487
J. Med. Chem. XXXX, XXX, XXX−XXX

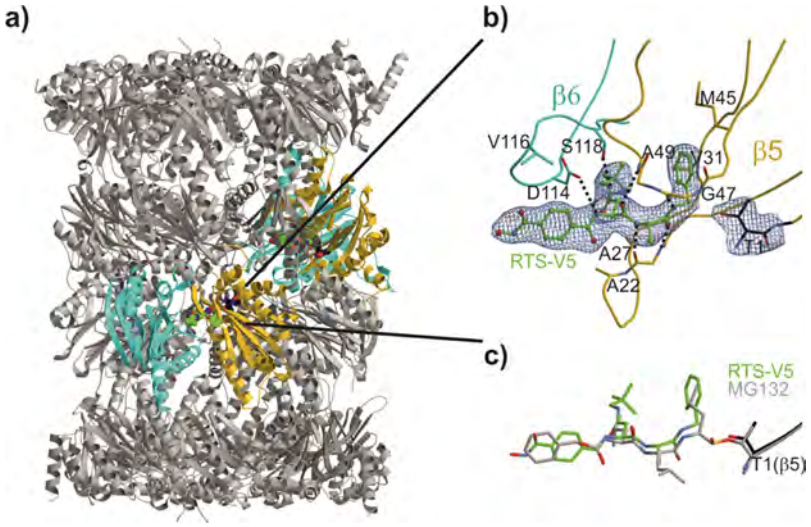

Figure 5. Yeast 20S proteasome in complex with RTS-V5. (a) Cartoon representation of the yeast 20S proteasome core particle (yCP) in complex with RTS-V5 (PDB 6H39). The decarboxylated ligand is presented as a sphere model, which is located at the intersection of the $\beta-\beta'$ rings. The molecule solely binds to the nonprimed substrate binding channel of the chymotrypsin-like active site, which is composed of subunits $\beta5$ (gold) and $\beta6$ (cyan), respectively. (b) The $2F_O - F_C$ electron density map of the noncovalent inhibitor is illustrated as blue mesh and contoured to 1σ. Hydrogen bonds forming the antiparallel β-sheet between ligand and protein main chain residues are indicated by black dashed lines. RTS-V5 intensely interacts with the S1 and S3 sites, whereas the P2-Ala side chain is solvent exposed. Amino acid numbering is according to Löwe et al.[18] and Groll et al.[19] (c) Structural superposition of RTS-V5 with the covalently acting aldehyde inhibitor MG132 (PDB 4NNN)[20] depicts a uniform arrangement. The hemiacetal bond is highlighted in gold.

monomers in this crystal form (rms deviation = 0.15 Å for 299 Cα atoms). Electron density for RTS-V5 is generally well-defined in both monomers (monomer A, Figure 4; monomer B, Figure S2, Supporting Information). Enzyme−inhibitor interactions are quite similar in both monomers, except for alternative interactions resulting from individual conformations of the benzyl-L-alanyl moiety in monomers A and B, respectively (Figure S3, Supporting Information).

In both monomers, the hydroxamate moiety of RTS-V5 coordinates to the active site Zn^{2+} ion in monodentate fashion, in a similar manner to that observed in complexes with other bulky phenylhydroxamate inhibitors such as HPOB, HPB, and ACY-1083.[17] This binding mode is characterized by the coordination of the ionized hydroxamate hydroxyl group to Zn^{2+} (average Zn^{2+}---O separation = 2.0 Å), while the hydroxamate carbonyl group accepts a hydrogen bond from a Zn^{2+}-bound water molecule (average O---O separation = 2.8 Å). The Zn^{2+}-bound N−O$^-$ group also accepts a hydrogen bond from Y745 (average O---O separation = 2.6 Å).

Beyond the Zn^{2+} coordination polyhedron, intermolecular interactions observed for RTS-V5 in both monomers contribute to inhibitor affinity and selectivity. The aromatic ring of the phenylhydroxamate is sandwiched between two fully conserved residues, F583 and F643. The *para*-substituted amide NH group forms a hydrogen bond with S531 on the L2 loop (average N---O separation = 3.0 Å). Notably, S531 is unique to HDAC6 and plays an important role in substrate binding.[17a] Thus, hydrogen bonds with S531 presumably contribute to HDAC6 inhibitor selectivity.

In monomer A, the carbonyl group of the neopentylamide moiety accepts a hydrogen bond from H463 in the L1 loop with an O---N separation of 2.9 Å; in monomer B, the O---N separation is 3.3 Å, which is slightly too long for, but perhaps within experimental error of, a hydrogen bond. Interestingly, H463 is unique to vertebrate HDAC6 isozymes, so this interaction may confer additional selectivity toward HDAC6.

Next, the crystal structure of the yeast 20S proteasome core particle (yCP) in complex with RTS-V5 was determined to 2.5 Å resolution (R_{free} = 0.217, PDB 6H39, Table S2, Supporting Information). Intriguingly, the $2F_O - F_C$ electron density map displays the entire inhibitor molecule only bound to the chymotrypsin-like active site by adopting an antiparallel β-sheet structure (Figure 5a,b). Importantly, the HDACi hydroxamic acid ZBG of RTS-V5 is solvent exposed and, thus, not in contact with protein residues. In agreement with our predictions, the complex structure depicts that the ligand acts noncovalently on the proteasome. Compared to standard inhibitors bound to the CP, such as the tripeptide aldehyde MG132,[20] our study revealed that RTS-V5 is solely stabilized by van der Waals interactions with its P1 benzene ring to Val31, Ala49, and predominantly Met45 of subunit $\beta5$, while its P3-neopentyl-Asn-moiety forms elaborate interactions with y$\beta5$-Ala49 as well as Asp114, Val116, and Ser118 of y$\beta6$ (Figure 5b,c). Notably, the electron density map uncovered the presence of an *N*-morpholino-ethane-sulfonic acid molecule (MES) in proximity to the inhibitor, which is derived from the crystallization buffer. Hereby, the sulfonate moiety of MES interacts with $\beta5$Gly47NH and, hence, occupies the oxyanion hole, an area normally populated by the active residue of ligands such as (i) the oxygen anion of the scissile peptide bond in its tetrahedral intermediate[21] or (ii) functional groups of covalently bound inhibitors.[22] Taken together, the crystallographic insights at the molecular resolution confirmed our structure−activity relationships, demonstrating that the noncovalent proteasome inhibitor RTS-V5 fulfils elaborate interactions with the distinct specificity pockets of the chymotrypsin-like substrate binding channel, hereby generating target specificity.

Specific Cytotoxic Activity of RTS-V5 against Cancerous Cells. To investigate the anticancer properties of our dual HDAC-proteasome inhibitor, RTS-V5 was screened for cytotoxicity against a panel of leukemia and multiple myeloma

DOI: 10.1021/acs.jmedchem.8b01487
J. Med. Chem. XXXX, XXX, XXX−XXX

cell lines using ricolinostat as a positive control (Table 1). Hereby, RTS-V5 showed comparable or higher cytotoxicity than ricolinostat with IC_{50} values in the single-digit micromolar to submicromolar concentration range. The highest activity of RTS-V5 was observed against the BCP-ALL cell line SEM (IC_{50}: 0.89 μM). Our dual inhibitor was also active against TKI-resistant SUP-B15r and KCL-22r cells,[16] with IC_{50} values of 1.83 and 2.58 μM, respectively (Table 1). Because of its encouraging activity against chemosensitive and chemoresistant BCP-ALL cell lines, RTS-V5 was further tested for activity against primary BCP-ALL cells derived from four therapy refractory patients (patients 1 and 2 from initial diagnosis and patients 3 and 4 from the relapse cohort) revealing IC_{50} values ranging from 1.51 to 5.23 μM (Table 1).

Table 1. Cytotoxicity of RTS-V5 and Ricolinostat against Selected Leukemia and Multiple Myeloma Cell Lines As Well As Patient-Derived BCP-ALL Cells

cell line	characteristic	RTS-V5 IC_{50} [μM]	ricolinostat IC_{50} [μM]
HL60	AML[a]	1.55 ± 0.02	2.36 ± 0.07
SEM	BCP-ALL[b]	0.89 ± 0.01	1.61 ± 0.02
SUP-B15	BCP-ALL[b]	1.77 ± 0.02	1.92 ± 0.07
KCL-22	CML[c]	3.14 ± 0.03	3.75 ± 0.09
SUP-B15r	BCP-ALL[b,d]	1.83 ± 0.03	3.54 ± 0.02
KCL-22r	CML[c,d]	2.58 ± 0.04	3.38 ± 0.03
RPMI-8226	MM[e]	1.75 ± 0.32	1.97 ± 0.12
U266	MM[e]	2.04 ± 0.37	3.52 ± 0.38
patient 1	BCP-ALL[b]	2.06 ± 0.16	0.29 ± 0.01
patient 2	BCP-ALL[b]	1.84 ± 0.07	0.58 ± 0.04
patient 3	BCP-ALL[b]	5.23 ± 0.13	4.45 ± 0.14
patient 4	BCP-ALL[b]	1.51 ± 0.05	0.54 ± 0.01

[a]Acute myeloid leukemia. [b]B-cell precursor acute lymphoblastic leukemia. [c]Chronic myeloid leukemia. [d]Imatinib resistant. [e]Multiple myeloma.

Next, we evaluated the cell viability in peripheral blood derived mononuclear cells (PBMCs) from healthy individuals. Strikingly, RTS-V5 showed only marginal toxicity against PBMCs (IC_{50} > 25 μM, Figure S4, Supporting Information). In contrast, the reference compounds ricolinostat, vorinostat, and bortezomib caused significant cytotoxicity against PBMCs, with IC_{50} values in the single-digit micromolar (ricolinostat, vorinostat) or even submicromolar concentration range (bortezomib) (Figure S4, Supporting Information). These data emphasize that RTS-V5 possesses promising anticancer properties against several leukemic and multiple myeloma cell lines as well as patient-derived BCP-ALL cells. Intriguingly, RTS-V5 acts in an encouraging therapeutic window.

On the basis of these promising results, the biological properties of RTS-V5 were analyzed in more detail using the BCP-ALL cell line SEM. RTS-V5 significantly inhibited the proliferation of SEM cells at its IC_{50} or 2× IC_{50} concentrations, comparable to ricolinostat (Figure S5, Supporting Information). RTS-V5 induced apoptosis in SEM cells as illustrated by Annexin V and PI staining with ∼5-fold increase in the apoptotic (annexin$^+$PI$^+$) cells upon 48 h treatment (Figure 6a). Comparable results were observed in a caspase 3/7 enzyme-dependent apoptosis assay with an induction of ∼6-fold of apoptotic cells at its IC_{50} concentration (Figure 6b). SEM cells were dose dependently arrested in S phase, and a reduction in G2/M phase was observed after exposure to RTS-V5 for 48 h (Figure 6c). The exposure of RTS-V5 induced early differentiation of SEM cells in the liquid medium marked by the expression of (CD14 and CD11b) myeloid markers (Figure S6, Supporting Information), and moreover, 48 h exposure of RTS-V5 to SEM cells significantly reduced their colony forming capacity (Figure 6d). In addition, exposure of RTS-V5 to SEM cells induces the heat shock response (HSR; marked by the overexpression of Grp94, HSP70, HSP40, and HSP27 proteins), and unfolded protein response (UPR; marked by the overexpression of BIP, ATF4, ATF6, and pJNK proteins) to combat the proteotoxic stress and autophagy (marked by the overexpression of LC3B and p62 proteins) (Figure 6e).

Aggresomes are inclusion bodies produced in response to inhibition of the ubiquitin−proteasome machinery. HDAC6 together with the motor protein dynein is required to recruit cytotoxic, ubiquitylated proteins to aggresomes. The effect of RTS-V5 on the aggresome accumulation was studied using fluorescence microscopy and FACS upon staining with an aggresome dye (Figure 7a,b). The well-known proteasome inhibitors MG132 and bortezomib were used as positive controls, whereas ricolinostat served as negative control. RTS-V5 significantly blocked aggresome accumulation at its inhibitory concentration as opposed to bortezomib and MG132 but in accordance with ricolinostat.

These results led us to conclude that RTS-V5 induces apoptosis and blocks proliferation, cell cycle, colony formation, and aggresome accumulation in the SEM cell line. Furthermore, the exposure of RTS-V5 leads to the activation of HSR and UPR. Hence, our findings together with the crystallographic and biochemical data demonstrate that RTS-V5 eradicates cancer cells by dual blockage of the aggresome-proteasome pathway.

■ DISCUSSION AND CONCLUSIONS

The "one-disease-one-drug" paradigm has dominated drug development strategies for decades.[23] However, the so-called magic bullets, molecules that exhibit high selectivity and potency for one target, are often not effective to treat multifactorial diseases such as cancer or neurological disorders.[4a] Consequently, combination therapy is a cornerstone of cancer therapy: the combination of anticancer drugs enhances efficacy compared to the monotherapy approach because it modulates key pathways in an additive or even synergistic manner.[24] Bortezomib is often given in combination with the pan-HDACi panobinostat. The combination of HDAC6i and proteasome inhibitors leads to increased α-tubulin acetylation as well as to accumulation of misfolded proteins.[25] Misfolded proteins accumulate because both clearance routes, the proteasome and the aggresome pathway, are blocked; in turn, this leads to apoptosis of the cell.[26] Thus, the simultaneous inhibition of both pathways could be of high clinical importance to combat hematological malignancies.

A phase I/II trial conducted for patients with relapsed or refractory multiple myeloma showed that therapy with ricolinostat as a single agent resulted in neither significant toxicity nor clinical responses.[27] However, combination therapy with the proteasome inhibitor bortezomib and dexamethasone achieved a response rate of 37%.[27] Similar results were reported in a study using a combination therapy including the proteasome inhibitor MG132 and vorinostat, which induced synergistic cytotoxicity in leukemia cells by

DOI: 10.1021/acs.jmedchem.8b01487
J. Med. Chem. XXXX, XXX, XXX−XXX

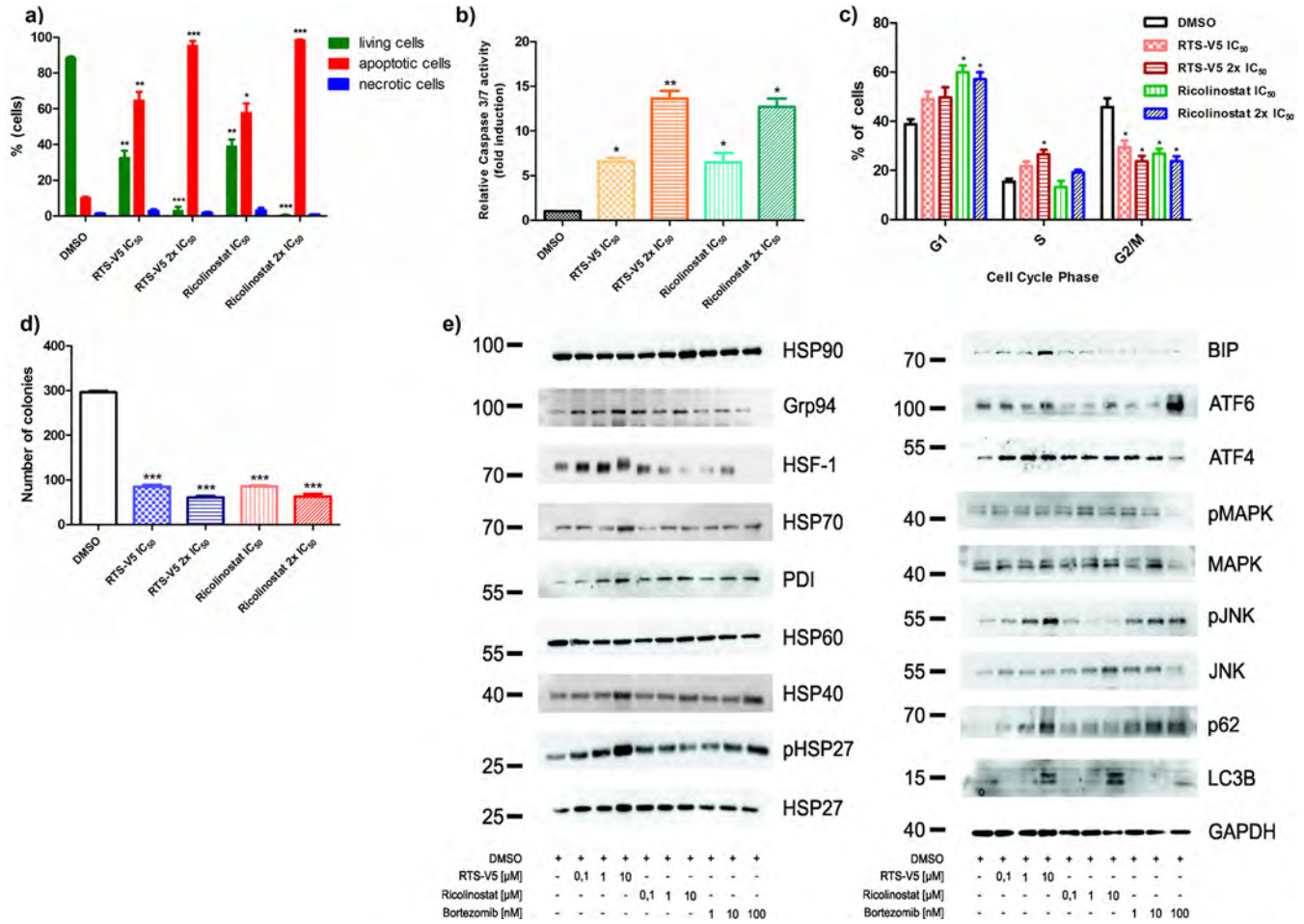

Figure 6. RTS-V5 as a potent inhibitor in a leukemic cell line. (a) SEM cells were treated with RTS-V5 and ricolinostat at IC_{50} or at 2× IC_{50} concentration for 48 h. Subsequently, dual staining was performed with annexin V/PI and measured by FACS. Viable cells (−ve for annexin V/PI) were analyzed if they are necrotic (+ve for PI) and are either in an early (+ve for annexin V) or in a late (+ve for both annexin/PI) apoptotic stage. The bar graph is depicting the percentage of living, apoptotic, and necrotic cells after 48 h exposure to RTS-V5 or ricolinostat. (b) SEM cells were treated with RTS-V5 for 48 h followed by determining the enzymatic activity of caspase 3/7 by applying a Glo assay (absorbance at 405 nm) to record the induction of apoptosis. (c) SEM cells were treated with RTS-V5 for 48 h, and after propidium iodide staining cell cycle analysis was carried out by FACS. (d) SEM cells were seeded in a semisolid methylcellulose-based medium after 48 h treatment with RTS-V5 or controls. Next, the impact of RTS-V5 on the differentiation ability of leukemic cells was evaluated. The bar graphs depict the colonies counted after 14 days. (e) SEM cells were treated with bortezomib, ricolinostat, and RTS-V5 at the indicated concentration for 18 h, after which the expression of proteins involved in the HSR, UPR, and autophagy were analyzed by Western blot analyses. The achieved values depicted in the Figure 6 are plotted as a bar graph. Columns depict the mean of three independent experiments ($n = 3$). Significance analyses of normally distributed data with variance similar between groups used paired, two-tailed Student's t test. * $p < 0.05$, ** $p < 0.005$, *** $p < 0.001$.

downregulating BCR-ABL1 expression and by inducing intracellular ROS levels.[28]

In recent years, multitarget drugs have emerged as a powerful alternative to combination chemotherapy. Although several HDACi-based multitarget drugs have been described before, no dual HDAC−proteasome inhibitor was reported to date. In this work, we have designed and synthesized RTS-V5 as a first-in-class dual HDAC−proteasome inhibitor. We have shown that this compound inhibits both HDAC6 and the chymotrypsin-like proteasome activity in the submicromolar range. RTS-V5 induces apoptosis, HSR, UPR, and autophagy in the SEM cell line. Furthermore, it blocks cell cycle, colony formation, and aggresome accumulation. It is an encouraging finding that RTS-V5 displayed potent anticancer activity against a panel of chemosensitive, chemoresistant leukemic and multiple myeloma cell lines, as well as against therapy refractory primary patient-derived leukemia cells without imposing toxicity against PBMC cells from healthy volunteers. In future studies, the efficacy and toxicity of RTS-V5 or improved analogues will be investigated in in vivo models in comparison to a combination treatment with a HDAC6 inhibitor and a proteasome inhibitor (e.g., ricolinostat combined with bortezomib) in order to further evaluate the therapeutic potential of this promising new class of multitarget ligands.

To the best of our knowledge, this is also the first report of a dual target binder with accompanying cocrystal structures of complexes with both protein targets. The X-ray structures confirmed several important features that might lead to fewer side effects. The noncovalent and selective inhibition of chymotrypsin-like proteasome activity may explain the selective toxicity profile of RTS-V5 compared to covalent proteasome inhibitors such as bortezomib.[12] Selective HDAC6 inhibition is clinically preferable because there is growing evidence that there are intrinsic toxic side effects associated with inhibition of HDAC1−3.[29] The monodentate zinc-

DOI: 10.1021/acs.jmedchem.8b01487
J. Med. Chem. XXXX, XXX, XXX−XXX

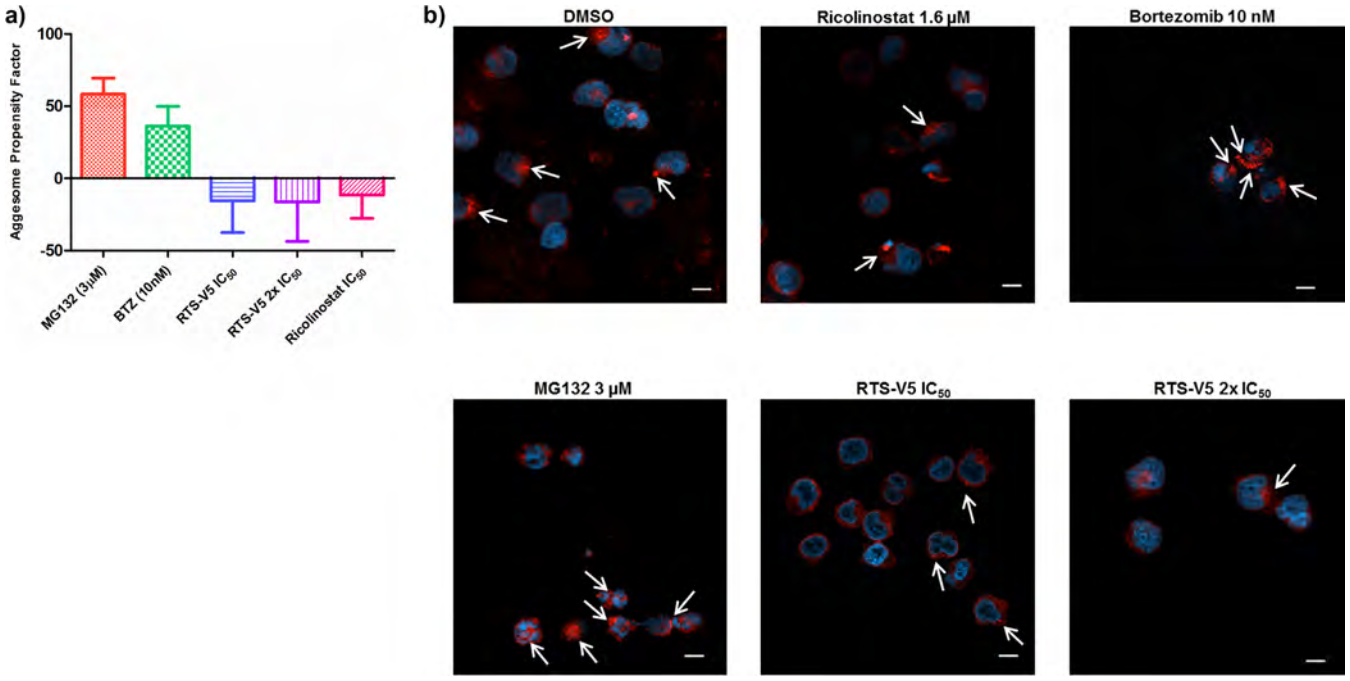

Figure 7. Effect of RTS-V5 on the aggresome accumulation. (a) SEM cells were treated with the respective compounds at their indicated concentration for 18 h. In the following, the Enzo proteostat aggresome detection kit was used to stain the cells along with their DNA. Pictures were taken with a 63× objective using fluorescence microscopy. Scale = 10 μm. (b) Treated SEM cells were analyzed by FACS upon staining with aggresome dye to determine the aggresome propensity factor according to the relative mean fluorescence intensity (MFI).

binding observed for RTS-V5 can be exploited by bulky phenylhydroxamate-based HDACi. However, binding of these inhibitors in the sterically constricted active site of HDAC1−3 would be disfavored.[17b] Thus, the monodentate zinc-binding mode is believed to contribute to the significantly reduced inhibition of HDAC1−3 and low toxicity of RTS-V5 compared to the pan-inhibitor vorinostat. Hence, our determined crystal structures of RTS-V5 in complex with HDAC6 and the 20S proteasome will ultimately pave the way for the structure-based optimization of dual HDAC−proteasome inhibitors for advanced preclinical studies.

■ EXPERIMENTAL SECTION

Chemistry. *General.* All reagents and solvents were purchased from commercial sources and used without further purification. Thin layer chromatography was carried out using Macherey-Nagel precoated aluminum foil sheets which were visualized using UV light (254 nm) and, in the case of hydroxamic acids, stained with a 1% solution of iron(III) chloride in methanol. ^{1}H NMR and ^{13}C NMR spectra were recorded at room temperature on Bruker Avance III HD (400 MHz), Bruker Avance III (600 MHz), Bruker Avance DRX (500 MHz), and Varian/Agilent Mercury-Plus (300 MHz) spectrometers. Chemical shifts (δ) are quoted in parts per million (ppm). All spectra were standardized in accordance with the signals of the deuterated solvent (DMSO-d_6: δ_H = 2.50 ppm, δ_C = 39.5 ppm). Coupling constants (J) are reported in hertz (Hz). Mass spectra were measured by the Leipzig University Mass Spectrometry Service, using electrospray ionization (ESI) on a Bruker Daltonics ESI-TOF micrOTOF. The uncorrected melting points were determined using a Barnstead Electrothermal 9100 apparatus. Analytical HPLC analysis were carried out using a Knauer Azura P 6.1L system equipped with P 6.1L (pumps), a Smartline UV detector 2600, and a Phenomenex Luna 5 μ C18(2) 1.8 μm particle (250 mm × 4.6 mm) column, supported by Phenomenex Security Guard Cartridge Kit C18 (4.0 mm × 3.0 mm). UV absorption was detected at 254 nm with a linear gradient of 10% B to 100% B within 20 min. HPLC-grade water (solvent A) and HPLC-grade acetonitrile (solvent B) were used for elution at a flow rate of 1 mL/min. Both solvents were enriched with 0.1% TFA. The purity of the final compound was at least 95%. The synthesis of 4-((benzyloxy)carbamoyl)benzoic acid is described in the Supporting Information.

*tert-Butyl ((S)-1-(((S)-1-(Benzylamino)-1-oxopropan-2-yl)-amino)-4-(neopentylamino)-1,4-dioxobutan-2-yl)carbamate (**3**).* *tert*-Butyl (*S*)-(1-benzylamino)-1-oxopropan-2-yl)carbamate (6.64 g, 23.85 mmol, 1 equiv) was dissolved in a mixture of trifluoroacetic acid/CH_2Cl_2 (1:2, 30 mL) and stirred at room temperature for 4 h. After completion of the reaction, the solution was basified (pH ≈ 9) using satd sodium carbonate solution. The mixture was extracted with CH_2Cl_2 (3 × 20 mL) and washed with 1 M sodium hydroxide solution (3 × 20 mL) and brine (3 × 20 mL). Subsequently, the collected organics were dried over sodium sulfate and the solvent was removed under reduced pressure to yield compound **2** as a crude product. The crude product **2** (1.9 g, 10.66 mmol, 1.1 equiv) was added to a mixture of **1** (2.93 g, 9.69 mmol, 1 equiv), diisopropylethylamine (1.65 mL, 9.69 mmol, 1 equiv), and HATU (3.68 g, 9.69 mmol, 1 equiv) in 10 mL of DMF and stirred at room temperature for 16 h. The mixture was extracted with CH_2Cl_2 (3 × 15 mL) and washed with H_2O (3 × 15 mL), citric acid (3 × 15 mL), and satd sodium carbonate solution (3 × 15 mL). The combined organics were dried over sodium sulfate, and the solvent was removed under reduced pressure. Product **3** was crystallized from *n*-hexane and ethyl acetate. White solid; 73% yield; mp 143−145 °C. ^{1}H NMR (400 MHz, DMSO-d_6) δ 8.45 (t, J = 5.4 Hz, 1H, NH), 8.02 (d, J = 7.4 Hz, 1H, NH), 7.83−7.67 (t, J = 5.4 Hz, 1H, NH), 7.37−7.22 (m, 5H, arom H), 6.91 (d, J = 6.9 Hz, NH), 4.36−4.19 (m, 4H, CH, CH, CH_2), 2.93−2.76 (m, 2H, CH_2), 2.75−2.57(m, 2H, CH_2), 1.36 (s, 9H, ^{t}Bu), 1.24 (d, J = 7.0 Hz, 3H, CH_3), 0.80 (s, 9H, ^{t}Bu) ppm. ^{13}C NMR (101 MHz, DMSO-d_6) δ 172.0, 171.0, 169.6, 155.0, 139.3, 128.2, 127.0, 126.7, 78.2, 51.5, 49.7, 48.4, 42.0, 37.7, 31.9, 28.1, 27.2, 18.2 ppm. HRMS (m/z): M^- calcd for $C_{24}H_{37}N_4O_5$ 461.2769, found 461.2755.

*(S)-2-Amino-N^1-((S)-1-(benzylamino)-1-oxopropan-2-yl)-N^4-neopentylsuccinamide (**4**).* Compound **3** (340 mg, 0.73 mmol, 1 equiv) was dissolved in a mixture of trifluoroacetic acid/CH_2Cl_2 (1:2.25, 13 mL) and stirred at room temperature for 4 h. After completion of the

DOI: 10.1021/acs.jmedchem.8b01487
J. Med. Chem. XXXX, XXX, XXX−XXX

reaction, the mixture was basified (pH ≈ 9) using satd sodium carbonate solution. The resulting solution was extracted with CH_2Cl_2 (3 × 20 mL) and washed with brine (1 × 10 mL). The collected organics were dried over magnesium sulfate, and the solvent was removed under reduced pressure. The crude product was recrystallized from methanol and diethyl ether to yield compound **4.** White solid; 75% yield; mp 160−163 °C. ^{1}H NMR (400 MHz, DMSO-d_6) δ 8.49 (t, J = 5.8 Hz, 1H, NH), 8.32 (d, J = 6.5 Hz, 1H, NH), 7.97 (t, J = 5.6 Hz, 1H, NH), 7.36−7.15 (m, 5H, arom H), 4.35−4.11 (m, 3H, CH, CH_2), 3.70−3.61 (m, 1H, CH), 2.84 (d, J = 6.2 Hz, 2H, CH_2), 2.68−2.53 (m, 2H, CH_2), 1.26 (d, J = 7.1 Hz, 3H, CH_3), 0.81 (s, 9H, ^{t}Bu) ppm. ^{13}C NMR (75 MHz, DMSO-d_6) δ 172.0, 171.9, 170.1, 169.9, 139.3, 128.2, 127.0, 126.7, 51.1, 49.7, 48.3, 42.0, 31.8, 27.2, 18.3 ppm. HRMS (m/z): MNa^+ calcd for $C_{19}H_{30}N_4NaO_3$ 385.2210, found 385.2210.

*N^1-((S)-1-(((S)-1-(Benzylamino)-1-oxopropan-2-yl)amino)-4-(neopentylamino)-1,4-dioxobutan-2-yl)-N^4-(benzyloxy)-terephthalamide (**5**).* A mixture of compound **4** (95 mg, 0.26 mmol, 1 equiv), ((benzyloxy)carbamoyl)benzoic acid (84 mg, 0.31 mmol, 1.2 equiv), and HATU (118 mg, 0.31 mmol, 1.2 equiv) was suspended in DMF (3 mL), and diisopropylethylamine (53 μL, 0.31 mmol, 1.2 equiv) was added. The resulting solution was stirred at room temperature for 24 h. After completion of the reaction, the solvent was removed under reduced pressure and the remaining solid was washed with satd sodium bicarbonate solution (2 × 15 mL), 10% HCl (2 × 15 mL), water (2 × 15 mL), and diethyl ether (2 × 15 mL). The crude product was recrystallized from methanol and diethyl ether to yield compound **5**. White solid; 65% yield; mp 232−236 °C. ^{1}H NMR (400 MHz, DMSO-d_6) δ 11.90 (s, 1H, NH), 8.70 (d, J = 7.6 Hz, 1H, NH), 8.43 (t, J = 6.1 Hz, 1H, NH), 8.25 (d, J = 7.4 Hz, 1H, NH), 7.94−7.87 (m, 2H, arom H), 7.84−7.78 (m, 2H, arom H), 7.48−7.17 (m, 10H, arom H), 4.94 (s, 1H, OCH_2), 4.82−4.73 (m, 1H, CH), 4.34−4.19 (m, 3H, CH_2, CH), 2.89−2.63 (m, 4H, CH_2, CH_2), 1.26 (d, J = 7.1 Hz, 3H, CH_3), 0.78 (s, 9H, ^{t}Bu) ppm. ^{13}C NMR (101 MHz, DMSO-d_6) δ 172.0, 170.7, 169.7, 165.4, 163.7, 139.4, 136.5, 135.8, 134.7, 129.0, 128.4, 128.2, 127.6, 127.1, 127.0, 126.7, 77.1, 50.9, 49.7, 48.6, 42.0, 37.5, 31.9, 27.2, 18.0 ppm. HRMS (m/z): M^- calcd for $C_{34}H_{40}N_5O_6$ 614.2984, found 614.2979.

N^1-((S)-1-(((S)-1-(Benzylamino)-1-oxopropan-2-yl)amino)-4-(neopentylamino)-1,4-dioxobutan-2-yl)-N^4-hydroxyterephthalamide (RTS-V5). Compound **5** (50 mg, 0.08 mmol, 1 equiv) was dissolved in 5 mL of MeOH, and Pd(C) (5 mg, 10 wt %, 4.70 μmol, 0.06 equiv) was added. The mixture was stirred under hydrogen atmosphere at room temperature for 4 h. After completion of the reaction, the mixture was filtered over Celite. The solvent was removed under reduced pressure, and the product RTS-V5 was crystallized from n-hexane and ethyl acetate. White solid; 98% yield; mp 220 °C (decomp); t_R 10.67 min; purity 95%. ^{1}H NMR (500 MHz, DMSO-d_6) δ 11.31 (bs, 1H, OH), 9.10 (bs, 1H, NH), 8.67 (d, J = 7.6 Hz, 1H, NH), 8.40 (t, J = 5.8 Hz, 1H, NH), 8.20 (d, J = 7.3 Hz, 1H, NH), 7.91−7.87 (m, 2H, arom H), 7.84−7.80 (m, 2H, arom H), 7.32−7.19 (m, 5H, arom H), 4.83−4.72 (m, 1H, CH), 4.34−4.21 (m, 3H, CH_2, CH), 2.91−2.79 (m, 2H, CH_2), 2.77−2.63 (m, 2H, CH_2), 1.26 (d, J = 7.1 Hz, 3H, CH_3), 0.78 (s, 9H, ^{t}Bu) ppm. ^{13}C NMR (126 MHz, DMSO-d_6) δ 171.9, 170.5, 169.6, 165.5, 139.2, 136.0, 135.2, 128.1, 127.3, 126.9, 126.7, 126.6, 50.9, 49.7, 48.5, 42.0, 37.4, 31.7, 27.1, 17.9 ppm. HRMS (m/z): MH^+ calcd for $C_{27}H_{36}N_5O_6$ 526.2660, found 526.2669.

Biological Evaluation. *Cell Culture.* SEM, HL60, KCL22, and K562 leukemic cell lines were cultured in RPMI1640 supplemented with 10% FCS and maintained at 37 °C with 5% CO_2, except for SUP-B15 (BCR-ABL1) BCP-ALL cell line, which was cultured in McCoy's 5A supplemented with 20% of FCS (DSMZ, Braunschweig, Germany). Mononuclear cells (MNC) were isolated by Ficoll density gradient centrifugation using standard procedures and later cultured in Mononuclear Cell Medium (PromoCell, Heidelberg, Germany). CD34+ cells were later sorted from these MNC using MACS (Miltenyi Biotec, Bergisch Gladbach, Germany). Primary patient samples were obtained from newly diagnosed patients or from relapse after informed consent approval of the local ethics committee and were cultured either in Stemline II hematopoietic stem cell expansion medium (Sigma-Aldrich) or in Mononuclear Cell Medium (PromoCell)

CellTiter-Glo Luminescent Cell Viability Assay. CellTiter-Glo luminescent cell viability assay (Promega, Madison, USA) was performed to determine the IC_{50} values for every cell line. Inhibitors were printed on white 384-well plates (Thermo Fisher Scientific, Waltham, USA) with increasing concentrations (50 nM-25 μM) by using a digital dispenser (D300e, Tecan, Männedorf, Switzerland). Cell viability was monitored after 72 h using CellTiter-Glo luminescent assay using a microplate reader (Spark, Tecan). IC_{50} for the compounds were determined by plotting raw data (normalized to controls) using sigmoid dose curve and nonlinear regression (GraphPad Prism Inc., San Diego, CA).

Proteasome Activity Assay. To analyze if treatment with RTS-V5 leads to decreased proteasome activity, chymotrypsin-like, trypsin-like, and caspase-like protease activities associated with the proteasome complex were measured. Therefore, cell-based Proteasome-Glo assay kits (Promega, Madison, USA) were used which contain luminogenic substrates that are recognized and cleaved by the proteasome into aminoluciferin. Aminoluciferin is consumed by Ultra-Glo luciferase, producing a luminescent signal correlating to proteasome activity. Luminescence was measured afterward using a microplate reader (Spark, Tecan).

Caspase Assay. Caspase-Glo 3/7 assay was used to show the impact of the inhibitors on the activity of caspase-3 and -7 in the cells. Caspase-3 and -7 are key players in apoptosis. The kit contains a luminogenic substrate of caspase-3 and -7 with a DEVD sequence. This sequence can be recognized and cleaved by caspase-3 and -7. The cleavage results in a luminescent signal which is proportional to the amount of caspase activity. Cells were seeded and treated with the IC_{50} or 2× IC_{50} concentrations of the inhibitors for 48 h, and later the luminescence was measured with a microplate reader (Spark, Tecan).

Proliferation Assay. To investigate the influence of the inhibitors on the proliferation, cells were counted after every 24 h interval through trypan exclusion method using automated cell counter (Vi-CELL XR, Beckman Coulter).

Annexin V Staining. For evaluating apoptosis, cells treated with respective compounds or control for 48 h were stained with annexin V and PI and later subjected to FACS, following supplier's guidelines (Invitrogen, Carlsbad, CA, USA).

Cell Cycle Analysis. To investigate if cells treated with the inhibitors show differences in the cell cycle progression as compared to untreated cells, cell cycle analysis was performed. Therefore, cells were permeabilized and DNA was stained with PI which binds stoichiometric, i.e., proportional to the amount of DNA present in the cell. Fluorescence was measured by flow cytometry with FACSCalibur (Becton Dickinson, Heidelberg, Germany).

Western Blotting. Cell lysates were generated after 24 h treatment with the respective inhibitors and later immunoblotted using anti-PARP (no. 9542), anti-acetyl-α-tubulin (no. 5335), anti-histone H3 (no. 9677), anti-HSP90 (no. 4877), anti-Grp94 (no. 2104), anti-HSF-1 (no. 4356), anti-HSP70 (no. 4872), anti-PDI (no. 2446), anti-HSP60 (no. 12165), anti-HSP40 (no. 4871), anti-pHSP27 (no. 9709), anti-HSP27 (no. 2402), anti-BIP (no. 3177), anti-ATF6 (no. 65880), anti-ATF4 (no. 11815), anti-pMAPK (no. 4370), anti-MAPK (no. 4695), anti-pJNK (no. 4668), anti-JNK (no. 9252), anti-p62 (no. 5114), anti-LC3B (no. 3868), and anti-GAPDH (no. 2118) (Cell Signaling Technology, Danvers, MA).

Differentiation Assay. Healthy cells differentiate into specialized cells when they mature. In contrast, cancer cells remain undifferentiated or poorly differentiated to maintain their ability of fast replication. Differentiation assay was performed to analyze if treatment with the inhibitors leads to increased differentiation of the cells. Therefore, antibodies against specific surface molecules that cells express depending on their stage of differentiation were used as differentiation markers. FACS was performed on FACSCalibur (Becton Dickinson, Heidelberg, Germany) by using fluorochrome coupled monoclonal antibodies (mAbs) along with matched isotype

DOI: 10.1021/acs.jmedchem.8b01487
J. Med. Chem. XXXX, XXX, XXX−XXX

controls: anti-CD11b (Bear1) and anti-CD14 (RMO52) (Beckman Coulter).

CFU Assay. Colony forming unit assays (CFU) were performed by initially treating the cells in the liquid medium for 24 h, and later the treated cells were seeded in the semisolid methylcellulose-based medium containing respective compounds or control. Colonies were counted after 14 days.

Aggresome Detection Assay. As RTS-V5 simultaneously blocks the 20S proteasome and HDAC6, we planned to evaluate its effect on aggresome production using a proteostat aggresome detection kit (Enzo Life Sciences). Cells were labeled using an aggresome detection kit following the manufacturer's guidelines. After 18 h treatment with the respective compounds, the aggresomes were detected using either fluorescence microscopy or FACS.

HDAC IC_{50} Profiling. The in vitro inhibitory activity of RTS-V5 against five human HDAC isoforms (1, 2, 3, 6, and 8) were determined at Reaction Biology Corporation (Malvern, PA) with a fluorescence-based assay according to the company's standard operating procedure using RHKK(Ac)AMC (HDACs 1, 2, 3, and 6) or RHK(Ac)K(Ac)AMC (HDAC8) as substrates. The IC_{50} values were determined in duplicate using 10 different concentrations with 3-fold serial dilution starting at 100 μM. TSA (HDAC1 IC_{50}, 9.4 nM; HDAC2 IC_{50}, 26.7 nM; $HDAC_3$ IC_{50}, 12.7 nM; HDAC6 IC_{50}, 8.5 nM; HDAC8 IC_{50}, 609 nM) was used as a reference compound.

X-ray Crystallography. Experimental details for the X-ray crystal structure determination of HDAC6 and the yeast 20S proteasome in complex with RTS-V5 can be found in the Supporting Information.

■ ASSOCIATED CONTENT

Supporting Information

The Supporting Information is available free of charge on the ACS Publications website at DOI: 10.1021/acs.jmedchem.8b01487.

Supplementary figures and tables, experimental procedures, compound characterization data, X-ray crystallography, HPLC traces, and NMR spectra of newly synthesized compounds (PDF)

Molecular formula strings and some data (CSV)

Accession Codes

Protein Data Bank (PDB): HDAC6−RTS-V5 complex, 6CW8; proteasome−RTS-V5 complex, 6H39.

■ AUTHOR INFORMATION

Corresponding Authors

*For F.K.H.: phone, (+49) 341 97 36801; fax, (+49) 341 97 36889; E-mail, finn.hansen@medizin.uni-leipzig.de.

*For J.H.: phone, (+49) 211 81 17680; fax, (+49) 211 81 16206, E-mail, julia.hauer@med.uni-duesseldorf.de.

ORCID

Michael Groll: 0000-0002-1660-340X

Thomas Kurz: 0000-0002-9474-4224

David W. Christianson: 0000-0002-0194-5212

Finn K. Hansen: 0000-0001-9765-5975

Author Contributions

S.B. and V.K. contributed equally to this work as first authors. J.H. and F.K.H. contributed equally to this work as senior authors. The manuscript was written through contributions of all authors. All authors have given approval to the final version of the manuscript.

Notes

The authors declare no competing financial interest.

■ ACKNOWLEDGMENTS

We thank Nicholas Porter for helpful scientific discussions. Additionally, we thank Alexei Soares and the beamline staff at the National Synchrotron Light Source II (NSLS-II) for assistance with data collection using AMX beamline 17-ID-1. NSLS-II is a U.S. Department of Energy (DOE) Office of Science User Facility operated by Brookhaven National Laboratory under contract no. DE-SC0012704. We are grateful to the staff of the beamline X06SA at the Paul-Scherrer-Institute, Swiss Light Source, Villigen (Switzerland), for assistance during data collection of the proteasome complex. Richard Feicht is acknowledged for the purification and crystallization of the yeast 20S core particle. Experimental support from Alexandra Herrlich is gratefully appreciated. This research was financially supported by NIH grant GM49758 (to D.W.C) and by the Deutsche Forschungsgemeinschaft (SFB1035, to M.G.). F.K.H. acknowledges financial support from the Fonds der Chemischen Industrie (FCI). J.H. has been supported by the German Children's Cancer Foundation (project 110997 and Translational Oncology Program 70112951), the German Carreras Foundation (DJCLS 02R/2016), the Kinderkrebsstiftung (2016/17), and the Elterninitiative Kinderkrebsklinik eV Düsseldorf. S.B. acknowledges financial support of an intramural grant (2018-04) from the Research Commission of the Medical Faculty of Heinrich Heine University Düsseldorf.

■ ABBREVIATIONS USED

CFU, colony forming assay; DMSO, dimethyl sulfoxide; HDAC, histone deacetylase; HDAC6 CD2, histone deacetylase 6 catalytic domain 2; PI, proteasome inhibitor; AML, acute myeloid leukemia; BCP-ALL, B-cell precursor acute lymphoblastic leukemia; CML, chronic myeloid leukemia; MM, multiple myeloma; TKI, tyrosine kinase inhibitor; PARP, poly(ADP-ribose) polymerase; PBMCs, peripheral blood derived mononuclear cells; HSR, heat shock response; UPR, unfolded protein response

■ REFERENCES

(1) Anighoro, A.; Bajorath, J.; Rastelli, G. Polypharmacology: challenges and opportunities in drug discovery. *J. Med. Chem.* **2014**, *57*, 7874−7887.

(2) Roche, J.; Bertrand, P. Inside HDACs with more selective HDAC inhibitors. *Eur. J. Med. Chem.* **2016**, *121*, 451−483.

(3) Maolanon, A. R.; Kristensen, H. M.; Leman, L. J.; Ghadiri, M. R.; Olsen, C. A. Natural and synthetic macrocyclic inhibitors of the histone deacetylase enzymes. *ChemBioChem* **2017**, *18*, 5−49.

(4) (a) Ganesan, A. Multitarget Drugs: an Epigenetic Epiphany. *ChemMedChem* **2016**, *11*, 1227−1241. (b) de Lera, A. R.; Ganesan, A. Epigenetic polypharmacology: from combination therapy to multitargeted drugs. *Clin. Epigenet.* **2016**, *8*, 105.

(5) (a) Millard, C. J.; Watson, P. J.; Fairall, L.; Schwabe, J. W. R. Targeting class I histone deacetylases in a "complex" environment. *Trends Pharmacol. Sci.* **2017**, *38*, 363−377. (b) Schobert, R.; Biersack, B. Multimodal HDAC inhibitors with improved anticancer activity. *Curr. Cancer Drug Targets* **2018**, *18*, 39−56.

(6) Hideshima, T.; Richardson, P. G.; Anderson, K. C. Mechanism of action of proteasome inhibitors and deacetylase inhibitors and the biological basis of synergy in multiple myeloma. *Mol. Cancer Ther.* **2011**, *10*, 2034−2042.

(7) Beck, P.; Dubiella, C.; Groll, M. Covalent and non-covalent reversible proteasome inhibition. *Biol. Chem.* **2012**, *393*, 1101−1120.

(8) Gallastegui, N.; Beck, P.; Arciniega, M.; Huber, R.; Hillebrand, S.; Groll, M. Hydroxyureas as noncovalent proteasome inhibitors. *Angew. Chem., Int. Ed.* **2012**, *51*, 247−249.

DOI: 10.1021/acs.jmedchem.8b01487
J. Med. Chem. XXXX, XXX, XXX−XXX

(9) Groll, M.; Koguchi, Y.; Huber, R.; Kohno, J. Crystal structure of the 20 S proteasome:TMC-95A complex: a non-covalent proteasome inhibitor. *J. Mol. Biol.* **2001**, *311*, 543−548.

(10) (a) Kaiser, M.; Groll, M.; Siciliano, C.; Assfalg-Machleidt, I.; Weyher, E.; Kohno, J.; Milbradt, A. G.; Renner, C.; Huber, R.; Moroder, L. Binding mode of TMC-95A analogues to eukaryotic 20S proteasome. *ChemBioChem* **2004**, *5*, 1256−1266. (b) Groll, M.; Gotz, M.; Kaiser, M.; Weyher, E.; Moroder, L. TMC-95-based inhibitor design provides evidence for the catalytic versatility of the proteasome. *Chem. Biol.* **2006**, *13*, 607−614. (c) Desvergne, A.; Genin, E.; Marechal, X.; Gallastegui, N.; Dufau, L.; Richy, N.; Groll, M.; Vidal, J.; Reboud-Ravaux, M. Dimerized linear mimics of a natural cyclopeptide (TMC-95A) are potent noncovalent inhibitors of the eukaryotic 20S proteasome. *J. Med. Chem.* **2013**, *56*, 3367−3378.

(11) (a) Blackburn, C.; Gigstad, K. M.; Hales, P.; Garcia, K.; Jones, M.; Bruzzese, F. J.; Barrett, C.; Liu, J. X.; Soucy, T. A.; Sappal, D. S.; Bump, N.; Olhava, E. J.; Fleming, P.; Dick, L. R.; Tsu, C.; Sintchak, M. D.; Blank, J. L. Characterization of a new series of non-covalent proteasome inhibitors with exquisite potency and selectivity for the 20S β5-subunit. *Biochem. J.* **2010**, *430*, 461−476. (b) Groll, M.; Gallastegui, N.; Marechal, X.; Le Ravalec, V.; Basse, N.; Richy, N.; Genin, E.; Huber, R.; Moroder, L.; Vidal, J.; Reboud-Ravaux, M. 20S proteasome inhibition: designing noncovalent linear peptide mimics of the natural product TMC-95A. *ChemMedChem* **2010**, *5*, 1701−1705.

(12) Huber, E. M.; Groll, M. Inhibitors for the immuno- and constitutive proteasome: current and future trends in drug development. *Angew. Chem., Int. Ed.* **2012**, *51*, 8708−8720.

(13) Hideshima, T.; Qi, J.; Paranal, R. M.; Tang, W.; Greenberg, E.; West, N.; Colling, M. E.; Estiu, G.; Mazitschek, R.; Perry, J. A.; Ohguchi, H.; Cottini, F.; Mimura, N.; Gorgun, G.; Tai, Y. T.; Richardson, P. G.; Carrasco, R. D.; Wiest, O.; Schreiber, S. L.; Anderson, K. C.; Bradner, J. E. Discovery of selective small-molecule HDAC6 inhibitor for overcoming proteasome inhibitor resistance in multiple myeloma. *Proc. Natl. Acad. Sci. U. S. A.* **2016**, *113*, 13162−13167.

(14) (a) Olson, D. E.; Wagner, F. F.; Kaya, T.; Gale, J. P.; Aidoud, N.; Davoine, E. L.; Lazzaro, F.; Weiwer, M.; Zhang, Y. L.; Holson, E. B. Discovery of the first histone deacetylase 6/8 dual inhibitors. *J. Med. Chem.* **2013**, *56*, 4816−4820. (b) Wagner, F. F.; Olson, D. E.; Gale, J. P.; Kaya, T.; Weïwer, M.; Aidoud, N.; Thomas, M.; Davoine, E. L.; Lemercier, B. C.; Zhang, Y.-L.; Holson, E. B. Potent and selective inhibition of histone deacetylase 6 (HDAC6) does not require a surface-binding motif. *J. Med. Chem.* **2013**, *56* (4), 1772−1776.

(15) Miyake, Y.; Keusch, J. J.; Wang, L.; Saito, M.; Hess, D.; Wang, X.; Melancon, B. J.; Helquist, P.; Gut, H.; Matthias, P. Structural insights into HDAC6 tubulin deacetylation and its selective inhibition. *Nat. Chem. Biol.* **2016**, *12*, 748−754.

(16) Bhatia, S.; Diedrich, D.; Frieg, B.; Ahlert, H.; Stein, S.; Bopp, B.; Lang, F.; Zang, T.; Kroger, T.; Ernst, T.; Kogler, G.; Krieg, A.; Ludeke, S.; Kunkel, H.; Rodrigues Moita, A. J.; Kassack, M. U.; Marquardt, V.; Opitz, F. V.; Oldenburg, M.; Remke, M.; Babor, F.; Grez, M.; Hochhaus, A.; Borkhardt, A.; Groth, G.; Nagel-Steger, L.; Jose, J.; Kurz, T.; Gohlke, H.; Hansen, F. K.; Hauer, J. Targeting HSP90 dimerization via the C-terminus is effective in imatinib resistant CML and lacks the heat shock response. *Blood* **2018**, *132*, 307−320.

(17) (a) Hai, Y.; Christianson, D. W. Histone deacetylase 6 structure and molecular basis of catalysis and inhibition. *Nat. Chem. Biol.* **2016**, *12*, 741−747. (b) Porter, N. J.; Mahendran, A.; Breslow, R.; Christianson, D. W. Unusual zinc-binding mode of HDAC6-selective hydroxamate inhibitors. *Proc. Natl. Acad. Sci. U. S. A.* **2017**, *114*, 13459−13464. (c) Mackwitz, M. K. W.; Hamacher, A.; Osko, J. D.; Held, J.; Schöler, A.; Christianson, D. W.; Kassack, M. U.; Hansen, F. K. Multicomponent Synthesis and binding mode of imidazo[1,2-*a*]pyridine-capped selective HDAC6 inhibitors. *Org. Lett.* **2018**, *20*, 3255−3258. (d) Porter, N. J.; Osko, J. D.; Diedrich, D.; Kurz, T.; Hooker, J. M.; Hansen, F. K.; Christianson, D. W. Histone deacetylase 6-selective inhibitors and the influence of capping groups on hydroxamate-zinc denticity. *J. Med. Chem.* **2018**, *61*, 8054−8060.

(18) Löwe, J.; Stock, D.; Jap, B.; Zwickl, P.; Baumeister, W.; Huber, R. Crystal structure of the 20S proteasome from the archaeon T. acidophilum at 3.4 A resolution. *Science* **1995**, *268*, 533−539.

(19) Groll, M.; Ditzel, L.; Lowe, J.; Stock, D.; Bochtler, M.; Bartunik, H. D.; Huber, R. Structure of 20S proteasome from yeast at 2.4 A resolution. *Nature* **1997**, *386*, 463−471.

(20) Stein, M. L.; Cui, H.; Beck, P.; Dubiella, C.; Voss, C.; Kruger, A.; Schmidt, B.; Groll, M. Systematic comparison of peptidic proteasome inhibitors highlights the alpha-ketoamide electrophile as an auspicious reversible lead motif. *Angew. Chem., Int. Ed.* **2014**, *53*, 1679−1683.

(21) Huber, E. M.; Heinemeyer, W.; Li, X.; Arendt, C. S.; Hochstrasser, M.; Groll, M. A unified mechanism for proteolysis and autocatalytic activation in the 20S proteasome. *Nat. Commun.* **2016**, *7*, 10900.

(22) Borissenko, L.; Groll, M. 20S proteasome and its inhibitors: crystallographic knowledge for drug development. *Chem. Rev.* **2007**, *107*, 687−717.

(23) Morphy, R.; Kay, C.; Rankovic, Z. From magic bullets to designed multiple ligands. *Drug Discovery Today* **2004**, *9*, 641−651.

(24) Mokhtari, R. B.; Homayouni, T. S.; Baluch, N.; Morgatskaya, E.; Kumar, S.; Das, B.; Yeger, H. Combination therapy in combating cancer. *Oncotarget* **2017**, *8*, 38022−38043.

(25) Hideshima, T.; Bradner, J. E.; Wong, J.; Chauhan, D.; Richardson, P.; Schreiber, S. L.; Anderson, K. C. Small-molecule inhibition of proteasome and aggresome function induces synergistic antitumor activity in multiple myeloma. *Proc. Natl. Acad. Sci. U. S. A.* **2005**, *102*, 8567−8572.

(26) Delic, J.; Morange, M.; Magdelenat, H. Ubiquitin pathway involvement in human lymphocyte gamma-irradiation-induced apoptosis. *Mol. Cell. Biol.* **1993**, *13*, 4875−4883.

(27) Vogl, D. T.; Raje, N.; Jagannath, S.; Richardson, P.; Hari, P.; Orlowski, R.; Supko, J. G.; Tamang, D.; Yang, M.; Jones, S. S.; Wheeler, C.; Markelewicz, R. J.; Lonial, S. Ricolinostat, the first selective histone deacetylase 6 inhibitor, in combination with bortezomib and dexamethasone for relapsed or refractory multiple myeloma. *Clin. Cancer Res.* **2017**, *23*, 3307−3315.

(28) Zhou, W.; Zhu, W.; Ma, L.; Xiao, F.; Qian, W. Proteasome inhibitor MG-132 enhances histone deacetylase inhibitor SAHA-induced cell death of chronic myeloid leukemia cells by an ROS-mediated mechanism and downregulation of the Bcr-Abl fusion protein. *Oncol. Lett.* **2015**, *10*, 2899−2904.

(29) Kalin, J. H.; Bergman, J. A. Development and therapeutic implications of selective histone deacetylase 6 inhibitors. *J. Med. Chem.* **2013**, *56*, 6297−6313.

DOI: 10.1021/acs.jmedchem.8b01487
J. Med. Chem. XXXX, XXX, XXX−XXX

Journal of Medicinal Chemistry

pubs.acs.org/jmc Article

Solid-Phase Synthesis of Cereblon-Recruiting Selective Histone Deacetylase 6 Degraders (HDAC6 PROTACs) with Antileukemic Activity

Published as part of the Journal of Medicinal Chemistry virtual special issue "New Drug Modalities in Medicinal Chemistry, Pharmacology, and Translational Science".

Laura Sinatra,[#] Jing Yang,[#] Julian Schliehe-Diecks, Niklas Dienstbier, Melina Vogt, Philip Gebing, Luisa M. Bachmann, Melf Sönnichsen, Thomas Lenz, Kai Stühler, Andrea Schöler, Arndt Borkhardt, Sanil Bhatia,* and Finn K. Hansen*

Cite This: https://doi.org/10.1021/acs.jmedchem.2c01659 Read Online

ABSTRACT: In this work, we utilized the proteolysis targeting chimera (PROTAC) technology to achieve the chemical knockdown of histone deacetylase 6 (HDAC6). Two series of cereblon-recruiting PROTACs were synthesized via a solid-phase parallel synthesis approach, which allowed the rapid preparation of two HDAC6 degrader mini libraries. The PROTACs were either based on an unselective vorinostat-like HDAC ligand or derived from a selective HDAC6 inhibitor. Notably, both PROTAC series demonstrated selective degradation of HDAC6 in leukemia cell lines. The best degraders from each series (denoted **A6** and **B4**) were capable of degrading HDAC6 via ternary complex formation and the ubiquitin−proteasome pathway, with DC_{50} values of 3.5 and 19.4 nM, respectively. PROTAC **A6** demonstrated promising antiproliferative activity via inducing apoptosis in myeloid leukemia cell lines. These findings highlight the potential of this series of degraders as effective pharmacological tools for the targeted degradation of HDAC6.

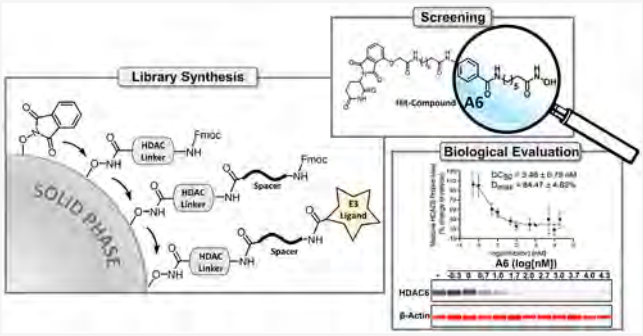

INTRODUCTION

The emerging technology of *pro*teolysis *ta*rgeting *c*himeras (PROTACs) opens new paths to modulate and study proteins for potential therapeutic approaches. PROTACs are molecules of bifunctional nature, incorporating two ligands, one for E3 ubiquitin ligase binding and one for the protein of interest (POI) binding, connected through a linker with variable length and chemical properties.[1−3] Once the chimeric molecule binds to the E3 ligase and the POI, an E3 ligase:PROTAC:POI ternary complex is formed, thereby inducing polyubiquitination of the POI and its subsequent degradation via the proteasome (Figure 1A). In recent years many efforts have been undertaken to drug new targets by targeted protein degradation and to develop new E3 ligase recruiting ligands.[4−6] In 2019, the first PROTAC entered clinical trials and the most advanced PROTACs bavdegalutamide (ARV-110, an androgen receptor degrader) and ARV-471 (an estrogen receptor degrader) have already reached phase II trials and showed promising early data in terms of tolerability, safety, and efficacy.[7,8] More than 10 targeted protein degraders had reached the clinic by the end of 2021[9] which underscores the vast potential of PROTACs and other targeted protein degraders as new therapeutic modalities.

Histone deacetylases (HDACs) are key players in the epigenetic network regulating the transcription of numerous proteins and many processes by removing acetyl and other acyl groups from histones as well as nonhistone proteins.[10,11] To date, 18 human HDAC isoforms have been identified: The Zn^{2+}-dependent HDACs, subdivided into three classes, including class I (HDAC1, -2, -3, -8), II (class IIa: HDAC4, -5, -7, -9; class IIb: HDAC6, -10), and IV (HDAC11) and the NAD^+-dependent class III enzymes (sirtuins 1−7).[12] Class I HDACs, mostly localized in the nucleus, are ubiquitously expressed and play a crucial role in cell survival and proliferation, whereas class II HDACs are expressed more

Received: October 12, 2022

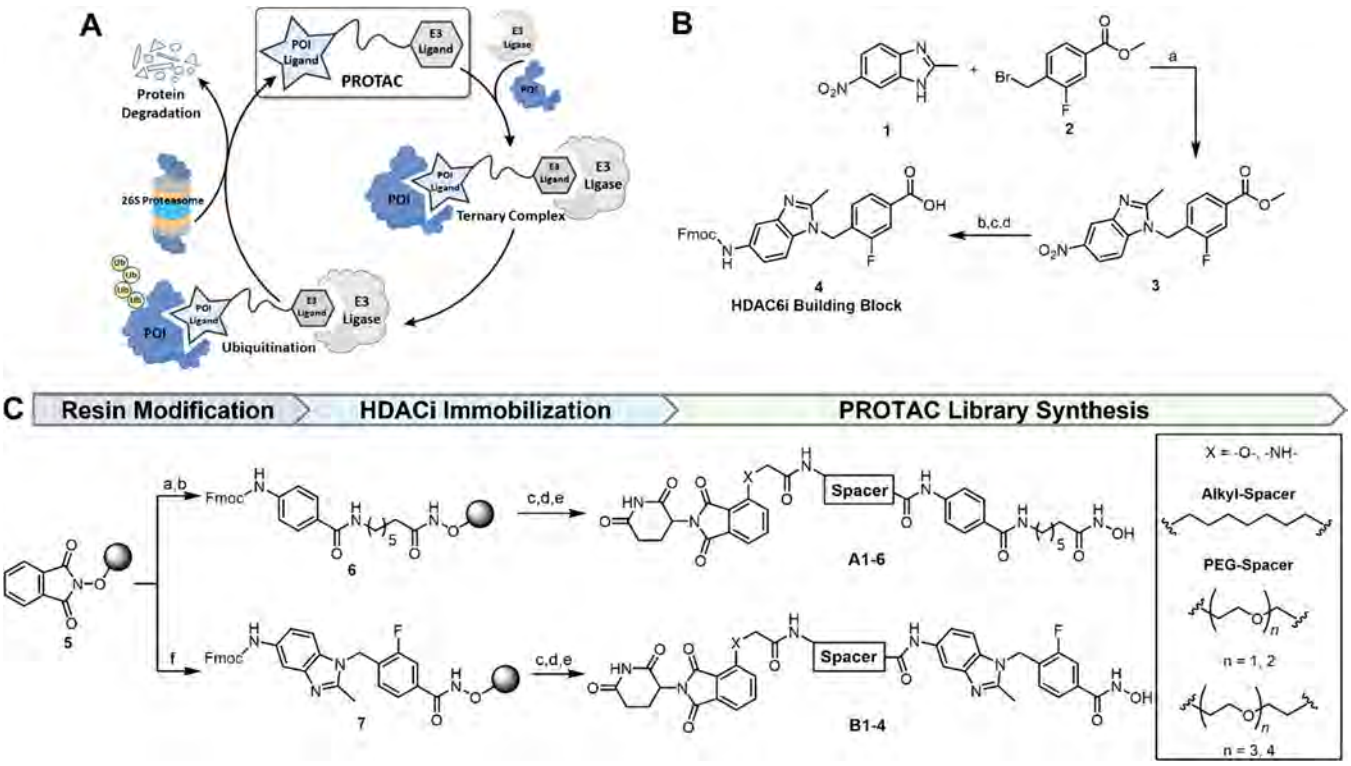

Figure 1. A. Schematic representation of the POI degradation mediated by a PROTAC. B. Solution-phase synthesis of the HDAC6i building block **4**: (a) Cs_2CO_3 (2.0 equiv), DMF, 80 °C, 2 h, 44%. (b) H_2, 10% Pd/C, MeOH/CH_2Cl_2 (5:1), rt, 4 h. (c) $NaOH_{aq}$ (4.0 equiv), THF/MeOH (5:1), rt, 2 h. (d) Fmoc-Cl (1.5 equiv), 5% $Na_2CO_{3\ aq}$/1,4-dioxane (3:2), 0 °C to rt, 18 h, 82% over three steps. C. Solid-phase synthesis of the first (**A1**−**6**) and second (**B1**−**4**) series of PROTACs: (a) i. 5% $N_2H_4{\cdot}H_2O$ in MeOH, rt, 2 × 15 min, ii. Fmoc-7-aminoheptanoic acid (2.0 equiv) HATU (2.0 equiv), HOBt·H_2O (2.0 equiv), DIPEA (3.0 equiv) DMF, rt, 20 h, loading determined: 0.77−0.97 mmol/g. (b) i. 20% piperidine, DMF, 2 × 5 min, ii. Fmoc-4-aminobenzoic acid (3.0 equiv), HATU (3.0 equiv), DIPEA (4.0 equiv), DMF, rt, 20 h. (c) i. 20% piperidine, DMF, 2 × 5 min, ii. Fmoc-spacer-COOH (3.0 equiv), HATU (3.0 equiv), DIPEA (4.0 equiv), DMF, rt, 4 h. (d) i. 20% piperidine, DMF, 2 × 5 min, ii. thalidomide-X-CH_2COOH building block (2.0 equiv), HATU (2.2 equiv), DIPEA (3.5 equiv), DMF, rt, 4 h, (e) 5% TFA, CH_2Cl_2, rt, 1 h, 27−71% over all solid-phase steps. (f) i. 5% $N_2H_4{\cdot}H_2O$ in MeOH, rt, 2 × 15 min, ii. **4** (2.0 equiv), HATU (2.0 equiv), HOBt·H_2O (2.0 equiv), DIPEA (3.0 equiv), DMF, rt, 20 h, loading determined: 0.60−0.62 mmol/g.

tissue specifically and can shuttle between the nucleus and cytoplasm.[13] An overexpression of HDACs is linked to various diseases including solid and hematological malignancies.[14] The efficacy of HDAC inhibitors (HDACi), especially of non-selective inhibitors, as anticancer agents has been widely proved.[15−18] However, pan-HDACi often possess serious adverse effects. Consequently, the development of selective HDACi, particularly HDAC6 selective inhibitors, is increasingly of interest to optimize the risk−benefit profile of HDACi.[19] However, besides the crucial catalytic functions mediated via the HDAC6 catalytic domain (CD2), HDAC6 can also influence cellular processes via the more enigmatic first catalytic domain (CD1) and the unique zinc-finger ubiquitin binding domain (ZnF-UBP), both of which are not inhibited by classical HDAC6 selective inhibitors.[20,21] Hence, the targeted degradation of HDAC6 may be advantageous over the well-established selective HDAC6 CD2 inhibition, because this approach eliminates both catalytic domains as well as the ubiquitin binding domain.[20]

The development of HDAC degraders is of emerging interest, and a few HDAC degraders were disclosed in recent years.[22−37] In 2017, Schiedel et al. described the first degraders of sirtuin 2 (Sirt2).[22] The first degraders of a Zn^{2+}-dependent HDAC were reported in 2018 by Yang et al. by utilizing pomalidomide as a recruiter for the E3 ligase cereblon (CRBN) and the unselective HDACi crebinostat as POI ligand.[23] Somewhat surprisingly, despite the unselective HDACi scaffold, the PROTACs achieved selective degradation of HDAC6. Subsequently, additional selective HDAC6 degraders were discovered based on the selective HDAC6i nexturastat A.[30−33,35] These findings raise the intriguing question, whether a selective or unselective HDAC6 ligand is superior to develop highly efficient and selective HDAC6 degraders. Even though most work on HDAC PROTACs has focused on HDAC6,[38] the first degraders of HDAC1, HDAC2, and/or HDAC3 utilizing a hydrazide or aminoanilide zinc-binding group were recently disclosed.[24,28,36,37] Furthermore, in 2022, the first selective HDAC4[39] and HDAC8[27,29,40] PROTACs were reported. Interestingly, a chemoproteomics study by Xiong et al. demonstrated that HDAC6 and HDAC3 are most amenable for targeted protein degradation.[26]

Degradation efficiency of PROTACs depends on multiple factors. One critical factor is the formation of the ternary complex, which still remains empirical and difficult to predict by rational design.[41] Thus, efficient synthesis protocols allowing the rapid preparation of different PROTACs with altered linker types and E3 ligase as well as POI ligands are an urgent need for hit optimization. Here we report a facile and straightforward synthetic gateway toward HDAC6 PROTACs using a combination of solution- and solid-phase chemistry. The synthesized PROTACs induced significant and selective degradation of HDAC6 in leukemia cells. The degradation

https://doi.org/10.1021/acs.jmedchem.2c01659
J. Med. Chem. XXXX, XXX, XXX−XXX

Table 1. In Vitro Inhibition of HDAC1 and -6 by the PROTACs A1−7 and B1−4

Code	Structure	HDAC Inhibition IC_{50} [μM] HDAC1	HDAC Inhibition IC_{50} [μM] HDAC6	SI	Code	Structure	HDAC Inhibition IC_{50} [μM] HDAC1	HDAC Inhibition IC_{50} [μM] HDAC6	SI
A1	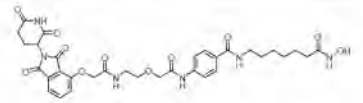	0.155 ± 0.027	0.012 ± 0.001	13	A7	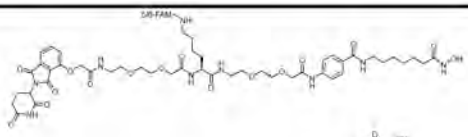	0.144 ± 0.009	0.0156 ± 0.0004	9
A2	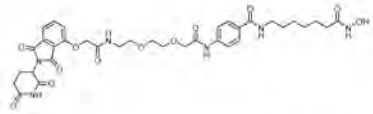	0.174 ± 0.009	0.0268 ± 0.0004	6	B1	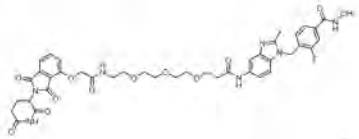	1.314 ± 0.134	0.0134 ± 0.0007	101
A3	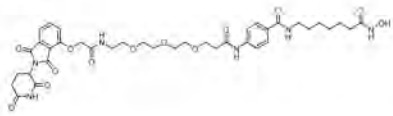	0.161 ± 0.015	0.017 ± 0.002	10	B2		1.494 ± 0.032	0.015 ± 0.001	100
A4		0.208 ± 0.005	0.0208 ± 0.0008	10	B3		1.420 ± 0.054	0.013 ± 0.001	110
A5	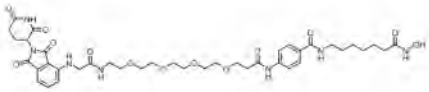	0.186 ± 0.018	0.015 ± 0.001	12	B4	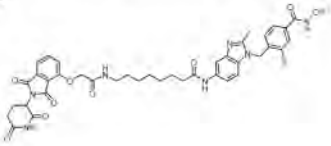	0.647 ± 0.087	0.00454 ± 0.0004	129
A6	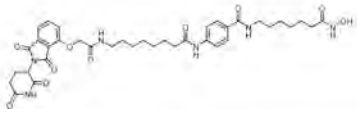	0.100 ± 0.011	0.00486 ± 0.0003	20	SAHA		0.088 ± 0.013	0.027 ± 0.007	3

efficiency and kinetics of the most promising degraders were further analyzed by automated capillary Western blot, fluorescence microscopy, and endogenously tagged HiBiT-HDAC6 K562 cells. The biological evaluation of the best degrader included viability, apoptosis, and caspase 3/7 assays as well as cell cycle analysis.

■ RESULTS AND DISCUSSION

Design and Synthesis of HDAC6 Degraders. To investigate whether a selective or an unselective HDAC ligand is superior for efficient and selective HDAC6 degradation, we designed two series of HDAC6 degraders. In the first series (**A1−6**), we utilized a vorinostat-like HDAC ligand based on an alkyl linker. In the second series (**B1−4**), we chose a selective benzimidazole-based HDAC6 ligand, which was derived from a selective HDAC6i reported by Shen et al.[42] For HDAC6i building block synthesis (Figure 1B), 2-methyl-6-nitro-1*H*-benzo[*d*]imidazole (**1**) was alkylated with methyl 4-(bromomethyl)-3-fluorobenzoate (**2**), yielding the intermediate **3**, which was separated from its minor regioisomer featuring the nitro group in the 6-position. The major isomer **3** was further treated in a reaction sequence including reduction of the nitro group, saponification of the ester, and Fmoc-protection without any purification steps in between to afford the Fmoc-protected building block **4**.

The designed PROTACs were synthesized following our previously published approach using hydroxamic acids immobilized on resins (HAIRs).[34] In detail, the preloaded resins were prepared by immobilization of hydroxylamine on commercially available 2-chlorotrityl chloride (2-CTC) resin, followed by coupling of the Fmoc-protected HDACi moieties. The synthesis of the first series (**A1−6**) was completely carried out on resin. To this end, the readily available phthaloyl-protected resin **5** was deprotected by treatment with hydrazine hydrate followed by an amide coupling with Fmoc-7-aminoheptanoic acid. The subsequent Fmoc deprotection and amide coupling with Fmoc-4-aminobenzoic acid afforded the preloaded resin **6** (Figure 1C). In contrast, the resin-bound benzimidazole-based HDAC6 ligand **7**, used for the synthesis of the second series of PROTACs (**B1−4**), was generated by immobilization of the previously synthesized building block **4**. Library synthesis of the desired PROTACs **A1−6** and **B1−4** was carried out starting from **6** or **7** using a solid-phase supported parallel synthesis approach. In the first step, we introduced different PEG-based linkers or 8-aminooctanoic acid as spacer moiety into both series (Figure 1C). For the E3 ligase-recruiting part, we chose the CRBN ligands hydroxythalidomide and pomalidomide, which were synthesized using modified literature known procedures, carrying an additional acetic acid residue for the following solid-phase approach.[43,44] Coupling of the E3 ligase component completed the PROTAC synthesis. The cleavage from the resin under gentle conditions generated the hydroxamic acids **A1−6** and **B1−4** in excellent crude purities of up to 91%. Before the biological evaluation, the compounds were further purified by preparative RP-HPLC to >95% purity, yielding the final PROTACs in total yields of 27−71%. Taken together, this synthetic strategy enabled PROTAC library generation in a highly time efficient fashion.

In Vitro HDAC Inhibition Assays. The synthesized PROTACs were first screened in biochemical assays to investigate their inhibition of HDAC1 and -6. The results are summarized in Table 1. All compounds from both series demonstrated potent inhibition of HDAC6 with IC_{50} values in double- or even single-digit nanomolar concentration range. As expected, the vorinostat-like derivatives of type **A1−6** turned out to be unselective inhibitors and also showed potent

https://doi.org/10.1021/acs.jmedchem.2c01659
J. Med. Chem. XXXX, XXX, XXX−XXX

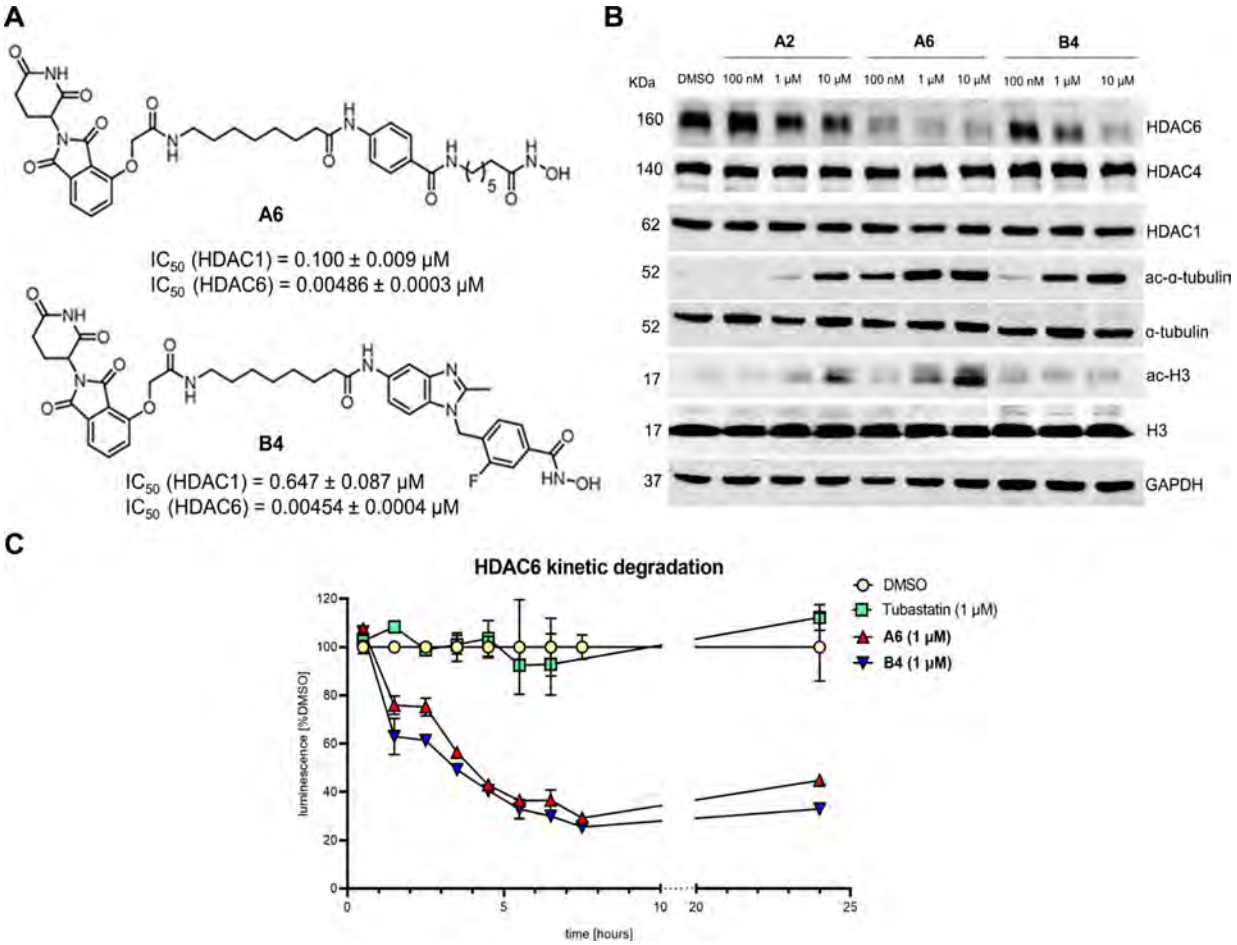

Figure 2. A. Structures of compounds **A6** and **B4**, which were selected for further biological evaluation. B. HL-60 cells were treated with 100 nM, 1 μM, 10 μM of **A2**, **A6**, **B4** for 6 h. Afterward, cell lysates were immunoblotted with anti-HDAC6, HDAC4, HDAC1, acetyl-α-tubulin, acetyl-histone H3, total α-tubulin, and total histone H3 antibodies. GAPDH was used as a loading control. C. Kinetic degradation of HDAC6 levels upon incubation with **A6** or **B4** (1 μM) in HiBit-tagged K562 cells, whereas tubastatin (1 μM) and DMSO served as a negative control. The luminescence was measured using Nano-Glo HiBit lytic detection system (n = 3).

inhibition of HDAC1, leading to selective indices ($SI^{1/6}$) ranging from 6 to 20. In contrast, the compounds from the benzimidazole series (**B1−4**) displayed high selectivity for HDAC6 ($SI^{1/6}$ = 100−129).

Selection and In Vitro Functional Evaluation of PROTACs. In the next step, all PROTACs were analyzed regarding their potential to degrade HDAC6 in the cellular context. To this end, HL-60 leukemia cells were treated for 6 or 24 h with different concentrations (0.1, 1, and 10 μM) of each PROTAC and subsequently investigated by Western blot in regards to degradation of HDAC1 and HDAC6 as well as hyperacetylation of α-tubulin (Figures S1−4, Supporting Information). Independent of the concentration used and the incubation time, there was no change observed in the protein level of HDAC1. In contrast, all PROTACs were able to reduce the HDAC6 levels although with different efficiency. Interestingly, in both series the PROTACs containing 8-aminooctanoic acid as linker moiety (**A6** and **B4**) demonstrated the most potent degradation of HDAC6 and the strongest hyperacetylation of α-tubulin, which is a marker of decreased HDAC6 activity. Consequently, both degraders were selected for a detailed biological investigation (Figure 2A).

In the first step, we compared the degradation efficiency of **A6** with our previously published prototypic HDAC6 degrader **A2**.[34] **A2** and **A6** are identical in terms of the HDAC warhead and E3 ligase ligand as well as chain length of the PROTAC linker. However, they differ in the linker type. Western blot experiments demonstrated that the HDAC6 degradation efficiency was clearly improved when the PEG-based linker present in **A2** (see Table S1) was replaced by the 8-aminooctanoic acid linker, as utilized in the case of **A6**. We calculated the physiochemical properties of PROTACs **A1−6** and **B1−4** using SwissADME (Table S1, Supporting Information). **A6** (log P: 2.37) displayed a significantly higher calculated log P value than **A2** (log P: 0.63) which makes it reasonable to assume that the improved degradation of HDAC6 arises from improved permeability due to a higher lipophilicity. When **A6** was analyzed head to head with the most potent PROTAC from the benzimidazole series (**B4**), **A6** turned out to be the slightly more efficient HDAC6 degrader (Figure 2B). Of note, no reduction of HDAC1 (as a representative class I isoform) and HDAC4 (as a representative class IIa isoform) protein levels was observed, demonstrating that **A6** and **B4** are potent and selective HDAC6 PROTACs (Figure 2B). On the other hand, while both compounds were capable of inducing hyperacetylation of α-

https://doi.org/10.1021/acs.jmedchem.2c01659
J. Med. Chem. XXXX, XXX, XXX−XXX

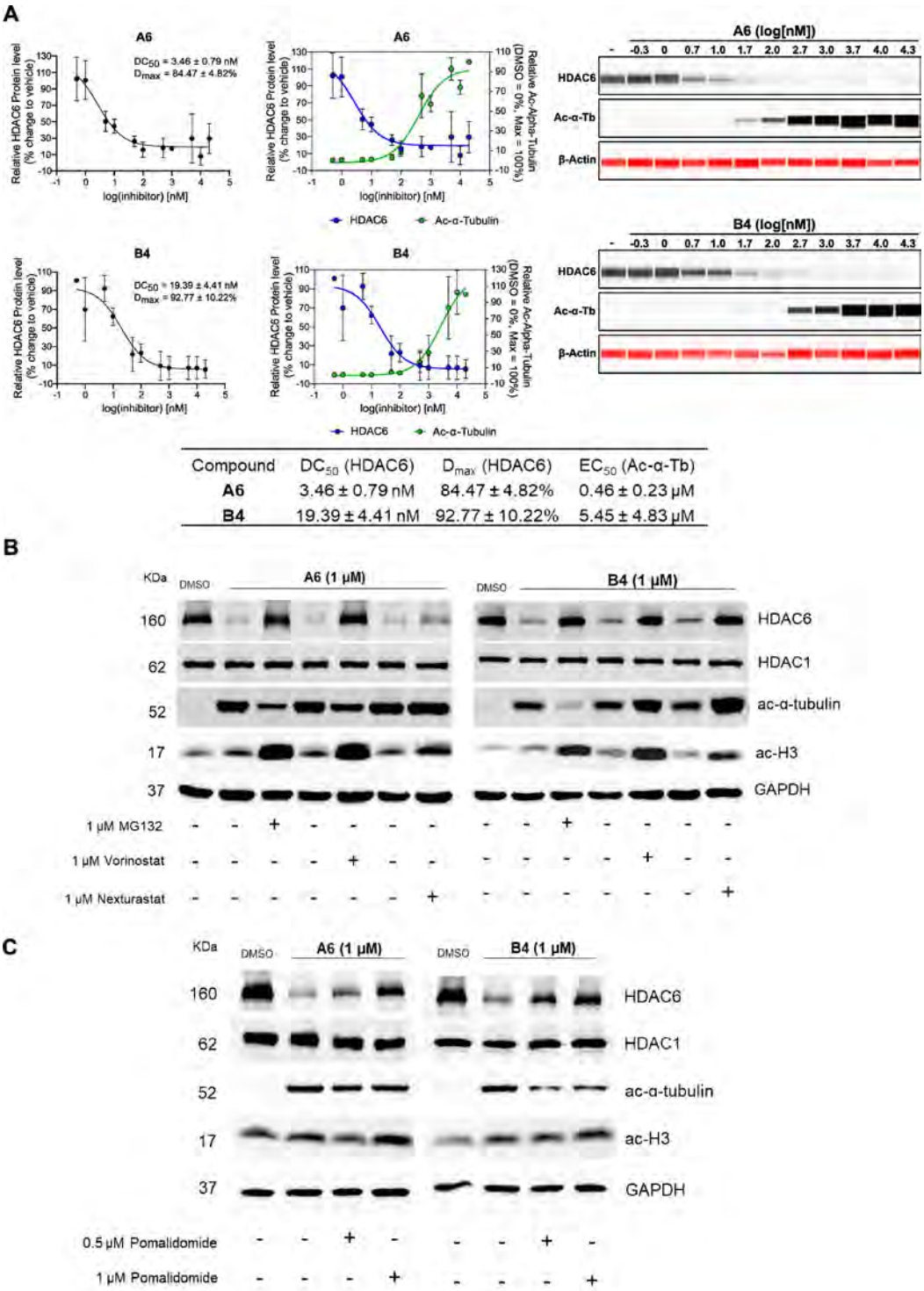

Compound	DC_{50} (HDAC6)	D_{max} (HDAC6)	EC_{50} (Ac-α-Tb)
A6	3.46 ± 0.79 nM	84.47 ± 4.82%	0.46 ± 0.23 μM
B4	19.39 ± 4.41 nM	92.77 ± 10.22%	5.45 ± 4.83 μM

Figure 3. A. Quantitative simple western immunoassay shows dose-dependent degradation of HDAC6 with subsequent increased levels of acetyl-α-tubulin. HL-60 cells were treated with the indicated concentrations of **A6** or **B4** for 6 h, and the resulting lysates (0.40 μg/sample) were analyzed utilizing simple western immunoassay technology (BioTechne). Samples were quantified by normalizing the area under the curve (AUC) values of the electropherogram from the vehicle control. DC_{50} and D_{max} were calculated using nonlinear regression (log(inhibitor) vs response (three parameters)). EC_{50} for α-tubulin hyperacetylation was calculated using nonlinear regression (log(agonist) vs normalized response−variable slope). Average DC_{50}, D_{max}, and EC_{50} values were calculated from three independent simple western immunoassay runs on the treated samples from two independent biological replicates. A representative immunoblot is depicted here. B. HL-60 cells were pretreated with vehicle (DMSO), MG132, vorinostat, or nexturastat A (1 μM) for 1 h, followed by treatment with **A6**, **B4** (1 μM), or DMSO for 6 h. Afterward, cell lysates were immunoblotted with anti-HDAC6, HDAC1, acetyl-α-tubulin, and acetyl-histone H3 antibodies. GAPDH was used as a loading control. C. HL-60 cells were pretreated with pomalidomide (0.5 μM or 1 μM) or vehicle (DMSO) for 1 h, followed by treatment with **A6**, **B4** (1 μM), or vehicle (DMSO) for 6 h. Afterward, cell lysates were immunoblotted with anti-HDAC6, HDAC1, acetyl-α-tubulin, and acetyl-histone H3 antibodies. GAPDH was used as a loading control.

https://doi.org/10.1021/acs.jmedchem.2c01659
J. Med. Chem. XXXX, XXX, XXX−XXX

tubulin in HL-60 cells, only **A6**, but not **B4**, caused hyperacetylation of histone H3. Because **A6** did not degrade HDAC1 (Figure 2B) but displayed submicromolar inhibitory activity toward HDAC1 (IC_{50}: 0.100 μM, Table 1), we assume that the observed hyperacetylation of histone H3 originates from unselective HDAC inhibition and not from degradation. These results indicate that the selectivity for increasing the level of acetylated tubulin over acetylated histone H3 can be improved by replacing an unselective HDACi by a selective HDAC6i as the HDAC6 ligand in PROTACs. These findings are in excellent agreement with the report of Tang and co-workers who showed that PROTACs based on the pan-HDACi crebinostat caused hyperacetylation of α-tubulin and histone H3, whereas PROTACs based on the HDAC6-selective inhibitor nexturastat A demonstrated selective hyperacetylation of α-tubulin.[45] Next, we evaluated the kinetics of HDAC6 degradation by generating (endogenous) HDAC6-fused HiBit[46] K562 cells and measured the degradation efficiency after incubation with **A6** or **B4** with a luminescent-based assay. The degradation profiles of both degraders were similar with comparable D_{max} values, and the most pronounced reduction of HDAC6 levels was observed in both cases between 5.5 and 7.5 h after treatment (Figure 2C). Furthermore, **A6** and **B4** (at 100 nM and 1000 nM) demonstrated potent HDAC6 degradation as well as hyper-acetylation of α-tubulin in a multiple myeloma cell line U266, thereby confirming that the activity of these degrader is not restricted to leukemia cell lines (Figure S5, Supporting Information). Next, we performed a quantitative mass spectrometry (MS) analysis to determine the effects of PROTACs on the global cellular proteome. Overall, we found no significant changes in protein expression pattern (4331 proteins identified with two or more Razor + unique peptides) after 6 h PROTAC treatment (**A6** or **B4** at 1 μM, Figure S6A,B, Supporting Information). In line with the immunoblot analysis (Figure 2B), HDAC6 was identified only in the cells that were not treated with the PROTACs (Table S2, Supporting Information). However, because of the small number of observations (one MS/MS count, respectively, in three of the five untreated replicates; three unique peptides in total), we did not perform a quantitative interpretation of HDAC6's MS data (Figure S6C and Table S3, Supporting Information). With regard to other HDAC related proteins (HDAC1−11, SIRT1−7, and HDRP), HDAC1/2/3/6/7/10 and SIRT1/2/3/5/6 were identified, of which HDAC1/2 and SIRT5 were reliably quantifiable but were not affected by the PROTACs (Table S2, Supporting Information).

Next, the degradation efficiency of **A6** and **B4** was quantified by automated capillary Western blot utilizing the simple western immunoassay technology (Figure 3A and Figure S7, Supporting Information). Both PROTACs revealed DC_{50} values for HDAC6 in the low nanomolar range and D_{max} values of over 80%. Degrader **A6** (DC_{50}: 3.5 nM) was slightly more efficient compared to **B4** (DC_{50}:19.4 nM). In addition, HDAC6 degradation was accompanied with dose-dependent α-tubulin hyperacetylation with an EC_{50} of 0.4 μM and 5.5 μM for **A6** and **B4**, respectively. Interestingly, **B4** required a higher concentration to induce α-tubulin hyperacetylation than **A6**. However, both HDAC6 inhibition and HDAC6 degradation contribute to the α-tubulin hyperacetylation. Keeping in mind that both compounds reduced HDAC6 levels to ∼10−15%, there is still HDAC6 available which can be inhibited. Differences in the intracellular target engagement of HDAC6 by **A6** and **B4** might explain the observed differences in the α-tubulin hyperacetylation in the quantitative simple western immunoassays (Figure 3A), which were also confirmed by classical Western blot experiments (Figure 2B).

Additional Western blot experiments were performed to confirm that the ubiquitin−proteasome system is involved in the decrease of HDAC6 protein levels. The pretreatment of HL-60 cells with the proteasome inhibitor MG132 for 1 h followed by the addition of PROTACs **A6** or **B4** inhibited the degradation of HDAC6 (Figure 3B). Moreover, pretreatment of HL-60 cells for 1 h with either the pan-HDACi vorinostat or the selective HDAC6i nexturastat A before treatment with **A6** or **B4** also rescued HDAC6 from degradation (Figure 3B). These results indicate that the formation of the CRBN:PROTAC:HDAC6 ternary complex, which was blocked by the respective HDACi, is crucial for HDAC6 degradation. Similarly, degradation of HDAC6 was rescued by pretreatment with the CRBN ligand pomalidomide (Figure 3C). Taken together, these data demonstrate that the degradation of HDAC6 occurs via the ternary complex formation and ubiquitin−proteasome pathway.

Fluorescence Microscopy. The degradation efficiency of the most potent degrader **A6** was further investigated by fluorescence microscopy (Figure 4). HL-60 cells were treated with either 100 nM or 1 μM **A6** for 3 and 6 h, after which they

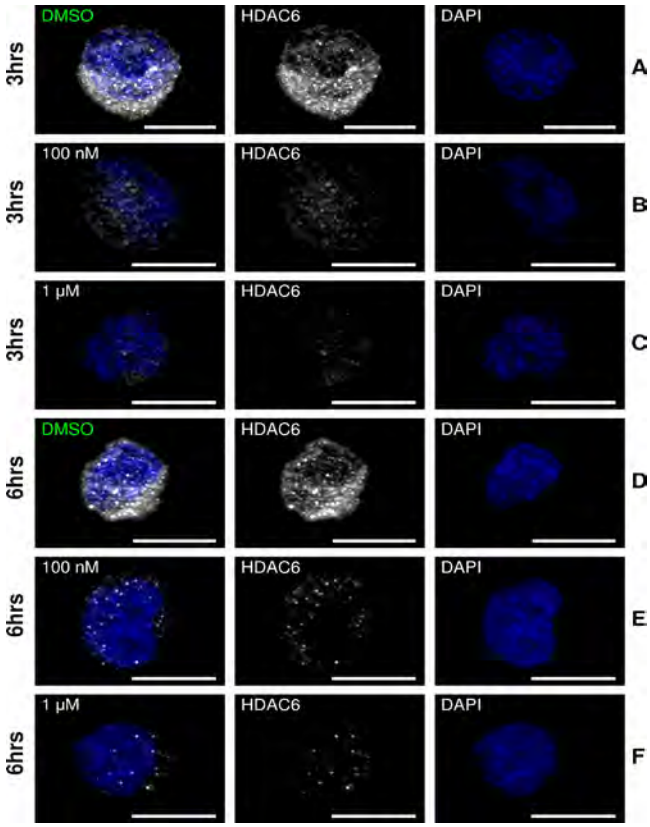

Figure 4. HDAC6 is degraded in HL-60 cells treated with 100 nM and 1 μM **A6** for 3 and 6 h. Row A/D: HL-60 cells treated control. Row B,C,E,F: HL-60 cells were treated with either 100 nM and 1 μM concentrations of **A6** for 3 or 6 h. All samples were stained with an anti-HDAC6 antibody (white), as well as DAPI nuclear stain (blue). HDAC6 is visibly reduced when treated with **A6** for both 3 and 6 h. Brightness and contrast were adjusted equally for all images. Scale bar = 10 μm.

https://doi.org/10.1021/acs.jmedchem.2c01659
J. Med. Chem. XXXX, XXX, XXX−XXX

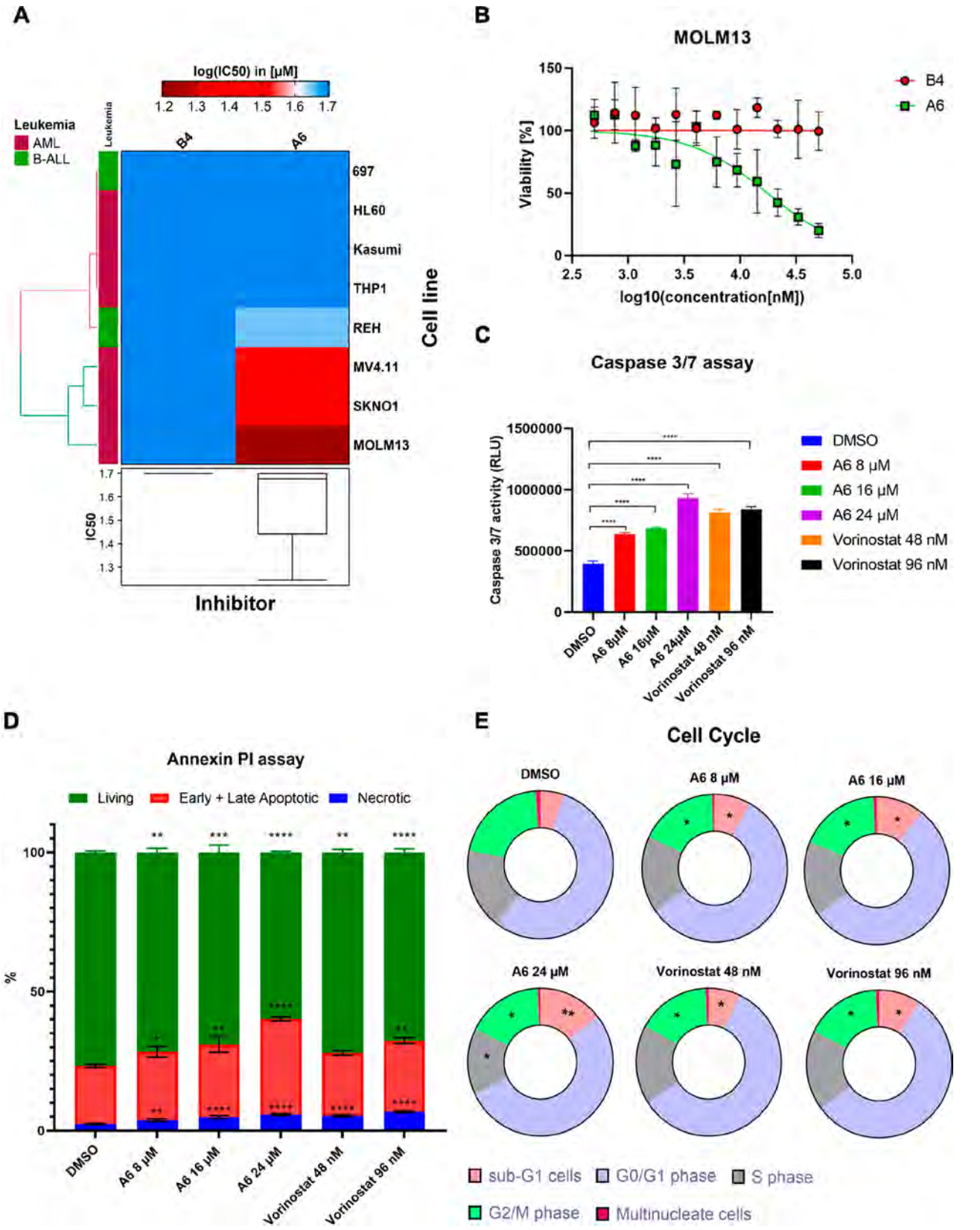

Figure 5. A. Comparative cellular viability (log IC_{50} (nM)) of different subgroups of leukemic cell lines (697, HL-60, KASUMI-1, MV4-11, REH, THP-1, SKNO-1, MOLM-13) after exposure to **A6** or **B4** for 72 h (n = 3). The IC_{50} data are plotted as a clustered heat map, followed by unsupervised hierarchical clustering. The vertical axis of the dendogram exemplifies the dissimilarity between clusters, whereas the color of the cell is related to its position along a log IC_{50} (nM) gradient. The boxplot shows the median IC_{50} (log IC_{50} (nM)) of the respective degrader across all tested leukemic cell lines. B. IC_{50} values of **A6** and **B4** in leukemia cell lines used in clustered heat map were calculated using nonlinear regression (log(antagonist) vs normalized response−variable slope). Representative example of MOLM13 regression curves shown here. C. MOLM-13 cells were treated with indicated concentrations of **A6**, vorinostat, or vehicle (DMSO) for 48 h. Treated cells were incubated with caspase-Glo 3/7

https://doi.org/10.1021/acs.jmedchem.2c01659
J. Med. Chem. XXXX, XXX, XXX−XXX

Figure 5. continued

substrate, and the enzymatic activity of caspase 3/7 was then examined by using a microplate reader (n = 3). D. MOLM-13-treated (48 h) cells with indicated concentrations of **A6**, vorinostat, or vehicle (DMSO) were stained with annexin V and propidium iodide (PI), and the apoptosis induced by these treatments was then assessed by flow cytometry analysis (n = 3). E. MOLM-13-treated (48 h) cells with indicated concentrations of **A6**, vorinostat, or vehicle (DMSO) were stained with PI. The effect of these treatments on the cell cycle were then assessed by flow cytometry analysis (n = 3). Significance analyses of normally distributed data with variance similar between groups, using paired, two-tailed Student's t test (*P < 0.05, **P < 0.01, ***P < 0.001, ****P < 0.0001).

were fixed and stained with anti-HDAC6 antibody to measure changes in HDAC6 signal intensity. We recorded z-stacks for all images with a conserved z-step size to create maximum intensity projections of each cell, which enabled us to display HDAC6 signals from the entire cell volume. Of note, acquisition settings were conserved between all the conditions. We observed that 3 h treatment with **A6** at 100 nM was sufficient to degrade HDAC6 as seen by the reduction in fluorescence intensity (Figure 4A−C). Extending the incubation period from 3 to 6 h appears to have a marginal effect on the HDAC6 signal (Figure 4A−C vs D−F). Furthermore, smaller differences in HDAC6 signals were visible when HL-60 cells were treated with 1 μM of **A6** (i.e., 10-fold higher). In line with the Western blot results, no change in the levels of HDAC1 was observed by fluorescence microscopy after 3 or 6 h treatment with either 100 nM or 1 μM **A6** (Figure S8, Supporting Information).

Next, to study the intracellular localization of our HDAC degraders, we synthesized the fluorescently tagged PROTAC **A7** (Figure S6, Supporting Information) by incorporating a fluorescein-labeled lysine in the middle of the PROTAC linker. HL-60 cells were treated with either 1, 10, or 50 nM concentrations of **A7** for 6 h. The signal intensity of HDAC6 did not change significantly when HL-60 cells were treated with 1 or 10 nM **A7**, whereas, 50 nM **A7** significantly reduced HDAC6 levels (Figure S6D, Supporting Information). However, the localization of HDAC6 was changed even at lower concentrations of **A7** (i.e., 1, 10, and 50 nM), as the dot-like signals for HDAC6 were more detached from the nuclear−cytoplasmic interface, when compared to the DMSO control (Figure S9, Supporting Information). We also paid close attention to the localization of our fluorescent compound **A7**. However, in contrast to changes in the HDAC6 intracellular localization, the colocalization of **A7** was not detected conclusively in the nucleus (Figure S9, Supporting Information).

Efficacy of A6 and B4 against Leukemia Cell Lines. After identifying **A6** and **B4** as the lead PROTACs that effectively reduced the HDAC6 levels, we further investigated their antileukemic activity. At first, we investigated the effect of **A6** and **B4** exposure on the cell viability of leukemia cell lines originated from different therapy refractory subgroups of acute myeloid leukemia or AML (HL-60, Kasumi, THP-1, HL-60, SKNO1, and MOLM13) and B-cell acute lymphoblastic leukemia or B-ALL (REH and 697), using an ATP-Glo based assay (Figure 5A,B and Table S4, Supporting Information). Exposure to **B4** did not display any inhibitory effects on the cellular viability of any tested leukemia cell line in the 0.5−50 μM concentration range, whereas **A6** revealed IC_{50} values in the double-digit micromolar range in three of the AML cell lines (MV4−11, SKNO-1, and MOLM13). The low effects of **B4** (a selective HDAC6 degrader and selective HDAC6 inhibitor) on the cellular viability is in agreement with recent reports that selective HDAC6 inhibitors do not show antiproliferative activities when used at selective concentrations.[47,48] The reduced cytotoxicity of **A6** (a selective HDAC6 degrader and unselective HDAC inhibitor) compared to vorinostat and nexturastat A is somewhat surprising, because its inhibitory properties against class I isoforms (similar HDAC1 inhibitory activity as vorinostat, see Table 1) should lead to more pronounced antiproliferative properties. For assessing the nuclear permeability **A6** vs vorinostat, HL60 cells were treated with vorinostat or **A6** at 1 μM for 24 h. Interestingly, a significantly higher H3 hyperacetylation was noticed upon incubation with vorinostat in comparison to **A6**. These results hint that the differences seen between the IC_{50} values of **A6** (double-digit micromolar) and vorinostat (submicromolar) likely arise due to reduced nuclear permeability of **A6** (Figure S10, Supporting Information).

Out of these three AML cell lines, **A6** displayed the lowest IC_{50} in the MOLM13 cell line (17.4 ± 3.1 μM), and therefore this cell line was selected for further validation studies, involving apoptosis induction and cell cycle progression. Exposure of MOLM13 to **A6** induced caspase 3/7-dependent apoptosis in dose-dependent fashion, which was further validated by annexin V and PI staining, whereas vorinostat at its IC_{25} and IC_{50} concentrations in MOLM13 cells was taken a positive control in both assays (Figure 5C,D). Next, the effect of **A6** on the cell cycle progression of MOLM13 cells was evaluated using flow cytometry (Figure 5E). A dose-dependent increase in the sub-G1 fraction (DNA fragmentation as a marker of apoptosis) with a concomitant reduction of cell population in G2/M phase was reported after 48 h exposure to **A6** (8, 16, and 24 μM), whereas vorinostat was taken as a control (Figure 5E). The proportions of the cells with the fragmented DNA (sub-G1 population) in the vehicle-treated group was 4.9%, which increased up to 7.5%, 9.9%, and 13.4% upon treatment with 8, 16, and 24 μM **A6**. These results specify that **A6** inhibits the cell cycle progression of MOLM13 cells, which explains the effect of **A6** exposure on cell viability and apoptosis induction.

Taken together, these results indicate that PROTAC **A6** reduces the cell viability in three AML cell lines in the double-digit micromolar range and also induces apoptosis of MOLM13 cells in a caspase 3/7-dependent fashion through arresting the cells in sub-G1 phase.

■ CONCLUSION

Using a combination of solution- and solid-phase protocols, we synthesized a series of HDAC6 degraders based on non-selective (**A1**−**7**) and HDAC6-selective (**B1**−**4**) ligands. Our protocols enabled the fast and efficient synthesis of the desired PROTACs in total yields of up to 71%. In both series, Western blotting experiments revealed that the PROTACs containing an 8-aminooctanoic acid-based spacer (**A6** and **B4**) demonstrated the most potent degradation of HDAC6. Although **A6** exhibited rather unselective HDAC6 inhibition, both **A6** as well as the selective HDAC6i **B4** displayed selective HDAC6

https://doi.org/10.1021/acs.jmedchem.2c01659
J. Med. Chem. XXXX, XXX, XXX−XXX

degradation. Of note, both degraders did not reduce the protein levels of the control HDAC isoforms HDAC1 (class I) and -4 (class IIa). In addition, automated capillary Western blotting was performed to quantify the degradation efficiency of the best HDAC6 degraders. Both **A6** and **B4** demonstrated DC_{50} values in the low nanomolar range (**A6**: 3.4 nM and **B4**: 19.3 nM) and comparable D_{max} values over 80%. Furthermore, we showed that pretreatment of the HL-60 cells with either a HDACi, a CRBN ligand, or the proteasome inhibitor MG132 rescued HDAC6 from degradation, suggesting that the degradation of HDAC6 occurs via the formation of a ternary complex and through the ubiquitin−proteasome system. Subsequently, to analyze the degradation kinetics of **A6** and **B4**, we performed a CRISPR-mediated HiBiT-tagging of HDAC6 in K562 cells and utilized the HiBiT+LgBiT complementation technology to monitor the reduction of HDAC6 levels over 24 h. Both PROTACs demonstrated similar degradation profiles, and the maximum degradation was observed between 5.5 and 7.5 h. Moreover, quantitative MS data did not reveal any significant changes in the overall cellular proteome profile after 6 h treatment of K562 cells with PROTACs **A6** or **B4** at 1 μM. Next, HDAC6 degradation of **A6** and intracellular localization of a fluorescein-labeled PROTAC (**A7**) were determined by fluorescence microscopy, which showed subcellular localization of the PROTAC **A7** in the cytoplasm/nuclear−cytoplasmic interphase. In contrast to An et al.,[32] we noticed a shift in the intracellular localization of HDAC6 from the cytoplasm/nuclear−cytoplasmic interphase into the nucleus upon **A6** (Figure 4) or **A7** (Figure S9, Supporting Information) exposure. HDAC6 is primarily located in the cytoplasm, but a fraction of HDAC6 can enter the nucleus in response to certain stimuli, where it can act as a transcription factor.[49] This is likely due to increased shuttling of HDAC6 into the nucleus in addition to its degradation, upon HDAC6-PROTAC exposure. In fact, high nuclear HDAC6 protein levels are associated with anticancer activity.[49] Notably, PROTAC **A6** exhibited encouraging antiproliferative activity in three AML cell lines, and **A6** induced apoptosis of MOLM13 cells in a caspase 3/7-dependent fashion through arresting the cells in sub-G1 phase.

Taken together, considering the powerful ability to degrade HDAC6, promising antileukemic activity, and the synthetic accessibility by a rapid and straightforward solid-phase protocol, **A6** can be considered as a promising starting point to develop new therapeutic modalities for HDAC6-driven diseases, while the selective HDAC6 inhibitor and degrader **B4** is a new effective pharmacological tool to study HDAC6 biology.

■ EXPERIMENTAL SECTION

Chemistry. *General Remarks.* For all solid-phase reactions, a 2-chlorotrityl chloride resin (200−400 mesh, 1.1−1.8 mmol/g) supplied by Iris Biotech was used. The manual solid-phase synthesis was carried out in a PP-reactor equipped with a PE frit (sizes: 2/10/20 mL, pore size 25 μm, MultiSynTech GmbH). Syntheses were carried out after the modification of the resin, and determination of the loading capacity of the preloaded resin followed the standard Fmoc-solid-phase method. After resin swelling for 30 min in DMF, the standard procedure was performed by repeating the Fmoc-deprotection and amide coupling steps. Completion of each coupling step was monitored via the TNBS-test using a TNBS test kit supplied by TCI. After the last coupling cycle, the PROTACs were cleaved from the resin using the standard cleavage cocktail (5% TFA in CH_2Cl_2 (v/v), treatment for 1 h at rt) and the compounds were purified by preparative RP-HPLC. Fractions containing the desired final compounds were collected and lyophilized, yielding the HDAC PROTACs **A1**−**A6** and **B1**−**4** with >95% purity in all cases. The FITC-labeled PROTAC **A7**, which was used for fluorescence microscopy studies, was obtained as a mixture of isomers in a purity of 88%. The Fmoc-protected building blocks (Fmoc-Ahp-COOH, Fmoc-*N*H-Ph-COOH) and PROTAC **A2** were synthesized as previously published.[34]

Fmoc-Deprotection. Piperidine (20% in DMF) was added to the resin, and the syringe was shaken for 5 min. The step was repeated once, followed by washing steps with DMF (5 × 2 mL), CH_2Cl_2 (5 × 2 mL), and DMF (5 × 2 mL). After the washing step, the needle was changed to prevent reactions with the remaining piperidine.

TNBS-Test. A small amount of resin-beads was placed in a 0.5 mL microcentrifuge tube. One drop of picrylsulfonic acid (∼1% in DMF) and two drops of DIPEA (10% in DMF) were added to the resin beads, and the resin beads were reacted for 5 min at room temperature.

Test Cleavage/Cleavage from the Resin. For a test cleavage, about 2 mg of the dried resin was weighed into a tube and treated with the standard cleavage solution (5% TFA in CH_2Cl_2) for 1 h. After the reaction period was finished, the filtrate was collected and the solvent was removed in vacuo, giving the crude products, which were solvated in Milli-Q H_2O/MeCN for analytical purposes via HPLC. A cleavage on a larger scale was carried out in the same way. For each 40 mg of resin, 1.0 mL of cleavage cocktail was used.

Determination of the Loading of the Preloaded Resin. A small part of the respective preloaded resin (∼5 mg) was weighed and treated with 500 μL of the deprotection solution (20% piperidine in DMF) for 5 min. The filtrate was collected, and the procedure was repeated once. The absorbance of the combined filtrates was measured at 300 nm, and the concentration was determined photometrically ($\varepsilon_{300\ nm}$(dibenzofulvene) = 7800 M^{-1} cm^{-1}).

Nuclear Magnetic Resonance (NMR) Spectroscopy. Proton (^1H), fluorine (^{19}F), and carbon (^{13}C) NMR spectra were recorded either on a Bruker AVANCE III HD 400 MHz or Varian/Agilent MERCURYplus 400 at a frequency of 400 MHz (^1H), 377 MHz (^{19}F), and 100 MHz (^{13}C) or a Varian/Agilent MERCURYplus 300 at a frequency of 300 MHz (^1H), 282 MHz (^{19}F) and 75 MHz (^{13}C) or a Bruker Fourier 300 at a frequency of 300 MHz (^1H) and 75 MHz (^{13}C). The residual solvent signal ($CDCl_3$: ^1H NMR: 7.26 ppm, ^{13}C NMR: 77.16 ppm, DMSO-d_6: ^1H NMR: 2.50 ppm, ^{13}C NMR: 39.52 ppm) was used for calibration as referred to tetramethylsilane. As solvents, deuterated chloroform ($CDCl_3$) and deuterated dimethyl sulfoxide (DMSO-d_6) were used. The chemical shifts are given in parts per million (ppm). The multiplicity of each signal is reported as singlet (s), doublet (d), triplet (t), quartet (q), multiplet (m), or combinations thereof. Multiplicities are reported as they were measured, and they might disagree with the expected multiplicity of a signal.

Mass Spectrometry. High resolution electrospray ionization mass spectra (HR-ESI-MS) were acquired either with a Bruker Daltonik GmbH microTOF coupled to a LC Packings Ultimate HPLC system and controlled by micrOTOFControl3.4 and HyStar 3.2-LC/MS or with a Bruker Daltonik GmbH ESI-qTOF Impact II coupled to a Dionex UltiMate 3000 UHPLC system and controlled by micrOTOFControl 4.0 and HyStar 3.2-LC/MS.

High Performance Liquid Chromatography (HPLC). For analytical purposes, a Thermo Fisher Scientific UltiMate 3000 UHPLC system with a Nucleodur 5 μm C18 100 Å (250 × 4.6 mm, Macherey Nagel) column was used. A flow rate of 1 mL/min and a temperature of 25 °C were set. For preparative purposes, either a Varian ProStar or Knauer Azura system with either a Jupiter 5 μm C18 100 Å-column (250 × 10 mm, Phenomenex) with 4 mL/min or a Nucleodur 5 u C18 HTec (150 × 32 mm, Macherey Nagel) column with 15 mL/min was used. Detection was implemented by UV absorption measurement at a wavelength of λ = 220 nm and λ = 254 nm. Bidistilled H_2O (A) and MeCN (B) were used as eluents with an addition of 0.1% TFA to eluent A. For analytical as well as preparative purposes after column equilibration for 5 min, a linear gradient from

https://doi.org/10.1021/acs.jmedchem.2c01659
J. Med. Chem. XXXX, XXX, XXX−XXX

5% A to 95% B in 15 min followed by an isocratic regime of 95% B for 5 min was used.

UV−Vis and Infrared Spectroscopy (IR). Loading determinations were performed on a Shimadzu UV-160A spectrometer at room temperature. All measurements were performed in a 3500 μL quartz cuvette (100-QS, Hellma Analytics) with a path length of 10 mm. Infrared spectroscopy measurements were performed on a PerkinElmer SpectrumTwo FT-IR spectrometer at room temperature.

General Procedure A. To a cooled (0 °C) solution of the appropriate amine (1.00 equiv) in 10% aq Na_2CO_3/1,4-dioxane (3:2, 20 mL/mmol) was added Fmoc-Cl (1.5 equiv) in five portions. The mixture was then allowed to warm to room temperature and stirred for 18 h. Upon completion of the reaction, the solution was diluted with distilled H_2O (30 mL) and washed with Et_2O (3 × 40 mL). Subsequently, the aqueous phase was acidified to pH 1 with 6 M HCl. Filtration of the resulting precipitate, followed by washing with distilled H_2O (100 mL) and drying in vacuo afforded the desired Fmoc-protected linker.

General Procedure B. The amounts of reagents and solvents used in the following synthesis protocol correspond to a 3.00−4.00 mmol scale. After swelling of the 2-chlorotrityl chloride resin (2.00 g, 3.20 mmol, 1.00 equiv., loading 1.60 mmol/g) for 30 min in DMF, a solution of *N*-hydroxyphthalimide (1.88 g, 11.5 mmol, 3.50 equiv) and Et_3N (1.60 mL, 11.5 mmol, 3.50 equiv) in DMF (1.5 mL/g resin) was added to the resin and reacted for 48 h. Afterward, the resin was washed with DMF (10 × 5 mL) and CH_2Cl_2 (10 × 5 mL). Capping of the modified resin was performed by treatment with a capping solution (CH_2Cl_2/MeOH/DIPEA, 80:15:5) two times for 15 min. Subsequently, the resin was washed with CH_2Cl_2 (10 × 5 mL) and dried in vacuo to afford the modified resin **5**.

General Procedure C. The amounts of reagents and solvents used in the following synthesis protocol correspond to a 0.09−0.20 mmol scale. After the HDACi-preloaded resin (1.00 equiv) was left to swell for 30 min in DMF, Fmoc deprotection was performed by treatment with 20% piperidine in DMF (1.5 mL, 2 × 5 min). Afterward, the resin was washed with DMF (5 × 3 mL), CH_2Cl_2 (5 × 3 mL) and DMF (5 × 3 mL). For the subsequent amide coupling reaction, a solution of the appropriate spacer Fmoc-R^2-COOH (3.00 equiv), HATU (3.00 equiv), and DIPEA (4.00 equiv) in DMF (1 mL/mmol acid) was agitated for 5 min and then added to the resin. After 4 h at room temperature, the resin was washed with DMF (5 × 3 mL) and CH_2Cl_2 (5 × 3 mL) and completion of the reaction was monitored via the TNBS-test. Again, washing with DMF (5 × 3 mL) and the repetition of the Fmoc-deprotection step gave the free amine which was reacted further in the last coupling cycle with the respective CRBN building block (1.50−2.20 equiv), HATU (2.00−2.20 equiv), and DIPEA (3.00−4.00 equiv) in DMF (500 μL) for 4 h at room temperature. After washing with DMF (5 × 3 mL) and CH_2Cl_2 (5 × 3 mL) and a negative TNBS-test, the resin was dried in vacuo followed by the cleavage of the crude products from the resin and purification via preparative HPLC.

2-Methyl-6-nitro-1H-benzo[d]imidazole (1). 4-Nitrobenzene-1,2-diamine (3.06 g, 20 mmol, 1.00 equiv) was dissolved in MeOH (8 mL). Triethyl orthoacetate (4.40 mL, 24 mmol, 1.20 equiv) and sulfamic acid (19.4 mg, 0.20 mmol, 1 mol %) were added to the solution, and the mixture was stirred for 4 h at room temperature. Afterward, the solvent was removed under reduced pressure and the product was resuspended in EtOAc and filtered. Subsequent purification by flash column chromatography using CH_2Cl_2/MeOH (gradient 0−10%) gave the desired product **1** as a beige solid (2.78 g, 15.7 mmol, 79%). ^{1}H NMR (400 MHz, DMSO-d_6, δ): 12.88 (s, 1H), 8.35 (dd, *J* = 2.3, 0.5 Hz, 1H), 8.05 (dd, *J* = 8.8, 2.3 Hz, 1H), 7.62 (dd, *J* = 8.8, 0.6 Hz, 1H), 2.56 (s, 3H) ppm. HRMS-ESI (*m*/*z*): $[M + H]^+$ calcd for $C_8H_7N_3O_2$: 178.0611, found: 178.0618. Analytical data are in agreement with the literature.[50]

Methyl 4-(Bromomethyl)-3-fluorobenzoate (2). Compound **16** (3.36 g, 20.0 mmol, 1.00 equiv) was dissolved in $CHCl_3$ (80 mL) under vigorous stirring. NBS (5.34 g, 30.0 mmol, 1.50 equiv) and AIBN (0.66 g, 4.02 mmol, 0.20 equiv) were added, and the orange reaction mixture was stirred for 16 h at 80 °C. The solvent was removed under reduced pressure, and the yellow/orange residue was purified by flash column chromatography (cyclohexane/EtOAc, 98:2), yielding the desired product **2** as a light yellowish solid (3.34 g, 13.5 mmol, 68%). ^{1}H NMR (400 MHz, $CDCl_3$, δ): 7.81 (dd, *J* = 8.0, 1.6 Hz, 1H), 7.72 (dd, *J* = 10.2, 1.6 Hz, 1H), 7.47 (t, *J* = 7.7 Hz, 1H), 4.52 (d, *J* = 1.1 Hz, 2H), 3.93 (s, 3H) ppm. ^{19}F NMR (377 MHz, $CDCl_3$, δ): −116.05 (m) ppm. ^{13}C NMR (101 MHz, $CDCl_3$, δ): 165.6 (d, $^4J_{C-F}$ = 2.8 Hz), 160.4 (d, $^1J_{C-F}$ = 251.1 Hz), 132.6 (d, $^3J_{C-F}$ = 7.7 Hz), 131.4 (d, $^3J_{C-F}$ = 3.1 Hz), 130.2 (d, $^2J_{C-F}$ = 14.7 Hz), 125.8 (d, $^4J_{C-F}$ = 3.7 Hz), 117.1 (d, $^2J_{C-F}$ = 23.3 Hz), 52.6, 24.7 (d, $^3J_{C-F}$ = 4.3 Hz) ppm. Analytical data are in agreement with the literature.[51]

Methyl 3-Fluoro-4-((2-methyl-5-nitro-1H-benzo[d]imidazol-1-yl)methyl)benzoate (3). **1** (1.42 g, 8.02 mmol, 1.00 equiv) and **2** (1.98 g, 8.01 mmol, 1.00 equiv) were dissolved in DMF (40 mL). Cs_2CO_3 (5.21 g, 16.0 mmol, 2.00 equiv) was added to the resulting yellow solution. The reaction was stirred for 2 h at 80 °C. Afterward, the reaction was cooled to room temperature, diluted with distilled H_2O (28 mL), and extracted with EtOAc (3 × 60 mL). The combined organic layers were washed with brine (1 × 70 mL) and dried over anhydrous $MgSO_4$. After filtration and removal of the solvent in vacuo, the crude product was purified by flash column chromatography (cyclohexane/EtOAc, 30:70), yielding the main isomer **3** as a beige solid (1.21 g, 3.52 mmol, 44%). ^{1}H NMR (400 MHz, $CDCl_3$, δ): 8.62 (d, *J* = 2.1 Hz, 1H), 8.16 (dd, *J* = 8.9, 2.1 Hz, 1H), 7.80 (dd, *J* = 10.5, 1.6 Hz, 1H), 7.74 (dd, *J* = 8.0, 1.6 Hz, 1H), 7.29 (d, *J* = 8.9 Hz, 1H), 6.83 (t, *J* = 7.6 Hz, 1H), 5.47 (s, 2H), 3.91 (s, 3H), 2.67 (s, 3H) ppm. ^{19}F NMR (377 MHz, $CDCl_3$, δ): −116.42 ppm. ^{13}C NMR (101 MHz, $CDCl_3$, δ): 165.3 (d, $^4J_{C-F}$ = 2.5 Hz), 160.0 (d, $^1J_{C-F}$ = 248.5 Hz), 155.7, 144.1, 141.9, 139.3, 132.9 (d, $^3J_{C-F}$ = 7.7 Hz), 128.0 (d, $^3J_{C-F}$ = 3.4 Hz), 126.9 (d, $^2J_{C-F}$ = 14.6 Hz), 126.2 (d, $^4J_{C-F}$ = 3.6 Hz), 118.8, 117.3 (d, $^2J_{C-F}$ = 22.9 Hz), 116.0, 109.3, 52.8, 42.0 (d, $^3J_{C-F}$ = 4.7 Hz), 14.3 ppm. HRMS-ESI (*m*/*z*): $[M + H]^+$ calcd for $C_{17}H_{14}FN_3O_4$: 344.1041, found: 344.1057.

4-((5-((((9H-Fluoren-9-yl)methoxy)carbonyl)amino)-2-methyl-1H-benzo[d]imidazol-1-yl)methyl)-3-fluorobenzoic Acid (4). Pd/C (10%) (124 mg) was added to a solution of **3** (1.24 g, 3.61 mmol, 1.00 equiv) in MeOH/CH_2Cl_2 (5:1, 120 mL), and the reaction was vigorously stirred under H_2-atmosphere. Full conversion was detected via HPLC after 4 h. The reaction solution was filtered through Celite, and the solvent was removed in vacuo. The light orange oily residue was dissolved in THF/MeOH (5:1, 90 mL), and $NaOH_{aq}$ (50 mg/mL, 11.5 mL, 14.4 mmol, 4.00 equiv) was added to the solution. Full conversion was monitored after 2 h via HPLC. The reaction solution was neutralized with 1 M HCl_{aq} (14.4 mL, 14.4 mmol, 4.00 equiv), and the solvent was removed in vacuo. The residue was dissolved in 5% Na_2CO_{3aq}/1,4-dioxane (3:2, 60 mL), and Fmoc-Cl (1.40 g, 5.41 mmol, 1.50 equiv) was added carefully in five portions at 0 °C. After stirring for 18 h, the reaction solution was acidified with 6 M HCl to pH 4 and the precipitate was filtered, washed with water, and dried in vacuo, yielding the desired product **4** as a beige solid (1.54 g, 2.95 mmol, 82%). Mp: 193 °C (decomp). ^{1}H NMR (300 MHz, DMSO-d_6, δ): 10.01 (s, 1H), 7.99 (s, 1H), 7.92 (s, 1H), 7.90 (s, 1H), 7.77 (s, 1H), 7.76−7.73 (m, 2H), 7.73−7.70 (m, 1H), 7.63 (d, *J* = 9.0 Hz, 1H), 7.39 (dtd, *J* = 24.2, 7.4, 0.9 Hz, 7H), 5.77 (s, 2H), 4.52 (d, *J* = 6.6 Hz, 2H), 4.32 (t, *J* = 6.6 Hz, 1H), 2.77 (s, 3H) ppm. ^{19}F NMR (377 MHz, DMSO-d_6, δ): −115.78 (t, *J* = 8.9 Hz) ppm. ^{13}C NMR (101 MHz, DMSO-d_6, δ): 166.0 (d, $^4J_{C-F}$ = 1.8 Hz), 163.2, 159.5 (d, $^1J_{C-F}$ = 246.6 Hz), 153.7, 152.5, 143.8, 142.4, 140.8, 133.6 (d, $^4J_{C-F}$ = 1.9 Hz), 131.3, 128.7 (d, $^3J_{C-F}$ = 4.2 Hz), 128.5 (d, $^2J_{C-F}$ = 14.8 Hz), 127.7, 127.1, 125.7 (d, $^3J_{C-F}$ = 3.3 Hz), 125.2, 120.2, 116.0 (d, $^2J_{C-F}$ = 22.3 Hz), 109.6, 65.5, 46.7, 41.0 (d, $^3J_{C-F}$ = 3.3 Hz), 13.5 ppm. HRMS-ESI (*m*/*z*): $[M + H]^+$ calcd for $C_{31}H_{24}FN_3O_4$: 522.1824, found: 522.1825. IR: $\tilde{\nu}$ = 3388 (w), 2872 (br), 2566 (br), 2346 (br), 1807 (br), 1720 (s), 1702 (m), 1621 (w), 1582 (w), 1536 (m), 1506 (m), 1427 (w), 1415 (w), 1329 (w), 1277 (m), 1220 (vs), 1182 (m), 1115 (w), 1083 (m), 1049 (m), 1006 (w), 961 (w), 933 (m), 855 (w), 803 (m), 760 (m), 737 (s), 675 (w), 632 (w), 614 (m), 565 (m), 538 (m), 505 (w), 472 (w) cm^{-1}.

https://doi.org/10.1021/acs.jmedchem.2c01659
J. Med. Chem. XXXX, XXX, XXX−XXX

*Nonselective HDACi Precursor (**6**).* After swelling of the modified resin **5** (500 mg, estimated loading 1.50 mmol/g, 0.75 mmol, 1.00 equiv) for 30 min in DMF, the resin was washed with MeOH (3 × 5 mL). The phthaloyl protecting group was removed by treatment with 5% hydrazine monohydrate in MeOH for 15 min (2 × 3 mL). Afterward, the resin was washed with DMF (3 × 5 mL), MeOH (3 × 5 mL), CH_2Cl_2 (3 × 5 mL), and DMF (3 × 5 mL). For the subsequent amide coupling reaction, a solution of Fmoc-amino-heptanoic acid (551 mg, 1.50 mmol, 2.00 equiv), HATU (570 mg, 1.50 mmol, 2.00 equiv), HOBt·H_2O (230 mg, 1.50 mmol, 2.00 equiv), and DIPEA (383 μL, 2.25 mmol, 3.00 equiv) in DMF (2 mL) was agitated for 5 min and then added to the resin. The amide coupling was performed for 20 h at room temperature. Afterward, the resin was washed with DMF (3 × 5 mL) and CH_2Cl_2 (3 × 5 mL). Completion of the reaction was monitored via the TNBS-test. Upon completion of the reaction and washing, the resin **17** was dried in vacuo and a loading between 0.77 mmol/g and 0.97 mmol/g was photometrically determined for different batches. The dried resin was stored at 4 °C.

After swelling of the resin **17** (676 mg, 0.97 mmol/g, 0.65 mmol, 1,00 equiv) in DMF for 30 min, Fmoc-deprotection was performed by treatment with 20% piperidine in DMF. Afterward, the resin was washed with DMF (3 × 5 mL), CH_2Cl_2 (3 × 5 mL), and DMF (3 × 5 mL). For the subsequent amide coupling reaction, a solution of Fmoc-aminobenzoic acid (701 mg, 1.95 mmol, 3.00 equiv), HATU (741 mg, 1.95 mmol, 3.00 equiv), and DIPEA (454 μL, 2.60 mmol, 4.00 equiv) in DMF (1.5 mL) was agitated for 5 min and then added to the resin. After a reaction time of 20 h at room temperature, the resin was washed with DMF (3 × 5 mL) and CH_2Cl_2 (3 × 5 mL). Completion of the reaction was monitored via the TNBS-test. The resin was dried in vacuo and stored at 4 °C.

*Selective HDAC6i Precursor (**7**).* After swelling of the modified resin **5** (133 mg, estimated loading 1.50 mmol/g, 0.20 mmol, 1.00 equiv) for 30 min in DMF, the resin was washed with MeOH (3 × 3 mL). The phthaloyl protecting group was removed by treatment with 5% hydrazine monohydrate in MeOH for 15 min (2 × 1.5 mL). Afterward, the resin was washed with DMF (3 × 3 mL), MeOH (3 × 3 mL), CH_2Cl_2 (3 × 3 mL), and DMF (3 × 3 mL). For the subsequent amide coupling reaction, a solution of **4** (208 mg, 0.40 mmol, 2.00 equiv), HATU (152 mg, 0.40 mmol, 2.00 equiv), HOBt·H_2O (61.0 mg, 0.40 mmol, 2.00 equiv), and DIPEA (102 μL, 0.60 mmol, 3.00 equiv) in DMF (900 μL) was agitated for 5 min and then added to the resin. The amide coupling was performed for 20 h at room temperature. Afterward, the resin was washed with DMF (3 × 3 mL) and CH_2Cl_2 (3 × 3 mL). Completion of the reaction was monitored via the TNBS-test. Upon completion of the reaction and washing, the resin was dried in vacuo and a loading of 0.60−0.62 mmol/g was photometrically determined for different batches of the preloaded resin. The dried resin was stored at 4 °C.

*8-((((9H-Fluoren-9-yl)methoxy)carbonyl)amino)octanoic Acid (**8a**).* Synthesized from 8-aminooctanoic acid (500 mg, 3.14 mmol, 1.00 equiv) and 9-fluorenylmethoxy-carbonyl chloride (1.22 g, 4.71 mmol, 1.50 equiv) according to general procedure A afforded the desired product **8** as a white solid (675 mg, 1.77 mmol, 56%). ^{1}H NMR (400 MHz, $CDCl_3$, δ): 7.79 (dt, *J* = 7.6, 1.0 Hz, 2H), 7.62 (dd, *J* = 7.6, 1.1 Hz, 2H), 7.46−7.38 (m, 2H), 7.34 (td, *J* = 7.4, 1.2 Hz, 2H), 4.78 (s, 1H), 4.43 (d, *J* = 6.9 Hz, 2H), 4.24 (t, *J* = 7.0 Hz, 1H), 3.27−3.04 (m, 2H), 2.38 (t, *J* = 7.4 Hz, 2H), 1.66 (p, *J* = 7.3 Hz, 2H), 1.52 (t, *J* = 7.0 Hz, 2H), 1.43−1.27 (m, 6H) ppm. HRMS-ESI (*m*/*z*): [*M* + Na]$^+$ calcd for $C_{23}H_{27}NO_4$: 404.1832, found: 404.1834. The analytical data are are in agreement with the literature.[52]

*tert-Butyl (2,6-Dioxopiperidin-3-yl)carbamate (**9**).* To a solution of Boc-L-Gln-OH (10.0 g, 40.6. mmol, 1.00 equiv) in dry THF (100 mL) were added CDI (7.00 g, 43.7 mmol, 1.08 equiv) and DMAP (21.0 mg, 0.17 mmol, 0.42 mol %). The reaction was heated to reflux for 24 h under argon atmosphere. The reaction mixture was concentrated to about half of the original volume in vacuo, resulting in precipitation of the desired product, which was filtered and washed with cold THF. Repeating this procedure once gave the desired product **9** as a white solid (4.53 g, 19.9 mmol, 49%). ^{1}H NMR (300 MHz, DMSO-d_6, δ): 10.72 (s, 1H), 7.11 (d, *J* = 8.7 Hz, 1H), 4.22 (q, *J* = 8.8 Hz, 1H), 2.81−2.60 (m, 1H), 2.44 (q, *J* = 4.0 Hz, 1H)*, 2.02−1.83 (m, 2H), 1.39 (s, 9H) ppm, *partially overlapping with DMSO signal. HRMS-ESI (*m*/*z*): [*M* + Na]$^+$ calcd for $C_{10}H_{16}N_2O_4$: 251.1002, found: 251.1009. Analytical data are in agreement with the literature.[52]

*2-(2,6-Dioxopiperidin-3-yl)-4-hydroxyisoindoline-1,3-dione (**10**).* 4-Hydroxyisobenzofuran-1,3-dione (492 mg, 3.00 mmol, 1.50 equiv) was suspended in acetic acid (20 mL). **9** (457 mg, 2.00 mmol, 1.00 equiv) and NaOAc (131 mg, 1.60 mmol, 0.80 equiv) were added, and the mixture was heated under reflux for 6 h. After expiration of this time, the reaction solution was cooled to room temperature. The mixture was diluted with H_2O (100 mL) and extracted with CH_2Cl_2 (10 × 50 mL). The combined organic phases were dried over anhydrous $MgSO_4$ and filtered, and the solvent was removed in vacuo. The crude product was purified by flash column chromatography (CH_2Cl_2/MeOH, 0 → 10%), yielding the desired product **10** as a beige solid (319 mg, 1.16 mmol, 39%). ^{1}H NMR (400 MHz, DMSO-d_6, δ): δ 11.19 (s, 1H, broad signal), 11.08 (s, 1H), 7.65 (dd, J = 8.4, 7.2 Hz, 1H), 7.32 (d, J = 7.1 Hz, 1H), 7.28−7.19 (m, 1H), 5.07 (dd, J = 12.9, 5.4 Hz, 1H), 2.95−2.82 (m, 1H), 2.64−2.45* (m, 2H), 2.07−1.98 (m, 1H) ppm, *partially overlapping with DMSO-signal. HRMS-ESI (*m*/*z*): [M + Na]$^+$ calcd for $C_{13}H_{10}N_2O_5$: 297.0482, found: 297.0494. Analytical data are in agreement with the literature.[52]

*Benzyl 2-((2-(2,6-Dioxopiperidin-3-yl)-1,3-dioxoisoindolin-4-yl)-oxy)acetate (**11**).* DIAD (950 μL, 4.84 mmol, 1.10 equiv) was added dropwise under argon atmosphere to a cooled (0 °C) solution of **10** (1.20 g, 4.40 mmol, 1.00 equiv), PPh_3 (1.73 g, 6.60 mmol, 1.50 equiv), and benzyl glycolate (687 μL, 4.84 mmol, 1.10 equiv) in dry THF (50 mL). The reaction was allowed to warm to room temperature and stirred for 20 h. Afterward, the reaction was quenched with distilled H_2O (50 mL) and diluted with EtOAc (50 mL). The aqueous phase was washed with EtOAc (3 × 50 mL), and the combined organic phases were dried over anhydrous $MgSO_4$, filtered, and concentrated in vacuo. The crude product was purified three times in total by flash column chromatography (cyclohexane/EtOAc) using a linear gradient from 5 to 95% EtOAc in 30 min, yielding **11** as a white foam (985 mg, 2.33 mmol, 53%). ^{1}H NMR (300 MHz, $CDCl_3$, δ): 8.12 (s, 1H), 7.62 (dd, *J* = 8.4, 7.3 Hz, 1H), 7.55−7.48 (m, 1H), 7.34 (d, *J* = 1.1 Hz, 5H), 7.08 (dd, *J* = 8.5, 0.8 Hz, 1H), 5.23 (s, 2H), 4.98 (d, *J* = 5.5 Hz, 1H), 4.94 (s, 2H), 3.03−2.61 (m, 3H), 2.24−2.07 (m, 1H) ppm. ^{13}C NMR (75 MHz, DMSO-d_6, δ): 171.0, 168.0, 167.9, 166.9, 165.5, 155.4, 136.5, 135.0, 134.1, 128.8, 128.8, 128.7, 120.3, 117.9, 117.3, 67.5, 66.5, 49.3, 31.5, 22.7 ppm. HRMS-ESI (*m*/*z*): [*M* + Na]$^+$ calcd for $C_{22}H_{18}N_2O_7$: 445.1006, found: 445.1004. Analytical data are in agreement with the literature.[52]

*2-((2-(2,6-Dioxopiperidin-3-yl)-1,3-dioxoisoindolin-4-yl)oxy)-acetic Acid (**12**).* Pd/C (10%) (28 mg) was added to a solution of **11** (280 mg, 0.66 mmol, 1.00 equiv) in 2.5:1 EtOAc/CH_2Cl_2 (30 mL), and the reaction was vigorously stirred under H_2-atmosphere. During the reaction, a gray suspension formed and more precipitation occurred. After 4 h, the reaction was gently flushed with argon and the mixture was diluted with MeOH (50 mL). The reaction mixture was heated carefully to reflux and filtered through Celite. The Celite was washed with hot MeOH (200 mL), and the combined organic phases were dried in vacuo, yielding **12** as a white solid (210 mg, 0.63 mmol, 95%), which was used for solid-phase synthesis without further purification. ^{1}H NMR (400 MHz, DMSO-d_6, δ): 11.10 (s, 1H), 7.79 (dd, *J* = 8.5, 7.3 Hz, 1H), 7.47 (d, *J* = 7.2 Hz, 1H), 7.38 (d, *J* = 8.5 Hz, 1H), 5.10 (dd, *J* = 12.8, 5.4 Hz, 1H), 4.96 (s, 2H), 2.89 (ddd, *J* = 17.3, 14.0, 5.3 Hz, 1H), 2.66−2.45 (m, 2H)*, 2.09−1.97 (m, 1H) ppm, *partially overlapping with DMSO signal. ^{13}C NMR (101 MHz, DMSO-d_6, δ): 172.8, 169.9, 169.5, 166.8, 165.2, 155.2, 136.7, 133.2, 119.9, 116.3, 115.7, 65.1, 48.8, 31.0, 22.0 ppm. HRMS-ESI (*m*/*z*): [*M* + Na]$^+$ calcd for $C_{15}H_{12}N_2O_7$: 355.0537, found: 355.0545. Analytical data are in agreement with the literature.[52]

*2-(2,6-Dioxopiperidin-3-yl)-4-fluoroisoindoline-1,3-dione (**13**).* 3-Fluorophthalic anhydride (3.08 g, 18.6 mmol, 1.50 equiv) was suspended in glacial acetic acid (60 mL). **9** (2.83 g, 12.4 mmol, 1.00

https://doi.org/10.1021/acs.jmedchem.2c01659
J. Med. Chem. XXXX, XXX, XXX−XXX

equiv) and NaOAc (814 mg, 9.92 mmol, 0.80 equiv) were added, and the mixture was heated to reflux for 6 h. The solution was cooled to room temperature and poured into H_2O (150 mL). The precipitate was collected by filtration and washed with H_2O (50 mL) and petroleum ether (30 mL). The solid was dried in vacuo, yielding the desired product **13** (2.47 g, 8.93 mmol, 72%) as a gray solid. ^{1}H NMR (400 MHz, DMSO-d_6, δ): 11.14 (s, 1H), 7.95 (ddd, J = 8.4, 7.3, 4.5 Hz, 1H), 7.79 (d, J = 7.3 Hz, 1H), 7.73 (t, J = 8.9 Hz, 1H), 5.16 (dd, J = 12.8, 5.4 Hz, 1H), 2.89 (ddd, J = 17.1, 13.9, 5.4 Hz, 1H), 2.66−2.43* (m, 2H), 2.07 (dtd, J = 13.0, 5.3, 2.3 Hz, 1H) ppm, *partially overlapping with DMSO-signal. ^{19}F NMR (377 MHz, DMSO-d_6, δ): −114.65 (dd, J = 9.5, 4.5 Hz) ppm. HRMS-ESI (m/z): $[M + Na]^+$ calcd for $C_{13}H_9FN_2O_4$: 299.0439, found: 299.0456. Analytical data are in agreement with the literature.[53]

*Benzyl (2-(2,6-Dioxopiperidin-3-yl)-1,3-dioxoisoindolin-4-yl)-glycinate (**14**).* **13** (300 mg, 1.09 mmol, 1.00 equiv), and H-Gly-OBz (269 mg, 1.63 mmol, 1.50 equiv) was dissolved in DMF (5 mL), and DIPEA (285 μL, 1.63 mmol, 1.50 equiv) was added to the solution. The reaction mixture was agitated at 150 °C for 5 min in a microwave-assisted reaction (150 W). The solution was cooled to room temperature, and the solvent was coevaporated with toluene (3 × 10 mL). Purification by preparative HPLC afforded **14** as a yellow powder (113 mg, 0.27 mmol, 25%). ^{1}H NMR (400 MHz, $CDCl_3$, δ): 8.12 (s, 1H), 7.49 (dd, J = 8.5, 7.2 Hz, 1H), 7.41−7.31 (m, 5H), 7.17 (dd, J = 7.1, 0.6 Hz, 1H), 6.81−6.61 (m, 1H), 6,69 (s, broad signal, 1H) 5.23 (s, 2H), 5.03−4.85 (m, 1H), 4.10 (s, 2H), 2.99−2.65 (m, 3H), 2.21−2.07 (m, 1H) ppm. ^{13}C NMR (101 MHz, $CDCl_3$-d_1, δ): 171.2, 169.6, 169.2, 168.3, 167.6, 145.8, 136.3, 135.2, 132.7, 128.8, 128.8, 128.7, 116.8, 112.8, 111.4, 67.6, 49.1, 44.6, 31.5, 22.9 ppm. HRMS-ESI (m/z): $[M + Na]^+$ calcd for $C_{22}H_{19}N_3O_6$: 444.1166, found: 444.1176. IR: $\tilde{\nu}$ = 3261 (br), 2871 (br), 1694 (s), 1625 (m), 1503 (m), 1407 (m), 1359 (m), 1320 (w), 1259 (m), 1197 (s), 1114 (s), 952 (w), 835 (w), 814 (w), 747 (m), 719 (m), 600 (w), 467 (w) cm^{-1}.

*(2-(2,6-Dioxopiperidin-3-yl)-1,3-dioxoisoindolin-4-yl)glycine (**15**).* 10% Pd/C (24.9 mg) was added to a solution of **14** (249 mg, 0.59 mmol, 1.00 equiv) in 1:2 MeOH/CH_2Cl_2 (25 mL), and the reaction was vigorously stirred under H_2-atmosphere. After 2 h, full conversion was monitored by RP-HPLC. After a change of the atmosphere, the reaction was diluted with warm MeOH (50 mL). The suspension was filtered through Celite, and the Celite was washed with warm MeOH until the Celite pad lost its yellow color. The combined organic phases were dried in vacuo and lyophilized, yielding **15** as a yellow solid (176 mg, 0.53 mmol, 90%). The product was used without further purification. HPLC: t_R = 14.28 min. ^{1}H NMR (400 MHz, DMSO-d_6, δ): δ 11.10 (s, 1H), 7.58 (dd, J = 8.5, 7.1 Hz, 1H), 7.07 (d, J = 7.1 Hz, 1H), 6.98 (d, J = 8.5 Hz, 1H), 6.86 (t, J = 5.7 Hz, 1H), 5.07 (dd, J = 12.9, 5.4 Hz, 1H), 4.07 (d, J = 5.7 Hz, 2H), 2.89 (ddd, J = 17.3, 13.9, 5.4 Hz, 1H), 2.65−2.52* (m, 2H), 2.07−1.99 (m, 1H) ppm, *partially overlapping with DMSO-signal, N*H* could not be detected due to solvent exchange. ^{13}C NMR (101 MHz, DMSO-d_6, δ): 172.8, 171.4, 170.1, 168.8, 167.3, 145.8, 136.1, 132.0, 117.7, 111.0, 109.6, 48.6, 43.9, 31.0, 22.1. HRMS-ESI (m/z): $[M + Na]^+$ calcd for $C_{15}H_{13}N_3O_6$: 354.0697, found: 354.0704. IR: $\tilde{\nu}$ = 3377 (w), 3182 (br), 3089 (br), 2906 (br), 1745 (w), 1688 (s), 1621 (m), 150 (w), 1445 (w), 1399 (m), 1295 (w), 1264 (m), 1198 (s), 1179 (m), 1148 (m), 1106 (m), 1017 (w), 945 (w), 921 (w), 814 (m), 741 (s), 679 (w), 601 (s), 471 (s) cm^{-1}.

*Methyl 3-Fluoro-4-methylbenzoate (**16**).* Thionyl chloride (3.06 mL, 42.2 mmol, 1.30 equiv) was added dropwise to a cooled (0 °C) solution of 3-fluoro-4-methylbenzoic acid (5.00 g, 32.4 mmol, 1.00 equiv) in dry MeOH (150 mL). The reaction was allowed to warm to room temperature and stirred for an additional 4 h at 50 °C. Afterward, the reaction was cooled to 0 °C and gently quenched with 1 M HCl (70 mL). Brine (20 mL) was added, and the yellow colored reaction solution was extracted with EtOAc (3 × 100 mL). The combined organic phases were dried over anhydrous Na_2SO_4 and filtered. Removal of the solvent in vacuo yielded the desired product **16** as a yellow/brown solid (5.09 g, 30.2 mmol, 93%). ^{1}H NMR (400 MHz, $CDCl_3$, δ): 7.72 (dd, J = 7.9, 1.7 Hz, 1H), 7.65 (dd, J = 10.2, 1.7 Hz, 1H), 7.25 (t, J = 7.7 Hz, 1H), 3.91 (s, 3H), 2.33 (d, J = 1.8 Hz, 3H) ppm. ^{19}F NMR (377 MHz, $CDCl_3$,δ): −116.75 (m) ppm. ^{13}C NMR (101 MHz, $CDCl_3$, δ): 166.3 (d, $^4J_{C-F}$ = 2.5 Hz), 161.1 (d, $^1J_{C-F}$ = 245.5 Hz), 131.5 (d, $^3J_{C-F}$ = 5.0 Hz), 130.7 (d, $^2J_{C-F}$ = 17.3 Hz), 129.8 (d, $^3J_{C-F}$= 7.5 Hz), 125.2 (d, $^4J_{C-F}$ = 3.5 Hz), 116.2 (d, $^2J_{C-F}$ = 24.1 Hz), 52.4, 15.0 (d, $^3J_{C-F}$ = 3.6 Hz) ppm. HRMS-ESI (m/z): $[M + Na]^+$ calcd for $C_9H_9FO_2$: 191.0479, found: 191.0485.

*4-(2-(2-(2-((2-(2,6-Dioxopiperidin-3-yl)-1,3-dioxoisoindolin-4-yl)-oxy)acetamido)ethoxy)acetamido)-N-(7-(hydroxyamino)-7-oxoheptyl)benzamide (**A1**).* Synthesized according to general procedure C using **6** (147 mg, 0.10 mmol, 1.00 equiv), Fmoc-O1Pen-OH (102 mg, 0.30 mmol, 3.00 equiv), HATU (114 mg, 0.30 mmol, 3.00 equiv), and DIPEA (70.0 μL, 0.40 mmol, 4.00 equiv) in DMF (300 μL). The second coupling cycle was performed using the hydroxythalidomide building block **12** (50.0 mg, 0.15 mmol, 1.50 equiv), HATU (76.0 mg, 0.20 mmol, 2.00 equiv), and DIPEA (52.0 μL, 0.30 mmol, 3.00 equiv) in DMF (500 μL). Purification by preparative HPLC afforded **A1** as a white powder (39.0 mg, 56.1 μmol, 56%) in >95% purity. HPLC: t_R = 13.56 min. ^{1}H NMR (400 MHz, DMSO-d_6, δ): 11.10 (s, 1H), 10.32 (s, 1H), 9.77 (s, 1H), 8.29 (t, J = 5.6 Hz, 1H), 8.20 (t, J = 5.8 Hz, 1H), 7.78 (dd, J = 8.6, 7.6 Hz, 3H), 7.72−7.62 (m, 2H), 7.45 (d, J = 7.2 Hz, 1H), 7.38 (d, J = 8.5 Hz, 1H), 5.08 (dd, J = 12.8, 5.4 Hz, 1H), 4.82 (s, 2H), 4.08 (s, 2H), 3.60 (t, J = 5.5 Hz, 2H), 3.46−3.34 (m, 2H*), 3.22 (q, J = 6.7 Hz, 2H), 2.87 (ddd, J = 16.9, 13.8, 5.4 Hz, 1H), 2.62−2.42 (m, 2H), 2.04−1.96 (m, 1H), 1.94 (t, J = 7.4 Hz, 2H), 1.53−1.44 (m, 4H), 1.33−1.22 (m, 4H) ppm, *overlapping with water signal, the C-N*H*-OH signal could not be detected due to solvent exchange. ^{13}C NMR (101 MHz, DMSO-d_6, δ): 172.8, 169.9, 169.1, 168.4, 167.2, 166.7, 165.5, 165.4, 155.1, 140.7, 136.9, 133.0, 129.6, 127.9, 120.3, 118.7, 116.8, 116.0, 70.0, 69.6, 67.6, 48.8,*, 38.3, 32.3, 31.0, 29.1, 28.4, 26.3, 25.1, 22.0 ppm, *overlapping with DMSO signal. HRMS-ESI (m/z): $[M + H]^+$ calcd for $C_{33}H_{38}N_6O_{11}$: 695.2671, found: 695.2695. IR: $\tilde{\nu}$ = 3251 (br), 2932 (br), 1774 (w), 1708 (s), 1667 (m), 1615 (m), 1532 (s), 1397 (m), 1261 (m), 1198 (m), 1110 (m), 1056 (m), 1016 (w), 989 (w), 853 (w), 747 (m), 601 (m), 466 (w) cm^{-1}.

*4-(1-((2-(2,6-Dioxopiperidin-3-yl)-1,3-dioxoisoindolin-4-yl)oxy)-2-oxo-6,9,12-trioxa-3-azapentadecan-15-amido)-N-(7-(hydroxyamino)-7-oxoheptyl)benzamide (**A3**).* Synthesized according to general procedure C using **6** (168 mg, 0.15 mmol, 1.00 equiv), Fmoc-NH-PEG(3)-OH (200 mg, 0.45 mmol, 3.00 equiv), HATU (171 mg, 0.45 mmol, 3.00 equiv), and DIPEA (105 μL, 0.60 mmol, 4.00 equiv) in DMF (500 μL). The second coupling cycle was performed using the hydroxythalidomide building block **12** (99.7 mg, 0.30 mmol, 2.00 equiv), HATU (125 mg, 0.33 mmol, 2.20 equiv), and DIPEA (92.0 μL, 0.53 mmol, 3.50 equiv) in DMF (500 μL). Purification by preparative HPLC afforded **A3** as a white powder (77.4 mg, 97.0 μmol, 65%) in >95% purity. HPLC: t_R = 13.80 min. ^{1}H NMR (400 MHz, DMSO-d_6, δ): 11.11 (s, 1H), 10.32 (s, 1H), 10.11 (s, 1H), 8.28 (t, J = 5.6 Hz, 1H), 7.99 (t, J = 5.7 Hz, 1H), 7.89−7.72 (m, 3H), 7.68−7.58 (m, 2H), 7.49 (d, J = 7.2 Hz, 1H), 7.39 (d, J = 8.5 Hz, 1H), 5.11 (dd, J = 12.9, 5.4 Hz, 1H), 4.78 (s, 2H), 3.69 (t, J = 6.2 Hz, 2H), 3.56−3.47 (m, 8H), 3.44 (t, J = 5.7 Hz, 2H), 3.30 (q, J = 5.7 Hz, 2H), 3.21 (q, J = 6.7 Hz, 2H), 2.89 (ddd, J = 17.3, 14.0, 5.4 Hz, 1H), 2.71−2.45 (m, 4H), 2.08−2.01 (m, 1H), 1.94 (t, J = 7.4 Hz, 2H), 1.49 (p, J = 7.0 Hz, 4H), 1.26 (dq, J = 8.4, 5.2, 4.4 Hz, 4H) ppm, C-N*H*-OH signal could not be detected due to solvent exchange. ^{13}C NMR (101 MHz, DMSO-d_6, δ): 172.8, 169.9, 169.6, 169.1, 166.9, 166.7, 165.5, 165.4, 155.0, 141.6, 136.9, 133.0, 129.1, 127.9, 120.4, 118.1, 116.8, 116.1, 69.7, 69.7, 69.7, 69.6, 68.8, 67.5, 66.5, 48.8, 40.2*, 38.4, 37.2, 32.2, 31.0, 29.1, 28.4, 26.2, 25.1, 22.0 ppm, *overlapping with DMSO signal. HRMS-ESI (m/z): $[M + Na]^+$ calcd for $C_{38}H_{48}N_6O_{13}$: 819.3172, found: 819.3188. IR: $\tilde{\nu}$ = 3261 (br), 2927 (br), 1773 (w), 1708 (s), 1659 (s), 1531 (m), 1395 (m), 1259 (m), 1099 (m), 1015 (w), 879 (w), 747 (m), 602 (m), 466 (m) cm^{-1}.

*4-(1-((2-(2,6-Dioxopiperidin-3-yl)-1,3-dioxoisoindolin-4-yl)oxy)-2-oxo-6,9,12,15-tetraoxa-3-azaoctadecan-18-amido)-N-(7-(hydroxyamino)-7-oxoheptyl)benzamide (**A4**).* Synthesized according to general procedure C using **6** (147 mg, 0.10 mmol, 1.00 equiv), Fmoc-NH-PEG(4)-OH (146 mg, 0.30 mmol, 3.00 equiv), HATU

https://doi.org/10.1021/acs.jmedchem.2c01659
J. Med. Chem. XXXX, XXX, XXX−XXX

(114 mg, 0.30 mmol, 3.00 equiv), and DIPEA (70.0 μL, 0.40 mmol, 4.00 equiv) in DMF (300 μL). The second coupling cycle was performed using the hydroxythalidomide building block **12** (50.0 mg, 0.15 mmol, 1.50 equiv), HATU (76.0 mg, 0.20 mmol, 2.00 equiv), and DIPEA (52.0 μL, 0.30 mmol, 3.00 equiv) in DMF (500 μL). Purification by preparative HPLC afforded **A4** as a white powder (55.7 mg, 66.2 μmol, 66%) in >95% purity. HPLC: t_R = 13.91 min. ^{1}H NMR (400 MHz, DMSO-d_6, δ): 11.11 (s, 1H), 10.32 (s, 1H), 10.12 (s, 1H), 8.29 (t, *J* = 5.6 Hz, 1H), 7.99 (t, *J* = 5.6 Hz, 1H), 7.84−7.74 (m, 3H), 7.68−7.61 (m, 2H), 7.49 (d, *J* = 7.2 Hz, 1H), 7.39 (d, *J* = 8.5 Hz, 1H), 5.11 (dd, *J* = 12.9, 5.4 Hz, 1H), 4.78 (s, 2H), 3.69* (t, *J* = 6.2 Hz, 2H), 3.56−3.38 (m, 14H), 3.31 (q, *J* = 5.7 Hz, 2H), 3.21 (q, *J* = 6.6 Hz, 2H), 2.89 (ddd, *J* = 17.4, 14.1, 5.4 Hz, 1H), 2.70−2.45 (m, 4H), 2.12−1.98 (m, 1H), 1.93 (t, *J* = 7.3 Hz, 2H), 1.48 (p, *J* = 7.1 Hz, 4H), 1.26 (dq, *J* = 10.0, 5.6 Hz, 4H) ppm, *overlapping with water signal, C-N*H*-OH signal could not be detected due to solvent exchange. ^{13}C NMR (101 MHz, DMSO-d_6, δ): 172.8, 169.9, 169.6, 169.1, 166.9, 166.7, 165.5, 165.4, 155.0, 141.6, 136.9, 133.0, 129.1, 127.9, 120.4, 118.1, 116.8, 116.1, 69.8 (2C), 69.7, 69.7 (2C), 69.6, 68.8, 67.5, 66.5, 48.8, 40.1*, 38.4, 37.2, 32.2, 30.9, 29.1, 28.4, 26.2, 25.1, 22.0 ppm, *overlapping with DMSO signal. HRMS-ESI (*m*/*z*): [*M* + Na]$^+$ calcd for $C_{40}H_{52}N_6O_{14}$: 863.3434, found: 863.3449. IR: $\tilde{\nu}$ = 3251 (br), 2932 (br), 1774 (w), 1708 (s), 1667 (m), 1615 (m), 1532 (s), 1439 (w), 1397 (m), 1261 (m), 1198 (m), 1110 (m), 1016 (w), 898 (w), 938 (w), 853 (w), 747 (m), 601 (m), 466 (w) cm^{-1}.

*4-(1-((2-(2,6-Dioxopiperidin-3-yl)-1,3-dioxoisoindolin-4-yl)-amino)-2-oxo-6,9,12,15-tetraoxa-3-azaoctadecan-18-amido)-N-(7-(hydroxyamino)-7-oxoheptyl)benzamide (**A5**).* Synthesized according to general procedure C using **6** (147 mg, 0.10 mmol, 1.00 equiv), Fmoc-NH-PEG(4)-OH (146 mg, 0.30 mmol, 3.00 equiv), HATU (114 mg, 0.30 mmol, 3.00 equiv), and DIPEA (70.0 μL, 0.40 mmol, 4.00 equiv) in DMF (300 μL). The second coupling cycle was performed using the pomalidomide building block **15** (33.1 mg, 0.10 mmol, 1.00 equiv), HATU (57.0 mg, 0.15 mmol, 1.50 equiv), and DIPEA (52.0 μL, 0.30 mmol, 3.00 equiv) in DMF (500 μL). For this coupling, a recoupling cycle using the same conditions was needed. Purification by preparative HPLC afforded **A5** as a yellow powder (52.1 mg, 62.0 μmol, 62%) in >95% purity. HPLC: t_R = 13.99 min. ^{1}H NMR (400 MHz, DMSO-d_6, δ): 11.09 (s, 1H), 10.32 (s, 1H), 10.12 (s, 1H), 8.29 (t, *J* = 5.6 Hz, 1H), 8.15 (t, *J* = 5.6 Hz, 1H), 7.86−7.74 (m, 2H), 7.69−7.62 (m, 2H), 7.58 (dd, *J* = 8.5, 7.1 Hz, 1H), 7.07 (d, *J* = 7.1 Hz, 1H), 6.94 (s, 1H), 6.86 (d, *J* = 8.6 Hz, 1H), 5.07 (dd, *J* = 12.9, 5.4 Hz, 1H), 3.93 (s, 2H), 3.69 (t, *J* = 6.2 Hz, 2H)*, 3.59−3.44 (m, 14H)*, 3.41 (t, *J* = 5.8 Hz, 2H), 3.23 (dq, *J* = 16.4, 6.7, 6.2 Hz, 4H), 2.89 (ddd, *J* = 17.4, 13.9, 5.5 Hz, 1H), 2.57 (t, *J* = 6.1 Hz, 2H), 2.03 (dtd, *J* = 13.0, 6.0, 2.8 Hz, 1H), 1.93 (t, *J* = 7.3 Hz, 2H), 1.57−1.39 (m, 4H), 1.36−1.14 (m, *J* = 6.4 Hz, 4H) ppm, *overlapping with water signal, C-N*H*-OH signal could not be detected due to solvent exchange. ^{13}C NMR (101 MHz, DMSO-d_6, δ): 172.8, 170.1, 169.6, 169.1, 168.7, 168.6, 167.3, 165.6, 145.8, 141.6, 136.2, 132.1, 129.1, 128.0, 118.1, 117.5, 111.0, 109.9, 69.8 (2C), 69.7, 69.7 (2C), 69.6, 68.9, 66.5, 48.6, 45.2, 40.2*, 38.7, 37.2, 32.2, 31.0, 29.1, 28.4, 26.2, 25.1, 22.2 ppm, *overlapping with DMSO signal. HRMS-ESI (*m*/*z*): [*M* + Na]$^+$ calcd for $C_{40}H_{53}N_7O_{13}$: 862.3594, found: 862.3596. IR: $\tilde{\nu}$ = 3262 (br), 2865 (br), 1757 (w), 1696 (s), 1624 (m), 1528 (m), 1505 (m), 1405 (m), 1359 (m), 1175 (m), 1111 (s), 1022 (w), 931 (w), 853 (w), 814 (w), 747 (m), 595 (w), 521 (w), 467 (w) cm^{-1}.

*4-(8-(2-((2-(2,6-Dioxopiperidin-3-yl)-1,3-dioxoisoindolin-4-yl)-oxy)acetamido)octanamido)-N-(7-(hydroxyamino)-7-oxoheptyl)-benzamide (**A6**).* Synthesized according to general procedure C using **6** (168 mg, 0.15 mmol, 1.00 equiv), **8** (172 mg, 0.45 mmol, 3.00 equiv), HATU (171 mg, 0.45 mmol, 3.00 equiv), and DIPEA (105 μL, 0.60 mmol, 4.00 equiv) in DMF (500 μL). The second coupling cycle was performed using the hydroxythalidomide building block **12** (99.7 mg, 0.30 mmol, 2.00 equiv), HATU (125 mg, 0.33 mmol, 2.20 equiv), and DIPEA (92 μL, 0.53 mmol, 3.50 equiv) in DMF (500 μL). Purification by preparative HPLC afforded **A6** as a white powder (49 mg, 66.8 μmol, 45%) in >95% purity. HPLC: t_R = 14.98 min. ^{1}H NMR (400 MHz, DMSO-d_6, δ): 11.11 (s, 1H), 10.32 (s, 1H), 10.04 (s, 1H), 8.28 (t, *J* = 5.6 Hz, 1H), 7.92 (t, *J* = 5.7 Hz, 1H), 7.81 (m, 1H), 7.79−7.73 (m, 2H), 7.66−7.60 (m, 2H), 7.48 (d, *J* = 7.2 Hz, 1H), 7.39 (d, *J* = 8.5 Hz, 1H), 5.12 (dd, *J* = 12.9, 5.4 Hz, 1H), 4.76 (s, 2H), 3.21 (q, *J* = 6.7 Hz, 2H), 3.14 (q, *J* = 6.6 Hz, 2H), 2.90 (ddd, *J* = 17.5, 14.0, 5.4 Hz, 1H), 2.66−2.46 (m, 2H), 2.31 (t, *J* = 7.4 Hz, 2H), 2.10−1.99 (m, 1H), 1.94 (t, *J* = 7.4 Hz, 2H), 1.58 (t, *J* = 7.1 Hz, 2H), 1.46 (dp, *J* = 20.0, 6.9 Hz, 6H), 1.27 (dd, *J* = 7.1, 3.1 Hz, 10H) ppm, C-N*H*-OH signal could not be detected due to solvent exchange. ^{13}C NMR (101 MHz, DMSO-d_6, δ): 172.8, 171.6, 169.9, 169.1, 166.7, 166.6, 165.6, 165.5, 155.1, 141.7, 136.9, 133.0, 128.9, 127.9, 120.4, 118.1, 116.8, 116.0, 67.7, 48.8, 40.2*, 38.3, 36.4, 32.2, 30.9, 29.1, 29.0, 28.6, 28.5, 28.4, 26.2, 26.2, 25.1, 24.9, 22.0 ppm, *overlapping with DMSO signal. HRMS-ESI (*m*/*z*): [*M* + Na]$^+$ calcd for $C_{37}H_{46}N_6O_{10}$: 757.3168, found: 757.3166. IR: $\tilde{\nu}$ = 3262 (br), 2928 (br), 1773 (w), 1708 (s), 1660 (s), 1531 (m), 1484 (w), 1394 (m), 1260 (m), 1198 (m), 1098 (w), 940 (w), 746 (m), 603 (m), 466 (w) cm^{-1}.

*N-((13S)-1-((2-(2,6-Dioxopiperidin-3-yl)-1,3-dioxoisoindolin-4-yl)oxy)-13-((2-(2-(2-((4-((7-(hydroxyamino)-7-oxoheptyl)-carbamoyl)phenyl)amino)-2-oxoethoxy)ethoxy)ethyl)carbamoyl)-2,11-dioxo-6,9-dioxa-3,12-diazaoctadecan-18-yl)-3′,6′-dihydroxy-3-oxo-3H-spiro[isobenzofuran-1,9′-xanthene]-5-carboxamide (**A7**).* Synthesized using **6** in a 0.15 mmol scale following the standard Fmoc-strategy solid-phase protocol. For the coupling of the PEG-linker, Fmoc-O2Oc-OH (231 mg, 0.60 mmol, 4.00 equiv), HATU (228 mg, 0.60 mmol, 4.00 equiv), and DIPEA (131 μL, 0.75 mmol, 5.00 equiv) were used. For coupling of the fluorescently labeled lysine, commercially available Fmoc-L-Lys(5/6FAM) (218 mg, 0.30 mmol, 2.00 equiv), Oxyma (64.0 mg, 0.45 mmol, 3.00 equiv), and DIC (70.5 μL, 0.45 mmol, 3.00 equiv) were used. CRBN ligand coupling was performed using (2-(2,6-dioxopiperidin-3-yl)-1,3-dioxoisoindolin-4-yl)glycine **12** (99.7 mg, 0.30 mmol, 2.00 equiv), HATU (125 mg, 0.33 mmol, 2.20 equiv), and DIPEA (92.6 μL, 0.53 mmol, 3.50 equiv). All couplings were performed in DMF (750 μL) for 4 h. Purification by preparative HPLC afforded **A7** as a yellow fluorescent powder (106 mg, 77.4 μmol, 52%). An isomer mixture containing 5/6-carboxyfluorescein in a ratio of 0.6:0.4 (determined by ^{1}H NMR) was isolated as product. The isomer determination was not further evaluated. **A7** was used as a mixture of both isomers. HPLC: t_R = 14.84. ^{1}H NMR (400 MHz, DMSO-d_6, δ): 11.10 (s, 1H), 10.33 (s, 1H), 9.83 (s, 0.6 H), 9.81 (s, 0.4 H), 8.77 (t, *J* = 4.7 Hz, 0.6 H), 8.63 (t, *J* = 4.4 Hz, 0.4 H), 8.43 (s, 0.6 H), 8.31 (t, *J* = 5.5 Hz, 1H), 8.22 (d, *J* = 8.1 Hz, 0.6H), 8.18−8.08 (m, 1.4 H), 8.05 (t, *J* = 6.3 Hz, 1.4H), 7.82−7.73 (m, 3H), 7.73−7.65 (m, 2.4 H), 7.59 (d, *J* = 8.4 Hz, 0.6 H), 7.54 (d, *J* = 8.5 Hz, 0.4 H), 7.47 (dd, *J* = 7.2, 3.5 Hz, 1H), 7.41−7.34 (m, 1.6 H), 6.69 (t, *J* = 2.4 Hz, 2H), 6.61−6.51 (m, 4H), 5.11 (dd, *J* = 12.8, 5.4 Hz, 1,2 H), 4.80 (s, 1.2 H), 4.78 (s, 0.8 H), 4.37−4.26 (m, 2 H), 4.09 (s, 1.2 H), 4.08 (s, 0.8 H), 3.97−3.78 (m, 2H), 3.69−3.09 (m, 20H), 2.94−2.83 (m, 1H), 2.68−2.53 (m, 2H), 2.08−1.99 (m, 1H), 1.93 (t, *J* = 7.3 Hz, 2H), 1.73−1.38 (m, 8H), 1.37−1.07 (m, 6H) ppm. ^{13}C NMR (101 MHz, DMSO-d_6, δ): 172.8, 171.4, 171.4, 169.9, 169.1, 168.9, 168.9, 168.6, 168.2, 168.1, 166.9, 166.7, 165.5, 165.4, 164.5, 164.3, 159.6, 158.5, 158.1, 155.0, 154.6, 152.7, 151.8, 140.8, 140.7, 136.9, 136.4, 134.7, 133.0, 129.6, 129.4, 129.2, 129.1, 128.1, 127.9, 126.4, 124.8, 124.2, 123.2, 122.2, 120.3, 118.7, 116.8, 116.0, 112.8, 112.7, 109.2, 109.1, 102.3, 83.4, 70.3, 70.3, 70.2, 69.7, 69.7, 69.4, 69.4, 68.9, 67.5, 51.7, 51.6, 48.8, 40.2*, 38.5, 38.4, 32.3, 32.2, 30.9, 29.1, 28.7, 28.6, 28.4, 26.2, 25.1, 22.7, 22.0 ppm, *overlapping with DMSO signal. HRMS-ESI (*m*/*z*): [*M* + Na]$^+$ calcd for $C_{68}H_{75}N_9O_{22}$: 1392,4919, found: 1392,4933. IR: $\tilde{\nu}$ = 3265 (br), 3095 (br), 2931 (br), 1773 (w), 1708 (s), 1639 (m), 1613 (m), 1531 (s), 1453 (s), 1396 (m), 1300 (m), 1262 (m), 1198 (s), 1116 (s), 1016 (w), 938 (w), 852 (w), 747 (m), 600 (m), 466 (m) cm^{-1}.

*4-((5-(1-((2-(2,6-Dioxopiperidin-3-yl)-1,3-dioxoisoindolin-4-yl)-oxy)-2-oxo-6,9,12-trioxa-3-azapentadecan-15-amido)-2-methyl-1H-benzo[d]imidazol-1-yl)methyl)-3-fluoro-N-hydroxybenzamide·TFA (**B1**).* Synthesized according to general procedure C using **7** (145 mg, 90.0 μmol, 1.00 equiv), Fmoc-NH-PEG(3)-OH (120 mg, 0.27 mmol, 3.00 equiv), HATU (103 mg, 0.27 mmol, 3.00 equiv), and DIPEA (64.0 μL, 0.36 mmol, 4.00 equiv) in DMF (300 μL). The second coupling cycle was performed using the hydroxythalidomide building block **12** (44.9 mg, 135 μmol, 1.50 equiv), HATU (68.4 mg,

https://doi.org/10.1021/acs.jmedchem.2c01659
J. Med. Chem. XXXX, XXX, XXX−XXX

0.18 mmol, 2.00 equiv), and DIPEA (46.8 μL, 0.27 mmol, 3.00 equiv) in DMF (300 μL). Purification by preparative HPLC afforded **B1** as a colorless TFA salt (58.0 mg, 61.3 μmol, 68%) in >95% purity. HPLC: t_R = 13.07. ^{1}H NMR (400 MHz, DMSO-d_6, δ): 11.35 (s, 1H), 11.11 (s, 1H), 10.29 (s, 1H), 8.29 (d, *J* = 1.9 Hz, 1H), 7.99 (t, *J* = 5.7 Hz, 1H), 7.80 (dd, *J* = 8.5, 7.3 Hz, 1H), 7.69 (d, *J* = 9.0 Hz, 1H), 7.64−7.55 (m, 2H), 7.52−7.44 (m, 2H), 7.38 (dt, *J* = 7.8, 3.6 Hz, 2H), 5.77 (s, 2H), 5.11 (dd, *J* = 12.9, 5.4 Hz, 1H), 4.78 (s, 2H), 3.70 (t, *J* = 6.2 Hz, 2H), 3.49 (dt, *J* = 6.4, 2.0 Hz, 8H), 3.43 (t, *J* = 5.7 Hz, 2H), 3.28 (q, *J* = 5.7 Hz, 2H), 2.89 (ddd, *J* = 17.4, 14.0, 5.4 Hz, 1H), 2.81 (s, 3H), 2.69−2.52 (m, 4H), 2.08−1.99 (m, 1H) ppm, C-N*H*-OH signal could not be detected due to solvent exchange. ^{19}F NMR (282 MHz, DMSO-d_6, δ): − 74.10 (s, TFA), − 115.73 (s) ppm. ^{13}C NMR (101 MHz, DMSO-d_6, δ): 172.7, 169.8, 169.7, 166.9, 166.7, 165.4, 159.8 (d, $^1J_{C-F}$ = 247.2 Hz), 158.2, 157.9, 154.9, 152.0, 137.2, 136.9, 135.1 (d, $^3J_{C-F}$ = 7.5 Hz), 133.0, 129.8 (d, $^3J_{C-F}$ = 3.2 Hz), 127.8, 124.3 (d, $^2J_{C-F}$ = 14.6 Hz), 123.2 (d, $^4J_{C-F}$ = 2.6 Hz), 120.3, 117.4, 116.7, 116.6 (q, $^1J_{C-F}$ = 295.9 Hz, TFA), 116.0, 114.2 (d, $^2J_{C-F}$ = 22.8 Hz), 112.8, 103.7, 69.7, 69.7, 69.7, 69.6, 68.8, 67.5, 66.5, 48.8, 42.4 (d, ^3J = 2.7 Hz), *, 38.4, 37.2, 30.9, 22.0, 11.9 ppm, *overlapping with DMSO signal. HRMS-ESI (*m*/*z*): [*M* + Na]$^+$ calcd for $C_{40}H_{42}FN_7O_{12}$: 854.2768, found: 854.2788. IR: $\tilde{\nu}$ = 2872 (br), 1711 (s), 1667 (m), 1553 (w), 1485 (w), 1394 (m), 1355 (w), 1263 (w), 1199 (s), 1124 (m), 880 (w), 748 (m), 603 (w), 527 (w), 467 (w) cm^{-1}.

*4-((5-(1-((2-(2,6-Dioxopiperidin-3-yl)-1,3-dioxoisoindolin-4-yl)-oxy)-2-oxo-6,9,12,15-tetraoxa-3-azaoctadecan-18-amido)-2-methyl-1H-benzo[d]imidazol-1-yl)methyl)-3-fluoro-N-hydroxybenzamide·TFA (**B2**).* Synthesized according to general procedure C using **7** (167 mg, 0.10 mmol, 1.00 equiv), Fmoc-NH-PEG(4)-OH (146 mg, 0.30 mmol, 3.00 equiv), HATU (114 mg, 0.30 mmol, 3.00 equiv), and DIPEA (70.0 μL, 0.40 mmol, 4.00 equiv) in DMF (550 μL). The second coupling cycle was performed using the hydroxythalidomide building block **12** (45.0 mg, 0.14 mmol, 1.35 equiv), HATU (76.0 mg, 0.20 mmol, 2.00 equiv), and DIPEA (52.0 μL, 0.30 mmol, 3.00 equiv) in DMF (550 μL). Purification by preparative HPLC afforded **B2** as a colorless TFA salt (61.2 mg, 61.8 μmol, 62%) in >95% purity. HPLC: t_R = 13.18. ^{1}H NMR (400 MHz, DMSO-d_6, δ): 11.36 (s, 1H), 11.11 (s, 1H), 10.31 (s, 1H), 8.29 (d, *J* = 1.9 Hz, 1H), 8.00 (t, *J* = 5.6 Hz, 1H), 7.80 (dd, *J* = 8.5, 7.3 Hz, 1H), 7.70 (d, *J* = 9.0 Hz, 1H), 7.64−7.55 (m, 2H), 7.52−7.46 (m, 2H), 7.44−7.36 (m, 2H), 5.77 (s, 2H), 5.11 (dd, *J* = 12.9, 5.4 Hz, 1H), 4.78 (s, 2H), 3.71 (t, *J* = 6.2 Hz, 2H), 3.57−3.38 (m, 14H), 3.30 (q, *J* = 5.7 Hz, 2H), 2.89 (ddd, *J* = 17.8, 14.2, 5.6 Hz, 1H), 2.82 (s, 3H), 2.70−2.51 (m, 4H), 2.07−1.97 (m, 1H) ppm, C-N*H*-OH signal could not be detected due to solvent exchange. ^{19}F NMR (376 MHz, DMSO-d_6, δ): −74.17 (s, TFA), −115.72 (dd, *J* = 10.9, 7.7 Hz) ppm. ^{13}C NMR (101 MHz, DMSO-d_6, δ): 172.8, 169.9, 169.7, 166.9, 166.7, 165.4, 159.8 (d, $^1J_{C-F}$ = 247.3 Hz), 158.2, 157.9, 155.0, 152.0, 137.2, 136.9, 135.1 (d, $^3J_{C-F}$ = 7.3 Hz), 133.0, 129.8 (d, $^3J_{C-F}$ = 3.0 Hz), 127.8, 124.3 (d, $^2J_{C-F}$ = 14.7 Hz), 123.2, 120.3, 117.4, 116.8, 116.5 (q, $^1J_{C-F}$ = 296.6 Hz, TFA) 116.1, 114.1 (d, $^2J_{C-F}$ = 22.7 Hz), 112.8, 103.7, 69.8 (2C), 69.7, 69.7, 69.6, 68.8, 67.5, 66.5, 48.8, 42.4, *, 38.4, 37.2, 30.9, 22.0, 12.0 ppm, *overlapping with DMSO signal. HRMS-ESI (*m*/*z*): [*M* + Na]$^+$ calcd for $C_{42}H_{46}FN_7O_{13}$: 898.3030, found: 898.3021. IR: $\tilde{\nu}$ = 3221 (br), 3094 (br), 2872 (br), 1773 (w), 1709(s), 1667 (s), 1554 (w), 1501 (w), 1485 (m), 1394 (m), 1262 (m), 1197 (s), 1121 (s), 1056 (m), 939 (w), 879 (w), 834 (m), 818 (m), 748 (m), 719 (m), 674 (w), 602 (m), 628 (w), 466 (m) cm^{-1}.

*4-((5-(1-((2-(2,6-Dioxopiperidin-3-yl)-1,3-dioxoisoindolin-4-yl)-amino)-2-oxo-6,9,12,15-tetraoxa-3-azaoctadecan-18-amido)-2-methyl-1H-benzo[d]imidazol-1-yl)methyl)-3-fluoro-N-hydroxybenzamide·TFA (**B3**).* Synthesized according to general procedure C using **7** (167 mg, 0.10 mmol, 1.00 equiv), Fmoc-NH-PEG(4)-OH (146 mg, 0.30 mmol, 3.00 equiv), HATU (114 mg, 0.30 mmol, 3.00 equiv), and DIPEA (70.0 μL, 0.40 mmol, 4.00 equiv) in DMF (550 μL). The second coupling cycle was performed using the pomalidomide building block **15** (49.0 mg, 0.15 mmol, 1.50 equiv), HATU (76.0 mg, 0.20 mmol, 2.00 equiv), and DIPEA (52.0 μL, 0.30 mmol, 3.00 equiv) in DMF (550 μL). Purification by preparative HPLC afforded **B3** as a yellow TFA salt (69.7 mg, 70.5 μmol, 71%) in >95% purity. HPLC: t_R = 13.22. ^{1}H NMR (400 MHz, DMSO-d_6, δ): 11.35 (s, 1H), 11.10 (s, 1H), 10.29 (s, 1H), 8.28 (d, *J* = 1.8 Hz, 1H), 8.15 (t, *J* = 5.6 Hz, 1H), 7.69 (d, *J* = 9.0 Hz, 1H), 7.64−7.54 (m, 3H), 7.47 (dd, *J* = 9.0, 1.9 Hz, 1H), 7.38 (t, *J* = 7.9 Hz, 1H), 7.06 (d, *J* = 7.0 Hz, 1H), 6.94 (s, 1H), 6.85 (d, *J* = 8.5 Hz, 1H), 5.76 (s, 2H), 5.07 (dd, *J* = 12.7, 5.4 Hz, 1H), 3.93 (d, *J* = 4.5 Hz, 2H), 3.71 (t, *J* = 6.2 Hz, 2H)*, 3.53−3.43 (m, 12H)*, 3.40 (t, *J* = 5.8 Hz, 2H)*, 3.24 (q, *J* = 5.7 Hz, 2H), 2.97−2.85 (m, 1H), 2.80 (s, 3H), 2.65−2.42 (m, 3H)**, 2.08−1.98 (m, 2H) ppm, *overlapping with water signal,**-overlapping with DMSO signal, C-N*H*-OH signal could not be detected due to solvent exchange. ^{19}F NMR (376 MHz, DMSO-d_6, δ): −74.03 (s, TFA), −115.73 t, *J* = 8.4 Hz) ppm. ^{13}C NMR (101 MHz, DMSO-d_6, δ): 172.8, 170.0, 169.7, 168.7, 168.6, 167.3, 159.8 (d, $^1J_{C-F}$ = 247.2 Hz), 158.3, 158.0, 152.0, 145.8, 137.2, 136.2, 135.1 (d, $^3J_{C-F}$ = 7.1 Hz), 132.0, 129.8 (d, $^3J_{C-F}$ = 2.8 Hz), 127.9, 124.4 (d, $^2J_{C-F}$ = 14.6 Hz), 123.3 (d, $^4J_{C-F}$ = 2.2 Hz), 117.5, 117.4, 116.7 (q, $^1J_{C-F}$ = 297.1 Hz, TFA), 114.2 (d, $^2J_{C-F}$ = 23.0 Hz), 112.7, 111.0, 109.8, 103.8, 69.8 (2C), 69.7, 69.7, 69.6, 68.9, 66.5, 48.6, 45.2, 42.4 (d, $^3J_{C-F}$ = 2.6 Hz), 40.2*, 38.6, 37.2, 31.0, 22.2, 12.0 ppm, *overlapping with DMSO signal. HRMS-ESI (*m*/*z*): [*M* + Na]$^+$ calcd for $C_{42}H_{47}FN_8O_{12}$: 897.3190, found: 897.3168. IR: $\tilde{\nu}$ = 2872 (br), 1695 (s), 1624 (m), 1554 (w), 1502 (m), 1407 (m), 1360 (m), 1322 (w), 1260 (m), 1199 (s), 1115 (m), 1024 (w), 880 (w), 814 (m), 747 (m), 719 (m), 677 (w), 602 (m), 525 (w), 468 (w) cm^{-1}.

*4-((5-(8-(2-((2-(2,6-Dioxopiperidin-3-yl)-1,3-dioxoisoindolin-4-yl)oxy)acetamido)octanamido)-2-methyl-1H-benzo[d]imidazol-1-yl)methyl)-3-fluoro-N-hydroxybenzamide (**B4**).* Synthesized according to general procedure C using **7** (167 mg, 0.10 mmol, 1.00 equiv), **8** (153 mg, 0.40 mmol, 4.00 equiv), HATU (152 mg, 0.40 mmol, 4.00 equiv), and DIPEA (87.5 μL, 0.50 mmol, 5.00 equiv) in DMF (600 μL). The second coupling cycle was performed using the hydroxythalidomide building block **12** (66.0 mg, 0.20 mmol, 2.00 equiv), HATU (84.0 mg, 0.22 mmol, 2.20 equiv), and DIPEA (61.1 μL, 0.35 mmol, 3.50 equiv) in DMF (600 μL). For this coupling step, a recoupling cycle using the same amounts of reagents in a mixture of DMF/CH_2Cl_2 (600 μL, 1:1) was needed. Purification by preparative HPLC afforded **B4** as a white powder (24.0 mg, 27.2 μmol, 27%) in >95% purity. HPLC: t_R = 14.01. ^{1}H NMR (400 MHz, DMSO-d_6, δ): 11.35 (s, 1H), 11.11 (s, 1H), 10.22 (s, 1H), 8.28 (d, *J* = 1.9 Hz, 1H), 7.93 (t, *J* = 5.7 Hz, 1H), 7.80 (dd, *J* = 8.5, 7.3 Hz, 1H), 7.68 (d, *J* = 9.0 Hz, 1H), 7.65−7.55 (m, 2H), 7.52−7.43 (m, 2H), 7.39 (d, *J* = 8.3 Hz, 2H), 5.77 (s, 2H), 5.11 (dd, *J* = 12.8, 5.4 Hz, 1H), 4.76 (s, 2H), 3.14 (q, *J* = 6.6 Hz, 2H), 2.97−2.82 (m, 1H), 2.81 (s, 3H), 2.69−2.53 (m, 2H), 2.33 (t, *J* = 7.4 Hz, 2H), 2.10−1.98 (m, 1H), 1.59 (t, *J* = 7.1 Hz, 2H), 1.44 (t, *J* = 6.9 Hz, 2H), 1.34−1.20 (m, 6H) ppm, C-N*H*-OH signal could not be detected due to solvent exchange. ^{19}F NMR (377 MHz, DMSO-d_6, δ): −73.20 (s, TFA), −114.91 (t, *J* = 9.1 Hz) ppm. ^{13}C NMR (101 MHz, DMSO-d_6, δ): 172.8, 171.7, 169.9, 166.7, 166.6, 165.5, 159.8 (d, $^1J_{C-F}$ = 247.0 Hz), 158.2, 157.9, 155.0, 151.9, 137.4, 136.9, 135.1 (d, $^3J_{C-F}$ = 7.1 Hz), 133.0, 129.8 (d, $^3J_{C-F}$ = 3.0 Hz), 127.7, 124.4 (d, $^2J_{C-F}$ = 14.3 Hz), 123.2 (d, $^4J_{C-F}$ = 2.5 Hz), 120.4, 117.4, 116.8, 116.6 (q, $^1J_{C-F}$ = 297.5, Hz, TFA), 116.0, 114.2 (d, $^2J_{C-F}$ = 22.7 Hz), 112.7, 103.7, 67.7, 48.8, 42.4 (d, $^3J_{C-F}$ = 3.0 Hz), 38.3, 36.4, 30.9, 29.0, 28.6, 28.5, 26.2, 25.0, 22.0, 12.0 ppm. HRMS-ESI (*m*/*z*): [*M* + Na]$^+$ calcd for $C_{39}H_{40}FN_7O_9$: 792.2764, found: 792.2754. IR: $\tilde{\nu}$ = 3226 (br), 2933 (br), 2859 (br), 1709 (s), 1666 (s), 1555 (m), 1486 (m), 1395 (m), 1323 (w), 1298 (w), 1263 (m), 1198 (s), 1124 (m), 1286 (w), 1018 (w), 942 (w), 825 (w), 746 (m), 720 (m), 676 (m), 663 (w), 604 (m), 567 (w), 528 (w), 468 (m) cm^{-1}.

In Vitro Human HDAC1 and HDAC6 Assay. In vitro inhibitory activities against HDAC1 and HDAC6 were measured using a previously published protocol.[54] OptiPlate-96 black microplates (PerkinElmer) were used with an assay volume of 50 μL.

Five microliters of test compound or control, diluted in assay buffer (50 mM Tris-HCl, pH 8.0, 137 mM NaCl, 2.7 mM KCl, 1 mM $MgCl_2$, 0.1 mg/mL BSA), was incubated with 35 μL of the fluorogenic substrate ZMAL (Z-Lys(Ac)-AMC) (21.43 μM in assay buffer) and 10 μL of human recombinant HDAC1 (BPS Bioscience, catalog no. 50051) or HDAC6 (BPS Bioscience, catalog no. 50006) at 37 °C. After an incubation time of 90 min, 50 μL of 0.4 mg/mL

https://doi.org/10.1021/acs.jmedchem.2c01659
J. Med. Chem. XXXX, XXX, XXX−XXX

trypsin in trypsin buffer (50 mM Tris-HCl, pH 8.0, 100 mM NaCl) was added, followed by further incubation at 37 °C for 30 min. Fluorescence was measured with an excitation wavelength of 355 nm and an emission wavelength of 460 nm using a Fluoroskan Ascent microplate reader (Thermo Scientific). All compounds were tested at least twice and in duplicates, and the 50% inhibitory concentration (IC_{50}) was determined by plotting dose−response curves and nonlinear regression with GraphPad Prism.

Cell Culture. The leukemic cell lines HL-60, MOLM-13, MV4-11, THP-1, KASUMI-1 (AML), 697, REH (B-ALL), and K562 (CML) were cultured in RPMI 1640 GlutaMax (Life Technologies, Carlsbad, CA, catalog no. 61870036) supplemented with 10−20% FCS. SKNO-1(AML) were cultured in RPMI 1640 GlutaMax supplemented with 10% FCS and 10 ng/mL GM-CSF. All cells were cultured in a 37 °C humidified incubator with 5% CO_2 according to the suggested culture conditions from DSMZ (https://www.dsmz.de), with the addition of 1% penicillin−streptomycin (catalog no. 15070063, Life Technologies, Carlsbad, CA).

Cell Viability Assay. The cell viability assay was performed to determine the IC_{50} values for the leukemic cell lines. The experimental compounds, vorinostat (catalog no. S1047) and nexturastat A (catalog no. S1047, Selleckchem, Houston, TX), were first dissolved in DMSO with an initial stock concentration of 10 mM and printed on white 384-well plates (catalog no. 3570, Thermo Fisher Scientific, MA) with increasing concentrations (0.5 μM to 50 μM) by using a digital dispenser (D300e, Tecan, Männedorf, Switzerland). Afterward, 30 μL of cell suspension/well was seeded with a concentration of 0.04×10^6 cells/mL and incubated under standard culture conditions. After 72 h the cell viability was measured utilizing the ATP-based CellTiter-Glo luminescent assay (Promega, Fitchburg, WI, catalog no. G7573) with a microplate reader (Spark, Tecan). The obtained raw data were normalized to DMSO-treated controls (DMSO < 0.5%) and the IC_{50} values calculated using the sigmoid dose curve (Hill slope) and nonlinear regression (GraphPad Prism Inc., San Diego, CA) ($n = 3$). The IC_{50} data were plotted as a clustered heat map, followed by unsupervised hierarchical clustering. Each box of the heatmap represents the mean of three independent experiments ($n = 3$). The average IC_{50} values of across all tested cell lines were used for statistical analysis, *, **, and n.s. indicate significant one-way ANOVA P values of <0.05, < 0.01, and >0.05, respectively. The IC_{50} values ± SD that were used for statistical analysis.

Immunoblot. Cells (0.5×10^6 cells/mL) were treated with the indicated concentration of the compound or vehicle (DMSO) for 6 or 24 h under standard culture conditions. Cell pellets were lysed with 300 μL of RIPA buffer (50 mM Tris-HCl pH 8.0, 1% Triton X-100, 0.5% sodium deoxycholate, 0.1% SDS, 150 mM sodium chloride, 2 mM EDTA, supplemented with protease inhibitors (Roche, Switzerland, catalog no. 11697498001) and phosphatase inhibitor (Roche, Switzerland, catalog no. 4906845001) cocktail tablets, Thermo Scientific, Wesel, Germany) according to manufactures guidelines. After centrifugation, the protein concentration of the whole cell extracts was determined using the Pierce BCA protein assay kit (catalog no. 23225, ThermoFisher Scientific, Waltham, MA), according to manufacturer's guidelines. Twenty micrograms of total protein extracts was resolved by a 8% or 12% SDS-PAGE at 60 mA for 60 min and transferred at 100 V for 60 min ∼120 min to nitrocellulose blotting membrane (catalog no. 10600002, GE Healthcare, Germany) utilizing the wet mini trans-blot electrophoretic transfer cell system (catalog no. 1703930. Bio-Rad, Hercules, CA). PageRuler Prestained Protein Ladder, 10 to 180 kDa (catalog no. 26616, ThermoFisher Scientific) was used as protein molecular weight marker. First, blots were incubated in 5% BSA in TBS-T blocking solution for 30 min under slight agitation at room temperature, followed by washing three times (5 min) with TBS-T. Afterward, the blots were incubated overnight at 4 °C with anti-HDAC6 (catalog no. 7558), anti-HDAC1 (catalog no. 5356), anti-HDAC4 (catalog no. 2072), anti-α-tubulin (catalog no. 2144), antiacetyl-α-tubulin (catalog no. 5335), antihistone H3 (catalog no. 4499), antiacetyl-histone H3 (catalog no. 9677), and anti-GAPDH (catalog no. 5174) antibodies (Cell Signaling Technology, Danvers, MA). All primary antibodies were diluted 1:1000 in 5% BSA/TBS-T. Afterward, blots were washed three times for 5 min in TBS-T. Next, blots were incubated with 1:2000 dilution of secondary horseradish peroxidase-conjugated antibodies (catalog no. 7074, Cell Signaling Technology) for 2 h at room temperature. Blots were washed three times with TBS-T and developed with the ECL system (catalog no. GERPN2109, GE Healthcare, Arlington Heights, IL), following manufacturer's guidelines. Blots were detected and analyzed with the Jess Western blot system (ProteinSimple, San Jose, CA).

Generation of HDAC6-HiBiT Knock-in Clones. The generation of HiBit-HDAC6 knock-in cells (K562) was performed following the published protocol,[46] with minor adaptions. See Table S5, Supporting Information, for crRNA and repair template (single-stranded oligodeoxynucleotide or ssODN) sequences.

Labeling of Single-Stranded Oligodeoxynucleotide (ssODN). Labeling of the donor DNA was carried out using LabelIT MFP488 Nucleic Acid Labeling Kit (catalog no. MIR7125; Mirus Bio, Madison, WI) according to the manufacturer's instructions. DNase- and RNase-free water, 10X labeling buffer A, ssODN (1 mg/mL) and 1:10 of labelIT Reagent was mixed and incubated at 37 °C for 1 h while centrifuging briefly after 30 min. Purification was conducted using G50 microspin columns. To this end, the total volume of 50 μL was slowly applied to the top center of the resin and centrifuged (700g, 2 min). Afterward, the purified sample was obtained and stored at −20 °C.

Transfection of Cells with CRISPR/Cas9-gRNA RNP Complex. Transfection was carried out using the Amaxa Nucleofection system (SF Cell Line Kit, catalog no. V4XC-2032). For 2×10^5 K562 cells, 100 pmol of Cas9 protein (Alt-R S.p. HiFi Cas9 nuclease V3, catalog no. 1081060; IDT, Coralville, IA) was mixed with 120 pmol of gRNA (crRNA:tracrRNA 1:1) and assembled for 20 min at room temperature. Afterward, the labeled ssODN was added and the mixture was combined with the cell suspension (resuspended cells in Nucleofector solution SF) and the electroporation enhancer. The complete volume was gently transferred to the nucleocuvette module, placed in the 4D-Nucleofector system, and electroporated with the program "CA-137". Prewarmed culture media was quickly added to the cells and transferred to a 96-well plate.

Generation of Monoclonal Cells. The generation of monoclonal cells was done via semisolid cloning. The cells were seeded (100 cells/mL) in methylcellulose medium for human cells (MethoCult H4100 STEMCELL, catalog no. 04100) supplemented with FCS (Sigma-Aldrich, St. Louis, MO) and penicillin−streptomycin (Invitrogen, Carlsbad, CA). After 10 days, the colonies were picked and transferred to a 96-well plate.

Validate Editing Event in Cells. Nano-Glo HiBiT Lytic Detection System (catalog no. N3030; Promega) was used to select positive clones. Briefly, 2×10^4 cells were taken 48 h postelectroporation and mixed 1:1 with Nano-Glo HiBiT Lytic Reagent (LgBiT Protein 1:100 and Nano-Glo HiBiT Lytic Substrate 1:50 in Nano-Glo HiBiT Lytic Buffer). The mixture was incubated 10 min at room temperature, and luminescence was measured using Tecan Spark microplate reader. The background luminescence was measured using unedited cells and was subtracted from all readings. Later, to ensure that the selected colonies are positive for the HiBiT constructs at the genomic (DNA) level and to omit any off target activity following CRISPR-Cas9 editing, Sanger sequencing was performed by designing the primers (for: 5′-cttgtggggactgtggaaca-3′ and rev: 5′-aggataacattggcgggagg-3′) spanning the donor template region. The clone(s) without any variations/mutations (SNPs, insertions, or deletions) were picked for the further degradation assay.

HDAC6-HiBiT PROTAC Degradation Assay. Validated HDAC6-HiBiT tagged monoclonal K562 cells were seeded (0.2×10^6 per mL) in FCS free media on 12-well cell culture plates. Compound was added into the seeding solution at a concentration of 1 μM, and DMSO was used as a vehicle control. For every time point of measurement and condition, one well was filled with 1 mL of seeding culture. The first measurement was performed after 30 min, followed by seven consecutive measurements every hour and a final

https://doi.org/10.1021/acs.jmedchem.2c01659
J. Med. Chem. XXXX, XXX, XXX−XXX

measurement at 24 h. Prior to each measurement, the cell culture plate was taken out of the incubator to acclimate to room temperature. Out of each well three times 100 μL was added to a white bottom Thermo Scientiffic Nunclon Delta Surface 96-well plate. Nano-Glo HiBiT Lytic (100 μL) reagent (LgBiT Protein 1:100 and Nano-Glo HiBiT Lytic Substrate 1:50 in Nano-Glo HiBiT Lytic Buffer) was later added to these wells (Promega). After 10 min of incubation at room temperature, the luminescence was measured with a Tecan Spark microplate reader. The luminescence signal of the treated cells was normalized to the DMSO signal.

Mass Spectrometry. *Sample Preparation.* K562 cells were lysed after 6 h treatment with **A6** or **B4** at 1 μM. Proteins were extracted from frozen cell pellets as described elsewhere.[55] Briefly, cells were lysed and homogenized in urea buffer using a TissueLyser (Qiagen) and, after centrifugation (15 min, 16000 rcf, 4 °C), supernatants were collected. After determination of protein concentration (Pierce 660 nm Protein Assay, Thermo Fischer Scientific), samples were adjusted to 0.5 mg/mL total protein concentration with SDS buffer (final 7.5% glycerol, 3% SDS, 37.5 mM Tris/HCl pH 7.0) and 10 μL was reduced (20 mM dithiothreitol, 20 min, 56 °C), alkylated (80 mM iodoacetamide, 15 min, RT, protected from light), and finally underwent tryptic digestion (200 ng of trypsin in 50 mM triethylammonium bicarbonate) after applying a slightly modified sp3 protocol[56] using 50 μg 1:1 mix Sera-Mag SpeedBeads. Twenty percent of the peptides were dissolved in 0.1% trifluoracetic acid and subjected to LC-MS analysis.

LC-MS Analysis. For the LC-MS analysis, a Q Exactive Plus Hybrid Quadrupole-Orbitrap mass spectrometer (Thermo Fisher Scientific), operated in positive mode and coupled with a nano electrospray ionization source connected with an Ultimate 3000 Rapid Separation liquid chromatography system (Dionex/Thermo Fisher Scientific, Idstein, Germany) equipped with an Acclaim PepMap 100 C18 column (75 μm inner diameter, 25 cm length, 2 mm particle size from Thermo Fisher Scientific), was applied using a 120 min LC gradient. Capillary temperature was set to 250 °C and source voltage to 1.4 kV. MS survey scans had a mass range from 350 to 2000 m/z at a resolution of 140 000. The automatic gain control was set to 3 000 000, and the maximum fill time was 80 ms. The 10 most intensive peptide ions were isolated and fragmented by high-energy collision dissociation.

Data Analysis. MaxQuant (version 2.0.3.0, Max Planck Institute for Biochemistry, Planegg, Germany) was used for peptide/protein identification and quantification, employing a human sequence database (UniProtKB, downloaded on 01/27/2021, 75 777 entries). Methionine oxidation and N-terminal acetylation as well as a carbamidomethylation at cysteine residues were considered as variable and fixed modifications, respectively. A false discovery rate of 1% on protein and peptide levels was set as identification threshold. Statistical analysis was performed based on experiment-pairwise median log 2(fold change) normalized MaxQuant protein group intensities and LFQ intensities using the "R" (v4.0.4) programming language after removing potential contaminants, reverse hits, and proteins only identified by modified peptides. Principal component analysis (PCA) was performed using the prcomp() function and cluster analysis using the heatmap() function with ward.D2 as the hclust method on protein groups with a complete set of valid values over all samples. Testing for significant protein up- or downregulation in differential analyses (**A6** vs DMSO or **B4** vs DMSO) was performed using the "Significance Analysis of Microarrays" (SAM) analysis method[57] within the Siggenes package. For this approach, a minimum of four valid values had to be present in at least one group (PROTAC treated or untreated), data were log 2 transformed to reach a normal distribution like data structure, and missing values were filled in with random values from samplewise downshifted normal distributions (0.3 s.d. width, 1.8 s.d. downshift). Even at very high permutation-based false discovery rate (FDR) settings of up to 50%, no statistically significant proteins were identified.

Simple Western Immunoassay. Fluorescent (5X) master mix, DTT, and biotinylated ladder were prepared per manufacturer's instruction (BioTechne). A 0.40 μg/μL sample per well was prepared by dilution of sample in 0.1x sample buffer and mixing it 5:1 with fluorescent 5x master mix. Incubation for 5 min at 95 °C in a PCR cycler (GeneAMP PCR System2700, Applied Biosystems, Woburn, MA) assures proper protein denaturation. After loading and centrifugation (5 min at 1000g at room temperature) of the assay plate, a 12−230 kDaA separation module with 25 cartridges (SM-W004, Bio-Techne, Minneapolis, MN) was used for the immune assay (JESS, Bio-Techne−ProteinSimple, Minneapolis, MN). Conditions include separation for 25 min at 375 V, blocking for 5 min with antibody diluent 2, 30 min incubation with primary antibody, and 30 min incubation with secondary antibody. Primary antibody multiplex mix consisted of 1:50 anti-HDAC6 (catalog no. 7558), 1:50 anti-GAPDH (catalog no. 5174, Cell Signaling Technology), and 1:50 anti-β-actin (catalog no. MAB8929, R&D Systems, Minneapolis, MN) was diluted in Antibody Diluent 2. Signals were detected using an antirabbit detection module of JESS (catalog no. DM-001, BioTechne), multiplexed with an antimouse secondary NIR antibody (catalog no. 043−821, BioTechne). Protein levels are calculated by area under the curves of electropherogramms. HDAC6 levels were normalized to the vehicle set to 100% whereas ac-α-tubulin levels were normalized to ac-α-tubulin levels after DMSO treatment set to 0% and maximum protein level set to 100%. DC_{50} was calculated via nonlinear regression (log(inhibitor) vs response (three paramters)). The nonlinear regression was used to generate D_{max} values by subtraction of 100% protein level by "bottom-best-fit value" (GraphPadPrism). EC_{50} of α-tubulin hyperacetylation was calculated via nonlinear regression (log(agonist) vs normalized response−variable slope). Average DC_{50}, D_{max} and EC_{50} values were calculated from three independent simple western immunoassay runs on the treated samples generated from two independent biological replicates.

Caspase 3/7 Assay. Cells (0.04×10^6 cells/mL) were treated with the indicated concentration of the compounds or vehicle (DMSO) for 48 h under standard culture conditions. Then cells were transferred to white 96-well plates and incubated with Caspase-Glo 3/7 Substrate (catalog no. G8091, Promega) for 30 min at room temperature, and later enzymatic activity of caspase 3/7 was examined by using Caspase-Glo 3/7 assay (absorbance at 405 nm), following manufacturer's instructions (Promega) using a microplate reader (Spark, Tecan). The average luminescence values ($n = 3$) of each condition was used for statistical analysis, *, **, and n.s. indicate significant one-way ANOVA P values of <0.05, < 0.01, and >0.05, respectively. The IC_{50} values ± SD were used for statistical analysis.

Annexin V/Propidium Iodide (PI) Apoptosis Assay. Cells (0.04×10^6 cells/mL) were treated with the indicated concentration of the compound or vehicle (DMSO) for 48 h under standard culture conditions. Cell pellets were washed in ice-cold PBS once and resuspended in 100 μL of Annexin-PI staining solution (containing 1.25 μL of Annexin and 2.5 μL of PI; FITC Annexin V Apoptosis Detection Kit with PI), catalog no. 640914, Biolegend, San Diego, CA. Following incubation at room temperature for 15 min in the dark, cells were analyzed using a flow cytometer (Beckman Coulter, Brea, CA). This allows for the discrimination of live cells (unstained with either fluorochrome) from apoptotic cells (stained only with Annexin V) and necrotic cells (stained with both Annexin V and PI). The average percentage ($n = 3$) of the stained or unstained cells across different conditions was used for statistical analysis, *, **, and n.s. indicate significant one-way ANOVA P values of <0.05, < 0.01, and >0.05, respectively.

Cell Cycle Analysis. Cells (0.04×10^6 cells/mL) were treated with the indicated concentration of the compound or vehicle (DMSO) for 48 h under standard culture conditions. Cell pellets were washed in ice-cold PBS twice and resuspended in 150 μL of staining solution containing 0.1% sodium citrate, 0.1% Triton X-100, 50 μg/mL propidium iodide (trisodium citrate 2-hydrate, catalog no. 3580.1; Triton X-100, Roth, Germany, catalog no. 3051.3; propidium iodide, Invitrogen, Waltham, MA, catalog no. P3566). Following incubation at room temperature for 15 min in the dark, cells were analyzed using a flow cytometer (Beckman Coulter). The average percentage of the cells in different cell cycle phase ($n = 3$) was used

https://doi.org/10.1021/acs.jmedchem.2c01659
J. Med. Chem. XXXX, XXX, XXX−XXX

for statistical analysis, *, **, and n.s. indicate significant one-way ANOVA P values of <0.05, < 0.01, and >0.05, respectively.

Immunofluorescence. The Lab-Tek II chamber slide w/Cover RS Glass slides (Nalgene Nunc International, catalog no. 154534) were chosen for this experiment and were coated with a 50 μg/mL solution of poly-D-lysine or PDL (Gibco, ThermoFisher Scientific, catalog no. A3890401) and incubated for 7 min to 24 h at 37 °C. All wells treated with PDL were washed three times with PBS before adding cells. Treated cells were resuspended and centrifuged at 400g for 5 min and then resuspended in 1 mL of Dulbecco's phosphate-buffered saline (PBS) (catalog no. D8537-500 ML, Sigma-Aldrich). Of the 1 mL cell mix, 400−500 μL of volume was added to each corresponding well. The microslides were then placed in the incubator for 30−60 min. After incubation, the slides were observed under a brightfield microscope (magn 10×) to identify cell attachment to the bottom of the slide. If sufficient cells were attached (∼50% confluency), all remaining cell media were removed and 200−300 μL of PBS was added. For fixation, PBS was removed and 200 μL of 4% formaldehyde (FA) (VWR Prolabo Chemical, catalog no. 9713.1000) was added to each well for 10 min at room temperature. A sufficient volume of 1xTBS (10XTBS: 100 mL of 1 M Tris (pH 7.5), 1400 mM NaCl, (in H_2O), 1xTBS is a 1:10 dilution of 10x TBS stock) was added as a quencher for 5 min to each well. For permeabilization, 200−300 μL of a 0.1% Triton X-100 solution was added for 15 min. A 200−300 μL amount of either 10% goat serum (Sigma-Aldrich, catalog no. G9023-10ML) in 1xTBS or 10% donkey serum (Sigma-Aldrich, catalog no. D9663-10ML) in 1xTBS blocking solution was added for either (i) 1 h at room temperature or (ii) overnight at 4 °C in a humidity cassette. Both primary and secondary antibodies were diluted in blocking solutions. A 100−200 μL amount of 1:200 HDAC6 (Cell Signaling Technology, catalog no. 7558S) antibody was added and left to incubate overnight at 4 °C in a humidity cassette. All wells were washed three times with an appropriate volume of 1xTBS for a total of 15 min between stainings. A 100−200 μL amount of secondary antibody (AlexaFluor, ThermoFischer) was added for 1−1.5 h at room temperature, protected from light. A 300 nM solution of DAPI (hydrochloride) (StemCell Technologies, Germany, catalog no. 75004) was prepared from an 8 μM stock and added for 5 min, followed by a single 1xTBS wash. After removing buffer from all wells, the chamber slide cover was removed and 1−2 drops of ProLong Gold Antifade reagent (Invitrogen, catalog no. P36934) was added to each well. Finally, a rectangular coverslip (24 × 50 mm, Menzel-Glaeser) was carefully placed on top. All samples were left to mount at 4 °C overnight.

Widefield Microscopy: All samples were imaged using a Zeiss Axioobserver.Z1/7 wide field microscope.

Aquisition Settings: Objective EC Plan-Neofluar 40×/1.30 oil. Filters 335−383, 420−470, 550−580, 690−650. Track 1 DAPI, beamsplitter (395), excitation 353 nm, emission 465 nm, light source (HXP 120 V), lamp intensity (24.95%), exposure 18.47 ms. Track 2 Alexa Fluor 568, beamsplitter (585), excitation 280 nm, emission 618 nm, light source (HXP 120BV), lamp intensity (87.55%), exposure 700 ms. Sensor resolution 4096 × 3008 pixels.

PAINS Analysis. We filtered all compounds for pan-assay interference compounds (PAINS) using the online filter http://zinc15.docking.org/patterns/home/.[58] No compound was flagged as PAINS.

■ ASSOCIATED CONTENT

Supporting Information

The Supporting Information is available free of charge at https://pubs.acs.org/doi/10.1021/acs.jmedchem.2c01659.

Supplemental figures and tables, NMR spectra, and HPLC traces (PDF)

Molecular strings formula (CSV)

■ AUTHOR INFORMATION

Corresponding Authors

Finn K. Hansen − *Pharmaceutical Institute, Department of Pharmaceutical and Cell Biological Chemistry, University of Bonn, 53121 Bonn, Germany;* orcid.org/0000-0001-9765-5975; Phone: (+49) 228 73 5213; Email: finn.hansen@uni-bonn.de; Fax: (+49) 228 73 7929

Sanil Bhatia − *Department of Pediatric Oncology, Hematology and Clinical Immunology, Medical Faculty, Heinrich Heine University Düsseldorf, 40225 Düsseldorf, Germany;* orcid.org/0000-0001-6494-7744; Phone: (+49) 211 81 04896; Email: sanil.bhatia@med.uni-duesseldorf.de; Fax: (+49) 211 81 16436

Authors

Laura Sinatra − *Institute for Drug Discovery, Medical Faculty, Leipzig University, 04103 Leipzig, Germany*

Jing Yang − *Department of Pediatric Oncology, Hematology and Clinical Immunology, Medical Faculty, Heinrich Heine University Düsseldorf, 40225 Düsseldorf, Germany; Department of Medicine, Yangzhou Polytechnic College, Yangzhou 225009, P.R. China*

Julian Schliehe-Diecks − *Department of Pediatric Oncology, Hematology and Clinical Immunology, Medical Faculty, Heinrich Heine University Düsseldorf, 40225 Düsseldorf, Germany*

Niklas Dienstbier − *Department of Pediatric Oncology, Hematology and Clinical Immunology, Medical Faculty, Heinrich Heine University Düsseldorf, 40225 Düsseldorf, Germany*

Melina Vogt − *Department of Pediatric Oncology, Hematology and Clinical Immunology, Medical Faculty, Heinrich Heine University Düsseldorf, 40225 Düsseldorf, Germany*

Philip Gebing − *Department of Pediatric Oncology, Hematology and Clinical Immunology, Medical Faculty, Heinrich Heine University Düsseldorf, 40225 Düsseldorf, Germany*

Luisa M. Bachmann − *Institute for Drug Discovery, Medical Faculty, Leipzig University, 04103 Leipzig, Germany;* orcid.org/0000-0003-0642-9361

Melf Sönnichsen − *Department of Pediatric Oncology, Hematology and Clinical Immunology, Medical Faculty, Heinrich Heine University Düsseldorf, 40225 Düsseldorf, Germany*

Thomas Lenz − *Molecular Proteomics Laboratory, Biological Medical Research Center, Heinrich-Heine-University Düsseldorf, 40225 Düsseldorf, Germany*

Kai Stühler − *Institute for Molecular Medicine, Proteome Research, University Hospital and Medical Faculty, Heinrich-Heine-University Düsseldorf, 40225 Düsseldorf, Germany*

Andrea Schöler − *Institute for Drug Discovery, Medical Faculty, Leipzig University, 04103 Leipzig, Germany*

Arndt Borkhardt − *Department of Pediatric Oncology, Hematology and Clinical Immunology, Medical Faculty, Heinrich Heine University Düsseldorf, 40225 Düsseldorf, Germany*

Complete contact information is available at: https://pubs.acs.org/10.1021/acs.jmedchem.2c01659

Author Contributions

[#]L.S. and J.Y. share the first authorship. S.B. and F.K.H. contributed equally to this work as senior authors. The

manuscript was written through contributions of all authors. All authors have given approval to the final version.

Notes

The authors declare no competing financial interest.

■ ACKNOWLEDGMENTS

S.B. acknowledges the financial support by Düsseldorf School of Oncology-Netzwerkverbundes and Forschungskommission (2018-04) HHU Düsseldorf. This study is funded in part by KinderKrebsForschung e.V. and the Deutsche Forschungsgemeinschaft (DFG, German Research Foundation) − 270650915 (Research Training Group GRK 2158, TP 2d to S.B.). A.B. is supported by the TransOnc priority program of the German Cancer Aid within grant #70112951 (ENABLE). A.B. additionally acknowledges the financial support from Katharina-Hardt Foundation, Christiane und Claudia Hempel-foundation, and especially Löwenstern e.V. for funding Simple Western system (JESS). Experimental support from Jannik Knoche is gratefully aknowledged.

■ ABBREVIATIONS USED

$CDCl_3$, chloroform-*d*; DMSO, dimethyl sulfoxide; DCM, dichloromethane; Et_2O, diethyl ether; EtOAc, ethyl acetate; MeOH, methanol; min, minutes; petrol, petroleum ether; PROTAC, proteolysis targeting chimera; rt, room temperature; TFA, trifluoroacetic acid

■ REFERENCES

(1) Neklesa, T. K.; Winkler, J. D.; Crews, C. M. Targeted Protein Degradation by PROTACs. *Pharmacol. Ther.* **2017**, *174*, 138−144.

(2) Paiva, S.-L.; Crews, C. M. Targeted Protein Degradation: Elements of PROTAC Design. *Curr. Opin. Chem. Biol.* **2019**, *50*, 111−119.

(3) Nalawansha, D. A.; Crews, C. M. PROTACs: An Emerging Therapeutic Modality in Precision Medicine. *Cell Chem. Biol.* **2020**, *27*, 998−1014.

(4) Ishida, T.; Ciulli, A. E3 Ligase Ligands for PROTACs: How They Were Found and How to Discover New Ones. *SLAS Discovery* **2021**, *26*, 484.

(5) Liu, J.; Chen, H.; Xie, L.; Chen, X.; Jin, J.; Wei, W.; Kaniskan, U. TF-PROTACs Enable Targeted Degradation of Transcription Factors. *J. Am. Chem. Soc.* **2021**, *143*, 8902.

(6) Zheng, M.; Huo, J.; Gu, X.; Wang, Y.; Wu, C.; Zhang, Q.; Wang, W.; Liu, Y.; Liu, Y.; Zhou, X.; Chen, L.; Zhou, Y.; Li, H. Rational Design and Synthesis of Novel Dual PROTACs for Simultaneous Degradation of EGFR and PARP. *J. Med. Chem.* **2021**, *64*, 7839.

(7) Trial numbers NCT03888612 and NCT04072952. https://clinicaltrials.gov/.

(8) Nalawansha, D. A.; Crews, C. M. PROTACs: An Emerging Therapeutic Modality in Precision Medicine. *Cell Chem. Biol.* **2020**, *27*, 998−1014.

(9) Mullard, A. Targeted Protein Degraders Crowd into the Clinic. *Nat. Rev. Drug Discovery* **2021**, *20*, 247−250.

(10) Strahl, B. D.; Allis, C. D. The Language of Covalent Histone Modifications. *Nature* **2000**, *403*, 41−45.

(11) Bolden, J. E.; Peart, M. J.; Johnstone, R. W. Anticancer Activities of Histone Deacetylase Inhibitors. *Nat. Rev. Drug Discovery* **2006**, *5*, 769−784.

(12) Park, S. Y.; Kim, J. S. A Short Guide to Histone Deacetylases Including Recent Progress on Class II Enzymes. *Exp. Mol. Med.* **2020**, *52*, 204−212.

(13) Hsu, K. C.; Liu, C. Y.; Lin, T. E.; Hsieh, J. H.; Sung, T. Y.; Tseng, H. J.; Yang, J. M.; Huang, W. J. Novel Class IIa-Selective Histone Deacetylase Inhibitors Discovered Using an in Silico Virtual Screening Approach. *Sci. Rep.* **2017**, *7*, 1−13.

(14) Xiao, Y.; Wang, J.; Zhao, L. Y.; Chen, X.; Zheng, G.; Zhang, X.; Liao, D. Discovery of Histone Deacetylase 3 (HDAC3)-Specific PROTACs. *Chem. Commun.* **2020**, *56*, 9866−9869.

(15) Glozak, M. A.; Seto, E. Histone Deacetylases and Cancer. *Oncogene* **2007**, *26*, 5420−5432.

(16) Wang, P.; Wang, Z.; Liu, J. Role of HDACs in Normal and Malignant Hematopoiesis. *Mol. Cancer* **2020**, *19*, 1−21.

(17) Ropero, S.; Esteller, M. The Role of Histone Deacetylases (HDACs) in Human Cancer. *Mol. Oncol.* **2007**, *1*, 19−25.

(18) Li, Y.; Seto, E. HDACs and HDAC Inhibitors in Cancer-Development and Therapy. *Cold Spring Harb Perspect Med.* **2016**, *6*, a026831.

(19) Clawson, G. A. Histone Deacetylase Inhibitors as Cancer Therapeutics. *Ann. Transl. Med.* **2016**, *4*, 287.

(20) Yang, K.; Wu, H.; Zhang, Z.; Leisten, E. D.; Nie, X.; Liu, B.; Wen, Z.; Zhang, J.; Cunningham, M. D.; Tang, W. Development of Selective Histone Deacetylase 6 (HDAC6) Degraders Recruiting von Hippel-Lindau (VHL) E3 Ubiquitin Ligase. *ACS Med. Chem. Lett.* **2020**, *11*, 575−581.

(21) Osko, J. D.; Christianson, D. W. Structural Basis of Catalysis and Inhibition of HDAC6 CD1, the Enigmatic Catalytic Domain of Histone Deacetylase 6. *Biochemistry* **2019**, *58*, 4912−4924.

(22) Schiedel, M.; Herp, D.; Hammelmann, S.; Swyter, S.; Lehotzky, A.; Robaa, D.; Oláh, J.; Ovádi, J.; Sippl, W.; Jung, M. Chemically Induced Degradation of Sirtuin 2 (Sirt2) by a Proteolysis Targeting Chimera (PROTAC) Based on Sirtuin Rearranging Ligands (SirReals). *J. Med. Chem.* **2018**, *61*, 482−491.

(23) Yang, K.; Song, Y.; Xie, H.; Wu, H.; Wu, Y.-T.; Leisten, E. D.; Tang, W. Development of the First Small Molecule Histone Deacetylase 6 (HDAC6) Degraders. *Bioorg. Med. Chem. Lett.* **2018**, *28*, 2493−2497.

(24) Xiao, Y.; Wang, J.; Zhao, L. Y.; Chen, X.; Zheng, G.; Zhang, X.; Liao, D. Discovery of Histone Deacetylase 3 (HDAC3)-Specific PROTACs. *Chem. Commun.* **2020**, *56*, 9866−9869.

(25) Lu, Y.; Sun, D.; Xiao, D.; Shao, Y.; Su, M.; Zhou, Y.; Li, J.; Zhu, S.; Lu, W. Design, Synthesis, and Biological Evaluation of HDAC Degraders with CRBN E3 Ligase Ligands. *Molecules* **2021**, *26*, 7241.

(26) Xiong, Y.; Donovan, K. A.; Eleuteri, N. A.; Kirmani, N.; Yue, H.; Razov, A.; Krupnick, N. M.; Nowak, R. P.; Fischer, E. S. Chemo-Proteomics Exploration of HDAC Degradability by Small Molecule Degraders. *Cell Chem. Biol.* **2021**, *28*, 1514−1527.

(27) Chotitumnavee, J.; Yamashita, Y.; Takahashi, Y.; Takada, Y.; Iida, T.; Oba, M.; Itoh, Y.; Suzuki, T. Selective Degradation of Histone Deacetylase 8 Mediated by a Proteolysis Targeting Chimera (PROTAC). *Chem. Commun.* **2022**, *58*, 4635−4638.

(28) Smalley, J. P.; Baker, I. M.; Pytel, W. A.; Lin, L.-Y.; Bowman, K. J.; Schwabe, J. W. R.; Cowley, S. M.; Hodgkinson, J. T. Optimization of Class I Histone Deacetylase PROTACs Reveals That HDAC1/2 Degradation Is Critical to Induce Apoptosis and Cell Arrest in Cancer Cells. *J. Med. Chem.* **2022**, *65*, 5642−5659.

(29) Sun, Z.; Deng, B.; Yang, Z.; Mai, R.; Huang, J.; Ma, Z.; Chen, T.; Chen, J. Discovery of Pomalidomide-Based PROTACs for Selective Degradation of Histone Deacetylase 8. *Eur. J. Med. Chem.* **2022**, *239*, 114544.

(30) Yang, H.; Lv, W.; He, M.; Deng, H.; Li, H.; Wu, W.; Rao, Y. Plasticity in Designing PROTACs for Selective and Potent Degradation of HDAC6. *Chem. Commun.* **2019**, *55*, 14848−14851.

(31) Wu, H.; Yang, K.; Zhang, Z.; Leisten, E. D.; Li, Z.; Xie, H.; Liu, J.; Smith, K. A.; Novakova, Z.; Barinka, C.; Tang, W. Development of Multifunctional Histone Deacetylase 6 Degraders with Potent Antimyeloma Activity. *J. Med. Chem.* **2019**, *62*, 7042−7057.

(32) An, Z.; Lv, W.; Su, S.; Wu, W.; Rao, Y. Developing Potent PROTACs Tools for Selective Degradation of HDAC6 Protein. *Protein Cell* **2019**, *10*, 606−609.

(33) Yang, K.; Zhao, Y.; Nie, X.; Wu, H.; Wang, B.; Almodovar-Rivera, C. M.; Xie, H.; Tang, W. A Cell-Based Target Engagement Assay for the Identification of Cereblon E3 Ubiquitin Ligase Ligands and Their Application in HDAC6 Degraders. *Cell Chem. Biol.* **2020**, *27*, 866−876.

(34) Sinatra, L.; Bandolik, J. J.; Roatsch, M.; Sönnichsen, M.; Schoeder, C. T.; Hamacher, A.; Schöler, A.; Borkhardt, A.; Meiler, J.; Bhatia, S.; Kassack, M. U.; Hansen, F. K. Hydroxamic Acids Immobilized on Resins (HAIRs): Synthesis of Dual-Targeting HDAC Inhibitors and HDAC Degraders (PROTACs). *Angew. Chem., Int. Ed.* **2020**, *59*, 22494−22499.
(35) Yang, K.; Wu, H.; Zhang, Z.; Leisten, E. D.; Nie, X.; Liu, B.; Wen, Z.; Zhang, J.; Cunningham, M. D.; Tang, W. Development of Selective Histone Deacetylase 6 (HDAC6) Degraders Recruiting Von Hippel-Lindau (VHL) E3 Ubiquitin Ligase. *ACS Med. Chem. Lett.* **2020**, *11*, 575−581.
(36) Smalley, J. P.; Adams, G. E.; Millard, C. J.; Song, Y.; Norris, J. K. S.; Schwabe, J. W. R.; Cowley, S. M.; Hodgkinson, J. T. PROTAC-Mediated Degradation of Class I Histone Deacetylase Enzymes in Corepressor Complexes. *Chem. Commun.* **2020**, *56*, 4476−4479.
(37) Cao, F.; de Weerd, S.; Chen, D.; Zwinderman, M. R. H.; van der Wouden, P. E.; Dekker, F. J. Induced Protein Degradation of Histone Deacetylases 3 (HDAC3) by Proteolysis Targeting Chimera (PROTAC). *Eur. J. Med. Chem.* **2020**, *208*, 112800.
(38) Keuler, T.; König, B.; Bückreiß, N.; Kraft, F. B.; König, P.; Schäker-Hübner, L.; Steinebach, C.; Bendas, G.; Gütschow, M.; Hansen, F. K. Development of the First Non-Hydroxamate Selective HDAC6 Degraders. *Chem. Commun.* **2022**, *58*, 11087−11090.
(39) Macabuag, N.; Esmieu, W.; Breccia, P.; Jarvis, R.; Blackaby, W.; Lazari, O.; Urbonas, L.; Eznarriaga, M.; Williams, R.; Strijbosch, A.; Van de Bospoort, R.; Matthews, K.; Clissold, C.; Ladduwahetty, T.; Vater, H.; Heaphy, P.; Stafford, D. G.; Wang, H.; Mangette, J. E.; McAllister, G.; Beaumont, V.; Vogt, T. F.; Wilkinson, H. A.; Doherty, E. M.; Dominguez, C. Developing HDAC4-Selective Protein Degraders To Investigate the Role of HDAC4 in Huntington's Disease Pathology. *J. Med. Chem.* **2022**, *65*, 12445−12459.
(40) Darwish, S.; Ghazy, E.; Heimburg, T.; Herp, D.; Zeyen, P.; Salem-Altintas, R.; Ridinger, J.; Robaa, D.; Schmidtkunz, K.; Erdmann, F.; Schmidt, M.; Romier, C.; Jung, M.; Oehme, I.; Sippl, W. Design, Synthesis and Biological Characterization of Histone Deacetylase 8 (HDAC8) Proteolysis Targeting Chimeras (PROTACs) with Anti-Neuroblastoma Activity. *Int. J. Mol. Sci.* **2022**, *23*, 7535.
(41) Paiva, S. L.; Crews, C. M. Targeted Protein Degradation: Elements of PROTAC Design. *Curr. Opin. Chem. Biol.* **2019**, *50*, 111−119.
(42) Shen, S.; Benoy, V.; Bergman, J. A.; Kalin, J. H.; Frojuello, M.; Vistoli, G.; Haeck, W.; Van Den Bosch, L.; Kozikowski, A. P. Bicyclic-Capped Histone Deacetylase 6 Inhibitors with Improved Activity in a Model of Axonal Charcot-Marie-Tooth Disease. *ACS Chem. Neurosci.* **2016**, *7*, 240−258.
(43) Lohbeck, J.; Miller, A. K. Practical Synthesis of a Phthalimide-Based Cereblon Ligand to Enable PROTAC Development. *Bioorg. Med. Chem. Lett.* **2016**, *26*, 5260−5262.
(44) Steinebach, C.; Kehm, H.; Lindner, S.; Vu, L. P.; Köpff, S.; López Mármol, Á.; Weiler, C.; Wagner, K. G.; Reichenzeller, M.; Krönke, J.; Gütschow, M. PROTAC-Mediated Crosstalk between E3 Ligases. *Chem. Commun.* **2019**, *55*, 1821−1824.
(45) Wu, H.; Yang, K.; Zhang, Z.; Leisten, E. D.; Li, Z.; Xie, H.; Liu, J.; Smith, K. A.; Novakova, Z.; Barinka, C.; Tang, W. Development of Multifunctional Histone Deacetylase 6 Degraders with Potent Antimyeloma Activity. *J. Med. Chem.* **2019**, *62*, 7042−7057.
(46) Schwinn, M. K.; Steffen, L. S.; Zimmerman, K.; Wood, K. V.; Machleidt, T. A Simple and Scalable Strategy for Analysis of Endogenous Protein Dynamics. *Sci. Rep.* **2020**, *10*, 8953.
(47) Depetter, Y.; Geurs, S.; De Vreese, R.; Goethals, S.; Vandoorn, E.; Laevens, A.; Steenbrugge, J.; Meyer, E.; de Tullio, P.; Bracke, M.; D'hooghe, M.; De Wever, O. Selective Pharmacological Inhibitors of HDAC6 Reveal Biochemical Activity but Functional Tolerance in Cancer Models. *Int. J. Cancer* **2019**, *145*, 735−747.
(48) Reßing, N.; Sönnichsen, M.; Osko, J. D.; Schöler, A.; Schliehe-Diecks, J.; Skerhut, A.; Borkhardt, A.; Hauer, J.; Kassack, M. U.; Christianson, D. W.; Bhatia, S.; Hansen, F. K. Multicomponent Synthesis, Binding Mode, and Structure-Activity Relationship of Selective Histone Deacetylase 6 (HDAC6) Inhibitors with Bifurcated Capping Groups. *J. Med. Chem.* **2020**, *63*, 10339−10351.
(49) Yang, C.-J.; Liu, Y.-P.; Dai, H.-Y.; Shiue, Y.-L.; Tsai, C.-J.; Huang, M.-S.; Yeh, Y.-T. Nuclear HDAC6 Inhibits Invasion by Suppressing NF-KB/MMP2 and Is Inversely Correlated with Metastasis of Non-Small Cell Lung Cancer. *Oncotarget* **2015**, *6*, 30263−30276.
(50) Yang, D.; Fu, H.; Hu, L.; Jiang, Y.; Zhao, Y. Copper-Catalyzed Synthesis of Benzimidazoles via Cascade Reactions of o-Haloacetanilide Derivatives with Amidine Hydrochlorides. *J. Org. Chem.* **2008**, *73*, 7841−7844.
(51) Álvarez, S.; Khanwalkar, H.; Álvarez, R.; Erb, C.; Martínez, C.; Rodríguez-Barrios, F.; Germain, P.; Gronemeyer, H.; de Lera, A. R. C3 Halogen and C8″ Substituents on Stilbene Arotinoids Modulate Retinoic Acid Receptor Subtype Function. *ChemMedChem* **2009**, *4*, 1630−1640.
(52) Galoppini, C.; Meini, S.; Tancredi, M.; Di Fenza, A.; Triolo, A.; Quartara, L.; Maggi, C. A.; Formaggio, F.; Toniolo, C.; Mazzucco, S.; Papini, A.; Rovero, P. A New Class of Pseudopeptide Antagonists of the Kinin B 1 Receptor Containing Alkyl Spacers. *J. Med. Chem.* **1999**, *42*, 409−414.
(53) Steinebach, C.; Kehm, H.; Lindner, S.; Vu, L. P.; Köpff, S.; López Mármol, Á.; Weiler, C.; Wagner, K. G.; Reichenzeller, M.; Krönke, J.; Gütschow, M. PROTAC-Mediated Crosstalk between E3 Ligases. *Chem. Commun.* **2019**, *55*, 1821−1824.
(54) Erdeljac, N.; Bussmann, K.; Schöler, A.; Hansen, F. K.; Gilmour, R. Fluorinated Analogues of the Histone Deacetylase Inhibitor Vorinostat (Zolinza): Validation of a Chiral Hybrid Bioisostere, BITE. *ACS Med. Chem. Lett.* **2019**, *10*, 1336−1340.
(55) Poschmann, G.; Seyfarth, K.; Besong Agbo, D.; Klafki, H.-W.; Rozman, J.; Wurst, W.; Wiltfang, J.; Meyer, H. E.; Klingenspor, M.; Stühler, K. High-Fat Diet Induced Isoform Changes of the Parkinson's Disease Protein DJ-1. *J. Proteome Res.* **2014**, *13*, 2339−2351.
(56) Hughes, C. S.; Moggridge, S.; Müller, T.; Sorensen, P. H.; Morin, G. B.; Krijgsveld, J. Single-Pot, Solid-Phase-Enhanced Sample Preparation for Proteomics Experiments. *Nat. Protoc.* **2019**, *14*, 68−85.
(57) Tusher, V. G.; Tibshirani, R.; Chu, G. Significance Analysis of Microarrays Applied to the Ionizing Radiation Response. *Proc. Natl. Acad. Sci. U.S.A.* **2001**, *98*, 5116−5121.
(58) Baell, J. B.; Holloway, G. A. New Substructure Filters for Removal of Pan Assay Interference Compounds (PAINS) from Screening Libraries and for Their Exclusion in Bioassays. *J. Med. Chem.* **2010**, *53*, 2719−2740.

https://doi.org/10.1021/acs.jmedchem.2c01659
J. Med. Chem. XXXX, XXX, XXX−XXX

Journal of Medicinal Chemistry

pubs.acs.org/jmc Article

Deciphering the Therapeutic Potential of Novel Pentyloxyamide-Based Class I, IIb HDAC Inhibitors against Therapy-Resistant Leukemia

Fabian Fischer,[○] Julian Schliehe-Diecks,[○] Jia-Wey Tu, Tanja Gangnus, Yu Lin Ho, Mara Hebeis, Leandro A. Alves Avelar, Katerina Scharov, Titus Watrin, Marie Kemkes, Pawel Stachura, Katharina Daugs, Lukas Biermann, Josefa Kremeyer, Nadine Horstick, Ingrid Span, Aleksandra A. Pandyra, Arndt Borkhardt, Holger Gohlke, Matthias U. Kassack, Bjoern B. Burckhardt, Sanil Bhatia,* and Thomas Kurz*

Cite This: https://doi.org/10.1021/acs.jmedchem.4c02024 Read Online

ABSTRACT: Histone deacetylase inhibitors (HDACi) are established anticancer drugs, especially in hematological cancers. This study aimed to design, synthesize, and evaluate a set of HDACi featuring a pentyloxyamide connecting unit linker region and substituted phenylthiazole cap groups. A structural optimization program yielded HDACi with nanomolar inhibitory activity against histone deacetylase class I/IIb enzymes. The novel inhibitors (**4d** and **4m**) showed superior antileukemic activity compared to several approved HDACi. Furthermore, **4d** and **4m** displayed synergistic activity when combined with chemotherapeutics, decitabine, and clofarabine. In vitro pharmacokinetic studies showed the most promising profile for **4d** with intermediate microsomal stability, excellent plasma stability, and concentration-independent plasma protein binding. Additionally, **4d** demonstrated comparable in vivo pharmacokinetics to vorinostat. When administered in vivo, **4d** effectively inhibited the proliferation of leukemia cells without causing toxicity. Furthermore, the binding modes of **4d** and **4m** to the catalytic domain 2 of HDAC6 from *Danio rerio* were determined by X-ray crystallography.

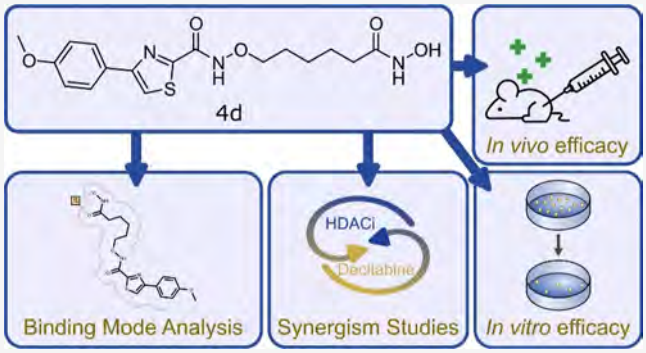

1. INTRODUCTION

Leukemia is characterized by genetic and epigenetic heterogeneity due to the presence of diverse molecular alterations, contributing to the formation of distinct subgroups and influencing the prognosis and therapeutic outcome of patients.[1−3] Leukemia is the most common cancer in children, with a 5 year-overall survival rate exceeding 85%.[4] However, approximately 20−25% of childhood leukemia patients experience relapsed or refractory leukemia; among those cases only around 15−50% of patients are able to achieve remission.[5] Another ongoing challenge in leukemia treatment is the therapy-related toxicity of routinely used drugs,[6,7] along with certain leukemia subtypes that continue to be linked to unfavorable outcomes.[8] In order to prevent long-term therapy-related health damage and to successfully treat therapy-refractory subtypes, new antileukemic drugs are urgently needed.

A possible target for new therapies is the characteristic perturbations of cancer cells in their epigenetic regulation.[9] Epigenetic dysregulation is common for all kinds of human cancer irrespective of solid tumors or hematological malignancies.[10] It has been argued that epigenetic disruption is the causative mechanism behind all hallmarks of cancer steering proliferation, growth suppressor evasion, or apoptosis of cancer cells.[11] Previous studies revealed that hematological malignant cells are especially sensitive to treatment with HDAC inhibitors (HDACi),[12] although the exact mechanism behind this observation remains elusive as it is not allocated to a single cause.[13] Today, all approved HDACi are approved for the therapy of hematological malignancies.[14] The epigenetic regulation of transcription is significantly governed by the acetylation status of histones.[15] This status is tightly regulated by the interplay of two families of enzymes that control the acetylation or deacetylation of ε-amino-groups of

Received: August 24, 2024
Revised: October 23, 2024
Accepted: October 30, 2024

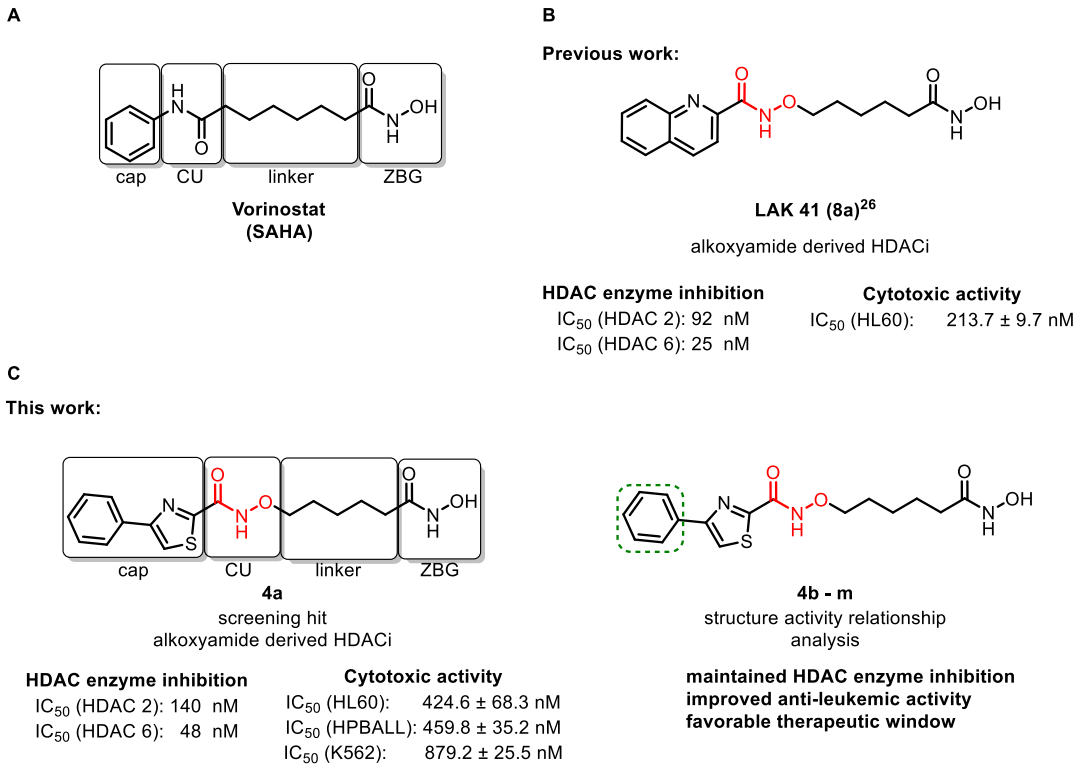

Figure 1. Development of novel pentyloxyamide-based HDACi (A) pharmacophore model of HDAC-inhibitors exemplified on vorinostat. CU = connecting unit and ZBG = zinc-binding-group. (B) Previously published pentyloxyamide-derived HDAC inhibitor.[26] (C) Initial screening hit **4a** showed nanomolar HDAC-isoenzyme inhibition and high nanomolar cytotoxic activity on three different leukemic cell lines. Derivatisation of the terminal phenyl moiety improved the antileukemic activity while retaining HDAC isoenzyme inhibition.

lysine residues: histone acetyltransferases acetylate the ε-amino group of lysine residues while HDAC remove acetyl groups from lysines.[16] HDAC enzymes are classified into four classes related to their homology toward yeast deacetylases.[17] Three of the four classes, namely class I, II, and IV HDAC enzymes, are zinc-dependent metalloenzymes. Class I consists of HDAC enzymes 1, 2, 3, and 8. Especially the nucleic HDAC enzymes 1, 2, and 3 are directly involved in the regulation of the acetylation status of histones.[18] Class IIb HDACs are formed by the cytosolic enzymes HDAC6 and 10. Substrates of HDAC6 are, among others, proteins that are found to be dysregulated in cancer like HSP90[19] or Ku70.[20]

In addition to their potent antileukemic effects used as mono treatment, HDACi are displaying strong synergistic effects in combination with a broad variety of anticancer drugs.[21] For instance, HDACi act synergistically with alkylating[22,23] and hypomethylating agents,[24] proteasome inhibitors,[25−27] and immunomodulating drugs.[28,29] In light of the promising results seen in preclinical studies, clinical trials are currently underway to investigate the potential of HDACi (vorinostat) in combination with the hypomethylating agent (azacytidine) for the treatment of pediatric or adult acute myeloid leukemia (AML) patients (NCT03843528 and NCT00392353). This provides the rationale for a systematic investigation of HDACi as synergistic combination partners for the therapy of resistant leukemic cells.

Our newly developed HDAC inhibitors, targeting class I and IIb, have demonstrated remarkable efficacy against different types of leukemic cells, including those resistant to standard therapies. Notably, these inhibitors exhibit a higher selectivity toward leukemic cells while minimizing damage to healthy cells, distinguishing them from several approved HDACi. Moreover, our most promising candidates (**4d** and **4m**) have displayed significant synergistic effects when combined with the approved chemotherapeutic agents, decitabine and clofarabine. Promising in vitro pharmacokinetic characteristics and in vivo activity encourage their further investigation.

2. RESULTS AND DISCUSSION

We screened our internal library for novel and easily accessible lead structures against three leukemic cell lines K562—(chronic myeloid leukemia or CML); HL60—(AML or AML); and HPBALL—(T-cell acute lymphoblastic leukemia or T-ALL) and identified HDACi **4a** as a hit compound. Strikingly, **4a** outperformed the approved HDACi, vorinostat, both in terms of the HDAC enzyme inhibitory activity and on cytotoxic activity on various leukemic cell lines. **4a** combines a phenylthiazole cap group that has been successfully deployed in the development of HDACi before[30−33] and an oxyamide group as a bioisosteric replacement for the common amide moiety[26,34] (Figure 1). Currently, the two clinically approved Mitogen-activated protein kinase (MEK) 1/2 inhibitors, binimetinib and selumetinib, are establishing the oxyamide group as a valuable structural motif in the field of anticancer drugs.[35,36] We have shown previously that HDACi with an oxyamide linker region are equally or even more potent than some approved HDACi with an amide connecting unit.[26,34] The oxyamide connecting unit extends the chemical space of amide bioisosters and may contribute to the recently emerging

https://doi.org/10.1021/acs.jmedchem.4c02024
J. Med. Chem. XXXX, XXX, XXX−XXX

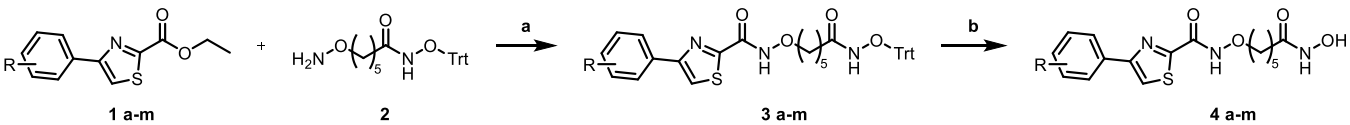

Figure 2. Reagents and conditions: (a) (1) 1M NaOH, THF, RT o.n., (2) HBTU, DIPEA, DMF, RT, o.n., and (b) TFA, Et_3SiH, DCM, RT, 30 min.

Table 1. Inhibition of Human HDAC2, 4, 6, and 8 by Compounds 4a−m and Reference Compounds Vorinostat, Panobinostat, and Tubastatin A

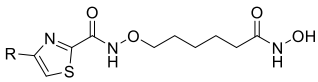

compound	R	IC_{50} (HDAC2) [μM]	IC_{50} (HDAC4) [μM]	IC_{50} (HDAC6) [μM]	IC_{50} (HDAC8) [μM]
4a		0.059 ± 0.012	> 100	0.075 ± 0.03	4.01 ± 0.9
4b		0.046 ± 0.009	> 100	0.026 ± 0.006	2.16 ± 0.3
4c		0.056 ± 0.013	> 100	0.026 ± 0.008	5.20 ± 1.0
4d		0.015 ± 0.004	> 100	0.038 ± 0.01	5.75 ± 0.9
4e		0.065 ± 0.008	> 100	0.051 ± 0.05	1.29 ± 0.3
4f		0.045 ± 0.011	> 100	0.047 ± 0.015	2.32 ± 0.3
4g		0.048 ± 0.012	> 100	0.045 ± 0.012	6.38 ± 1.6
4h		0.047 ± 0.008	> 100	0.081 ± 0.03	2.51 ± 0.3
4i		0.105 ± 0.016	> 100	0.049 ± 0.017	5.41 ± 0.3
4j		0.060 ± 0.03	> 100	0.064 ± 0.03	7.01 ± 1.9
4k		0.065 ± 0.03	> 100	0.108 ± 0.004	4.86 ± 0.5
4l		0.010 ± 0.003	> 100	0.030 ± 0.01	3.68 ± 0.5
4m		0.0045 ± 0.0007	> 100	0.064 ± 0.03	4.80 ± 1.6
Vorinostat	-	0.165 ± 0.006	47.8 ± 6.0	0.047 ± 0.003	5.85 ± 0.7
Panobinostat	-	N.D.	0.725 ± 0.06	N.D.	0.299 ± 0.07
Tubastatin	-	N.D.	N.D.	0.033 ± 0.017	N.D.

[a]All compounds were evaluated in duplicate in two independent experiments. Values represent the mean ± SEM. N.D. = not determined.

https://doi.org/10.1021/acs.jmedchem.4c02024
J. Med. Chem. XXXX, XXX, XXX−XXX

Table 2. Inhibition of Human HDAC1, 2, 3, 4, 6, 8, and 11 by Compounds 4d and 4m and Reference Compounds Vorinostat, Panobinostat, and Tubastatin A

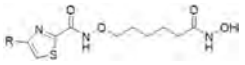

compound	R	IC_{50} (HDAC1) [μM]	IC_{50} (HDAC2) [μM]	IC_{50} (HDAC3) [μM]	IC_{50} (HDAC4) [μM]	IC_{50} (HDAC6) [μM]	IC_{50} (HDAC8) [μM]	IC_{50} (HDAC11) [μM]
4d		0.0045 ± 0.0010	0.015 ± 0.004	0.013 ± 0.002	> 100	0.038 ± 0.012	5.8 ± 0.8	26 ± 4
4m		0.012 ± 0.003	0.0045 ± 0.0007	0.048 ± 0.012	> 100	0.06 ± 0.03	4.8 ± 1.6	36 ± 7
Vorinostat	-	0.082 ± 0.018	0.165 ± 0.006	0.073 ± 0.010	47 ± 6	0.047 ± 0.003	5.9 ± 0.7	> 100
Panobinostat	-	0.0082 ± 0.0015	N.D.	0.014 ± 0.003	0.72 ± 0.06	N.D.	0.30 ± 0.07	2.9 ± 0.2
Tubastatin	-	N.D.	N.D.	N.D.	N.D.	0.033 ± 0.017	N.D.	N.D.

[a]All compounds were evaluated in duplicate in two independent experiments. Values represent the mean ± SEM. N.D. = not determined.

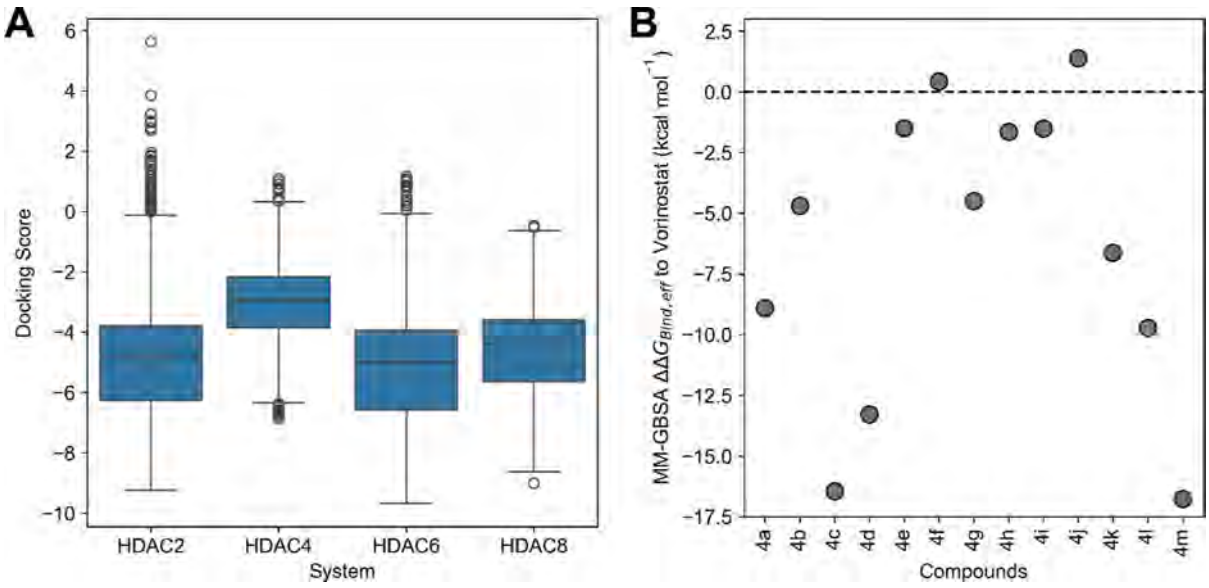

Figure 3. (A) Comparison of the docking results between the isoenzymes HDAC2, 4, 6, and 8 for compounds **4a**−**4m**. The results mirror the enzyme assay data in that the compounds on average show better inhibition of HDAC2, HDAC6, and HDAC8 than HDAC4. (B) MM-GBSA results of the best-docked pose of a compound in HDAC2. In line with the results of the enzyme assay, **4m** is predicted to have the best effective binding energy.

topic of hydroxylamine analogs to established amine moieties.[37,38]

As starting materials for a diverse set of phenylthiazole analogs were readily available, we aimed in this study to further develop **4a** into a new antileukemic lead structure by elucidating the structure−activity relationship of its terminal phenyl moiety.

2.1. Synthesis. The synthesis of the novel HDACi (**4a**−**m**) started with the saponification of phenylthiazole carboxylic esters (**1a**−**m**) followed by HBTU-mediated coupling reactions of the generated corresponding sodium salts with the hydroxylamine linker **2** containing the *O*-trityl-protected hydroxamic acid zinc binding group using a modified protocol of Goodreid et al.[39] (Figure 2). The coupling reactions for the construction of the pentyloxyamide moiety were performed utilizing the in situ generated sodium salts of the respective carboxylic acids as the corresponding acids of **1a**−**m** were prone to decarboxylation. The synthesis of the hydroxylamine linker **2** was previously published by our group.[26] Subsequent TFA and triethylsilane-mediated deprotection of the *O*-trityl-protected hydroxamates yielded the hydroxamic acids **4a**−**m**.

2.2. HDAC Enzyme Inhibition. All synthesized HDACi are nanomolar inhibitors of HDAC2, a representative of HDAC class I, and of HDAC6, a representative of HDAC class IIb. The HDAC enzyme inhibition profile did not differ remarkably among the improved analogs (Table 1). Derivate **4m** was the most potent HDAC2 inhibitor improving the IC_{50} of the parent compound **4a** (IC_{50} 0.140 μM) significantly by a factor of 13 (IC_{50} 0.0045 μM). Also, compounds **4d** (IC_{50} 0.015 μM) and **4l** (IC_{50} 0.010 μM) improved HDAC2 inhibition in comparison to **4a** by a factor of 4 or 6, respectively. Interestingly, HDAC6 inhibition was not improved to the same extent as HDAC2 inhibition. **4c** is the most active HDAC6 inhibitor in this series and exceeded the activity of the parent compound by a factor of about three (IC_{50} 0.026 μM). However, each newly synthesized HDAC inhibitor surpassed vorinostat in regards to HDAC2 inhibition and was similarly potent as tubastatin A in HDAC6 enzyme inhibition.

https://doi.org/10.1021/acs.jmedchem.4c02024
J. Med. Chem. XXXX, XXX, XXX−XXX

Encouraged by the promising results of **4m** and **4d**, these compounds were subjected to an expanded HDAC isozyme analysis (Table 2), which demonstrated nanomolar inhibition of HDAC 1 and 3 but only weak HDAC11 inhibition.

2.3. Docking Studies. Molecular docking was performed to assess the binding affinities of the compounds **4a**−**4m** to human HDAC2, 4, 6, and 8 from a structural perspective. Binding affinities predicted with the Glide SP scoring function of the Schrödinger Suite[40] generally align with the enzyme assay results when considered on a per-isoform basis (Table 1, Figure 3): On average, **4a**−**4m** yield more favorable docking scores in HDAC2, HDAC6, and HDAC8 (−5.1 ± 1.8 kcal mol^{-1}, −5.3 ± 1.5 kcal mol^{-1}, and −4.7 ± 1.2 kcal mol^{-1}, respectively) than in HDAC4 (−3.0 ± 1.4 kcal mol^{-1}). Although predicting binding affinities with scoring functions requires caution when the differences are small,[41] this agreement mirrors that IC_{50} values for HDAC4 are one to two orders of magnitude larger than for the other isoforms. To support the results, Molecular Mechanics - Generalized Born Surface Area (MM-GBSA) computations were used to predict effective binding energies for the best-docked pose of each compound in HDAC2. The results identify **4m** as the compound with the highest binding affinity, which agrees with the experimental data. The other compounds cannot be expected to be ranked well due to the small value range (a factor of ∼2 except for **4d**, **4l**, which are predicted second and third best, qualitatively in line with the experimental data; **4c** is overpredicted; Table 1) and SEM values of up to ∼50% of the mean value.

The docking poses of **4m** and the unsubstituted compound **4a** (Figure 4) in human HDAC2 show an interaction of the hydroxamate moiety with the zinc ion, hydrogen bonds with D100 and Y304, and stacking interactions of the phenyl moiety with H29 close to the rim of the binding tunnel. The *p*-substitution of the phenyl ring with pyrrolidine in **4m** increases the interaction surface of the complex, allowing for additional apolar interactions. The entropic penalty for extending the ligand with the pyrrolidine moiety is likely small since free rotation about the *C*−*N* axis is already restricted in solution due to conjugation such that only a few degrees of freedom are lost upon binding.

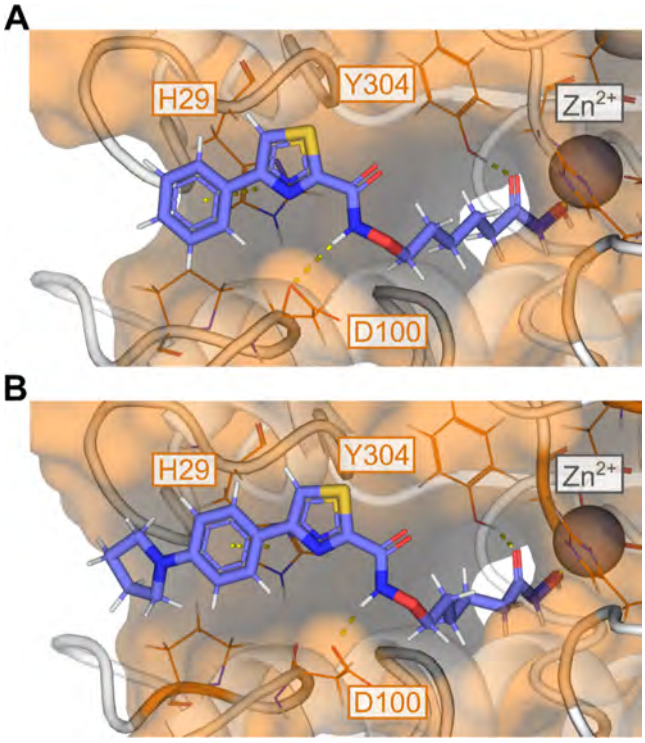

Figure 4. Predicted binding poses of compounds **4a** (A) and **4m** (B) to human HDAC2 (PDB-ID: 7KBG).[42]

2.4. Crystal Structures of 4d and 4m in Complex with HDAC6. To analyze the binding mode of **4d** and **4m** to HDAC6, both inhibitors were cocrystallized with the catalytic domain 2 (CD2) of HDAC6 from *Danio rerio* (zebrafish). This enzyme can be used as a model for human HDAC6 due to high structural similarity and high conservation of the active site.[43]

The crystal structures of CD2 from *Dr*HDAC6 bound to **4d** and **4m** were solved at 1.90 and 2.14 Å resolutions, respectively (Figure 5 and Supporting Information Table S1), providing, for the first time, insights into the binding mode of pentyloxyamide-based HDACi. The structures do not reveal pronounced conformational changes relative to the HDAC6 structure in the absence of any ligands (PDB ID: 5EEM).[44] The root-mean-square deviation (rmsd) between unliganded and **4d**-bound structures is 0.4 Å for 353 Cα atoms and between unliganded and **4m**-bound structures is 0.5 Å for 353 Cα atoms.

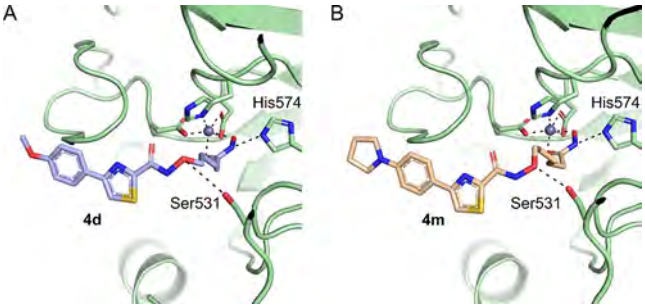

Figure 5. Crystal structures of (A) HDAC6−**4d** complex and (B) HDAC6−**4m** complex. The HDAC6 protein is shown as a cartoon and colored pale green. Close-up view of the active site with the ligands and the side chains of the amino acids coordinated to the zinc ion shown as a stick model and colored light blue (**4d**) and wheat (**4m**). The ligands and amino acid side chains are colored according to the element-specific color code. The zinc ion is shown as a sphere and colored gray. A figure displaying the simulated annealing omit map of the ligands is shown in the Supporting Information (Figure S1) (PDB ID: 9GGH and 9GGK).

The inhibitors **4d** and **4m** bind in a similar conformation to *Dr*HDAC6 with the hydroxamate group coordinated to the zinc ion in the active site. The flexible pentyloxyamide connecting unit linker region is able to enter the narrow channel to the active site and enable a tight coordination to the zinc with O−Zn distances of 2.0 Å. The higher electron density observed in the simulated annealing omit map of the inhibitor shows that the sulfur atom of the thiazole group has the same orientation in both inhibitors, suggesting that only one conformation is adopted (Supporting Information Figure S1). Interestingly, the oxygen and nitrogen atoms of the oxyamide connecting unit of **4d** and **4m** are in a similar position despite not forming a specific interaction with the protein surface. In addition to the coordination of the hydroxamate group to the zinc ion, we observe two

https://doi.org/10.1021/acs.jmedchem.4c02024
J. Med. Chem. XXXX, XXX, XXX−XXX

Table 3. Comparison of the IC_{50} of the Experimental Compounds in Three Different Leukemia Entities

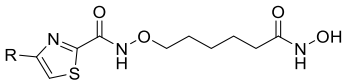

compound	R	IC_{50} (HL60) [nM]	IC_{50} (HPBALL) [nM]	IC_{50} (K562) [nM]
4a		424.6 ± 68.3	459.8 ± 35.2	879.2 ± 25.5
4b		332.1 ± 56.2	523.1 ± 58.2	993 ± 128.2
4c		670.7 ± 74.8	714.6 ± 55.2	1478.7 ± 53
4d		76.8 ± 8.2	110.6 ± 15.2	180.8 ± 55.7
4e		352.4 ± 25.5	359.9 ± 20	873.9 ± 238.4
4f		249.8 ± 84.5	421.2 ± 44.7	656.1 ± 264.7
4g		380.3 ± 36.8	465.3 ± 73.1	786.4 ± 230.9
4h		168.1 ± 104	355.9 ± 19.6	526.5 ± 28
4i		313.7 ± 96.5	403.8 ± 46.2	722 ± 164
4j		192.4 ± 22.4	279 ± 20.7	414.6 ± 38.8
4k		263.7 ± 70.7	446.4 ± 65.7	629.6 ± 69.6
4l		86 ± 10.4	119.4 ± 6.2	242.5 ± 52
4m		49.1 ± 5.4	100.1 ± 6	141.9 ± 13.2
Vorinostat	-	318.03 ± 36.7	823.53 ± 27	577.4 ± 119.8
Ricolinostat	-	2190.3 ± 24.9	2583.7 ± 71.16	2933 ± 79.5
CI994	-	1578.7 ± 92.5	4703.3 ± 117.2	5331.3 ± 948.17
Belinostat	-	157.7 ± 13.9	269.1 ± 5	217.9 ± 51.8

interactions with the HDAC6 protein. The imidazole ring of H574 interacts with the nitrogen atom in the hydroxamate group of the inhibitor, and the oxygen atom in the hydroxy group of S531 interacts with the bivalent oxygen atom of the oxyamide connecting unit. Notably, the predicted binding mode of **4m** to human HDAC2 differs from the conformation observed in the crystal structure of *Dr*HDAC6, which may be due to the differences in the sequence between human HDAC2 and zebrafish HDAC6. Taken together, the crystal structures of **4d** and **4m** in CD2 of *Dr*HDAC6 provide important insights into the binding mode of the novel pentyloxyamide-based HDACi.

2.5. High Throughput Drug Screening on Cytotoxicity of Novel HDACi. A HTDS[45] was conducted to evaluate the activity of 13 new synthesized HDACi across three leukemia cell lines: K562, HPBALL, and HL60 (Table 3). By representing the IC_{50} values of each HDACi through heatmaps and performing unsupervised clustering, three

https://doi.org/10.1021/acs.jmedchem.4c02024
J. Med. Chem. XXXX, XXX, XXX−XXX

distinct clusters were identified (Supporting Information Figure S2). Compared to the lead inhibitor **4a**, the first cluster had similar activity against the three entities, while the second cluster consisted of HDACi with slightly lower IC_{50} and the third one showed significantly lower IC_{50} (~0.7 $\log_{10}$ fold change). In the HL60 cell line, which is the most sensitive, HDACi **4d**, **4m**, and **4l** showed IC_{50} values between 0.049 and 0.086 μM, whereas in the K562 cell line, the range was 0.141 to 0.242 nM. Throughout all three cell lines the inhibitor with the most potent anticancer activity is **4m**, followed by **4d** and **4l**.

2.6. Structure−Activity-Relationship Analysis. First, we modulated the electronic properties of the terminal phenyl ring by introducing a methoxy or fluorine substituent at the 1′, 2′, or 3′-position. Though the introduction of fluorine did not influence the antileukemic effect of the HDAC inhibitors significantly regardless of the ring position (**4e**−**g**), the introduction of a methoxy substituent at the 4′-position (**4d**) enhanced the cytotoxic activity against leukemia cells in comparison to the 2′ or the 3′ derivates (**4b**, **4c**).

Second, the replacement of the phenyl ring with thiophene was tolerated (**4h** and **4i**). Interestingly, the sulfur in the 2′-position (**4h**) proved to be beneficial for the antileukemic activity. However, the overall influence on the cytotoxic activity against leukemic cells remained rather small.

Third, we focused on the optimization of the substituent in 4′-position. The molecular docking studies suggested that the introduction of a larger substituent would favor additional apolar interactions with the HDAC2 enzyme. Correlating with the molecular docking studies, the pyrrolidine analog **4m** is a compound with strong antileukemic activity and low nanomolar inhibition of the HDAC2 enzyme. Further agreeing with that, extending the size of the cap group with a 2′-benzofuran moiety (**4l**) also enhanced the cytotoxic activity remarkably in comparison to **4a**. Overall, the introduction of larger substituents in 4′-position in combination with electron donating heteroatoms (**4d**, **4m**) and the 2′ substitued benzofuran (**4l**) improved the antileukemic activity in comparison to the unsubstituted compound **4a** remarkably (Figure 5). In addition, there is also a good correlation between the antileukemic activity and the inhibition of HDAC2 and 6.

2.7. Western Blot Analysis. The HDAC inhibitory effects of the three most promising derivatives (**4d**, **4l**, and **4m**) were next evaluated through cell-based assays using the HL60 cell line. Treatment of HL60 cells with compounds **4d**, **4l**, and **4m** resulted in notable α-tubulin acetylation (indicating effective inhibition of HDAC6), as determined by Western blot analysis. Vorinostat was utilized as a control for comparison (Figure 6). When evaluating HDAC class I inhibition, the optimized inhibitors displayed higher histone H3 acetylation levels compared to vorinostat. Furthermore, correlating with the H3 acetylation, we observed higher PARP cleavage (indicator of apoptosis induction) with **4d**, **4l** and **4m**, suggesting their enhanced effectiveness in comparison to vorinostat.

2.8. Selective Cytotoxicity of 4d and 4m against Leukemia Cells Surpasses Various Commercial HDAC Inhibitors. Following the confirmation of cellular HDAC inhibition by the promising new HDACi series, we selected two most potent HDACi (**4d** and **4m**) for an extended drug screening analysis. This analysis involved evaluating their

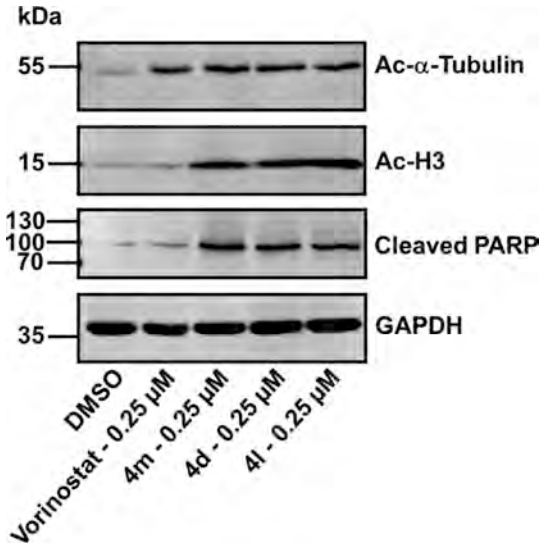

Figure 6. Western Blot analysis was conducted to assess the effects on HDAC inhibition markers (ac-H3 and ac-Tubulin) and the induction of apoptosis marker (cleaved PARP) following a 24 h treatment with **4d**, **4m**, and vorinostat (control) in HL60 leukemia cells (n = 3). A representative blot is shown here with GAPDH serving as the loading control.

effectiveness against 12 commercially available HDAC inhibitors using 7 leukemia cell lines (Figure 7A and Supporting Information Tables S2−S4) and 27 leukemia patient-derived xenograft (PDX) cells (Figure 7B and Supporting Information Tables S2−S4) across distinct therapy response subgroups. We incorporated healthy controls into our screens to determine whether **4d** and **4m** operate within a safe therapeutic window. These controls comprised $CD34^+$ hematopoietic stem and progenitor cells derived from cord blood and T-cells from healthy donors. By determining drug sensitivity scores (DSS) and generating selective or differential DSS (dDSS),[46] we obtained comparative data to evaluate their selectivity on the leukemia cells compared to the healthy controls. In comparative studies, both **4d** and **4m** demonstrated superior efficacy compared to clinically advanced HDAC inhibitors including tubastatin A, ricolinostat, CI994, romidepsin, and vorinostat. This was evidenced by their significantly elevated sDSS values when assayed against a panel of leukemia cell lines and PDX cells. Moreover, **4d** and **4m** consistently displayed selective antileukemic effects in the majority of tested leukemia cell types, suggesting their superiority over other examined HDACi. Additionally, standard chemotherapeutics used in leukemia treatment protocols, including cytarabine, idarubicin, daunorubicin, and azacitidine, were incorporated into the PDX drug screening analysis. Both **4d** and **4m** demonstrated significantly higher sDSS values, indicative of an improved therapeutic window and relatively similar cytotoxic profiles toward both chemotherapy-sensitive and chemotherapy-resistant subgroups (Figure 7B).

2.9. 4d and 4m Induce Cell Cycle Arrest and Apoptosis in Leukemia Cells. HDAC inhibition commonly leads to cell cycle arrest as an initial response, followed by the induction of apoptosis.[47,48] Analysis of the cell cycle demonstrated that treatment with **4d** in a concentration of 0.15 μM and **4m** at both concentrations significantly increased the proportion of HL60 cells in the G1 phase.

https://doi.org/10.1021/acs.jmedchem.4c02024
J. Med. Chem. XXXX, XXX, XXX−XXX

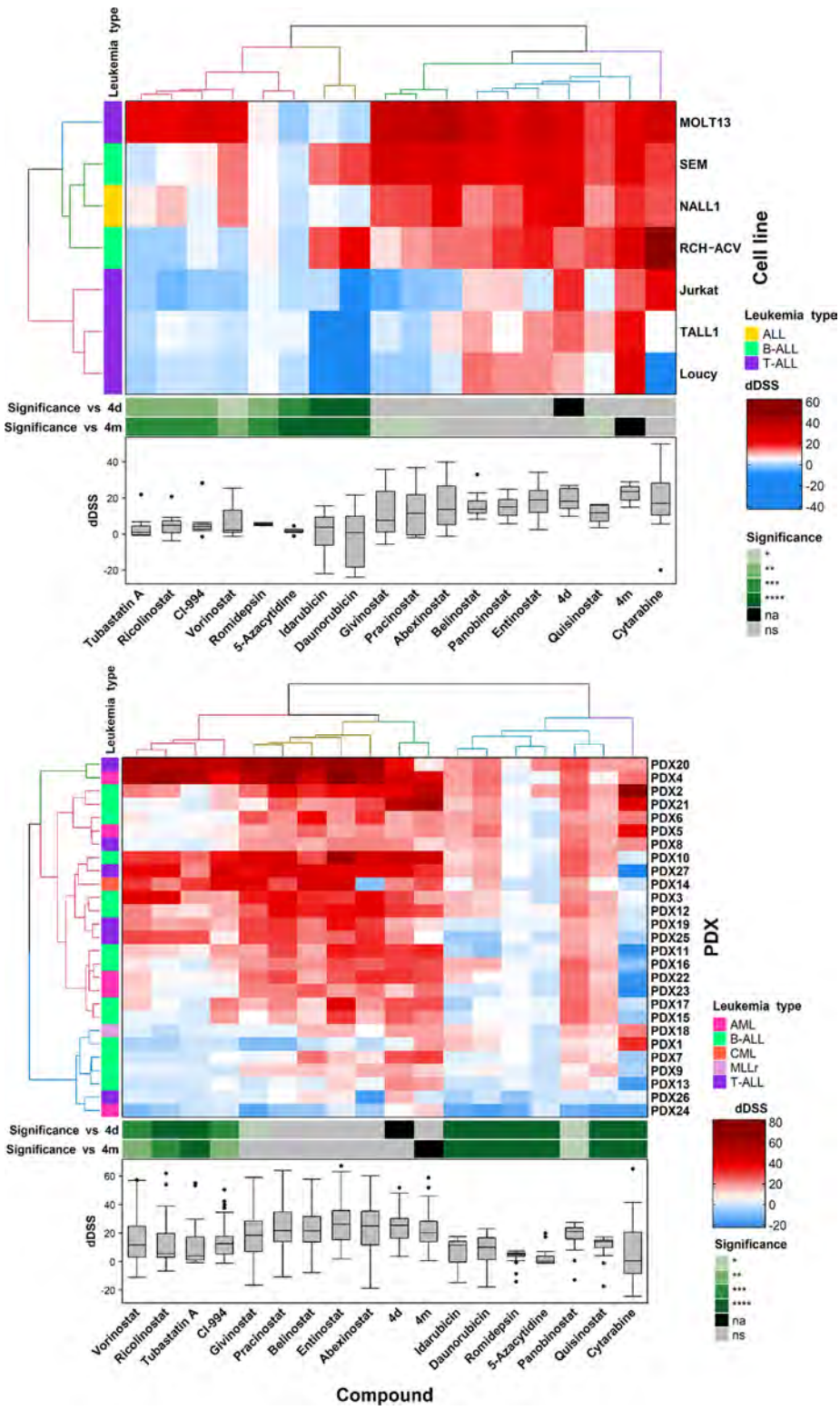

Figure 7. Unsupervised clustered heatmap displaying the differential drug sensitivity score (dDSS) of (A) leukemia cell lines and (B) PDX-grown leukemia cells. The statistical analysis was conducted using one-way ANOVA, $n = 1$. ALL = acute lymphoblastic leukemia, AML = acute myeloid leukemia, B-ALL = B-cell acute lymphoblastic leukemia, CML = chronic myeloid leukemia, MLLr = MLL rearranged leukemia, T-ALL = T-cell acute lymphoblastic leukemia, na = not applicable, ns = not significant, * = $p(\text{adj}) > 0.05$, ** = $p(\text{adj}) > 0.01$, *** = $p(\text{adj}) > 0.001$, and **** = $p(\text{adj}) > 0.0001$.

4d and **4m** reduced the number of cells in the S and G2/M phases significantly (Figure 8). Furthermore, an increased population of cells exhibited sub G1 labeling, indicating DNA fragmentation and confirming the induction of apoptosis. In comparison, **4m** exhibited greater potency than **4d** in inducing cell cycle arrest at the same concentration, which can be attributed to the lower IC_{50} value reported for **4m** as compared to **4d** (Table 3).

https://doi.org/10.1021/acs.jmedchem.4c02024
J. Med. Chem. XXXX, XXX, XXX−XXX

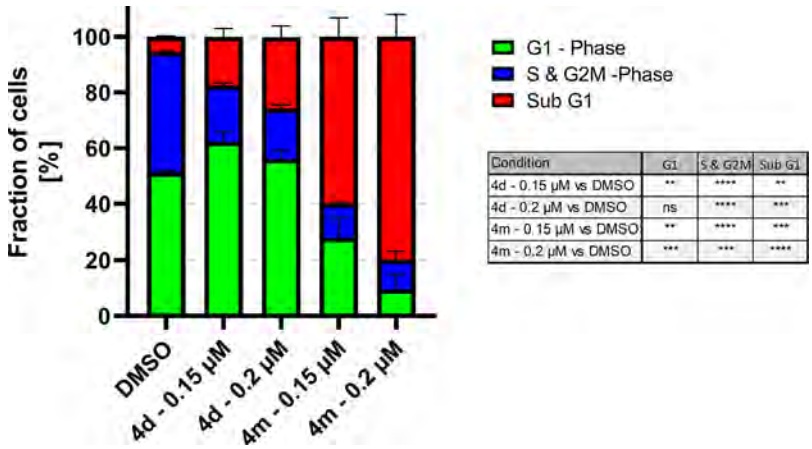

Figure 8. Bar graph depicting a cell cycle analysis via propidium iodide staining of HL60 leukemia cells treated with **4m** or **4d**, while the bar graphs displays statistical significance (unpaired student *t*-test, $n = 3$). ns = not significant, ** = $p(\text{adj}) > 0.01$, *** = $p(\text{adj}) > 0.001$, and **** = $p(\text{adj}) > 0.0001$.

To assess apoptosis induction by **4d** and **4m** further, we employed a trypan blue staining in conjunction with a caspase 3/7 assay on HL60 leukemia cells. As a control, we used the pan-caspase inhibitor Q-VD.[49] Treatment with **4d** or **4m** resulted in a significant reduction of viability ∼20% after 24 h and 70% after 48 h (Figure 9A). Q-VD reduced the loss of viability by 50%, suggesting that the cytotoxic effects triggered by both compounds are associated with apoptosis and are largely caspase-dependent. The caspase 3/7 assay further validated these findings, showing a marked increase in caspase activity after 48 h treatments with **4d** or **4m** (Figure 9B). Notably, Q-VD effectively negated this caspase 3/7 activity. In sum, the findings robustly indicate that both **4d** and **4m** induce apoptosis, leading to cytotoxic impacts on leukemia cells.

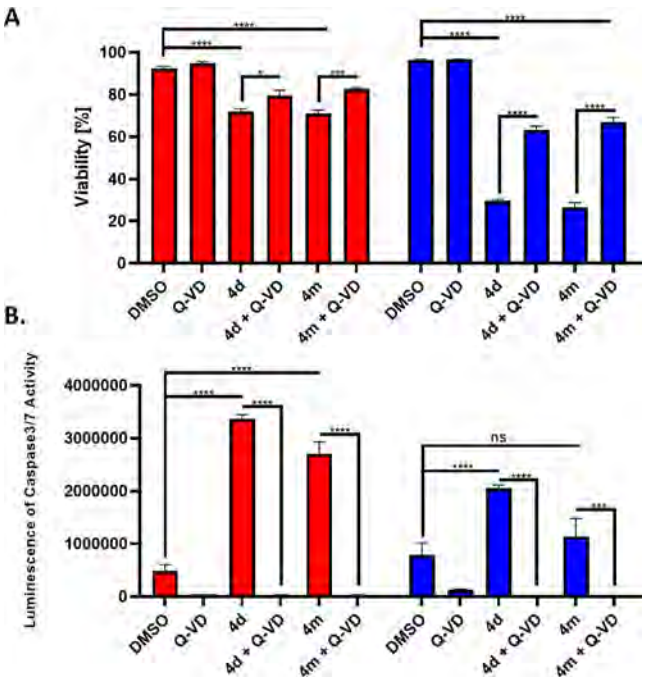

Figure 9. Bar diagram comparing the changes in (A) viability and (B) apoptosis induction via caspase 3/7 activity of HL60 leukemia cells treated with **4m** or **4d** and Q-VD (pan-Caspase inhibitor) via trypan blue or caspase3/7 assay, respectively. The statistical analysis was conducted using unpaired student *t*-test, $n = 3$. ns = not significant, * = $p(\text{adj}) > 0.05$, ** = $p(\text{adj}) > 0.01$, *** = $p(\text{adj}) > 0.001$, and **** = $p(\text{adj}) > 0.0001$.

2.10. 4d and 4m Synergize Effectively with the Standard Chemotherapy Drugs Decitabine and Clofarabine. Current clinical therapeutic strategies acknowledge the shortcomings of singular drug treatments, advocating for the utilization of synergistic drug combinations. These combinations aim to reduce cytotoxicity, exploit the unique susceptibilities of cancer cells, and avert drug resistance development. Therefore, we investigated potential synergistic drug combinations with the novel HDACi **4d** and **4m**. Decitabine, a first line chemotherapeutic, functions as a DNA methyltransferase inhibitor resulting in DNA hypomethylation. Synergistic drug effects between decitabine and HDACi have been well characterized, particularly in the context of AML.[50,51] Utilizing a matrix synergy screening method with the zero-interaction potency (ZIP) algorithm, we identified high ZIP synergy scores ranging from 60 to 80 across various concentration for both **4d** and **4m** when combined with decitabine (Figure 10A,B). Subsequently, we looked into the underlying mechanism of this drug synergy by evaluating the acetylation levels of histone H3 (Figure 10C). Although decitabine alone did not augment H3 acetylation, its combination with **4d** or **4m** showcased more pronounced bands compared to the individual HDACi treatment.

The combination ratio of decitabine to **4d** (5:1) was determined through synergy analysis, as this concentration ratio exhibited the highest synergistic interaction between them against AML cells. We have conducted additional combination experiments using a broad range of **4d** concentrations in conjunction with decitabine (Figure 10D). We included vorinostat as a positive control, maintaining the same concentrations as for **4d**. Notably, at equivalent concentrations, **4d** significantly increased actylated-H3 levels and cleaved PARP levels (a marker of apoptosis) compared to vorinostat in combination with decitabine (Figure 10E,F). Therefore, this enhanced effect on protein acetylation (Ac−H3) likely contributes to the observed synergistic cytotoxicity outcomes.

https://doi.org/10.1021/acs.jmedchem.4c02024
J. Med. Chem. XXXX, XXX, XXX−XXX

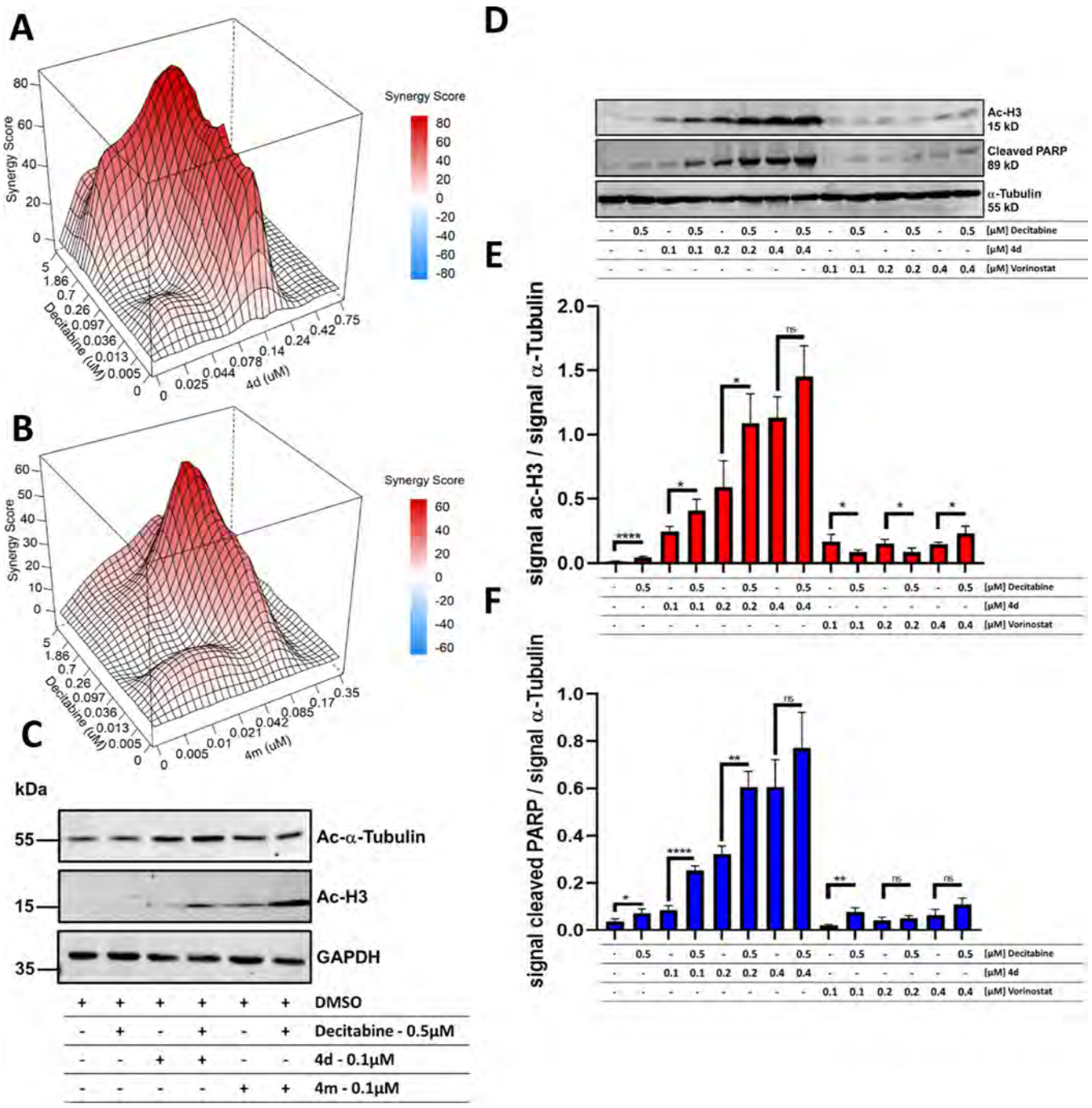

Figure 10. 3D synergy plots of HL60 cells treated with drug combinations for 72 h. The plots represent synergy scores from a combination matrix analyzed by the ZIP algorithm: (A) **4d** + decitabine and (B) **4m** + decitabine (n = 2). (C) Western blot analysis illustrating the differences in HDAC inhibition markers, ac-H3 and ac-Tubulin, in HL60 cells. The comparison is between solo treatment and combination treatments of either **4d** or **4m** with decitabine (n = 3) for 24 h. A representative blot is displayed with GAPDH as the loading control. (D) Western blot with increasing concentrations of **4d** and vorinostat combined with a fixed concentration of decitabine (n = 3). (E/F) Quantification of the signal of ac-H3 or cleaved PARP of D (unpaired student t-test, n = 3). ns = not significant, ** = p(adj) > 0.01, *** = p(adj) > 0.001, and **** = p(adj) > 0.0001.

The observed synergy of the epigenetic combination, which includes HDACi (**4d**) and DNMTi (Decitabine), has been corroborated by our studies and others, demonstrating significant synergistic activity against AML cells.[24,50−52] In fact, the safety, tolerability, and antileukemia activity of this combination have led to clinical trials involving AML patients.[53,54] Mechanistic insights suggest that the observed synergistic interaction is due to the crosstalk between DNA methylation and HDAC pathways. This mechanism involves a 5-methylcytosine-binding protein binding to gene promoters and recruiting HDACs.[55] In AML cells, this interaction is significant for the activation of tumor suppressor genes, including CDKN2B.[56] However, we acknowledge that the detailed mechanism underlying enhanced cytotoxicity upon combining HDAC and DNMT inhibitors is still unclear.

https://doi.org/10.1021/acs.jmedchem.4c02024
J. Med. Chem. XXXX, XXX, XXX−XXX

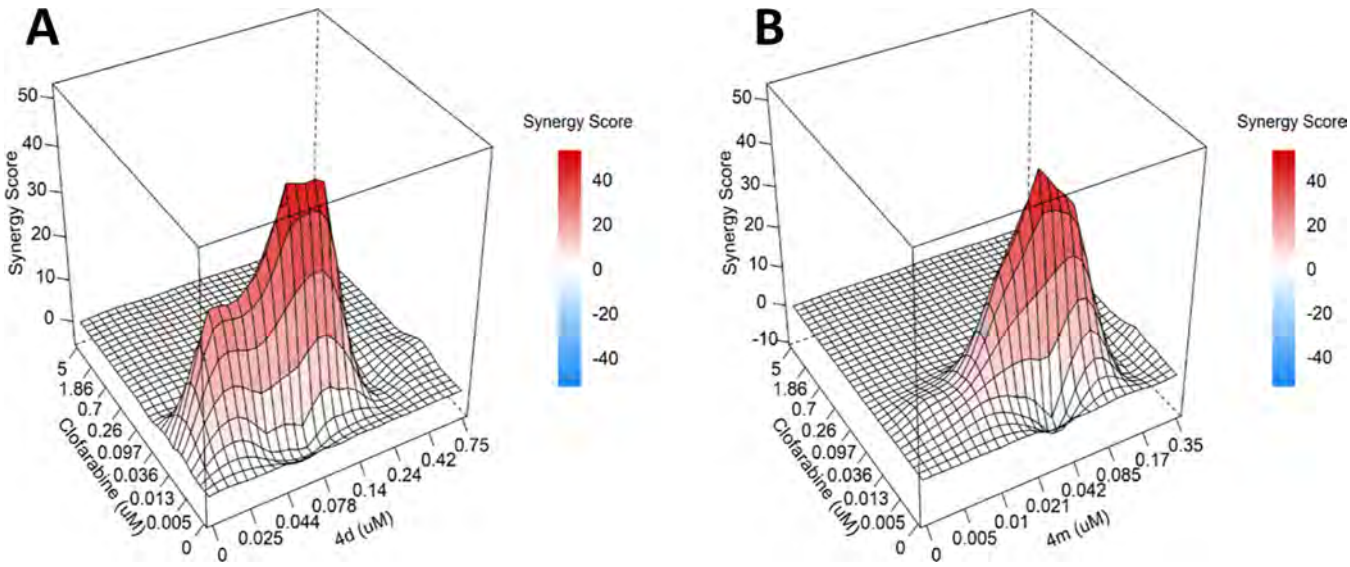

Figure 11. 3D synergy plots of HL60 cells treated with drug combinations for 72 h. The plots represent synergy scores from a combination matrix analyzed by the ZIP algorithm: (A) **4d** + clofarabine and (B) **4m** + clofarabine (n = 2).

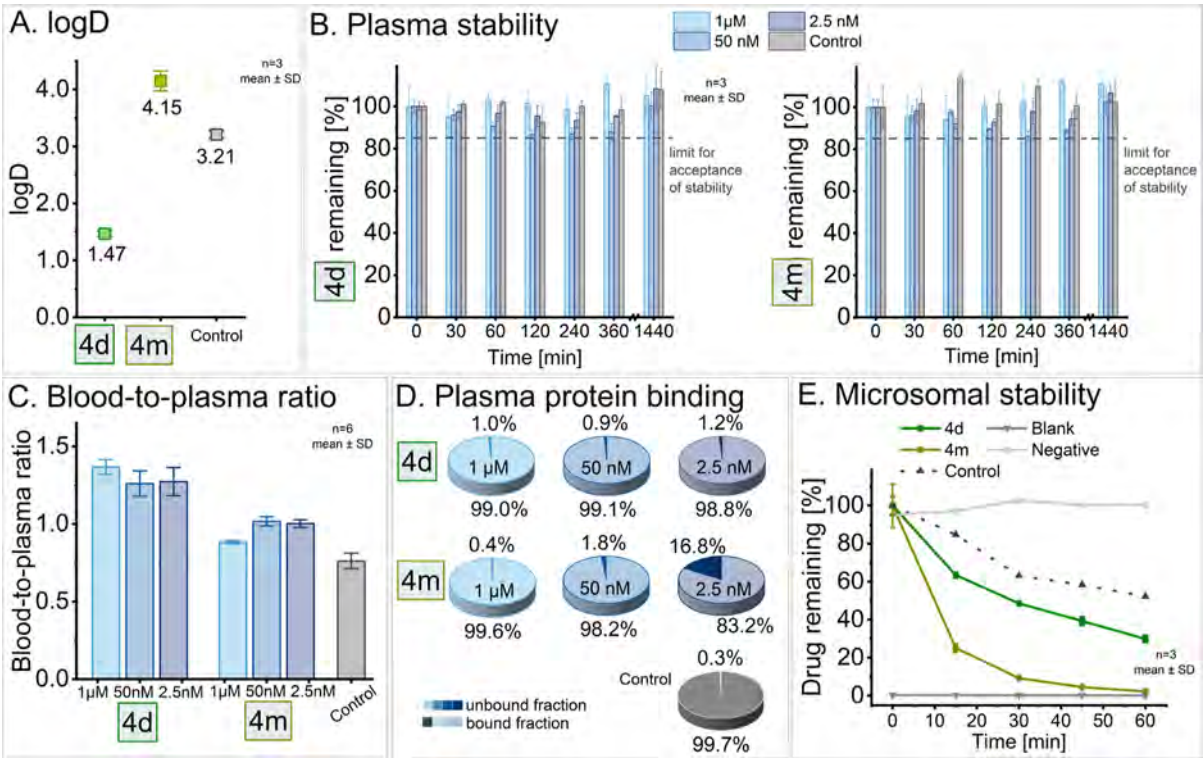

Figure 12. Overview of in vitro pharmacokinetics of **4d** and **4m**. (A) Interval plot of the determination of the coefficient of distribution (log D). Carvedilol was used as a control. (B) Stability of **4d** and **4m** in human plasma over 24 h at three different concentrations. A limit of −15% was set as acceptance criterium for stability according to bioanalytical guidelines. 4% bovine serum albumin (BSA) (absence of plasma enzymes) was used as a control spiked with a concentration of 50 nM of the drug. (C) Blood-to-plasma ratio of **4d** and **4m** for the three assessed concentration levels applying carvedilol as a control. (D) Plasma protein binding for **4d** and **4m** at three different concentration levels. The mean value of n = 3 is displayed. Itraconazol was used as a control. (E) Microsomal stability of **4d** and **4m** in HLMs. Propranolol was used as a control. The blank contains no drug, while the negative is free of HLMs. BSA: bovine serum albumin, HLM: HLMs, and SD: standard deviation.

HDAC inhibition contributes to increased DNA damage.[57] We examined the synergistic impact of combining **4d** and **4m** with clofarabine, a purine nucleoside analog and DNA synthesis inhibitor. In line with our previous observations, we found in a similar matrix synergy approach, ZIP synergy scores around 50 when **4d** and **4m** were administered in combination with clofarabine (Figure 11A,B).

These findings indicate that HDAC inhibitors **4d** and **4m** enhance the effectiveness of first line chemotherapeutics

https://doi.org/10.1021/acs.jmedchem.4c02024
J. Med. Chem. XXXX, XXX, XXX−XXX

Table 4. Comparison of In Vitro Pharmacokinetic Data of 4d and 4m to Vorinostat[a]

	vorinostat	4d	4m
log D	1.46[63]	1.47 ± 0.05	4.15 ± 0.18
plasma stability/$t_{1/2}$	75 min[63]	>24 h	>24 h
$K_{B/P}$	2.0[64]	1.26 ± 0.16 (50 nM)	1.02 ± 0.06 (50 nM)
plasma protein binding	71%[65] (1.89 μM)	99.0% (1 μM)	99.6% (1 μM)
microsomal stability/$t_{1/2}$(clearance category)	60 min[66] (intermediate)	35.9 min[66] (intermediate)	11.2 min (high)

[a]$K_{B/P}$: blood-to-plasma ratio, log D: coefficient of distribution at pH 7.4, $t_{1/2}$: half-life.

Table 5. Pharmacokinetic Parameters (AUC_{last}, C_{max}, T_{max}, and $t_{1/2}$) Were Calculated According to a Noncompartmental Analysis (NCA) from the Blood Concentration of 4d Based on Actual Blood Sampling Time Pre-Dose and Post-Dose[a]

variable	mouse 1	mouse 2	mouse 3	mean [±SD]	vorinostat	
	intraperitoneal 10 mg/kg				per oral 50 mg/kg	
C_{max} (ng/mL)	1490	1030	1230	1250 [±232]	501[67]	580[68]
T_{max} (h)	0.25	0.25	0.25	0.25 [±0]	na[67]	0.08[68]
AUC_{last} (h·ng/mL)	523	396	480	466 [±65]	619[67]	347[68]
$t_{1/2}$ (h)	0.275	0.554	0.227	0.352 [±0.177]	0.75[67]	0.8[68]

[a]Na: not applicable.

decitabine and clofarabine potentially allowing for dose reduction and decreasing the likelihood of drug resistance.

2.11. 4d Shows Promising Human In Vitro Pharmacokinetics Superior to 4m. Determination of in vitro pharmacokinetic properties of new chemical entities is a key step in drug discovery and aids in nonclinical evaluation. To assess the initial ADME characteristics (absorption, distribution, metabolism, and elimination) of **4d** and **4m**, coefficient of distribution, plasma stability, blood-to-plasma ratio, microsomal stability, and plasma protein binding were investigated.

Good oral absorption can be assumed for the coefficient of distribution (log D) between 0 and 3.[58] The log D value was determined as 1.47 ± 0.05 for **4d** and 4.15 ± 0.18 for **4m** (Figure 12A), favoring **4d**. Carvedilol acted as a control and confirmed the assay validity (obtained: 3.21 vs in literature: 3.2).[59]

Further, in vitro plasma stability was determined, as instability is an indicator for rapid clearance or a short half-life ($t_{1/2}$), resulting in poor in vivo performance. **4d** and **4m** demonstrated excellent stability over the 24 h period monitored in human plasma at 37 °C (Figure 12B).

4m showed equal affinity to plasma and red blood cells, while **4d** tended toward higher distribution into red blood cells (Figure 12C), as determined by the blood-to-plasma ratio ($K_{B/P}$). One-way ANOVA confirmed no concentration dependency over the range of 2.5 nM to 1 μM for **4d** ($K_{B/P}$: 1.27 at 2.5 nM, 1.26 at 50 nM, and 1.37 at 1 μM), while for **4m** the $K_{B/P}$ at the highest concentration level investigated (1 μM) was significantly lower if compared to the lower concentration levels ($K_{B/P}$: 1.00 at 2.5 nM, 1.02 at 50 nM, and 0.88 at 1 μM). The control compound carvedilol validated the assay performance ($K_{B/P}$ obtained: 0.76 vs $K_{B/P}$ in literature: 0.76).[60]

Plasma protein binding was high for **4d** with a mean of 99.0% over the observed concentration range with no concentration-dependency. **4m** exhibited an atypical concentration-dependent plasma protein binding with lower binding for lower concentrations (Figure 12D). If proceeding in drug development, this phenomenon needs to be further investigated.[61] Itraconazol as control showed high plasma protein binding throughout all cavities confirming no leakage and being in line with values reported in the literature.[62]

While **4m** was extensively metabolized by hepatic enzymes, such as Cytochrome P450 and Uridine 5′-diphosphoglucuronosyltransferases, in Human liver microsomes (HLMs), **4d** showed moderate metabolism (Figure 12E). The half-life of **4d** was 35.9 min, with an intrinsic clearance of 38.6 μL/min/mg. When corrected for nonspecific protein binding in the incubation mixture, the unbound intrinsic clearance was determined as 54.7 μL/min/mg. The half-life of **4m** was substantially shorter with 11.2 min. While the corresponding intrinsic clearance resulted in 123.6 μL/min/mg, its unbound intrinsic clearance was 466.4 μL/min/mg.

Using the collected data, the in vivo hepatic clearance was estimated to be 0.39 L/min for **4d** and 8.18 L/min for **4m**. Assuming a hepatic blood flow of 1500 mL/min, **4d** can therefore be classified as a low hepatic extraction drug (calculated hepatic extraction ratio (E_h) < 0.3) and **4m** as high hepatic extraction drug (E_h > 0.7).

Finally, the collected in vitro pharmacokinetic data of **4d** and **4m** were compared to that of the approved drug vorinostat (Table 4). In comparison to vorinostat, **4d** appeared most promising for further pharmacokinetic investigation.

2.12. Preclinical Pharmacokinetic Study of 4d in Mice Showed Comparability to Vorinostat. Building on our human in vitro pharmacokinetic data, an in vivo pharmacokinetic study using **4d** was performed in three C57BL/6 mice. After intraperitoneal application of 10 mg/kg, a rapid onset of the compound was observed with a t_{max} of 0.25 h (mean) and C_{max} of 1250 ± 232 ng/mL (mean ± SD). Remarkably, dose adjusted overall exposure (AUC_{inf}/dose) of **4d** in mice was higher if compared to vorinostat (47 vs 12 h·kg·ng/mL/mg). Similar to vorinostat ($t_{1/2}$ = 0.75), **4d** was characterized by a short elimination half-life of 0.35 h (mean), indicating a substantial metabolism/elimination of **4d** in mice. A summary of pharmacokinetic data and a comparison with vorinostat is shown in Table 5.

2.13. 4d Suppresses In Vivo Growth of Myeloid Leukemia (MV4-11 and C1498) Cells. The pronounced cytotoxic effect of **4d** on leukemia cells, combined with the comparatively promising in vitro pharmacokinetic character-

https://doi.org/10.1021/acs.jmedchem.4c02024
J. Med. Chem. XXXX, XXX, XXX−XXX

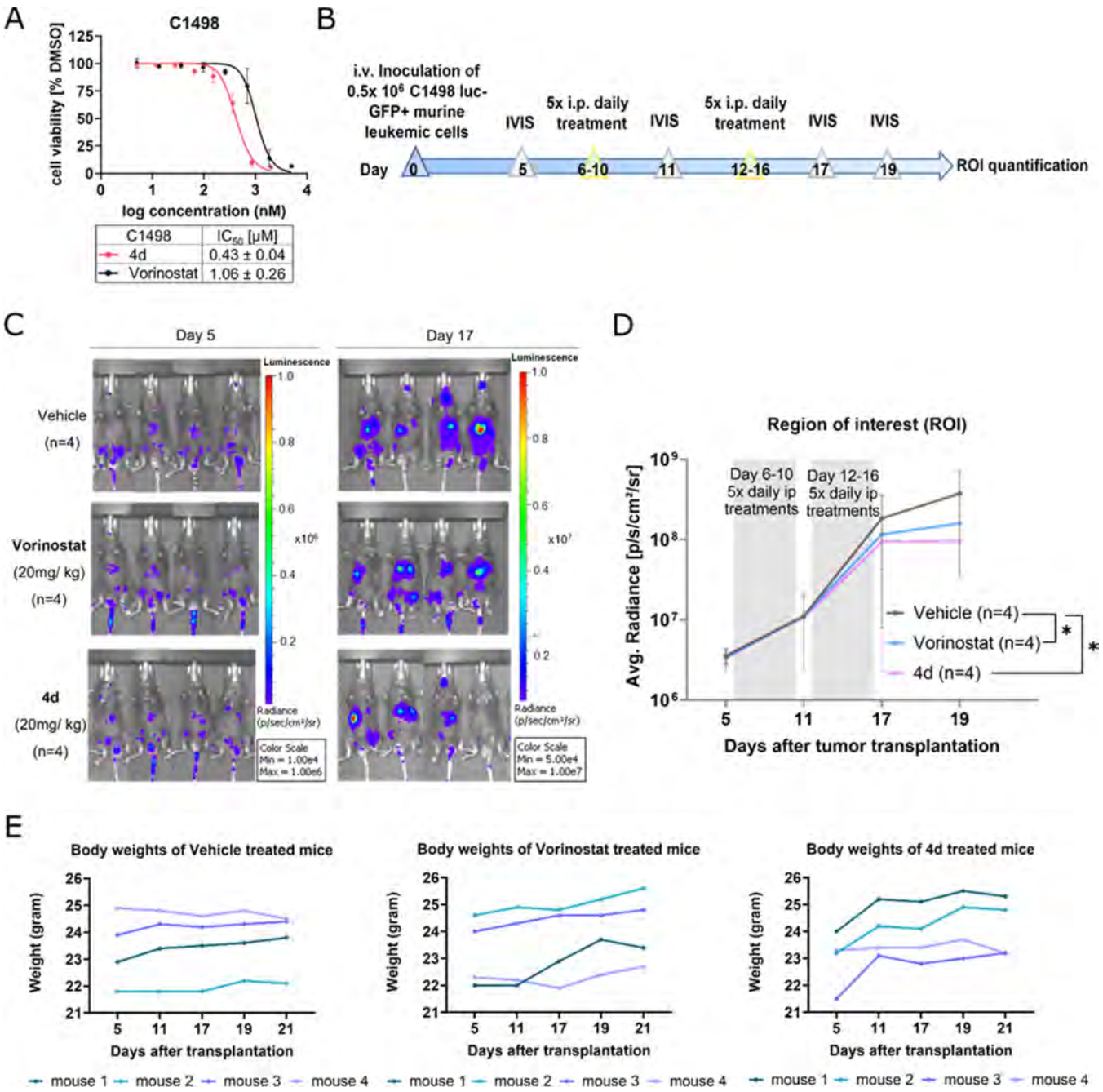

Figure 13. (A) Dose−response curve with IC_{50} value showing the inhibitory effect of vorinostat and compound **4d** on the proliferation of the C1498 cell line. The curve and IC_{50} values were generated with GraphPad Prism software by measuring the percentage of viable cells after 72 h incubation of cells with vorinostat and compound **4d** via CellTiter-Glo assay. Cell viability was normalized to DMSO (solvent)-treated controls. This curve and each point represent the results of the mean ± SD of biological and technical triplicates. (B) Schematic timeline of the experimental design. Each mouse received 0.5×10^6 C1498 luc-GFP$^+$ murine leukemic cells. After confirmation of tumor engraftment via monitoring the bioluminescence-based in vivo imaging system (IVIS) on day5, mice were grouped into three treatment groups, Vehicle (n = 4), Vorinostat (n = 4), and **4d** (n = 4). All mice received daily treatments accordingly via intraperitoneal injection. Tumor progression was examined by measuring bioluminescent signals with IVIS and ROI (p/s/cm^2/sr) quantification. (C) IVIS images of treated mice were taken on days 5 and 17. (D) ROI values at various time points, representing the measurement of leukemia cell growth. Statistical analysis was performed using a two-way mixed ANOVA with Greenhouse-Geisser correction. (E) Changes in body weight of each mouse from the three treatment groups before and after the treatment course.

istics of **4d**, prompted us to evaluate its effectiveness in a preclinical leukemic xenograft mouse (NSG) model using human AML cell line MV4-11. Initially, we determined the IC_{50} of **4d** in the MV4-11 cell line using the CellTiter-Glo assay, with vorinostat serving as a positive control, as described in prior methods. The dose−response curve and corresponding IC_{50} values were generated by applying a nonlinear regression algorithm to plot the log of inhibitor concentrations against normalized cell viability (Supporting Information Figure S3A). **4d** demonstrated an IC_{50} of 0.036 μM in MV4-11 cells, exhibiting over a 7-fold increase in potency compared to vorinostat. The in vivo experimental

https://doi.org/10.1021/acs.jmedchem.4c02024
J. Med. Chem. XXXX, XXX, XXX−XXX

design is illustrated in Supporting Information Figure S3B. Briefly, mice were first intravenously (i.v.) injected with (0.5 × 10^6) human AML (MV4-11) cells, stably expressing luciferase-GFP for tracking in vivo transplantation. The in vivo growth of the leukemia cells was examined after 14 days of injection via bioluminescence measurement using in vivo imaging system (IVIS). Next, the leukemia bearing mice were distributed randomly to two groups. From day 16 onward, the mice were treated for 8 consecutive days with intraperitoneal injections of either with a vehicle control or **4d** (at a dose of 10 mg/kg). The IVIS images (Supporting Information Figure S3C) and the quantified region of interest (ROI) measurements during the treatment period indicated that the treatment with **4d** significantly (p = 0.002) suppresses the in vivo growth of MV4-11 leukemia cells as compared to the vehicle control group (Supporting Information Figure S3D). At day 42, which is 3 weeks after discontinuing the **4d** treatment, no differences in the growth of leukemia cells was observed between **4d** treated and vehicle group. Importantly, for measuring the potential signs of toxicity, such as body weight alterations, the **4d** treatment group exhibited a minor (not significant) reduction during and after the treatment course when compared to the vehicle control group (Supporting Information Figure S3E).

Next, given the growing evidence of immunomodulatory effects of HDAC inhibitors in cancer therapy,[69] we utilized an allograft leukemia model. In this model, leukemia is established by injecting (C57BL/6) derived murine AML (C1498) cells by intravenous injection in immunocompetent wildtpye (C57BL/6) mice.[70] Similarly, we initially determined the IC_{50} of **4d** in C1498 cells, with vorinostat serving as a positive control. Both **4d** and vorinostat affected C1498 cell growth in a concentration-dependent manner with IC_{50} of 0.425 and 1.06 μM, respectively (Figure 13A). Similar to human leukemia cells, exposure to **4d** or vorinostat increased actylated-H3 levels in murine C1498 leukemia cells (Supporting Information Figure S4). The in vivo experimental design is illustrated in Figure 13B. Briefly, leukemia was established by injecting (0.5 × 10^6) murine AML (C1498) cells, stably expressing luciferase-GFP by intravenous injection in C57BL/6 mice.[70] Confirmation of tumor engraftment was assessed on day 5 after injection of leukemia cells by measuring the luminescence signals in the mice following D-Luciferin intraperitoneal injection (Figure 13C). Starting on day 6, the mice were divided into three treatment groups and administered intraperitoneally with either vehicle, positive control vorinostat (20 mg/kg), or **4d** (20 mg/kg) for 2 weeks. Compared to the vehicle control group, both the vorinostat- (p = 0.0249) and **4d** (p = 0.0326)-treated groups exhibited significantly lower leukemia burden after the second treatment cycle, with this difference becoming more pronounced by day 19 (Figure 13D). Additionally, no significant differences in body weight were observed during the treatment course (Figure 13E). Additionally, for the target engagement studies, we isolated liver cells from mice 24 h post-treatment with **4d**. Consistent with our in vitro observations, the intracellular staining intensity of acetylhistone H3 in liver cells was markedly increased in the **4d**-treated mice, pointing toward target engagement inside the organ tissues (Supporting Information Figure S5).

3. CONCLUSIONS

We developed a novel pentyloxyamide-based HDACi with substituted phenylthiazole cap groups and evaluated their potential as novel antileukemic lead structures. The leading candidates from this series, **4d** and **4m**, exhibited nanomolar inhibition toward HDAC2 and HDAC6 and demonstrated cytotoxic effects against a wide range of therapy-sensitive and therapy-resistant leukemia cell lines as well as against patient-derived leukemia cells. In addition, the binding modes of both inhibitors were determined by X-ray crystallography, revealing specific interactions with the CD2 of HDAC6 from *D. rerio* (zebrafish).

Importantly, **4d** and **4m** exhibited comparable or even higher DSS than well-established and clinically used HDAC inhibitors, along with greater selectivity toward malignant cells relative to healthy controls. Considering the current reliance on combination therapies in modern cancer treatment, drugs that demonstrate synergistic interactions can significantly influence the therapeutic outcome, delay or prevent the development of resistance, and increase the treatable population of patients. In this regard, the combination of **4d** and **4m** with the routinely used chemotherapeutic agents clofarabine and decitabine exhibited a notable synergistic cytotoxic effect. The promising in vitro pharmacokinetic characteristics and first in vivo pharmacokinetic data support comprehensive in vivo investigation of **4d**. Notably, in vivo administration of **4d** effectively suppressed the growth of leukemia cells without inducing any observable signs of toxicity in mice. Overall, these findings position **4d** and **4m** as novel lead structures with potential for further preclinical development, as they not only demonstrate a therapeutic window but also promising antileukemic effects when used in combination with established antileukemic drugs. Current challenges, such as the improvable in vivo pharmacokinetics of HDAC inhibitors **4d** and **4m** will be addressed along with further structure−activity relationship (SAR) studies in a follow-up lead optimization program.

4. EXPERIMENTAL SECTION

4.1. Chemistry. Chemicals and solvents were purchased from commercial suppliers (Acros Organics, TCI, abcr, Alfa Aesar, Ambeed, BLDpharm, and Merck) and used without further purification. Dry solvents were purchased from Acros Organics. The reactions were monitored by thin-layer chromatography (TLC) using Macherey-Nagel precoated ALUGRAM Xtra SIL G/UV_{254} plates. Spots were visualized either by irradiation with ultraviolet light (254 nm) or staining in potassium permanganate solution. Hydroxamic acids were further stained using a 1% solution of iron(III) chloride in ethanol. Flash chromatography was performed on a CombiFlash RF 200 or a Büchi Pure C-810 Flash using RediSep Rf-columns using the solvent mixtures of *n*-hexane/ethyl acetate or dichloromethane/methanol according to the separation. Melting points (mp) analyses were performed using a Büchi M-565 melting point apparatus and are uncorrected. Proton (^{1}H) and carbon (^{13}C) NMR spectra were recorded on a Bruker Avance III 300 or 600 MHz using DMSO-d_6 as the solvent. Chemical shifts are given in parts per million (ppm) relative to the residual solvent peak for ^{1}H and ^{13}C NMR. Coupling constants, J, were reported in Hertz (Hz). High-resolution mass spectra (HRMS) analysis was performed on a UHR-QTOF maXis 4G, Bruker Daltonics, by electrospray ionization (ESI). Analytical HPLC analyses were carried out on an Knauer AZURA system equipped with AZURA 6.1L (pumps), AZURA column thermostat CT 2.1 and AZURA UVD 2.1L (UV-detector), and a Spark Holland B.V. OPTIMAS model 820 autosampler, or on a Agilent LC 1260 Infinity II system equipped

https://doi.org/10.1021/acs.jmedchem.4c02024
J. Med. Chem. XXXX, XXX, XXX−XXX

with an G7116A Infinity II Multicolumn Thermostat, a G7104C Infinity II Flexible Pump a G7129C Infinity II Vialsampler and a G7114A Infinity II Variable Wavelength Detector. The separation took place on a Eurospher II 100 5 C18 (150 × 4 mm) column. UV absorption was detected at 254 nm. HPLC-grade water +0.1% TFA (solvent A) and HPLC-grade acetonitrile +0.1% TFA (solvent B) were used for elution at a flow rate of 1 mL/min. A linear gradient of 10% B to 100% B within 30 min was used. In the case of the *O*-trityl protected compounds **3a-m** HPLC-grade water (solvent A) and HPLC-grade acetonitrile (solvent B) were used for elution at a flow rate of 1 mL/min. A linear gradient of 10% B to 100% B within 30 min was used. All compounds are >95.0% pure by HPLC.

4.1.1. General Procedure for the Preparation of Phenylthiazoles ***1a−1m***. The respective 2-bromoketone (1.0 equiv) and ethyl thiooxamate (1.0 equiv) were dissolved in ethanol (7 mL/mmol) and heated at 70 °C. If the TLC (eluent: ethyl acetate/*n*-hexane) showed incomplete conversion after 7 h of heating, the reaction was stirred at room temperature overnight. After evaporation of the solvent, the resulting residue was diluted with ethyl acetate and washed three times with 50 mL of saturated sodium bicarbonate solution and once with 50 mL of brine. The organic phase was dried over anhydrous sodium sulfate and filtrated, and the solvent was evaporated under reduced pressure. The crude product was purified using flash chromatography using ethyl acetate and *n*-hexane as the eluent (0−30% ethyl acetate) to yield phenylthiazoles **1a−m**.

4.1.1.1. ***1a*** *Ethyl 4-Phenylthiazole-2-carboxylate.* Synthesis according to general procedure A using phenacyl bromide (4.1 g, 20.0 mmol) afforded **1a** as a light yellow solid (3.3 g, 14.1 mmol, 71%). mp 36.9 °C, t_r 14.47 min, purity: 99.3%.

^{1}H NMR (300 MHz, DMSO-d_6): δ 1.36 (t, J = 7.1 Hz, 3H), 4.42 (q, J = 7.1 Hz, 2H), 7.36−7.44 (m, 1H), 7.45−7.53 (m, 2H), 7.98−8.00 (m, 1H), 8.02 (d, J = 1.5 Hz, 1H), 8.53 (s, 1H).

^{13}C NMR (75 MHz, DMSO-d_6): δ 14.1, 62.2, 121.0, 126.2, 128.7, 129.0, 133.2, 156.3, 157.5, 159.4.

HRMS (m/z): MH$^+$ calcd for $C_{12}H_{11}NO_2S$ 234.0583; found, 234.0584.

4.1.1.2. ***1b*** *Ethyl 4-(2-Methoxyphenyl)thiazole-2-carboxylate.* Synthesis according to general procedure A using 2-bromo-1-(2-methoxyphenyl)ethanone (2.3 g, 10,0 mmol) afforded **1b** as a white solid (2.0 g, 7.6 mmol, 76%). mp 70.3 °C, t_r 15.21 min purity: 99.1%.

^{1}H NMR (300 MHz, DMSO-d_6): δ 1.36 (t, J = 7.1 Hz, 3H), 3.94 (s, 3H), 4.41 (q, J = 7.1 Hz, 2H), 7.09 (ddd, J = 7.8, 7.3, 1.1 Hz, 1H), 7.18 (dd, J = 8.4, 1.1 Hz, 1H), 7.40 (ddd, J = 8.3, 7.3, 1.8 Hz, 1H), 8.13 (dd, J = 7.7, 1.8 Hz, 1H), 8.45 (s, 1H).

^{13}C NMR (75 MHz, DMSO-d_6): δ 14.1, 55.6, 62.1, 111.9, 120.7, 121.6, 124.2, 129.4, 129.9, 152.3, 155.8, 156.6, 159.5.

HRMS (m/z): MH$^+$ calcd for $C_{13}H_{13}NO_3S$ 264.0689; found, 264.0696.

4.1.1.3. ***1c*** *Ethyl 4-(3-Methoxyphenyl)thiazole-2-carboxylate.* Synthesis according to general procedure A using 3-methoxyphenacyl bromide (2.3 g, 10.0 mmol) afforded **1c** as a white solid (1.9 g, 7.4 mmol, 74%). mp 76.6 °C, t_r 14.36 min purity: 98.9%.

^{1}H NMR (300 MHz, DMSO-d_6): δ 1.36 (t, J = 7.1 Hz, 3H), 3.83 (s, 3H), 4.42 (q, J = 7.1 Hz, 2H), 6.98 (ddd, J = 8.2, 2.6, 1.0 Hz, 1H), 7.40 (ddd, J = 8.2, 7.7, 0.4 Hz, 1H), 7.51−7.62 (m, 2H), 8.56 (s, 1H).

^{13}C NMR (75 MHz, DMSO-d_6): δ 14.1, 55.2, 62.2, 111.6, 114.4, 118.6, 121.3, 130.1, 134.6, 156.1, 157.3, 159.3, 159.7.

HRMS (m/z): MH$^+$ calcd for $C_{13}H_{13}NO_3S$ 264.0689; found, 264.0693.

4.1.1.4. ***1d*** *Ethyl 4-(4-Methoxyphenyl)thiazole-2-carboxylate.* Synthesis according to general procedure A using 4-methoxyphenacyl bromide (2.3 g, 10.0 mmol) afforded **1d** as a white solid (1.9 g, 7.3 mmol, 73%). mp 150.5 °C, t_r 14.40 min purity: 97.7%.

^{1}H NMR (300 MHz, DMSO-d_6): δ 1.36 (t, J = 7.1 Hz, 3H), 3.81 (s, 3H), 4.41 (q, J = 7.1 Hz, 2H), 6.99−7.09 (m, 2H), 7.90−7.98 (m, 2H), 8.37 (s, 1H).

^{13}C NMR (75 MHz, DMSO-d_6): δ 14.1, 55.2, 62.1, 114.3, 119.0, 126.0, 127.7, 156.3, 157.2, 159.4, 159.7.

HRMS (m/z): MH$^+$ calcd for $C_{13}H_{13}NO_3S$ 264.0689; found, 264.0693.

4.1.1.5. ***1e*** *Ethyl 4-(2-Fluorophenyl)thiazole-2-carboxylate.* Synthesis according to general procedure A using 2-bromo-2′fluoroacetophenone (2.2 g, 10.0 mmol) afforded **1e** as a white solid (1.3 g, 5.2 mmol, 52%). mp 65.7 °C, t_r 15.25 min purity: 99.8%.

^{1}H NMR (300 MHz, DMSO-d_6): δ 1.36 (t, J = 7.1 Hz, 3H), 4.42 (q, J = 7.1 Hz, 2H), 7.31−7.43 (m, 2H), 7.48 (tdd, J = 7.2, 5.3, 2.7 Hz, 1H), 8.11 (td, J = 7.8, 1.7 Hz, 1H), 8.37 (d, J = 2.4 Hz, 1H).

^{13}C NMR (75 MHz, DMSO-d_6): δ 14.0, 62.3, 116.3 (d, J = 22.0 Hz), 121.0 (d, J = 11.5 Hz), 124.8−125.2 (m), 129.8 (d, J = 2.8 Hz), 130.6 (d, J = 8.7 Hz), 149.8 (d, J = 2.3 Hz), 157.1, 157.8, 159.3, 161.1.

HRMS (m/z): MH$^+$ calcd for $C_{12}H_{10}FNO_2S$ 252.0489; found, 252.0490.

4.1.1.6. ***1f*** *Ethyl 4-(3-Fluorophenyl)thiazole-2-carboxylate.* Synthesis according to general procedure A using 2-bromo-1-(3-fluorophenyl)ethan-1-one (2.2 g, 10.0 mmol) afforded **1f** as a white solid (1.6 g, 6.5 mmol, 65%). mp 66.0 °C, t_r 14.81 min purity: 99.7%.

^{1}H NMR (300 MHz, DMSO-d_6): δ 1.36 (t, J = 7.1 Hz, 3H), 4.42 (q, J = 7.1 Hz, 2H), 7.24 (dddd, J = 9.1, 8.3, 2.6, 1.0 Hz, 1H), 7.41−7.66 (m, 1H), 7.73−7.92 (m, 2H), 8.64 (s, 1H).

^{13}C NMR (75 MHz, DMSO-d_6): δ 14.1, 62.3, 112.8 (d, J = 23.2 Hz), 115.5 (d, J = 21.2 Hz), 121.1−123.0 (m), 131.1 (d, J = 8.4 Hz), 135.5 (d, J = 8.3 Hz), 154.8 (d, J = 2.9 Hz), 157.7, 159.3, 161.0, 164.2.

HRMS (m/z): MH$^+$ calcd for $C_{12}H_{10}FNO_2S$ 252.0489; found, 252.0489.

4.1.1.7. ***1g*** *Ethyl 4-(4-Fluorophenyl)thiazole-2-carboxylate.* Synthesis according to general procedure A using 2-bromo-1-(4-fluorophenyl)ethan-1-one (1.1 g, 5.0 mmol) afforded **1g** as a white solid (0.8 g, 3.3 mmol, 66%). mp 74.0 °C t_r 14.79 min purity: 99.9%.

^{1}H NMR (300 MHz, DMSO-d_6): δ 1.36 (t, J = 7.1 Hz, 3H), 4.41 (q, J = 7.1 Hz, 2H), 7.25−7.39 (m, 2H), 7.96−8.13 (m, 2H), 8.51 (s, 1H).

^{13}C NMR (126 MHz, DMSO-d_6): δ 13.9, 62.1, 115.7 (d, J = 21.7 Hz), 120.6, 128.3 (d, J = 8.3 Hz), 129.8 (d, J = 3.1 Hz), 155.2, 157.5, 159.2, 161.3, 163.2.

HRMS (m/z): MH$^+$ calcd for $C_{12}H_{10}FNO_2S$ 252.0489; found, 252.0494.

4.1.1.8. ***1h*** *Ethyl 4-(Thiophen-2-yl)thiazole-2-carboxylate.* Synthesis according to general procedure A using 2-bromo-1-(thiophen-2-yl)ethanone (2.1 g, 10.0 mmol) afforded **1h** as a black solid (1.3 g, 10.0 mmol, 54%). mp 53.4 °C t_r 13.81 min purity: 96.5%.

^{1}H NMR (300 MHz, DMSO-d_6): δ 1.35 (t, J = 7.1 Hz, 3H), 4.41 (q, J = 7.1 Hz, 2H), 7.16 (dd, J = 5.1, 3.6 Hz, 1H), 7.61 (dd, J = 5.1, 1.2 Hz, 1H), 7.68 (dd, J = 3.6, 1.2 Hz, 1H), 8.37 (s, 1H).

^{13}C NMR (75 MHz, DMSO-d_6): δ 14.1, 62.3, 119.3, 125.5, 126.9, 128.2, 136.8, 151.1, 157.4, 159.2.

HRMS (m/z): MH$^+$ calcd for $C_{10}H_9NO_2S_2$ 240.0147; found, 240.0149.

4.1.1.9. ***1i*** *Ethyl 4-(Thiophen-3-yl)thiazole-2-carboxylate.* Synthesis according to general procedure A using 3-(bromoacetyl)-thiophene (1.0 g, 4.7 mmol) afforded **1i** as a brown oil (0.7 g, 3.0 mmol, 63%). T_r 13.43 min purity: 99.0%.

^{1}H NMR (300 MHz, DMSO-d_6): δ 1.35 (t, J = 7.1 Hz, 3H), 4.41 (q, J = 7.1 Hz, 2H), 7.63−7.69 (m, 2H), 8.03 (dd, J = 2.6, 1.6 Hz, 1H), 8.36 (s, 1H).

^{13}C NMR (151 MHz, DMSO-d_6): δ 14.1, 62.2, 120.3, 123.3, 126.2, 127.4, 135.4, 152.6, 157.3, 159.4.

HRMS (m/z): MH$^+$ calcd for $C_{10}H_9NO_2S_2$ 240.0147; found, 240.0151.

4.1.1.10. ***1j*** *Ethyl 4-(p-Tolyl)thiazole-2-carboxylate.* Synthesis according to general procedure A using 2-bromo-1-(*p*-tolyl) (2.2 g, 10.0 mmol) afforded **1j** as a white solid (1.7 g, 6.9 mmol, 69%). mp 60.0 °C, t_r 15.59 min purity: 99.3%.

https://doi.org/10.1021/acs.jmedchem.4c02024
J. Med. Chem. XXXX, XXX, XXX−XXX

^{1}H NMR (300 MHz, DMSO-d_6): δ 1.36 (t, J = 7.1 Hz, 3H), 2.35 (s, 3H), 4.41 (q, J = 7.1 Hz, 2H), 7.29 (dd, J = 7.9, 0.7 Hz, 2H), 7.84−7.94 (m, 2H), 8.45 (s, 1H).

^{13}C NMR (75 MHz, DMSO-d_6): δ 14.1, 20.8, 62.2, 120.1, 126.2, 129.5, 130.6, 138.2, 156.4, 157.3, 159.4.

HRMS (m/z): MH$^+$ calcd for $C_{13}H_{13}NO_2S$ 248.0740; found, 248.0744.

4.1.1.11. ***1k*** *Ethyl 4-(4-(Trifluoromethyl)phenyl)thiazole-2-carboxylate.* Synthesis according to general procedure A using 2-bromo-4′-(trifluoromethyl)acetophenone (2.8 g, 10.0 mmol) afforded **1k** as a white solid (2.3 g, 7.7 mmol, 77%). mp 134.3 °C, t_r 16.36 min purity: 96.4%.

^{1}H NMR (300 MHz, DMSO-d_6): δ 1.36 (t, J = 7.1 Hz, 3H), 4.43 (q, J = 7.1 Hz, 2H), 7.85 (d, J = 8.1 Hz, 2H), 8.23 (d, J = 8.0 Hz, 2H), 8.74 (s, 1H).

^{13}C NMR (75 MHz, DMSO-d_6): δ 14.1, 62.3, 123.3, 125.9 (d, J = 4.1 Hz), 126.9, 128.5, 128.9, 136.9, 154.5, 158.0, 159.3.

HRMS (m/z): MH$^+$ calcd for $C_{13}H_{10}F_3NO_2S$ 302.0457; found, 302.0465.

4.1.1.12. ***1l*** *Ethyl 4-(Benzofuran-2-yl)thiazole-2-carboxylate.* Synthesis according to general procedure A using 2-(bromoacetyl)-benzofuran (1.0 g, 4.1 mmol) afforded **1l** as a brown solid (0.5 g, 1.7 mmol, 42%). mp 128.6 °C, t_r 16.02 min purity: 99.4%.

^{1}H NMR (300 MHz, DMSO-d_6): δ 1.37 (t, J = 7.1 Hz, 3H), 4.43 (q, J = 7.1 Hz, 2H), 7.25−7.41 (m, 2H), 7.42 (d, J = 0.9 Hz, 1H), 7.69 (ddq, J = 17.4, 8.1, 0.8 Hz, 2H), 8.49 (s, 1H).

^{13}C NMR (151 MHz, DMSO-d_6): δ 14.1, 62.4, 104.2, 111.3, 121.8, 122.5, 123.5, 125.3, 128.2, 147.3, 150.3, 154.3, 158.7, 159.1.

HRMS (m/z): MH$^+$ calcd for $C_{14}H_{11}NO_3S$ 274.0532; found, 274.0534.

4.1.1.13. ***1m*** *Ethyl 4-(4-(Pyrrolidine-1-yl)phenyl)thiazole-2-carboxylate.* Synthesis according to general procedure A using 2-bromo-4′-(1-pyrrolidinyl)acetophenone (2.8 g, 10.0 mmol) afforded **1m** as a dark yellow solid (0.9 g, 2.9 mmol, 29%). mp 180.5 °C, t_r 15.15 min purity: 99.3%.

^{1}H NMR (300 MHz, DMSO-d_6): δ 1.35 (t, J = 7.1 Hz, 3H), 1.88−2.04 (m, 4H), 3.21−3.32 (m, 4H), 4.40 (q, J = 7.1 Hz, 2H), 6.54−6.67 (m, 2H), 7.75−7.87 (m, 2H), 8.16 (s, 1H).

^{13}C NMR (151 MHz, DMSO-d_6): δ 14.1, 25.0, 47.2, 62.0, 111.6, 116.5, 120.5, 127.3, 147.8, 156.7, 157.5, 159.5.

HRMS (m/z): MH$^+$ calcd for $C_{16}H_{18}N_2O_2S$ 303.1162; found, 303.1167.

4.1.1.14. 6-(Aminooxy)-N-(trityloxy)hexanamide. The synthesis of the linker **2** was performed after an adapted protocol of Avelar et al.[71]

4.1.1.15. 6-Bromo-N-(trityloxy)hexanamide. To a stirred solution of 6-bromohexanoic acid (7.4 g, 38 mmol, 1.0 equiv) in 100 mL THF, isobutyl chloroformate (IBCF) (5.8 mL, 45 mmol, 1.2 equiv) and *N*-methylmorpholine (NMM) (5.0 mL, 45 mmol, 1.2 equiv) were added at 10 °C. After stirring for 15 min *O*-tritylhydroxylamine (13 g, 38 mmol, 1.0 equiv) dissolved in 50 mL, THF was carefully added, and the reaction was left stirring at room temperature overnight. The precipitate was filtered off, the filtrate was evaporated, and the crude residue was dissolved in ethyl acetate and washed three times with 100 mL of saturated sodium bicarbonate solution and once with 100 mL of brine. The organic phase was dried over anhydrous sodium sulfate, filtrated, and evaporated. The crude product was recrystallized from ethyl acetate/n hexanes to yield **I** (14 g, 30 mmol, 80%) as a white solid. mp 128.0 °C, t_r 17.58 min purity: 99.6%.

^{1}H NMR (300 MHz, DMSO-d_6): δ 1.07 (dd, J = 15.6, 6.6 Hz, 1H), 1.14−1.28 (m, 1H), 1.64 (p, J = 6.9 Hz,1H), 1.79 (t, J = 7.2 Hz, 1H), 3.41 (t, J = 6.8 Hz, 2H), 7.33 (s, 8H), 10.18 (s, 1H) ^{13}C NMR (75 MHz, DMSO-d_6): δ 23.8, 26.9, 31.7, 31.9, 34.9, 91.7, 127.4, 127.5, 128.9, 142.4, 170.1.

HRMS (m/z): MNa$^+$ calcd for $C_{25}H_{26}BrNO_2$ 474.1039; found, 474.1041.

4.1.1.16. 6-((1,3-Dioxoisoindolin-2-yl)oxy)-N-(trityloxy)-hexanamide. **I** (7.1 g, 16 mmol, 1.0 equiv), *N*-hydroxyphthalimide (NHPI) (2.6 g, 16 mmol, 1.0 equiv), and triethylamine (4.5 mL, 31 mmol, 2.0 equiv) were suspended in 100 mL acetonitrile and refluxed for 12 h. The solvent was removed, the residue dissolved in ethyl acetate and extracted with saturated sodium bicarbonate solution until the aqueous phase did not show any left NHPI. The organic phase was dried over anhydrous sodium sulfate, filtrated, and evaporated. The crude product was recrystallized using ethyl acetate/n hexanes to yield **II** (6.2 g, 12 mmol, 74%) as a white solid. mp 142.0 °C, HPLC t_r 16.72 min purity: 96.9%.

^{1}H NMR (300 MHz, DMSO-d_6): δ 1.11 (d, J = 16.0 Hz, 2H), 1.18−1.30 (m, 2H), 1.52 (t, J = 7.4 Hz, 2H), 1.72−1.85 (m, 2H), 4.03 (t, J = 6.7 Hz, 2H), 7.32 (s, 15H), 7.86 (s, 4H), 10.19 (s, 1H) ^{13}C NMR (75 MHz, DMSO-d_6): δ 24.4, 27.3, 77.5, 91.7, 123.2, 127.4, 127.5, 128.6, 129.0, 134.7, 142.5, 163.3, 170.2.

HRMS (m/z): MH$^+$ calcd for $C_{33}H_{30}N_2O_5$ 535.2227; found, 535.2237.

4.1.1.17. Synthesis of 6-(Aminooxy)-N-(trityloxy)hexanamide. **II** (2.1 g, 4.0 mmol, 1.0 equiv) was dissolved in 40 mL dichloromethane; subsequently, hydrazine monohydrate (0.4 mL, 8 mmol, 2.0 equiv) was added, and the reaction was left stirring overnight. The precipitate was filtered off, and the filtrate was washed three times with 50 mL of saturated sodium bicarbonate solution and once with 50 mL of brine. The organic phase was dried over anhydrous sodium sulfate, filtrated, and evaporated to yield the **2** (1.5 g, 3.7 mmol, 94%) as a white wax, which was suitable to use without any further purification. HPLC: tr 13.17 min purity: 96.0%.

^{1}H NMR (300 MHz, DMSO-d_6): δ 0.98 (q, J = 8.5 Hz, 2H), 1.18 (t, J = 7.6 Hz, 2H), 1.32 (q, J = 7.0 Hz, 2H), 1.77 (t, J = 7.4 Hz, 2H), 3.40 (t, J = 6.7 Hz, 2H), 5.84 (s, 2H), 7.32 (s, 15H), 10.16 (s, 1H).

^{13}C NMR (75 MHz, DMSO-d_6): δ 24.7, 25.0, 27.7, 31.9, 74.7, 91.7, 127.4, 127.5, 128.9, 142.5, 170.2.

HRMS (m/z): MH$^+$ calcd for $C_{25}H_{28}N_2O_3$ 405.2173; found, 405.2172.

4.1.2. General Procedure for the Preparation of the O-Trityl-Protected Hydroxamates ***3a−m***. The synthesis of the *O*-trityl-protected hydroxamates was performed after an adapted protocol of Goodreid et al.[39]

After solving the corresponding phenylthiazole (**1a−m**) (1.0 equiv) in tetrahydrofuran (15 mL/mmol), an equimolar amount of 1 M sodium hydroxide solution in water was added. The reaction was monitored via TLC (eluent ethyl acetate/*n*-hexane). After complete consumption of the starting material, the solvent was evaporated under reduced pressure, and the resulting solid was dried in a vacuum. The dried product was suspended in *N*,*N*-dimethylformamide (2.2 mL/mmol). HBTU (1.1 equiv) and DIPEA (1.1 equiv) were added, and the resulting suspension was left stirring until a clear solution was formed (usually after 1 h). To that solution **2** (1.1 equiv) solved in *N*,*N*-dimethylformamide (2.2 mL/mmol) was added, and the reaction was left stirring overnight. The solvent was removed under reduced pressure, the resulting product diluted with 50 mL dichloromethane and washed three times with 50 mL of saturated sodium bicarbonate solution and three times with 50 mL of brine. The organic layer was dried over anhydrous sodium sulfate, filtrated, and the solvent was removed under reduced pressure. The obtained crude product was purified via flash chromatography, unless otherwise stated, using *n*-hexane/ethyl acetate (0−100%) as the eluent to yield the *O*-trityl-protected hydroxamates **3a−m**.

4.1.2.1. ***3a*** *N-((6-Oxo-6-((trityloxy)amino)hexyl)oxy)-4-phenylthiazole-2-carboxamide.* Synthesis according to general procedure B using **2a** (114 mg, 0.5 mmol) afforded **3a** as a white solid (150 mg, 0.25 mmol, 51%). mp 130.0 °C, t_r 17.46 min purity: 99.6%.

^{1}H NMR (600 MHz, DMSO-d_6): δ 1.11 (dd, J = 14.8, 7.9 Hz, 2H), 1.25 (dq, J = 11.3, 5.4 Hz, 2H), 1.45−1.53 (m, 2H), 1.82 (t, J = 7.3 Hz, 2H), 3.86 (t, J = 6.6 Hz, 2H), 7.26−7.38 (m, 15H), 7.40 (t, J = 7.4 Hz, 1H), 7.49 (t, J = 7.7 Hz, 2H), 8.07 (d, J = 7.3 Hz, 2H), 8.44 (s, 1H), 10.21 (s, 1H), 12.15 (s, 1H).

^{13}C NMR (151 MHz, DMSO-d_6): δ 25.0, 25.2, 27.8, 32.4, 76.0, 92.2, 119.8, 126.8, 127.9, 128.0, 129.1, 129.3, 129.4, 133.8, 142.9, 155.9, 157.1, 162.0, 170.7.

https://doi.org/10.1021/acs.jmedchem.4c02024
J. Med. Chem. XXXX, XXX, XXX−XXX

HRMS (m/z): MNa^+ calcd for $C_{35}H_{33}N_3O_4S$ 614.2084; found, 614.2092.

4.1.2.2. ***3b*** *4-(2-Methoxyphenyl)-N-((6-oxo-6-((trityloxy)amino)-hexyl)oxy)thiazole-2-carboxamide.* Synthesis according to general procedure B using **2b** (0.8 g, 3.0 mmol) afforded **3b** as a white solid (1.7 g, 2.2 mmol, 74%). mp 190.6 °C, t_r 17.66 min purity: 98.8%.

^{1}H NMR (300 MHz, DMSO-d_6): δ 1.04−1.17 (m, 2H), 1.18−1.31 (m, 2H), 1.48 (t, J = 7.8 Hz, 2H), 1.80 (t, J = 7.0 Hz, 2H), 3.84 (t, J = 6.7 Hz, 2H), 3.94 (s, 3H), 7.03−7.13 (m, 1H), 7.17 (d, J = 8.4 Hz, 1H), 7.33 (s, 16H), 8.29−8.37 (m, 2H), 10.19 (s, 1H), 12.12 (s, 1H).

^{13}C NMR (75 MHz, DMSO-d_6): δ 24.5, 24.7, 27.3, 31.9, 55.6, 75.5, 91.7, 111.7, 120.4, 121.7, 122.6, 127.4, 127.5, 129.0, 129.7, 129.8, 142.4, 151.4, 156.6, 159.8, 170.2.

HRMS (m/z): MH^+ calcd for $C_{36}H_{35}N_3O_5S$ 622.2370; found, 622.2373.

4.1.2.3. ***3c*** *4-(3-Methoxyphenyl)-N-((6-oxo-6-((trityloxy)amino)-hexyl)oxy)thiazole-2-carboxamide.* Synthesis according to general procedure B using **2c** (0.8 g, 3.0 mmol) afforded **3c** as a white solid (1.2 g, 1.9 mmol, 62%). mp 142.8 °C, t_r 17.36 min purity: 99.3%.

^{1}H NMR (300 MHz, DMSO-d_6): δ 12.15 (s, 1H), 10.20 (s, 1H), 8.46 (s, 1H), 7.73−7.58 (m, 2H), 7.33 (d, J = 4.6 Hz, 16H), 6.96 (dd, J = 8.2, 2.6 Hz, 1H), 3.84 (d, J = 5.5 Hz, 5H), 1.81 (t, J = 6.9 Hz, 2H), 1.59−1.40 (m, 2H), 1.24 (s, 2H), 1.19−1.01 (m, 2H).

^{13}C NMR (75 MHz, DMSO-d_6): δ 24.5, 24.7, 27.3, 31.9, 55.2, 75.5, 91.7, 111.9, 114.2, 118.6, 119.6, 127.4, 127.5, 129.0, 129.9, 134.7, 142.4, 155.3, 156.5, 159.7, 161.4, 170.2.

HRMS (m/z): MH^+ calcd for $C_{36}H_{35}N_3O_5S$ 622.2370; found, 622.2373.

4.1.2.4. ***3d*** *4-(4-Methoxyphenyl)-N-((6-oxo-6-((trityloxy)amino)-hexyl)oxy)thiazole-2-carboxamide.* Synthesis according to general procedure B using **2d** (263 mg, 1.0 mmol) afforded **3d** as a white solid (150 mg, 0.24 mmol, 24%). mp 195.4 °C, t_r 17.34 min purity: 98.2%.

^{1}H NMR (300 MHz, DMSO-d_6): δ 1.11 (q, J = 7.7 Hz, 2H), 1.16−1.33 (m, 2H), 1.48 (p, J = 7.0 Hz, 2H), 1.81 (t, J = 7.3 Hz, 2H), 3.83 (d, J = 10.2 Hz, 5H), 6.99−7.08 (m, 2H), 7.33 (d, J = 4.7 Hz, 15H), 7.95−8.04 (m, 2H), 8.27 (s, 1H), 10.20 (s, 1H), 12.11 (s, 1H).

^{13}C NMR (75 MHz, DMSO-d_6): δ 24.5, 24.7, 27.3, 31.9, 55.2, 75.5, 91.7, 114.2, 117.3, 126.2, 127.4, 127.5, 127.7, 129.0, 142.5, 155.4, 156.6, 159.6, 161.3, 170.2.

HRMS (m/z): MNa^+ calcd for $C_{36}H_{35}N_3O_5S$ 644.2189; found, 644.2196.

4.1.2.5. ***3e*** *4-(2-Fluorophenyl)-N-((6-oxo-6-((trityloxy)amino)-hexyl)oxy)thiazole-2-carboxamide.* Synthesis according to general procedure B using **2e** (0.8 g, 3.0 mmol) afforded **3e** as a white solid (1.3 g, 2.1 mmol, 70%). mp 159.2 °C, t_r 17.87 min purity: 98.6%.

^{1}H NMR (300 MHz, DMSO-d_6): δ 1.00−1.18 (m, 2H), 1.24 (s, 2H), 1.47 (d, J = 8.2 Hz, 2H), 1.80 (t, J = 7.1 Hz, 2H), 3.85 (t, J = 6.6 Hz, 2H), 7.33 (s, 16H), 7.46 (dt, J = 7.9, 5.4 Hz, 1H), 8.21−8.34 (m, 2H), 10.19 (s, 1H), 12.18 (s, 1H).

^{13}C NMR (75 MHz, DMSO-d_6): δ 24.5, 24.7, 27.3, 31.9, 75.5, 91.7, 116.2 (d, J = 22.0 Hz), 121.0 (d, J = 11.5 Hz), 123.5 (d, J = 13.5 Hz), 124.8 (d, J = 3.4 Hz), 127.4, 127.5, 129.0, 130.1, 130.5 (d, J = 8.8 Hz), 142.5, 148.9, 156.4, 157.9, 161.2, 170.2.

HRMS (m/z): MH^+ calcd for $C_{35}H_{32}FN_3O_4S$ 610.2170; found, 610.2163.

4.1.2.6. ***3f*** *4-(3-Fluorophenyl)-N-((6-oxo-6-((trityloxy)amino)-hexyl)oxy)thiazole-2-carboxamide.* Synthesis according to general procedure B using **2f** (0.8 g, 3.0 mmol) afforded **3f** as a white solid (0.6 g, 1.0 mmol, 34%). mp 142.8 °C, t_r 17.85 min purity: 99.1%.

^{1}H NMR (300 MHz, DMSO-d_6): δ 1.11 (d, J = 7.2 Hz, 2H), 1.23 (d, J = 7.0 Hz, 2H), 1.48 (t, J = 7.3 Hz, 2H), 1.80 (t, J = 7.1 Hz, 2H), 3.85 (t, J = 6.6 Hz, 2H), 7.17−7.41 (m, 16H), 7.53 (td, J = 8.2, 6.2 Hz, 1H), 7.88−7.97 (m, 2H), 8.55 (s, 1H), 10.19 (s, 1H), 12.16 (s, 1H).

^{13}C NMR (75 MHz, DMSO-d_6): δ 24.7, 27.3, 75.6, 91.8, 113.3, 115.3 (d, J = 21.5 Hz), 120.6, 122.3, 127.4, 127.5, 129.0, 130.9 (d, J = 9.1 Hz), 135.7 (d, J = 8.4 Hz), 142.5, 154.0, 156.4, 161.7.

HRMS (m/z): MH^+ calcd for $C_{35}H_{32}FN_3O_4S$ 610.2170; found, 610.2173.

4.1.2.7. ***3g*** *4-(4-Fluorophenyl)-N-((6-oxo-6-((trityloxy)amino)-hexyl)oxy)thiazole-2-carboxamide.* Synthesis according to general procedure B using **2g** (253 mg, 1.0 mmol) afforded **3g** as a white solid (313 mg, 0.5 mmol, 51%). mp 163.0 °C, t_r 17.57 min purity: 99.6%.

^{1}H NMR (300 MHz, DMSO-d_6): δ 1.11 (d, J = 7.3 Hz, 2H), 1.24 (s, 2H), 1.40−1.55 (m, 2H), 1.79 (d, J = 7.5 Hz, 2H), 3.84 (t, J = 6.6 Hz, 2H), 7.24−7.41 (m, 17H), 8.06−8.15 (m, 2H), 8.41 (s, 1H), 10.18 (s, 1H), 12.13 (s, 1H).

^{13}C NMR (75 MHz, DMSO-d_6): δ 24.5, 24.7, 27.3, 31.9, 75.5, 91.7, 115.7 (d, J = 21.7 Hz), 119.1, 127.4, 127.5, 128.4 (d, J = 8.3 Hz), 128.9, 130.0 (d, J = 2.9 Hz), 142.4, 154.4, 156.5, 160.6, 161.6, 163.9, 170.2.

HRMS (m/z): MH^+ calcd for $C_{35}H_{32}FN_3O_4S$ 610.2170; found, 610.2180.

4.1.2.8. ***3h*** *N-((6-Oxo-6-((trityloxy)amino)hexyl)oxy)-4-(thiophen-2-yl)thiazole-2-carboxamide.* Synthesis according to general procedure B using **2h** (0.7 g, 3.0 mmol) afforded **3h** as a white solid (1.6 g, 2.6 mmol, 88%). mp 174.6 °C, t_r 17.23 min purity: 98.1%.

^{1}H NMR (600 MHz, DMSO-d_6): δ 1.09 (p, J = 7.9 Hz, 2H), 1.24 (p, J = 7.5 Hz, 2H), 1.47 (p, J = 7.0 Hz, 2H), 1.80 (q, J = 7.9 Hz, 2H), 3.84 (t, J = 6.6 Hz, 2H), 7.15 (dd, J = 5.0, 3.6 Hz, 1H), 7.25−7.38 (m, 15H), 7.58−7.62 (m, 1H), 7.64−7.68 (m, 1H), 8.25 (s, 1H), 10.19 (s, 1H), 12.09 (s, 1H).

^{13}C NMR (151 MHz, DMSO-d_6): δ 24.5, 24.7, 27.3, 31.9, 75.4, 91.7, 118.0, 125.4, 126.8, 127.4, 127.5, 128.1, 129.0, 136.8, 142.5, 150.3, 156.4, 161.8, 170.2.

HRMS (m/z) MH^+ calcd for $C_{33}H_{31}N_3O_4S_2$ 598.1829, found 598.1832.

4.1.2.9. ***3i*** *N-((6-Oxo-6-((trityloxy)amino)hexyl)oxy)-4-(thiophen-3-yl)thiazole-2-carboxamide.* Synthesis according to general procedure B using **2i** (665 mg, 2.8 mmol) afforded **3i** after recrystallization in n-hexane/ethyl acetate as a white solid (1.5 g, 2.6 mmol, 92%). mp 214.7 °C, t_r 16.91 min purity: 96.9%.

^{1}H NMR (300 MHz, DMSO-d_6): δ 1.10 (d, J = 7.2 Hz, 2H), 1.23 (d, J = 6.8 Hz, 2H), 1.46 (d, J = 7.2 Hz, 2H), 1.79 (d, J = 7.5 Hz, 2H), 3.84 (t, J = 6.6 Hz, 2H), 7.33 (d, J = 4.3 Hz, 15H), 7.62−7.73 (m, 2H), 8.01 (dd, J = 2.8, 1.5 Hz, 1H), 8.25 (s, 1H), 10.19 (s, 1H), 12.09 (s, 1H).

^{13}C NMR (126 MHz, DMSO-d_6): δ 24.9, 25.1, 27.7, 32.3, 75.9, 92.2, 119.0, 123.3, 126.7, 127.6, 127.8, 127.9, 129.3, 136.1, 142.9, 152.1, 157.0, 161.8, 170.6.

HRMS (m/z): MH^+ calcd for $C_{33}H_{31}N_3O_4S_2$ 598.1829; found, 598.1836.

4.1.2.10. ***3j*** *N-((6-Oxo-6-((trityloxy)amino)hexyl)oxy)-4-(p-tolyl)-thiazole-2-carboxamide.* Synthesis according to general procedure B using **2j** (742 mg, 3.0 mmol) afforded **3j** as a white solid (313 mg, 0.5 mmol, 17%). mp 163.2 °C, t_r 17.93 min purity: 95.1%.

^{1}H NMR (300 MHz, DMSO-d_6): δ 1.10 (d, J = 6.4 Hz, 2H), 1.23 (s, 2H), 1.46 (d, J = 7.7 Hz, 3H), 1.79 (d, J = 7.6 Hz, 2H), 2.35 (s, 3H), 3.84 (t, J = 6.6 Hz, 2H), 7.24−7.41 (m, 17H), 7.95 (d, J = 8.1 Hz, 2H), 8.36 (s, 1H), 10.19 (s, 1H), 12.11 (s, 1H).

^{13}C NMR (75 MHz, DMSO-d_6): δ 20.9, 24.5, 24.7, 27.3, 31.9, 75.5, 91.7, 118.5, 126.2, 127.4, 127.5, 129.0, 129.4, 130.7, 138.0, 142.5, 156.6, 161.4, 170.2.

HRMS (m/z): MNa^+ calcd for $C_{36}H_{35}N_3O_4S$ 628.2240; found, 628.2244.

4.1.2.11. ***3k*** *N-((6-Oxo-6-((trityloxy)amino)hexyl)oxy)-4-(4-(trifluoromethyl)phenyl)thiazole-2-carboxamide.* Synthesis according to general procedure B using **2k** (904 mg, 3.0 mmol) afforded **3k** as a white solid (499 mg, 0.8 mmol, 25%). mp 182.5 °C, t_r 19.44 min purity: 99.8%.

^{1}H NMR (300 MHz, DMSO-d_6): δ 1.11 (q, J = 7.7 Hz, 2H), 1.25 (t, J = 7.3 Hz, 2H), 1.48 (t, J = 7.4 Hz, 2H), 1.81 (t, J = 7.0 Hz, 2H), 3.85 (t, J = 6.6 Hz, 2H), 7.33 (s, 15H), 7.86 (d, J = 8.2 Hz, 2H), 8.29 (d, J = 8.1 Hz, 2H), 8.66 (s, 1H), 10.19 (s, 1H), 12.22 (s, 1H).

https://doi.org/10.1021/acs.jmedchem.4c02024
J. Med. Chem. XXXX, XXX, XXX−XXX

^{13}C NMR (75 MHz, DMSO-d_6): δ 24.4, 24.6, 27.2, 31.7, 75.4, 91.6, 121.6, 125.7, 126.8, 127.3, 127.4, 128.8, 137.0, 142.3, 153.6, 156.3, 162.0, 170.1.

HRMS (*m*/*z*): MNa^+ calcd for $C_{36}H_{32}F_3N_3O_4S$ 682.1958; found, 682.1966.

4.1.2.12. ***3l*** *4-(Benzofuran-2-yl)-N-((6-oxo-6-((trityloxy)amino)-hexyl)oxy)thiazole-2-carboxamide.* Synthesis according to general procedure B using **2l** (547 mg, 2.0 mmol) afforded **3l** after recrystallization in dichlorormethane/ethyl acetate as a light brown solid (408 mg, 0.7 mmol, 32%). mp 200.7 °C, t_r 18.46 min purity: 97.9%.

^{1}H NMR (300 MHz, DMSO-d_6): δ 1.03−1.19 (m, 2H), 1.14−1.34 (m, 3H), 1.42−1.56 (m, 2H), 1.74−1.87 (m, 2H), 3.85 (t, *J* = 6.6 Hz, 2H), 7.20−7.43 (m, 18H), 7.63−7.69 (m, 1H), 7.74 (dd, *J* = 7.3, 1.4 Hz, 1H), 8.42 (s, 1H), 10.19 (s, 1H), 12.24 (s, 1H).

^{13}C NMR (75 MHz, DMSO-d_6): δ 24.5, 24.7, 27.3, 31.9, 75.5, 91.7, 104.0, 111.2, 121.2, 121.8, 123.5, 125.3, 127.4, 127.5, 128.1, 129.0, 142.5, 146.5, 150.5, 154.3, 156.3, 163.1, 170.2.

HRMS (*m*/*z*): MH^+ calcd for $C_{37}H_{33}N_3O_5S$ 532.2214; found, 632.2211.

4.1.2.13. ***3m*** *N-((6-Oxo-6-((trityloxy)amino)hexyl)oxy)-4-(4-(pyrrolidin-1-yl)phenyl)thiazole-2-carboxamide.* Synthesis according to general procedure B using **2m** (907 mg, 3.0 mmol) afforded **3m**, after flash chromatography with dichloromethane/30% methanol in dichloromethane as a eluent, as a yellow solid (487 mg, 0.7 mmol, 25%). mp 192.1 °C, t_r 20.03 min purity: 95.3%.

^{1}H NMR (300 MHz, DMSO-d_6): δ 1.05−1.17 (m, 2H), 1.18−1.30 (m, 2H), 1.43−1.53 (m, 2H), 1.79 (d, *J* = 7.2 Hz, 2H), 1.92−2.02 (m, 4H), 3.27 (q, *J* = 5.1 Hz, 4H), 3.84 (t, *J* = 6.6 Hz, 2H), 6.56−6.64 (m, 2H), 7.31 (q, *J* = 5.1 Hz, 15H), 7.81−7.91 (m, 2H), 8.05 (s, 1H), 10.20 (s, 1H), 12.05 (s, 1H).

^{13}C NMR (75 MHz, DMSO-d_6): δ 24.5, 24.7, 25.0, 26.3, 27.3, 31.9, 47.3, 75.5, 91.7, 111.5, 114.7, 120.7, 127.4, 127.5, 129.0, 142.5, 147.8, 156.6, 156.8, 170.2.

HRMS (*m*/*z*): MH^+ calcd for $C_{39}H_{40}N_4O_4S$ 661.2843; found, 661.2838.

4.1.2.14. General Procedure for the Preparation of the Hydroxamates ***4a−4m***. *O*-trityl-protected hydroxamate (**4a−m**) was dissolved in DCM (30 mL/mmol). Et_3SiH (10 equiv) and TFA (10 equiv) were added successively, and the reaction was left stirring for 30 min at room temperature. After that time, the reaction mixture was purified via flash chromatography using dichloromethane and 30% methanol in dichloromethane as eluents to yield hydroxamic acids **4a−m**.

4.1.2.15. ***4a*** *N-((6-(Hydroxyamino)-6-oxohexyl)oxy)-4-phenylthiazole-2-carboxamide.* Synthesis according to general procedure C using **3a** (296 mg, 0.5 mmol) afforded **4a** as a colorless wax (240 mg, 0.41 mmol, 81%). t_r 9.32 min purity: 95.1%.

^{1}H NMR (600 MHz, DMSO-d_6): δ 1.38 (qd, *J* = 9.0, 6.2 Hz, 2H), 1.55 (p, *J* = 7.5 Hz, 2H), 1.62 (p, *J* = 6.8 Hz, 2H), 1.98 (t, *J* = 7.4 Hz, 2H), 3.94 (t, *J* = 6.5 Hz, 2H), 7.40 (t, *J* = 7.3 Hz, 1H), 7.49 (t, *J* = 7.7 Hz, 2H), 8.07 (d, *J* = 7.4 Hz, 2H), 8.43 (s, 1H), 8.68 (s, 1H), 10.37 (s, 1H), 12.18 (s, 1H).

^{13}C NMR (151 MHz, DMSO-d_6): δ 25.3, 25.5, 27.8, 32.7, 76.1, 119.8, 126.8, 129.1, 129.3, 133.8, 155.9, 157.1, 162.0, 169.5.

HRMS (*m*/*z*): MH^+ calcd for $C_{16}H_{19}N_3O_4S$ 349.1096; found, 350.1170.

4.1.2.16. ***4b*** *N-((6-(Hydroxyamino)-6-oxohexyl)oxy)-4-(2-methoxyphenyl)thiazole-2-carboxamide.* Synthesis according to general procedure C using **3b** (622 mg, 1.0 mmol) afforded **4b** as a white solid (284 mg, 0.75 mmol, 75%). mp 137.4 °C, t_r 9.84 min, purity: 99.6%.

^{1}H NMR (300 MHz, DMSO-d_6): δ 1.26−1.47 (m, 2H), 1.58 (dp, *J* = 22.2, 7.0 Hz, 4H), 1.97 (t, *J* = 7.3 Hz, 2H), 3.93 (d, *J* = 4.0 Hz, 5H), 7.08 (td, *J* = 7.5, 1.1 Hz, 1H), 7.17 (dd, *J* = 8.4, 1.1 Hz, 1H), 7.39 (ddd, *J* = 8.4, 7.3, 1.8 Hz, 1H), 8.31 (dd, *J* = 7.8, 1.8 Hz, 1H), 8.35 (s, 1H), 8.67 (s, 1H), 10.35 (s, 1H), 12.14 (s, 1H).

^{13}C NMR (75 MHz, DMSO-d_6): δ 24.9, 25.0, 27.4, 32.2, 55.6, 75.6, 111.8, 120.5, 121.7, 122.6, 129.8, 129.8, 151.4, 156.6, 156.7, 159.8, 169.0.

HRMS (*m*/*z*): MH^+ calcd for $C_{17}H_{21}N_3O_5S$ 380.1275; found, 380.1272.

4.1.2.17. ***4c*** *N-((6-(Hydroxyamino)-6-oxohexyl)oxy)-4-(3-methoxyphenyl)thiazole-2-carboxamide.* Synthesis according to general procedure C using **3c** (622 mg, 1.0 mmol) afforded **4c** as a yellow wax (253 mg, 0.67 mmol, 67%). t_r 9.53 min purity 99.9%.

^{1}H NMR (300 MHz, DMSO-d_6): δ 1.38 (ddd, *J* = 12.4, 6.0, 3.2 Hz, 2H), 1.58 (dp, *J* = 22.5, 7.0 Hz, 4H), 1.97 (t, *J* = 7.3 Hz, 2H), 3.84 (s, 3H), 3.93 (t, *J* = 6.4 Hz, 2H), 6.96 (ddd, *J* = 8.3, 2.6, 1.0 Hz, 1H), 7.39 (t, *J* = 7.9 Hz, 1H), 7.57−7.72 (m, 2H), 8.46 (s, 1H), 8.67 (d, *J* = 1.8 Hz, 1H), 10.35 (s, 1H), 12.17 (s, 1H).

^{13}C NMR (75 MHz, DMSO-d_6): δ 24.9, 25.0, 27.4, 32.2, 55.3, 75.6, 111.9, 114.2, 118.6, 119.6, 129.9, 134.7, 155.3, 156.5, 159.7, 161.3, 169.0.

HRMS (*m*/*z*): MH^+ calcd for $C_{17}H_{21}N_3O_5S$ 380.1275; found, 380.1276.

4.1.2.18. ***4d*** *N-((6-(Hydroxyamino)-6-oxohexyl)oxy)-4-(4-methoxyphenyl)thiazole-2-carboxamide.* Synthesis according to general procedure C using **3d** (1.8 g, 3.0 mmol) afforded **4d** as a white solid (603 mg, 1.59 mmol, 53%). mp 151.1 °C, t_r 9.46 min purity 98.1%.

^{1}H NMR (300 MHz, DMSO-d_6): δ 1.38 (q, *J* = 8.1 Hz, 2H), 1.58 (dp, *J* = 22.1, 7.0 Hz, 4H), 1.97 (t, *J* = 7.3 Hz, 2H), 3.81 (s, 3H), 3.92 (t, *J* = 6.4 Hz, 2H), 6.92−7.18 (m, 2H), 7.85−8.13 (m, 2H), 8.27 (s, 1H), 8.67 (d, *J* = 1.8 Hz, 1H), 10.35 (d, *J* = 1.9 Hz, 1H), 12.13 (s, 1H).

^{13}C NMR (75 MHz, DMSO-d_6): δ 24.9, 25.0, 27.4, 32.2, 55.2, 75.6, 114.2, 117.3, 126.2, 127.7, 155.4, 156.6, 159.6, 161.3, 169.0.

HRMS (*m*/*z*): MH^+ calcd for $C_{17}H_{21}N_3O_5S$ 380.1275; found, 380.1277.

4.1.2.19. ***4e*** *4-(2-Fluorophenyl)-N-((6-(hydroxyamino)-6-oxohexyl)oxy)thiazole-2-carboxamide.* Synthesis according to general procedure C using **3e** (610 mg, 1.0 mmol) afforded **4e** as an orange wax (221 mg, 0.6 mmol, 60%). t_r 9.93 min purity 99.2%.

^{1}H NMR (300 MHz, DMSO-d_6): δ 1.28−1.46 (m, 2H), 1.58 (dp, *J* = 22.5, 7.0 Hz, 4H), 1.97 (t, *J* = 7.3 Hz, 2H), 3.93 (t, *J* = 6.4 Hz, 2H), 7.28−7.41 (m, 2H), 7.41−7.52 (m, 1H), 8.21−8.36 (m, 2H), 8.67 (d, *J* = 1.8 Hz, 1H), 10.35 (d, *J* = 1.8 Hz, 1H), 12.21 (s, 1H).

^{13}C NMR (126 MHz, DMSO-d_6): δ 24.7, 24.9, 27.3, 32.1, 75.5, 116.1 (d, *J* = 22.0 Hz), 121.0 (d, *J* = 11.5 Hz), 123.2 (d, *J* = 13.4 Hz), 124.7 (d, *J* = 3.4 Hz), 130.0 (d, *J* = 2.8 Hz), 130.3 (d, *J* = 8.7 Hz), 148.9, 156.4, 158.4, 160.4, 161.0, 168.9.

HRMS (*m*/*z*): MH^+ calcd for $C_{16}H_{18}FN_3O_4So$ 368.1075; found, 368.1067.

4.1.2.20. ***4f*** *4-(3-Fluorophenyl)-N-((6-(hydroxyamino)-6-oxohexyl)oxy)thiazole-2-carboxamide.* Synthesis according to general procedure C using **3f** (505 mg, 0.8 mmol) afforded **4f** as a colorless wax (258 mg, 0.7 mmol, 85%). t_r 9.89 min purity 95.9%.

^{1}H NMR (300 MHz, DMSO-d_6): δ 1.30−1.48 (m, 2H), 1.46−1.70 (m, 4H), 1.97 (t, *J* = 7.3 Hz, 2H), 3.93 (t, *J* = 6.5 Hz, 2H), 7.23 (td, *J* = 8.6, 2.5 Hz, 1H), 7.53 (td, *J* = 8.1, 6.1 Hz, 1H), 7.87−7.99 (m, 2H), 8.54 (s, 1H), 8.67 (s, 1H), 10.36 (s, 1H), 12.18 (s, 1H).

^{13}C NMR (75 MHz, DMSO-d_6): δ 24.9, 25.0, 27.4, 32.2, 75.6, 113.1 (d, *J* = 23.6 Hz), 115.3 (d, *J* = 20.7 Hz), 120.5, 122.3, 130.9 (d, *J* = 8.5 Hz), 135.8, 154.0, 156.4, 161.0, 161.7, 164.3, 169.0.

HRMS (*m*/*z*): MH^+ calcd for $C_{16}H_{18}FN_3O_4S$ 368.1075; found, 368.1081.

4.1.2.21. ***4g*** *4-(4-Fluorophenyl)-N-((6-(hydroxyamino)-6-oxohexyl)oxy)thiazole-2-carboxamide.* Synthesis according to general procedure C using **3g** (260 mg, 0.4 mmol) afforded **4g** as a white solid (99 mg, 0.3 mmol, 63%). mp 170.7 °C, t_r 9.65 min purity 98.5%.

^{1}H NMR (300 MHz, DMSO-d_6): δ 1.38 (q, *J* = 7.8 Hz, 2H), 1.45−1.67 (m, 4H), 1.97 (t, *J* = 7.2 Hz, 2H), 3.92 (t, *J* = 6.4 Hz, 2H), 7.26−7.39 (m, 2H), 8.03−8.16 (m, 2H), 8.41 (s, 1H), 8.68 (s, 1H), 10.36 (s, 1H), 12.17 (s, 1H).

^{13}C NMR (75 MHz, DMSO-d_6): δ 24.9, 25.0, 27.4, 32.2, 75.6, 115.7 (d, *J* = 21.6 Hz), 119.1, 128.5 (d, *J* = 8.3 Hz), 130.0 (d, *J* = 3.0 Hz), 154.4, 156.5, 160.6, 161.6, 163.9, 169.0.

https://doi.org/10.1021/acs.jmedchem.4c02024
J. Med. Chem. XXXX, XXX, XXX−XXX

HRMS (m/z): MH^+ calcd for $C_{16}H_{18}FN_3O_4S$ 368.1075; found, 368.1074.

4.1.2.22. ***4h*** *N-((6-(Hydroxyamino)-6-oxohexyl)oxy)-4-(thiophen-2-yl)thiazole-2-carboxamide.* Synthesis according to general procedure C using **3h** (598 mg, 1.0 mmol) afforded **4h** as a white solid (226 mg, 0.6 mmol, 63%). mp 123.4 °C, t_r 8.87 min purity 98.8%.

^{1}H NMR (300 MHz, DMSO-d_6): δ 1.28−1.47 (m, 2H), 1.44−1.75 (m, 4H), 1.97 (t, J = 7.3 Hz, 2H), 3.92 (t, J = 6.4 Hz, 2H), 7.15 (dd, J = 5.1, 3.6 Hz, 1H), 7.54−7.71 (m, 2H), 8.25 (s, 1H), 8.67 (s, 1H), 10.35 (s, 1H), 12.12 (s, 1H).

^{13}C NMR (75 MHz, DMSO-d_6): δ 24.9, 25.0, 27.4, 32.2, 75.5, 118.0, 125.4, 126.8, 128.1, 136.8, 150.3, 156.4, 161.8, 169.0.

HRMS (m/z): MH^+ calcd for $C_{14}H_{17}N_3O_4S_2$ 356.0733; found, 356.0735.

4.1.2.23. ***4i*** *N-((6-(Hydroxyamino)-6-oxohexyl)oxy)-4-(thiophen-3-yl)thiazole-2-carboxamide.* Synthesis according to general procedure C using **3i** (598 mg, 1.0 mmol) afforded **4i** as a white solid (198 mg, 0.6 mmol, 56%). mp 140.4 °C, t_r 8.79 min purity 98.6%.

^{1}H NMR (300 MHz, DMSO-d_6): δ 1.38 (tt, J = 11.3, 6.3 Hz, 2H), 1.58 (dp, J = 22.1, 7.0 Hz, 4H), 1.97 (t, J = 7.3 Hz, 2H), 3.92 (t, J = 6.4 Hz, 2H), 7.42−7.81 (m, 2H), 8.01 (dd, J = 2.7, 1.6 Hz, 1H), 8.25 (s, 1H), 8.67 (s, 1H), 10.35 (s, 1H), 12.12 (s, 1H).

^{13}C NMR (75 MHz, DMSO-d_6): δ 24.8, 25.0, 27.3, 32.1, 75.5, 118.7, 122.9, 126.3, 127.3, 135.7, 151.7, 156.5, 161.4, 169.0.

HRMS (m/z): MH^+ calcd for $C_{14}H_{17}N_3O_4S_2$ 356.0733; found, 356.0734.

4.1.2.24. ***4j*** *N-((6-(Hydroxyamino)-6-oxohexyl)oxy)-4-(p-tolyl)-thiazole-2-carboxamide.* Synthesis according to general procedure C using **3j** (606 mg, 1.0 mmol) afforded **4j** as a white solid (212 mg, 0.6 mmol, 58%). mp 134.3 °C, t_r 10.20 min purity 97.8%.

^{1}H NMR (600 MHz, DMSO-d_6): δ 1.37 (tt, J = 9.5, 6.2 Hz, 2H), 1.54 (p, J = 7.5 Hz, 2H), 1.61 (p, J = 6.7 Hz, 2H), 1.97 (t, J = 7.4 Hz, 2H), 2.35 (s, 3H), 3.92 (t, J = 6.5 Hz, 2H), 7.22−7.34 (m, 2H), 7.90−8.00 (m, 2H), 8.35 (s, 1H), 8.67 (s, 1H), 10.35 (s, 1H), 12.14 (s, 1H).

^{13}C NMR (151 MHz, DMSO-d_6): δ 20.9, 25.0, 25.0 (d, J = 9.3 Hz), 27.4, 32.2, 75.6, 118.5, 126.2, 129.4, 130.7, 138.0, 155.6, 156.6, 161.4, 169.0.

HRMS (m/z): MH^+ calcd for $C_{17}H_{21}N_3O_4S$ 364.1326; found, 364.1330.

4.1.2.25. ***4k*** *N-((6-(Hydroxyamino)-6-oxohexyl)oxy)-4-(4-(trifluoromethyl)phenyl)thiazole-2-carboxamide.* Synthesis according to general procedure C using **3k** (382 mg, 0.6 mmol) afforded **4k** as a light brown solid (134 mg, 0.3 mmol, 56%). mp 127.2 °C, t_r 11.278 min purity 98.5%.

^{1}H NMR (300 MHz, DMSO-d_6): δ 1.37 (qd, J = 8.7, 5.5 Hz, 2H), 1.48−1.68 (m, 4H), 1.97 (t, J = 7.3 Hz, 2H), 3.93 (t, J = 6.4 Hz, 2H), 7.86 (d, J = 8.2 Hz, 2H), 8.23−8.33 (m, 2H), 8.66 (s, 2H), 10.36 (s, 1H), 12.25 (s, 1H).

^{13}C NMR (75 MHz, DMSO-d_6): δ 24.9, 25.0, 27.4, 32.2, 75.6, 121.7, 122.4, 125.8 (d, J = 3.2 Hz), 126.0, 126.9, 127.9−129.4 (m), 137.1, 153.7, 156.4, 162.1, 169.0.

HRMS (m/z): MH^+ calcd for $C_{17}H_{18}F_3N_3O_4S$ 418.1043; found, 418.1041.

4.1.2.26. ***4l*** *4-(Benzofuran-2-yl)-N-((6-(hydroxyamino)-6-oxohexyl)oxy)thiazole-2-carboxamide.* Synthesis according to general procedure C using **3l** (316 mg, 0.5 mmol) afforded **4l** as a off-white solid (112 mg, 0.3 mmol, 58%). Yield 58%, mp 150.4 °C, t_r 10.70 min purity 99.3%.

^{1}H NMR (300 MHz, DMSO-d_6): δ 1.18−1.45 (m, 2H), 1.58 (dp, J = 22.2, 7.0 Hz, 4H), 1.97 (t, J = 7.3 Hz, 2H), 3.93 (t, J = 6.4 Hz, 2H), 7.25−7.43 (m, 3H), 7.66 (dq, J = 8.2, 0.9 Hz, 1H), 7.70−7.78 (m, 1H), 8.42 (s, 1H), 8.67 (d, J = 1.8 Hz, 1H), 10.35 (d, J = 1.8 Hz, 1H), 12.27 (s, 1H).

^{13}C NMR (75 MHz, DMSO-d_6): δ 24.9, 25.0, 27.4, 32.2, 75.6, 104.1, 111.2, 121.3, 121.8, 123.5, 125.3, 128.1, 146.5, 150.5, 154.3, 156.3, 163.1, 169.0.

HRMS (m/z): MH^+ calcd for $C_{18}H_{19}N_3O_5S$ 390.1118; found, 390.1117.

4.1.2.27. ***4m*** *N-((6-(Hydroxyamino)-6-oxohexyl)oxy)-4-(4-(pyrrolidin-1-yl)phenyl)thiazole-2-carboxamide.* Synthesis according to general procedure C using **3m** (500 mg, 0.8 mmol) afforded as **4m** a yellow solid (93 mg, 0.2 mmol, 29%). mp 136.2 °C, t_r 9.29 min purity 98.9%.

^{1}H NMR (300 MHz, DMSO-d_6): δ 1.28−1.47 (m, 2H), 1.58 (dp, J = 21.9, 6.9 Hz, 4H), 1.86−2.07 (m, 6H), 3.23−3.34 (m, 4H), 3.92 (t, J = 6.4 Hz, 2H), 6.48−6.81 (m, 2H), 7.75−8.01 (m, 2H), 8.05 (s, 1H), 8.67 (s, 1H), 10.35 (s, 1H), 12.07 (s, 1H).

^{13}C NMR (151 MHz, DMSO-d_6): δ 24.9, 25.0, 25.0, 27.4, 32.2, 47.3, 48.6, 75.5, 111.5, 114.7, 120.7, 127.4, 147.8, 156.6, 156.8, 160.8, 169.0.

HRMS (m/z): MH^+ calcd for $C_{20}H_{26}N_4O_4S$ 419.1748; found, 419.1746.

4.2. Biological Evaluation. *4.2.1. Enzyme Assay.* HDAC1, 2, 3, 4, 6, and 8 human recombinant enzymes were purchased from Reaction Biology Corp. (Malvern, PA). HDAC 11 was purchased from Sigma-Aldrich (Saint Louis, MO). The HDAC activity assay of HDAC1 (catalog no. KDA-21-365), 2 (catalog no. KDA-21-277), 3 (catalog no. KDA-22-278), 4 (catalog no. KDA-21-279), 6 (catalog no. KDA-21-213), 8 (catalog no. KDA-21-481), and 11 (catalog no. SRP0113) was performed in 96-well plates (Corning Incorporated, New York City, NY). Briefly, 20 ng of HDAC1, 2, 3, and 8, 2 ng of HDAC4, 17.5 ng of HDAC6, and 30 ng of HDAC11 per reaction were used. Recombinant enzymes were diluted in assay buffer (50 mM Tris−HCl, pH 8.0, 137 mM NaCl, 2.7 mM KCl, 1 mM MgCl2, and 1 mg/mL BSA). 80 μL of this dilution was incubated with 10 μL of different concentrations of inhibitors in assay buffer. After a 5 min incubation step, the reaction was started with 10 μL of 400 μM (HDAC1), 300 μM (HDAC2), 500 μM (HDAC3), 150 μM (HDAC6) Boc-Lys(Ac)-AMC (Bachem, Bubendorf, Switzerland) or 100 μM (HDAC4), 60 μM (HDAC8), 500 μM (HDAC11) Boc-Lys(TFA)-AMC (Bachem, Bubendorf, Switzerland). The reaction was stopped after 90 min by adding 100 μL stop solution 16 mg/mL trypsin, 8 μM vorinostat for HDAC1, 2, and 3, 8 μM panobinostat for HDAC4, 8, and 11, and 4 μM tubastatin for HDAC6 in 50 mM Tris−HCl, pH 8.0, and 100 mM NaCl. Fifteen min after the addition of the stop solution, the fluorescence intensity was measured at an excitation of 355 nm and emission of 460 nm in a NOVOstar microplate reader (BMG Lab-Tech, Ortenburg, Germany).

4.2.2. Cell Culture. All leukemic cell lines were cultured at 37 °C with 5% CO_2 in RPMI 1640 GlutaMax medium supplemented with 10−20% fetal bovine serum (FBS), depending on the recommendation of the German collection of microorganisms and cell culture (DSMZ). PDX samples were generated by (intravenously) injecting leukemia cells, isolated from patients into immune-deficient *NOD.Cg-Prkdcscid Il2rgtm1Wjl/SzJ* or NSG mice aged 8−12 weeks.[45,72] The transplanted leukemia cells were isolated from the spleen or the bone marrow of the mice. If the proportion of human cells was below 90%, a mouse cell depletion kit (Miltenyi Biotec) was used to enrich the human cells. Subsequently, leukemia cells (≥90% human) derived from the bone marrow and spleen of the mice were utilized to conduct a short-term ex vivo drug sensitivity assay. PDX cells were short-term cultured in RPMI 1640 GlutaMax with 15% FBS, 0.1 mM 2- Mercaptoethanol, 1 mM Sodium Pyruvate, and Gentamicin 0.5 μg/mL. All animal experiments were conducted in accordance with the regulatory guidelines of the official committee at LANUV (Akt. 81-02.04.2017.A441), under the authorization of the animal research institute (ZETT) at the Heinrich Heine University Düsseldorf. Patient samples were received after obtaining informed consent in accordance with the Declaration of Helsinki. The experiments were approved by the ethics committee of the medical faculty of the Heinrich Heine University (Study no.: 2019-566).

4.2.3. High Throughput Drug Screening. All compounds were used in 10 mM stock solutions and dissolved in DMSO.[45] Drug screening plates were preprinted with the Tecan D300e in 384 or

https://doi.org/10.1021/acs.jmedchem.4c02024
J. Med. Chem. XXXX, XXX, XXX−XXX

1536 well plates. To avoid plate effects, all plates were randomized, and all wells were further on normalized to the highest DMSO volume on the plate. Plates were stored at −80 °C and thawed 1 h prior to the experiment. Cells concentration and viability was determined via the Vi-CELL BLU cell counter. Only if cells exceeded 90% viability they were deemed acceptable for seeding. Cell lines were seeded at a concentration of 0.04×10^6 cells/mL in 384 well plates or at 0.5×10^6 cells/mL in 1536 well plates, while PDX samples were seeded in 1536 well plates at 1.5×10^6 cells/mL via the Multidrop reagent dispenser. The seeded plates were incubated for 72 h and subsequently evaluated via CellTiter-Glo. A Tecan Spark microplate reader was used to measure the emerging luminescence.

Initial IC_{50} determination of all experimental compounds was done in 11 concentrations (from 0.005 to 25 μM) three times with the three cell lines, K562 (CML), HL60 (AML), and HPBALL (T-ALL). The viability was determined in relation to the DMSO controls, and IC_{50} was calculated via Prism (log(inhibitor) vs normalized response − Variable slope). Screening with commercially available inhibitors was done in 6 concentration from 0.005−25 μM. Viability and inhibition curves were determined in the same way. DSS was calculated via the R package *DSS*. The dDSS was calculated by subtracting the DSS value of five healthy controls from the leukemia value. Significance was calculated by comparing all dDSS values of two drugs in a one-way Anova test. Heatmaps were generated via the complex heatmap package.

4.2.4. Synergy Drug Screening. Drug synergy was investigated by a matrix screening approach. Plates were designed by combining each concentration of drug A with each concentration of drug B. All drugs were printed in 8 concentrations on 384 well plates. (**4d**: 0.025−0.75 μM, **4m**: 0.005−0.35 μM, decitabine and clofarabine 0.005−5 μM). HL60 were seeded with a concentration of 0.1×10^6 cells/ml and afterward processed by the previously described protocol.[26] After the viability calculation, ZIP scores were generated through the "SynergyFinder" package.

4.2.5. Immunoblotting. Leukemia cells were treated with the indicated concentrations for 24 h. Afterward, the cells were collected and washed three times with cold PBS and, in the end, snap frozen with liquid nitrogen. Cells were lysed in Pierce RIPA buffer (with cOmplete Protease Inhibitor cocktail, PhosSTOP & Dithiothreitol), and DNA was removed via high speed centrifugation. The protein concentration was determined via the BCA assay. Protein lysates were diluted via 5× laemmli buffer and denatured at 95 °C for 5 min. Into every pocket of a 10% acryl amid gel, a volume with 20 μg of protein was added. SDS-Page were run for 90 min at 100 mV in 1× running buffer. The proteins were transferred with 1× transfer buffer with 10% methanol onto nitrocellulose membranes at 100 mV for 90 min.

The membranes were blocked with 3% BSA in Tris buffered saline with Tween for 1 h. The membranes were incubated overnight at 4 °C with primary antibodies, including antiacetyl-α-tubulin (catalog no. 5335), antiacetyl-histone H3 (catalog no. 9677S), anticleaved PARP (catalog no. 9541), and anti-GAPDH (catalog no. 97166), following the manufacturer's guidelines (Cell Signaling Technology). Signals were quantified via ImageJ and divided by the signal of the housekeeper.

4.2.6. Caspase 3/7 and Trypan Blue Assay. At a concentration of 0.25 μM, either **4d** or **4m** was introduced to wells containing HL60 leukemia cells. Additionally, compounds were coadministered with a caspase inhibitor Q-VD at a concentration of 10 μM in separate wells. Control conditions encompassed wells treated solely with DMSO or exclusively with Q-VD. Each experimental condition was executed in quadruplicate. Following a 24 or 48 h incubation period, the cells underwent treatment with a Caspase 3/7 Kit (Promega), and luminescence was quantified using the Tecan Spark microplate reader. In parallel, the identical cell solutions was dispensed into 24-well plates, and cell enumeration was conducted employing the Vi-CELL BLU (Beckman Coulter) cell counter after 24 or 48 h.

4.2.7. Cell Cycle Analysis. HL60 cells were plated in a concentration of 0.1×10^6 cells/ml in 12 well plates with a volume of 1.5 mL. Both **4d** and **4m** were added to the cultures at 0.15 or 0.20 μM. After 24 h of incubation, the cells were centrifuged and incubated with 0.2 mL Nicoletti assay buffer (0.1% trisodium citrate dehydrate, 0.1% Triton X-100, 50 μg/mL propidium iodide, 0.5 mg/mL RNase A). The solution was incubated 15 min at 4 °C and afterward measured via CytoFLEX (Beckman Coulter).

4.3. Molecular Modeling Studies. *4.3.1. Molecular Docking.* The cryo-EM structures of HDAC2 (PDB-ID: 7KBG),[42] HDAC4 (PDB-ID: 2VQM),[73] and HDAC8 (PDB-ID: 1T69)[74] were prepared for molecular docking using the Protein Preparation Wizard as implemented in the Maestro GUI of the Schrödinger Suite version 2024-1. Protonation states for Asp, Glu, His, and Lys, tautomers for His, and chi flips for Asp, Glu, and His were calculated at pH 7.0 ± 2.0 using the PROPKA[75] implementation within Maestro. A restrained energy minimization was performed focusing only on hydrogen atoms. Three-dimensional structures of the ligands **4a**−**4m** and vorinostat were generated and prepared using the LigPrep module in Maestro. Docking studies were performed with Glide (Schrödinger Release 2024-1) using the Glide XP docking protocol,[40] generating 75 poses for each ligand.

4.3.2. Effective Binding Energy Computations. To estimate relative affinities of compounds **4d** and **4m**, the best scoring pose of each ligand in HDAC2 was postprocessed using the MM-GBSA method in Prime with the VSGB 2.1 solvation model.[76] Side-chain flexibility of the protein was considered for all residues within 8 Å of the ligand pose.

4.4. Structure Determination. *4.4.1. Protein Preparation.* CD2 from *Dr*HDAC6 was recombinantly expressed using His_6-MBP-TEV-HDAC-pET28a(+) vector and purified as previously described with minor modifications.[77] Briefly, HDAC6 was expressed using the *Escherichia coli* strain BL21(DE3) grown in 2× yeast extract tryptone media (2YT) supplemented with 0.02 M glucose and kanamycin (50 mg/mL). Expression was induced at an optical density at 600 nm (OD_{600}) of 1.5 with 0.1 mM isopropyl-β-D-1-thiogalactopyranoside (IPTG) along with the addition of 0.2 mM zinc sulfate. Cultures were then incubated at 20 °C overnight and harvested by centrifugation.

To isolate the protein, cells were resuspended in wash buffer (50 mM K_2HPO_4/KH_2PO_4 pH 8.0, 300 mM NaCl, 5% Glycerol, 1 mM TCEP) and lysed by sonication. The crude lysate was clarified by centrifugation and then applied to a Protino Ni-NTA 5 mL column (Macherey-Nagel, Düren, Germany) using an ÄKTA Go system (Cytiva, Marlborough, Massachusetts, United States). The His_6-MBP-TEV-HDAC6 fusion protein was eluted using 150 mM imidazole. The fractions containing protein were combined, and the buffer exchanged with wash buffer. To remove the maltose binding protein and the affinity tag from the fusion protein TEV cleavage was performed. TEV cleavage was performed by adding the protease in a ratio of 1:10 in a buffer containing 1 mM DTT and 0.5 mM EDTA at 4 °C overnight. Subsequently, the solution was applied to an HisTrap Excel 5 mL column (Cytiva). Fractions were collected while washing the column with 10 mM imidazole. The volume of the combined fractions was reduced, and the solution loaded onto an HiLoad 16/600 Superdex 75 pg column (Cytiva). The column was washed with buffer (50 mM HEPES, 100 mM KCl and 5% Glycerol, pH 7.5). The purity of the target protein was monitored throughout using SDS-PAGE.

4.4.2. Crystallization. All HDAC6−inhibitor complexes were crystallized in sitting drops by the vapor diffusion method at 18 °C. For cocrystallization of the inhibitors with HDAC6, the protein solution (14.7 mg/mL in 50 mM HEPES, 100 mM KCl, and 5% Glycerol, pH 7.5) was incubated with 2 mM inhibitor. Then, 1 μL of the HDAC6−inhibitor complex solution was mixed with 1 μL of a reservoir solution. The structure of the HDAC6−**4d** complex was determined from a crystal obtained in 0.1 M sodium acetate, pH 8.7, 0.1 M sodium formiate, and 28% PEG3350. The structure of the HDAC6−**4m** complex was determined from a crystal obtained in 0.1 M sodium acetate, pH 8.7, 0.1 M sodium formiate, and 22%

https://doi.org/10.1021/acs.jmedchem.4c02024
J. Med. Chem. XXXX, XXX, XXX−XXX

PEG3350. Crystals were harvested after 6 weeks and flash frozen in liquid nitrogen using a 50% aqueous PEG3350 solution as the cryoprotectant.

4.4.3. Data Collection and Structure Determination. X-ray diffraction data was collected at 100 K using synchrotron radiation on beamline MASSIF-3 (ID30A-3) at the European Synchrotron Radiation Facility, Grenoble, France.[78,79] The data was processed using XDS,[80] molecular replacement, and structure refinement were performed using CCP4i2.[81] Data reduction was performed with AIMLESS,[82] and molecular replacement was performed using Phaser[83] with the coordinates of CD2 of HDAC6 from *D. rerio* in complex with trichostatin A (TSA) (PDB ID: 5WGI).[77] Model building and refinement were performed with Coot[84] and Refmac.[85] PyMOL[86] was used to prepare the figures and to calculate the root-mean-square deviation (RMSD) of the Cα atoms using the align command with the number of cycles set to 0, thus, not including outlier rejection. The atomic coordinates have been deposited with the Protein Data Bank, Research Collaboratory for Structural Bioinformatics at Rutgers University (PDB ID: 9GGH and 9GGK). Authors will release the atomic coordinates upon article publication.

4.5. In Vitro Pharmacokinetics. *4.5.1. LC−MS/MS Method.* For the determination of in vitro pharmacokinetics of **4d** and **4m**, a tailored liquid chromatography coupled with tandem mass spectrometry (LC−MS/MS) assay was developed. Chromatographic separation was performed using a Luna Pentafluorophenyl (PFP (2)) column (100.0 × 2.0 mm; 3 μm; Phenomenex Ltd., Aschaffenburg, Germany). For the mobile phase, 0.1% FA in water (v/v) and 0.1% FA in methanol (v/v, B) were applied. Gradient separation at a flow rate of 0.4 mL/min was used, involving the following steps: 0.0−1.5 min: 5% B, 1.5−2.5 min: 5%−20% B, 2.5−4.5 min: 20%−95% B, 4.5.−7.5 min: 95% B, and 7.5−8.0 min: 95%−5% B. The injection volume was set to 20 μL, and the column oven was maintained at 60 °C. A TSQ Quantum Ultra triple quadrupole mass spectrometer (Thermo Fisher Scientific, Waltham, Massachusetts) with an ESI interface was used for the mass spectrometric detection. A spray voltage of 4000 V and a capillary temperature of 300 °C were applied. The vaporizer temperature was maintained at 380 °C, the sheath gas at 50 au, aux gas pressure at 5 au and ion sweep gas at 1.0 au. Argon was utilized as the collision gas with a pressure of 1.6 mTorr. **4j** was used as the internal standard for **4d** and **4m**, while deuterated standards were used for the control compounds in the respective in vitro pharmacokinetic assays. The following multiple reaction monitoring transitions with their collision energy and tube lens voltage (TL) were monitored in the positive ion mode: **4d**: 380.23 → 175.0 mass-to-charge ratio (m/z) (CE: 40 V, TL: 96 V), **4m**: 419.19 → 229.1 m/z (CE: 26 V, TL: 100 V), 4j: 364.15 → 217.1 m/z (CE: 17 V, TL: 158 V), Carvedilol: 407.04 → 224.07 m/z (CE: 22 V, TL: 150 V), Carvedilol d5 CE: 412.28 → 229.1 m/z (CE: 23 V, TL: 116 V), Propranolol 260.0 → 155.0 m/z (CE: 24 V, TL: 86 V), Propranolol d7 267.18 → 116.12 m/z (CE: 20 V, TL: 88 V), Itraconazol 705.4 → 392.18 m/z (CE: 34 V, TL: 154 V), Itraconazol d4 709.6 → 396.23 m/z (CE: 36 V, TL: 165 V).

4.5.2. Distribution Coefficient (log D). The log D determination was based on the shake flask method optimized for mass spectrometric analysis.[87] The distribution of test compounds was investigated between buffer presaturated octanol and octanol-presaturated 0.1 M potassium phosphate buffer pH 7.4. A 10 mM solution of the test compounds in DMSO and the control carvedilol were diluted 1:100 in buffer. A 200 μL aliquot was directly taken and 1:1 diluted in acetonitrile (v/v, standard). To the residual buffer volume, octanol was added in different v/v ratios: 1:0.1, 1:0.01, 3:0.01, and 5:0.01. Samples were shaken for 1 h to reach equilibrium before the two phases were separated by centrifugation at 13.200g for 10 min. Determinations were performed in triplicate for each compound from the aqueous phase. For the calculation of log D, the buffer/octanol v/v ratio was used in which the amount of drug was most similar in order to obtain the most precise measurement. The log D was then calculated by the following eq 1:

Calculation of log D. A_{St}: area ratio standard, A_w: area ratio after partition, V_w: volume aqueous phase, and V_o: volume octanol.

$$\log D = \log\left(\left(\frac{A_{St}}{A_w} - 1\right)\frac{V_w}{V_o}\right) \quad (1)$$

4.5.3. Plasma Stability. Ex vivo plasma stability was studied in fresh human plasma at 37 °C. Plasma was prewarmed to 37 °C, and reactions were started by spiking **4d** and **4m** to the plasma to a final concentration of 1 μM, 50 nM, and 2.5 nM. Sample aliquots of 100 μL were taken at 0, 30, 60, 120, 240, and 360 min and after 24 h. Each aliquot was mixed with 300 μL ice-cold acetonitrile containing the internal standards and directly vortexed, followed by 15 min shaking at 800 rpm at room temperature. Then, samples were centrifuged for 5 min at 13.200g. 300 μL of the supernatant was evaporated to dryness under heated nitrogen stream at 50 °C. Samples were stored at 4 °C, until completion of the assay and reconstituted in 100 μL 50/50 acetontitrile/water (v/v). This customized sample preparation protocol was characterized by good recoveries of 104.7 ± 6.7% for **4d** and 104.5 ± 6.6% for **4m** and low matrix effects of less than 11% for both compounds. The assay was conducted in triplicate. As a control, the compounds were incubated in 4% BSA to identify potential enzyme-related degradation in plasma. In vitro plasma half-life ($t_{1/2}$) was calculated by $t_{1/2} = \ln 2/k_e$, where k_e is the slope in the linear fit of the natural logarithm of the fraction remaining of the parent compound vs incubation time.

4.5.4. Blood-To-Plasma Ratio. The blood-to-plasma ratio ($K_{B/P}$) was determined to investigate the drug binding to erythrocytes. Therefore, freshly drawn whole blood was spiked to a final concentration of 1 μM, 50 nM, and 2.5 nM and cautiously shaken to avoid lysis and incubated at 37 °C for 30 min. Spiked whole blood was centrifuged at room temperature for 10 min at 2,000g, and the obtained plasma was used for analysis. Additionally, plasma was directly spiked to a final concentration of 1 μM, 50 nM, and 2.5 nM and also incubated for 30 min at 37 °C (reference plasma; not considering distribution into the red blood fraction). 100 μL of reference plasma and of plasma separated from spiked whole blood were precipitated with 300 μL of ice-cold acetonitrile containing 3.33 ng/mL of the internal standards. Following immediate vortexing, samples were shaken for 15 min at 800 rpm at room temperature. Subsequently, samples were centrifuged for 5 min at 13,200g and 300 μL of the supernatant was evaporated to dryness under a heated nitrogen stream at 50 °C. The residue was reconstituted in 100 μL 50/50 acetonitrile/water (v/v). Whole blood and plasma of two donors (male and female) in three independent replicates were used for the analysis. Carvedilol was used as a control compound with known $K_{B/P}$. The hematocrit was determined volumetrically. The blood-to-plasma-ratios were calculated according to eqs 2 and 3:[88,89]

Calculation of the Red blood cell partitioning coefficient. H: hematocrit; $K_{e/p}$: red blood cell partition coefficient, pref: reference plasma; and p: plasma separated from spiked whole blood.

$$K_{e/p} = \frac{1}{H} x \left(\frac{\text{Area ratio}_{\text{pRef}}}{\text{Area ratio}_{\text{p}}} - 1\right) + 1 \quad (2)$$

Calculation of the Blood-to-plasma ratio ($K_{e/p}$). H: hematocrit; $K_{e/p}$: red blood cell partition coefficient.

$$K_{b/p} = (K_{e/p} \times H) + (1 - H) \quad (3)$$

4.5.5. Plasma Protein Binding. Plasma protein binding was determined using equilibrium dialysis. A 20% ethanol regenerated dialysis membrane with a molecular weight cutoff of 6 kDa (Reichelt Chemietechnik GmbH + Co, Heidelberg, Germany) was placed into a 96-well dialysis apparatus to obtain two chambers. 150 μL of plasma spiked to a final concentration of 1 μM, 50 nM, and 2.5 nM of the test compounds and 150 μL of 0.9% saline were added to the respective sides of the 96-well dialysis plate; wells were sealed and

https://doi.org/10.1021/acs.jmedchem.4c02024
J. Med. Chem. XXXX, XXX, XXX−XXX

the plate was placed into an incubator at 37 °C to dialyze for 24 h. Following 24 h of incubation, 100 μL of plasma were removed, directly precipitated with ice-cold acetonitrile containing the internal standards, and prepared as described above. 100 μL of methanol with internal standards was added to the saline at the acceptor chamber to keep the compounds dissolved before taking the respective aliquot. Plasma protein binding was analyzed in three independent replicates and itraconazole was used as a control in each chamber to account for potential leaking of the dialysis membrane. Plasma protein binding was calculated according to eq 4, where f_b is the fraction bound, c_{te} is the total plasma drug concentration at equilibrium, c_f is the free drug concentration of the acceptor side, V_{pi} is the initial plasma volume, and V_{pe} is the equilibrium plasma volume.[90]

Calculation of drug fraction bound.

$$f_b\,[\%] = \frac{(c_{te} - c_f) \times \frac{V_{pe}}{V_{pi}}}{\left[(c_{te} - c_f) \times \frac{V_{pe}}{V_{pi}}\right] + c_f} \times 100 \tag{4}$$

To determine plasma protein binding >99% more accurately, the dilution method was applied.[91] For this purpose, a 1:10 and a 1:20 dilution of plasma in 0.9% saline was additionally used as the donor. The diluted plasma was spiked to a final concentration of 1 μM, 50 nM, and 2.5 nM of **4d** and **4m** and incubated with 0.9% saline in the acceptor chamber for 24 h at 37 °C. Sample purification was performed as for the classical approach. Calibration curves from 1:10 and 1:20 diluted plasma were used to determine the corresponding donor concentrations. Plasma protein binding was analyzed in triplicates. As a control, the plasma protein binding of itraconazole was determined. Plasma protein binding was calculated according to eqs 5, 6, and 7 where f_u is the fraction unbound and D is the dilution level of the plasma.

Calculation of diluted fraction unbound. $f_{u,d}$: free fraction from diluted plasma.

$$f_{u,d}\,[\%] = \left(1 - \frac{(c_{te} - c_f) \times \frac{V_{pe}}{V_{pi}}}{\left[(c_{te} - c_f) \times \frac{V_{pe}}{V_{pi}}\right] + c_f}\right) \times 100 \tag{5}$$

Calculation of undiluted fraction unbound. D: plasma dilution factor, f_u: fraction unbound, $f_{u,d}$: fraction unbound from diluted plasma.

$$\text{Undiluted}\, f_u = \frac{\frac{1}{D}}{\left[\left(\frac{1}{f_{u,d}}\right) - 1\right] + \frac{1}{D}} \tag{6}$$

Calculation of undiluted fraction bound.

$$\text{Undiluted}\, f_b\,[\%] = (1 - f_u) \times 100 \tag{7}$$

4.5.6. Microsomal Stability. HLMs were used to determine microsomal stability using the cosolvent method. For this purpose, 905 μL of 0.1 M potassium phosphate buffer pH 7.4 and 25 μL of 20 mg/mL pooled (from 150 donors) HLMs (Corning, New York, USA) were added and gently inverted for mixing. 10 μL of a 100 μM working solution for **4d**, **4m**, and the control compound propranolol in acetonitrile/DMSO 80/20 (v/v) was added and gently inverted for three times. 47 μL of this mix was aliquoted into three reaction tubes per time point. To start the reaction, 3 μL of a freshly prepared mix of 125 μL NADPH Regenerating System Solution A and 25 μL NADPH Regenerating System Solution B (Corning, New York, USA) was added. The tubes were incubated at 37 °C and 300 rpm, and reactions were stopped at the time points 0, 15, 30, 45, and 60 min by adding 150 μL of ice-cold acetonitrile (containing 100 ng/mL of the internal standards). Each sample was directly vortexed and placed on ice. Following, samples were centrifuged at 13,200*g* for 10 min, and the supernatant was diluted 1:10 with acetonitrile/water 50/50 (v/v). A negative control (no HLMs) and a blank (no analytes) were used as controls besides propranolol. First-order kinetics was used to calculate half-life ($t_{1/2}$) and intrinsic clearance (Cl_{int}) (eqs 8 and 9).

Calculation of half-life ($t_{1/2}$). k_e: elimination rate constant.

$$t_{1/2} = \frac{\ln 2}{k_e} \tag{8}$$

Calculation of intrinsic clearance. $t_{1/2}$: half-life.

$$Cl_{int}\,[\mu L/\text{min}\,/\text{mg protein}] = \frac{\ln(2)}{t_{1/2}} \times \frac{\text{volume of incubation}\,[\mu L]}{\text{protein amount in incubation}\,[mg]} \tag{9}$$

The elimination rate constant (k_e) was determined as the negative slope of the plotted natural logarithm of the test compound peak area ratio versus time.

To correct for nonspecific binding in the HLM incubation, plasma protein binding of **4d** and **4m** to HLMs was determined by equilibrium dialysis. The procedure was conducted as described above, replacing plasma by a 0.5 mg/mL HLM mixture (no NADPH). The unbound intrinsic clearance, which is solely influenced by the activity of metabolizing enzymes, was calculated (eq 10).

Calculation of unbound intrinsic clearance. Cl_{int}: intrinsic clearance and f_{umic}: unbound fraction microsomal incubation.

$$\text{Unbound}\, Cl_{int} = \frac{CL_{int}}{f_{u_{mic}}} \tag{10}$$

4.5.7. In Vitro–In Vivo Extrapolation of Hepatic Clearance. The in vivo hepatic clearance of **4d** and **4m** was estimated using the in vitro determined $K_{B/P}$, unbound intrinsic clearance, and plasma protein binding at 50 nM according to eq 11. A hepatic blood flow of 1500 mL/min was used for calculation, displaying the normal value in the healthy male.[92] In addition, the hepatic extraction ratio was calculated according to eq 12. Drugs with an extraction ratio <0.3 were classified as low hepatic extraction drugs, 0.3–0.7 as intermediate hepatic extraction drugs, and >0.7 as high hepatic extraction drugs.

Calculation of hepatic clearance. Cl_H: hepatic clearance, $Cl_{int,u}$: unbound intrinsic clearance, f_u: fraction unbound in plasma, $K_{B/P}$, blood-to-plasma ratio, and Q_H: hepatic blood flow.

$$Cl_H = Q_H \times \frac{\frac{f_u}{K_{B/P}} \times Cl_{int,u}}{Q_H + \frac{f_u}{K_{B/P}} \times Cl_{int,u}} \tag{11}$$

Calculation of the hepatic extraction ratio (E_H). Cl_H: hepatic clearance and Q_H: hepatic blood flow.

$$E_H = \frac{Cl_H}{Q_H} \tag{12}$$

4.5.7.1. Preclinical Pharmacokinetic Study and Assessment. The pharmacokinetics of **4d** were assessed (by Pharmacelsus GmbH) following a single intraperitoneal dose (10 mg/kg) in C57BL/6 mice. Blood samples were collected from the tail vein of C57BL/6 mice at 0.25, 0.5, 1, 2, 4, 7, and 24 h post dose. The pharmacokinetic parameters were calculated based on the concentration time profiles of three mice using a standard NCA method. The maximum concentration (C_{max}) and the time to reach C_{max} (t_{max}) were directly acquired from the concentration–time curves. The apparent elimination half-life ($t_{1/2}$) was calculated as 0.693/λz, where λz was the elimination rate constant calculated by linear regression of the terminal linear portion of the ln-concentration–time curve. The area under the plasma concentration–time curve (AUC) from time 0 to the last time point (AUC_{last}) was calculated using the linear trapezoidal rule method. The AUC from 0 to infinity (AUC_{inf}) was calculated as AUC_{last} + Ct/λz, where Ct is the

https://doi.org/10.1021/acs.jmedchem.4c02024
J. Med. Chem. XXXX, XXX, XXX−XXX

last measurable concentration. Oral clearance (CL/F) was calculated as dose/AUC_{inf}, and apparent volume of distribution (V_d/F) was obtained by dividing CL/F by λz.

4.5.7.2. Animal Experiment. The periclinal animal experiments were conducted to evaluate the therapeutic efficacy of **4d** on two in vivo leukemic mouse models encompassing cell line -derived xenograft (CDX) and mouse tumor allografts.

A CDX model was constructed by transplanting MV4-11 (DSMZ, no. ACC 102), a human AML cell line, into immunodeficient mice. MV4-11 cells were maintained in RPMI 1640 medium supplemented with 20% FBS. Luc-GFP-expressing MV4-11 cells were generated by lentiviral transduction with the luciferase reporter gene.[93] MV4-11 cells were maintained in RPMI 1640 medium supplemented with 20% FBS. MV4-11 GFP-Luc (0.5×10^6) cells were intravenously injected into 6 to 8 weeks old immunodeficient NSG mice (NOD.Cg-Prkdcscid Il2rgtm1Wjl/SzJ, Jackson laboratory). Engraftments of the leukemia cells was verified by the in vivo imaging system (IVIS Spectrum In Vivo Imaging System, PerkinElmer) 14 days after injection. The leukemia bearing mice were randomly divided to two treatment groups (4 mice/group), vehicle control (10% DMSO$^+$ 18% PEG300 + 5% TWEEN 20$^+$ 68% dH_2O), and compound **4d** (10 mg/kg). Starting from day 16, a total of 8 daily doses were administered through intraperitoneal (i.p.) injections.

A murine cell line-derived syngeneic model was constructed by transplanting C1498 (ATCC, TIB-49), an AML cell line that originated from a female C57BL/6 mouse, into immunocompetent mice.[70] C1498 cells were maintained in RPMI 1640 medium supplemented with 20% FBS. Luc-GFP-expressing C1498 cells were generated according to methods described above. C1498 GFP-Luc (0.5×10^6) cells were intravenously injected into 6 weeks old male C57BL/6J mice (Janvier). Verification of leukemic engraftments was done with IVIS imaging 5 days after tumor inoculation. The tumor-bearing mice were randomly divided into three treatment groups (4 mice/group), namely vehicle control, vorinostat (HDACi) (20 mg/kg), and compound **4d** (20 mg/kg). From day 6 to 10, daily treatments were administered i.p. for 5 consecutive days, followed by an IVIS imaging on day 11 and another successive 5 day treatment course. Body weight from each mouse was recorded every day. Treatment efficacy and tumor progression were monitored by means of IVIS and quantification of ROI values (radiance, p/s/cm^2/sr). The animal experiments were conducted in accordance with the regulatory guidelines of the official committee at LANUV, under the authorization of the animal research institute (ZETT) at the Heinrich Heine University Düsseldorf.

4.5.7.3. Flow Cytometry. In order to investigate changes in intracellular expression levels of histone 3 acetylation upon compound **4d** treatment, C1498 tumor-bearing C57B6/LJ mice were treated with vehicle or **4d** (20 mg/kg). For preparation of mice liver cells, liver tissue of vehicle or **4d** (20 mg/kg) treated mice were excised 12 h post treatment administration. The liver cells were isolated by smashing and filtering the liver tissue through a 40 μm cell strainer filter (Greiner cat. no. 542040). Erythrocyte lysis was performed by washing the cells once in ammonium chloride isotonic buffer. The liver cells acquired from both vehicle control or **4d** treated mice were harvested and fixed with fixation/permeabilization concentrate (Invitrogen cat. no. 00-5123-43) for 30 min at room temperature in the dark and were washed with permeabilization buffer (Invitrogen cat. no. 00-8333-56). Afterward, the cells were stained with Acetyl-Histone H3 (Lys9) antibody (Cell signaling, cat. no. 9649) for 3 h at room temperature in the dark. After incubation, the cells were washed again with the permeabilization buffer and stained with the 1:300 diluted Cyanine3 Donkey antirabbit IgG antibody (BioLegend, cat. no. 406402), and were then suspended in FACS buffer (PBS, 1% FCS, 5 mM EDTA) for flow cytometric analysis. Flow cytometry was performed by utilizing the Beckman Coulter CytoFLEX Cytometer, and the results were analyzed with FlowJo software.

■ ASSOCIATED CONTENT

Supporting Information

The Supporting Information is available free of charge at https://pubs.acs.org/doi/10.1021/acs.jmedchem.4c02024.

Simulated annealing omit map of **4d** and **4m** in the CD2 of *D. rerio* HDAC6 data collection and refinement statistics, comparison of the cytotoxic data of compounds **4a**−**4m** in a heatmap format effectiveness of **4d** in a MV4-11 leukemia xenograft mouse model, Western blot showing induction of ac-H3 in the C1498 cell line Histogram plot of ac-H3 intracellular staining in liver cells from C1498 tumor bearing mice, and NMR spectra and HPLC traces of synthesized compounds Raw IC_{50}, DSS, and dDSS values (PDF)

Molecular formular strings (CSV)

Atomic coordinates of HDAC2_4a_noH (PDB)

Atomic coordinates of HDAC2_4m_noH (PDB)

■ AUTHOR INFORMATION

Corresponding Authors

Sanil Bhatia − *Department of Pediatric Oncology, Hematology and Clinical Immunology, Medical Faculty, Heinrich-Heine University Düsseldorf, 40225 Düsseldorf, Germany*; orcid.org/0000-0001-6494-7744; Phone: (+49) 211 81 04896; Email: sanil.bhatia@med.uni-duesseldorf.de; Fax: (+49) 211 81 16436

Thomas Kurz − *Institute of Pharmaceutical und Medicinal Chemistry, Heinrich-Heine University Düsseldorf, 40225 Düsseldorf, Germany*; orcid.org/0000-0002-9474-4224; Phone: (+49) 211 81 14894; Email: thomas.kurz@hhu.de

Authors

Fabian Fischer − *Institute of Pharmaceutical und Medicinal Chemistry, Heinrich-Heine University Düsseldorf, 40225 Düsseldorf, Germany*

Julian Schliehe-Diecks − *Department of Pediatric Oncology, Hematology and Clinical Immunology, Medical Faculty, Heinrich-Heine University Düsseldorf, 40225 Düsseldorf, Germany*

Jia-Wey Tu − *Department of Pediatric Oncology, Hematology and Clinical Immunology, Medical Faculty, Heinrich-Heine University Düsseldorf, 40225 Düsseldorf, Germany*

Tanja Gangnus − *Individualized Pharmacotherapy, Institute of Pharmaceutical and Medicinal Chemistry, University of Münster, 48149 Münster, Germany*; orcid.org/0009-0005-7573-6631

Yu Lin Ho − *Institute of Pharmaceutical und Medicinal Chemistry, Heinrich-Heine University Düsseldorf, 40225 Düsseldorf, Germany*

Mara Hebeis − *Bioinorganic Chemistry, Friedrich-Alexander-Universität Erlangen-Nürnberg, 91058 Erlangen, Germany*

Leandro A. Alves Avelar − *Institute of Pharmaceutical und Medicinal Chemistry, Heinrich-Heine University Düsseldorf, 40225 Düsseldorf, Germany*

Katerina Scharov − *Department of Pediatric Oncology, Hematology and Clinical Immunology, Medical Faculty, Heinrich-Heine University Düsseldorf, 40225 Düsseldorf, Germany*

Titus Watrin − *Department of Pediatric Oncology, Hematology and Clinical Immunology, Medical Faculty,*

Heinrich-Heine University Düsseldorf, 40225 Düsseldorf, Germany; orcid.org/0009-0003-2665-9639

Marie Kemkes − *Department of Pediatric Oncology, Hematology and Clinical Immunology, Medical Faculty, Heinrich-Heine University Düsseldorf, 40225 Düsseldorf, Germany*

Pawel Stachura − *Department of Pediatric Oncology, Hematology and Clinical Immunology, Medical Faculty, Heinrich-Heine University Düsseldorf, 40225 Düsseldorf, Germany; Department of Molecular Medicine II, Medical Faculty, Heinrich-Heine University, 40225 Düsseldorf, Germany*

Katharina Daugs − *Department of Pediatric Oncology, Hematology and Clinical Immunology, Medical Faculty, Heinrich-Heine University Düsseldorf, 40225 Düsseldorf, Germany*

Lukas Biermann − *Institute of Pharmaceutical und Medicinal Chemistry, Heinrich-Heine University Düsseldorf, 40225 Düsseldorf, Germany*

Josefa Kremeyer − *Institute of Pharmaceutical und Medicinal Chemistry, Heinrich-Heine University Düsseldorf, 40225 Düsseldorf, Germany*

Nadine Horstick − *Institute of Pharmaceutical und Medicinal Chemistry, Heinrich-Heine University Düsseldorf, 40225 Düsseldorf, Germany*

Ingrid Span − *Bioinorganic Chemistry, Friedrich-Alexander-Universität Erlangen-Nürnberg, 91058 Erlangen, Germany;* orcid.org/0000-0002-2892-4825

Aleksandra A. Pandyra − *Department of Pediatric Oncology, Hematology and Clinical Immunology, Medical Faculty, Heinrich-Heine University Düsseldorf, 40225 Düsseldorf, Germany; Institute of Clinical Chemistry and Clinical Pharmacology, University Hospital Bonn, 53127 Bonn, Germany; German Center for Infection Research (DZIF), 53127 Bonn, Germany*

Arndt Borkhardt − *Department of Pediatric Oncology, Hematology and Clinical Immunology, Medical Faculty, Heinrich-Heine University Düsseldorf, 40225 Düsseldorf, Germany*

Holger Gohlke − *Institute of Pharmaceutical und Medicinal Chemistry, Heinrich-Heine University Düsseldorf, 40225 Düsseldorf, Germany; Institute of Bio- and Geosciences (IBG-4: Bioinformatics), Forschungszentrum Jülich, 52425 Jülich, Germany;* orcid.org/0000-0001-8613-1447

Matthias U. Kassack − *Institute of Pharmaceutical und Medicinal Chemistry, Heinrich-Heine University Düsseldorf, 40225 Düsseldorf, Germany;* orcid.org/0000-0002-9094-8481

Bjoern B. Burckhardt − *Individualized Pharmacotherapy, Institute of Pharmaceutical and Medicinal Chemistry, University of Münster, 48149 Münster, Germany;* orcid.org/0000-0002-1782-9937

Complete contact information is available at: https://pubs.acs.org/10.1021/acs.jmedchem.4c02024

Author Contributions

○F.F. and J.S.-D. contributed equally to this work. F.F. and J.S.-D. share first authorship. S.B. and T.K. contributed equally to this work as senior authors. F.F. and L.A.A.A. synthesized all intermediates and target compounds. J.K. contributed to the characterization of all intermediates and target compounds. M.H. and I.S. performed X-ray crystallography. J.S.-D., J.-W.T., K.S., M.K., P.S., A.A.P., and T.W. performed the biological evaluation. L.B. and N.H. provided the HDAC enzyme data. T.G. and B.B.B. performed the bioanalytical determination and evaluation of in vitro and in vivo pharmacokinetics. Y.L.H. performed molecular modeling, Y.L.H. and H.G. analyzed the results. A.B., H.G., M.U.K., B.B.B., S.B., and T.K. acquired funding and provided resources. F.F., J.S-D., S.B., and T.K. designed the study. The manuscript was written through the contributions of all authors. All authors have given approval to the final version.

Funding

This work was funded by the Deutsche Forschungsgemeinschaft (DFG, German Research Foundation) 270650915 (Research Training Group GRK 2158). S.B. additionally acknowledges financial support from Elterninitiative Kinderkrebsklinik e.V and Deutsche Forschungsgemeinschaft (DFG, German Research Foundation) BH 162/4-1 (528968169). A.B. acknowledges the financial support from the Katharina-Hardt Foundation, the Christiane and Claudia Hempel Foundation, and Löwenstern e.V. M.U.K. acknowledges financial support from the Deutsche Forschungsgemeinschaft (DFG, German Research Foundation) KA 1942/2-1.

Notes

The authors declare no competing financial interest.

■ ACKNOWLEDGMENTS

F.F., L.A.A.A., and T.K. thank the CeMSA@HHU (Center for Molecular and Structural Analytics @ Heinrich Heine University) for recording the mass-spectrometric and the NMR-spectroscopic data. We are grateful for computational support and infrastructure provided by the "Zentrum für Informations-und Medientechnologie" (ZIM) at the Heinrich Heine University Düsseldorf and the computing time provided by the John von Neumann Institute for Computing (NIC) to HG on the supercomputer JUWELS at the Jülich Supercomputing Centre (JSC) (user IDs: VSK33). We further thank Pharmacelsus for performing the preclinical in vivo study in mice. We acknowledge the European Synchrotron Radiation Facility (ESRF) for provision of synchrotron radiation facilities under proposal number mx2499 and we would like to thank Lindsay McGregor for assistance and support in using beamline ID30A-3 / MASSIF-3.

■ ABBREVIATIONS

AML, acute myeloid leukemia; AUC_{inf}, area under the curve from 0 to infinity; AUC_{last}, area under the curve from 0 to the time of the last quantifiable concentration; BCP-ALL, B cell precursor acute lymphoblastic leukemia; BSA, bovine serum albumin; CE, collision energy; CL/F, apparent total body clearance following extravascular administration; C_{max} (ng/mL), maximum observed concentration; CML, chronic myeloid leukemia; dDSS, differential DSS; DSMZ, german collection of microorganisms and cell culture; DSS, drug sensitivity scores; ESI, electrospray ionization; FBS, fetal bovine serum; HAT, histone acetyltransferases; HBTU, *O*-(benzotrialzol-1-yl)-*N, N,N′,N′*,-tetramethyluroniumhexafluorophosphat; HDAC, histone deacetylases; HDACi, HDAC inhibitors; HLM, human liver microsomes; HRMS, high-resolution mass spectra; HSCs, hematopoietic stem cells; HTDS, high throughput drug screening; Hz, Hertz; $K_{B/P}$, blood-to-plasma ratio; mp, melting points; MRM, multiple

reaction monitoring; PDX, patient-derived xenograft; ppm, parts per million; $t_{1/2}$, Terminal elimination half-life or apparent terminal elimination half-life; T-ALL, T cell acute lymphoblastic leukemia; TBST, tris buffered saline with Tween; TFA, trifluoroacetic acid; TL, Tube lens; TLC, thin-layer chromatography; tmax (h), time to reach the maximum concentration; V_z/F, apparent volume of distribution following extravascular administration; Λz, first order terminal elimination rate constant; ZIP, zero interaction potency

■ REFERENCES

(1) Cordo', V.; van der Zwet, J. C. G.; Canté-Barrett, K.; Pieters, R.; Meijerink, J. P. P. T-Cell Acute Lymphoblastic Leukemia: A Roadmap to Targeted Therapies. *Blood cancer Discovery* **2021**, *2* (1), 19−31.

(2) Ratti, S.; Lonetti, A.; Follo, M. Y.; Paganelli, F.; Martelli, A. M.; Chiarini, F.; Evangelisti, C. B-All Complexity: Is Targeted Therapy Still a Valuable Approach for Pediatric Patients? *Cancers* **2020**, *12* (12), 3498.

(3) Rooij, J. D. E. d.; Michel Zwaan, C.; van den Heuvel-Eibrink, M. Pediatric AML: From Biology to Clinical Management. *J. Clin. Med.* **2015**, *4* (1), 127−149.

(4) Pui, C. H.; Yang, J. J.; Hunger, S. P.; Pieters, R.; Schrappe, M.; Biondi, A.; Vora, A.; Baruchel, A.; Silverman, L. B.; Schmiegelow, K.; Escherich, G.; Horibe, K.; Benoit, Y. C. M.; Izraeli, S.; Yeoh, A. E. J.; Liang, D. C.; Downing, J. R.; Evans, W. E.; Relling, M. V.; Mullighan, C. G. Childhood Acute Lymphoblastic Leukemia: Progress through Collaboration. *J. Clin. Oncol.* **2015**, *33* (27), 2938−2948.

(5) Nguyen, K.; Devidas, M.; Cheng, S. C.; La, M.; Raetz, E. A.; Carroll, W. L.; Winick, N. J.; Hunger, S. P.; Gaynon, P. S.; Loh, M. L. Factors Influencing Survival after Relapse from Acute Lymphoblastic Leukemia: A Children's Oncology Group Study. *Leukemia* **2008**, *22* (12), 2142−2150.

(6) Schmiegelow, K.; Müller, K.; Mogensen, S. S.; Mogensen, P. R.; Wolthers, B. O.; Stoltze, U. K.; Tuckuviene, R.; Frandsen, T. Non-Infectious Chemotherapy-Associated Acute Toxicities during Childhood Acute Lymphoblastic Leukemia Therapy. *F1000Res.* **2017**, *6*, 444.

(7) O'Connor, D.; Bate, J.; Wade, R.; Clack, R.; Dhir, S.; Hough, R.; Vora, A.; Goulden, N.; Samarasinghe, S. Infection-Related Mortality in Children with Acute Lymphoblastic Leukemia: An Analysis of Infectious Deaths on UKALL2003. *Blood* **2014**, *124* (7), 1056−1061.

(8) Gu, Z.; Churchman, M. L.; Roberts, K. G.; Moore, I.; Zhou, X.; Nakitandwe, J.; Hagiwara, K.; Pelletier, S.; Gingras, S.; Berns, H.; Payne-Turner, D.; Hill, A.; Iacobucci, I.; Shi, L.; Pounds, S.; Cheng, C.; Pei, D.; Qu, C.; Newman, S.; Devidas, M.; Dai, Y.; Reshmi, S. C.; Gastier-Foster, J.; Raetz, E. A.; Borowitz, M. J.; Wood, B. L.; Carroll, W. L.; Zweidler-McKay, P. A.; Rabin, K. R.; Mattano, L. A.; Maloney, K. W.; Rambaldi, A.; Spinelli, O.; Radich, J. P.; Minden, M. D.; Rowe, J. M.; Luger, S.; Litzow, M. R.; Tallman, M. S.; Racevskis, J.; Zhang, Y.; Bhatia, R.; Kohlschmidt, J.; Mrózek, K.; Bloomfield, C. D.; Stock, W.; Kornblau, S.; Kantarjian, H. M.; Konopleva, M.; Evans, W. E.; Jeha, S.; Pui, C. H.; Yang, J.; Paietta, E.; Downing, J. R.; Relling, M. V.; Zhang, J.; Loh, M. L.; Hunger, S. P.; Mullighan, C. G. PAX5-Driven Subtypes of B-Progenitor Acute Lymphoblastic Leukemia. *Nat. Genet.* **2019**, *51* (2), 296−307.

(9) Cheng, Y.; He, C.; Wang, M.; Ma, X.; Mo, F.; Yang, S.; Han, J.; Wei, X. Targeting Epigenetic Regulators for Cancer Therapy: Mechanisms and Advances in Clinical Trials. *Signal Transduction Targeted Ther.* **2019**, *4* (1), 62.

(10) Gopi, L. K.; Kidder, B. L. Integrative Pan Cancer Analysis Reveals Epigenomic Variation in Cancer Type and Cell Specific Chromatin Domains. *Nat. Commun.* **2021**, *12* (1), 1419.

(11) Timp, W.; Feinberg, A. P. Cancer as a Dysregulated Epigenome Allowing Cellular Growth Advantage at the Expense of the Host. *Nat. Rev. Cancer* **2013**, *13* (7), 497−510.

(12) Zeng, H.; Qu, J.; Jin, N.; Xu, J.; Lin, C.; Chen, Y.; Yang, X.; He, X.; Tang, S.; Lan, X.; Yang, X.; Chen, Z.; Huang, M.; Ding, J.; Geng, M. Feedback Activation of Leukemia Inhibitory Factor Receptor Limits Response to Histone Deacetylase Inhibitors in Breast Cancer. *Cancer Cell* **2016**, *30* (3), 459−473.

(13) Ceccacci, E.; Minucci, S. Inhibition of Histone Deacetylases in Cancer Therapy: Lessons from Leukaemia. *Br. J. Cancer* **2016**, *114* (6), 605−611.

(14) Bondarev, A. D.; Attwood, M. M.; Jonsson, J.; Chubarev, V. N.; Tarasov, V. V.; Schiöth, H. B. Recent Developments of HDAC Inhibitors: Emerging Indications and Novel Molecules. *Br. J. Clin. Pharmacol.* **2021**, *87* (12), 4577−4597.

(15) Shvedunova, M.; Akhtar, A. Modulation of Cellular Processes by Histone and Non-Histone Protein Acetylation. *Nat. Rev. Mol. Cell Biol.* **2022**, *23* (5), 329−349.

(16) Yang, X. J.; Seto, E. HATs and HDACs: From Structure, Function and Regulation to Novel Strategies for Therapy and Prevention. *Oncogene* **2007**, *26* (37), 5310−5318.

(17) Park, S. Y.; Kim, J. S. A Short Guide to Histone Deacetylases Including Recent Progress on Class II Enzymes. *Exp. Mol. Med.* **2020**, *52* (2), 204−212.

(18) Ho, T. C. S.; Chan, A. H. Y.; Ganesan, A. Thirty Years of HDAC Inhibitors: 2020 Insight and Hindsight. *J. Med. Chem.* **2020**, *63*, 12460−12484.

(19) Liu, P.; Xiao, J.; Wang, Y.; Song, X.; Huang, L.; Ren, Z.; Kitazato, K.; Wang, Y. Posttranslational Modification and beyond: Interplay between Histone Deacetylase 6 and Heat-Shock Protein 90. *Mol. Med.* **2021**, *27* (1), 110.

(20) Kerr, E.; Holohan, C.; McLaughlin, K. M.; Majkut, J.; Dolan, S.; Redmond, K.; Riley, J.; McLaughlin, K.; Stasik, I.; Crudden, M.; Van Schaeybroeck, S.; Fenning, C.; O'Connor, R.; Kiely, P.; Sgobba, M.; Haigh, D.; Johnston, P. G.; Longley, D. B. Identification of an Acetylation-Dependant Ku70/FLIP Complex That Regulates FLIP Expression and HDAC Inhibitor-Induced Apoptosis. *Cell Death Differ.* **2012**, *19* (8), 1317−1327.

(21) Zhou, M.; Yuan, M.; Zhang, M.; Lei, C.; Aras, O.; Zhang, X.; An, F. Combining Histone Deacetylase Inhibitors (HDACis) with Other Therapies for Cancer Therapy. *Eur. J. Med. Chem.* **2021**, *226*, 113825.

(22) Diyabalanage, H. V. K.; Granda, M. L.; Hooker, J. M. Combination Therapy: Histone Deacetylase Inhibitors and Platinum-Based Chemotherapeutics for Cancer. *Cancer Lett.* **2013**, *329* (1), 1−8.

(23) Stenzel, K.; Hamacher, A.; Hansen, F. K.; Gertzen, C. G. W.; Senger, J.; Marquardt, V.; Marek, L.; Marek, M.; Romier, C.; Remke, M.; Jung, M.; Gohlke, H.; Kassack, M. U.; Kurz, T. Alkoxyurea-Based Histone Deacetylase Inhibitors Increase Cisplatin Potency in Chemoresistant Cancer Cell Lines. *J. Med. Chem.* **2017**, *60* (13), 5334−5348.

(24) Reßing, N.; Schliehe-Diecks, J.; Watson, P. R.; Sönnichsen, M.; Cragin, A. D.; Schöler, A.; Yang, J.; Schäker-Hübner, L.; Borkhardt, A.; Christianson, D. W.; Bhatia, S.; Hansen, F. K. Development of Fluorinated Peptoid-Based Histone Deacetylase (HDAC) Inhibitors for Therapy-Resistant Acute Leukemia. *J. Med. Chem.* **2022**, *65* (22), 15457−15472.

(25) Laporte, A. N.; Barrott, J. J.; Yao, R. J.; Poulin, N. M.; Brodin, B. A.; Jones, K. B.; Underhill, T. M.; Nielsen, T. O. HDAC and Proteasome Inhibitors Synergize to Activate Pro-Apoptotic Factors in Synovial Sarcoma. *PLoS One* **2017**, *12* (1), No. e0169407.

(26) Avelar, L. A. A.; Schrenk, C.; Sönnichsen, M.; Hamacher, A.; Hansen, F. K.; Schliehe-Diecks, J.; Borkhardt, A.; Bhatia, S.; Kassack, M. U.; Kurz, T. Synergistic Induction of Apoptosis in Resistant Head and Neck Carcinoma and Leukemia by Alkoxyamide-Based Histone Deacetylase Inhibitors. *Eur. J. Med. Chem.* **2021**, *211*, 113095.

(27) Bhatia, S.; Krieger, V.; Groll, M.; Osko, J. D.; Reßing, N.; Ahlert, H.; Borkhardt, A.; Kurz, T.; Christianson, D. W.; Hauer, J.; Hansen, F. K. Discovery of the First-in-Class Dual Histone

https://doi.org/10.1021/acs.jmedchem.4c02024
J. Med. Chem. XXXX, XXX, XXX−XXX

Deacetylase-Proteasome Inhibitor. *J. Med. Chem.* **2018**, *61* (22), 10299−10309.

(28) Hideshima, T.; Cottini, F.; Ohguchi, H.; Jakubikova, J.; Gorgun, G.; Mimura, N.; Tai, Y. T.; Munshi, N. C.; Richardson, P. G.; Anderson, K. C. Rational Combination Treatment with Histone Deacetylase Inhibitors and Immunomodulatory Drugs in Multiple Myeloma. *Blood Cancer J.* **2015**, *5* (5), No. e312.

(29) Knox, T.; Sahakian, E.; Banik, D.; Hadley, M.; Palmer, E.; Noonepalle, S.; Kim, J.; Powers, J.; Gracia-Hernandez, M.; Oliveira, V.; Cheng, F.; Chen, J.; Barinka, C.; Pinilla-Ibarz, J.; Lee, N. H.; Kozikowski, A.; Villagra, A. Selective HDAC6 Inhibitors Improve Anti-PD-1 Immune Checkpoint Blockade Therapy by Decreasing the Anti-Inflammatory Phenotype of Macrophages and down-Regulation of Immunosuppressive Proteins in Tumor Cells. *Sci. Rep.* **2019**, *9* (1), 6136.

(30) Kozikowski, A. P.; Chen, Y.; Gaysin, A. M.; Savoy, D. N.; Billadeau, D. D.; Kim, K. H. Chemistry, Biology, and QSAR Studies of Substituted Biaryl Hydroxamates and Mercaptoacetamides as HDAC Inhibitors - Nanomolar-Potency Inhibitors of Pancreatic Cancer Cell Growth. *ChemMedChem* **2008**, *3* (3), 487−501.

(31) Curtin, M.; Glaser, K. Histone Deacetylase Inhibitors: The Abbott Experience. *Curr. Med. Chem.* **2003**, *10* (22), 2373−2392.

(32) Mo, H.; Zhang, R.; Chen, Y.; Li, S. T.; Wang, Y.; Zou, W.; Lin, Q.; Zhao, D. G.; Du, Y.; Zhang, K.; Ma, Y. Y. Synthesis and Anticancer Activity of Novel Histone Deacetylase Inhibitors That Inhibit Autophagy and Induce Apoptosis. *Eur. J. Med. Chem.* **2022**, *243* (August), 114705.

(33) Peng, X.; Li, L.; Chen, J.; Ren, Y.; Liu, J.; Yu, Z.; Cao, H.; Chen, J. Discovery of Novel Histone Deacetylase 6 (HDAC6) Inhibitors with Enhanced Antitumor Immunity of Anti-PD-L1 Immunotherapy in Melanoma. *J. Med. Chem.* **2022**, *65* (3), 2434−2457.

(34) Asfaha, Y.; Schrenk, C.; Alves Avelar, L. A.; Lange, F.; Wang, C.; Bandolik, J. J.; Hamacher, A.; Kassack, M. U.; Kurz, T. Novel Alkoxyamide-Based Histone Deacetylase Inhibitors Reverse Cisplatin Resistance in Chemoresistant Cancer Cells. *Bioorg. Med. Chem.* **2020**, *28* (1), 115108.

(35) Tran, B.; Cohen, M. S. The Discovery and Development of Binimetinib for the Treatment of Melanoma. *Expert Opin. Drug Discovery* **2020**, *15* (7), 745−754.

(36) Markham, A.; Keam, S. J. Selumetinib: First Approval. *Drugs* **2020**, *80* (9), 931−937.

(37) Lassalas, P.; Gay, B.; Lasfargeas, C.; James, M. J.; Tran, V.; Vijayendran, K. G.; Brunden, K. R.; Kozlowski, M. C.; Thomas, C. J.; Smith, A. B.; Huryn, D. M.; Ballatore, C. Structure Property Relationships of Carboxylic Acid Isosteres. *J. Med. Chem.* **2016**, *59* (7), 3183−3203.

(38) Hill, J.; Crich, D. The N,N,O-Trisubstituted Hydroxylamine Isostere and Its Influence on Lipophilicity and Related Parameters. *ACS Med. Chem. Lett.* **2022**, *13* (5), 799−806.

(39) Goodreid, J. D.; Duspara, P. A.; Bosch, C.; Batey, R. A. Amidation Reactions from the Direct Coupling of Metal Carboxylate Salts with Amines. *J. Org. Chem.* **2014**, *79* (3), 943−954.

(40) Friesner, R. A.; Murphy, R. B.; Repasky, M. P.; Frye, L. L.; Greenwood, J. R.; Halgren, T. A.; Sanschagrin, P. C.; Mainz, D. T. Extra Precision Glide: Docking and Scoring Incorporating a Model of Hydrophobic Enclosure for Protein-Ligand Complexes. *J. Med. Chem.* **2006**, *49* (21), 6177−6196.

(41) Ramírez, D.; Caballero, J. Is It Reliable to Use Common Molecular Docking Methods for Comparing the Binding Affinities of Enantiomer Pairs for Their Protein Target? *Int. J. Mol. Sci.* **2016**, *17* (4), 525.

(42) Liu, J.; Yu, Y.; Kelly, J.; Sha, D.; Alhassan, A. B.; Yu, W.; Maletic, M. M.; Duffy, J. L.; Klein, D. J.; Holloway, M. K.; Carroll, S.; Howell, B. J.; Barnard, R. J. O.; Wolkenberg, S.; Kozlowski, J. A. Discovery of Highly Selective and Potent HDAC3 Inhibitors Based on a 2-Substituted Benzamide Zinc Binding Group. *ACS Med. Chem. Lett.* **2020**, *11* (12), 2476−2483.

(43) Osko, J. D.; Christianson, D. W. Methods for the Expression, Purification, and Crystallization of Histone Deacetylase 6-Inhibitor Complexes. *Methods Enzymol.* **2019**, *626*, 447−474.

(44) Hai, Y.; Christianson, D. W. Histone Deacetylase 6 Structure and Molecular Basis of Catalysis and Inhibition. *Nat. Chem. Biol.* **2016**, *12* (9), 741−747.

(45) Oikonomou, A.; Valsecchi, L.; Quadri, M.; Watrin, T.; Scharov, K.; Procopio, S.; Tu, J. W.; Vogt, M.; Savino, A. M.; Silvestri, D.; Valsecchi, M. G.; Biondi, A.; Borkhardt, A.; Bhatia, S.; Cazzaniga, G.; Fazio, G.; Bardini, M.; Palmi, C. High-Throughput Screening as a Drug Repurposing Strategy for Poor Outcome Subgroups of Pediatric B-Cell Precursor Acute Lymphoblastic Leukemia. *Biochem. Pharmacol.* **2023**, *217* (May), 115809.

(46) Yadav, B.; Pemovska, T.; Szwajda, A.; Kulesskiy, E.; Kontro, M.; Karjalainen, R.; Majumder, M. M.; Malani, D.; Murumägi, A.; Knowles, J.; Porkka, K.; Heckman, C.; Kallioniemi, O.; Wennerberg, K.; Aittokallio, T. Quantitative Scoring of Differential Drug Sensitivity for Individually Optimized Anticancer Therapies. *Sci. Rep.* **2014**, *4*, 5193.

(47) Nalawansha, D. A.; Gomes, I. D.; Wambua, M. K.; Pflum, M. K. H. HDAC Inhibitor-Induced Mitotic Arrest Is Mediated by Eg5/KIF11 Acetylation. *Cell Chem. Biol.* **2017**, *24* (4), 481−492.e5.

(48) Stockhammer, P.; Okumus, O. ⋯; Hegedus, L.; Rittler, D.; Ploenes, T.; Herold, T.; Kalbourtzis, S.; Bankfalvi, A.; Sucker, A.; Kimmig, R.; Aigner, C.; Hegedus, B. HDAC Inhibition Induces Cell Cycle Arrest and Mesenchymal-Epithelial Transition in a Novel Pleural-Effusion Derived Uterine Carcinosarcoma Cell Line. *Pathol. Oncol. Res.* **2021**, *27* (March), 1−10.

(49) Caserta, T. M.; Smith, A. N.; Gultice, A. D.; Reedy, M. A.; Brown, T. L. Q-VD-OPh, a Broad Spectrum Caspase Inhibitor with Potent Antiapoptotic Properties. *Apoptosis* **2003**, *8* (4), 345−352.

(50) Kalac, M.; Scotto, L.; Marchi, E.; Amengual, J.; Seshan, V. E.; Bhagat, G.; Ulahannan, N.; Leshchenko, V. V.; Temkin, A. M.; Parekh, S.; Tycko, B.; O'Connor, O. A. HDAC Inhibitors and Decitabine Are Highly Synergistic and Associated with Unique Gene-Expression and Epigenetic Profiles in Models of DLBCL. *Blood* **2011**, *118* (20), 5506−5516.

(51) Blagitko-Dorfs, N.; Schlosser, P.; Greve, G.; Pfeifer, D.; Meier, R.; Baude, A.; Brocks, D.; Plass, C.; Lübbert, M. Combination Treatment of Acute Myeloid Leukemia Cells with DNMT and HDAC Inhibitors: Predominant Synergistic Gene Downregulation Associated with Gene Body Demethylation. *Leukemia* **2019**, *33* (4), 945−956.

(52) Tretbar, M.; Schliehe-Diecks, J.; von Bredow, L.; Tan, K.; Roatsch, M.; Tu, J. W.; Kemkes, M.; Sönnichsen, M.; Schöler, A.; Borkhardt, A.; Bhatia, S.; Hansen, F. K. Preferential HDAC6 Inhibitors Derived from HPOB Exhibit Synergistic Antileukemia Activity in Combination with Decitabine. *Eur. J. Med. Chem.* **2024**, *272* (April), 116447.

(53) Kirschbaum, M.; Gojo, I.; Goldberg, S. L.; Bredeson, C.; Kujawski, L. A.; Yang, A.; Marks, P.; Frankel, P.; Sun, X.; Tosolini, A.; Eid, J. E.; Lubiniecki, G. M.; Issa, J. P. A Phase 1 Clinical Trial of Vorinostat in Combination with Decitabine in Patients with Acute Myeloid Leukaemia or Myelodysplastic Syndrome. *Br. J. Hamaetol.* **2014**, *167* (2), 185−193.

(54) How, J.; Minden, M. D.; Brian, L.; Chen, E. X.; Brandwein, J.; Schuh, A. C.; Schimmer, A. D.; Gupta, V.; Webster, S.; Degelder, T.; Haines, P.; Stayner, L. A.; McGill, S.; Wang, L.; Piekarz, R.; Wong, T.; Siu, L. L.; Espinoza-Delgado, I.; Holleran, J. L.; Egorin, M. J.; Yee, K. W. L. A Phase i Trial of Two Sequence-Specific Schedules of Decitabine and Vorinostat in Patients with Acute Myeloid Leukemia. *Leuk. Lymphoma* **2015**, *56* (10), 2793−2802.

(55) Jones, P. L.; Veenstra, G. J. C.; Wade, P. A.; Vermaak, D.; Kass, S. U.; Landsberger, N.; Strouboulis, J.; Wolffe, A. P. Methylated DNA and MeCP2 Recruit Histone Deacetylase to Repress Transcription. *Nat. Genet.* **1998**, *19* (2), 187−191.

(56) Cameron, E. E.; Bachman, K. E.; Myöhänen, S.; Herman, J. G.; Baylin, S. B. Synergy of Demethylation and Histone Deacetylase

https://doi.org/10.1021/acs.jmedchem.4c02024
J. Med. Chem. XXXX, XXX, XXX−XXX

Inhibition in the Re- Expression of Genes Silenced in Cancer. *Nat. Genet.* **1999**, *21* (1), 103−107.
(57) Gkotzamanidou, M.; Terpou, E.; Kentepozidis, N.; Terpos, E. Targeting the Interplay between Hdacs and Dna Damage Repair for Myeloma Therapy. *Int. J. Mol. Sci.* **2021**, *22* (19), 10406.
(58) Di, L.; Kerns, E. H. Profiling Drug-like Properties in Discovery Research. *Curr. Opin. Chem. Biol.* **2003**, *7* (3), 402−408.
(59) Markovic, M.; Zur, M.; Fine-Shamir, N.; Haimov, E.; González-Álvarez, I.; Dahan, A. Segmental-Dependent Solubility and Permeability as Key Factors Guiding Controlled Release Drug Product Development. *Pharmaceutics* **2020**, *12* (3), 295.
(60) Gangnus, T.; Burckhardt, B. B. Low-Volume LC-MS/MS Method for the Pharmacokinetic Investigation of Carvedilol, Enalapril and Their Metabolites in Whole Blood and Plasma: Application to a Paediatric Clinical Trial. *Drug Test. Anal.* **2021**, *13* (3), 694−708.
(61) Nation, R. L.; Theuretzbacher, U.; Tsuji, B. T. Concentration-Dependent Plasma Protein Binding: Expect the Unexpected. *Eur. J. Pharm. Sci.* **2018**, *122* (May), 341−346.
(62) Schafer-Korting, M.; Korting, H. C.; Amann, F.; Peuser, R.; Lukacs, A. Influence of Albumin on Itraconazole and Ketoconazole Antifungal Activity: Results of a Dynamic in Vitro Study. *Antimicrob. Agents Chemother.* **1991**, *35* (10), 2053−2056.
(63) Konsoula, R.; Jung, M. In Vitro Plasma Stability, Permeability and Solubility of Mercaptoacetamide Histone Deacetylase Inhibitors. *Int. J. Pharm.* **2008**, *361* (1−2), 19−25.
(64) Europe, Middle East, and Africa. *Withdrawal Assessment Report Vorinostat MSD 100 Mg Hard Capsules (Vorinostat)*, 2009.
(65) 021991s000_Zolinza_ClinPharmR.Pdf.
(66) Venkatesh, P. R.; Goh, E.; Zeng, P.; New, L. S.; Xin, L.; Pasha, M. K.; Sangthongpitag, K.; Yeo, P.; Kantharaj, E. In Vitro Phase I Cytochrome P450 Metabolism, Permeability and Pharmacokinetics of SB639, a Novel Histone Deacetylase Inhibitor in Preclinical Species. *Biol. Pharm. Bull.* **2007**, *30* (5), 1021−1024.
(67) Yeo, P.; Xin, L.; Goh, E.; New, L. S.; Zeng, P.; Wu, X.; Venkatesh, P.; Kantharaj, E. Development and Validation of High-performance Liquid Chromatography-Tandem Mass Spectrometry Assay for 6-(3-benzoyl-ureido)-hexanoic Acid Hydroxyamide, a Novel HDAC Inhibitor, in Mouse Plasma for Pharmacokinetic Studies. *Biomed. Chromatogr.* **2007**, *21* (2), 184−189.
(68) Hiriyan, J.; Shivarudraiah, P.; Gavara, G.; Annamalai, P.; Natesan, S.; Sambasivam, G.; Sukumaran, S. K. Discovery of PAT-1102, a Novel, Potent and Orally Active Histone Deacetylase Inhibitor with Antitumor Activity in Cancer Mouse Models. *Anticancer Res.* **2015**, *35* (1), 229−238.
(69) Hull, E. E.; Montgomery, M. R.; Leyva, K. J. HDAC Inhibitors as Epigenetic Regulators of the Immune System: Impacts on Cancer Therapy and Inflammatory Diseases. *Biomed. Res. Int.* **2016**, *2016*, 1−15.
(70) Mopin, A.; Driss, V.; Brinster, C. A Detailed Protocol for Characterizing the Murine C1498 Cell Line and Its Associated Leukemia Mouse Model. *J. Visualized Exp.* **2016**, No. 116, 54270.
(71) Avelar, L. A. A.; Held, J.; Engel, J. A.; Sureechatchaiyan, P.; Hansen, F. K.; Hamacher, A.; Kassack, M. U.; Mordmüller, B.; Andrews, K. T.; Kurz, T. Design and Synthesis of Novel Anti-Plasmodial Histone Deacetylase Inhibitors Containing an Alkoxyamide Connecting Unit. *Arch. Pharm.* **2017**, *350* (3−4), 1600347.
(72) Vogt, M.; Dienstbier, N.; Schliehe-Diecks, J.; Scharov, K.; Tu, J. W.; Gebing, P.; Hogenkamp, J.; Bilen, B. S.; Furlan, S.; Picard, D.; Remke, M.; Yasin, L.; Bickel, D.; Kalia, M.; Iacoangeli, A.; Lenz, T.; Stühler, K.; Pandyra, A. A.; Hauer, J.; Fischer, U.; Wagener, R.; Borkhardt, A.; Bhatia, S. Co-Targeting HSP90 Alpha and CDK7 Overcomes Resistance against HSP90 Inhibitors in BCR-ABL1+ Leukemia Cells. *Cell Death Dis.* **2023**, *14* (12), 799.
(73) Bottomley, M. J.; Surdo, P. L.; Giovine, P. D.; Cirillo, A.; Scarpelli, R.; Ferrigno, F.; Jones, P.; Neddermann, P.; De Francesco, R.; Steinkühler, C.; Gallinari, P.; Carfí, A.; Carfí, A. Structural and Functional Analysis of the Human HDAC4 Catalytic Domain Reveals a Regulatory Structural Zinc-Binding Domain. *J. Biol. Chem.* **2008**, *283* (39), 26694−26704.
(74) Somoza, J. R.; Skene, R. J.; Katz, B. A.; Mol, C.; Ho, J. D.; Jennings, A. J.; Luong, C.; Arvai, A.; Buggy, J. J.; Chi, E.; Tang, J.; Sang, B. C.; Verner, E.; Wynands, R.; Leahy, E. M.; Dougan, D. R.; Snell, G.; Navre, M.; Knuth, M. W.; Swanson, R. V.; McRee, D. E.; Tari, L. W. Structural Snapshots of Human HDAC8 Provide Insights into the Class I Histone Deacetylases. *Structure* **2004**, *12* (7), 1325−1334.
(75) Olsson, M. H. M.; Søndergaard, C. R.; Rostkowski, M.; Jensen, J. H. PROPKA3: Consistent Treatment of Internal and Surface Residues in Empirical p K a Predictions. *J. Chem. Theory Comput.* **2011**, *7* (2), 525−537.
(76) Li, J.; Abel, R.; Zhu, K.; Cao, Y.; Zhao, S.; Friesner, R. A. The VSGB 2.0 Model: A next Generation Energy Model for High Resolution Protein Structure Modeling. *Proteins: Struct., Funct., Bioinf.* **2011**, *79* (10), 2794−2812.
(77) Porter, N. J.; Mahendran, A.; Breslow, R.; Christianson, D. W. Unusual Zinc-Binding Mode of HDAC6-Selective Hydroxamate Inhibitors. *Proc. Natl. Acad. Sci. U.S.A.* **2017**, *114* (51), 13459−13464.
(78) Von Stetten, D.; Carpentier, P.; Flot, D.; Beteva, A.; Caserotto, H.; Dobias, F.; Guijarro, M.; Giraud, T.; Lentini, M.; McSweeney, S.; Royant, A.; Petitdemange, S.; Sinoir, J.; Surr, J.; Svensson, O.; Theveneau, P.; Leonard, G. A.; Mueller-Dieckmann, C. ID30A-3 (MASSIF-3) - A Beamline for Macromolecular Crystallography at the ESRF with a Small Intense Beam. *J. Synchrotron Radiat.* **2020**, *27*, 844−851.
(79) Theveneau, P.; Baker, R.; Barrett, R.; Beteva, A.; Bowler, M. W.; Carpentier, P.; Caserotto, H.; Sanctis, D. d.; Dobias, F.; Flot, D.; Guijarro, M.; Giraud, T.; Lentini, M.; Leonard, G. A.; Mattenet, M.; McCarthy, A. A.; McSweeney, S. M.; Morawe, C.; Nanao, M.; Nurizzo, D.; Ohlsson, S.; Pernot, P.; Popov, A. N.; Round, A.; Royant, A.; Schmid, W.; Snigirev, A.; Surr, J.; Mueller-Dieckmann, C. The Upgrade Programme for the Structural Biology Beamlines at the European Synchrotron Radiation Facility-High Throughput Sample Evaluation and Automation. *J. Phys.: Conf. Ser.* **2013**, *425* (1), 012001.
(80) Kabsch, W. *XDS. Acta Crystallogr., Sect. D: Biol. Crystallogr.* **2010**, *66*, 125−132.
(81) Winn, M. D.; Ballard, C. C.; Cowtan, K. D.; Dodson, E. J.; Emsley, P.; Evans, P. R.; Keegan, R. M.; Krissinel, E. B.; Leslie, A. G. W.; McCoy, A.; McNicholas, S. J.; Murshudov, G. N.; Pannu, N. S.; Potterton, E. A.; Powell, H. R.; Read, R. J.; Vagin, A.; Wilson, K. S. Overview of the CCP4 Suite and Current Developments. *Acta Crystallogr., Sect. D: Biol. Crystallogr.* **2011**, *67* (4), 235−242.
(82) Evans, P. R.; Murshudov, G. N. How Good Are My Data and What Is the Resolution? *Acta Crystallogr., Sect. D: Biol. Crystallogr.* **2013**, *69* (7), 1204−1214.
(83) McCoy, A. J.; Grosse-Kunstleve, R. W.; Adams, P. D.; Winn, M. D.; Storoni, L. C.; Read, R. J. Phaser Crystallographic Software. *J. Appl. Crystallogr.* **2007**, *40* (4), 658−674.
(84) Emsley, P.; Lohkamp, B.; Scott, W. G.; Cowtan, K. Features and Development of Coot. *Acta Crystallogr., Sect. D: Biol. Crystallogr.* **2010**, *66* (4), 486−501.
(85) Murshudov, G. N.; Vagin, A. A.; Dodson, E. J. Refinement of Macromolecular Structures by the Maximum-Likelihood Method. *Acta Crystallogr., Sect. D: Biol. Crystallogr.* **1997**, *53* (3), 240−255.
(86) Schrodinger LLC. *The PyMOL Molecular Graphics System.* version 3.0, 2015.
(87) Andrés, A.; Rosés, M.; Ràfols, C.; Bosch, E.; Espinosa, S.; Segarra, V.; Huerta, J. M. Setup and Validation of Shake-Flask Procedures for the Determination of Partition Coefficients (Log D) from Low Drug Amounts. *Eur. J. Pharm. Sci.* **2015**, *76*, 181−191.
(88) Yu, S.; Li, S.; Yang, H.; Lee, F.; Wu, J. T.; Qian, M. G. A Novel Liquid Chromatography/Tandem Mass Spectrometry Based Depletion Method for Measuring Red Blood Cell Partitioning of Pharmaceutical Compounds in Drug Discovery. *Rapid Commun. Mass Spectrom.* **2005**, *19* (2), 250−254.

(89) Hinderling, P. H. Red Blood Cells: A Neglected Compartment in Pharmacokinetics and Pharmacodynamics. *Pharmacol. Rev.* **1997**, *49* (3), 279−295.

(90) Banker, M. J.; Clark, T. H.; Williams, J. A. Development and Validation of a 96-Well Equilibrium Dialysis Apparatus for Measuring Plasma Protein Binding. *J. Pharm. Sci.* **2003**, *92* (5), 967−974.

(91) Riccardi, K.; Cawley, S.; Yates, P. D.; Chang, C.; Funk, C.; Niosi, M.; Lin, J.; Di, L. Plasma Protein Binding of Challenging Compounds. *J. Pharm. Sci.* **2015**, *104* (8), 2627−2636.

(92) Rocha, F. G. *Liver Blood Flow: Physiology, Measurement, and Clinical Relevance*, 5th ed; Elsevier Inc., 2012..

(93) Bhatia, S.; Diedrich, D.; Frieg, B.; Ahlert, H.; Stein, S.; Bopp, B.; Lang, F.; Zang, T.; Kröger, T.; Ernst, T.; Kögler, G.; Krieg, A.; Lüdeke, S.; Kunkel, H.; Rodrigues Moita, A. J.; Kassack, M. U.; Marquardt, V.; Opitz, F. V.; Oldenburg, M.; Remke, M.; Babor, F.; Grez, M.; Hochhaus, A.; Borkhardt, A.; Groth, G.; Nagel-Steger, L.; Jose, J.; Kurz, T.; Gohlke, H.; Hansen, F. K.; Hauer, J. Targeting HSP90 Dimerization via the C Terminus Is Effective in Imatinib-Resistant CML and Lacks the Heat Shock Response. *Blood* **2018**, *132* (3), 307−320.

https://doi.org/10.1021/acs.jmedchem.4c02024
J. Med. Chem. XXXX, XXX, XXX−XXX